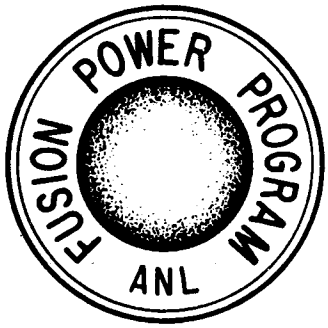
ANL/FPP-84-1
VOLUME 2
CHAPTER 6

ANL/FPP-84-1
VOLUME 2
CHAPTER 6

BLANKET COMPARISON AND SELECTION STUDY
FINAL REPORT



FUSION POWER PROGRAM

Argonne National Laboratory
9700 South Cass Avenue
Argonne, Illinois 60439

Operated by
The University of Chicago
for the U. S. Department of Energy
under Contract W-31-109-Eng-38

Argonne National Laboratory, with facilities in the states of Illinois and Idaho, is owned by the United States government, and operated by The University of Chicago under the provisions of a contract with the Department of Energy.

DISCLAIMER

This report was prepared as an account of work sponsored by an agency of the United States Government. Neither the United States Government nor any agency thereof, nor any of their employees, makes any warranty, expressed or implied, or assumes any legal liability or responsibility for the accuracy, completeness, or usefulness of any information, apparatus, product, or process disclosed, or represents that its use would not infringe privately owned rights. Reference herein to any specific commercial product, process, or service by trade name, trademark, manufacturer, or otherwise, does not necessarily constitute or imply its endorsement, recommendation, or favoring by the United States Government or any agency thereof. The views and opinions of authors expressed herein do not necessarily state or reflect those of the United States Government or any agency thereof.

Printed in the United States of America
Available from
National Technical Information Service
U. S. Department of Commerce
5285 Port Royal Road
Springfield, VA 22161

NTIS price codes
Printed copy: A28
Microfiche Copy: A01

Distribution Categories:
Magnetic Fusion Energy (UC-20)
MFE--Fusion Systems (UC-20d)

ANL/FPP-84-1

ARGONNE NATIONAL LABORATORY
9700 South Cass Avenue
Argonne, Illinois 60439

BLANKET COMPARISON AND SELECTION STUDY - FINAL REPORT

Contributors

D. L. Smith (ANL) G. D. Morgan (MDAC)

M. A. Abdou (UCLA)
C. C. Baker (ANL)
D. H. Berwald (TRW)
M. Billone (ANL)
W. D. Bjorndahl (TRW)
R. F. Bourque (GA)
D. A. Bowers (MDAC)
Y. S. Cha (ANL)
E. T. Cheng (GA)
R. Clemmer (ANL)
R. L. Creedon (GA)
C. F. Dahms (GA)
J. W. Davis (MDAC)
G. Deis (EG&G)[1]
J. DeVan (ORNL)
D. Diercks (ANL)
P. Finn (ANL)
A. Fischer (ANL)
J. Foley (ANL)[2]
K. Furuta (ANL)[3]
J. K. Garner (TRW)
Y. Gohar (ANL)
J. D. Gordon (TRW)
C. Gung (UCLA)
A. Hassanein (ANL)
S. Herring (EG&G)
G. Hollenberg (LLNL)
C. Johnson (ANL)
J. Jung (ANL)
T. Lechtenberg (GA)
J. D. Lee (LLNL)
R. Leonard (ANL)
Y. Y. Liu (ANL)
B. Loomis (ANL)
S. Majumdar (ANL)
R. C. Maninger (LLNL)
H. C. Mantz (MDAC)
R. F. Mattas (ANL)
I. Maya (GA)
T. J. McCarville (TRW)
R. Micich (Grumman)
B. Misra (ANL)
R. W. Moir (LLNL)
W. S. Neef, Jr. (LLNL)
B. Picologlou (ANL)
S. Piet (EG&G)
D. E. Ruester (MDAC)
R. Ryder (GA)
K. R. Schultz (GA)
A. E. Sherwood (LLNL)
K. Shin (UCLA)[4]
W. G. Steele (TRW)
D. K. Sze (ANL)
S.-W. Tam (ANL)
A. Tobin (Grumman)
P. Tortorelli (ORNL)
L. Turner (ANL)
D. Vasquez (GA)
S. Vogler (ANL)
E. Vold (UCLA)
L. M. Waganer (MDAC)
K. Wenzel (ANL)[5]
F. W. Wiffen (ORNL)
C. P. C. Wong (GA)
L. Yang (GA)
S. Yang (ANL)
M. Z. Youssef (UCLA)

September 1984

Study supported by
Office of Fusion Energy
U. S. Department of Energy

[1]Presently with LLNL.
[2]Graduate Student, Princeton University.
[3]University of Tokyo.
[4]Kyoto University, Japan.
[5]Graduate Student, MIT.

TABLE OF CONTENTS

Page

ACKNOWLEDGMENTS.....xix

ABSTRACT.....xxi

1. INTRODUCTION.....1-1

2. OVERVIEW AND SUMMARY

2.1 Introduction.....2-1

2.2 Design Guidelines and Evaluation Methodology.....2-6

2.2.1 Design Guideline.....2-6

2.2.2 Evaluation Methodology.....2-7

2.3 Special Issues... 2-8

2.3.1 Structural Materials.....2-9

2.3.2 Corrosion/Compatibility.....2-11

2.3.2.1 Liquid Metal Corrosion/Compatibility.....2-11

2.3.2.2 Molten Salts.....2-14

2.3.2.3 Water Corrosion.....2-16

2.3.2.4 Gaseous Corrosion/Compatibility of Vanadium Base Alloys.....2-16

2.3.3 Breeder Materials.....2-16

2.3.3.1 Solid Breeder Materials.....2-17

2.3.3.2 Liquid Breeder Materials.....2-20

2.3.4 Special Materials.....2-21

2.3.4.1 Beryllium.....2-21

2.3.4.2 Electrical Insulators.....2-22

2.3.4.3 Nitrate Salts.....2-23

2.3.5 Tritium Containment.....2-24

2.3.6 Tritium Breeding Requirements.....2-25

2.3.7 3-D Tritium Breeding Analysis.....2-26

2.3.8 Shielding Assessment.....2-29

2.3.9 Activation/Waste Management.....2-31

2.3.10 Electromagnetic Effects.....2-31

2.4 Design Concepts.....2-32

2.4.1 Self-Cooled Liquid-Metal Blanket Concepts.....2-32

2.4.1.1 Final Rankings for Self-Cooled Liquid Metal Concepts.....2-33

2.4.1.2 Reference Designs for Concepts Ranked R=1 (Tokamak and TMR).....2-33
2.4.2 Helium-Cooled Blanket Concepts.....2-37
2.4.2.1 Final Rankings for Helium-Cooled Concepts....2-37
2.4.2.2 Blanket Configuration for Reference Helium-Cooled Concepts.....2-38
2.4.3 Water-Cooled Concepts.....2-43
2.4.3.1 Final Rankings for Water-Cooled Concepts.....2-44
2.4.3.2 $LiAlO_2/H_2O$/FS/Be Concept Reference Design (Tokamak and TMR).....2-45
2.4.4 Molten-Salt-Cooled Blanket Concept.....2-45
2.4.4.1 Final Rankings for NS-Cooled Concepts.....2-47
2.4.4.2 $LiAlO_2$/NS/FS/Be Concept Reference Design (Tokamak and TMR).....2-47
2.5 Evaluation of Leading Blanket Concepts.....2-48
2.5.1 Engineering Feasibility.....2-49
2.5.1.1 Methodology for Engineering Evaluation.....2-49
2.5.1.2 Results and Conclusions of Engineering Evaluation.....2-50
2.5.2 Economic Evaluation.....2-53
2.5.3 Safety Evaluation.....2-58
2.5.4 Summary of Research and Development Concept Evaluation Results.....2-63
2.5.4.1 R&D Investment Evaluation Results.....2-63
2.5.4.2 R&D Risk Evaluation Results.....2-65
2.5.4.3 Composite R&D Evaluation Results.....2-69
2.5.5 Overall Evaluation.....2-69
2.6 Summary.....2-73
REFERENCES.....2-76

3. CONCEPT EVALUATION RESULTS
3.1 Engineering Feasibility.....3-1
3.1.1 Tritium Breeding and Inventory (I_1; 25 points).....3-2
3.1.2 Engineering Complexity and Fabrication (I_2; 25 points)..3-4
3.1.3 Maintenance and Repair (I_3; 15 points).....3-6
3.1.4 Resource Requirements (I_4; 5 points).....3-6
3.1.5 Allowable Power Variation (I_5; 10 points).....3-9
3.1.6 Capability for Increases in Power Loading, Surface Heating and Particle Flux (I_6; 10 points).....3-11

3.1.7 Startup/Shutdown (SU/SD) Requirements (I_7; 10 points)..3-14
3.1.8 Summary and Conclusions.....3-15
3.2 Economics Evaluation Results.....3-20
3.2.1 Discussion of Major Economic Factors.....3-20
3.2.2 Overall Economic Evaluation.....3-37
3.2.3 Economic Sensitivity Studies.....3-45
3.3 Safety.....3-57
3.3.1 Methodology and Results.....3-57
3.3.1.1 Accident Source Term Characterization.....3-60
3.3.1.2 Accident Fault Tolerance.....3-61
3.3.1.3 Effluent Control.....3-63
3.3.1.4 Maintenance and Waste Management.....3-64
3.3.1.5 Overall Safety Figure-of-Merit.....3-65
3.3.2 Sensitivity Cases.....3-68
3.3.2.1 "Low-Activation" Steels.....3-68
3.3.2.2 Risk-Based Safety Figure-of-Merit.....3-70
3.3.2.3 Optimistic Effluent Control.....3-70
3.3.2.4 Pessimistic Effluent Control.....3-71
3.3.2.5 Optimistic Chemical Reaction Control.....3-72
3.3.2.6 Pessimistic Chemical Reaction Control.....3-72
3.3.2.7 Impact of Deviation from 5 MW/m^2 Neutron Wall Loading.....3-73
3.3.2.8 Other Physics Confinement Concepts.....3-74
3.3.3 Discussion of Results by Blanket.....3-74
3.3.4 Conclusions.....3-77
3.4 Research and Development Concept Evaluation Results.....3-81
3.4.1 R&D Investment Evaluation Results.....3-81
3.4.2 R&D Risk Evaluation Results.....3-83
3.4.3 Composite R&D Evaluation Results.....3-93
3.5 Overall Evaluation.....3-96

4. R&D ASSESSMENT

Introduction.....4-1
4.1 Welding/Fabrication of Structural Alloys.....4-3
4.2 Embrittlement of Structural Materials by Hydrogen.....4-5
4.3 Radiation-Induced Embrittlement of the Structural Alloys.....4-7

4.5 Risk from Reactivity of Structure with Environment (Inability to Use Inert Atmosphere).....4-9
4.6 Risk from Reactivity of Coolant and Breeder with Environment (Inability to Use Inert Atmosphere.....4-9
4.7 Liquid Metal Corrosion.....4-10
4.8 MHD Effects Substantially Worse.....4-13
4.9 Insulators Not Developed for Liquid Metal Blanket.....4-13
4.10 Risk from Presence of Water in Near Blanket Components.....4-16
4.11 Difficult to Meet Seismic Requirements.....4-18
4.12 Adequacy of Tritium Breeding.....4-19
4.13 Inability to Accommodate Breeder Swelling.....4-21
4.14 Temperature Range for Tritium Release Much Less Than Predicted.....4-22
4.15 Unacceptable Temperature Predictability of Breeder (e.g., Breeder-to-Structure Gaps are Created).....4-25
4.16 Unacceptable Power Variation Capability.....4-27
4.17 Fabrication/Refabrication of Solid Breeder.....4-29
4.18 Tritium Recovery/Containment and Control.....4-30
4.19 Loss of Be Integrity.....4-32
4.20 Inability to Reprocess Be at Low Loss Rates.....4-33
4.21 Tritium Release from Be to Primary Coolant.....4-34
4.22 Excessive Chemical Reactivity of Be with Salt.....4-35
4.23 Salt Stability/Decomposition Worse Than Predicted.....4-36
4.24 Grooved First Wall.....4-37
4.25 Excessive Leakage of Coolant to Plasma Chamber.....4-39
4.26 Coolant/Breeder Cleanup after Spills.....4-40
4.27 Coolant Containment Reliability of Doulbe Wall Tubes Less Than Predicted.....4-42
4.28 Excessive Activation Products from Nitrate Salt and 17Li-83Pb.....4-43
4.29 Electromagnetic Effects.....4-45
REFERENCES.....4-46

5. EVALUATION METHODOLOGY
5.1 Design Guidelines.....5-4
References - Section 5.1.....5-17
5.2 Engineering Feasibility.....5-18
5.2.1 Tritium Breeding and Inventory.....5-19

5.2.2 Engineering Complexity and Fabrication.....5-23
5.2.3 Maintenance and Repair.....5-26
5.2.4 Resources.....5-26
5.2.5 Accommodation of Power Variations.....5-27
5.2.6 Ability to Increase Neutron Power Loading.....5-28
5.2.7 Higher Surface Heat Flux and Higher Erosion Rates.....5-29
5.2.8 Startup/Shutdown Operations.....5-30
References - Section 5.2.....5-31
5.3 Economics 5-32
5.3.1 Economic Evaluation Methodology.....5-32
5.3.2 Economic Groundrules.....5-37
5.3.3 Costing Methodology for the Blanket Tritium Processing Systems.....5-52
5.3.3.1 Basic Assumptions.....5-52
5.3.3.2 Subsystem Assumptions.....5-55
5.3.3.3 Calculated System Costs.....5-59
5.3.3.4 Conclusions for the Fuel Handling and Storage System.....5-63
5.3.4 Economic Analyses.....5-64
References - Section 5.3.....5-70
5.4 Safety.....5-71
5.4.1 Introduction.....5-71
5.4.1.1 Purpose.....5-72
5.4.1.2 Past Studies.....5-73
5.4.1.3 General Approach.....5-75
5.4.1.4 Interactions With Other Evaluation Areas.....5-82
5.4.1.5 Key Assumptions and Limitations.....5-85
5.4.2 Source Term Characterization.....5-86
5.4.2.1 General Approach.....5-87
5.4.2.2 Structure Source Term Characterization, Index 1.....5-94
5.4.2.3 Breeder/Multiplier Source Term Characterization, Index 2.....5-104
5.4.2.4 Coolant Source Term Characterization, Index 3.....5-118
5.4.2.5 Results.....5-122
5.4.3 Fault Tolerance.....5-128
5.4.3.1 General Approach.....5-128

5.4.3.2 Fault Tolerance to Breeder--Coolant Mixing, Index 4.....5-130
5.4.3.3 Fault Tolerance to Cooling Transients, Index 5.....5-137
5.4.3.4 Fault Tolerance to External Forces, Index 6.....5-150
5.4.3.5 Fault Tolerance to Near-Blanket System Interactions, Index 7.....5-155
5.4.3.6 Fault Tolerance of the Reactor Building to Blanket Transients, Index 8.....5-179
5.4.3.7 Summary.....5-187
5.4.4 Normal Radioactivity Effluents, Index 9.....5-192
5.4.4.1 Sources of Effluents.....5-192
5.4.4.2 Design Philosophy.....5-201
5.4.4.3 Evaluation Scheme.....5-202
5.4.4.4 Index 9 Results.....5-208
5.4.5 Occupational Exposure and Waste Management.....5-216
5.4.5.1 Occupational Exposure, Index 10.....5-217
5.4.5.2 Waste Management, Index 11.....5-224
5.4.5.3 Summary.....5-239
5.4.6 Results and Conclusions.....5-240
5.4.6.1 Safety Rankings and Key Sensitivities.....5-242
5.4.6.2 Discussion of Results by Material.....5-257
5.4.6.3 Discussion of Results by Blanket.....5-265
5.4.6.4 Conclusions.....5-267
References - Section 5.4.....5-273
5.5 R&D Evaluation Methodology.....5-281
5.5.1 R&D Investment Cost.....5-281
5.5.2 R&D Risk 5-283
5.5.3 R&D Evaluation Composite Rating.....5-284

6. SPECIAL ISSUES
6.1 STRUCTURAL MATERIALS.....6.1-1
6.1.1 Austenitic Stainless Steel.....6.1-1
6.1.1.1 Prime Candidate Alloy (PCA).....6.1-2
6.1.1.2 Manganese Stabilized Steels.....6.1-13
6.1.2 Ferritic Steels.....6.1-18
6.1.2.1 HT-9 Ferritic Steel.....6.1-19

6.1.2.2 Modified Ferritic Steels.....6.1-23
6.1.3 Vanadium Alloys.....6.1-27
6.1.3.1 Thermophysical Properties.....6.1-28
6.1.3.2 Nuclear Properties.....6.1-29
6.1.3.3 Welding/Fabrication of Vanadium Alloys.....6.1-29
6.1.3.4 Unirradiated Mechanical Properties V-15Cr-5Ti Alloy.....6.1-31
6.1.3.5 Radiation Effects.....6.1-35
6.1.3.6 Low Activation Considerations.....6.1-39
REFERENCES.....6.1-40

6.2 CORROSION/COMPATIBILITY.....6.2-1
6.2.1 Liquid Metal Corrosion/Compatibility.....6.2-1
6.2.1.1 Corrosion of Austenitic and Ferritic Steels.6.2-2
6.2.1.2 Corrosion of Vanadium-Base Alloys.....6.2-11
6.2.1.3 Corrosion in Li.....6.2-13
6.2.1.4 Criteria and Corrosion Limits.....6.2-17
6.2.1.5 Mechanical Property Degradation.....6.2-19
6.2.1.6 Mass Transfer Model.....6.2-22
6.2.1.7 Corrosion Inhibition in Liquid Metal Systems.....6.2-23
6.2.2 Molten Salt Corrosion.....6.2-26
6.2.2.1 Nitrate Salts.....6.2-26
6.2.2.2 FLIBE.....6.2-26
6.2.3 Water Corrosion.....6.2-27
6.2.4 Gaseous Corrosion/Compatibility.....6.2-27
REFERENCES.....6.2-29

6.3 SOLID BREEDER MATERIALS.....6.3-1
6.3.1 Fabrication.....6.3-2
6.3.1.1 Pressed and Sintered Solid Breeders.....6.3-3
6.3.1.2 Sphere-Pac Solid Breeders.....6.3-12
6.3.1.3 Fabrication/Microstructure/Impurities/ Properties/Stability/Performance.....6.3-14
6.3.2 Properties.....6.3-15
6.3.2.1 Thermodynamic/Chemical.....6.3-15
6.3.2.2 Thermophysical/Transport.....6.3-24

6.3.2.3 Mechanical....6.3-33
6.3.2.4 Compatibility/Mass Transfer....6.3-38
6.3.3 Irradiation Experiments....6.3-43
6.3.3.1 TULIP....6.3-44
6.3.3.2 FUBR-1A....6.3-57
6.3.3.3 TRIO-1....6.3-63
6.3.3.4 VOM-15H....6.3-75
6.3.3.5 Sealed Capsule Versus In-Situ Experiments..6.3-79
6.3.4 Design Guidelines....6.3-82
6.3.5 Modeling....6.3-87
6.3.5.1 Steady-state Tritium Inventory....6.3-88
6.3.5.2 Transient Tritium Release Behavior....6.3-111
6.3.5.3 Tritium Permeation/Leakage/Containment....6.3-115
6.3.5.4 Physical Integrity/Gap Conductance....6.3-127
6.3.5.5 Solid Breeder/Structure Mechanical Interaction....6.3-138
REFERENCES....6.3-145

6.4 LIQUID BREEDER MATERIALS....6.4-1
6.4.1 Lithium Properties....6.4-1
6.4.2 Lithium-Lead Properties....6.4-3
6.4.3 FLIBE Properties....6.4-12
6.4.3.1 Thermophysical Properties....6.4-12
6.4.3.2 High-Temperature Stability....6.4-14
6.4.3.3 Corrosion Properties....6.4-16
6.4.3.4 Tritium Chemistry....6.4-17
REFERENCES....6.4-19

6.5 SPECIAL MATERIALS....6.5-1
6.5.1 Neutron Mutipliers (Be Only)....6.5-1
6.5.1.1 Trace Impurities....6.5-2
6.5.1.2 Irradiation Effects....6.5-2
6.5.1.3 Fabrication and Recycling Technology....6.5-7
6.5.1.4 Design Considerations....6.5-13
6.5.2 Electrical Insulators....6.5-16
6.5.2.1 Candidate Materials....6.5-18

6.5.2.2 Fabrication Technology....6.5-18
6.5.2.3 Insulator/Liquid-Metal Compatibility....6.5-19
6.5.2.4 Irradiation Effects....6.5-20
6.5.3 Nitrate Salt....6.5-21
6.5.3.1 Thermophysical Properties....6.5-22
6.5.3.2 Thermal Stability....6.5-23
6.5.3.3 Radiation Stability....6.5-27
6.5.3.4 MHD Effects....6.5-29
6.5.3.5 Tritium Chemistry....6.5-31
6.5.3.6 Handling....6.5-31
6.5.3.7 Corrosion Properties....6.5-32
REFERENCES....6.5-36

6.6 TRITIUM CONTAINMENT....6.6-1
6.6.1 Introduction....6.6-1
6.6.2 Release of Tritium from Solid Breeders....6.6-3
6.6.2.1 Introduction....6.6-3
6.6.2.2 Results from Post-Irradiation Extraction Experiments....6.6-4
6.6.2.3 Results from In-Situ Experiments....6.6-4
6.6.2.4 Recommended Criterion from the Evaluation of Tritium Leakage....6.6-6
6.6.3 Oxidation of Tritium in a Double-Walled Heat Exchanger Tube....6.6-7
6.6.4 Tritium Permeation....6.6-14
6.6.4.1 Tritium Permeation and Inventory in First Wall....6.6-14
6.6.4.2 Tritium Permeation in HT-9....6.6-19
6.6.5 Isotopes Effect....6.6-19
6.6.6 Tritium Release Guidelines....6.6-23
6.6.7 Conclusions and Summary....6.6-23
REFERENCES....6.6-31

6.7 STRUCTURAL ANALYSIS....6.7-1
6.7.1 Load Definition....6.7-1
6.7.2 Design Criteria....6.7-2
6.7.2.1 Classification of Stresses....6.7-2

6.7.2.2 Stress Allowables.....6.7-3
6.7.2.3 Crack Growth Life.....6.7-14
6.7.3 Comparison of PCA, HT-9 and V-15Cr-5Ti as Structural Materials.....6.7-21
6.7.4 R&D Requirements for Structural Design and Analysis..6.7-29

6.8 TRITIUM BREEDING REQUIREMENTS AND UNCERTAINTIES.....6.8-1
6.8.1 Introduction.....6.8-1
6.8.2 Definition of the Problem.....6.8-1
6.8.3 Model for Required TBR.....6.8-4
6.8.4 Calculations of Required Breeding Ratio.....6.8-13
6.8.4.1 Base Case.....6.8-13
6.8.4.2 Sensitivity to Single Parameter Variation..6.8-16
6.8.4.3 Sensitivity to Variations in Two Parameters.....6.8-24
6.8.5 Uncertainties in System Definition.....6.8-33
6.8.5.1 Introduction.....6.8-33
6.8.5.2 Geometrical Description of the Standard Model.....6.8-38
6.8.5.3 Calculational Method.....6.8-39
6.8.5.4 Results of Uncertainty Analysis.....6.8-39
6.8.5.5 Variation in Blanket Material Composition..6.8-51
6.8.6 Uncertainties in Nuclear Data.....6.8-60
6.8.6.1 Introduction.....6.8-60
6.8.6.2 Theoretical Background for the Cross-Section Sensitivity/Uncertainty Analysis.....6.8-62
6.8.6.3 Blanket Concepts Considered for the Analysis and the Calculational Procedures.....6.8-64
6.8.6.4 Calculation Results.....6.8-67
6.8.6.5 Comparison of the Uncertainty Analysis Results to Results from the Non-Statistical Treatment.....6.8-93
6.8.6.6 Estimates for the Uncertainty in the Tritium Breeding Ratio for Other Blanket Concepts..6.8-97
6.8.6.7 Conclusions on Nuclear Data Uncertainty...6.8-100
REFERENCES.....6.8-102

6.9 IMPACT OF THE REACTOR DESIGN CHOICES ON THE NEUTRONICS PERFORMANCE OF THE TOKAMAK BLANKET CONCEPTS.....6.9-1
6.9.1 Computational Models.....6.9-1
6.9.2 Tritium Breeding and Energy Deposition Analyses.....6.9-7
REFERENCES.....6.9-16

6.10 MULTIDIMENSIONAL NUCLEAR ANALYSIS.....6.10-1
6.10.1 General Remarks.....6.10-1
6.10.2 Tritium Breeding and Energy Multiplication.....6.10-8
6.10.2.1 TMR Designs.....6.10-8
6.10.2.2 Tokamak Designs.....6.10-20
REFERENCES.....6.10-33

6.11 ENERGY MULTIPLICATION, FIRST WALL ATOMIC DISPLACEMENT, AND SHIELDING REQUIREMENTS FOR ALL BLANKET CONCEPTS.....6.11-1
6.11.1 Design Criteria.....6.11-1
6.11.2 Procedure and Assumptions for the Analysis.....6.11-4
6.11.3 Energy Deposition and First Wall Atomic Displacement.6.11-5
6.11.4 Shielding Requirements.....6.11-9
REFERENCES.....6.11-20

6.12 ACTIVATION/WASTE MANAGEMENT.....6.12-1
6.12.1 Introduction.....6.12-1
6.12.2 Qualitative Comparisons of Remote Maintenance Ratings.....6.12-3
6.12.3 Qualitative Comparisons of Waste Disposal Ratings....6.12-5
REFERENCES.....6.12-19

6.13 ELECTROMAGNETIC EFFECTS.....6.13-1
6.13.1 Mirror Plasma Loss.....6.13-1
6.13.2 Tokamak Plasma Disruption.....6.13-1
6.13.2.1 Pressure on First Wall.....6.13-2
6.13.2.2 Forces on Sides of Blanket Sector.....6.13-2
6.13.2.3 Loss of Plasma Diamagnetism.....6.13-3
6.13.2.4 Semi-Cylindrical First Wall Modules.....6.13-3
6.13.3 Assumptions.....6.13-3
6.13.3.1 Tokamak Fields and Time Constants.....6.13-3

6.13.3.2 Tokamak Field Solution.....6.13-4
6.13.3.3 Diamagnetism in a Tokamak Plasma.....6.13-4
6.13.3.4 Pulsed Loads on Mirror First Wall & Blanket.....6.13-5
6.13.4 Conclusions.....6.13-6

7. LIQUID METAL-COOLED BLANKET CONCEPTS
7.1 Introduction.....7-1
7.2 Summary of Final Rankings.....7-2
7.3 Key Factors.....7-5
7.3.1 MHD Analysis.....7-5
7.3.2 Thermal Hydraulics.....7-7
7.3.3 Stress Analysis.....7-8
7.3.4 Neutronics.....7-9
7.3.5 Tritium Recovery.....7-11
7.3.5.1 Tritium Recovery from 17Li-83Pb.....7-11
7.3.5.2 Tritium Recovery from Lithium.....7-11
7.4 Tokamak R=1 Concepts.....7-12
7.4.1 Mechanical Design.....7-12
7.4.2 Integral Analysis and Design Window.....7-14
7.4.3 Design Summary.....7-21
7.5 Tandem Mirror R=1 Concept.....7-25
7.6 Concepts Ranked R=2A.....7-31
7.6.1 Tokamak.....7-31
7.6.1.1 Li/Li/HT-9 Blanket.....7-32
7.6.1.2 LiPb/LiPb/V Blanket.....7-32
7.6.2 Tandem Mirror.....7-34
7.7 Concepts Ranked R=2B/3.....7-36
7.7.1 Tokamak.....7-36
7.7.1.1 Li/Li/PCA Blanket.....7-36
7.7.1.2 LiPb/LiPb/HT-9 Blanket.....7-36
7.7.1.3 LiPb/LiPb/PCA Blanket.....7-38
7.7.2 Tandem Mirror.....7-38
7.7.2.1 LiPb/LiPb/HT-9 Blanket.....7-38
7.7.2.2 LiPb/LiPb/PCA Blanket.....7-40
7.8 Analysis of Special Issues.....7-40

7.8.1 MHD Analysis....7-40
7.8.1.1 Introduction....7-40
7.8.1.2 MHD Analysis....7-42
7.8.1.3 Laminated Wall Construction with Insulators..7-46
7.8.1.4 Tokamak Reactor....7-48
7.8.1.5 Tandem Mirror....7-52
7.8.1.6 Pressure Drop Calculations....7-54
7.8.2 Thermal Hydraulic Analysis....7-56
7.8.2.1 Analyses....7-56
7.8.2.2 Results....7-58
7.8.3 Stress Analysis....7-66
7.8.3.1 Tokamak Design (Lithium Cooled Vanadium Structure)....7-66
7.8.3.2 Tandem Mirror Design....7-72
7.8.4 Nucleonic Analyses....7-82
7.8.4.1 Tritium Breeding....7-83
7.8.4.2 Blanket Energy Multiplication....7-93
7.8.4.3 Shield Energy Deposition....7-99
7.8.4.4 Tritium Breeding Benchmark Calculations for Liquid Lithium Blanket Concept....7-105
7.8.4.5 Optimum Design Range for the Liquid Metal Blanket Concepts....7-109
7.8.5 Tritium Recovery....7-111
7.8.5.1 Tritium Recovery from LiPb....7-111
7.8.5.2 Tritium Recovery from Liquid Lithium....7-121
7.8.6 Liquid-Metal-Cooled Limiter for Tokamaks....7-123
7.8.6.1 Introduction....7-123
7.8.6.2 Mechanical Design....7-124
7.8.6.3 MHD Analysis....7-127
7.8.6.4 Thermal Hydraulic Analysis....7-128
7.8.6.5 Stress Analysis....7-130
REFERENCES....7-139

8. HELIUM-COOLED BLANKET CONCEPTS
8.1 Introduction....8-1
8.2 Summary of Final Ranking....8-5
8.3 Key Factors....8-9

8.3.1 Tokamak Reactor....8-9
8.3.2 Tandem Mirror Reactor....8-11
8.3.3 Helium Flow Thermodynamics....8-13
8.3.4 Tritium Breeding....8-13
8.3.5 Tritium Control....8-14
8.4 Li_2O/Helium/HT-9 (R=1)....8-15
8.4.1 Tokamak....8-15
8.4.1.1 Blanket Configuration....8-15
8.4.1.2 Design Summary and Issues....8-17
8.4.2 Tandem Mirror Reactor....8-22
8.4.2.1 Blanket Configuration....8-22
8.4.2.2 Design Summary and Issues....8-23
8.5 Li/Helium/HT-9 (R=1)....8-27
8.5.1 Tokamak....8-28
8.5.1.1 Blanket Configuration....8-28
8.5.1.2 Design Summary and Issues....8-28
8.5.2 Tandem Mirror Reactor....8-34
8.5.2.1 Blanket Configuration....8-34
8.5.2.2 Design Summary and Issues....8-35
8.6 $LiAlO_2$/Be/Helium/HT-9 (R=1)....8-41
8.6.1 Tokamak....8-41
8.6.1.1 Blanket Configuration....8-41
8.6.1.2 Design Summary and Issues....8-43
8.6.2 Tandem Mirror Reactor....8-48
8.6.2.1 Blanket Configuration....8-48
8.6.2.2 Design Summary and Issues....8-49
8.7 FLIBE/Be/He/FS Concept (R=1)....8-54
8.7.1 Design Choices....8-54
8.7.2 Tokamak Blanket Configuration....8-57
8.7.3 Tandem Mirror Blanket Configuration....8-57
8.7.4 Design Summary and Issues....8-57
8.8 Attractive Concepts, Ranked 1B and 2A....8-61
8.8.1 R=1B Concepts....8-61
8.8.1.1 Solid Breeders....8-62
8.8.1.2 Liquid Breeders....8-63
8.8.2 R=2A Concepts....8-64

8.8.2.1 Solid Breeders....8-64
8.8.2.2 Liquid Breeders....8-65
8.8.2.3 Multiple Structural Materials....8-66
8.9 Concepts Ranked R=2B and R=3....8-67
8.9.1 Less Attractive Concepts, Ranked R=2B....8-67
8.9.1.1 R=2B Solid Breeders....8-68
8.9.1.2 R=2B Liquid Breeders....8-68
8.9.1.3 Different Inboard/Outboard Blanket....8-70
8.9.2 Concepts Ranked 3, Infeasible....8-71
8.9.2.1 R=3 Solid Breeders....8-71
8.9.2.2 R=3 Liquid Breeders....8-71
8.10 Analysis of Special Issues....8-72
8.10.1 Mechanical Design....8-72
8.10.1.1 Solid and Lithium Breeder Designs....8-72
8.10.1.2 FLIBE/He/FS/Be Concept....8-86
8.10.2 Neutronics Designs....8-90
8.10.2.1 Solid Breeder Designs....8-90
8.10.2.2 Li/He Designs....8-102
8.10.2.3 FLIBE/He/Design....8-106
8.10.3 Thermal-Hydraulics Design....8-120
8.10.3.1 Solid Breeder Designs....8-123
8.10.3.2 Li/He Designs....8-129
8.10.3.3 FLIBE/He Concept....8-134
8.10.4 Tritium Extraction and Control....8-145
8.10.4.1 Solid Breeder Designs....8-145
8.10.4.2 Li/He Designs....8-153
8.10.4.3 Tritium Permeation and Recovery for the FLIBE/He Blanket Design....8-158
8.10.4.4 Tritium Inventory/Containment Structure Corrosion in Oxidized FLIBE Environment....8-164
References - Section 8.10....8-173
8.11 Potential Design Improvements....8-174
8.11.1 Li_2O, Li and $LiAlO_2$/Be Blankets....8-174

9. WATER-COOLED BLANKET CONCEPTS
9.1 Introduction....9-1
9.2 Final Rankings for Water-Cooled Blanket Concepts....9-1

9.2.1 General Conclusions for Water-Cooled Blanket Concepts...9-3
9.2.2 Summary of Rationale for Rankings.....9-3
9.3 Key Factors for H_2O-Cooled Blanket Concepts.....9-4
9.3.1 Key Factors Generic to H_2O-Cooled Blanket Concepts.....9-5
9.3.1.1 Reliability of Coolant Tubes.....9-5
9.3.1.2 Tritium Control.....9-7
9.3.1.3 Breeder Physical Integrity.....9-8
9.3.1.4 Breeder Temperature Predictability.....9-9
9.3.1.5 Breeder Allowable Temperature Limits.....9-10
9.3.1.6 Li-6 Burnup Effects.....9-12
9.3.2 Differences for Tokamak and TMR Concepts.....9-13
9.3.2.1 Blanket Thickness.....9-13
9.3.2.2 First Wall.....9-15
9.3.2.3 Module Shape.....9-16
9.3.2.4 Manifolds.....9-17
9.4 $LiAlO_2/H_2O/FS/Be$ Concept - Tokamak (R=1).....9-18
9.4.1 Reference Blanket Design Configuration.....9-18
9.4.1.1 General Description.....9-18
9.4.1.2 First Wall.....9-22
9.4.1.3 Neutron Multiplier and Breeding Zone.....9-24
9.4.1.4 Tritium Purge.....9-24
9.4.1.5 Manifold Region.....9-27
9.4.2 Concept Evaluation Summary.....9-28
9.4.2.1 Engineering.....9-28
9.4.2.2 Economics.....9-28
9.4.2.3 Safety and Environmental.....9-29
9.4.2.4 Research and Development.....9-29
9.4.3 Design Details and Related Issues.....9-29
9.4.3.1 Mechanical and Structural Design.....9-30
9.4.3.2 Thermal-Hydraulics.....9-37
9.4.3.3 Neutronics.....9-43
9.4.3.4 Tritium Control.....9-44
9.5 $LiAlO_2/H_2O/FS/Be$ Concept - TMR (R=1).....9-46
9.5.1 Reference Blanket Design Configuration.....9-47
9.5.2 Concept Evaluation Summary.....9-47
9.5.3 Design Details and Related Issues.....9-50

9.6 Concepts Ranked R=2A - Tokamak and TMR.....9-50
9.6.1 Li_2O/H_2O/(STRUC)/Be (R=2A).....9-50
9.6.1.1 Concept Reference Design.....9-51
9.6.1.2 Key Issues.....9-51
9.7 Concepts Ranked R=2B and R=3 - Tokamak and TMR.....9-53
9.7.1 $LiPb/H_2O$/(STRUC) Concept (R=2B).....9-54
9.7.2 Li_2O/H_2O/(STRUC) Concept (R=2B).....9-55
9.7.3 Li_8ZrO_6/H_2O/(STRUC) Concept (R=2B).....9-56
9.7.4 Li_8ZrO_6/H_2O/(STRUC)/Be Concept (R=2B).....9-56
9.7.5 $LiAlO_2/H_2O$/(STRUC)/Pb Concept (R=2B).....9-57
9.7.6 $LiAlO_2/H_2O$/(STRUC)/Pb Concept (R=2B).....9-59
9.7.7 $LiAlO_2/H_2O$/(STRUC) Concept (R=3).....9-59
9.7.8 Li/H_2O/(STRUC) Concept (R=3).....9-59
9.8 Special Issues.....9-60
9.8.1 Thermal Hydraulics - Design Considerations for Solid Breeder Blankets.....9-60
9.8.1.1 Introduction.....9-60
9.8.1.2 Analytical Approach.....9-60
9.8.1.3 The Role of Thermal Conductivity.....9-62
9.8.1.4 The Role of Temperature Window.....9-64
9.8.1.5 The Role of Interfacial Contact Resistance...9-68
9.8.1.6 Sphere-Pac Concept.....9-70
9.8.1.7 Tritium Inventory.....9-72
9.8.1.8 Partial Power Operation.....9-73
9.8.1.9 Summary.....9-75
9.8.2 Thermal Hydraulics - First Wall.....9-75
9.8.2.1 Analytical Approach.....9-76
9.8.2.2 Discussion of Results.....9-77
9.8.3 Structural Analyses.....9-80
9.8.3.1 Introduction/Summary.....9-80
9.8.3.2 Applied Loads and Design Allowables.....9-81
9.8.3.3 Comparison of Flat First Wall With a Lobe-Shaped First Wall.....9-81
9.8.3.4 Thermal Stresses for TMR and Tokamak First Walls.....9-86
9.8.3.5 Electromagnetic Forces on the First Wall/Blanket Due to Plasma Disruption or Loss of Plasma.....9-87

9.8.3.6 Seismic Loads on First Wall/Blanket Module...9-88
9.8.3.7 Magnetic Loads on the Ferritic Steel Lobe-Shaped First Wall.....9-88
9.8.4 Nuclear Analysis.....9-90
9.8.4.1 Evolution of the $LiAlO_2/H_2O$/FS/Be Reference Blanket Design.....9-91
9.8.4.2 Multi-Dimensional Analysis of Water-Cooled Solid-Breeder Blanket Designs.....9-99
9.8.4.3 Nuclear Analysis of the Reference Blanket Design.....9-103
REFERENCES.....9-111

10. MOLTEN SALT COOLED BLANKET CONCEPTS
10.1 Introduction.....10-1
10.2 Evaluation of Salt-Cooled Blankets.....10-3
10.3 Major Issues.....10-5
10.4 Lithium Aluminate, Nitrate Salt, Beryllium Blanket Concepts....10-6
10.4.1 Overview.....10-6
10.4.2 Mechanical Design.....10-7
10.4.3 Neutronics.....10-14
10.4.4 Heat Transfer and Thermal Hydraulics.....10-16
10.4.5 Tritium Inventories.....10-17
10.4.6 Design Issues.....10-22
10.5 Summary.....10-24
10.6 Concepts Set Aside for Possible Future Consideration.....10-25
10.7 Concepts Judged to be Less Promising or Clearly Inferior.....10-26
10.8 Recommended Research.....10-27
10.8.1 Excessive Salt Decomposition.....10-27
10.8.2 Excessive Chemical Reactivity.....10-28
10.8.3 Excessive Activation Products from NS.....10-29
10.8.4 Tritium Control.....10-29
10.8.5 Corrosion Effects.....10-30
10.8.6 Solid Breeder Temperature Control.....10-31
10.8.7 Beryllium Reprocessing.....10-32
REFERENCES.....10-33

ACKNOWLEDGMENTS

The BCSS Project gratefully acknowledges the support of A. L. Opdenaker, Program Administrator, Reactor Systems Design Branch, OFE/DOE, and P. Stone, Chief, Reactor Systems Design Branch, OFE/DOE.

The Project would also like to thank members of the BCSS Review Committee for their interest and comments during the course of the study: R. Krakowski (Chm.) (LANL), D. Cohn (MIT), C. Flanagan (W/FEDC), R. Gold (W), C. Henning (LLNL), G. Kulcinski (U of WI), R. Little (PPPL), J. Scott (ORNL), and F. Garner (HEDL).

The Project is also indebted to the management of all participating organizations, particularly C. Baker (Director, Fusion Power Program) and J. Roberts (Associate Laboratory Director) of Argonne National Laboratory, for their support and encouragement throughout the study.

We would like to acknowledge the outstanding effort of L. Ciarlette who coordinated the typing and assembly of this report and to C. Bury for administrative support. We would also like to express our appreciation to J. Ruettiger and R. Johns of ANL for their contributions to the typing of the final manuscript and to the secretarial staffs of MDAC, GA, TRW, EG&G, LLNL, and UCLA for their contributions to the typing of the report.

ABSTRACT

The Blanket Comparison and Selection Study (BCSS) was a two-year, multi-laboratory project initiated by the U.S. Department of Energy/Office of Fusion Energy (DOE/OFE) with the primary objectives of: (1) defining a limited number of blanket concepts that should provide the focus of the blanket R&D program, and (2) identifying and prioritizing critical issues for the leading blanket concepts. The BCSS focused on the mainline approach for fusion reactor (TMR) development, viz., the D-T-Li fuel cycle, tokamak and tandem mirror reactors for electrical energy production, and a reactor parameter space that is generally considered achievable with modest extrapolations from the current data base. The STARFIRE and MARS reactor and plant designs, with a nominal first wall neutron load of 5 MW/m^2, were used as reference designs for the study.

The study focused on:

- Development of reference design guidelines, evaluation criteria, and a methodology for evaluating and ranking candidate blanket concepts.
- Compilation of the required data base and development of a uniform systems analysis for comparison.
- Development of conceptual designs for the comparative evaluation.
- Evaluation of leading concepts for engineering feasibility, economic performance, and safety.
- Identification and prioritization of R&D requirements for the leading blanket concepts.

Sixteen concepts (nine TMR and seven tokamak) which were identified as leading candidates in the early phases of the study, were evaluated in detail. The overall evaluation concluded that the following concepts should provide the focus for the blanket R&D program:

(Breeder/Coolant/Structure)

Lithium/Lithium/Vanadium Alloy

Li_2O/Helium/Ferritic Steel

LiPb Alloy/LiPb Alloy/Vanadium Alloy

Lithium/Helium/Ferritic Steel

The primary R&D issues for the Li/Li/V concept are the development of an advanced structural alloy, resolution of MHD and corrosion problems, provision for an inert atmosphere (e.g., N_2) in the reactor building, and the development of non-water cooled near-plasma components, particularly for the tokamak. The main issues for the LiPb/LiPb/V concept are similar to the Li/Li/V blanket with the addition of resolving the tritium recovery issue. Furthermore, resolution of MHD and corrosion problems will be more severe for LiPb/LiPb/V than for the Li/Li/V; on the other hand, the LiPb blanket has reduced concerns with respect to chemical reactivity with environment. The R&D issues for Li_2O/He/FS concept include resolution of the tritium recovery/containment issue, achieving adequate tritium breeding and resolving other solid breeder issues such as swelling and fabrication concerns. Major concerns for the Li/He/FS concept are related to its rather poor economic performance. Improvement of its economic performance will be somewhat concept-dependent and will be more of a systems engineering issue.

BLANKET COMPARISON AND SELECTION STUDY

C H A P T E R 6

BLANKET COMPARISON AND SELECTION STUDY

SECTION 6.1 - STRUCTURAL MATERIALS

TABLE OF CONTENTS

SECTION 6.1 -STRUCTURAL MATERIALS

SECTION	TITLE	PAGE
6.1	Structural Materials	6.1-1
6.1.1	Austenitic Stainless Steels	6.1-1
6.1.1.1	Prime Candidate Alloy (PCA)	6.1-2
6.1.1.2	Manganese Stabilized Steels	6.1-13
6.1.2	Ferritic Steels	6.1-18
6.1.2.1	HT-9 Ferritic Steel	6.1-19
6.1.2.2	Modified Ferritic Steels	6.1-23
6.1.3	Vanadium Alloys	6.1-27
6.1.3.1	Thermophysical Properties	6.1-28
6.1.3.2	Nuclear Properties	6.1-29
6.1.3.3	Welding/Fabrication	6.1-29
6.1.3.4	Unirradiated Mechanical Properties - V-15Cr-5Ti Alloy	6.1-31
6.1.3.5	Radiation Effects	6.1-35
6.1.3.6	Low Activation Considerations	6.1-39
References		6.1-40

LIST OF TABLES FOR SECTION 6.1

TABLE NO.	TITLE	PAGE
6.1-1	Selected Physical and Nuclear Properties of Three Reference Alloys	6.1-2
6.1-2	Composition of Manganese-Stabilized Stainless Steel in the Current Data Base	6.1-13
6.1-3	Summary of Data Base for Irradiation Effects in Manganese-Stabilized Austenitic Stainless Steels	6.1-16
6.1-4	Ranges of Impurities in 9-12Cr Steels (wt %)	6.1-26
6.1-5	Tensile Properties of V-15Cr-5Ti Sheet	6.1-32
6.1-6	Creep Strength of V-15Cr-5Ti Sheet	6.1-33

LIST OF FIGURES FOR SECTION 6.1

FIGURE NO.	TITLE	PAGE
6.1-1	Specific heat of reference alloys	6.1-4
6.1-2	Thermal conductivity of reference alloys	6.1-4
6.1-3	Electrical resistivity of reference alloys	6.1-5
6.1-4	Mean thermal expansion coefficient of reference alloys	6.1-5
6.1-5	Modulus of elasticity of reference alloys	6.1-6
6.1-6	Average ultimate tensile strength of reference alloys	6.1-6
6.1-7	Average yield strength of reference alloys	6.1-7
6.1-8	Total elongation of 25% CW PCA	6.1-7
6.1-9	Uniform elongation of 25% CW PCA	6.1-8
6.1-10	Swelling responses of austenitic steels from EBR-II irradiations	6.1-9
6.1-11	Predicted dependence of swelling on dpa for the three primary structural materials	6.1-9
6.1-12	Predicted effect of irradiation on UTS of 25% CW PCA	6.1-11
6.1-13	Predicted effect of irradiation on yield strength of 25% CW PCA	6.1-11
6.1-14	Uniform elongation of irradiated CW PCA	6.1-12
6.1-15	HT-9 - Predicted average and minimum tensile ultimate and tensile yield strengths and measured data	6.1-21
6.1-16	Alloy HT-9 - Predicted average 1% creep curves and measured data	6.1-21
6.1-17	HT-9 - Predicted average and minimum creep rupture curves and measured data	6.1-22
6.1-18	Tensile properties of V-15Cr-5Ti	6.1-32
6.1-19	Creep-rupture behavior of V-3Ti-13Cr	6.1-34
6.1-20	Swelling of vanadium and vanadium-base alloys on neutron and ion irradiation	6.1-37

6.1 Structural Materials

Three classes of alloys are currently considered as leading candidates for the first wall/blanket structure of a commercial fusion reactor: austenitic stainless steels, ferritic (martensitic) steels and vanadium-base alloys. A representative alloy from each class has been selected by the BCSS for analysis.

The materials assessment conducted as part of the BCSS includes: (1) a compilation of available materials properties data, (2) specification of limiting criteria for materials performance, (3) determination of design allowable parameters, and (4) evaluation of compositions in each alloy class with potential for low activation[1]. Where data were insufficient for a reliable assessment, best estimates based on extrapolation of available information were used to provide a consistent basis for evaluation of various designs. Established design rules and codes, e.g., ASME Pressure Vessel Code, were applied where possible (see Sec. 6.7).

This section provides a review of (1) the critical thermophysical, neutronic and mechanical properties; (2) the welding/fabrication characteristics; (3) the effects of the radiation environment on the above properties; and (4) the potential for low activation compositions. The corrosion and compatibility assessment of these alloys in various chemical environments is presented in Sec. 6.2.

6.1.1 Austenitic Stainless Steel

Austenitic stainless steels have been used extensively in fission reactor applications, and therefore possess the most developed data base for nuclear applications. For this reason the austenitic steels have been generally regarded as a reference for comparison with other candidate alloys. In addition to the substantial data base for both irradiated and unirradiated material, the austenitic steels are readily fabricated and welded. Primary limitations of the austenitic steels relate to critical physical properties, such as low thermal conductivity which can result in relatively high thermal stresses. As discussed in Sec. 6.2, corrosion in the liquid metal breeders is also a concern.

6.1.1.1 Prime Candidate Alloy (PCA)

The primary candidate alloy (PCA), which has been developed in the U.S. Alloy Development for Irradiation Performance Program, is selected as the reference austenitic steel. This alloy is similar to Type 316, but with a somewhat higher nickel concentration, lower chromium concentration and a small amount (~0.3%) of titanium. This chemistry modification, derived from several years of development, has provided improved resistance to radiation-induced swelling. To further enhance the swelling resistance of this alloy and to increase its elevated temperature strength, this material will be used in the 20-25% cold-worked (CW) condition with aging treatments to control precipitate distribution.

Physical Properties - The reference physical properties for PCA are summarized in this section. In most cases the data are assumed to be the same as for Type 316 stainless steel. Temperature independent or temperature insensitive properties are given in Table 6.1-1[2]. The thermal stress factors, which provide a figure of merit for accommodating thermal stresses,

TABLE 6.1-1. SELECTED PHYSICAL AND NUCLEAR PROPERTIES OF THREE REFERENCE ALLOYS

	PCA	HT-9	V-15Cr-5Ti
Melting Temperature, ^{0}C	1400	1420	1890
Density, g/cm^3	8.0	7.8	6.1
Poisson's Ratio	0.27	0.27	0.36
Thermal Stress Factor, MW/m^2-mm (500^{0}C)	3.2	4.8	9.8
Nuclear Properties[a]			
dpa/MW-y/m^2	11	11	11
appm He/MW-y/m^2	174	130	57
appm H/MW-y/m^2	602	505	240
W/cm^3/MW-y/m^2	40	40	25

[a]Nuclear properties for first wall of lithium blanket.

based on the physical properties at 500^{0}C are listed in Table 6.1-1. A higher value of the thermal stress factor indicates lower thermal stresses for a comparable thermal gradient or heat flux. The specific heat[3], electrical resistivity[4], thermal conductivity[5], thermal expansion coefficient[6] and the modulus of elasticity[7] are plotted as a function of temperature in Figs. 6.1-1 through 6.1-5.

Nuclear Properties - Several important nuclear properties for the reference structural alloys are listed in Table 6.1-1. The listed values are characteristic of the first wall of a lithium breeder blanket. Although these values will vary with blanket concept, the relative values for the three alloys do not change substantially. The displacement damage rates are similar for all three candidate materials. However, the gas (He and H) generation rates and nuclear heating rates differ significantly with material.

Welding/Fabrication - Extensive experience exists for the welding/fabrication of austenitic steels. The Type 300 series stainless steels are readily weldable by all methods of interest.

Baseline Mechanical Properties - The unirradiated tensile properties of cold-worked PCA are presented in Figs. 6.1-6 through 6.1-9.[8] The ultimate and yield strengths of PCA at low temperatures (500^{0}C) are slightly below those of 20% CW stainless steel. However, at temperatures above 500^{0}C the strength of PCA is above that of Type 316. The strength differences may be due to the titanium additions or may be a result of differences in test conditions. The cold-worked austenitic steel provides an advantage of ~100% in ultimate strength and over 300% in yield strength compared to annealed material at temperatures of interest. The uniform and total elongations of PCA are similar to those determined for cold-worked Type 316 CW stainless steel. In the case of PCA, there is a region of low elongation around 250-300^{0}C. Examination of the data indicates that this trend is probably characteristic of austenitic stainless steels and is not unique to PCA. However, it does point out that care needs to be exercised when designing for maximum loads in this temperature region.

Radiation Swelling and Creep Effects - The effects of radiation on the projected performance characteristics of PCA are based partially on data for

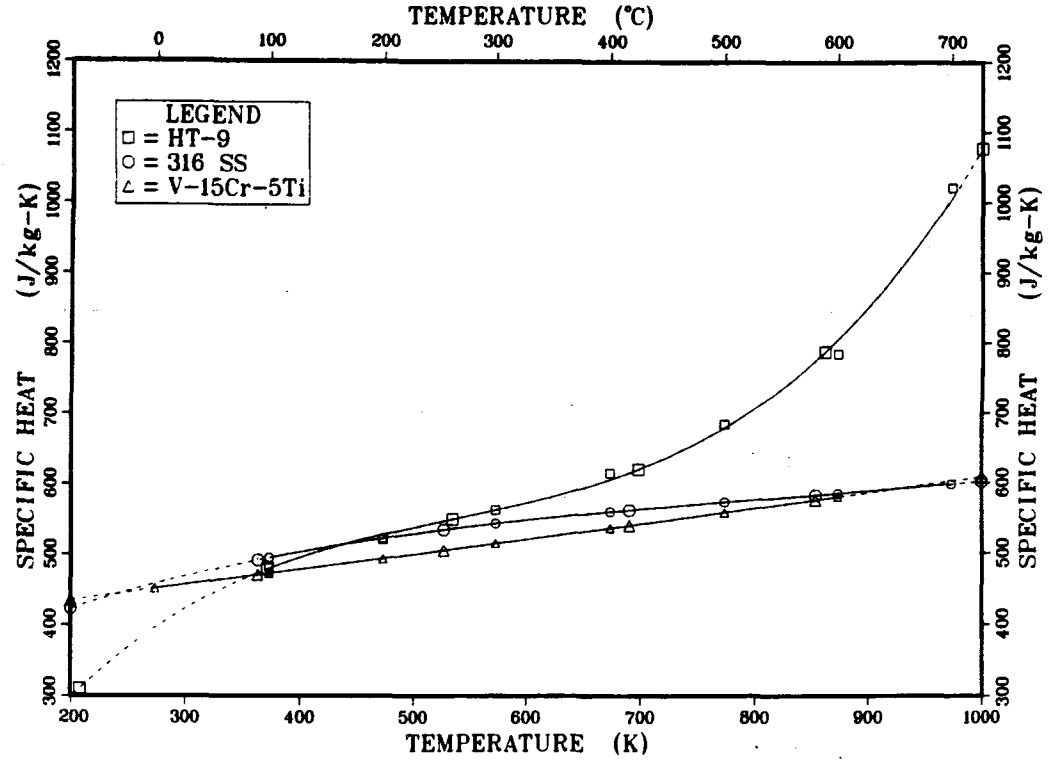


Fig. 6.1-1 Specific heat of reference alloys

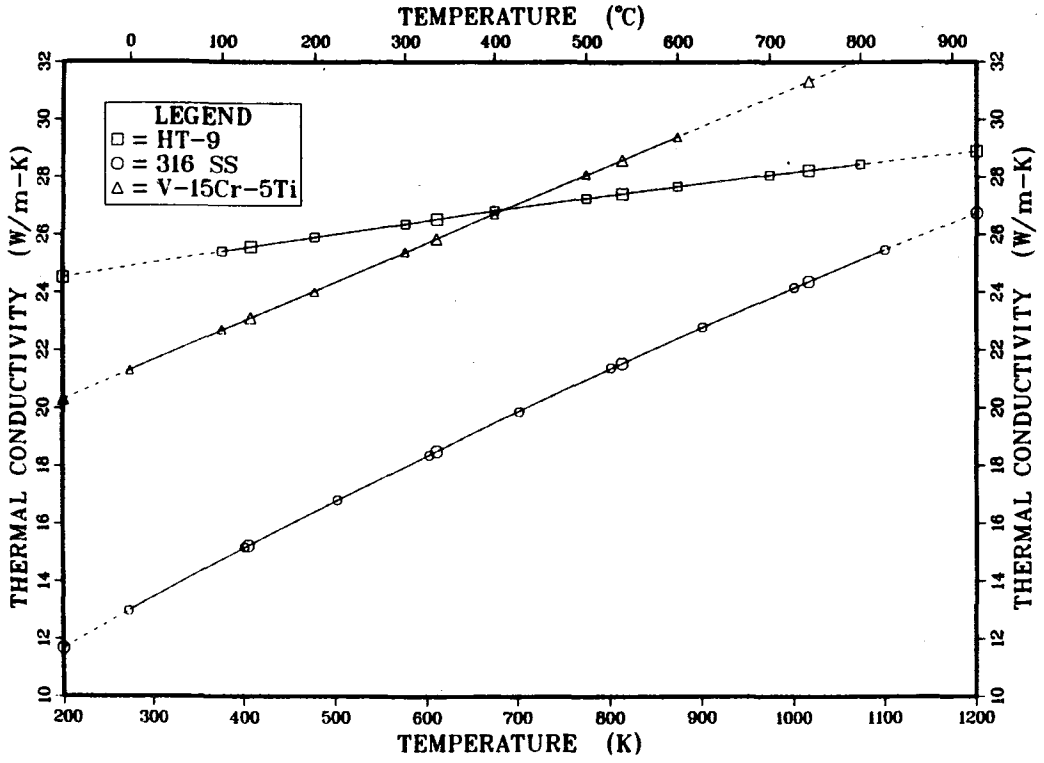


Fig. 6.1-2 Thermal conductivity of reference alloys

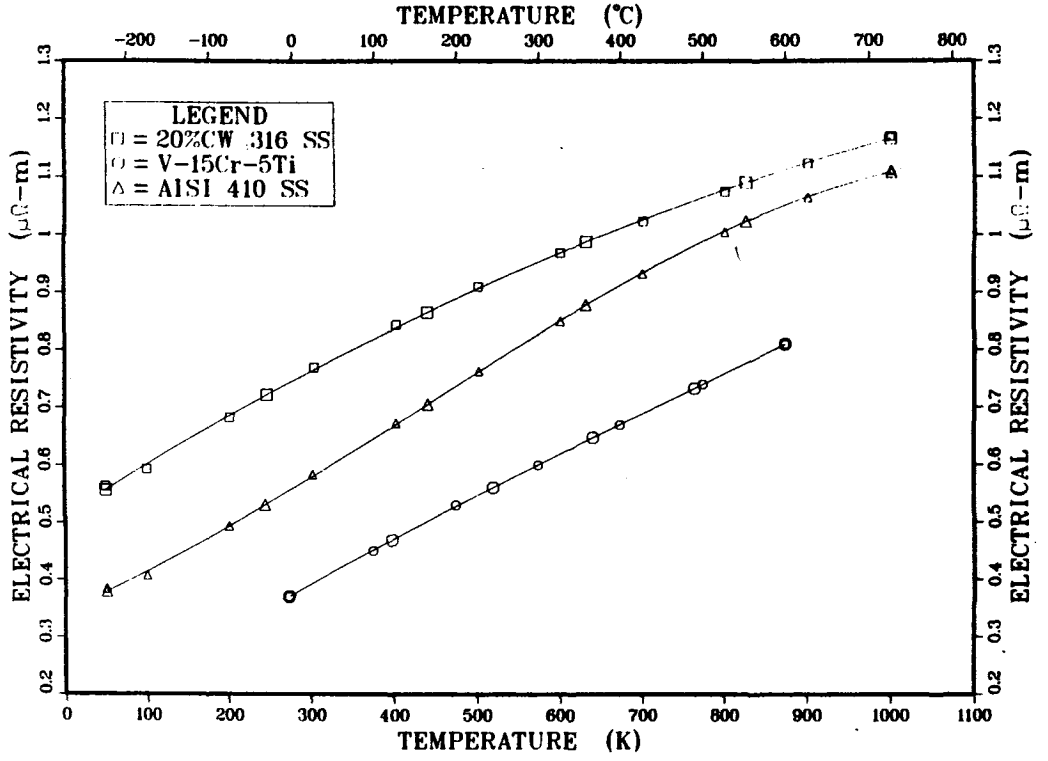


Fig. 6.1-3 Electrical resistivity of reference alloys

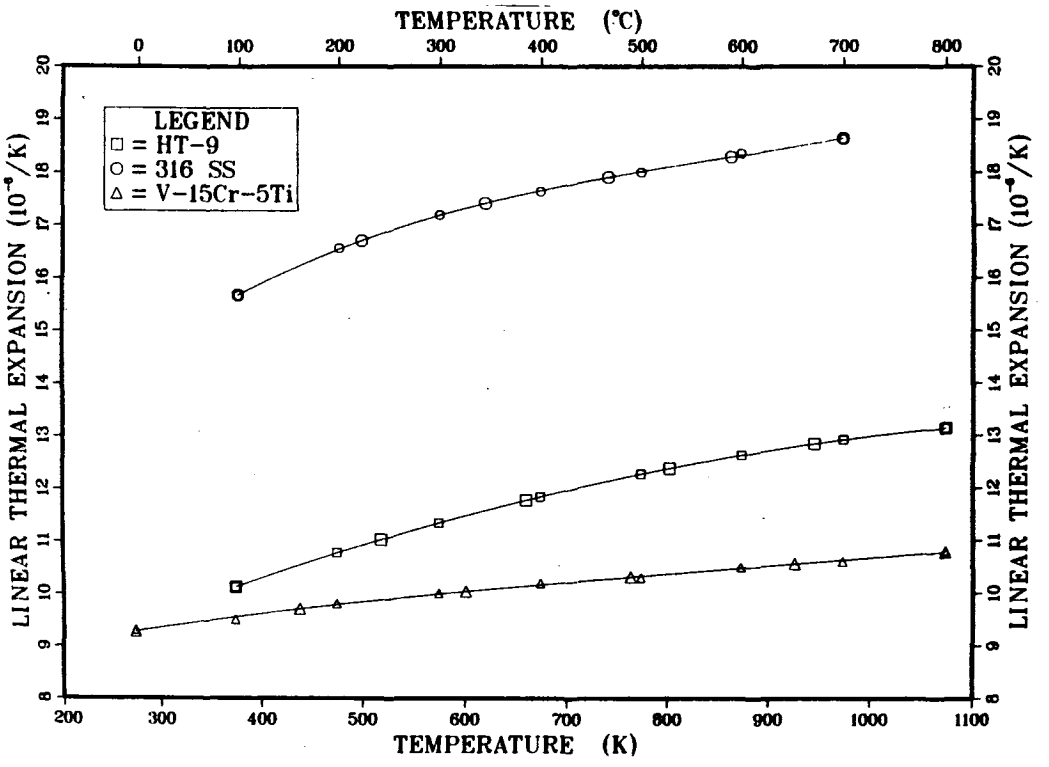


Fig. 6.1-4 Mean thermal expansion coefficient of reference alloys

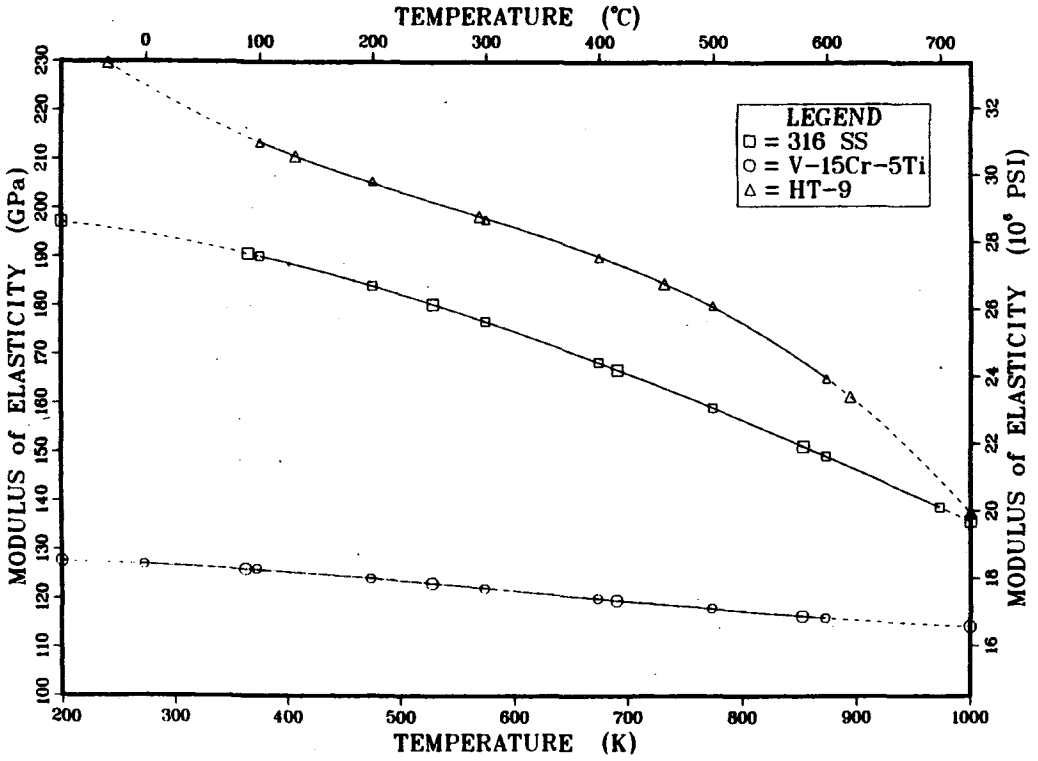


Fig. 6.1-5 Modulus of elasticity of reference alloys

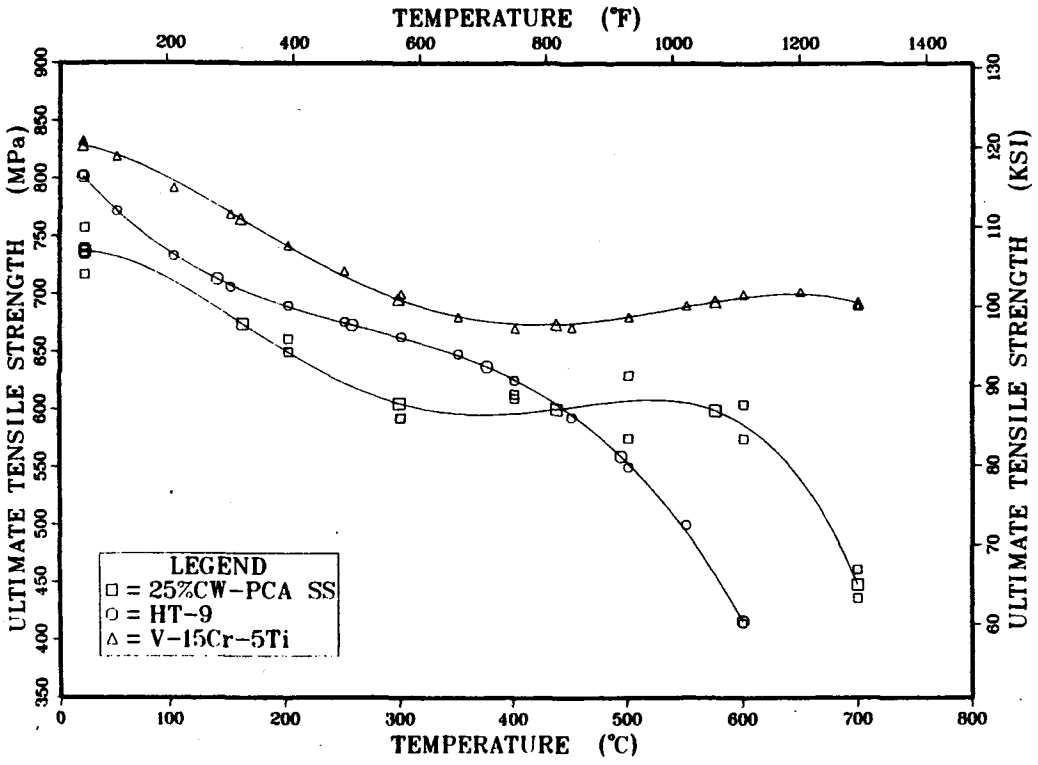


Fig. 6.1-6 Average ultimate tensile strength of reference alloys

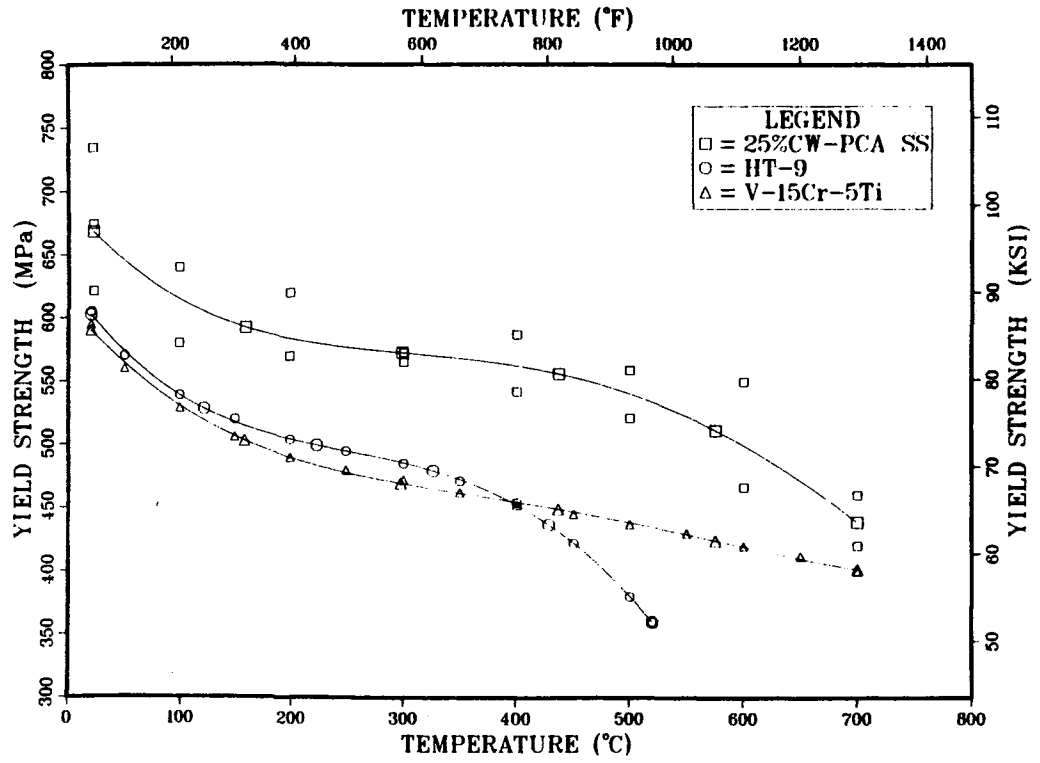


Fig. 6.1-7 Average yield strength of reference alloys

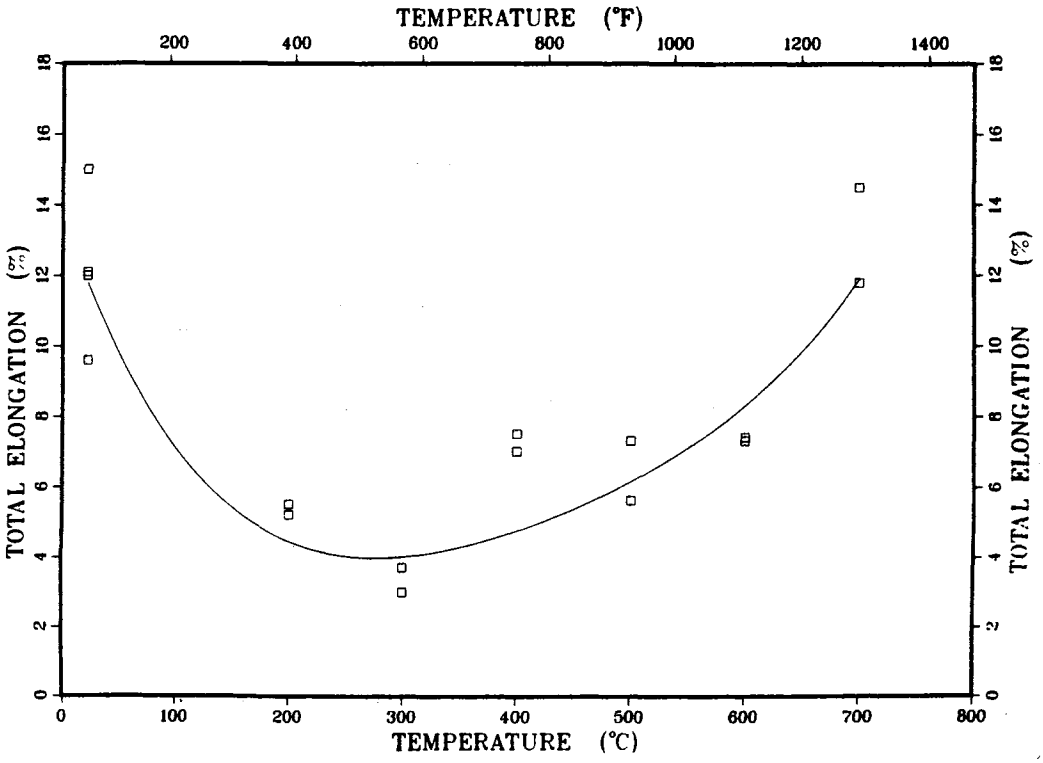


Fig. 6.1-8 Total elongation of 25% CW PCA

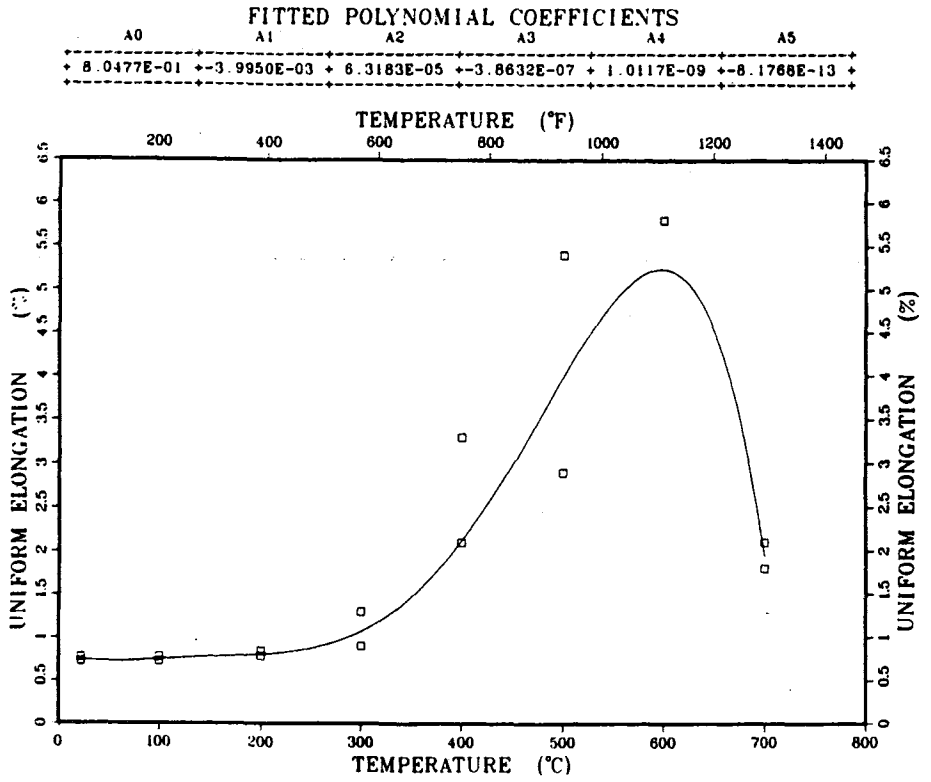


Figure 6.1-9. Uniform elongation of 25% CW PCA.

Type 316 stainless steel. The swelling of PCA is modeled on the assumption that it will behave similarly to Type 316 stainless steels. The high fluence data have been obtained from fast breeder reactor irradiations, primarily EBR-II, in which the helium generation rates are low. Extensive data produced by EBR-II irradiations are summarized in Fig. 6.1-10[9]. Effects of helium are based primarily on lower fluence, mixed spectrum reactor (HFIR) irradiations. The swelling response of PCA assumed for the present study is approximated by a bilinear swelling curve as shown in Fig. 6.1-11. Based on available information, the experimental data have been extrapolated to predict an incubation period of 150 dpa for irradiation temperatures of $\leq 400^0$C and 100 dpa for irradiation temperatures in the range 450-550^{0}C. The initial swelling rate is assumed to be 0.02%/dpa (2% at 100 dpa). Above the incubation fluence limit, breakaway swelling at ~ 0.5%/dpa is predicted. For the present study a swelling limit of 5% (volumetric) is assumed, based on macroscopic dimensional changes for projected blanket-size components. Because of the high swelling

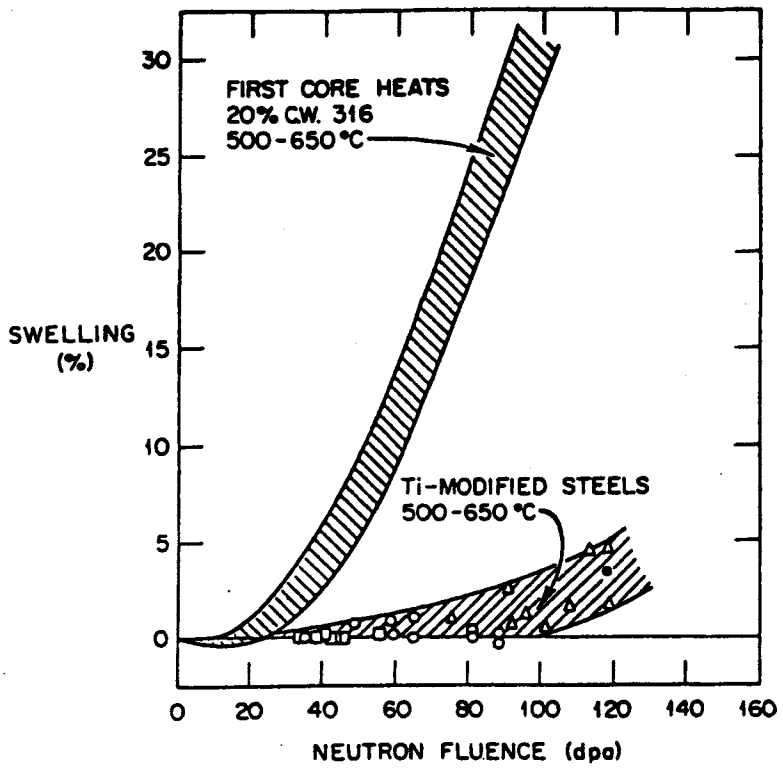


Fig. 6.1-10 Swelling responses of austenitic steels from EBR-II irradiations

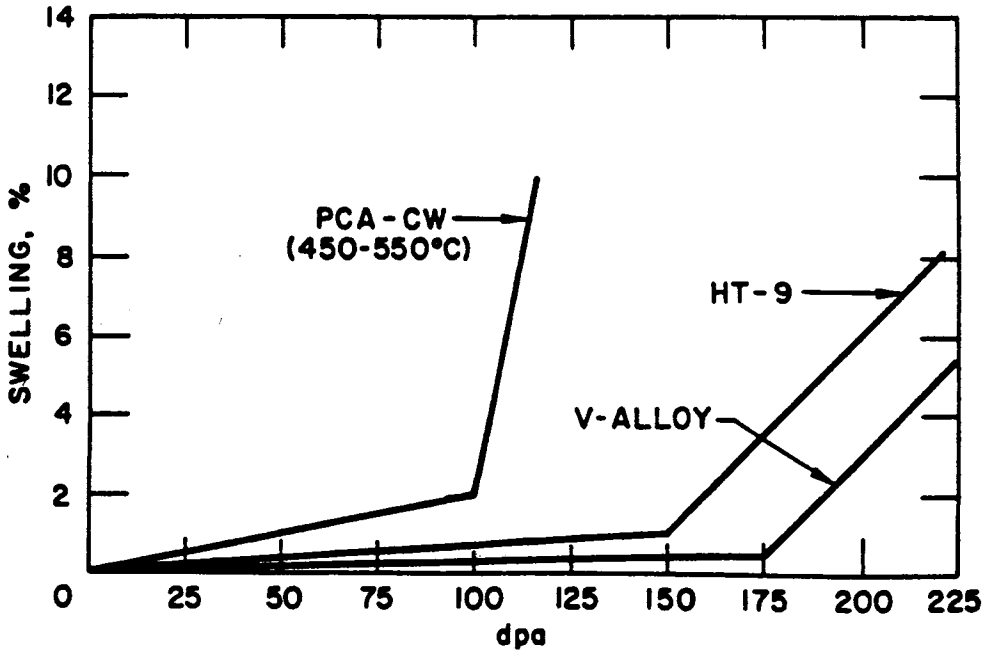


Fig. 6.1-11 Predicted dependence of swelling on dpa for the three primary structural materials

rate above the incubation fluence, the lifetime is quite insensitive to the exact value of the swelling limit. Therefore, in the present study, a lifetime corresponding to 100 dpa is recommended for PCA at temperatures of 450-550^{0}C.

The radiation creep characteristics of PCA have not been extensively investigated. A radiation creep equation developed by Mattas[10], which takes into consideration the lower swelling rates of PCA compared to Type 316 stainless steel, is used in the present analysis. Estimates of the effects of radiation creep on the allowable design stresses for PCA are presented in Section 6.7.

Effects of Radiation on Mechanical Properties - Information on the effects of irradiation on the mechanical properties of PCA is limited. Therefore, the results of HFIR irradiations on a special heat of Type 316 stainless steel (referred to as the MFE heat) were utilized.[11] There does not appear to be a strong influence of transmuted helium on either the tensile or yield strength of the MFE heat. In general, the response of the material is similar to that experienced in previous stainless steel irradiations without helium. Examination of the data shows that for irradiation temperatures > 400^{0}C, both the tensile and yield strength increase as a result of matrix hardening up to approximately 25-30 dpa, at which point saturation occurs with very little subsequent change. Above this temperature, the opposite effect on strength is produced, with significant softening occurring during irradiation.

Using these trends, the irradiated tensile and yield strengths of PCA were developed (Figs. 6.1-12 and 6.1-13). The same approach was used to develop the uniform elongation curve presented in Fig. 6.1-14. The trends shown in this figure are different from those previously presented in the literature, and reflect recently acquired irradiation data on Type 316 and Ti-modified 316 stainless steel. This figure shows about the same trend as seen in the strength curves, with saturation occurring at a damage level ~ 30 dpa. It is significant to note that at 575^{0}C the uniform elongation with up to 3000 appm helium is still quite high and substantially above the 0-0.2% previously reported.[12] However, for temperatures below ~300^{0}C the uniform

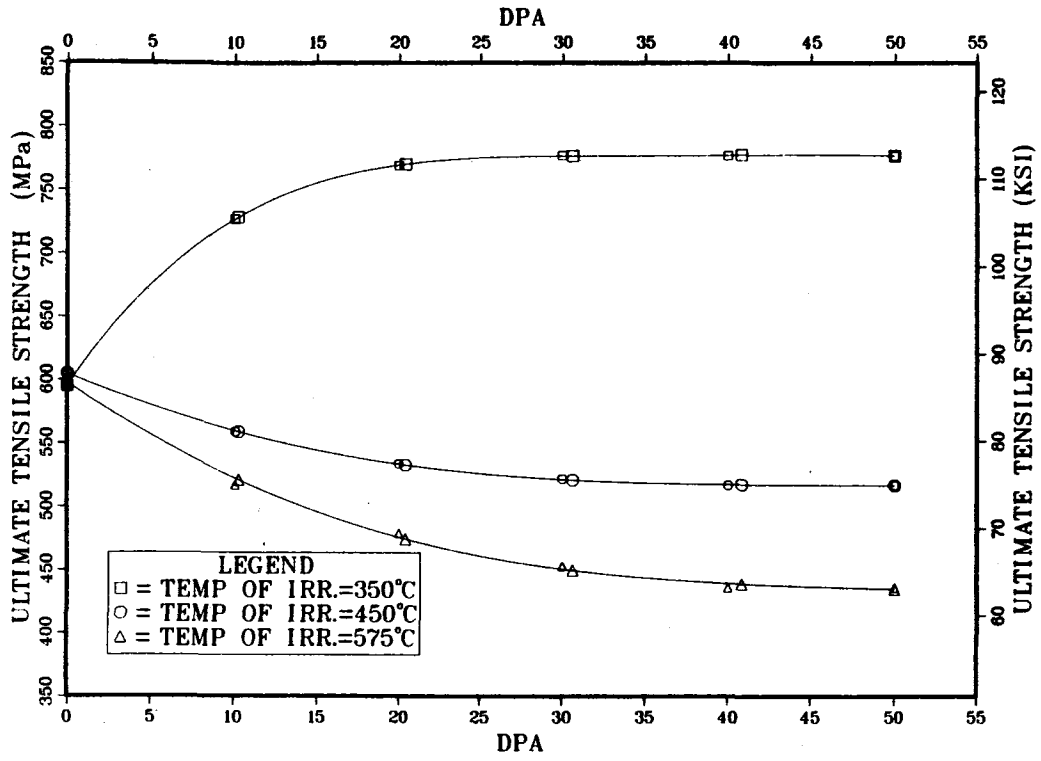


Fig. 6.1-12 Predicted effect of irradiation on UTS of 25% CW PCA

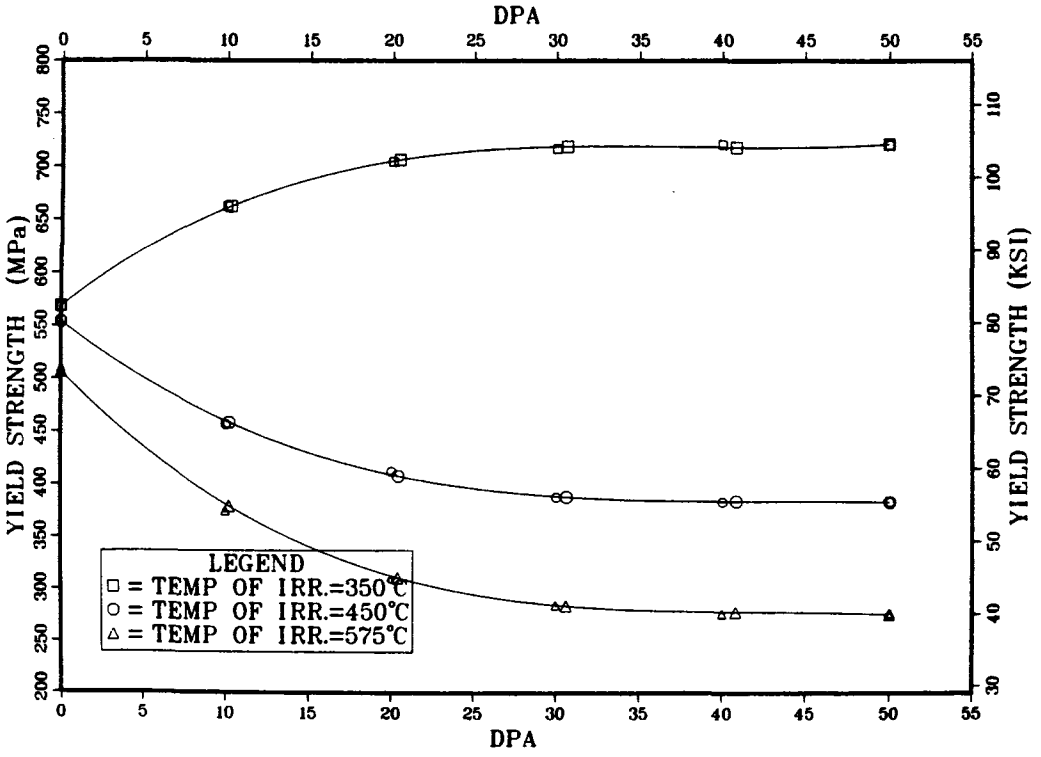


Fig. 6.1-13 Predicted effect of irradiation on yield strength of 25% CW PCA

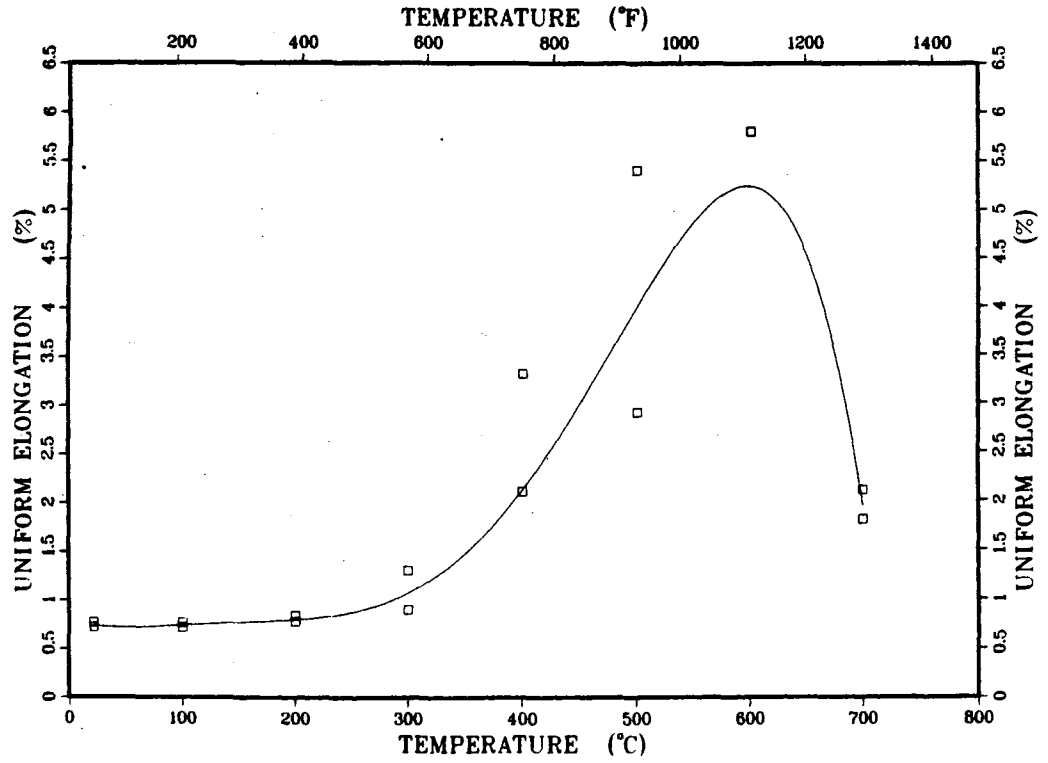


Fig. 6.1-14 Uniform elongation of irradiated CW PCA

elongation is less than 1%.[13,14] A reason proposed for the change is that earlier irradiations were performed using material with a different heat treatment.

Most materials exhibit severe loss of ductility at temperatures $\geq$ 0.5 T_m (melting temperature) due to helium embrittlement. A maximum operating temperature of (0.5 T_m - 50°C) was recommended by the BCSS to avoid this problem. A temperature increment of 50°C is considered adequate to allow for both data and operating uncertainties.

A maximum operating temperature limit of 550°C was recommended for PCA in the high fluence region. Since a ductile-brittle transition temperature (DBTT) is not observed in austenitic stainless steels above room temperature, a minimum operating temperature for this alloy was not specified.

6.1.1.2 Manganese Stabilized Steels

Austenitic stainless steels, particularly Type 316, are of interest in fusion reactors because of the extensive data base and ease of fabrication. However, because they are heavily alloyed with nickel and molybdenum, these steels do not qualify as a low activation material. Therefore, one of the objectives in the BCSS was to find a steel with the same type of microstructure but free of the high activation elements.

One type of steel that appears to meet these requirements is manganese stabilized steel, that uses this element to stabilize the austenite phase. These steels were initially developed for use in wear resistant applications and are noted for their hardenability. Because they rapidly work harden, they are normally not supplied in the shapes needed in fusion applications and are generally considered to be non-machineable. However, recent efforts in Japan have been conducted to develop a more fabricable steel. Based on the optimistic results of these investigations, it may be possible to develop a low activation form of a manganese-stabilized austenitic steel. It should be noted, however, that the level of understanding of the metallurgy of this steel is much less than that of the ferritic steels, and as a result the risk of failure to develop a qualified alloy is substantially greater than for the low-activation ferritic steel.

Approach - There are currently a number of commercialy available manganese stabilized steels. Compositions for the steels considered by the BCSS are listed in Table 6.1-2. However, it does not appear that the simple alloy

TABLE 6.1-2. COMPOSITION OF MANGANESE-STABILIZED AUSTENITIC STAINLESS STEELS IN THE CURRENT DATA BASE

Alloy[a]	Composition[a] (wt %)						
	Cr	Mn	Ni	Mo	C	Si	Ti
EP-838	11.6	13.5	4.2	0.9	0.02	0.42	<0.02
ICL 016	17.3	8.3	7.2	1.4	0.02	0.51	--
AMCR	10	17.5	0.67	--	0.2	--	--
UKAEA Experimental	~12	1-30	11-35	0-3	0.3-0.7	0.4-1.0	0.2-0.3
AISI 216	20	8.5	6.7	2.7	0.07	0.32	--

[a]Balance iron. More complete chemistry is given for some of these alloys in the original papers. See Table 6.1-3 for reference citations.

substitution approach used in developing the low activation ferritic steel (Sec. 6.1.2.2) will work with this type of steel. The requirements for developing a low activation manganese steel have been analyzed.[15] The analysis suggests that manganese is not as good an austenite-stabilizing element as nickel and as a result other elements, e.g., N, C, Cu and Co, will have to be considered in addition to manganese. Copper will not meet the low activation requirements and the nitrogen concentration would have to be limited to <0.09 wt%. Cobalt, while it has a short half life, produces high energy gammas and as a result is not a desirable alloying element. The composition recommended in Ref. 15 for consideration consisted of 15-20% Mn, 0.05-0.1% C, <0.01% N, and 10-15% Cr. Chromium, while it tends to promote the formation of ferrite, is needed for corrosion resistance. The nominal composition selected for the BCSS was 15Mn-15Cr-0.05C-0.01N. Other compositions of potential interest are listed in Table 6.1-2.

Physical Properties - Comparison of the physical properties of various 300 series stainless steels with those of several manganese steels indicates that there is very little difference between the two groups. Therefore, it was assumed in this study that the physical properties of the low activation austenitic steel were the same as those of PCA.

Nuclear Properties - The nuclear properties of the manganese steels will be similar to those of the ferritic steel (Table 6.1-1). The displacement damage rate is similar for all alloys considered. Both the helium and hydrogen generation rates for manganese are less than for iron. Therefore, the gas generation rates and the heating rate will be similar to those for the ferritic steels.

Unirradiated Mechanical Properties - In the annealed condition the manganese steels appear to have slightly lower strength than the 300 series steels. However, the austenitic steels in the annealed condition experience higher swelling rates than other materials, and as a result cold working will be required for radiation damage resistance. Based on this need to cold work the structure, it was felt that the resultant properties of the manganese steel would be equivalent to cold-worked PCA. Therefore, the mechanical properties of the low activation manganese steel for this study were assumed to be the same as those presented for PCA.

Effects of Radiation on Properties - Available irradiation effects data show that the partial replacement of nickel by manganese has relatively little effect on property changes in austenitic steels. Therefore, it is likely that the first alloys developed in this class with full replacement of nickel will respond to irradiation in a manner similar to the standard grades of Types 304 and 316 stainless steel. It is anticipated that the alloys of this class which are optimized for radiation resistance will exhibit a behavior similar to PCA and other optimized austenitic steels containing nickel.

The scant data base that is available for use in predicting the irradiation response of this alloy class has been generated mainly on alloys in which only part of the nickel (in conventional austenitic stainless steels) has been replaced by manganese. In many of these alloys, the concentrations of molybdenum, nitrogen, and niobium are far in excess of limits imposed for a low activation steel.[1] These data are summarized qualitatively in Table 6.1-3 for the steels whose compositions are shown in Table 6.1-2.

The post-irradiation tensile properties of the USSR EP-838 steel were reported by Klueh and Grossbeck[15] and by Votinov et al.[16] Both of these experiments compared the tensile results for EP-838 steel to Type 316 stainless steel which was irradiated in the same capsules. In the Klueh and Grossbeck experiment, both materials were in the 20% cold worked condition and the temperature of irradiation was 50^0C. After irradiation to a damage level of 5.2 dpa, the specimens were tensile tested at 20 and 300^0C In the Votinov experiment, the specimens were in the solution annealed condition and the temperature of irradiation was 150^0C. These specimens were irradiated to a damage level of 0.2 dpa and the post irradiation test temperatures were 20 to 750^0C. Both of these experiments showed that the behavior of the two types of steels were remarkably similar. The difference in tensile strength between the two steels was smaller in the as-irradiated condition than in the unirradiated condition. Typically the strength values were increased and ductility was reduced by irradiation. Irradiation at 50^0C resulted in near-zero elongation for the manganese steel as well as for the austenitic stainless steel, but total elongation was in the range of 2-9% indicating a tough material. Votinov's tests at 700^0C and higher temperatures did not show evidence of helium embrittlement at these low fluence levels. He did report,

TABLE 6.1-3. SUMMARY OF DATA BASE FOR IRRADIATION EFFECTS IN MANGANESE-STABILIZED AUSTENITIC STAINLESS STEELS

Alloy[a]	Reference	Irradiation Species	Fluence (dpa)	Temperature (^{0}C)	Measurements	Observations
EP-838	15	Neutrons	5.2	~50	Tensile properties (20 and 300^{0}C)	20%-cold-worked material response very similar to Type 316 for equivalent conditions.
EP-838	16	Neutrons	~0.2	150	Tensile properties (20 to 750^{0}C)	Annealed material response similar to Type 316 for same conditions.
ICL 016	17	46 MeV Ni^{6+}	60	625	Microstructure	Swelling sensitivity to helium; no advantage over other austenitic steels; some phase instability.
AMCR	18	1.25 MeV e^-	10	400-600	Microstructure	Swelling equivalent to austenitic stainless steel FV 548 for some conditions; phase instability; high manganese does not have adverse effect on swelling.
UKAEA Experimental	19	46 MeV Ni^{6+}	60	625	Microstructure	Swelling similar to other austenitic alloys, decreases as manganese or Mn + Ni increases; phase instability.
AISI 216	20	Neutrons	16-27	400-650	Density, microstructure	Substitution of manganese for nickel does not appear to alter the swelling response from 300-series steels; insensitive to temperature in this range.

[a]Compositions given in Table 6.1-2.

however, that embrittlement has been observed in some other steels under the same irradiation and test conditions.

Embrittlement related to a DBTT or a shift in the DBTT resulting from irradiation is not expected in the manganese-stabilized austenitic steels since this phenomenon is generally restricted to the body-centered-cubic (bcc) ferritic or martensitic steels.

There are apparently no determinations of irradiation-induced creep rates in the manganese-stabilized steels. However, the similarity of the swelling response of these steels to the conventional austenitic stainless steels suggests the assumption of similar irradiation creep behavior in these two classes of steels.

Several experimenters have used charged particle bombardment to simulate fusion reactor irradiations of manganese-containing steels.[17-19] Transmission electron microscopy of the damage region was used to determine swelling and phase stability. A range of alloy compositions has been examined by this approach with the general finding that the substitution of manganese for nickel does not alter the swelling resistance or phase stability of these alloys. All experiments showed some swelling with the amount usually characterized as that expected for Fe-Cr-Ni austenitic stainless steels irradiated under similar conditions. These investigators have also reported that the manganese-containing steels develop a large amount of precipitate phase at elevated temperatures. However, most of this appears to be a result of thermal instability of the alloy, and the additional contribution of irradiation to the precipitation process may not be large. The high carbon content in many of these alloys may also be a contributing factor.

Gelles and Garner have reported the swelling behavior of the manganese-bearing AISI 216 steel irradiated in a fast reactor.[20] Fluences producing 16 to 27 dpa were achieved at temperatures in the range of 400 to 650^{0}C. Swelling values ranged from 0.4 to 3.4%. They concluded that the swelling was not temperature dependent over the range studied and was similar to the behavior of other austenitic stainless steels, with composition typified by Types 304 and 316 stainless steels. If the swelling data are described by the standard bilinear behavior, then the incubation fluence would be between 15 and 22 dpa. Very little precipation was observed in this steel.

In summary, the scant experimental data indicate that the partial substitution of manganese for nickel in an austenitic steel does not significantly alter the irradiation response of the alloy. Therefore, it is reasonable to assume that the properties for this steel should be roughly equivalent to the behavior of PCA.

Compatibility - The compatibility of the manganese-containing steels with helium and water coolants should be similar to the austenitic stainless steels. The considerations for PCA regarding water chemistry will also apply for manganese steel. To minimize the water corrosion, the manganese steel should have at least 12% Cr. In the case of liquid metal compatibility, manganese is more soluble than nickel in lithium. As a result, to produce the same rate of corrosion as PCA, the manganese steel will have to operate at a lower temperature. The recommended operating temperature for the manganese steel was 50^0C below that of PCA.

Uncertainties for Manganese Steels - The level of understanding of the metallurgy of the manganese steels is much lower than for either ferritic steels or vanadium alloys and as a result the risk of not achieving desired characteristics through alloy development is greater. The manganese steels have been made in thick plate or bar for commercial purposes. It is only recently that effort has been initiated to develop more fabricable steels, for example NM-1. None of these steels were developed for elevated temperature operation.

The irradiation data base is very limited. Substantial effort will be required to scope the radiation response of these materials before any definitive judgement can be made regarding their usefulness for fusion applications, and before the development of optimized compositions and microstructures can begin.

6.1.2 Ferritic Steels

High chromium martensitic stainless steels such as Sandvik HT-9 and Fe-9Cr-1Mo are of considerable interest because of their superior resistance to neutron-induced swelling, elevated temperature strength, liquid-metal compatibility and thermal stress resistance. Section 6.1.2.1 presents a brief review of the HT-9 data which was compiled and used as a reference in the BCSS

designs. The discussion is divided into physical properties, mechanical properties, and radiation effects. Section 6.1.2.2 reviews the results of efforts to develop low activation ferritic steels.

6.1.2.1 HT-9 Ferritic Steel

Physical Properties - The melting temperature, density,[21] Poisson's ratio and thermal stress factor for the HT-9 ferritic steel are listed in Table 6.1-1. The specific heat[22], thermal conductivity,[22] Young's modulus[22], coefficient of thermal expansion[21], and modulus of elasticity recommended for this study are presented in Figs. 6.1-1 through 6.1-5. The electrical resistivity of AISI 410 steel (Fe-12Cr) which was assumed to approximate the resistivity of HT-9 (Fe-12Cr-1Mo) is given in Fig. 6.1-3.

Nuclear Properties - Several important nuclear properties of the ferritic steel are given in Table 6.1-1. The displacement damage rate is similar for all alloys considered. The helium and hydrogen production rates are less than those for PCA but greater than those for the vanadium alloy. Nuclear heating rates are similar to those of the austenitic steel.

Welding/Fabrication - Large commercial heats of the 9-12Cr class of steels have been made to specifications and fabricated into product forms in the U.S. and abroad. This experience has shown that electroslag refining (ESR) produced a more uniform microstructure in HT-9 than the argon-oxygen decarburization process (AOD). Control of impurities such as phosphorous, sulphur, and tin should be a consideration in procuring material in the future in order to decrease the effects of segregation. This could be accomplished by incorporating an empirical relationship, such as the Watanabe factor, in the specifications.

A considerable amount of effort has been spent on determining the welding characteristics of HT-9. While the ferritic steels are not as easy to weld as the austenitic steels, investigations have shown that the HT-9 alloy can be readily welded with welds meeting ASME Code requirements. In welding high strength ferritic steel such as HT-9, preheat of the weld zone is needed to minimize cracking. However, it has been shown, from Y-groove weld cracking tests, that the weld procedures recommended by Sandvik of preheat/interpass temperatures between 250-400^{0}C are unnecessarily restrictive, and that lower

preheats of around 100^0C could be used on welds in many fusion-relevant sections. Furthermore, the lower preheat decreases the DBTT after welding. A significant amount of effort has been placed on understanding the metallurgy of the weld and heat-affected zones. Much of the metallurgy of these weld areas has been identified and the effects on mechanical properties are being measured both by Gleeble simulations and innovative testing techniques.

The requirement for post weld heat treatment (PWHT) has been identified as an issue. The HT-9 alloy has a recommended PWHT of 760^0C for 2-1/2 hours. A recent study has shown that a TASKA blanket module could be manufactured, and the PWHT could be given at the recommended temperatures and times. This assessment was based on information from industrial heat treating firms such as Cooperheat Company, Los Angeles, and Whessoe, Ltd, England. It was concluded that PWHT is an engineering problem, and that the method of performing the PWHT is design-dependent. The implications of this are that an assessment of the method of fabrication and building of a first wall/blanket module should consider the accessibility of weldments for post weld heat treatment.

There are significant amounts of information on the 9-12Cr steel in Europe and in the U.S. on the 2-1/4Cr class alloys. The USDOE LMFBR program has developed substantial knowledge of the PWHR behavior of 9Cr-1Mo. Information and experience is extensive on post weld heat treatment, but the temperature "window" in the martensitic steels is not fully characterized. Further work is needed to determine the latitude in PWHT temperatures and times.

In regard to the low activation ferritic steel, the weldability should be equivalent to the 9Cr-1Mo steel because of a lower initial DBTT.

Mechanical Properties - Factors that influence the unirradiated value of the design allowable stresses according to the ASME nuclear pressure vessel code include mechanical strength (UTS and yield), and thermal creep. The code has certain criteria for selecting the allowable limits of stress on a component, the result of which is a factor called S_{mt} which incorporates the tensile and creep property requirements. The tensile properties, stress rupture, and time to 1% creep strain for several heats of HT-9 are given in Figs. 6.1-15 through 6.1-17.[24] The dependence of the ultimate and yield strength on temperature for HT-9 is compared with values for PCA and V-15Cr-5Ti in Figs. 6.1-6 and 6.1-7.

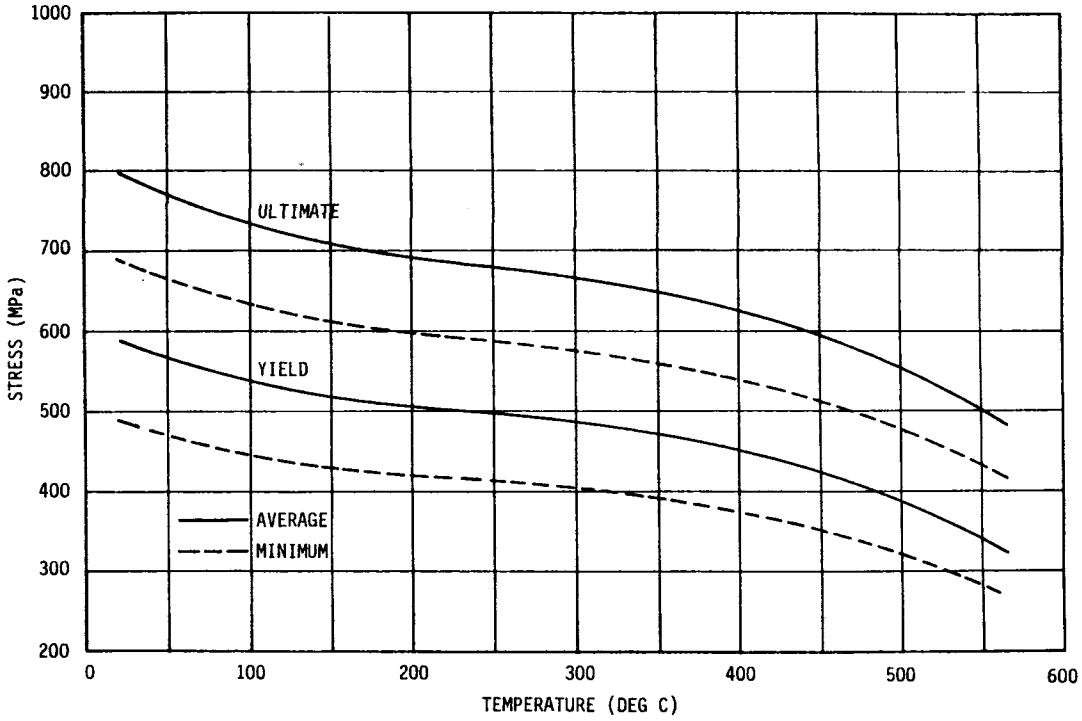


Fig. 6.1-15 HT-9 - Predicted average and minimum tensile ultimate and tensile yield strengths and measured data

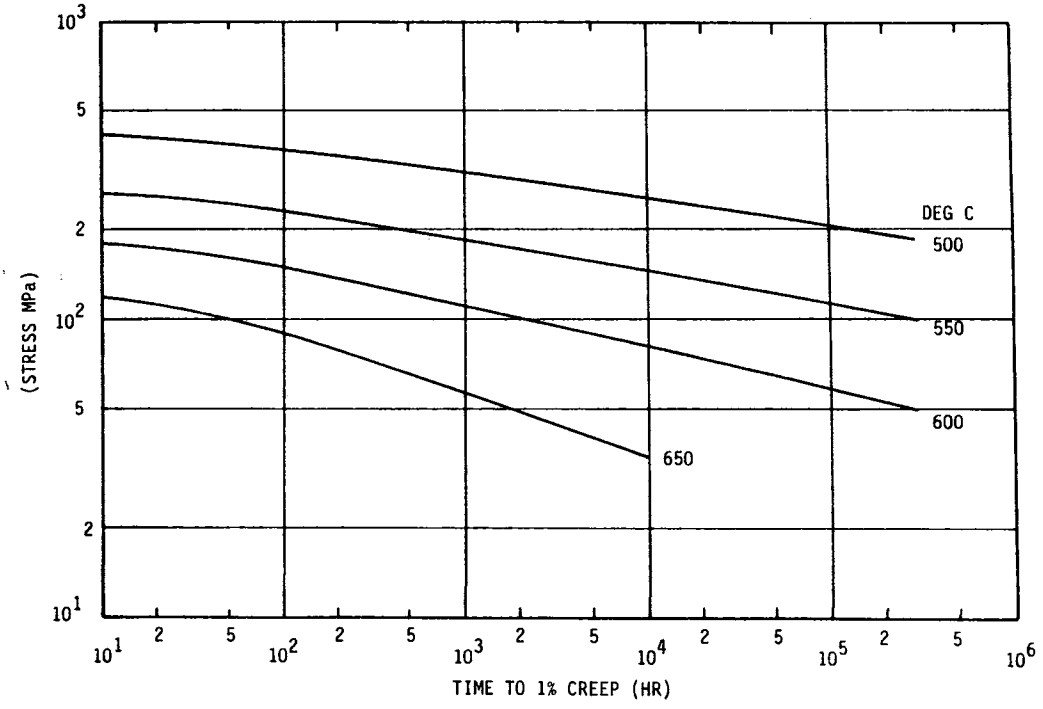


Fig. 6.1-16 Alloy HT-9 - Predicted average 1% creep curves and measured data

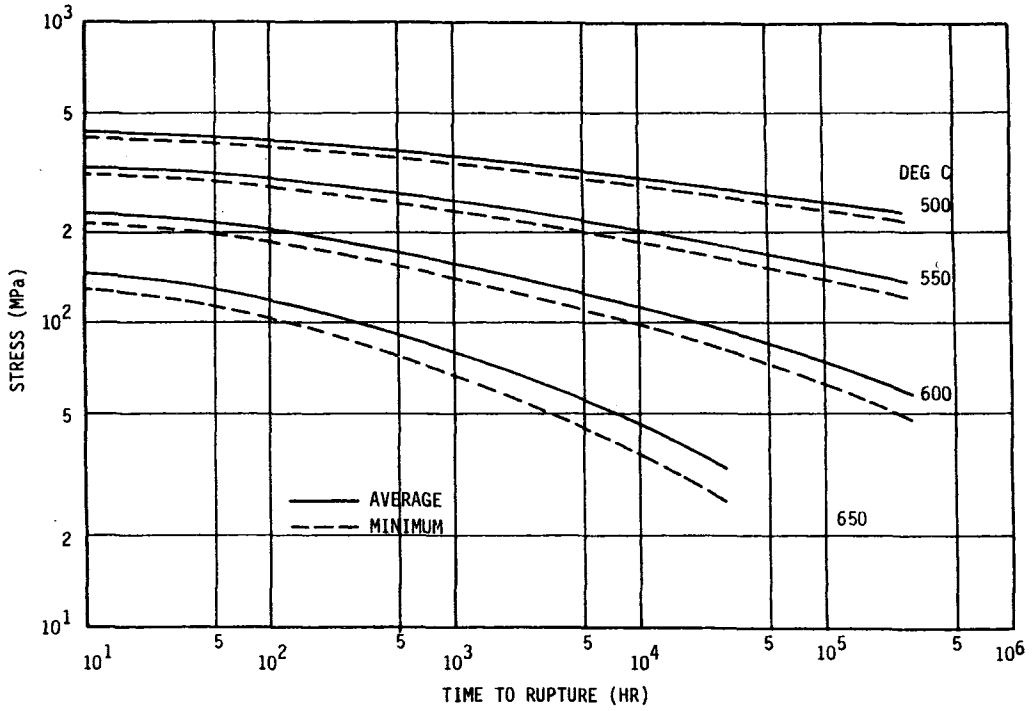


Fig. 6.1-17 HT-9 - Predicted average and minimum creep rupture curves and measured data

Radiation Swelling and Creep Effects - The effects of irradiation on the properties of HT-9 include dimensional changes (swelling and irradiation-induced creep), and embrittlement due to an upward shift in the ductile-brittle transition temperature or helium generation.

Theoretical analyses of the swelling of ferritic steels indicate that the maximum swelling rate of these steels will be approximately an order of magnitude less than that for the austenitic steels. Although high fluence data with appropriate helium generation rates do not exist for HT-9, data to > 100 dpa with low helium content show that the swelling rates were measured to be very small.[25] In Fig. 6.1-11, it has been assumed that HT-9 has a bilinear swelling response similar to that for austenitic steel. Although limited data suggest that swelling may increase at higher helium contents, significant increases in swelling rate are not expected to occur until a very high incubation dose. For the recommended swelling limit of 5% volumetric, the predicted lifetime for HT-9 corresponds to ~ 190 dpa.

The radiation creep characteristics of HT-9 have not been extensively investigated. Based on a comparison with austenitic steels, the bcc ferritic steels generally exhibit lower radiation creep rates.[26] Estimates of the radiation creep on the allowable design stress are presented in Section 6.7.

Effects of Radiation on Mechanical Properties - Limited data indicate that the strength of HT-9 increases during irradiation.[27] For BCSS design purposes, unirradiated tensile properties were used to obtain allowable design stresses.

The shift in the DBTT during neutron irradiation is an important issue for ferritic steels.[28] It is known that the substantial change in DBTT of low alloy pressure vessel steels saturates at relatively low fluences (~10 dpa) due to the precipitation of a copper-rich strengthening phase. As the alloy matrix is depleted of copper, there is a corresponding increase in the DBTT. Since the shift in DBTT in bcc materials is probably due to the hardening that occurs during irradiation, the DBTT tends to approach a limiting value as the matrix depletes itself of the elements needed in the precipitate. In the HT-9 alloy, the irradiation strengthening effect is probably due to the formation of a silicon-rich G-phase, and thus the change in DBTT of HT-9 may diminish at high fluences. Data on HT-9 irradiated at 390^{0}C to 13 dpa show a DBTT of ~150^{0}C. If HT-9 behaves similar to the low alloy pressure vessel steels mentioned above, the DBTT may be well below the lowest proposed operating temperature (250^{0}C).[29] A critical question remains as to whether a greater shift in the DBTT occurs for HT-9 at lower irradiation temperatures as is the case for some pressure vessel steels.

It has been assumed for this study that the DBTT stays below the coolant temperature, and therefore is not prohibitive. However, further experimental investigations at 100-400^{0}C are warranted. Other factors such as afterheat to maintain a temperature above the DBTT even after shutdown, novel thermomechanical treatments, and alloy composition modifications may further ensure that the structure never operates on the lower shelf of the fracture strength curve.

6.1.2.2 Modified Ferritic Steels

The Fe-Cr-Mo class of ferritic steels have found extensive use in a number of applications such as turbine blades, shells, rotors, boilers, super

heaters, and reheater tubing. As a result of these extensive applications, the physical metallurgy for these steels has been studied in detail since the late 1950's. The effect of various alloying additions, particularly chromium (up to 12%) and molybdenum (up to 2%), is well understood.[30] The level of metallurgical understanding gives high confidence that tailoring of the alloy composition to obtain a low activation ferritic steel is achievable.

Approach to Alloy Development - To develop a steel capable of achieving a disposal requirement of Class C or better after reactor shutdown, certain alloying elements must be avoided. For ferritic steel these elements are molybdenum and nickel, which are currently used as alloying elements in HT-9, and niobium, which exists as an alloying or impurity element. Molybdenum has traditionally been used as an elevated temperature strengthener primarily because of its low cost and potent strengthening ability in relation to other alloying elements.

Tungsten may be used as an alternative to molybdenum as an elevated temperature strengthener in ferritic steels. The metallurgy of the Fe-Cr-W system has not been studied as extensively as the Fe-Cr-Mo system. However, analogies can be drawn from the work done on the Cr-Mo-W class of steels.[31,32] While this class of steels is essentially a mixture of ferrite and martensite, and HT-9 is fully martensite, compositional limits for an all-martensite structure can be estimated by using chromium-equivalent and nickel-equivalent equations such as those developed by Schneider.[33,34] Based on these calculations, the level of tungsten required would be ~2.5%, and the level of nickel could be reduced from ~0.5% to 0.009%. The resultant alloy would contain 2.5% W, 11% Cr, and 0.15% C. The nickel, which contributes to phase stability, would be held to a maximum of 0.009%. Since tungsten is not as strong a carbide former as molybdenum, a reactive element addition might be required. The candidate reactive elements that have potential for low activation are Si, Ta, Ti, and V. For this study vanadium was selected based on its ability to form the stable $M_{23}C_6$ phase.[35]

The reduction of the impurity elements, e.g., niobium, is not as straightforward as elemental tailoring. To get a sense of the impurity level practically achievable, chemical analyses were obtained on ultrapure heats of steels. Results of these analyses suggest that the desired compositional limits for the impurity elements can be obtained using existing technology.

The recommended compositional limits for commercial HT-9 and the low activation ferritic steel based on the HT-9 chemistry is shown in Table 6.1-4 along with the limits for the impurity elements.

Physical Properties - The recommended physical properties for the low activation ferritic steel for use in this study were assumed to be the same as those used for HT-9. This assumption was based on the fact that the low activation steel to be developed would be a chemical and microstructural analogue of HT-9.

Nuclear Properties - The pertinent nuclear properties of the low-activation structural material should also be very similar to the reference ferritic steel (HT-9).

Welding/Fabrication - The welding/fabrication characteristics of the low-activation ferritic steel should be similar to those for the reference alloys.

Unirradiated Mechanical Properties - Tensile data developed for 12Cr-2(Mo,W) steels shows that substituting tungsten for molybdenum produces strengths (ultimate and yield) equivalent to the same alloy with 2% Mo. In the case of the 12Cr steel with tungsten additions and/or substitutions, the creep-rupture strength was found to be similar to that of the 12Cr-2Mo steel and higher than that of the Sandvik HT-9.[36,37] Based on these data, the unirradiated mechanical properties for the low activation ferritic steel were assumed to be the same as those presented for HT-9 in Section 6.1.2.1.

Effects of Radiation on Properties - There are currently no irradiation effects data on molybdenum-free martensitic steels. Therefore, the irradiation response must be inferred from the sparse data base currently available on the "conventional" class of ferritic steels, viz., 12Cr-1MoVW (HT-9), 9Cr-1MoVNb, and 2-1/4Cr-1Mo.

Based on the information available, the radiation response of the low activation ferritic steel and the standard HT-9 is assumed to be the same with regard to the effects on the mechanical properties. The published information on HT-9 shows that the tensile strength increases with irradiation until saturation occurs. The information is not sufficient to develop a trend curve. Therefore, for the purposes of this study, the irradiated mechanical properties of HT-9 were assumed to be the same as the unirradiated.

TABLE 6.1-4. RANGES OF IMPURITIES IN 9-12Cr STEELS (wt%)

Element	9Cr-1Mo Mod.[a]	HT-9[b]	Low Activation Ferritic Steel
Li	--	--	--
Be	--	--	--
B	<.001	<.001	<.0001
C	.039	0.20	0.15
N	--	.0001*-.047	0.0001
O	.005-.009	.001-.013	.0001
Na	--	--	--
Mg	--	--	--
Al	.001-.010	.006-.01	.0006
Si	.01-.03	.17-.22	.001
P	.012-.022	.006-.02	.0006
S	.004-.017	.002-.006	.0002
Cl	--	--	--
K	--	.0003*	.0003
Ca	--	--	--
Ti	<.01	.003-.01	.0003
V	--	.30	0.30
Cr	9.5-10.5	11.9-12.1	11.0
Mn	.43-.61	.50-.57	0.01
Fe	balance	balance	balance
Co	.024-.028	.02-.08	.002
Ni	.09-.42	.50-.58	.009
Cu	.01-.10	.003*-.07	.003
Zn	--	--	--
As	.0005-.004	.003-.01	.00005
Sr	--	--	--
Zr	<.001	.002	.0001
Nb	.009-.061	.002*-.01	.002
Mo	.85-1.02	1.0-1.04	.001
Ag	--	.000064‡	.000064
Cd	<.001	--	.00001
Sn	.001-.005	.001-.004	.0001
Sb	<.0005	<.0005	.00005
Ba	--	<.0002*	.0002
Ta	--	<.0004‡-<.01	.0004
W	<.01	.45-.52	2.5
Pb	<.0005	<.0001-.01	.00001
Bi	<.0005	<.0002*	.0002
Se	<.0005	--	.00005
Tb	--	<.0002*	.0002
Ir	--	.00005‡-<.0003*	.0003

[a] Heat numbers 31377, 31378, 31446, 91887 (ORNL/BRP-79/4 and ORNL SUB-4291/1, TRMCD-015 CE Report).

[b] Heat number Cartech 91353, Electralloy 9607 and 9607R2 (ESR).

‡ Neutron activation estimate from oxidation safety study at GA for EG&G.

* Virgin charge melt on HT-9 by Spark Source Mass Spectrometry (HEDL).

Concern was expressed in Sec. 6.1.2.1 about the possible magnitude of the shift in the DBTT of HT-9 as a function of neutron fluence. Based on information available for other compositions of ferritic steels, it appears that the shift in DBTT observed in HT-9 may not be as severe in all ferritic steels. Results from limited data indicate that there are compositions and microstructures within this class that exhibit smaller shifts in the DBTT and also have lower initial DBTT's.[38] Based on this potential for lowering the DBTT, it was assumed in this study that while the irradiation-induced shift in the DBTT for the low activation steel may be the same as that of the standard HT-9, the final DBTT would likely be lower.

Information now available on the swelling of ferritic steels indicates that for irradiations up to 125 dpa, very little swelling is observed.[39] However, these steels contained relatively little transmutation helium product. For irradiations that produce amounts of helium which are large but still lower than anticipated in a fusion reactor, some cavity formation was observed at doses around 40 dpa.[40] The swelling was larger in the delta ferrite phase, and therefore the microstructure should consist of fully tempered martensite or bainite. Dual phase microstructures should not be used. Since the microstructure of low activation ferritic steel is martensitic, it was assumed that the swelling resistance of this steel should be as good as HT-9 for the same temperatures and fluences used in this study.

Uncertainties for Low Activation Ferritic Steel - While there is a reasonable metallurgical basis for designing an alloy for use outside a radiation environment, this level of understanding has not been developed for use in a radiation environment. To improve the understanding, the Alloy Development for Irradiation Performance (ADIP) program is currently conducting a series of studies designed to scope the irradiation response of the ferritic steels and to provide the data base for alloy development to produce an optimized ferritic steel for fusion.

6.1.3 Vanadium Alloys

Vanadium-base alloys offer the potential of significant advantages over other candidate alloys as a fusion reactor structural material. Modest fluence irradiations under LMFBR conditions and high damage level ion irradiations have demonstrated an inherent resistance of certain vanadium alloys to

void swelling and ductility loss in comparison to most other candidate alloys. Of particular importance in projecting the potential radiation damage resistance of vanadium alloys to fusion reactor conditions is the apparent insensitivity to moderate compositional and microstructural variations. The relatively high thermal conductivity and low thermal expansion coefficient, which result for a given heat flux in lower thermal stresses compared to the other candidate alloys (Table 6.1-1). The lower stresses provide for improved wall load and lifetime capabilities. Since the mechanical strength of vanadium alloys is retained at relatively high temperatures, higher operating temperatures are projected for vanadium alloys than for austenitic or ferritic steels. Vanadium alloys produce the least impact on tritium breeding of the primary candidate alloys and selected vanadium alloys offer the potential for low long term (> 30 y) neutron-induced activation.

Major concerns regarding the use of vanadium-base alloys relate primarily to their reactivity with nonmetallic elements, e.g., oxygen and nitrogen as impurities in liquid metal systems, during accidental exposure to air at high temperature, and as contaminants during welding or fabrication. A second problem arises from the relatively limited data base for this alloy system.

The V-15Cr-5Ti alloy exhibits many favorable characteristics for the fusion reactor application, and is therefore used as a reference material in the present study. Further investigations may provide more optimized alloys with improved performance characteristics. This section presents a summary of the physical properties, mechanical properties and radiation effects data for the V-15Cr-5Ti alloy. For cases where insufficient data exist for reliable evaluation, projections based on available information are presented for use in this study. Further effort will be required to verify and more reliably predict the alloy performance for conditions of interest. Data for corrosion/compatibility of vanadium alloys in liquid metal, water, and gaseous systems are presented in Sec. 6.2.

6.1.3.1 Thermophysical Properties

The temperature-dependent thermophysical properties of V-15Cr-5Ti are given in Figs. 6.1-1 through 6.1-5. The specific heat values are for vanadium[41]; thermal conductivity, thermal expansion[42] and elastic modulus

values are those for a similar alloy (V-15Ti-7.5Cr)[43]. The melting temperature of the alloy is estimated to be 2163 K, which is slightly below that of pure vanadium. The density of V-15Cr-5Ti is 6.16 g/cm^3, and Poisson's Ratio is 0.36[43]. The electrical resistivity for the alloy is somewhat higher than that for pure vanadium.[44]

6.1.3.2 Nuclear Properties

Representative nuclear properties for the V-15Cr-5Ti alloy are presented in Table 6.1-1. The displacement damage rate is similar to the rate for the ferrous alloys. However, the helium and hydrogen generation rates in the vanadium alloy are considerably less than either the austenitic steels or the ferritic steels. Also, the heat generation rate in the first wall is considerably less than that for either of the steels.

6.1.3.3 Welding/Fabrication of Vanadium Alloys

In general, the welding characteristics of vanadium and vanadium-base alloys have not been thoroughly investigated, and the parameters for optimum welds have not been defined. However, the limited experience available on the welding of these alloys generally indicates favorable weld characteristics, provided contamination by oxygen and nitrogen is avoided. Consequently, welding must be carried out under high vacuum or in an inert gas environment. To date, vanadium-base alloys have been successfully welded using electron beam welding (EBW) and gas tungsten-arc welding (GTAW), otherwise known as tungsten inert gas (TIG) welding, techniques. Resistance welding of 1.25-mm (0.050 in.)-thick sheet has also been reported.[45]

Among the earliest reported work on the welding of vanadium-base alloys is that of Rajala in 1961,[46] who successfully joined 1.25-mm (0.050 in.)-thick sheet of V-5Ti-20Nb by GTAW in a helium environment. Tensile specimens cut from the weldments failed in the heat-affected zone or the base metal, and no serious degradation in alloy properties as a result of welding was observed.

In the mid-1960's, several studies were conducted on the welding of vanadium-base alloys for aerospace and nuclear reactor applications. Bill[45] reported good weldability of a V-20Nb-4Ti-1Zr-0.07C alloy using GTAW techniques. Post-weld tensile tests showed the weldments to have strength

properties equal to those of the unwelded base metal, and only a modest loss of ductility at and near the weld was noted in bend tests. Royster[47] performed both EBW and GTAW welding of V-20Nb and Nb-40V. Sound welds were obtained in both alloys by both techniques, although the V-20Nb alloy exhibited some slight cracking in bend tests.

Three alloys (V-7.5Cr-1.5Ti, V-15Cr-5Ti, and V-15Cr-7.5Ti) were successfully welded by Kramer et al.[48] for two different product forms. End plugs were joined to 6.6 mm (0.26 in.) diameter, 0.38 mm (0.015 in.) wall thickness tubing using GTAW procedures in Ar and He-Ar environments. The same alloys in the form of 1.5-mm (0.059 in.)-thick sheet were welded by EBW. Post-weld tensile tests and metallographic examinations indicated generally good quality welds, even though no serious attempt was made to optimize weld parameters. Similarly, Pollack et al.[49] produced satisfactory welds in unalloyed V and eight different vanadium-base alloys by GTAW. However, most of the alloys showed substantial increases in the bend ductile-to-brittle transition temperature (BDBTT) as welded, an effect apparently associated with the dissolution of interstitial O, N, and C during the welding thermal transient. Post-weld heat treatments reduced the transition temperatures to or below room temperature in all cases.

More recently, Smith et al.[50] successfully welded 12.5 mm (0.50 in.) OD x 1.25 mm (0.050 in.) wall thickness tubes of V-10Cr, V-15Cr, V-15Cr-5Ti, and V-10Ti by GTAW in helium. In addition, the dissimilar metal welds V-20Ti/V-15Cr and V-15Cr/Type 304 stainless steel were made. Gold and Bajaj[51] have investigated in some detail the ductilities of V-20Ti, V-15Cr-5Ti, and VANSTAR-7 joined by GTAW in argon. While the first two alloys produced satisfactory weldments, VANSTAR-7 exhibited cracking in the fusion zone, suggesting that further optimization of welding parameters is needed. After welding, the V-20Ti had the lowest DBTT and V-15Cr-5Ti the highest. Glenn et al.[52] conducted tensile tests and metallographic examinations on electron beam welds of six different heats of nominally pure vanadium containing various interstitial levels. The effect of interstitial content on strength was significant, but the influence on ductility was less apparent, probably because of variations in grain size.

In summary, a number of studies have indicated that vanadium-base alloys can, in general, be welded without undue difficulty using GTAW and EBW procedures. Excessive interstitial element content can lead to weld embrittlement, but with proper precautions most vanadium-base alloys can apparently be welded without the need for post-weld heat treatment. Possible exceptions are some of the more complex alloys such as the VANSTARS.

Further investigations are required to determine the sensitivities of alloy composition to weld characteristics and to define the optimum weld procedures and parameters. However, some perspective can be gained about the ability of achieving success by looking at the welding experience that exists for niobium alloys, which are comparable to vanadium in sensitivity for interstitial contamination. Niobium alloys have been used extensively by the aerospace industry in a number of applications ranging from rocket nozzle extensions to re-entry vehicles that are several feet in diameter and many feet in length. The shapes ranged from simple cylinders to complex shapes with penetrations and compound curves. To be able to weld these structures required the modification of welding techniques and equipment so that it was possible to weld in the field or to accomplish blind welding in which the back side of the weld piece could not be reached. In the vast majority of the cases, the resulting welds were successfully made and the components successfully performed their function. In the instances where difficulties were encountered, it was usually a result of the selection of the wrong alloy, and when substitution was made in the same alloy system, successful welds were obtained.

6.1.3.4 Unirradiated Mechanical Properties - V-15Cr-5Ti Alloy

Tensile Properties - Tensile properties for the recrystallized material are presented in Table 6.1-5. Details of the testing conditions and material chemistry can be found in Ref. 53. The tensile properties show only a small dependence on temperature in the range 450-750^{0}C. The strength data are plotted as a function of test temperature in Fig. 6.1-18. The total and uniform elongations of V-15Cr-5Ti exceed 16% and 12%, respectively, over the temperature range of 25-750^{0}C. The slight increase in strength in the 550-750^{0}C temperature range is due to dynamic strain aging and is regularly observed in vanadium alloys in the 0.35-0.45 T_m range. The yield

TABLE 6.1-5. TENSILE PROPERTIES OF V-15Cr-5Ti SHEET[a]

Temperature (^{0}C)	Strength (MPa)		Elongation (%)	
	0.2% YS	UTS	Uniform	Total
25	490	690	23	28
450	340	540	13	17
500	320	530	14	17
550	330	550	15	19
600	305	555	13	16
650	310	550	14	17
700	310	590	16	19
750	305	560	12	16

[a]Sheet thickness = 0.76 mm.

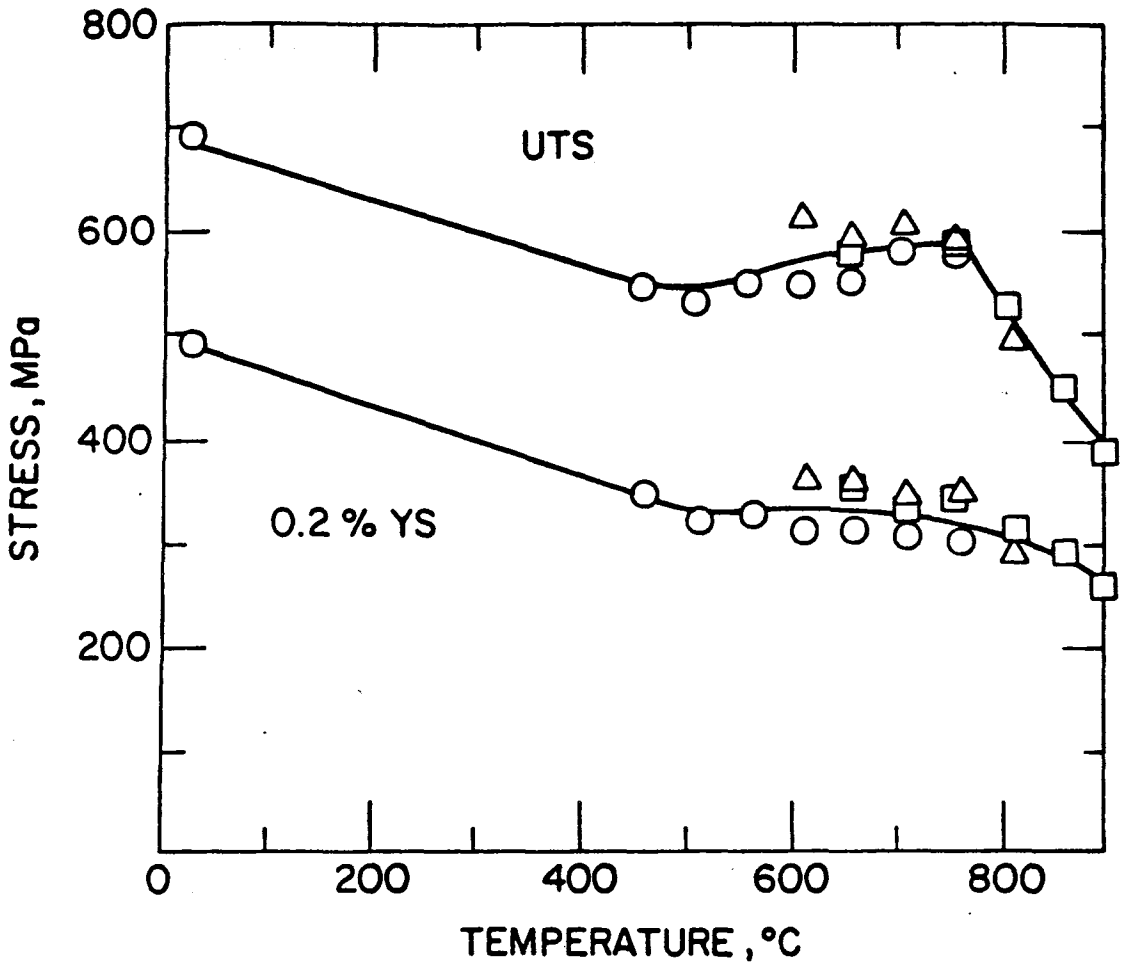


Fig. 6.1-18 Tensile properties of V-15Cr-5Ti

strength and ultimate tensile strength of the V-15Cr-5Ti alloy are compared with these properties for austenitic and ferritic steels in Figs. 6.1-6 and 6.1-7.

Thermal Creep Behavior - The creep strength of V-15Cr-5Ti sheet specimens, expressed as the stress to produce 1% strain in 1000 h, is summarized in Table 6.1-6[54]. These data have been extrapolated or interpolated from creep tests performed in ultra-high vacuum (< 10^{-8} torr) on the same heat of material for which tensile data were given above.

TABLE 6.1-6. CREEP STRENGTH OF V-15Cr-5Ti SHEET[a]

Temperature (^{0}C)	Stress for 1% Thermal Creep in 1000 h (MPa)
25 - 550	>> 400
600	> 400
650	> 400
700	380
750	330
800	~ 270

[a]Sheet thickness = 0.76 mm.

The creep data[54] are plotted in terms of rupture properties, along with data for a V-13Cr-3Ti alloy,[55] in Fig. 6.1-19. The creep strength of these two alloys appears to be comparable for the 650-750^{0}C temperature range. Rupture strains for the specimens tested at 650-800^{0}C and reported in Refs. 54 and 55 were in the 13-33% range.

Discussion - In dealing with alloys based on metals of Group V (V, Nb, Ta), it is important to consider the possibility of an unacceptably high DBTT

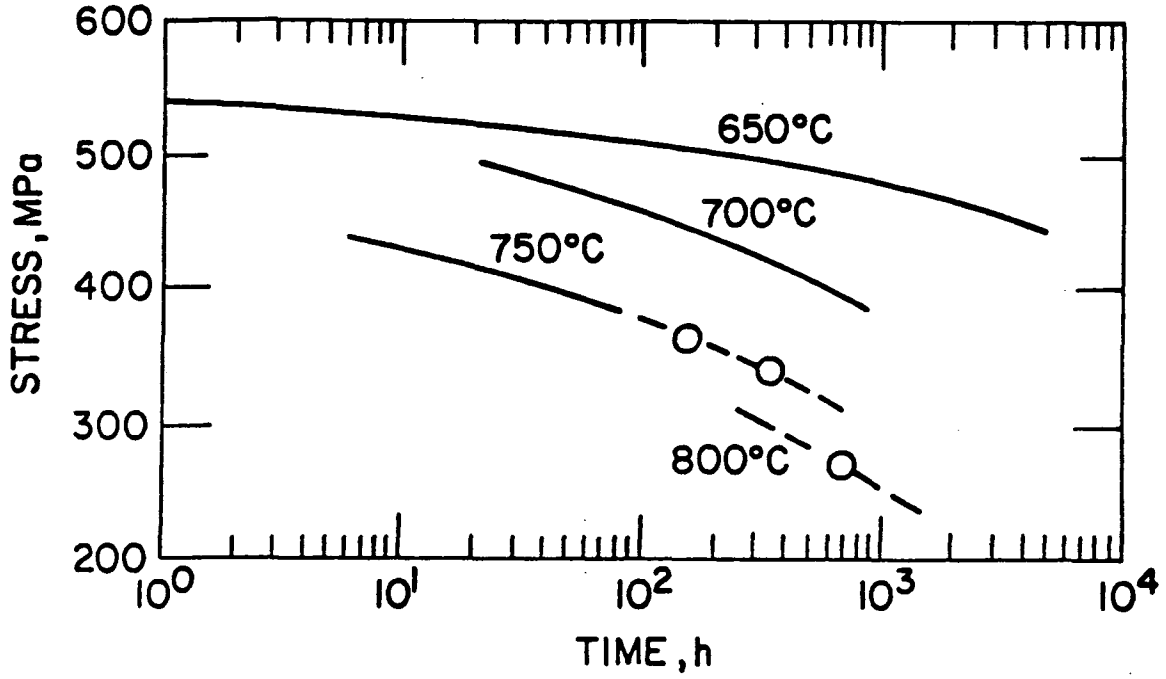


Fig. 6.1-19 Creep-rupture behavior of V-3Ti-13Cr

and the consequences of nonmetallic contamination. The data presented in Table 6.1-5 show very high uniform and total elongations (23 and 28%, respectively). While not definitive in establishing the DBTT, these values and the 100% ductile shear failure mode reported in Ref. 53 for these specimens suggest the nonirradiated DBTT is well below room temperature. In addition, intentional increases of up to 1200 wppm oxygen to these specimens did not induce brittle (cleavage) behavior at room temperature. These results, albeit limited, do not indicate a problem for the V-15Cr-5Ti alloy over the temperature range of interest to this study.

The mechanical properties of V-15Cr-5Ti may also be enhanced by strain hardening. Strain hardening is known to be a potent means of increasing the strength of metal alloys, including the bcc refractory metal alloys.[56,57] The levels of strength increase which can be realized are comparatively less than those attainable in face-centered-cubic metal alloys, such as stainless steels or aluminum alloys.

Strain hardening is regularly used to advantage with the Group VI (Mo, W) bcc alloys where an additional advantage is gained by the lowering of the DBTT. In reviewing the elevated temperature creep data for the refractory metals, however, Begley et al.[58] found that, for temperatures above about ~0.4 T_m, V, Nb and Ta-base alloys exhibited inferior time-dependent strength in the strain hardened condition compared to the fully recrystallized, fine grain microstructural condition. This partially explains why essentially all long-time mechanical property testing is carried out on fully recrystallized V, Nb or Ta alloys. This practice has been biased in the past by the fact that the applications of interest have usually been at quite high temperatures (to $\gtrsim$0.45 T_m) in space power conversion systems.

The relationship of strain hardening of vanadium alloys with temperature was discussed in Ref. 59. It seems likely that a minimum increase of 20% could be attained over the tensile properties presented in Tables 6.1-5 and 1-6. Recommended values for the temperature dependent ultimate and yield strength of the V-15Cr-5Ti alloy are presented in Figs. 6.1-6 and 6.1-7. In view of the fusion radiation environment, it is probably prudent to assume this strain hardening increment would be stable only to ~500°C (~0.35-0.36 T_m). However, at that temperature, and probably to $\gtrsim$ 600°C, additional strengthening will be realized due to the radiation-induced production of matrix-hardening dislocation microstructures.

6.1.3.5. Radiation Effects

In general, the data base for vanadium-base alloys is much more limited than for the other candidate alloys; however, data are more extensive than for the other low activation alloy candidates. Since vanadium alloys were once considered as possible fuel cladding for fast breeder reactor applications, most of the data used in this study was obtained from those investigations. The V-15Cr-5Ti alloy was originally developed in the fast breeder reactor program. Although this alloy was found to be highly radiation damage resistant, it does not necessarily represent an optimized alloy. Efforts are continuing to develop vanadium base alloys with improved radiation damage resistance.

Swelling - The projected swelling response of the V-15Cr-5Ti alloy is based on neutron (fast reactor) and ion irradiation data. Vanadium and

vanadium alloys exhibit peak swelling at ~525^{0}C under fast neutron irradiation. Neutron irradiation to ~ 20 dpa for V-15Cr-5Ti and ~ 35 dpa for V-20Ti indicated no tendency for swelling. Experiments have shown that titanium concentrations of only a few percent greatly suppress swelling compared to unalloyed vanadium.(60) Swelling resistance has been demonstrated in a number of vanadium alloys, including V-15Cr-5Ti and V-15Ti-7.5Cr irradiated to ~425^{0}C and 30 dpa. A few isolated cavities were observed in both alloys after irradiation at 550 to 600^{0}C to a fluence of 40 dpa. The low number density of the voids produced negligible swelling.(61,62)

Resistance to swelling has been observed under both single and dual-ion irradiations at high damage levels. Ion irradiations using 3-4 MeV $^{51}V^{+}$ and $^{58}Ni^{++}$ ions on V-15Cr-5Ti over the temperature range of 400 to 725^{0}C at damage levels of up to 205 dpa tend to verify the results of the lower neutron damage studies.(64,65) Dual-ion irradiations (3 MeV $^{51}V^{+}$ + degraded 0.83 MeV He^{+} ions, 3 to 50 appm He/dpa or 3 MeV $^{58}Ni^{++}$ + 0.25 MeV He^{+} ions, 9.3 appm He/dpa) of the V-15Cr-5Ti alloy to 125 dpa result in negligible swelling (0.1%) for irradiation temperatures to at least 725^{0}C. (62,63)

Experimental results on the swelling of vanadium and selected vanadium-base alloys are summarized in Fig. 6.1-20. Although these data are limited, comparison with swelling data under similar conditions for either PCA or HT-9 indicate lower swelling for the vanadium alloy. Effects of helium are also projected to be less for the V-CR-Ti alloys since the helium generation rate is much less than for PCA or HT-9. Based on this limited data and the comparison with irradiation data for the other alloys, the projected bilinear swelling curve for the V-CR-Ti alloys is given in Fig. 6.1-11.

Radiation Creep - The radiation creep characteristics of V-20Ti at 650^{0}C following irradiation at 585^{0}C to fluences of 2 x 10^{22} cm^2 indicate no effect on the minimum creep rate of the unirradiated alloy.(61) For purposes of the present study, the creep characteristics of VCrTi are assumed to be similar to those for HT-9. The temperature dependence has been modified by the ratio of the absolute melting temperatures of the two alloys.

Mechanical Properties - Only limited information exists on the effect of irradiation on the mechanical properties of the V-15Cr-5Ti alloy. Therefore, the predicted mechanical response of this alloy is based partially on results

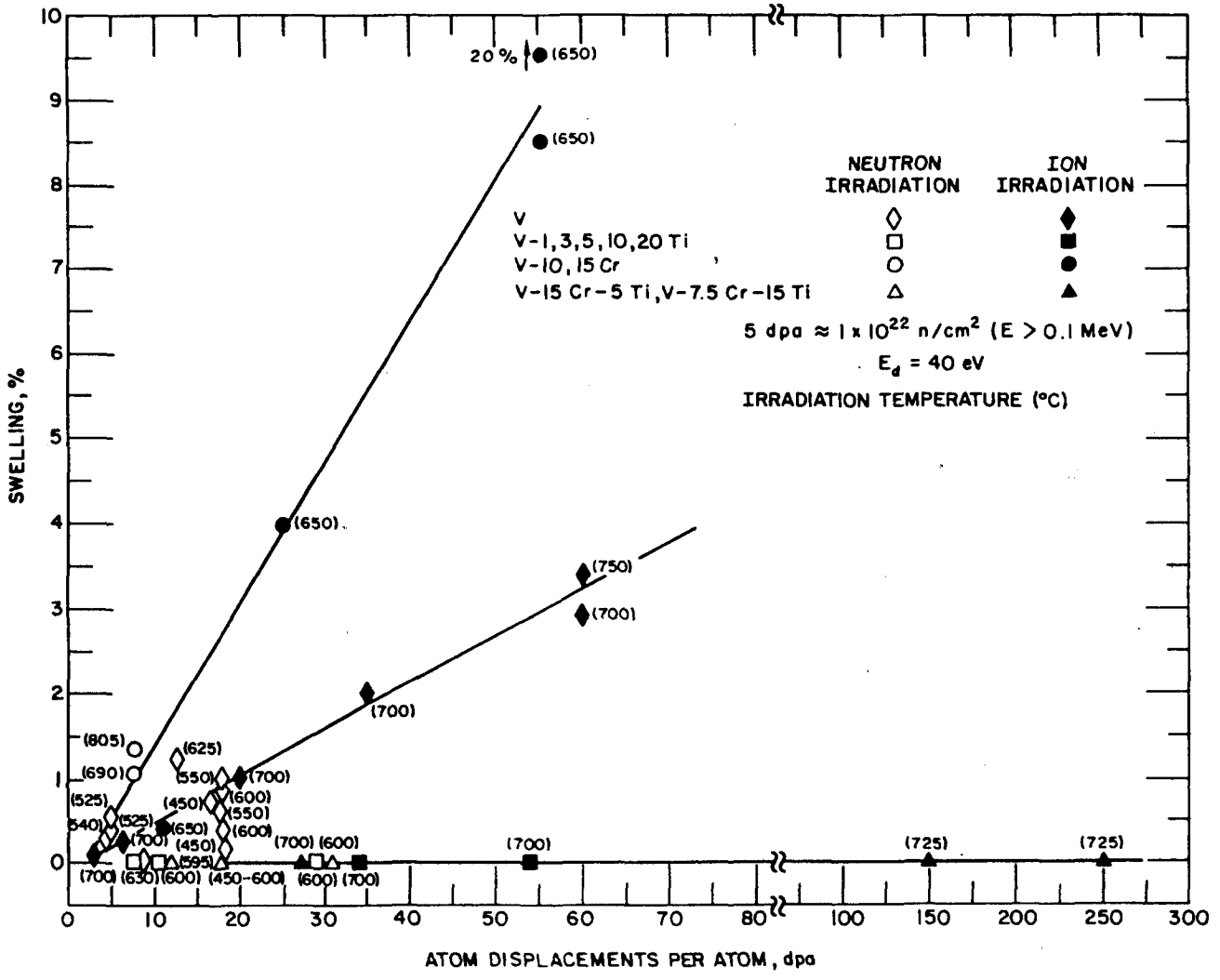


Figure 6.1-20. Swelling of vanadium and vanadium-base alloys on neutron and ion irradiation.

from other vanadium-base alloys, e.g., V-20Ti, Vanstar 7 (V-9Cr-3Fe-1Zr), and other V-Cr-Ti ternaries.

Increases in the ultimate and yield strength of several alloys have been observed after neutron irradiation at temperature to 750-800^{0}C and fluences of 10^{21} to $6x10^{22}$ cm^{-2} (0.5 to 30 dpa).[60,64] For example, the V-15Ti-7.5Cr alloy exhibited ~25% increase in yield stress when tested at 600^{0}C, after irradiation at 600^{0}C to a fluence of ~$4x10^{21}$ cm^{-2} (~3 dpa).[65] Also, the tensile properties of several ternary alloys, viz., V-2Cr-10Ti, V-5Cr-5Ti, V-5Cr-10Ti and V-15Cr-5Ti, have been shown to be insensitive to composition over the temperature range of 25-800^{0}C even after low fluence irradiations.[66] Therefore, the unirradiated tensile properties are used as a basis for obtaining design stress limits for the BCSS.

Loss of ductility caused by radiation hardening, helium embrittlement or increases in the DBTT is a major concern for all alloys, including the vanadium-base alloys. Again, data for the vanadium alloy system are quite sparse; however, results from several investigations have been reported. The data generally indicate that although substantial reductions in ductility (total and uniform elongation) are observed in V-Cr-Ti, V-Ti and V-Cr alloys after irradiation, significant (a few percent) residual ductility is retained. Carlander[65] reported elongations of 8-20% for V-15Ti-7.5Cr at 25-750^{0}C after irradiation to 3 dpa at 600^{0}C. Bohm[66] reported total elongations of 2-3% at temperatures of 25-400^{0}C after irradiation of V-15Cr-5Ti and three other V-Cr-Ti alloys at 100^{0}C to ~1 dpa. Higher residual ductilities were observed after testing at 400-800^{0}C. Wiffen[67] reported total elongations for Vanstar 7 of > 5% after irradiation at 70, 500 and 700^{0}C to fluences of ~1 dpa and testing at temperatures of 25 to 650^{0}C. Wiffen also reported similar results for V-10Cr after testing at 400 and 650^{0}C. Several investigators[60,61,65,68,69] have reported even higher residual ductilities in V-Ti alloys after irradiation to ~30 dpa, e.g., typical uniform elongation of 5-10% and total elongation of 10-20%. Tanaka[68] has reported results on the effects of helium preinjection (on 90 and 200 appm) on the irradiated (17 dpa) properties of V-20Ti. Uniform elongations of 5, 12, and 3% were observed after irradiation and testing at 400, 575 and 700^{0}C, respectively, with 200 appm He. A significant helium effect was observed only at the highest temperature.

More recent irradiations of V-15Cr-5Ti at 375,550, and 600^{0}C to 5 dpa have indicated severe embrittlement when tested at 25 and 375^{0}C.[64] This embrittlement is tentatively attributed to possible sulfur concentrations (> 3%) were observed on the fracture surfaces. Additional investigations of unirradiated material from the same test heat indicated extensive intergranular fracture with > 10% sulfur on the fracture surface. This heat of material also contained a large amount (~1200 wppm) of oxygen. Intergranular fracture was not observed with higher purity V-15Cr-5Ti (unirradiated) when tested in a similar manner.

For purposes of the present study, it is assumed that the strength of the V-15Cr-5Ti alloy will increase upon irradiation at reactor temperatures. Therefore, the ultimate, yield, and creep strength for the alloy in the unirradiated condition can be used for the design allowable stresses.

Existing data indicate that the DBTT of vanadium alloys will remain below room temperature during irradiation. Since DBTT shifts are typically observed to saturate at relatively low fluences, it is assumed for the present study that this constraint is not critical for the VCrTi alloy.

A maximum design temperature limit of 750^{0}C is recommended for V-15Cr-5Ti for the present study. This limit is based on helium embrittlement which is commonly observed in metals at temperatures > 0.5 T_m. A margin of ~50^{0}C results in the allowable limit of 750^{0}C.

6.1.3.6 Low Activation Considerations

Vanadium, alloyed with either tungsten, chromium, silicon or titanium, will meet the Class B and/or C criteria for waste storage.[1] Therefore, the need for development of low activation alloys that exists for the ferritic steel and the manganese steels does not exist for the vanadium-base alloys. For the vanadium alloys, the issue is not whether one can develop a low activation alloy, but whether the impurity elements can be maintained at a low enough level for the alloy to be considered low activation. Niobium concentrations as low as 4 wppm or less are considered attainable.

REFERENCES FOR SECTION 6.1

1. R. W. Conn et al., "Report of the DOE Panel on Low Activation Materials for Fusion Applications," UCLA Center for Plasma Physics and Fusion Engineering, PPG-728, June 1983.

2. D. L. Smith et al., "Fusion Reactor Blanket/Shield Design Study," ANL/FPP/79-1, Argonne National Laboratory, pp. 4-8 (1979).

3. Anon., Aerospace Structural Metals Handbook, Ferrous Alloys - Type 316 and 317, Metal and Ceramics Information Center, Battelles Columbus Laboratories, p. 1307-5 (1974).

4. J. W. Davis, editor, Material Handbook for Fusion Energy Systems, U.S. Department of Energy, p. AB02-3201 (1982).

5. T. K. Chu and C. Y. Ho, "Thermal Conductivity and Electrical Resistivity of Eight Selected AISI Steels," Thermal Conductivity, 18 pp. 79-104 (1978).

6. C. F. Lucks and H. W. Deem, "Thermal Properties of 13 Metals," ASTM STP-227 (1958) and D. E. Furman, "Thermal Expansion Characteristics of Stainless Steels between 300 and 1000^{0}C," Journal of Metals 188 (1950).

7. F. Garofalo, "Temperature Dependence of the Elastic Moduli of Several Stainless Steels," Proceedings BSTM, 60, pp. 738-749 (1960).

8. D. N. Braski and P. J. Maziasz, "The Tensile Properties of Unirradiated Path A - PCA," Alloy Development for Irradiation Performance - Semiannual Progress Report, DOE/ER-0045/9, pp. 63-70 (February 1983) and DOE/ER-0045/10, pp. 49-52 (October 1983).

9. P. J. Maziasz and D. N. Braski, "Swelling of Path A - PCA Irradiated to 10 dpa in HFIR," Alloy Development for Irradiation Performance - Semiannual Progress Report, DOE/ER-0045/8, pp. 98-117 (September 1982).

10. Personal Communication, R. F. Mattas and D. L. Smith, January 1983.

11. R. L. Klueh and M. L. Grossbeck, Tensile Properties and Swelling of 20% Cold Worked Type 316 Stainless Steel Irradiated in HFIR, Alloy Development for Irradiation Performance - Quarterly Progress Report DOE/ER-0045/6, pp. 58-69 (July 1981) and Semiannual Progress Report DOE/ER-0045/9, pp. 71-77 (February 1983).

12. E. E. Bloom and F. W. Wiffen, "The Effects of Large Concentrations of Helium on the Mechanical Properties of Neutron Irradiated Stainless Steel," Journal of Nuclear Materials, 58, pp. 171-184 (1975).

13. R. L. Klueh and M. L. Grossbeck, "Tensile Properties and Swelling of 20% Cold Worked Type 316 Stainless Steel Irradiated in HFIR," Alloy Development for Irradiation Performance, Semiannual Progress Report DOE/ER-0045/10, pp. 60-66 (October 1983).

14. R. L. Klueh and M. L. Grossbeck, "Tensile Properties of U.S.S.R. Austenitic Stainless Steel After Low Temperature High Flux Reactor Irradiation," Alloy Development for Irradiation Performance - Semiannual Progress Report, DOE/ER-0045/8, pp. 266-275 (September 1982).

15. R. L. Klueh and M. L. Grossbeck, "A Comparison of the Irradiated Tensile Properties of a High-Manganese Austenitic Steel and Type 316 Stainless Steel," J. Nucl. Mater., 122 & 123, pp. 294-298 (1984).

16. S. N. Votinov et al., "Effects of Neutron Irradiation on Mechanical Properties of EP-838 and 316 Steels," Fizika i Khimiya Obrabotki Malerialov, 1, p. 50 (1981), (English Translation ORNL-TR-4812).

17. D. J. Mazey et al., "Observations of the Microstructure of a 8% Manganese Stainless Steel (ICL 016) Before and After Irradiation with 46 MeV Nickel Ions," J. Nucl. Mater., 107, p. 2 (1982).

18. M. Snykers and E. Ruedl, "The Influence of Helium on the Swelling Behavior by Electron Irradiation of a Mn-Cr Austenitic Stainless Steel," J. Nucl. Mater. 103 & 104, p. 1075 (1981).

19. R. M. Boothby, D. R. Harries, and T. M. Williams, "Precipitation and Void Swelling in Nickel-Manganese Austenitic Stainless Steels," J. Nucl. Mater. 115, p. 16 (1983).

20. D. S. Gelles and F. A. Garner, "Swelling Behavior of Manganese Bearing Steel AISI 216," Alloy Development for Irradiation Performance: Semiannual Progress Report for Period Ending March 31, 1984, ORNL, DOE/ER-0045/12, pp. 55-58 (July 1984).

21. J. W. Davis, editor, Materials Handbook for Fusion Energy Systems (1983) density p. AA01-3304, thermal expansion p. AA01-3114.

22. Personal Communication, J. W. Davis - proposed datasheet for Materials Handbook for Fusion Energy Systems.

23. T. K. Chu and C. Y. Ho, op. cit.

24. J. E. Chafey and J. B. Wattier, "Estimation of Allowable Design Stress Values for 12Cr-1Mo-0.3V Steel," General Atomic Company Report GA-A14610.

25. J. L. Straalsand and D. S. Gelles, "Assessment of the Performance Potential of the Martensitic Alloy HT-9 for Liquid Metal Fast Breeder Reactor Applications," presented at Topical Conference on Ferritic Alloys for Use in Nuclear Energy Technologies, Snowbird, Utah, June 19-23, 1983.

26. R. J. Puigh and G. L. Wire, "In-Reactor Creep Behavior of Selected Ferritic Alloys," presented at Topical Conference on Ferritic Alloys in Nuclear Energy Technologies, Snowbird, Utah, June 19-23, 1983.

27. T. Lauritzan et al., Effects of Irradiation on the Mechanical Properties of Ferritic Alloys HT-9 and 2.25 Cr-1Mo," presented at Topical Conference on Ferritic Alloys in Nuclear Energy Technologies, Snowbird, Utah, June 19-23, 1983.

28. T. V. Marston, "Use of Ferritic Steels in Light Water Reactor Plants," presented at Topical Conference on Ferritic Alloys in Nuclear Energy Technologies, Snowbird, Utah, June 19-23, 1983.

29. W. L. Hu and D. S. Gelles, "Miniature Charpy Impact Test Results for the Irradiated Ferritic Alloys HT-9 and Modified 9Cr-1Mo," presented at Topical Conference on Ferritic Alloys in Nuclear Energy Technologies, Snowbird, Utah, June 19-23, 1983.

30. J. W. Davis and D. J. Michel, Proceedings of the Topical Conference on Ferritic Alloys for Use in Nuclear Energy Technologies, AIME, June 1984.

31. T. Wada, "The Effects of Tungsten on Mechanical Properties and Hardenability of 2.25Cr-1Mo Steel," Climax Molybdenum Company of Michigan, 1-323-02, July 1982.

32. E. J. Vineberg and T. B. Cox, "Development of a Ferritic Low-Carbon Steel for Elevated Temperature Service," Proceedings of the Topical Conference on Ferritic Alloys for Use in Nuclear Energy Technologyes, AIME, pp. 291-298, June 1984.

33. H. Schneider, "Investment Casting of High Hot-Strength 12% Chromium Steel," Foundary Trade Journal, 108, p. 562 (1960).

34. J. Briggs and T. Parker, "The Super 12% Cr Steels," Climax Molybdenum Company of Michigan, 6 (1965).

35. R. L. Klueh and E. E. Bloom, "Alloy Development for Fast Induced Radioactivity Decay for Fusion Reactor Applications," Oak Ridge National Laboratory, ORNL/TM-8994, March 1984.

36. P. Billard et al., "Relationship Between Microstructural Evolution, Mechanical Properties and Creep Behavior of 9%Cr-2%Mo-Nb-V Ferritic Steel," Proceedings of the Topical Conference on Ferritic Alloys for Use in Nuclear Energy Technologies, AIME, pp. 425-434, June 1984.

37. E. Vineberg, "Rupture Strength, Phase Stability, and Weldability Characteristics of Duplex Structure 12Cr-(Mo,W) Steels," Climax Molybdenum Company of Michigan, Report 1-323-01, July 1982.

38. J. R. Hawthorne, J. R. Reed, and J. A. Sprague, "Post-irradiation Fractur Toughness Tests of ESR Alloy HT-9 and Modified 9Cr-1Mo Alloy for UBR Reactor Experiments," Alloy Development for Irradiation Performance: Semiannual Progress Report for Period Ending March 31, 1984, Oak Ridge National Laboratory, DOE/ER-0045/12, pp. 86-89 (1984).

39. D. S. Gelles, "Swelling in Several Commercial Alloys Irradiated to Very High Neutron Fluence," J. Nucl. Mater., 122 & 123, pp. 207-213 (1984).

40. J. M. Vitek and R. L. Klueh, "Microstructure of HFIR-Irradiated 12Cr-1MoVW Ferritic Steel," Proceedings of the Topical Conference on Ferritic Alloys for Use in Nuclear Energy Technologies, AIME, pp. 551-558, June 1984.

41. Y. S. Touloukian, editor, Thermophysical Properties of High Temperature Solid Materials, The MacMillan Company, New York (1967).

42. F. L. Yaggee et al., "Thermal Expansivities, Thermal Conductivities, and Densities of Vanadium, Titanium, Chromium, and Some Vanadium Base Alloys," Journal of the Less-Common Metals, 19, pp. 39-51 (1969).

43. R. E. Gold et al., "Technical Assessment of Vanadium Base Alloys for Fusion Reactor Applications," Westinghouse Electric Corporation Report COO-4540-1, Vol. 2 (April 1978).

44. B. A. Loomis and D. L. Smith, "Evaluation and Development of Vanadium Base Alloys for Fusion Reactor Applications," Alloy Development for Irradiation Performance - Semiannual Progress Report DOE/ER-0045/10, pp. 87-90 (October 1983).

45. R. W. Bill, "Evaluation of Vanadium Alloy V-20Cb-4Ti-1Zr-0.07C Sheet," McDonnell Aircraft Report 513-414 (September 1964).

46. B. R. Rajala et al., "The Development of Improved Vanadium Base Alloys for Use at Temperatures to 1800^{0}F," J. Less-Common Metals 3, 489 (1961).

47. D. M. Royster, R. Manning, Jr., and A. Dysleski, "Mechanical Properties, Oxidation Characteristics, and Weldability of Two Uncoated and Coated Vanadium-Base Alloys," NASA Technical Note NASA TN-D-2616 (February 1965).

48. W. C. Kramer, W. R. Burt, Jr., F. J. Karasek, J. E. Flinn, and R. M. Mayfield, "Vanadium Alloy Screening Studies and Fabrication of V-15 w/o Ti-7.5 w/o Cr Tubing for Nuclear Fuel Cladding," Argonne National Laboratory Report ANL-7206 (August 1966).

49. W. Pollack et al., "Development of High Strength Vanadium Alloys - Final Report," Westinghouse Electric Corporation, WCAP-3487-16 (June 1967).

50. D. L. Smith, R. H. Lee, and R. M. Yonco, "Investigation of Nonmetallic Element Interactions in Vanadium-Alloy/Lithium Systems," Proc. Second Intl. Conf. on Liquid Metals in Energy Production, Richland, WA (April 1980).

51. R. E. Gold and R. Bajaj, "The Weldability of Candidate Vanadium Alloys for Fusion Applications," Proc. Third Topical Meeting on Fusion Reactor Materials, Albuquerque, NM (September 1983).

52. T. G. Glenn, G. W. Elliston, C. M. Edstrom, and W. L. Johns, "Effect of Chemistry on the Weldability of Commercially Pure Vanadium Sheet," Rockwell International Energy Systems Group, RFP-3217 (February 1982).

53. Tensile curves developed using data obtained from following four references. The curves were increased by 20% to allow for strength enhancement as a result of strain hardening.

    a) R. F. Mattas, et al., "Elevated Temperature Tensile Properties of V-15Cr-5Ti Containing Helium Induced by Ion Bombardment and Tritium Decoy," Proceeding of the 2nd Topical Meeting on the Technology of Controlled Nuclear Fusion, CONF-760935-P1, Volume 1, p. 199 (1977).

    b) A. T. Santhanan, et al., Journal of Nuclear Materials, 18, p. 302 (1973).

    c) R. E. Gold, op. cit.

    d) R. E. Gold and R. L. Ammon, "Mechanical Property Evaluations of Patch C Vanadium Scoping Alloys," Alloy Development for Irradiation Performance - Quarterly Progress Report DOE/ER-0045/6, pp. 96-105 (July 1981).

54. The creep data was extracted from the following sources:

    a) R. E. Gold and R. Bajaj, "Mechanical Property Evaluation of Path C Vanadium Scoping Alloys," Alloy Development for Irradiation Performance - Semiannual Progress Report DOE/ER-0045/9, pp. 122-141 (February 1983).

    b) R. Bajaj and R. E. Gold, "Mechanical Property Evaluations of Path C Vanadium Scoping Alloys," Alloy Development for Irradiation Performance - Semiannual Progress Report DOE/ER-0045/10, pp. 74-80 (October 1983).

55. M. Schirra, "Creep and Creep-Rupture Behavior of Vanadium Based Alloys," United States - Euratom Fast Reactor Exchange Program, EURFNR-1449 (1977).

56. T. E. Tietz and J. W. Wilson, "Behavior and Properties of Refractory Metals," Stanford University Press, Stanford, CA (1965).

57. B. A. Wilcox, "Basic Strengthening Mechanisms in Refractory Metals," Refractory Metals Alloys, Tetallurgy and Technology, I. Machlin, et al., editors, Plenum Press, NY, pp. 1-40 (1968).

58. R. T. Begley, D. L. Harrod and R. E. Gold, "High Temperature Creep and Fracture Behavior of the Refractory Metals," Refractory Metal Alloys, Metallurgy and Technology, J. Machlin, et al., editors, Plenum Press, NY, pp. 41-84 (1968).

59. M. Abdou, et al., "Blanket Comparison and Selection Study - Interim Report," report ANL/FPP-82-1, Argonne National Laboratory (October 1983).

60. R. Carlander, et al., "Effects of Radiation on Substructure and Mechanical Properties of Metals and Alloys," American Society for Testing and Material publication ASTM-STP529, p. 399 (1973).

61. A. T. Santhanam, et al., Defects and Defect Clusters in B.C.C. Metals and Their Alloys, Nuclear Metallurgy, 18, p. 302 (1973).

62. B. A. Loomis and G. Ayrault, "Cavity Formation in Single- and Dual-Ion Irradiated V-15Cr-5Ti Alloy," Damage Analysis and Fundamental Studies - Quarterly Progress Report DOE/ER-0046/12, pp. 194-205 (February 1983).

63. B. A. Loomis and D. L. Smith, "Swelling of V-15Cr-5Ti Alloy on Single- and Dual-Ion Irradiation," Alloy Development for Irradiation Performance - Semiannual Progress Report, DOE/ER-0045/12, pp. 66-71 (March 31, 1984).

64. R. Bajaj and R. E. Gold, Report WAESD-TR- , Westinghouse Electric Corp. (1983).

65. R. Carlander, Argonne National Laboratory (unpublished data).

66. H. Bohm et al., ASTM Spec. Tech. Publ. 426, p. 95 (1967).

67. F. W. Wiffen, Nucl. Metall. 18, 176 (1973).

68. M. F. Tanaka et al., J. Nucle. Mater. 103 & 104, 895 (1981).

69. J. A. Horak, report ORNL-5082, Oak Ridge National Laboratory (1975).

BLANKET COMPARISON AND SELECTION STUDY

SECTION 6.2 - CORROSION/COMPATIBILITY

SECTION 6.2

TABLE OF CONTENTS

PAGE NO.

6.2 Corrosion of Structural Alloys.....6.2-1

6.2.1 Liquid Metal Corrosion/Compatibility.....6.2-1

6.2.1.1 Corrosion of Austenitic and Ferritic Steels.....6.2-2

6.2.1.2 Corrosion of Vanadium-Base Alloys.....6.2-11

6.2.1.3 Corrosion in Li.....6.2-13

6.2.1.4 Criteria and Corrosion Limits.....6.2-17

6.2.1.5 Mechanical Property Degradation.....6.2-19

6.2.1.6 Mass Transfer Model.....6.2-22

6.2.1.7 Corrosion Inhibition in Liquid Metal Systems.....6.2-23

6.2.2 Molten Salt Corrosion.....6.2-26

6.2.2.1 Nitrate Salts.....6.2-26

6.2.2.2 FLIBE.....6.2-26

6.2.3 Water Corrosion.....6.2-27

6.2.4 Gaseous Corrosion/Compatibility.....6.2-27

REFERENCES.....6.2-29

LIST OF FIGURES FOR SECTION 6.2

FIGURE NO.	TITLE	PAGE NO.
6.2-1	Depth of internal corrosion of Type 316 stainless steel exposed to flowing lithium	6.2-7
6.2-2	Arrhenius plot of corrosion rate data for Types 304 and 316 stainless steel, PCA alloy, HT-9 alloy and Fe-9Cr-1Mo steel exposed to flowing lithium	6.2-10
6.2-3	Arrhenius plot of corrosion rate data for austenitic Type 316 stainless steel and ferritic HT-9 alloy and Fe-9Cr-1Mo steel in flowing Pb-17Li	6.2-12
6.2-4	Effect of temperature on the corrosion rate of PCA and HT-9 alloy in flowing lithium	6.2-15
6.2-5	Effect of temperature on the corrosion rate of 20% cold worked Type 316 stainless steel and HT-9 alloy in flowing Pb-17Li	6.2-16

LIST OF TABLES FOR SECTION 6.2

TABLE NO.	TITLE	PAGE NO.
6.2-1	SUMMARY OF SYSTEM AND MATERIAL CONDITIONS FOR CORROSION DATA IN LIQUID LITHIUM	6.2-3
6.2-2	SUMMARY OF SYSTEM AND MATERIAL CONDITIONS FOR CORROSION DATA IN LIQUID LEAD - 19 AT.% LITHIUM	6.2-4
6.2-3	PRELIMINARY DESIGN TEMPERATURE LIMITS (°C)	6.2-18

6.2 Corrosion of Structural Alloys

Critical aspects of liquid metal, molten salt, water, and gaseous corrosion/compatibility for the three candidate structural materials have been evaluated as part of the present study. The following assessments and analyses have been conducted.

- Liquid Metal Corrosion/Compatibility (Li and Li-Pb)
  - Lithium
  - 17Li-83Pb

- Molten Salt
  - Nitrate Salt
  - FLIBE

- Water (200-350°C)
  - Vanadium Alloys
  - Cold-Worked Austenitic Steel

- Gaseous Corrosion/Compatibility Vanadium
  - Helium with Impurities
  - Air or Oxygen Characteristic of Accident Conditions
  - Hydrogen Plasma Environment

6.2.1 Liquid Metal Corrosion/Compatibility

Compatibility considerations with liquid metals have a major influence on the material selection and operating limitations of the structural materials for liquid metal fusion reactor blankets. The two major compatibility concerns arising from the use of liquid metals, such as lithium or Pb-17Li, are (a) corrosion/mass transfer, and (b) degradation of mechanical strength of the containment material. The corrosion and mass transfer of structural material can be deleterious in any application of circulating liquid metals. Corrosion in the form of uniform or selective dissolutive, intergranular penetration, and interstitial-element transfer to and from the liquid metal can result in (a) significant wall thinning/wastage and (b) deposition of corrosion products that may cause severe flow restrictions and excessive accumulation of radio-

active material in unshielded regions. The former consequence results in a loss of mechanical integrity and the latter phenomenon would increase pumping power requirements, decrease the energy conversion efficiency, and complicate system maintenance. The corrosion and mass transfer problem varies for different combinations of containment material and liquid metals and depends on many variables. These include the liquid metal and its purity (i.e., concentration of N, O, C, etc. in the liquid metal); composition and microstructure of the containment material; temperature; exposure time; and system parameters such as flow velocity (including MHD effects), ΔT (difference in temperature across the circulating system), surface area and temperature profile of the system, and material combination (i.e., bimetallic or monometallic system).

Deterioration of the mechanical properties of structural materials can result from the influence of the environment itself and the effects of microstructural and compositional changes that occur in the material during long-term high-temperature exposure to the liquid metal environment. Liquid metals can influence the surface-active properties of the material through liquid metal embrittlement (LME), oxidation, nitridation, or carburization-decarburization phenomena, all of which can alter the near-surface deformation behavior and thus affect mechanical properties such as fatigue crack propagation, creep ductility, etc. The long-term exposure of the material to a liquid metal environment can change bulk properties, primarily through compositional and microstructural modifications caused by selective corrosion, interstitial-element transfer, and thermal aging. The environmental interactions and the nature and extent of the changes in the material depend on liquid metal chemistry, temperature, time, and material composition and microstructure.

6.2.1.1 Corrosion of Austenitic and Ferritic Steels

Experimental data on the corrosion behavior of several austenitic and ferritic steels in liquid lithium and Pb-17Li environments have been obtained in static liquid-metal pots or capsules as well as in circulating systems such as thermal convection loops (TCLs) and forced-circulation loops (FCLs).[6.2-1] The experimental conditions for the corrosion data in liquid lithium and Pb-17Li are summarized in Tables 6.2-1 and 6.2-2, respectively. Relatively little data are available on corrosion in Pb-17Li environment. Recent experiments with static and circulating Pb-17Li indicate that the dissolution rates are substantially greater than those in lithium. In both environments, auste-

TABLE 6.2-1. SUMMARY OF SYSTEM AND MATERIAL CONDITIONS FOR CORROSION DATA IN LIQUID LITHIUM

Lab.[a]	Ref.	System Conditions							Material Conditions			Results[e]
		Type[b]	Material	Velocity m/s	Impurity	Temp. °C	ΔT °C	Max. Time h	Material[c]	TMT[d]	Stress	
ORNL	1-3	Capsule	316 SS, HT-9, 9 Cr, 2 1/4 Cr	-	0, N < 175 ppm Li_3N Addition	400-700	-	10,000	Same	2 1/4 Cr	-	W,P
ORNL	4-9	TCL	316 SS, HT-9	0.03	0, N < 175 ppm	500-650	150	16,000	PCA, 316 SS, LRO, HT-9, 9 Cr	PCA	-	W/L/ M, P
ORNL	10	TCL	Alloy 800	0.03	0, N < 175 ppm	500	175	3,000	Path B, Alloy 800	-	-	W, M
UW	11	FCL	316 SS	0.45-1.36	N = 50-120 ppm O = 275 ppm	440,490	110-195	4,000	Same	-	-	W/L
SU	12	FCL	304 SS	0.16-0.85	-	421-612	10-212	100	Same	-	-	W
ANL	13,14	FCL	304 SS	~0.03	N = 50-250 ppm	427-482	70	5,000	316 SS, 304 L, PCA HT-9, 9 Cr	316 CW	Yes	W, P
WARD	15	FCL	Austenitic	1.82	-	538	150	1,000	316 SS, 304 SS, 9 Cr	-	-	W/L
JAERI	16	TCL	-	0.03	-	600	100	2,500	316 SS	-	-	W
CSM	17,18	Pot	Armco Iron	-	N > 3000 ppm	565-592	-	135	Same	-	Yes	P
CSM	19	Pot	304 L	-	N > 1.2%	800	-	35	Same	-	-	P
ISPRA	20	Capsule	γ-Mn Steel	-	N = 20 ppm	600	-	6,000	Same	-	-	P

[a] ORNL - Oak Ridge National Laboratory
UW - University of Wisconsin
SU - Syracuse University
ANL - Argonne National Laboratory
WARD - Westinghouse Advanced Reactor Division
JAERI - Japan Atomic Energy Research Institute
CSM - Colorado School of Mines
ISPRA - Commission of European Communities, Joint Research Centre

[b] TCL - Thermal Convection Loop
FCL - Forced Circulation Loop with Cold Trap Purification System

[c] Materials other than the lithium system construction material are listed.

[d] Materials tested in various thermo-mechanical conditions are listed.

[e] W = weight loss in $mg/m^2.h$.
W/L = weight change as a function of loop position.
P = depth of corrosive penetration.
M = mass transfer/deposition.

TABLE 6.2-2. SUMMARY OF SYSTEM AND MATERIAL CONDITIONS FOR CORROSION DATA IN LIQUID LEAD - 19 at.% LITHIUM

Lab.[a]	Ref.	System Conditions						Material Conditions		Results[d]
		Type[b]	Material	Velocity	Temp.	ΔT	Max. Time	Material	TMT[c]	
ORNL	6.2-23	Capsule	316 SS, HT-9	-	300-700	-	5,000	316 SS, HT-9	-	W, P
ORNL	6.2-24	TCL	316 SS, HT-9	0.03	500	150	500	316 SS, HT-9	-	W, P
ANL	6.2-27	FCL	Carbon Steel/304 SS	0.03	427,454	150	3,500	316 SS, PCA, HT-9 9Cr	PCA 316 SS	W, P
CSM	6.2-1	Pot	2 1/4 Cr	-	300-600	-	135	2 1/4 Cr	-	P
ISPRA	6.2-1	Pot	Armco Iron	-	400-600	-	6,000	316 L	-	P
		Capsule	304 L	-	400	-	1,000	316 L	-	P
USSR	6.2-25	Pot	-	-	430	-	1500	16Cr15Ni2MO,13Cr1Mo	-	W
		TCL	-	0.18	430	60	1500	16Cr15Ni2Mo,13Cr1Mo	-	W

[a] ORNL - Oak Ridge National Laboratory
ANL - Argonne National Laboratory
CSM - Colorado School of Mines
ISPRA - Commission of European Communities, Joint Research
USSR - Contribution to the Phase IIA of the INTOR Workshop

[b] TCL - Thermal Convection Loop
FCL - Forced Circulation Loop

[c] Materials tested in various thermo-mechanical treatment are listed.

[d] W - Weight change in $mg/m^2.h$
P - depth of corrosive penetration

nitic stainless steels, e.g., types 316 and 304 stainless steel and primary candidate alloy (PCA) develop a ferrite layer due to preferrential depletion of nickel and to a lesser extent chromium from the surface, whereas, the ferritic steels, e.g., HT-9 alloy and Fe-9Cr-1Mo steel, show little or no surface degradation. Intergranular penetration of both ferritic and austenitic steels has been observed in lithium containing high (> 1000 ppm) concentrations of nitrogen.

For most studies, the corrosion behavior has been evaluated in terms of weight loss per unit surface area and/or as depth of internal corrosive penetration. However, the rate of weight loss is expressed either as the average value for the entire time of exposure or as the steady state value attained after the initial transient period of high dissolution rates. For austenitic stainless steels, the difference between the average and steady-state dissolution rates can be significant, particularly for long exposure times. Furthermore, the system parameters, such as flow velocity, ΔT, surface area of the liquid metal system, and liquid metal purity, vary significantly for the various investigations. The existing experimental data are insufficient to accurately establish the influence of the different material and system parameters on the corrosion behavior of structural materials. It is possible, however, to qualitatively assess the corrosion behavior of various alloys and determine the preliminary operating temperature limits for circulating and static liquid-metal systems.

Lithium System

Corrosion tests in static lithium systems have been used in identifying and characterizing the various reactions between lithium and containment materials and to study the influence of lithium purity, stress, and material variables on these interactions. For most studies, the corrosion behavior in static lithium has been evaluated in terms of the depth of internal corrosive penetration. The dissolution and mass transfer behavior has been investigated from data in circulating lithium systems. The significant results from corrosion tests in lithium are summarized as follows:

(a) The dissolution rates for austenitic stainless steels reach steady-state values after an initial period of 1500-3000 h characterized by

higher, rapidly changing rates. The weight loss, W (mg/m^2), may also be expressed by a power-law relationship with time, t, given by $W = kt^n$. For the data in TCL and FCL systems, the average value of the time exponent is 0.7.

(b) The weight loss for ferritic HT-9 alloy and Fe-9Cr-9Mo steel in circulating lithium systems follows a linear relationship with time.

(c) The dissolution rates of austenitic stainless steels in FCL are a factor of 5 to 20 greater than in TCL. All FCL systems used for corrosion studies are equipped with a cold trap purification loop. The greater dissolution rates in FCL may be attributed to greater mass transfer/deposition behavior because of the cold trap/purification loop. The dissolution rates for ferritic steels are comparable in TCL and FCL.

(d) After exposure to flowing lithium, the austenitic stainless steel develop a very porous ferrite layer due to preferential depletion of nickel and to a lesser extent chromium from the material. Data indicate that the thickness of the ferrite layer may increase linearly with time. Figure 6.2-1 shows the thickness of the ferrite layer for type 316 stainless steel in TCL and FCL systems. The results yield a growth rate of ~ 100 μm/y at 482°C in FCL and 55 μm/y at 570°C in TCL. Furthermore, the ferrite layer on austenitic stainless steel is very weak and may spall off under thermal transients or cyclic straining.

(e) The ferritic steel show little or no internal corrosive attack in low-nitrogen flowing lithium. The near-surface region shows slight depletion of chromium.

(f) Weight loss for 20% cold-worked type 316 stainless steel is a factor of ~ 2 greater than that for annealed steel.

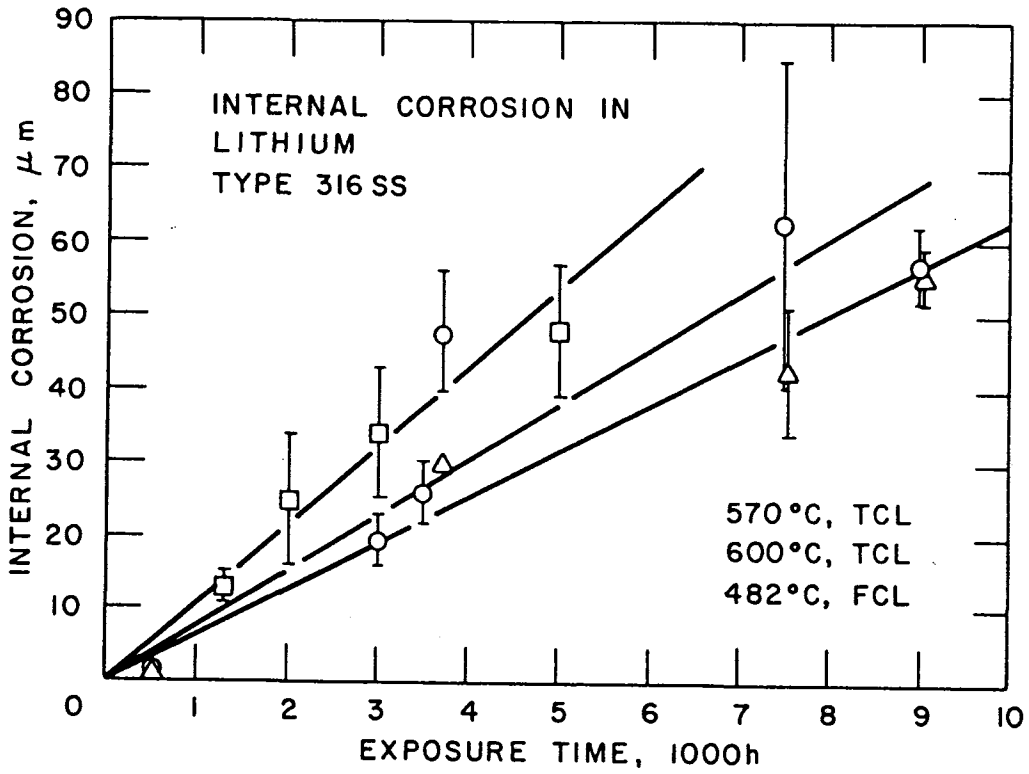


Figure 6.2-1. Depth of internal corrosion of Type 316 stainless steel exposed to flowing lithium.

(g) Dissolution rates of austenitic steels increase with an increase in the nickel content. Weight loss for cold-worked PCA is a factor of ~ 1.5 greater than that for cold-worked type 316 SS.

(h) For FCL systems, the dissolution rates for ferritic steels are an order of magnitude lower than the steady-state dissolution rates for annealed type 316 stainless steel. However, dissolution rates for ferritic HT-9 alloy and type 316 stainless steel are comparable in TCL system. Additional long-term data are needed to establish the effects of material composition on corrosion.

(i) Weight loss for types 304 and 316 stainless steel in flowing lithium are comparable, although the data from different FCL systems show significant scatter.

(j) FCL data indicate that the dissolution rates in flowing lithium increase with an increase in flow velocity or an increase in ΔT in the system. However, the data are insufficient to obtain accurate correlations.

(k) Limited data in FCL show that the weight loss for both ferritic and austenitic steels in lithium containing 50 ppm nitrogen is a factor of 2 to 5 lower than in lithium with 200 ppm nitrogen. Similar changes in nitrogen content in TCL show no effect on corrosion. Additional data are required to establish the effects of lithium purity on corrosion and mass transfer in flowing lithium systems.

(l) The variation in dissolution rates with temperature have been investigated for type 316 SS in TCL systems at 500, 550, and 600°C. An Arrhenius plot of dissolution rate data yield an activation energy of 38 kcal/mole. The data from FCL systems show considerable scatter and yield values of activation energy between 11 and 30 kcal/mole. However, such analyses are based on data obtained for $<$ 100 h exposure time or $<$ 50°C difference in exposure temperature. Long-term data in FCL systems under controlled liquid metal and system

conditions, at temperatures between 350 and 500°C are needed to determine the variation in dissolution rates with temperature.

Because of the many variables, viz., lithium purity, temperature,ΔT, surface area, etc., it is difficult to compile a definitive data set of measured corrosion rates in flowing lithium. An activation energy of 38 kcal/mole measured for TCL systems is comparable to the value of 36 kcal/mole observed for type 316 stainless steel and Alloy 800 in large flowing sodium systems. When exposed to high temperature sodium, Alloy 800 develops a porous ferrite layer similar to that observed for type 316 stainless steel in flowing lithium. Figure 6.2-2 shows an Arrhenius plot of dissolution rate data for various ferritic and austenitic steels in flowing lithium. The data in lithium were normalized for velocity effects using the relationship for corrosion of stainless steel in sodium. In sodium, the corrosion rate, R, is expressed as

$$R \alpha (2.97 + 2.71\ V) \qquad [6.2\text{-}1]$$

where V is the velocity in m/s. The data for FCL systems fall within a wide scatter band. The Arrhenius temperature dependence for the dissolution rate of type 316 SS in TCL and FCL systems was assumed to be the same as that observed in sodium. The results show that the dissolution rates for type 316 SS in FCLs are an order of magnitude greater than in TCL systems. Dissolution rates for HT-9 alloy in TCL and FCL are identical and similar to those for type 316 SS in TCLs.

Pb-17Li System

Relatively little data are available for corrosion and mass transfer behavior of structural materials in Pb-17Li. The significant results from corrosion tests in static capsules and FCL system are as follows:

(a) The dissolution rates for austenitic Type 316 SS in flowing Pb-Li are an order of magnitude greater than in lithium. At temperatures between 410 and 460°C, the weight loss in Pb-Li follows a power-law relationship with time (the time exponent vary between 0.5 and 0.9). A linear increase in weight loss is observed at 500°C.

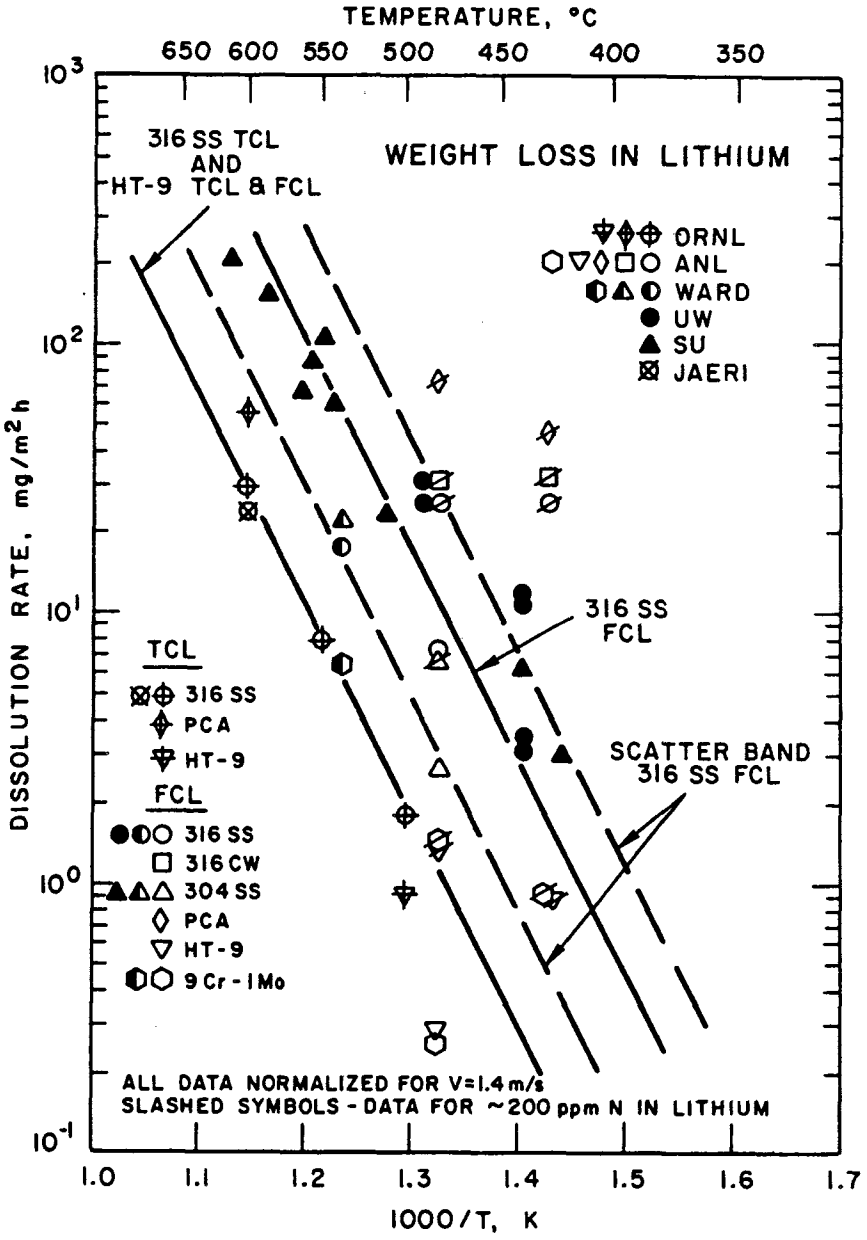


Figure 6.2-2. Arrhenius plot of corrosion rate data for types 304 and 316 stainless steel, PCA alloy, HT-9 alloy and Fe-9Cr-1Mo steel exposed to flowing lithium.

(b) The weight loss for both ferritic and austenitic steels in static Pb-Li capsules is significantly lower than that in flowing Pb-Li and reaches a constant value after a short period of 1000 to 3000 h.

(c) The weight loss for ferritic HT-9 alloy and Fe-9Cr-1Mo steel in flowing Pb-Li are a factor of 5 to 10 lower than type 316 SS and shows a linear relationship with time.

(d) Dissolution rates of PCA are a factor of 4 greater than those for the annealed or cold-worked Type 316 SS.

(e) After exposure to flowing Pb-Li the austenitic steels develop a very porous and weak ferrite layer which spalls off easily. The ferritic HT-9 alloy and Fe-9-Cr-1Mo steel show little or no internal corrosion.

(f) Figure 6.2-3 shows an Arrhenius plot of the dissolution rate data for annealed and cold-worked type 316 SS, PCA, HT-9 alloy, and Fe-9Cr-1Mo steel in flowing Pb-17Li. The data are normalized for velocity effects using Eq. 6.2-1. The temperature dependence is identical to that observed for lithium TCLs or for sodium systems.

6.2.1.2 Corrosion of Vanadium-Base Alloys

The data base for corrosion of vanadium-base alloys in lithium and 17Li-83Pb is very limited. Therefore, the projected corrosion resistance of vanadium and vanadium base alloys in lithium and Li-Pb is based on (1) very limited experimental data for the systems of interest, (2) reported corrosion resistance vanadium alloys in sodium, (3) reported corrosion resistance of similar refractory alloys, viz., niobium and tantalum alloys, in lithium, and (4) reported low solubilities of group V and VI refractory metals in lithium and lead.

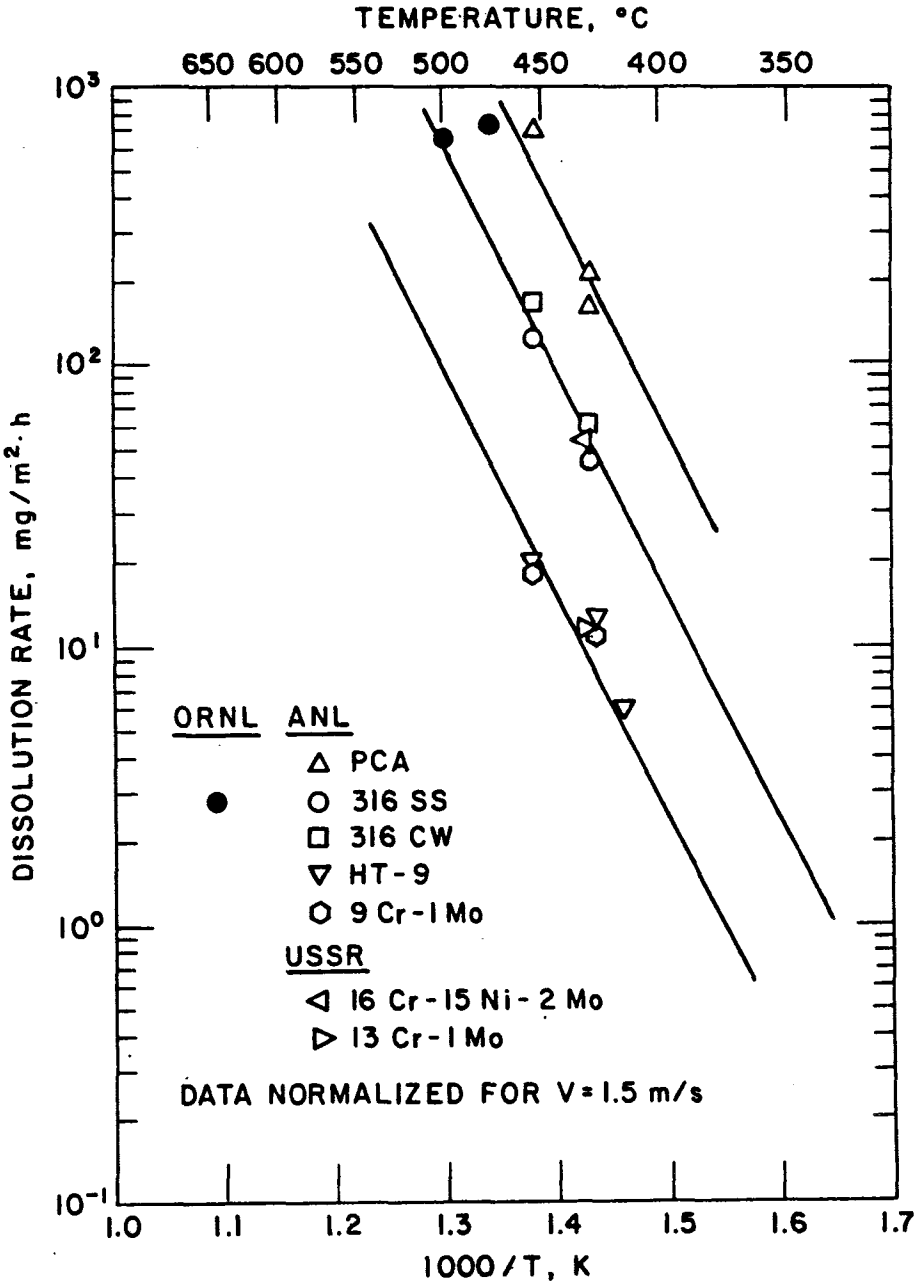


Figure 6.2-3. Arrhenius plot of corrosion rate data for austenitic Type 316 stainless steel and ferritic HT-9 alloy and Fe-9Cr-1Mo steel in flowing Pb-17Li.

6.2.1.3 Corrosion in Li

The data on corrosion of vanadium alloys in lithium derive primarily from (1) forced-circulation loop tests conducted by Pratt-Whitney and others in the late 50's and early 60's as part of the space power program; (2) capsule tests conducted in the early 1960's at Oak Ridge National Laboratory as part of the high temperature materials program, and (3) forced-circulation loop tests conducted at Argonne National Laboratory in the late 70's and early 80's as part of the fusion materials program. The most relevant data related to the current vanadium-lithium blanket concept is the high temperature results from Pratt-Whitney.[6.2-2] Several refractory metals and alloys were tested. Unalloyed vanadium was exposed for 1170 h in a forced circulation loop at a lithium velocity of 4 m/s, maximum temperature of 870°C, and a loop ΔT of 220°C. The reported corrosion indicated for vanadium was "nil", but this is not well defined. Since the lowest reported corrosion value reported for other alloys in this series of tests is 0.15 mg/cm^2, it seems reasonable to assume that the designation "light" corresponds to <0.1 mg/cm^2 and "nil" probably corresponds to approximately 10^{-2} mg/cm^2 or less. A corrosion rate of 10^{-2} mg/cm^2 in 1000 h corresponds to ~0.1 $mg/m^2 \cdot h$ or ~0.1 $\mu m/y$.

The limited capsule tests conducted at Oak Ridge National Laboratory [6.2-3] (816°C) confirm the corrosion resistance of vanadium to lithium. Redistribution of nonmetallic elements, e.g., oxygen was observed in these tests; however, vanadium did not exhibit the severe penetration rate when oxygen was present as was observed for tantalum and niobium.

The forced circulation loop tests at Argonne (600-650°C) further confirmed the corrosion resistance of vanadium and V-15Cr-5Ti alloy.[6.2-4] Very small weight changes in the vanadium samples were observed. The primary focus of these tests were on the redistribution of nonmetallic impurity elements. Acceptable nonmetallic impurity levels were maintainable in the small loop. Scoping tests indicated that the tensile properties of high purity alloys were not significantly altered after exposures at 600 to 650°C for up to 500 h. However, degradation of the ductility was observed in some less pure alloys after exposure. It was not clear from the limited tests whether the loss of ductility was caused by thermal aging or the lithium environment. Also, the cause of the different response of similar alloys was not determined. The

test loop, which was constructed of V-10Cr alloy, was operated for a total of ~30,000 h at a maximum temperature of 600-650°C.

Much of the available corrosion data are for temperatures above those considered in the current blanket study. Also, insufficient data exist to develop a temperature dependent corrosion curve. For purposes of the current study, it is recommended that the same activation energy be assumed for the vanadium-lithium system as is proposed for the ferritic and austenitic steels. From this assumption, the inferred corrosion rate at 816°C from the Pratt-Whitney data, and an order of magnitude increase for conservatism, the recommended corrosion curve for the V-15Cr-5Ti alloy in lithium is given in Fig. 6.2-4. No significant differences between unalloyed vanadium and the V-15Cr-5Ti alloy are expected in the lithium environment. Future work will be required to confirm these predicted corrosion rates. Also, the ability to control nonmetallic elements at acceptable levels in a large heat transport system must be demonstrated.

Corrosion in Li-Pb

No data on the corrosion of vanadium alloys in Li-Pb has been reported in the literature. Based on the low solubilities of the group V and VI refractory metals in both lithium and lead, good corrosion resistance for vandium is predicted. Initial scoping tests at Argonne National Laboratory indicate no measurable corrosion of V-15Cr-5Ti alloy after 2300 h exposure at ~430°C. (6.2-5) Additional tests are currently in progress.

For purposes of the BCSS, recommended corrosion rates for V-15Cr-5Ti alloy have been developed from the vanadium-lithium corrosion data and the observed differences in the corrosion rates of ferritic steels in lithium-lead and lithium. The proposed corrosion rate for ferritic steel in LiPb is a factor of 50 higher than that for lithium. The recommended curve for V-15Cr-5Ti in LiPb is, therefore, taken as a factor of 50 higher than that for vanadium in lithium (see Fig. 6.2-5). While the existing information leads one to believe the corrosion resistance of vanadium in LiPb is quite good, obviously supporting data will be required.

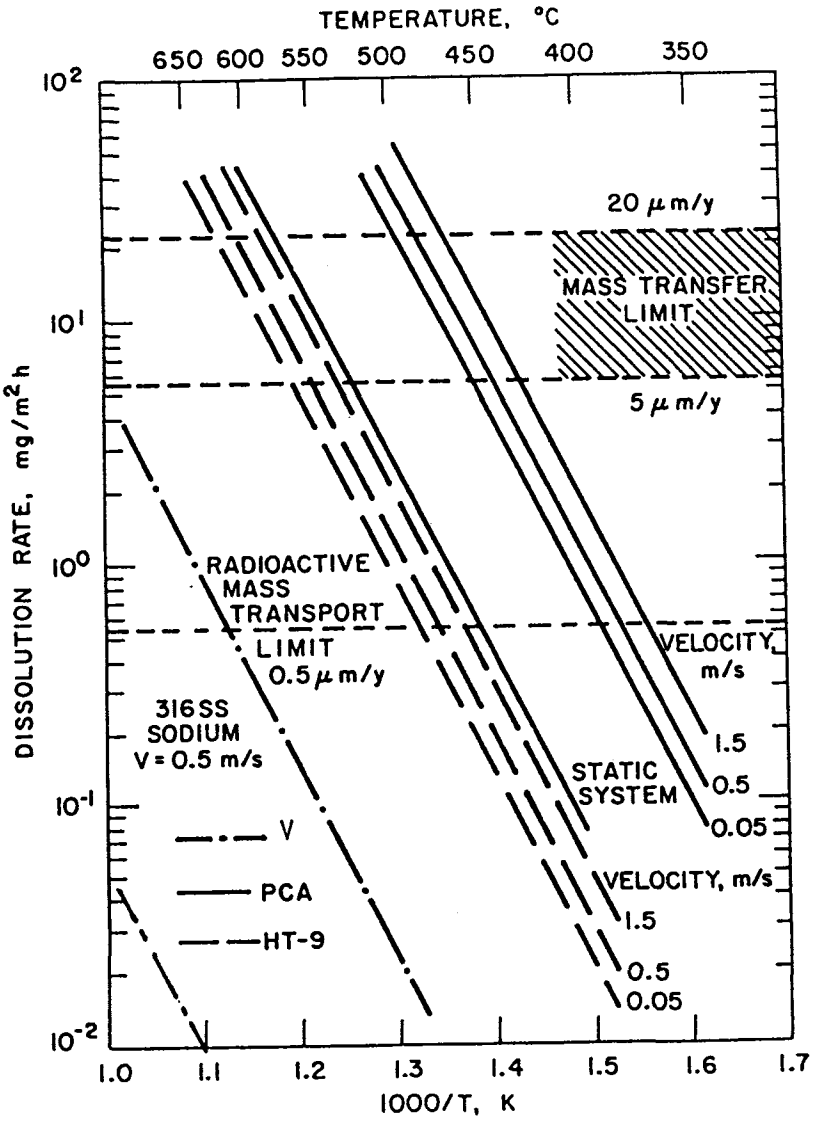


Figure 6.2-4. Effect of temperature on the corrosion rate of PCA and HT-9 alloy in flowing lithium.

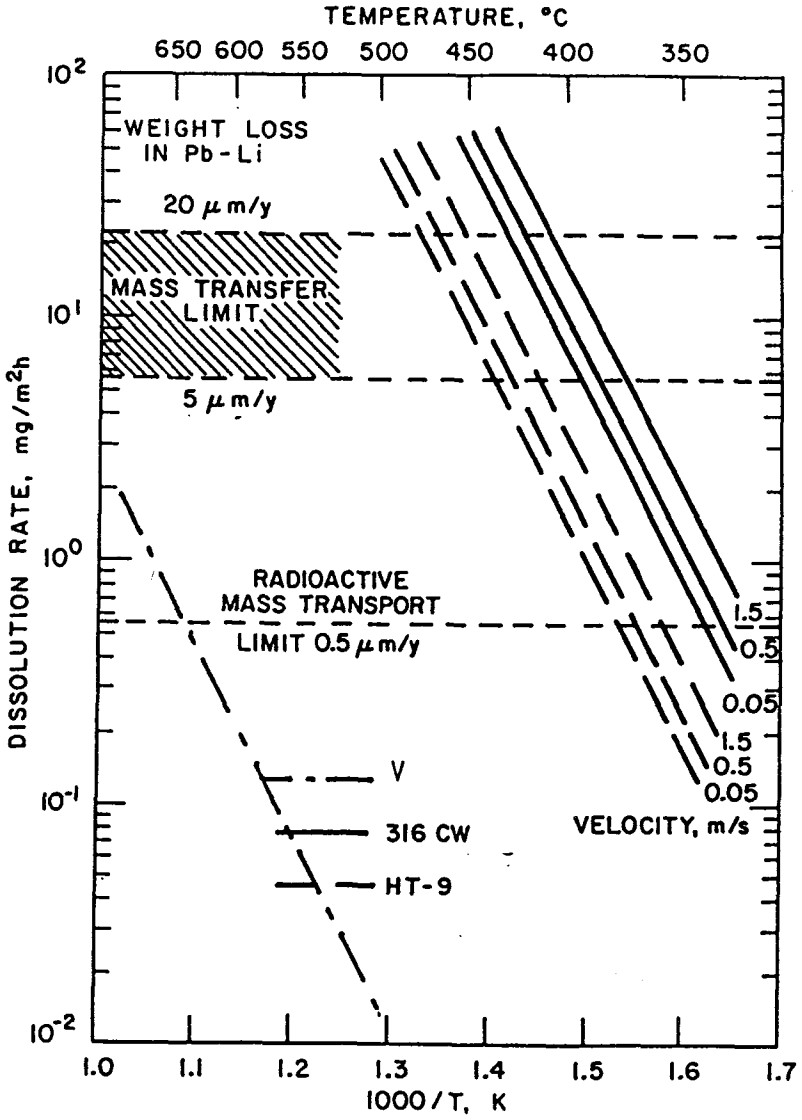


Figure 6.2-5. Effect of temperature on the corrosion rate of 20% cold worked Type 316 stainless steel and HT-9 alloy in flowing Pb-17Li.

6.2.1.4 Criteria and Corrosion Limits

The corrosion and mass transfer behavior of structural material depend on the particular liquid-metal blanket design. For example, a liquid metal system used solely for tritium breeding could be isothermal and have very low flow velocities, but the use of liquid metals as a coolant requires large ΔT and high flow velocities. Ideally, the corrosion limits for an isothermal semistagnant blanket system should be determined from the static lithium data and the FCL data should be used to establish the limits for coolant system. However, even the semistagnant tritium breeding blanket systems will have some ΔT and thus mass transfer, particularly during off normal operating conditions. Some blanket systems are designed for use as a coolant during loss of flow accidents. Consequently, the design limits for the static or semistagnant blanket systems are determined from the TCL data.

The basis for a temperature limit from corrosion considerations can be from radioactive mass transport, wall thinning/wastage, or mass transfer and deposition. Based primarily on sodium-cooled fact breeder reactor experience, corrosion rate limits for hands-on maintenance of intermediate heat exchangers (IHX) are estimated to be ~ 0.5 μm/y. Although these values are based on austenitic steel systems, the same values are recommended as limits for other structural materials in the present study. The temperature limit for radioactive mass transport based on a corrosion rate of 0.5 μm/y is too restrictive for acceptable performance of most blanket systems considered. Therefore, remote maintenance of the IHX (or steam generators if no IHX is used) will probably be required.

The allowance for wall thinning/wastage from corrosion of breeder reactor cladding is generally established as 10% of the wall thickness. A similar value is recommended for the present blanket study. This criterion is not likely to be restrictive for section thicknesses > 1 mm during a service life of 2 to 3 years.

Mass transfer and deposition is likely to be the most restrictive criterion for corrosion under most conditions of interest. Based primarily on experience from operation of liquid sodium systems, a reference corrosion limit of 5 μm/y is recommended. Plugging flow perturbations, and effects on pumps and values are frequently encountered when corrosion rates significantly exceed this limit. One must also consider enhanced corrosion caused by local

"hot spot" conditions and high velocity or turbulent regions. The benefits of using an optimistic limit of 20 μm/y is evaluated for comparison.

Figures 6.2-4 and 6.2-5 show the Arrheneus temperature dependence of the corrosion rates for PCA alloy and HT-9 in lithium and Pb-17Li environments. The curves for PCA alloy in lithium were obtained from the type 316 stainless steel data in FCLs and applying a factor 3 increase (i.e., a factor of 2 increase for cold-worked 316 SS and a factor of 1.5 increase for PCA alloy) in dissolution rates. The curve for the static lithium system was obtained from the TCL data. The operating temperature limits for static and circulating (at three different velocities) liquid metal systems are listed in Table 6.2-3. The temperatures within brackets are based on an optimistic value of allowable corrosion rate, i.e., 4 x 5 = 20 μm/y. The results show that the use of austenitic stainless steels with Pb-17 Li environment may not be practical.

TABLE 6.2-3. PRELIMINARY DESIGN TEMPERATURE LIMITS (°C)[a]

System	Flow Velocity m/s	Austenitic Steel (PCA)[b]	Ferritic Steel (HT-9)	Vanadium Alloy[c] (V-15Cr-5Ti)
Lithium				
Circulating	1.5	470 (430)	(585) 535	> 750
	0.5	480 (445)	(605) 550	
	0.05	495 (455)	(620) 565	
Static	-	575 (525)	(620) 565	> 750
Pb-17Li				
Circulating	1.5	410 (375)	450 (415)	> 750
	0.5	420 (385)	465 (425)	
	0.05	430 (395)	475 (435)	
Static	-	430 (395)	475 (435)	> 750

[a] Limits based on a uniform dissolution rate of 20 μm/y (or ~ 22 mg/m^2.h). The values within brackets correspond to a rate of μm/y.

[b] Temperature limits for Pb-17Li system are for 20% cold worked type 316 SS.

[c] Nonmetallic element transfer are expected to dominate corrosion limits.

6.2.1.5 Mechanical Property Degradation

Environmental effects on the mechanical properties of materials can be divided into two classes: the influence of the environment itself and the effects of microstructural and compositional changes that occur in the material during long-term high-temperature exposure to the environment. The influence of the environment itself on mechanical behavior of materials is evaluated by conducting mechanical tests in the liquid-metal environment of controlled purity and comparing the results with data obtained in other environments, such as air, vacuum, or inert gas. The long-term effects of environment, i.e., interstitial- or substitutional-element transfer and thermal aging, on the mechanical properties are determined by conducting tests on material that is either pre-exposed to the liquid-metal environment or thermally aged in an inert environment. Preexposure of the material is carried out in liquid metals of known purity, namely service conditions anticipated in real systems.

The tensile, creep, fatigue, and crack-growth properties of various austenitic and ferritic steels have been investigated in liquid lithium environment. Most of the data have been obtained by conducting tensile or creep tests in static lithium pots or on tube specimens filled with lithium. However, the purity of the lithium is not specified for all the tests. Corrosion phenomena, such as intergranular penetration or preferential leaching of substitutional elements, are likely to have a profound effect on mechanical properties. Studies on the corrosion behavior of materials in liquid lithium indicate that the nature and kinetics of corrosive attack, strongly depends on the impurity content in the environment. For example, it is well known that an increase in the concentration of nitrogen in lithium increases the corrosion rates and causes intergranular penetration of most materials. Consequently, mechanical property data obtained in liquid metal of unknown purity may be biased by the effects of the corrosive interactions and not representative of the anticipated service conditions.

Relatively little or no information is available on the influence of liquid Pb-17Li on the mechanical properties of materials. The influence of applied stress on the corrosion behavior and the effects of preexposure on tensile properties of materials have been investigated in Pb-17Li. However, the current assessment of the environmental effects in Pb-17Li are based on

mechanical property data obtained in liquid lead, bismuth, or lead-bismuth environments.

The significant results from these studies can be summarized as follows:

(a) Tensile and creep strength of austenitic stainless steels is not significantly affected by both static or flowing lithium. The influence on tensile ductility depends on strain rate, e.g., elongation is slightly reduced at slow strain rates ($\sim 4 \times 10^{-5} s^{-1}$).

(b) The tensile strength and, most particularly, ductility of Armco iron in static lithium are considerably lower than in vacuum. The reduction in tensile properties occurs in the temperature range of 200 to 500°C and is more pronounced at slow strain rates. At the critical temperatures the material fails by a brittle fracture mode and the elongation is ~ 5%.

(c) The creep-rupture strength of Armco iron is also reduced in lithium at temperatures < 500°C.

(d) Addition of hydrogen (up to ~ 40 ppm) in lithium has little or no effect on the tensile properties of austenitic stainless steels. Influence of other impurities (e.g., N, O, or C) in lithium is not established.

(e) Preexposure of austenitic and ferritic steels to flowing lithium reduces the tensile strength owing to the formation of a weak ferrite layer in austenitic steels or decarburization of the ferritic steels (particularly low-alloy ferritic steels).

(f) Nitrogen content in lithium plays an important role in controlling the fatigue properties of materials. Low-cycle fatigue life of austenitic and ferritic steels in low-nitrogen flowing lithium (i.e., < 100 ppm) is superior to that in air. Limited data also indicate that fatigue life is independent of strain rate in low-nitrogen lithium. However, fatigue life is significantly reduced in flowing

lithium containing > 1000 ppm nitrogen due to intergranular attack of the material. The reduction in life is greater at slow strain rates.

(g) Preexposure of medium chromium ferritic steels (e.g., HT-9 alloy) to low-nitrogen lithium has no effect on fatigue life, whereas preexposure of austenitic stainless steel to lithium reduces fatigue life because of the formation of the ferrite layer.

(h) Fatigue crack propagation rates (da/dN) for type 304 stainless steel and Fe-2¼Cr-1Mo ferritic steel are greater in static lithium than in argon. The growth rates depend on temperature and test frequency. For austenitic type 304 SS, the growth rates increase with a decrease in frequency, whereas the crack growth rates show a minima at intermediate frequencies for the Fe-2¼Cr-Mo steel. The increase in growth rates is attributed to corrosive interactions at low frequencies and due to strain-rate-induced liquid-metal-embrittlement at high frequencies.

(i) Data are not available on the mechanical behavior of materials in liquid Pb-17Li environment. Severe loss in ductility and reduction in fatigue strength have been observed for austenitic and ferritic steels wetted with liquid Pb, Bi, or Pb-Bi.

These results indicate that a low-nitrogen lithium environment itself has no deleterious effects on the mechanical properties of austenitic stainless steels. In a lithium environment of controlled purity, the tensile and creep properties are similar and the fatigue properties are superior to that in air. Limited data indicate that exposure of austenitic stainless steels to flowing lithium can reduce mechanical strength due to the formation of the ferrite layer (i.e., a reduction in the load bearing area of the material). Long-term corrosion data in flowing lithium of controlled purity are required to determine the growth rates of the ferrite layer as a function of time and temperature, and to establish an allowance for wall thinning/wastage over the service life of the component. Data are also needed on the creep-fatigue behavior of austenitic stainless steels.

The results also indicate that embrittlement of ferritic steels, particularly low-alloy steels, may occur in lithium at temperatures between 200 and 400°C. However, data are insufficient for a reliable assessment of the environmental effects on the mechanical properties of ferritic steels. For example, the low-cycle fatigue data on HT-9 alloy show that the fatigue life in low-nitrogen lithium is independent of strain rate and is superior to that in air. Fatigue crack propagation studies on Fe-2¼Cr-1Mo steel indicate that at temperatures < 500°C the crack growth rates in lithium increase with an increase in test frequencies. Also, the crack growth rates in lithium are greater than that in argon. Additional data are needed to evaluate the possible embrittlement of ferritic steels in lithium. Limited data indicate that preexposure of ferritic steels to lithium has no effect on fatigue strength, while the tensile strength is reduced due to decarburization of the steel.

No data are available to evaluate the influence of Pb-17Li environment on mechanical properties. The current assessment of environmental effects is based on data for Pb or Bi. The results indicate that Pb-17Li may significantly affect mechanical properties of materials.

6.2.1.6 Mass Transfer Model

A computer model has been developed to predict dissolution and deposition rates in a liquid metal primary coolant loop of a fusion reactor.[6.2-6] The model is general in that it can be applied to any liquid metal coolant loop as long as one provides the proper geometrical design parameters (i.e., tube diameters, surface areas, etc.). To date, we have applied the computer model to the MARS design which has 83Pb-17Li coolant and HT-9 structure. Also the considerations and methods used in this model have been used to evaluate potential mass transfer concerns in other blanket designs.

The parameters which can be included in the model are the following:

- Coolant (Li or 83Pb-17Li)
- Local Wall Temperature
- Total Temperature Difference (ΔT) in the Loop
- Coolant Velocity
- Geometry of Flow (e.g., in a Tube or Across a Tube Bundle as is the

Case for a Shell and Tube Heat Exchanger)

6.2.1.7 Corrosion Inhibition in Liquid Metal Systems

General Considerations

In certain applications corrosion rates of structural alloys in liquid metal systems may be altered by each of the following:

(1) elemental additions to the liquid metal to promote the formation of a surface layer on the exposed containment material or to reduce the activity of impurities in the liquid metal (for example, aluminum in lithium,[6.2-7] titanium in lead[6.2-8],

(2) surface modification of the containment material prior to exposure to the liquid metal (for example, aluminized ferrous alloys exposed to lithium,[6.2-9,-10] and lead[6.2-11]), or

(3) design of the liquid metal circuit to control deposition, e.g., corrosion product traps.

The first two methods modify the composition of the containment surfaces or the chemical reactivity of the liquid metal such that overall solution rates into a liquid metal are reduced.[6.2-7-6.2-12] Surface composition modification can also hinder deposition in the cold zone (and thereby reduce the plugging tendency) by increasing the required degree of supersaturation needed for precipitation because of the difference in composition between the nucleated particle in the melt and the altered surface of the cold zone containment material.[6.2-12] Of these two methods for compositional modification of a surface, use of elemental additions to the liquid metal has the advantage of being an in situ method that modifies the composition of only those surfaces that are exposed to the liquid metal. Furthermore, the coating can be renewed during service. On the other hand, the coating of the surfaces prior to liquid metal exposure allows a greater variety of surface compositions. However, such coatings can sometimes be ineffective due to adherence problems (see, for example. Ref. 6.2-11). In some cases it is not clear whether elemental additions to the liquid metal perform as true "inhibitors" or whether the elemen-

tal additions act as dissolved getters, thereby altering the activity of non-metallic impurities such as nitrogen which is known to affect corrosion rates.

One variant of the third method listed above involves the use of a cold trap on a side stream of the liquid metal circuit.[6.2-13] Such a system is designed to reduce the concentration of dissolved elements below that necessary for deposition in the mainstream. Such a procedure is therefore not a true "inhibition" technique. Indeed, it would actually lead to greater dissolution in the circuit's hot zone because of the lower solute levels and therefore be appropriate only where deposition is more of a problem than metal wastage by dissolution (but this normally is the case).

The kinetics of the deposition process is an important consideration in evaluating mass transfer control by cold trapping. The deposition rate, R_D, can usually be described as

$$R_D = k\Delta C$$

where k is the rate and ΔC is the amount of supersaturation above the critical value needed for deposition. R_D is thus related to two factors that vary oppositely with temperature and, as such, the effectiveness of a cold trap system may be limited. For example, if k decreases rapidly with decreasing temperature, the deposition rate in the cold trap may be insignificant compared to the deposition rate near the entrance to the heat exchanger. Indeed, maximum deposition at temperatures significantly higher than the minimum temperature has been experimentally observed in lithium systems.[6.2-14] Given such effects, the use of magnetic fields to preferentially trap dissolved magnetic elements may possibly be an alternate design modification for deposition control.

Corrosion Inhibition in Lithium Systems

Aluminized layers formed by additions of aluminum to lithium have been found to reduce corrosion of alloy 600 [76 Ni-8 Fe-16 Cr (wt %] in static lithium and to decrease the mass transfer of type 316 stainless steel in flowing lithium by a factor of 5.[6.2-7] Work with preformed aluminide diffusion coatings showed that such coatings reduced the attack of high-nickel alloys by flowing lithium at 400°C.[6.2-9] At this low temperature, however no real

benefit of the aluminide coatings was found for type 316 stainless and ferritic steels.[6.2-9] Nickel-bearing alloys with adherent coatings of Mo, Mo-Ti, and Al (applied from a molten sodium solution) were resistant to corrosive attack by flowing lithium at temperatures up to 900°C.[6.2-10] Furthermore, the addition of aluminum to static nitrogen-contaminated lithium decreased the corrosiveness of this melt.[6.2-15] This observation may also be interpreted such that the dominant effect of aluminum is to reduce the nitrogen activity in lithium by the formation of aluminum nitride, which is predicted. Experiments in flowing lithium systems have shown a large effect of nitrogen concentration in lithium on the corrosion rates of austenitic and ferritic steels in lithium.[2.6-16,-17]

Corrosion Inhibition in Lead-Lithium Systems

There has been no reported work on corrosion inhibition in lead-lithium. However, it is expected that the most appropriate guidance for possible ways to reduce the very corrosive nature of 17Li-83Pb comes from earlier studies with pure lead. In these experiments,[6.2-8,-11,-18,-19] the addition of titanium to lead was found to inhibit dissolution. It was thought that (in analogy with zirconium in bismuth[6.2-12,-18] the titanium reacted with the nitrogen and/or carbon of the containment steel to form a protective surface film of TiN and/or TiC.[6.2-15,6.2-20] As in the case for lithium, the dominant effect of the elemental additions may simply be to reduce the activity of nonmetallic elements whose presence enhances corrosion. If this is the case, the lithium in Li-Pb may act in a similar fashion as titanium additions; e.g., reduce the oxygen activity. The possibility of a protective iron-titanium intermetallic surface compound has also been suggested.[6.2-10] On the other hand, the use of externally applied coatings for protection against lead corrosion has not been very successful (because of adherence problems) with the exception of plasma-sprayed molybdenum on 2¼Cr-1Mo steel and aluminized specimens of the same steel.[6.2-11] In the former case, protection was afforded by the high corrosion resistance of molybdenum, and in the latter, it was probably provided by formation of protective oxide films. While oxide surface films can afford corrosion protection from lead attack,[6.2-11] certain types of oxides will not be stable in 17Li-83Pb because of its greater reducing potential.

Because of the importance of corrosion to the satisfactory performance of liquid metal blankets, further work should be conducted to evaluate the potential of possible inhibition methods. At the present time, neither a specific inhibition method nor a good estimate of the reduction in corrosion and mass transfer can be made until definitive inhibition experiments with 17Li-83Pb are performed.

6.2.2 Molten Salt Corrosion

6.2.2.1 Nitrate Salts

An adequate data base exits for design of nonnuclear nitrate salt heat transfer systems with austenitic steels to temperatures of 600°C. No data have been reported on the corrosion of high Cr ferritic steels such as HT-9 or Fe-9Cr-1Mo. The only corrosion effect observable in austenitic steel heat transfer systems with the nitrate salt is the formation of a duplex spinel/ magnetite oxide film and an uptake of oxidized chromium (+6) by the molten salt. There is no measurable thermal gradient mass transfer up to 600°C, and oxide films have resisted spalling up to 600°C in virtually all tests for times in excess of three years. For non-nuclear applications, a corrosion allowance of 13 μm/year appears adequate up to 600°C. Operation above this temperature is not realistic because of salt decomposition and steeply increasing corrosion rates. For purposes of this study it is assumed that the corrosion behavior of ferritic steel is similar to the austenitic steels; this must be verified.

The salts are somewhat conducting and, when moved through a magnetic field, will generate a voltage which can cause disassociation of the salt. Increasing the ionic content of the salt will increase the corrosion of the structure. Preliminary estimates indicate that there is no problem. However, this is based primarily on data for fluoride salts, which itself is sparse. Thus, there is an issue that the effects are worse and that restrictions on flow channel size and flow velocity would ensue.

6.2.2.2 FLIBE

The majority of the relevant corrosion data for FLIBE have been obtained with austenitic stainless steels. Based on the Molten Salt Reactor Experi-

ment, corrosion rates of Type 316 stainless steel loops containing $2LiF-BeF_2$ mixture under heat transfer conditions average about 8 μm/year at 650°C. These rates can be lowered significantly by chemically buffering the salt and/or reducing the chromium content of the steel. The high nickel alloys generally exhibit superior corrosion resistance than the austenitic steels. The high chromium ferritic steels have not been investigated.

Currently there is a great uncertainty in the FLIBE corrosion properties in a magnetic field. Further tests are required to evaluate the potential for electromagnetic effects on the corrosion by the salts.

6.2.3 Water Corrosion

Most earlier studies have concluded that vanadium alloys could not be used in pressurized water-cooled systems because of excessive corrosion. An evaluation of recent scoping data concludes that selected alloys such as VCrTi may be acceptable for use in pressurized water. Observed corrosion rates in 288°C water for 500 hours indicate corrosion rates less than an order of magnitude greater than those typically observed for austenitic stainless steels.(6.2-21)

Although austenitic stainless steels have been used extensively in pressurized water systems, stress corrosion problems have frequently been observed under certain conditions. The combination of cold-work and reduced ductility under irradiation may exacerbate this problem. Further investigations should be conducted to more thoroughly evaluate the seriousness of this problem. For the present study, it is assumed that this problem will not prevent the use of cold-worked PCA in pressurized water systems.

6.2.4 Gaseous Corrosion/Compatibility

The thermodynamic and kinetic processes for vanadium and VCrTi exposed to helium with low impurity concentrations have been evaluated. Details of this evaluation were presented in the BCSS Interim Report.(6.2-22) Since data are very limited, unalloyed vanadium has been evaluated and extrapolations to VCrTi have been made. For purposes of the present design study, it is concluded that oxidation will be excessive (unacceptable) if VCrTi is exposed to helium with greater than ~0.1 ppm moisture at temperatures above ~500°C. At temperatures below 450°C, kinetic mechanisms become controlling and may permit

limited use of VCrTi in high purity (<1 ppm H_2O) helium. This alloy is significantly more resistant to oxidation than unalloyed vanadium. An evaluation of the helium coolant cleanup indicates that the purities required here are extremely difficult to attain economically in practical systems.

The potential effects of short therm exposure of VCrTi to air and/or oxygen has been investigated to evaluate potential effects of accident conditions. No severe effects are predicted for exposures to air for a few hours at temperatures ≤650°C. However, since one oxide of vanadium melts at ~670°C, rapid attack may occur at higher temperatures. As in the case of moisture in helium, the alloy is much more resistant to oxidation than unalloyed vanadium.

The potential for hydrogen pickup in VCrTi exposed to the hydrogenous plasma environment was evaluated. The tritium inventory in vanadium exposed to projected hydrogen pressures is predicted to be sufficiently low that hydrogen embrittlement is not projected to be a problem.

REFERENCES FOR SECTION 6.2

6.2-8 M. A. Abdou et al., "Blanket Comparison and Selection Study," Argonne National Laboratory, ANL/FPP-83-1, October 1983.

6.2-2 M. S. Freed and K. J. Kelly, PWAC-355 (1961).

6.2-3 J. R. DiStefano, ORNL-3551 (1964).

6.2-4 D. L. Smith, R. H. Lee, and R. M. Yonco, Proc. Second Inter. Conf. Liquid Metal Technology in Energy Production, Richland, WA, April 20-24, 1980, pp. 2-72.

6.2-5 O. K. Chopra and D. L. Smith, Argonne National Laboratory (unpublished data, July, 1984).

6.2-6 S. Malang and D. L. Smith, "Modeling of Liquid Metal Corrosion/Deposition in a Fusion Reactor Blanket," Argonne National Laboratory, ANL/FPP/TM-192, in press.

6.2-7 P. F. Tortorelli, J. H. DeVan, J. E. Selle, and H. D. Upton, Proc. 8th Symp. Engineering Problems of Fusion Research, Vol. 3, IEEE (USA) Publ. 79CH1441-5 NPS (1979) pp. 1610-1613.

6.2-8 A. J. Romano, C. J. Klamut, and D. H. Gurinsky, Brookhaven National Laboratory (USA) Report BNL-811 (1963).

6.2-9 G. C. Burrow, M. G. Down, and C. Bagnall, J. Nucl. Mater. 103&104 (1981) 657-662.

6.2-10 M. S. Goikhman, V. F. Shatinskii, and S. V. Rybakov, Sov. Mater. Sci. (Engl. Transl.) 15 (1979) 510-511.

6.2-11 R. C. Asher, D. Davies, and S. A. Beetham, Corros. Sci. 17 (1977) 545-557.

6.2-12 O. F. Kammerer, J. R. Weeks, J. Sadofsky, W. E. Miller, and D. H. Gurinsky, Trans. AIME 212 (1958) 20-25.

6.2-13 B. G. Logan et al., "Mirror Advanced Reactor Study Final Design Report," Lawrence Livermore National Laboratory, UCRL-53480, 1984.

6.2-14 P. F. Tortorelli and J. H. DeVan, "Mass Transfer Kintics in Lithium-Stainless Steel Systems," Proc. Third Int'l. Conf. Liq. Metal Eng. and Technol., April 1984, British Nuclear Energy Society.

6.2-15 P. F. Tortorelli and J. H. DeVan, ADIP Quarterly Progress Report, June 30, 1979, U.S. Department of Energy Report DOE/ET-0058/6, pp. 82-88.

6.2-16 O. K. Chopra and D. L. Smith, ADIP Semiannual Prog. Rep. September 30, 1982, DOE/ER-0045/9, U.S. Department of Energy, Office of Fusion Energy, pp. 309.

6.2-17 O. K. Chopra and D. L. Smith, ADIP Semiannual Prog. Rep. March 31, 1984, DOE/ER-0045/12, U.S. Department of Energy, Office of Fusion Energy.

6.2-18 J. A. James and J. Trotman, J. Iron Steel Inst. London 194 (1960) 319-323.

6.2-19 G. W. Honsley and J. T. Maskney, J. Iron Steel Inst. London 189 (1958) 139-148.

6.2-20 Private communication, D. H. Gurinsky to J. H. DeVan, 1964.

6.2-21 D. Diercks and D. L. Smith, unpublished data.

6.2-22 M. A. Abdou et al., "Blanket Comparison and Selection Study - Interim Report," Argonne National Laboratory, ANL/FPP-83-1, October 1983.

6.2-23 P. F. Tortorelli and J. H. DeVan, J. Materials for Energy Systems 4 (2) (1982), pp. 78-83.

BLANKET COMPARISON AND SELECTION STUDY

SECTION 6.3 - SOLID BREEDER MATERIALS

SECTION 6.3

TABLE OF CONTENTS

PAGE NO.

6.3 Solid Breeders 6.3-1

6.3.1 Fabrication.....6.3-2

6.3.1.1 Pressed and Sintered Solid Breeders.....6.3-3

6.3.1.2 Sphere-Pac Solid Breeders.....6.3-12

6.3.1.3 Fabrication/Microstructure/Impurities/ Properties/Stability/Performance.....6.3-14

6.3.2 Properties.....6.3-15

6.3.2.1 Thermodynamic/Chemical.....6.3-15

6.3.2.2 Thermophysical/Transport.....6.3-24

6.3.2.3 Mechanical.....6.3-33

6.3.2.4 Compatibility/Mass Transfer.....6.3-38

6.3.3 Irradiation Experiments.....6.3-43

6.3.3.1 TULIP.....6.3-44

6.3.3.2 FUBR-1A.....6.3-57

6.3.3.3 TRIO-1.....6.3-63

6.3.3.4 VOM-15H.....6.3-75

6.3.3.5 Sealed Capsule Versus In-Situ Experiments.....6.3-79

6.3.4 Design Guidelines.....6.3-82

6.3.5 Modeling 6.3-87

6.3.5.1 Steady-state Tritium Inventory.....6.3-88

6.3.5.2 Transient Tritium Release Behavior.....6.3-111

6.3.5.3 Tritium Permeation/Leakage/Containment.....6.3-115

6.3.5.4 Physical Integrity/Gap Conductance.....6.3-127

6.3.5.5 Solid Breeder/Structure Mechanical Interaction..6.3-138

LIST OF FIGURES FOR SECTION 6.3

FIGURE NO.	TITLE	PAGE NO.
6.3-1	Open versus closed porosities in sintered Li_2O as a function of bulk density (from Ref. 6.3-11)	6.3-5
6.3-2	Weight gain of lithium ceramic pellets exposed to laboratory air (from Ref. 6.3-10)	6.3-9
6.3-3	Concentration of LiOH in Li_2O as a function of partial pressure of water vapor in helium carrier gas	6.3-17
6.3-4	Concentration of LiOH as a function of temperature	6.3-17
6.3-5	Thermal conductivity of sintered Li_2O as a function of temperature	6.3-27
6.3-6	Thermal conductivity of sintered γ-$LiAlO_2$ as a function of temperature	6.3-27
6.3-7	Thermal conductivity of sphere-pac Li_2O as a function of temperature and helium fill-gas pressure	6.3-28
6.3-8	Thermal conductivity of sphere-pac γ-$LiAlO_2$ as a function of temperature and helium fill-gas pressure	6.3-28
6.3-9	Thermal expansion of solid breeder and structural materials	6.3-30
6.3-10	Temperature dependence of diffusion coefficients of tritium, oxygen, lithium, hydrogen, and deuterium in Li_2O	6.3-32
6.3-11	Internal penetration and total scale thickness for austenitic and ferritic steels exposed with Li_2O pellets at 823 K in flowing helium containing 93 or 1 ppm H_2O and 1 ppm H_2	6.3-40
6.3-12	Weight loss for Li_2O pellets exposed at 823 K in flowing helium containing 1 ppm each of H_2O and H_2. Each symbol type represents weight loss for a single specimen after various times	6.3-42
6.3-13	Sealed-capsule design used in the TULIP (Li_2O) experiment	6.3-46
6.3-14	Unirradiated Li_2O - (a) intergranular fracture, 200 x, (b) intergranular fracture, 1000 x, (c) transgranular fracture, 200 x, (d) transgranular fracture, 1000 x	6.3-47

6.3-15 Specimen 403-1, (a) fracture surface, 200 x, (b) intergranular fracture, 1000 x, (c) transgranular fracture, 1000 x, (d) transgranular fracture, 5000 x....6.3-49

6.3-16 Specimen 403-4, (a) fracture surface, 200 x, (b) transgranular fracture showing large bubbles, 1000 x, (c) bubbles showing faceted appearance, 10,000 x, (d) fracture surface showing rows of bubbles, 500 x.....6.3-50

6.3-17 Specimen 404-4, (a) fracture surface, 100 x, (b) middle of (a) showing transgranular fracture, 500 x, (c) middle of (b) showing rows of bubbles, 2000 x, (d) bubbles at 10,000 x.....6.3-51

6.3-18 Specimen 404-2, (a) fracture surface, 500 x, (b) transgranular fracture showing bubbles, 10,000 x.....6.3-52

6.3-19 Percent tritium retention in Li_2O as a function of irradiation temperature and burnup.....6.3-53

6.3-20 Percent helium retention in Li_2O as a function of irradiation temperature and burnup.....6.3-54

6.3-21 Post-irradiation grain growth measurements of lithium ceramics (G. W. Hollenberg, HEDL).....6.3-59

6.3-22 Percent tritium retention in Li_2O, γ-$LiAlO_2$, and Li_4SiO_4 irradiated in the FUBR-1A experiment in EBR-II (from Ref. 6.3-93).....6.3-59

6.3-23 Percent helium retention in Li_2O, $LiAlO_2$ and Li_4SiO_4 irradiated in the FUBR-1A experiment in EBR-II (from Ref. 6.3-93).....6.3-61

6.3-24 Irradiation-induced swelling in lithium ceramics (G. W. Hollenberg, HEDL).....6.3-61

6.3-25 Irradiation-induced swelling in Li_2O as a function of burnup (G. W. Hollenberg, HEDL).....6.3-62

6.3-26 Capsule design used in the TRIO-1 in-situ tritium recovery experiment on γ-$LiAlO_2$.....6.3-64

6.3-27 Tritium release results from γ-$LiAlO_2$ in the first nine runs of the TRIO-1 experiment.....6.3-67

6.3-28 Tritium permeation from 304 stainless steel cladding in TRIO-1.....6.3-70

6.3-29 Thermal conductivity data of γ-$LiAlO_2$ from the TRIO experiment.....6.3-72

6.3-30 Effect of purge gas composition on fractional tritium release (R/B) from Li_2O in the VOM-15H experiment (from Ref. 6.3-96).....6.3-76

6.3-31 Temperature dependence of tritium release from Li_2O pellets in VOM-15H (from Ref. 6.3-96).....6.3-78

6.3-32 Tritium release data obtained during the four reactor cycles of the VOM-15H experiment (from Ref. 6.3-96).....6.3-80

6.3-33 Representative cross-sections of unit cells for cylindrical and plate geometries. Purge stream channels are not shown.....6.3-90

6.3-34 Distribution of tritium concentration in the BCSS (LOBE-2B) γ-$LiAlO_2$/Be/H_2O/HT9 blanket for the case of 0.1% H_2 added to the purge stream (T_{max} = 950°C, T_{min} = 360°C, G = 866 g/day, r_g = 0.1 μm). 6.3-98

6.3-35 Diffusion coefficient for tritium in $LiAlO_2$ determined from selected TRIO runs in which intragranular diffusion appeared to be the rate limiting phenomenon in tritium transport. The one-sigma bands are based on uncertainties in the experimental generation rate ($\dot{G}$) and inventory (I).....6.3-100

6.3-36 Comparison of selected data for tritium diffusion in γ-$LiAlO_2$ with the TRIO-1 correlation (includes uncertainties in grain size, inventory, and generation rate).....6.3-101

6.3-37 Predicted diffusive inventory for the BCSS γ-$LiAlO_2$/Be/H_2O/HT9 design as a function of T_{min} for T_{max} = 1000°C, $\dot{G}$ = 866 g/day and r_g = 0.1 μm. 6.3-102

6.3-38 Estimation of "surface-adsorption" inventory for TRIO-1 runs 9-27 as a function of purge stream chemistry and average γ-$LiAlO_2$ temperature.....6.3-105

6.3-39 Measured tritium inventory in the FUBR-1A experiment (105 FPD) minus the calculated diffusive inventory.....6.3-107

6.3-40 Tritium response to an instantaneous reactor startup for the $LiAlO_2$/H_2O/Be/HT-9 design with T_{min} = 350°C and T_{max} = 1000°C. Assumed grain diameter is 0.2 μm.....6.3-114

6.3-41 Limiting tritium partial pressure in the purge channel plotted as a function of maximum tritium leakage rate ($\dot{m}_\ell$) into the primary coolant loop (γ-$LiAlO_2$/H_2O/HT9/Be blanket).....6.3-125

6.3-42 Limiting volumetric gas flow rate in the purge channel plotted as a function of maximum tritium leakage rate ($\dot{m}_g$) into the primary coolant loop (γ-$LiAlO_2$/H_2O/HT9/Be blanket).....6.3-126

6.3-43 Purge channel pressure drop (Δp) plotted as a function of maximum tritium leakage rate ($\dot{m}_g$) into the primary coolant loop (γ-$LiAlO_2$/H_2O/HT9/Be blanket).....6.3-128

6.3-44 Variation of gas-phase conductance with temperature and gap size d.....6.3-137

6.3-45 Variation of maximum gas-phase conductance (d=0) with temperature.....6.3-139

LIST OF TABLES FOR SECTION 6.3

TABLE NO.	TITLE	PAGE NO.
6.3-1	CATION IMPURITIES (wt %) IN Li_2O GRANULES AND SINTERED PELLETS (FROM REF. 6.3-11)	6.3-6
6.3-2	CHEMICAL ANALYSIS OF γ-$LiAlO_2$	6.3-7
6.3-3	FUBR-1A PELLET CHARACTERIZATION (FROM REF. 6.3-10)	6.3-10
6.3-4	RESULTS OF SOLID BREEDER THERMAL STABILITY AFTER 8 HRS AT 900°C (FROM REF 6.3-10)	6.3-11
6.3-5	Li_2O IRRADIATION CONDITIONS AND TRITIUM/HELIUM RETENTIONS (TULIP)	6.3-45
6.3-6	TEMPERATURE AND SWEEP GAS COMPOSITIONS FOR THE TRIO-1 EXPERIMENT	6.3-66
6.3-7	SUMMARY OF TRITIUM RETENTIONS IN FOUR SOLID BREEDER IRRADIATION EXPERIMENTS	6.3-81
6.3-8	BCSS DESIGN GUIDLINES FOR SOLID BREEDERS	6.3-84
6.3-9	TIMES TO REACH 67.4% AND 99% OF THE STEADY-STATE RELEASE RATE AS A FUNCTION OF MINIMUM BLANKET TEMPERATURE FOR A WATER-COOLED γ-$LiAlO_2$ BLANKET WITH A MAXIMUM TEMPERATURE OF 1000°C	6.3-113
6.3-10	SOLID BREEDER BLANKET DESIGN PARAMETERS USED IN TRITIUM PERMEATION AND PURGE FLOW DESIGN CALCULATIONS	6.3-121
6.3-11	INPUT VALUES ASSUMED FOR THERMAL STRESS/CRACKING ANALYSIS OF PLATE- OR BEAM-LIKE SOLID BREEDERS	6.3-132
6.3-12	PLATE- AND BEAM-LIKE SOLID BREEDER HALF THICKNESS (h) REQUIREMENTS	6.3-132
6.3-13	INTERFACE PRESSURE AND CLADDING STRESSES DUE TO Li_2O/HT9 MECHANICAL INTERACTION (SHRINK-FIT ANALOGY)	6.3-143

6.3 Solid Breeder Materials

Subsections in 6.3 are organized based on three criteria: (1) division by technical discipline, (2) update/addition from the interim BCSS report, and (3) emphasis on common bases (methodology) in addressing technical disciplinary areas with regard to all solid breeder blanket designs. These criteria reflect the spirit of all the BCSS Special Issues Tasks which attempt to prevent uneven blanket design evaluation arising from the difference in methodologies.

The logic of the subsection sequence is as follows: a state-of-the-art assessment of solid breeder fabrication technology is given in Section 6.3.1. Powders, sintered pellets and plates of Li_2O and γ-$LiAlO_2$ have been successfully fabricated; the attention will be placed on the sphere-pac forms of these solid breeders, and on advanced materials. The advanced solid breeders include other lithium-ceramic compounds, as well as added value products (such as Li_2O and γ-$LiAlO_2$ with microstructure tailoring and property enhancement).

Advanced materials cannot be properly defined unless their properties are characterized in sufficient detail. The same statement can be made when comparing different solid breeders. Four topics on solid breeder properties are covered in Section 6.3.2: thermodynamic/chemical, thermophysical/transport, mechanical, and mass transfer/compatibility.

Irradiation effects on solid breeders, particularly the tritium, helium, and swelling behavior, are addressed in Section 6.3.3. Key observations from four irradiation experiments will be summarized. Among these four experiments, two are of the sealed capsule type, TULIP and FUBR-1A; two are in-situ tritium recovery experiments, TRIO-1 and VOM-15H. While both types of experiments have their unique test objectives, the presence/absence of a purge flow environment permit a direct comparison of the differences in tritium behavior.

Design guidelines (Section 6.3.4) follow logically after solid breeder properties are characterized and irradiation effects examined. Major updates of design guidelines were made on solid breeder temperature limits, thermal conductivities of sintered and sphere-pac Li_2O and γ-$LiAlO_2$ with irradiation effects, and the specification of grain size which has a decisive influence on the low temperature limit. It must be said that these temperature limits, though consistent with the existing ex- and in-reactor data, may still be

optimistic because long-term fluence effects cannot be properly assessed at this time.

Significant work has been done on modeling the tritium and solid breeder behavior during irradiation. The five topics covered in Section 6.3.5 are steady-state tritium inventory, transient tritium behavior, tritium permeation/leakage/ containment, physical integrity/gap-conductance, and solid-breeder/structure mechanical interaction. In many cases the available ex- and in-reactor data are translated into blanket design evaluation via mathematical models.

Research and Development (R&D) assessment of solid breeders is done by subjects at subsection levels. Based on these assessments, the R&D needs and priorities for solid breeders are established in Chapter 4.

6.3.1 Fabrication

There are several possible blanket configurations for solid breeders: monolithic block, pressed and sintered plates, and spherical particles (sphere-pac). The monolithic block configuration was adopted in the STARFIRE[6.3-1] and DEMO[6.3-2] blankets for γ-$LiAlO_2$ and Li_2O, respectively. Thermal-stress induced cracking (due to temperature gradients) and cracked fragment relocation impose difficulties in precise temperature control of these monolithic breeder blankets.[6.3-3] To overcome the cracking problem and the associated gap conductance uncertainties (which lead to blanket temperature variability), the leading BCSS solid-breeder blanket designs (Chapters 8, 9, and 10) employ either pressed and sintered plates for Li_2O and γ-$LiAlO_2$, or sphere-pac configuration for γ-$LiAlO_2$. Not only does the fabrication of these breeders into the desired forms need to be demonstrated, attention also needs to be placed on breeder microstructural tailoring (i.e., controlled density, grain size, and pore morphology), impurities, and stability. The attention is well justified because of the intimate relationships between breeder microstructure and properties (Section 6.3.2), between impurities and properties, between properties and performance, and between stability and performance. Understanding of these relationships are fundamental to the development of advanced solid breeders with superior properties and performance than those of the current-generation materials.

Fabrication technology of solid breeders has been assessed previously in

the BCSS interim report[6.3-3] and in the 1984 U.S. contribution to the INTOR study.[6.3-4] The salient features from these earlier assessments are summarized below, along with highlights of the new development results.

6.3.1.1 Pressed and Sintered Solid Breeders

Cold pressing and sintering techniques were developed for (1) Li_2O, Li_4SiO_4, and $LiAlO_2$ samples irradiated in ORR,[6.3-5] (2) Li_2O cylinders used in the TFTR Lithium Blanket Module (LBM) Program,[6.3-6] (3) γ-$LiAlO_2$ pellets with tailored microstructure[6.3-7] used in the TRIO-1 experiment (Section 6.3.3.3), (4) γ-$LiAlO_2$ plates[6.3-8] to be used in the ANL microwave heating experiment, and (5) Li_2O pellets and pebbles[6.3-9] used in the various Japanese experiments. Hot pressing techniques were developed for Li_2O, Li_4SiO_4, γ-$LiAlO_2$, Li_2ZrO_3, and Li_8ZrO_4 pellets; these pellets were either used or to be used in the FUBR-1A and -1B experiments.[6.3-10] Product dimensions vary from small pellets to relatively large γ-$LiAlO_2$ plates; production scale varies from laboratory to relatively large throughput operation for the LBM program.

Powder Preparation

Powder preparation is the first step involved in the fabrication of pressed and sintered solid breeders. Candidate materials have been prepared using either solid state reaction techniques or bringing together in an inert solvent metal organic adducts in the desired stoichiometry. For the FUBR-1A experiment (Section 6.3.3.2), the Li_2O powder was fabricated by thermal dissociation of the enriched Li_2CO_3 starting materials. The γ-$LiAlO_2$ powder was generated by spary drying a mixture of Li_2CO_3, water and Al_2O_3, followed by calcination. Both the Li_2ZrO_3 and the Li_4SiO_4 powders were obtained by an organometallic approach in which Li_2CO_3 and $Si(C_2H_5O)_4$ or $ZrOCl_2 6H_2O$ were used to form a gel which was subsequently calcined into fine grained powders. Although these recently developed techniques represent state-of-the-art technology, only the γ-$LiAlO_2$ powder possessed less than a 1 μm particle size.

Initially, chloride and fluoride contamination was observed in unacceptable powder lots of the γ-$LiAlO_2$, Li_4SiO_4 and Li_2ZrO_3. The chloride level in γ-$LiAlO_2$ (1500 μg/g) can be reduced to approximately 100 μg/g by off-gassing at 800°C for 16 hours in a vacuum system incorporating a liquid nitrogen cold

trap.[6.3-10] A similar off-gassing of the Li_2ZrO_3 powder at 650°C for 65 hours and a subsequent off-gassing at 750°C for 68 hours was found to adequately remove excess Cl and F from contaminated Li_2ZrO_3 powders. Vacuum off-gassed Li_4SiO_4 powders with acceptable halide content were not suitable for hot pressing and the Li_4SiO_4 powder had to be refabricated. The synthesized Li_4SiO_4 powder possessed acceptable halide levels but was vacuum off-gassed at 450°C for 4 hours to remove moisture prior to hot pressing. The initial Li_2O powder contained low levels of halide but was vacuum off-gassed at 750°C to remove moisture, organics and CO_2. The Li_2O powder was heated on an 8-hour ramp to 750°C during the vacuum off-gas treatment to avoid excessive increases in particle size.

Cold Pressing and Sintering

Based on the LBM fabrication experience, Yang[6.3-3] recommended a procedure for cold pressing and sintering of Li_2O: the walls of the cavity of the steel die and the surfaces of the steel plungers should be brushed with a solution of 2 wt% stearic acid in absolute ethyl alcohol. A known amount of lithium oxide powder of minus 100 mesh size should be added to the cavity of the steel die and pressed at a pressure of 69 or 104 MPa, then sintered in vacuum at 1050°C (for a cold pressing pressure of 10 ksi) or 950°C (for a cold pressing pressure of 104 MPa).

The reproducibility of the cold pressed and sintered Li_2O cylinders was assessed.[6.3-3] The average density of 27 sintered pellets is 80.6% of the theoretical value, with a standard deviation of ±0.6%. The average diameter is 0.9851 in., with a standard deviation of ±0.0032 in. In addition to density and diameter, the microstrcture of one sample from each of the five runs was examined at the edge, the center, and midway between the edge and center. No significant difference was observed among the samples or for the same sample at different locations. The porosity in these samples appears "open", which should facilitate the release of the bred tritium.

Using a similar technique with pressure ranging from 97 to 490 MPa and slightly higher sintering temperatures (1100-1200°C), Takahashi and Kikuchi[6.3-9] fabricated Li_2O pellets with densities ranging from 70 to 93.4%. Figure 6.3-1 shows the percent porosity in Li_2O as a function of bulk density (% TD)[6.3-11]. Above 88% TD the closed pores are more abundant than

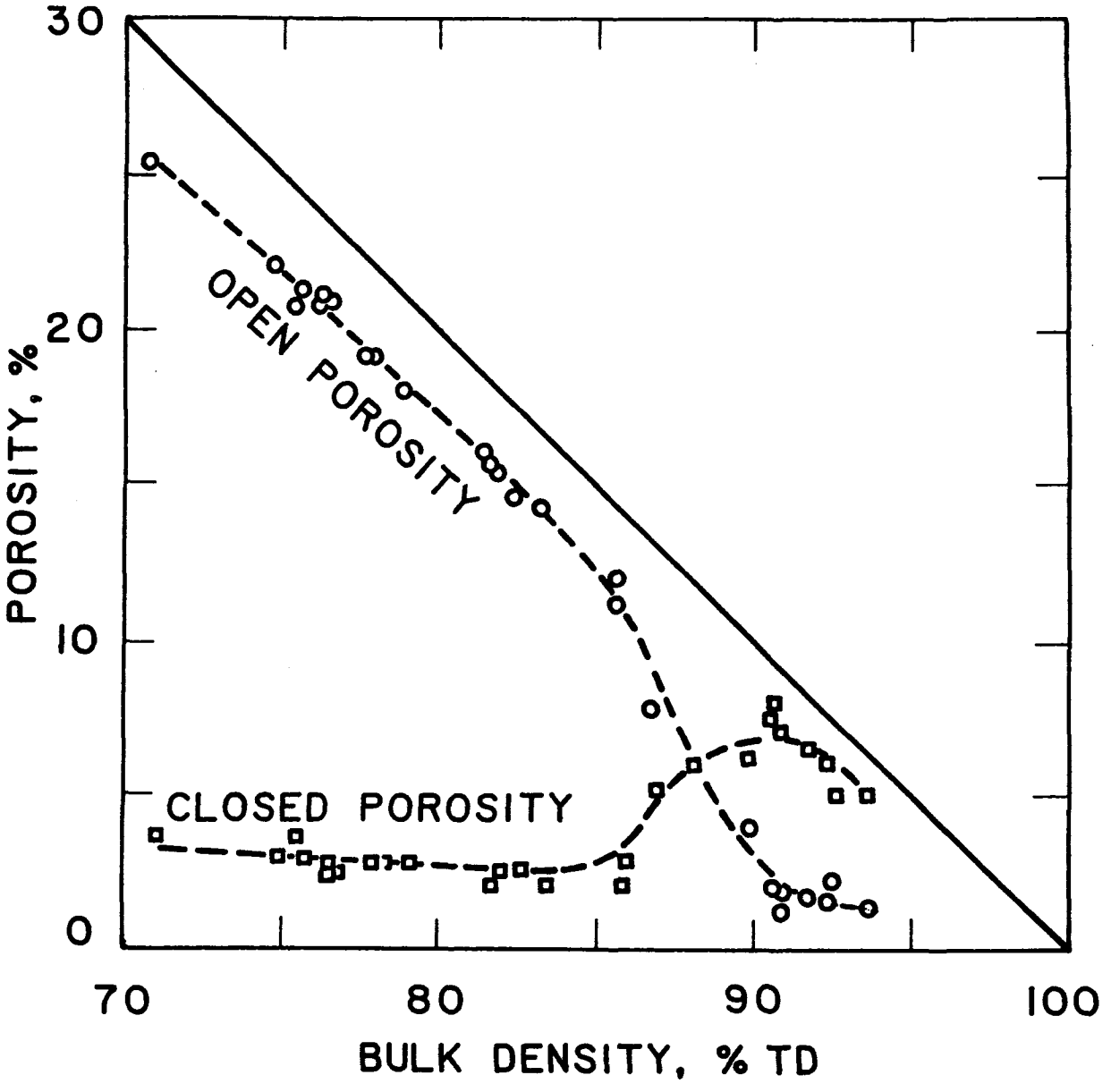


Figure 6.3-1. Open versus closed porosities in sintered Li_2O as a function of bulk density (from Ref. 6.3-11).

the open pores, whereas below 88% TD the open pores are more numerous than the closed ones. The Fraction of closed pores changed little in the range of 70-85% TD, however. In the microstructure examination of polished sections of the Li_2O pellets, Takahashi and Kikuchi[6.3-11] found that the higher the density, the smaller the porosity and the larger the crystal grain growth. The average dimension of the crystal grain was ~20 μm in the 79.8% TD Li_2O and ~60 μm in the 93.4% TD Li_2O. Analysis results of cation impurities in the Li_2O granules and sintered pellets are shown in Table 6.3-1. These impurities are later used in the activation/waste management analysis (Section 6.12).

TABLE 6.3-1 CATION IMPURITIES (WT %) IN Li_2O GRANULES AND SINTERED PELLETS (from Ref. 6.3-11)

Element	Granule	Sintered Pellet[a]
Na	0.066	0.005
K	0.111[b]	---[b]
Ca	0.029	0.021
Fe	0.006	0.010
Pb	0.008	0.008
Mn	0.002	0.002
Ni	0.002	0.002
Mo	---[b]	---[b]
Al	0.002	0.002
Cu	0.0006	0.0013
Si	0.001	0.001
Ti	---[b]	---[b]
Mg	---[b]	---[b]

[a]Sintered at 1000°C for 4 h under vacuum in a platinum crucible.
[b]Concentrations of these elements are unspecified. They are probably below detection level.

The γ-$LiAlO_2$ pellets used in the TRIO-1 experiment were fabricated by preparing agglomerates of appropriate size, and then by cold-pressing and firing agglomerates. The agglomerates were prepared by first mixing 12 g of polyvinyl alcohol (PVA) in 300 cc of water at 60°C, mixing in the 120 g of $LiAlO_2$ powder, and then heating the mixture until a thick paste was obtained. The paste was then vacuum dried at ~80°C for 8 hours with periodic stirring. The resultant agglomerates were weakly bound; ball-milling produced an exces-

sively high fraction of fines. The lithium aluminate was then mixed with water (200 cc), dried into a cake, and manually ground with a mortar and pestle, and once again there were too many fines. The material was then added to 300 cc of warm water with an additional 3.6 g of PVA, dried as before, manually ground in a mortar and pestle, and seived to retain the fraction passing 200 mesh but not passing 325 mesh. The fines were again added to water and reworked to produce 200-325 mesh agglomerates. These agglomerates from the second batch were added to those of the first batch and the prepared material was then cold-pressed at 14,000 pounds, producing a green pellet having dimensions of 1.18 in. OD x 0.695 in. ID x 0.512 in. height. After several trials of the firing schedule, the one chosen for the TRIO-1 pellets was 17 hrs at 1050°C. This resulted in the desired bimodal microstructure with coarse agglomerates and fine grains (<0.2 μm diameter), and an interconnected porosity of ~35%. Chemical analyses of the cation impurities in γ-$LiAlO_2$ are given in Table 6.3-2.

TABLE 6.3-2. CHEMICAL ANALYSIS OF γ-$LiAlO_2$[a]

Element	w/o	Element	w/o
Li	13.9	Ni	0.002
Be	0.001	Cu	0.001
B	0.001	Zn	0.05
O	31.9	As	0.05
Na	0.005	Sr	0.10
Al	53.8	Zr	0.01
P	0.05	Mo	0.003
Cl	0.01	Ag	0.001
Ca	0.003	Cd	0.01
Ti	0.003	Sn	0.03
V	0.003	Sb	0.01
Cr	0.003	Ba	0.01
Mn	0.001	Pb	0.001
Fe	0.003	Bi	0.001
Co	0.003		

[a]Methods used were emission spectroscopy and neutron activation.

Recent efforts in the γ-$LiAlO_2$ plate fabrication for the planned ANL microwave heating experiment have produced satisfactory results after several modifications to the fabrication procedure (i.e., a combination of preslugg-

ing, use of binder, lubricant, and dispersant, and the firing schedule). γ-$LiAlO_2$ plates with dimensions of 10 x 10 x 0.5 cm can now be fabricated using cold pressing and sintering to achieve densities of 65-85% TD while keeping grain size small.

Hot Pressing

Hot pressing is an alternative to cold pressing and sintering for solid breeder fabrication. Hot pressing was chosen over cold pressing and sintering for FUBR-1A and -1B pellet fabrication in order to achieve well controlled density while avoiding excessive grain growth.[6.3-10] Density control was accomplished by accurately pre-weighing (±1 mg) a powder charge for a precisely manufactured graphite die and punch assembly (±0.001 in.). Hot press dies were filled with powder in an argon-atmosphere glove box and then transferred to the hot press which was operated with a vacuum or inert atmosphere.

Each material had its own hot pressing characteristics. As the temperature of the die increased, the pressure on the punches was slowly increased to a maximum of 34 MPa (5000 psi). After the intended density was achieved, power to the hot press furnace was reduced and the pellets were allowed to cool. Typical maximum hot pressing temperatures for each material were: Li_2O (680°C), Li_4SiO_4 (750°C), Li_2ZrO_3 (1050°C) and $LiAlO_2$ (1250°C).

In order to obtain the specified diameters, the pellets were removed from the argon glove box and centerless ground in laboratory air. The air exposure time for centerless grinding of Li_2O pellets was approximately four minutes. Weight gain measurements (Fig. 6.3-2) indicate that the Li_2O pellets should not have gained more than 0.1% moisture during this process.

To remove moisture gained during grinding, pellets were vacuum off-gassed using a liquid nitrogen cold trap under the following conditions: γ-$LiAlO_2$, 600°C for 4 hours; Li_2ZrO_3, 750°C for 68 hours; Li_4SiO_4, 550°C for 18 hours; and Li_2O, 450°C for 18 hours.

Table 6.3-3 shows the characteristics of the pellets fabricated by hot pressing. Pellet densities were all within the prescribed theoretical density requirements, either 85 ± 2% TD or 95 ± 2% TD. The pellet diameters were all within the 0.375 ± 0.001 requirement of the specification. All materials were

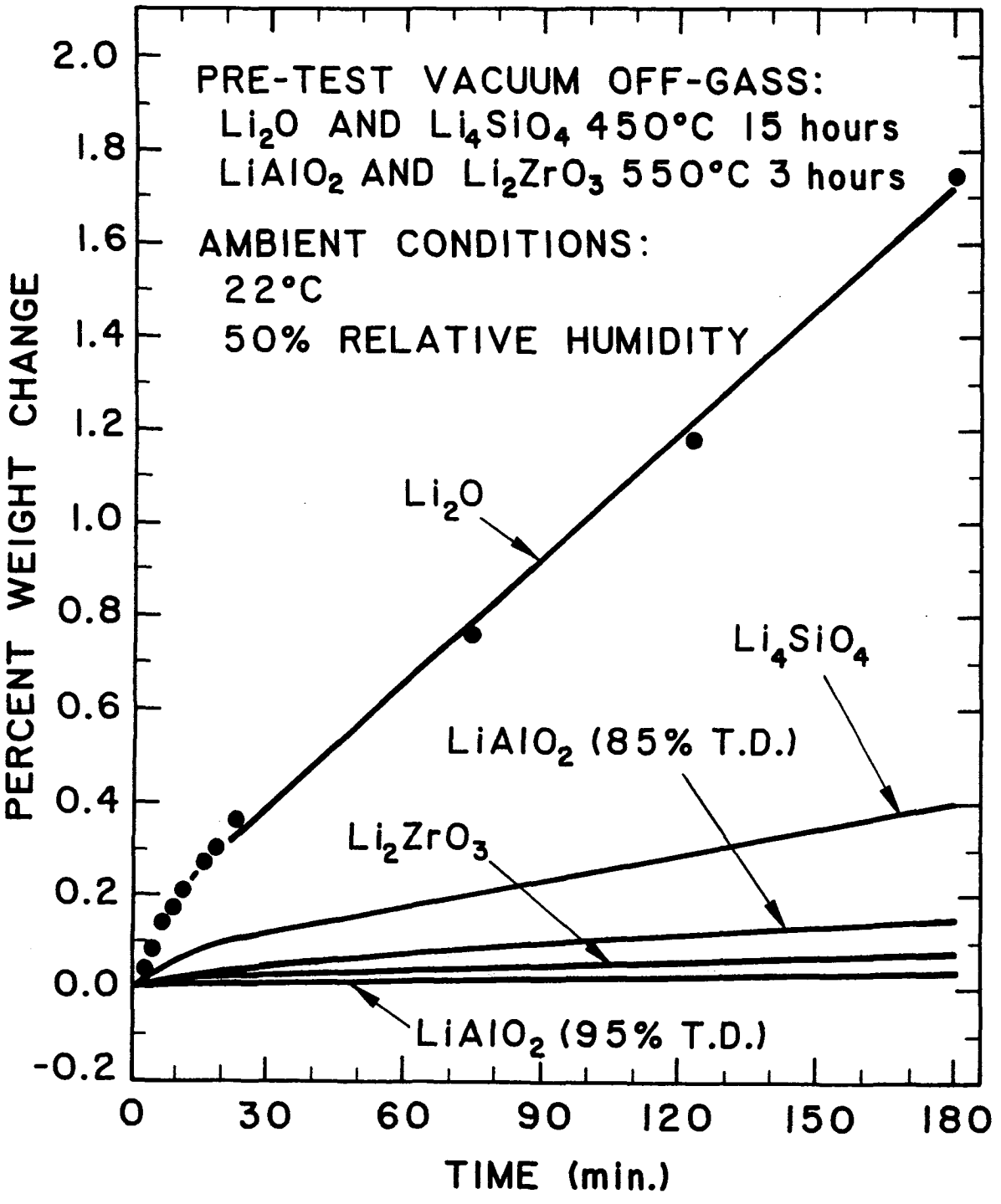


Figure 6.3-2. Weight gain of lithium ceramic pellets exposed to laboratory air (from Ref. 6.3-10).

TABLE 6.3-3. FUBR-1A PELLET CHARACTERIZATION (FROM REF. 6.3-10)

	γ-$LiAlO_2$	γ-$LiAlO_2$	Li_2O	Li_2ZrO_3	Li_4SiO_4
Density (% T.D.)	83.47 to 86.84	93.34 to 96.00	84.6 to 86.55	84.69 to 85.80	84.10 to 86.80
Diameter (in.)	0.3744 to 0.3750	0.3745 to 0.3748	0.3742 to 0.3757	0.3741 to 0.3750	0.3743 to 0.3750
Length (in.)	0.5492 to 0.5662	0.5581 to 0.5670	0.5606 to 0.5657	0.5561 to 0.5659	0.5510 to 0.5669
Phase Purity	XRD Phase Pure	XRD Phase Pure	XRD Phase Pure	XRD Phase Pure	XRD Phase Pure
Enrichment (% ^6Li)	95.5	95.5	45.0	69.3	69.0
Impurities (μg/g)					
Cl	100	100	10	30	20
F	10	10	5	100	120
Cation	1140	1140	<500	<500	<500
Grain Size (μm)	<1	<1	[6][a]	[2][a]	[2][a]
Surface Area m^2/cm^3	1.31	0.103	0.17	1.40	0.77
Powder Processing	Spray Drying	Spray Drying	Li_2CO_3 Decomposition	Organometallic	Organometallic

[a]Average measurements.

also phase pure as determined by x-ray diffraction and the ^{6}Li enrichment was within specification for all four material types.

As a result of the significant effort devoted to obtaining low Cl and F levels, the final pellet Cl and F concentrations were less than the specified 150 μg/g limit for all four materials. Metallic impurities did not appear to be a significant problem in these fabrication processes.

Fabrication of small-grained solid breeders may be crucial from the tritium release standpoint. The γ-$LiAlO_2$ pellets were the only material that achieved a grain size of less than 1 μm. The Li_2ZrO_3 pellets possessed an average grain size of slightly greater than 1 μm. The Li_4SiO_4 pellets possessed a bimodal grain size distribution with most of the grains averaging 2 μm, while a few ranged up to an average size of 20 μm. The Li_2O pellets possessed an average grain size of 6 μm. The 6 μm grain size is considerably less than that obtained by cold pressing and sintering.

In order to evaluate the thermal stability of these four materials at the peak irradiation temperature, each material was annealed for eight hours at 900°C. The results, shown in Table 6.3-4, indicate that $LiAlO_2$ and Li_2ZrO_3 are relatively stable at 900°C.

TABLE 6.3-4. RESULTS OF SOLID BREEDER THERMAL STABILITY TEST AFTER 8 HRS AT 900°C (FROM REF. 6.3-10)

Material	Weight Loss (%)	Dimensional Change (%)	Grain Growth Before/After (μm)
γ-$LiAlO_2$	0.04	0.00	<1/<1
Li_2ZrO_3	0.08	-0.03	2/ 2
Li_4SiO_4	0.30	-0.74	2/20
Li_2O	1.34	-2.4	6/80

Both densification and grain growth occurred in the Li_4SiO_4 pellet. The grain size of the Li_4SiO_4 pellet increased an order of magnitude from 2 μm to 20 μm during the 900°C anneal.

In Li_2O, the grains grew from a 6 μm average up to 60 to 100 μm range during the thermal stability test.[6.3-10] Arons et al.[6.3-7] have also observed substantial grain growth in Li_2O, and they have attributed this phenomena to liquid-phase-(i.e., LiOH)-enhanced sintering. Independent assessment by Wilson and Hollenberg[6.3-10] also leads to the conclusion that Li_2O microstructural thermal stability is limited by impurity-induced, liquid-phase-enhanced sintering. Since LiOH (as LiOT) is produced in Li_2O during irradiation, microstructural thermal stability at an irradiation temperature of 900°C is not anticipated for Li_2O. As will be discussed later in Section 6.3.3, irradiation adds other dimensions to solid breeder stability, so does the purge environment to be discussed in Section 6.3.2.4.

6.3.1.2 Sphere-Pac Solid Breeders

There have been few direct experiences in fabricating sphere-pac solid breeders. In the nuclear fission industry, the sphere-pac route for fabrication of fissile fuel has been demonstrated for UO_2. With the sphere-pac process, high density ceramic spheres of controlled sizes are produced, and these are subsequently loaded into cladding tubes with low-energy vibration to facilitate dense packing.

For fission fuels the gel-sphere-pac prepration[6.3-12 - 6.3-16] is based upon three major steps: (1) preparation of a sol or special solution ("broth"), (2) gelation of droplets of sol or broth to give semi-rigid spheres, and (3) drying and sintering these spheres to a high density. Gelation (gel) may be accomplished by two methods: water extraction (suitable only for sols), or ammonia gelation (suitable for both sols and broths, but used almost exclusively with broths). Ammonia gelation can be accomplished either externally, via ammonia gas and ammonium hydroxide, or internally via hexamethylene tetramine which generates ammonia when thermally decomposed; internal gelation is followed by treatment with ammonium hydroxide to complete the reaction.

Sphere-pac requires three sizes of high-density (>98% TD) spheres to achieve about 88% smear density.[6.3-17] These sizes have diameter ratios of 40:10:1. The actual diameters currently used for fission fuels are 1200, 300, and 30 μm. The same sizes have also been recommended for blankets using solid breeders in sphere-pac form. If a lower smear density is acceptable, two

sizes will yield ~85% smear density. The loading of sphere-pac fuel involves vibratory packing of spheres of the proper size ratio.

Considerable sphere-pac technology has been developed regarding the identification of proper sizes, size ratios, blending ratios, and loading sequences to fabricate maximum smear densities at minimum loading times. Simultaneous loading of all three size fractions showed promise of overcoming the problem of excessive loading times for long but relatively small-diameter rods. A typical water-cooled γ-$LiAlO_2$ blanket module has the dimension of 0.3 x 0.5 x 4 m. More than 200 coolant tubes run through the module which would have to be in place before the spheres are poured and vibratorily packed. In addition to near-flat surfaces at the module walls, there are many convex surfaces at the coolant tube outer walls, as opposed to concave surfaces at the inner walls of the fission-reactor fuel rods. Whether the same 88% smear density can be achieved in a blanket module with such a complicated geometry needs to be demonstrated.

Other fabrication issues for the sphere-pac solid breeder are the grain size, particle size, and particle porosity (or density). The size ratio is probably more important than the actual sizes in determining the solid-breeder smear density in a blanket module. For example, a 70% solid-breeder smear density can be achieved in the Japanese blanket design with single-size Li_2O pebbles of 10 mm diameter. For other solid breeders, γ-$LiAlO_2$ in particular, tritium inventory considerations (Section 6.3.4.1) dictate grain size in the micron range so that the recommended spherical particles must be made of fine-grained material. If porosity is needed in the spherical particles to aid tritium release, the overall smear density must come down from 88% with a concomittant decrease in the effective thermal conductivity (Section 6.3.2.2). Whether the spherical solid breeders with fine grain and tailored microstructure can be fabricated by the sol-gel or other processes also remains to be demonstrated.

Finally, thermal and irradiation-enhanced particle sintering needs to be considered. In contrast to the porosity elimination occurring in relatively low-density sintered products, the spherical particles can sinter together and develop necks at the particle contact regions. Besides a strong temperature dependence, solid-state sintering generally increases with time (t) at temperature ($\propto t^m$, $m < 1$), and with decreasing particle size r($\propto r^{-n}$, $n < 1$).[6.3-18]

Together these will place a limit on the smallest particle size to prevent particle sintering which is a concern for breeder stability. For Li_2O there is a patent by Research Dynamics Inc.[6.3-19] for producing porous lithium oxide spheres. Mass transfer tests[6.3-20] (8 hrs at 1000°C) conducted on much larger (10-mm diameter) 85%-dense Li_2O pebbles showed not only materials loss, but also shrinkage and neck development. Sphere-pac Li_2O has not been considered in any of the BCSS solid-breeder blanket designs.

6.3.1.3 Fabrication/Microstructure/Impurities/Properties/Stability/Performance

In the development of solid-breeder blankets for D-T fusion reactors, fabrication technology for solid breeders occupies the first step from which all subsequent materials development efforts originate, a base that must be firmly built to meet the performance requirements of tritium generation and recovery, heat generation and removal, and lifetime of a solid breeder blanket. The assessment of solid-breeder fabrication technology in the two preceding sections gives the state-of-the-art development in this field; much more work is needed in order to improve the current-generation materials and/or develop advanced solid breeders.

The importance of microstructure and impurities on properties, stability, and performance of ceramics has long been recognized.[6.3-18] For solid breeders microstructure and impurities have trickle-down effects that permeate through all categories of blanket design and performance. For example, porosity, pore morphology, and grain size have profound effects on thermal conductivity (Sections 6.3.2.2), mechanical properties (Section 6.3.2.3), stability (this section), and tritium inventory (Section 6.3.4.1). Impurities can have significant impact on thermodynamic/chemical properties (Section 6.3.2.1) as well as on transport properties (Section 6.3.2.2). These intrinsic materials properties of the current-generation solid breeders and their irradiation data (Section 6.3.3) largely determine the design guidelines (Section 6.3.5). In some cases the limits may cause severe constraints on blanket design and great penalty on blanket performance.

Although the relationships of fabrication/microstructure/impurities/properties/stability/performance are generally recognized, fabrication development itself can be a long and tedious process even for ceramicists who have

considerable fabrication experience. Adequate lead time should, therefore, be provided for fabrication in the solid breeder development cycles which also include properties characterization and performance evaluation.

In summary, several forms of solid breeders have been successfully prepared and used in various experimental programs. Microstructural tailoring and property enhancement are the goals for the development of advanced solid breeders that will offer better properties and performance than those of the current-generation materials. Since one can anticipate potentially high payoffs from these advanced materials, and since long lead time will be required for their development, the fabrication R&D efforts should be supported at stable levels. In the case of sphere-pac breeder fabrication, there are still several feasibility issues (i.e., grain size, particle size, porosity) and performance issues (i.e., stability, tritium release) that remain to be resolved.

6.3.2 Properties

6.3.2.1 Thermodynamic/Chemical

For accuracy and self-consistency in thermodynamic/chemical data assessment for solid breeder materials, basic thermodynamic data (e.g., free energies, enthalpies of formation, entropies, heat capacities, and free energy functions) should be taken from a critically evaluated source. It is probably well to defer adoption of the latest data that might appear in the literature (unless nothing else exists) until a qualified critique has been made. The recommended source is the JANAF tables.[6.3-21]

Lithium Oxide

The solubility of hydroxide in Li_2O has been measured by Tetenbaum[6.3-22] as a function of the partial pressure of H_2O in the gas phase and temperature. The equation expressing the solubility of LiOH as mol fraction, X, partial pressure of water vapor in atm, p, and temperature, T(K) is:

$$\log(X) = (0.495 + 13.4/T)\log(p) + (1.238 - 3738/T). \qquad [6.3\text{-}1]$$

The temperature range of the measurements is 973 to 1273 K. The activity coefficient γ for LiOH in these dilute solutions in Li_2O is expressed in the Margules form as a function of temperature and the mole fraction of Li_2O, (1-X):

$$\log(\gamma) = (563.57 - 708681.7/T)\ (1-X)^2 + (-566.00 + 714023.6/T)\ (1-X)^3. \quad [6.3\text{-}2]$$

The partial pressure of water vapor in the 3-phase system $Li_2O(s)$ -LiOH(s or l) -$H_2O(g)$ was measured by Tetenbaum[6.3-23]. Below the melting point of LiOH (744 K) the water vapor pressure is given in atm by:

$$\log(p) = -6718/T + 6.45. \quad [6.3\text{-}3]$$

Above the melting point of LiOH, it is given by:

$$\log(p) = -4406/T + 3.27. \quad [6.3\text{-}4]$$

These results agree substantially with the earlier studies by Gregory and Mohr[6.3-24] and by Norman and Hightower.[6.3-25]

Figures 6.3-3 and 6.3-4 present the solubility information in terms of mol fraction LiOH (X_{LiOH}) as a function of temperature and partial pressure H_2O. Figure 6.3-4 displays the data in a fashion of direct interest to breeder blanket designers. Current blanket designs use helium purge flow for tritium recovery (Chapters 8 and 9); the data display the interrelationship between temperature, concentration and purge gas composition. At 900 K and 1×10^{-5} atm $T_2O(g)$, the solubility of tritium as LiOT in an Li_2O solid breeder blanket is 0.14 wppm T. This would correspond to ~0.14 kg of tritium in a STARFIRE-like blanket.

The solubility values derived from measurements[6.3-22] are smaller than the ones estimated from thermochemical calculations using an ideal solution model and JANAF data.[6.3-21] Such ideal solution calculations predicted decreasing solubility of LiOH in Li_2O with increasing temperature at a fixed partial pressure of water vapor. In contrast, the measurements show that the solubility increases with temperature under these conditions. From the observed solubility relationship, it also follows that the dissolution of LiOH

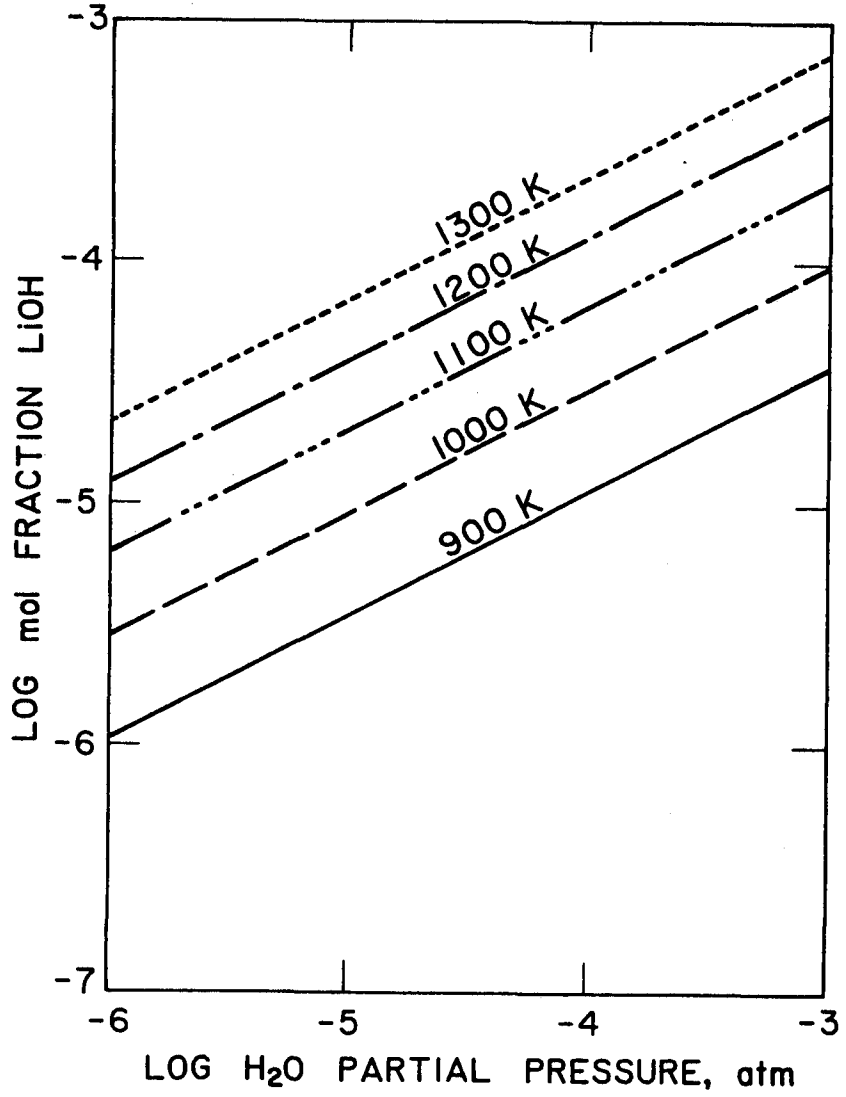


Figure 6.3-3. Concentration of LiOH in Li_2O as a function of partial pressure of water vapor in helium carrier gas.

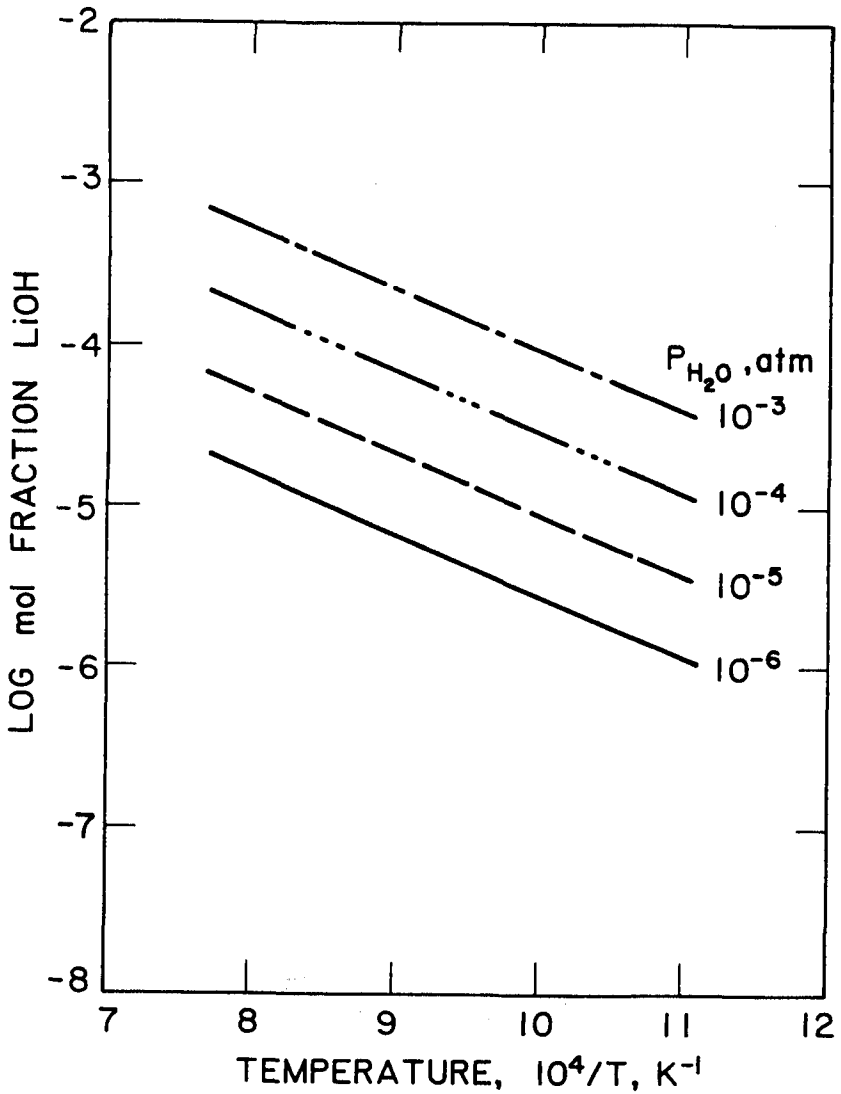


Figure 6.3-4. Concentration of LiOH as a function of temperature.

in Li_2O is an endothermic process; this conclusion is consistent with observations from differential scanning calorimetric analysis of Li_2O in a flowing argon atmosphere[6.3-25]. The observed solubility-temperature trend is that commonly observed for most solutes. In this case, the solute, LiOH, is the product of the reaction between gaseous H_2O and the solvent, solid Li_2O. In the thermodynamic analysis, we do not consider that we are dealing with the solubility of H_2O in Li_2O, but simply relate the behavior of the solute to pure LiOH, whatever the exact chemical nature of the solute might be. Consequently, in speaking of the solubility of lithium hydroxide, we do so without implying that a molecular species "LiOH" is in solution. The exact nature of this species is an interesting issue. An unresolved question is whether, in solid Li_2O, the hydroxide is an OH^- ion or a labile proton transiently associated with a succession of O^{2-} ions in the lattice.

Advanced calculations have been made (using the experimentally determined activity coefficients) to study the equilibrium thermodynamic behavior of the Li_2O system containing certain fixed amounts of tritium and protium. The calculations address matters of the (HT + T_2) : (HTO + T_2O) ratio in the gas phase, gas phase concentrations of LiOH and LiOT and their dimers, gas phase tritium enhancement by protium purging, tritium retention in the condensed phase, and elemental lithium formation. Oxygen activity is a variable common to all these phenomena which requires close attention. Major conclusions from the above study are summarized below.

For each temperature, there is a critical value of the oxygen activity above which the dominant gaseous species is the oxidized form (HTO or T_2O) rather than the reduced form (HT or T_2). In the tritium management for a breeder blanket, therefore, the form of the swept species is dependent on the local oxygen activity. At least three areas are seen as influencing oxygen activity: the purge gas, the materials of construction, and radiation effects. Some measure of oxygen activity control can be achieved by controlling the H_2O:H_2 ratio in the purge gas, but both quantities in the ratio must be known. An additional degree of control is provided by the material of construction in the region of the breeder; as long as the metal-metal oxide equilibrium that is characteristic of this material prevails, so does its characteristic oxygen activity. As for the radiation damage aspect, it is noteworthy that evidence of lithium globules has been reported by two research groups in

neutron-irradiated lithium ceramics. This phenomenon should be regarded as a radiation damage effect which introduces a potent reducing agent with the thermodynamic consequence of reducing the oxygen activity strongly.

At high temperatures and low oxygen activities, the activity of elemental lithium will increase; under these conditions, greater vaporization of elemental lithium and increased quantities of LiT (and LiH) in the condensed phase should be expected. At low oxygen activities, the concentration (therefore, inventory) of tritoxide and hydroxide in the condensed phase will decline. The converse is important: increased retention of tritoxide in the condensed phase at high oxygen activity.

Vaporization of LiOH and LiOT would increase as the $H_2O(g)$, HTO(g), and $T_2O(g)$ partial pressures increase, provided the oxygen activity is relatively high. However, since these partial pressures are themselves related to the prevailing oxygen activity, at low oxygen activity vaporization of LiOH and LiOT would be less significant.

Protium purging, the process of promoting tritium sweep-out by deliberately introducing protium in the purge gas, must be evaluated carefully. The oxygen activity will be related to the ratio of the forms in which protium is introduced, both as H_2O and H_2. At high oxygen activity, release of tritium (favored to be HTO) is enhanced by lowering the temperature and by increasing, up to a point, the H:T ratio; for higher H:T ratios a reverse temperature trend is found. At low oxygen activity, there is a general trend for tritium release (favored to be HT) to decline at lower temperatures and for this trend to become sharper as the H:T ratio rises. The technique is <u>not</u> necessarily a panacea and can even be counterproductive.

Oxygen activity is seen as having a mechanistic as well as a thermodynamic impact on tritium removal from a breeder by virtue of its relationship to the lattice oxide vacancy concentration. Higher oxygen activity is related to a decline in the vacancy concentration so that the diffusion of tritons (or tritoxide) would be impeded. A converse vacancy-oxygen activity effect would be expected: increased vacancy concentration at low oxygen activity leading to enhanced diffusion of tritium. This aspect of breeder behavior has not been quantified yet, but the effects that can be explained by it have been observed at rather high oxygen activities, e.g., 10^{-3}.

In light of the importance of oxygen activity in determining the thermodynamic state of the system, some studies on the "solubility" of H_2 or D_2 in Li_2O still need to address the oxygen activity question before a firm understanding of the results is possible. Ignoring oxygen activity control in earlier experiments could have contributed to data discrepancies and difficulties of interpretation. For example, the experiments of Katsuta, et al[6.3-27] and of Ihle and Wu[6.3-28] could have been reflecting at least in part the solubility of H_2O or D_2O, as well as the surface adsorption of H_2 or D_2 on Li_2O, in addition to the claimed solubility of H_2 and D_2.

Finally, the composition of the vapor phase over Li_2O and over the Li_2O-LiOH system has been addressed by several experimental studies.[6.3-29 - 6.3-36] The earlier papers[6.3-29 - 6.3-32] formed the basis of the JANAF[6.3-21] tables for the major species. The later papers[6.3-33 - 6.3-36] identified additional but minor species. For a detailed consideration of the relationships among the vapor species on thermodynamic grounds, practical needs will be served adequately by calculations based on the JANAF data for the gaseous species referred to above. Additional species that can be included in the calculations and which are in JANAF are Li(l and g), LiH(s, l, and g).

Lithium Aluminate

JANAF[6.3-21] data are available for most species of interest in the $LiAlO_2$ system. These species include $LiAlO_2$(s and l), AlOH(g), AlO_2H(g), HAlO(g), Al_2O_3(s and l). For gaseous Li-O species, see above discussions for Li_2O.

Data from experimental studies of the gas-phase thermochemical behavior over $LiAlO_2$ (as well as over Li_5AlO_4 and $LiAl_5O_8$), have been reported in preliminary and final form by Ikeda, et al.[6.3-37,6.3-38]

A calorimetric study[6.3-39] of the heat capacity of $LiAl_5O_8$(s) has been reported for the temperature range from 5 to 545 K. The standard enthalpy of formation at 298 K was calculated to be -1082 kcal/mol. This value is in fair agreement with that (-1094 kcal/mol) calculated by Ikeda, et al[6.3-38] from their vaporization study. However, the standard Gibbs free energy of formation in Ref. 6.3-39 is not consistent with their enthalpy and entropy values

and might reflect a typographical error. The value recalculated from their enthalpy and entropy values is -1021 kcal/mol[6.3-40].

For the temperatures of interest, estimates have to be made for the standard Gibbs free energy of formation of $LiAl_5O_8$(s). This was done by Fischer[6.3-40] by linear interpolation between the JANAF values for $LiAlO_2$ and Al_2O_3, on a total g • atom basis. The result is expressed as -4435193 + 9.38415T + 108.347T(lnT) in joules/mol between 700 to 1300 K.

Lithium Silicates

Gas phase relationships among Li-O species can be calculated as discussed above for Li_2O. The species in the vapor over Li_2SiO_3 have been identified.[6.3-41] The important ones are Li, Li_2O, LiO, SiO, and Li_2SiO_3. Data for all these except Li_2SiO_3 are in JANAF.[6.3-21] Estimates are possible for the free energy of formation of Li_2SiO_3(g), a minor species, from the data in Ref. 6.3-41 for temperatures above 1474 K, but this is probably of lesser fusion technology interest.

For the condensed phase, data are in JANAF for Li_2SiO_3(s and l). The solid phase species likely to form from burnup of Li in Li_2SiO_3 is $Li_2Si_2O_5$ for which there are data in JANAF for solid and liquid states. For the Li_4SiO_4 breeder, the burnup product is expected to be Li_2SiO_3.

Estimates need to be made for the free energy of formation of Li_4SiO_4(s) at the temperatures of interest. There is in the literature[6.3-42] an estimated value for this quantity at 298 K which, however, did not appear to provide a reliable basis for estimates at higher temperatures. Instead estimates were made[6.3-40] by linear interpolation on a total g • atom basis between the JANAF values for Li_2SiO_3 and Li_2O. The resulting expression for the standard Gibbs free energy of formation (G) of Li_4SiO_4(s) is: G(joules/mol) = $-2263610 + 468.888T - 0.008333T^2$, where T(K) is between 700 and 1300 K.

Lithium Zirconates

The vaporization of Li(g) from Li_2ZrO_3, Li_4ZrO_4, and Li_8ZrO_6 has been studied.[6.3-43] Up to about 1650 K, no zirconium-bearing species were detected in the vapor. Li and O_2 were the main species, with minor

contributions from LiO, Li_2, and O. Using these data and the extrapolated heat capacities, the thermodynamic quantities, including free energy functions (not Gibbs free energies) were calculated for Li_2ZrO_3. The enthalpies of formation of all three zirconates at 298 K are: Li_2ZrO_3, -419.6 ± 2; Li_4ZrO_4, -565.0 ± 4; Li_8ZrO_6, -851.8 ± 4, all in kcal/mol.

Lithium Titanate

Data for Li_2TiO_3(s and l) can be found in JANAF.[6.3-21] Calculations have not been performed yet.

Advanced calculations of a scope to match those done for Li_2O have just been initiated at ANL for $LiAlO_2$ but not yet for the other breeders. Comparison of the breeders on this basis is, therefore, not yet possible. However, certain relationships that became evident from the Li_2O calculations discussed above are expected to hold qualitatively for other materials.

Measurements of the solubility of tritiated species in the breeders cannot be separated from the need for measurements of surface adsorption of these species. For breeders other than Li_2O, the surface adsorption is likely to be a greater contributor than solubility to tritium retention. Lithium oxide is unique in its strong reactive affinity for H_2O to form LiOH so that the solubility of hydroxide is a dominant issue. For the other breeders, this hydrolysis reaction is not as extensive and there is greater significance in the potential for H_2O and perhaps H_2 simply to be adsorbed. This expectation, however, must be tempered with cognizance of the role of oxygen activity. It is now recognized from thermodynamic considerations that, at low oxygen activities (at levels that could prevail in a breeder because of container effects), retention of tritium because of solubility as tritoxide will be reduced. At high oxygen activities, retention as the solute, tritoxide, will be enhanced. It is not known if there are concomitant effects at the surface that would either increase or reduce adsorption. Quite likely, oxidic, hydroxidic, and cationic sites on the surface would be involved in adsorbing H_2O and H_2 to different degrees depending on oxygen activity.

The research activity that would be appropriate, therefore, and which is being pursued at Argonne National Laboratory, is measurements of the adsorption isotherms for the adsorbates H_2O and H_2 on solid breeders as a function of temperature and of oxygen activity. The adsorption isotherms

provide data directly for the amount of adsorbed material but they also provide the means for: (1) deriving heats of adsorption which will distinguish between chemisorption and physiosorption; (2) distinguishing between solute and adsorbed species by means of deuterium-substitution and exchange techniques; (3) distinguishing between single site and multiple site adsorption; and (4) deriving other surface thermodynamic quantities like the entropy of adsorption.

In addition to the adsorption measurements, there is also the complementary need for measurements to determine the concentration and the atomic and molecular nature of surface species. These, too, would need to be done as a function of temperature and oxygen activity. The data would be valuable adjuncts in the interpretation of the adsorption isotherm measurements. One appropriate technique would be surface reflectance infra-red spectroscopy. However, unless resources are ample, it is probably best to defer studies that require samples to be handled in vacuum because the surface phenomena of interest involve features that would be altered or destroyed in a vacuum environment.

There should be early examination of the magnitude of impurity effects. Considering that in the tabulation of impurities in the BCSS reference blanket material (Section 6.12), the amounts of impurities for $LiAlO_2$ totaled several tenths of a percent, and that the tritium inventory at a given time is much less, the meaning of tritium release data from tests on such materials becomes arguable. Impurities introduce new thermodynamic variables, and importantly, they affect the defect structure of the solid state. Diffusional properties and processes related to diffusion would be affected. The adsorption isotherm measurements could, in principle, provide one avenue toward an answer if the breeder compositions (impurities) are accurately controlled. However, perhaps enough is known about solid state theory and about measurements on analogous systems so that an informed estimate can be made.

For some of the solid breeders, Li_4SiO_4 and Li_8ZrO_6 particularly, accurate free energy of formation data as a function of temperature up to 1300K are needed for good thermodynamic calculations. The most accurate measurements to yield such data would be calorimetric measurements of the enthalpy of formation at a reference temperature, 298K, and accurate heat capacity measurements up to the temperature of interest.

6.3.2.2 Thermophysical/Transport

Thermophysical properties of solid breeders covered in this section include: thermal conductivity, specific heat, and thermal expansion; transport properties covered include tritium diffusivities. These properties largely determine the thermal performance and tritium recovery of the solid breeder blankets.

Thermal Conductivity

A review of literature data on the thermal conductivity (k) of unirradiated sintered solid breeder materials has been carried out by Suiter.[6.3-44] The data reviewed include Li_2O, γ-$LiAlO_2$, a mixture of γ- and α-$LiAlO_2$, Li_4SiO_4, Li_2TiO_3, and Li_2ZrO_3. In general at comparable temperatures Li_2O has the highest thermal conductivity. For example, at 500°C $k(Li_2O)$ ~5 W/mK whereas the thermal conductivity of all the other materials mentioned above ranges between 1.75 and 2.5 W/mK.

At low to intermediate temperatures, heat conduction in dielectric solids is mainly determined by phonon scattering. A general correlation[6.3-45] for the lattice thermal conductivity (k_o) may be written as

$$k_o = \frac{1}{A + BT\varepsilon} + C \ , \qquad [6.3\text{-}5]$$

where T is the temperature and A incorporates all other sources of phonon scattering except phonon-phonon processes. Examples of the non phonon-phonon processes are effects due to impurities, defects, specimen sizes, and microstructure. These are mostly temperature independent.[6.3-46] The parameter B in Eq. [6.3-5] is a material-specific parameter related to the phonon-phonon scattering mechanism[6.3-46] and ε usually ranges between 1 and 2.[6.3-47,6.3-48] The parameter C in Eq. [6.3-5] represents a saturation term for which the thermal conductivity reaches a minimum value which is insensitive to temperature.[6.3-47 - 6.3-50] Equation [6.3-5] represents well the temperature dependence of k_o when electronic and radiative contributions[6.3-46] are negligible.

Equation [6.3-5] describes only the lattice component of the thermal conductivity. When porosity (P) is present in the solid, a correction factor needs to be applied, i.e.,

$$K = K_o\, f(P) \ . \qquad [6.3\text{-}6]$$

For low porosity (i.e., $P \lesssim 30\%$) the standard Maxwell-Euken porosity[6.3-51] correction applies which gives

$$f(P) = \frac{1 - P}{1 + bP} \ , \qquad [6.3\text{-}7]$$

where b is an empirical parameter that is usually temperature dependent. For Li_2O the value of b has been determined by fitting to the experimental data.[6.3-11] The same value of b has also been used in Eq. [6.3-7] to correct for porosity effect for γ-$LiAlO_2$, Li_4SiO_4, and $LiZrO_3$.[6.3-51]

For higher porosity (i.e., $P > 30\%$) the correction may depend not only on P as in Eq. [6.3-7] but also on details of the microstructure. This is well illustrated by the experiment of Leibowitz and Bloomquist[6.3-50, 6.3-52] in which the high temperature ($T > 800°C$) thermal conductivity of γ-$LiAlO_2$ was found to decrease by a factor of 4 when the porosity varies from 22% to 35%. The large reduction may result from the presence of interconnected porosity; the Maxwell-Euken type porosity correction no longer applies under such conditions.

The presence of gases in the pores will affect the thermal conductivity. This is also true for the sphere-pac (or powder-like) breeders for which the interparticle spacings can be considered as interconnected porosity. Gas species, gas pressure, and solid types will all enter into the thermal conductivity consideration.[6.3-53]

Irradiation generally degrades thermal conductivity by introducing defects in the material. This can be incorporated into the parameter A in Eq. [6.3-5]. Irradiation effects on thermal conductivity are relatively large at low temperatures (e.g., room temperature) where 50-100% reductions from the unirradiated values have been noted.[6.3-53] Typically the reductions also exhibited a saturation behavior beyond which the thermal conductivity became insensitive to further irradiation. At higher temperatures irradiation effect diminishes since the phonon-phonon scattering becomes more important. In addition, some of the irradiation-induced defects (which serves to reduce k) tend to be annealed out at higher temperatures. Together these two factors reduce the effects of irradiation on k at higher temperature. The TRIO-1

results[6.3-54] provide the only known experimental data on the thermal conductivity of irradiated γ-$LiAlO_2$ (in He environment). Determined from heat transfer calculations and the thermocouple recordings, the thermal conductivity of the irradiated γ-$LiAlO_2$ (65% TD) is reported to be 1.2 W/mK at 700 K, about 10% lower than the unirradiated value.

Design curves (Figs. 6.3-5 through 6.3-8) have been generated for the thermal conductivities of sintered and sphere-pac Li_2O and γ-$LiAlO_2$, with and without irradiation effects. Details of the materials data bases, physical models, estimation procedures, and limited model verifications can be found in Ref. 6.3-53. These design curves provide the basis for the recommended thermal conductivities (Section 6.3.5) which were used in the design of the BCSS solid breeder blankets (Chapters 8, 9 and 10).

Specific Heat

In cases where the thermal conductivities of solid breeders are deduced from measured thermal diffusivities (e.g., by laser pulse type dynamic experiments), the knowledge of the specific heat of the relevant breeder materials is required. At relatively low temperatures (i.e., 300-400°C for lithium ceramic breeders), the specific heat follows the familiar temperature pattern as prescribed by the Debye Model and increases relatively rapidly with temperature. Above 300-400°C the specific heat still increases with temperature but at a much lower rate. It does not settle into the classical Dulong-Petit value of 3R (R = gas constant) mainly because of the anharmonic effects such as thermal expansion.

The available specific heat data of lithium ceramics has been collected. These include: (1) Measurements on Li_2O up to 1073 K from a number of experiments;[6.3-55 - 6.3-59] (2) Data of γ-$LiAlO_2$[6.3-51] (398-700 K) and mixed phase $LiAlO_2$[6.3-60] (298-1800 K); (3) Experimental results on Li_4SiO_4 (with a 1 wt% Li_2SiO_3[6.3-51] over a temperature range of 373-773 K) and on phase pure Li_2SiO_3 and $Li_2Si_2O_5$ over a temperature range of 298-1098 K; (4) Measurements on Li_2TiO_3[6.3-60] covering the temperature range of 298-1173 K; (5) Data of monoclinic Li_2ZrO_3 (373 to 773 K).[6.3-51, 6.3-57]

A survey of these results indicates that a reasonable data base exists on the specific heats of solid breeders for fusion application.

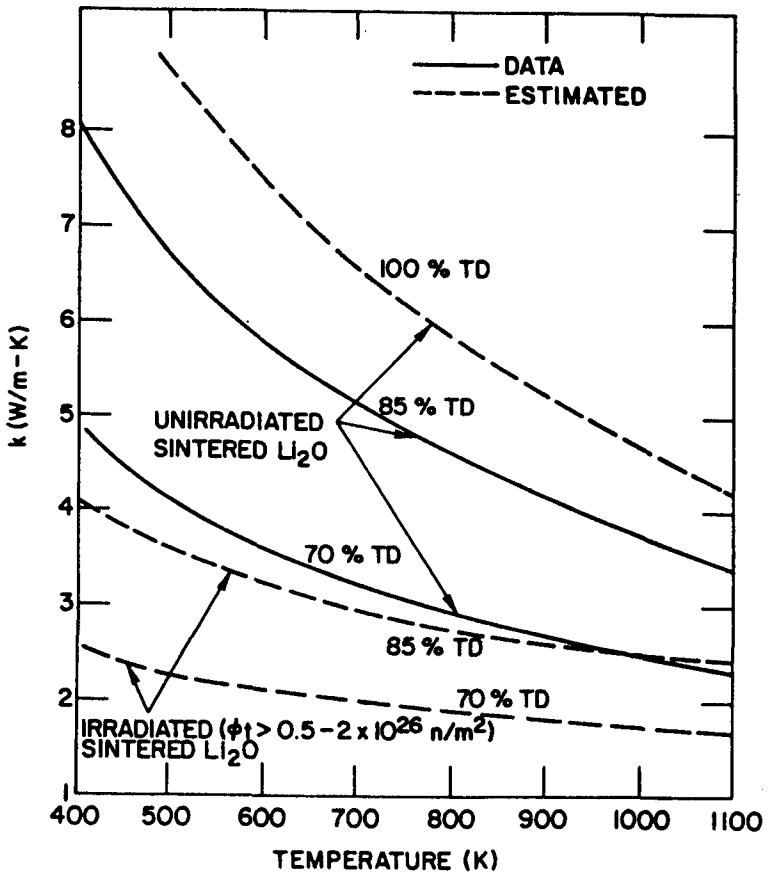


Figure 6.3-5. Thermal conductivity of sintered Li_2O as a function of temperature.

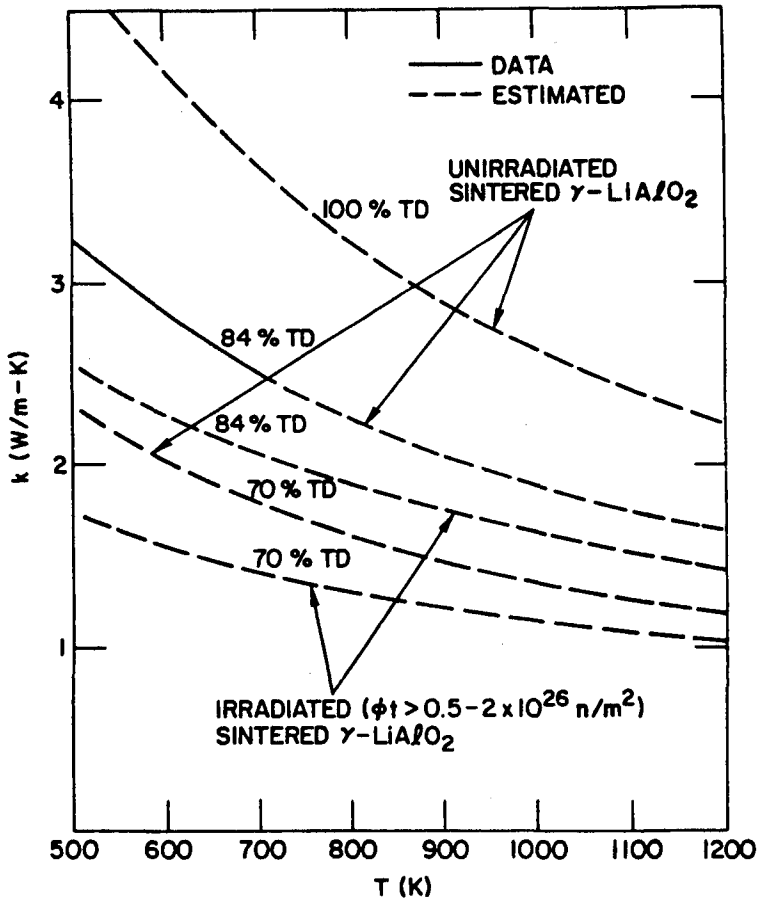


Figure 6.3-6. Thermal conductivity of sintered γ-$LiAlO_2$ as a function of temperature.

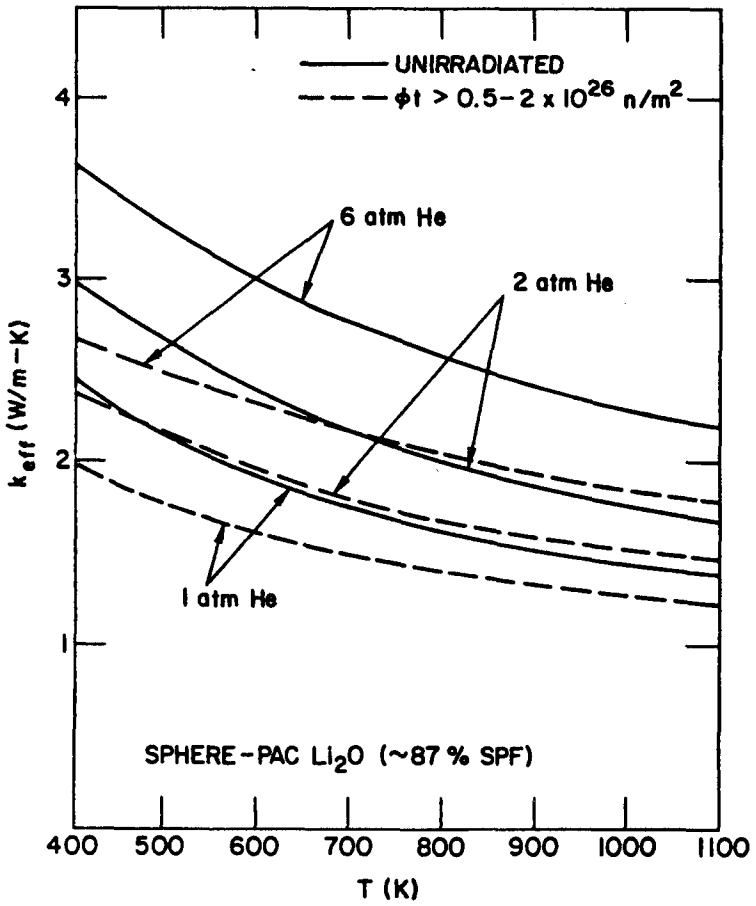


Figure 6.3-7. Thermal conductivity of sphere-pac Li_2O as a function of temperature and helium fill-gas pressure.

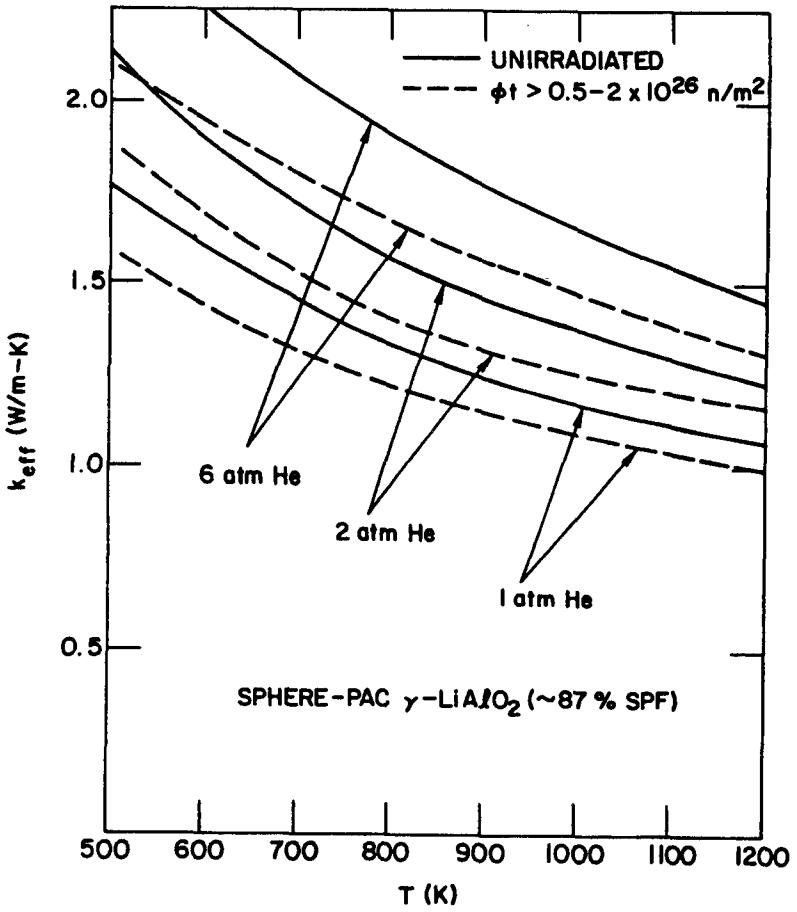


Figure 6.3-8. Thermal conductivity of sphere-pac γ-$LiAlO_2$ as a function of temperature and helium fill-gas pressure.

Thermal Expansion

To determine the solid breeder thermal responses as required for heat transfer and mechanical analyses, one needs to know the thermal expansion behavior of the breeder materials. A review of the existing literature has been given by Suiter.[6.3-44] The available data include: (1a) Li_2O pellets[6.3-51] (85% TD, 373 K to 1273 K),[6.3-61] and (1b) single crystal Li_2O (373 K to 1273 K);[6.3-61] (2a) pure γ-$LiAlO_2$ (373 K to 1173 K),[6.3-51] and (2b) γ-$LiAlO_2$ with some possible mixing of $LiAl_5O_8$ (373 K to 1173 K).[6.3-62] The data agree closely with those from 2a; (3a) Li_4SiO_4 [6.3-51,6.3-63] (from 298 K to 1173 K), and (3b) Li_2SiO_3 and $Li_2Si_2O_5$[6.3-64] (from 373 K to 973 K). In general the data of Li_2SiO_3 and $Li_2Si_2O_5$ are close to each other and lower than that of Li_4SiO_4; (4) Li_2TiO_3[6.3-65] ($\gtrsim$ 90% TD, 373 K to 1073 K); (5) Li_2ZrO_3[6.3-51] (85% TD, 373 K to 1073 K). These existing measurements indicate that aside from possible extension, the current data base on the solid breeder thermal expansion are reasonably complete.

Figure 6.3-9 shows the length change $(\Delta L/L_o)$ due to thermal expansion for four solid breeder materials. The Li_2O has the largest thermal expansion, whereas those of the γ-$LiAlO_2$ and Li_2ZrO_3 are the smallest. Also plotted on Fig. 6.3-9 are the thermal expansions of two structural materials, PCA which is a T_i-modified 316 stainless steel and a ferritic alloy HT9. The difference in the thermal expansion between solid breeders and structural materials will give rise to solid-breeder/structure mechanical interaction, the magnitude of which is apparently the largest for the Li_2O/HT9 combination. The resulting interface pressure due to breeder/structure differential thermal expansion and the associated stresses in the structural materials will be discussed later in Section 6.3.4.5.

Tritium Diffusivities

Data of tritium diffusion in various solid ceramic breeders have been determined primarily from release-type experiments (both laboratory and in-reactor experiments). The laboratory experiments were usually conducted on irradiated lithium ceramic samples from which the tritium release data can be obtained as a function of time at various temperatures. Tritium diffusion

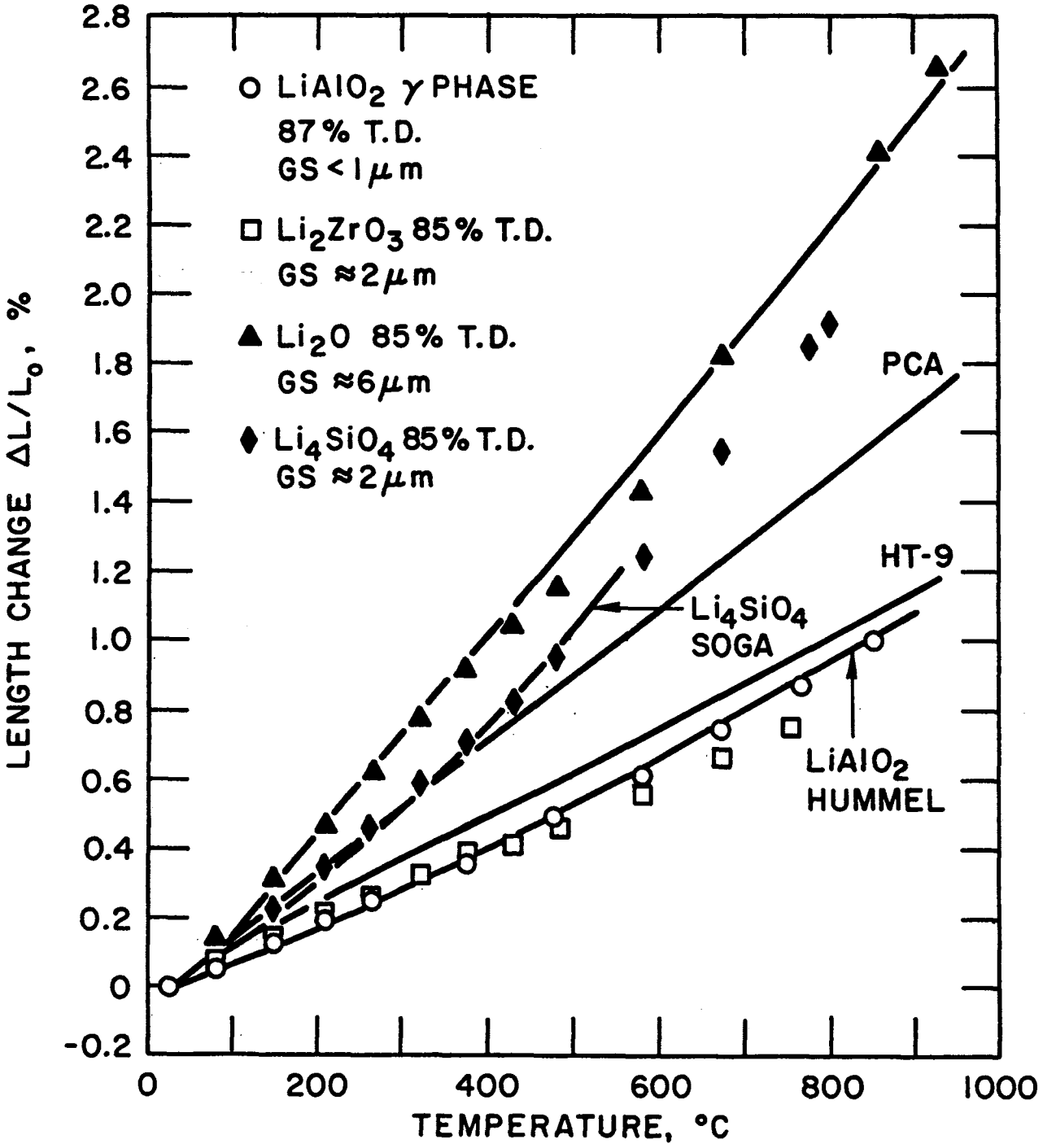


Figure 6.3-9. Thermal expansion of solid breeder and structural materials.

coefficients in solid breeder materials may be extracted from these release data, assuming the release process is diffusion-controlled.

The majority of the release data pertained to Li_2O.[6.3-66 - 6.3-71] Below 400°C the activation energy varies between 1 and 1.45 eV among four separate groups of data.[6.3-66 - 6.3-69] However, only one data set[6.3-69] exhibits a relatively large activation energy of ~ 1.48 eV. The rest of the data[6.3-66 - 6.3-68] show activation energies clustering around 1 eV (23000 cal/mol). It must be noted that the absolute values of D_T, as determined from the tritium release data, depend critically on the values of grain size which are characteristically poorly defined. The activation energies, on the other hand, were determined from the slope of the ln(D) versus 1/T plot and should be insensitive to the uncertainty in grain size, provided a consistent grain size is used throughout.

There are yet several more sets of data between 500 and 950°C.[6.3-70-6.3-75] The activation energy among these data sets varies considerably from ~0.3 eV, [6.3-70 - 6.3-72] to ~ 0.8 eV,[6.3-73] to a value of ~1.2 eV.[6.3-70,6.3-71, 6.3-74] The last two values are reasonably close to the low temperature (i.e., $\lesssim$ 400°C) results.[6.3-66 - 6.3-68] However, the low value of 0.3 eV is consistent with the activation energies of deuterium and hydrogen diffusion in Li_2O.[6.3-71,6.3-75]

The various data of tritium diffusivity in Li_2O have been analyzed by Shearer et al.[6.3-3] and shown in Fig. 6.3-10. The most recent data[6.3-73] determined from single-crystal Li_2O are also included for purposes of comparison. It is noted that the single-crystal tritium diffusivity data of Guggi et al. are 3 orders of magnitudes higher than the previous results at comparable temperatures. Application of the single-crystal tritium diffusivity will thus result in a markedly lower calculated tritium diffusive inventory in Li_2O. As will be discussed in subsequent sections, the calculated tritium diffusive inventories are much lower than the measured residual tritium in Li_2O after irradiation, thus indicating possible roles of irradiation-induced defect trapping of tritium and purge chemistry effects.

Several sets of tritium release data are available for $LiAlO_2$ between 400 and 800°C. The derived tritium diffusion coefficients (D_T) generally clustered into two groups. One group[6.3-68-6.3-70,6.3-75,6.3-76] has activation energies between 0.5 to 0.7 eV. Typical value of D_T at 600°C is ~ 10^{-9} cm^2/

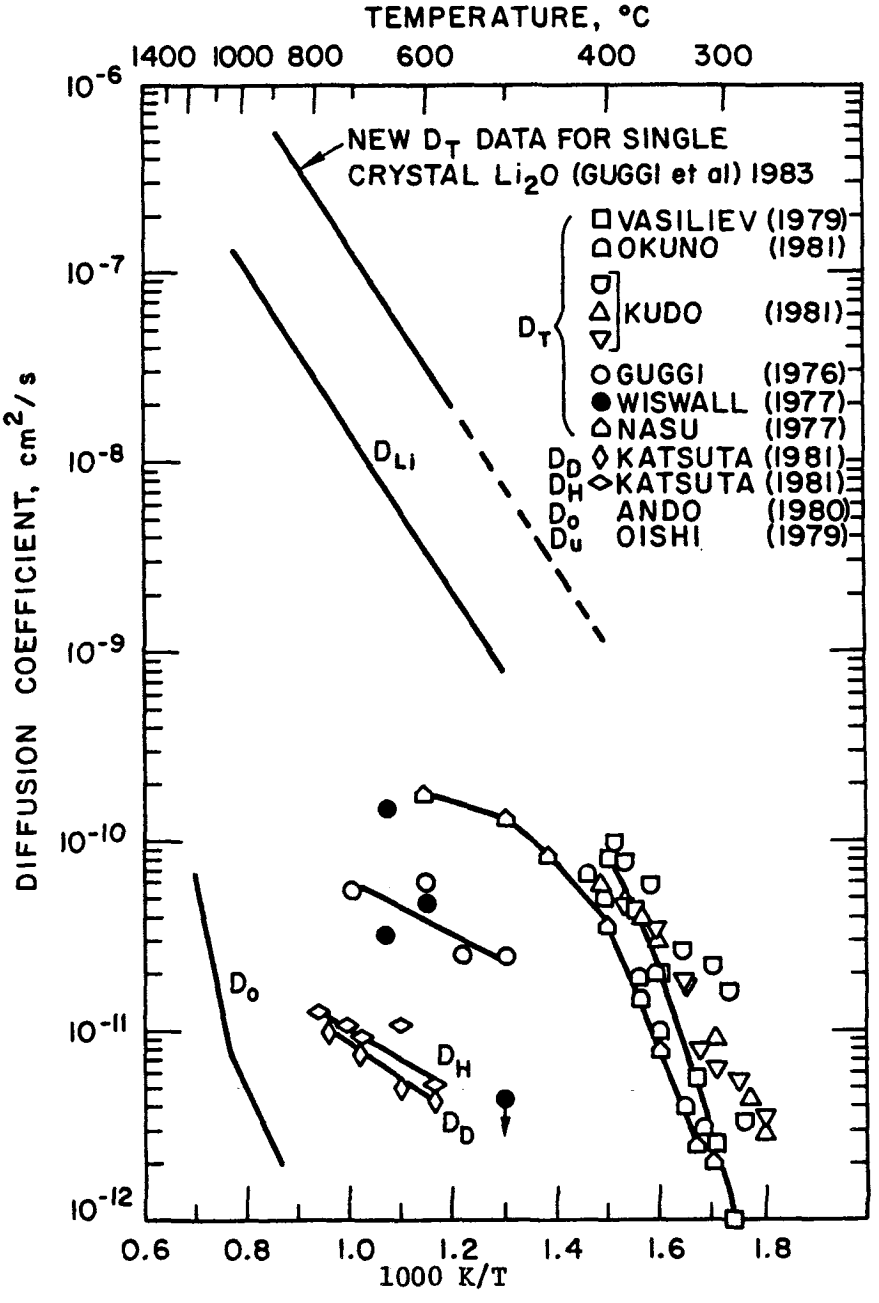


Figure 6.3-10. Temperature dependence of diffusion coefficients of tritium, oxygen, lithium, hydrogen, and deuterium in Li_2O.

sec.[6.3-70] The other group[6.3-74,6.3-77] has much larger activation energies (1.5-1.9 eV). The D_T of one member of this group is derived from the TRIO-1 irradiation experiment which will be discussed later in Section 6.3.4.1.

The data of Li_2SiO_3 indicate that D_T has an activation energy of ~ 0.5 eV in the temperature range of 200-700°C[6.3-69]; its value at 600°C is ~ 10^{-9} $cm^2/sec.$[6.3-69,6.3-74]

The above survey of tritium diffusivities in solid breeders showed a considerable spread in the apparent activation energies for tritium diffusivity in solid breeders. A consistent understanding is not available at present. Possible causes for the data scatter include (a) different experimental conditions (e.g., wet or dry), (b) different sample characteristics (e.g., single crystal versus polycrystalline, pellets, powder forms), and (c) effects of other mechanisms besides bulk diffusion that may contribute to the tritium release process in the release-type experiments.

In terms of the R&D requirements for solid breeder thermophysical and transport properties, additional studies are necessary for thermal conductivity and tritium diffusivity. In the area of thermal conductivity, the effects of porosity (especially for P > 30%) and irradiation (level of degradation, saturation phenomenon) need to be established experimentally. For the sphere-pac breeders, measurements of the effective thermal conductivity as a function of temperature and filled-gas pressure are also required. In the area of tritium diffusivity, measurements for single-crystal γ-$LiAlO_2$ are highly recommended. Additional experimental studies of the effects of extrinsic impurities and defects in solid breeders are also necessary as they generally exert significant influence on transport properties. Finally as pointed out in Section 6.3.2.1, the oxygen activity is another important variable which should be considered in tritium diffusivity measurements.

6.3.2.3 Mechanical

Among the various solid breeder properties, the least known are the mechanical properties which include elastic moduli, strength, and high-temperature deformation behavior. These mechanical properties are particularly important to the engineering design of solid breeder blankets.

During the first year of BCSS, estimates of elastic moduli and fracture strength of Li_2O were given based on previous work.[6.3-3,6.3-78] No experimental data on solid breeders existed then, very few data exist to date. An experimental program on solid-breeder mechanical properties has been initiated at ANL; information on selected materials will become available in the near future.

The existence of an experimental program on solid-breeder mechanical properties indicates a recognition of their R/D needs in the U.S. Fusion Program (note: both the Japanese and The Joint European Fusion Materials Programs have also recently initiated efforts on solid-breeder mechanical properties). The impending availability of data diminishes the need for mechanical properties estimates (such as those done before for Li_2O). Discussions below shall thus briefly review the reasons for their R/D needs and the areas where they are of crucial importance.

Elastic Moduli

Frequently the term elastic moduli are associated with the Young's modulus (E) and Poisson's (ν) ratio of materials deformed (in the elastic range) under external loads. If materials are not isotropic, more than two constants (E and ν) are required to characterize the elastic behavior. The elastic moduli reflect the atomic bond strength of materials; their effects enter into tensile fracture strength (especially brittle fracture of ceramics), wave velocity in solids (needed to compute phonon lattice thermal conductivity), and all continuum mechanics analysis of stresses and strains. Elastic moduli also provide information on lattice defects; their measurements are useful in investigating the nature of radiation damage. Elastic moduli are thus both scientifically and technologically important.

Several issues related to the BCSS solid-breeder blanket designs cannot be fully addressed owing to the lack of data on elastic moduli. A notable example is the Li_2O swelling accommodation in the Li_2O/He/HT9 design. Even before irradiation-induced swelling takes place in Li_2O, differential thermal expansion between Li_2O and the HT9 cladding will already cause breeder/structure mechanical interaction (BSMI). If Li_2O or the HT9 cladding cannot deform easily, the Li_2O/HT9 interface pressure will build up, leading to large cladding stresses and/or premature failure. This is a potential

concern for the Li_2O/He/HT9 blanket, the resolution of which depends on the Li_2O mechanical properties/behavior. Not only are the elastic moduli necessary for a proper assessment of the severity of BSMI (thereby effecting design modifications if necessary), data on fracture strength and high-temperature deformation behavior of Li_2O are also required.

Other blanket designs with γ-$LiAlO_2$ face similar BSMI problems, but with less expected severity than that of Li_2O. Compared to Li_2O, γ-$LiAlO_2$ exhibited little dimensional change under neutron irradiation (Section 6.3.3); the use of sphere-pac, rather than sintered, γ-$LiAlO_2$ further lessens BSMI. Small spherical particles can rearrange themselves easier under load than the sintered product, which is likely to crack, translate, and deform during blanket operation.

Strength

General tendency of brittle fracture in ceramics is well known. Macrocracking of sintered solid breeders has been predicted analytically[6.3-2, 6.3-79] and observed in both ex-[6.3-80] and in-reactor[6.3-81] experiments. Tensile stresses, generated by temperature gradients in solid breeders (either during steady-state or temperature cyclings), were responsible for the observed macrocracking. To a good approximation, a stress criterion may be used for brittle fracture below which cracking will not occur. Tensile fracture strengths of solid-breeder ceramics provide such a criterion.

Two important aspects of macrocracking are related to the performance of blankets using sintered solid breeders. The first is the cracked fragment relocation which will alter the separation distance between solid breeder and structural material. If the solid breeder (such as Li_2O) has a narrow operating temperature window, the change in gap conductance due to breeder relocation can easily cause breeder temperatures to exceed either the upper and/or the lower temperature limit (see Performance/Lifetime Analysis, Chapter IX.2, Ref. 6.3-3 for full discussion). The second aspect of macrocracking is related to stress intensification in the structural materials near the region of breeder macrocracks. The magnitude of BSMI will be amplified adjacent to the breeder macrocracks to cause even larger localized structural deformation, with an increasing likelihood for premature structure failure (see earlier discussion on BSMI under elastic moduli).

As a result of the first year BCSS investigation,[6.3-3] two methods, breeder segmentation and transformation toughening, were suggested as possible means to overcome the difficulties associated with breeder macrocracking. Sphere-pac breeders fall into the first class which can be thought of as a form of precracking. The small particle sizes mean that temperature gradient across particles should be insignificant, and that the resultant thermal stresses should be insufficient to cause particle cracking. Because these particles are in discrete contact with the surrounding structural materials and among themselves, gap conductance variation is also much smaller as long as particle sintering, particle breakup and resettlement do not occur during blanket operation. Transformation toughening is another approach through which solid breeder strengths may be enhanced to a point to prevent thermal-gradient induced cracking. The method has been employed with success on certain ceramics for which toughness is an important requirement. Solid breeder toughening is an area most suitably placed under advanced solid-breeder materials (Section 6.3.1) for future R&D.

One might argue that the R&D need for tensile fracture strength diminishes for all sphere-pac solid breeders (e.g., γ-$LiAlO_2$) by virtue of their equivalence to precracking. However, there remains the question of whether the spheres will remain intact during blanket operation. While the particle thermal stresses are expected to be insignificant, the Hertzian contact stresses (again tensile in nature) may become high enough to cause particle breakup. If particle cracking occurs, BSMI will be temporarily relieved owing to particle resettlement. However, the risk of these broken particles being displaced into undesirable blanket locations (i.e., purge channels) should be considered.

Finally it is noted that in the case of γ-$LiAlO_2$, strong justification has <u>not</u> been found for the necessity of a sphere-pac configuration. One can probably design a monolithic, sintered γ-$LiAlO_2$ blanket (i.e., STARFIRE design) within the same temperature limits and live with the gap conductance uncertainties. Inherent stabilities (thermal, chemical, and irradiation) and the wider design temperature window of γ-$LiAlO_2$ make design requirements less constraining for this material than those for Li_2O.

High-Temperature Deformation Behavior

Sintering, hot pressing and creep, with and without irradiation enhancement, belong to this class of mechanical properties or behaviors. Sintering refers to porosity elimination in sintered solid breeders; it also applies to neck growth between particles in sphere-pac form. Crack healing, which usually occurs concurrent with sintering, is another manifestation of sintering and grain growth. All of these processes involve mass transport of atomic species via various diffusional mechanisms, which generally have a strong temperature dependence. Hot pressing and creep differ from sintering in that external loads are present, in addition to high temperatures. They differ from each other in the form of deformation; hot pressing (shrinkage) does not conserve volume, whereas creep generally does. All of these deformation processes have an irradiation-enhanced component, so that ex-reactor data alone are insufficient to characterize solid-breeder deformation behavior during blanket operation.

High-temperature deformation behavior and mass transfer determine the upper temperature limits for solid breeders. Other than vapor-phase mass transfer which moves solid breeders in the blanket by vaporization and condensation (see discussions on thermodynamic/chemical and mass transfer/compatibility, this section), the concern over any undesirable solid-breeder microstructural changes (e.g., grain growth and porosity elimination will increase tritium diffusion path length and seal off release pathways) is related to tritium release. Since tritium diffusivities in solid breeders increase rapidly with temperatures, the negative effect of grain growth on tritium diffusion is compensated by the increased tritium diffusivities. In Li_2O with high tritium diffusivity, limited grain growth may be tolerable. The situation is unclear, however, with the other solid breeders. Nevertheless, it remains valid to state that significant microstructural changes in solid breeders should be avoided, otherwise microstructural tailoring for specific purposes (i.e., tritium release, toughening, etc.) loses its footing. If the solid breeder microstructure is mandated to remain as fabricated, the effects of irradiation naturally gain more significance (therefore their R/D needs are more important) because radiation enhancement of these high-temperature processes may be regarded as equivalent to lowering the upper temperature limit (as determined from ex-reactor and short term in-reactor experiments).

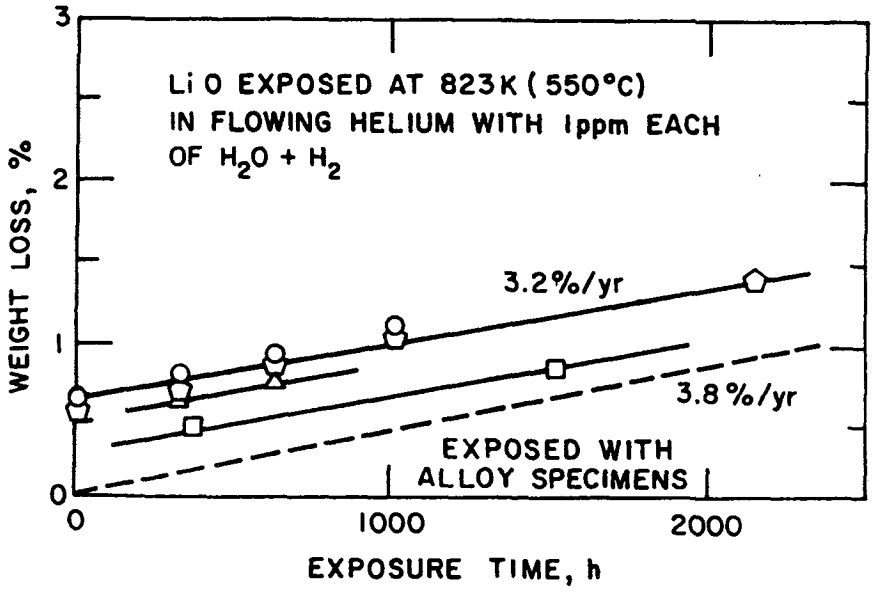


Figure 6.3-12. Weight loss for Li_2O pellets exposed at 823 K in flowing helium containing 1 ppm each of H_2O and H_2. Each symbol type represents weight loss for a single specimen after various times.

initial transient, with or without prior baking, are comparable after exposure to the flowing gas environment. This observation indicates that any residual LiOH in the specimens is released at 550°C in a short time compared to the length of these tests. The results yielded a weight loss of 3.2%/yr for Li_2O pellets exposed to the flowing-gas environment. This value is similar to that observed for Li_2O pellets exposed with alloy specimens.

Two additional tests of Li_2O pellets in a flowing helium environment containing 1 ppm each of H_2O and H_2 are now in progress. Prior to the test, the Li_2O pellets were baked at the test temperatures (450 and 650°C) for ~7 h under dynamic vacuum in order to reduce the residual LiOH concentration. At both temperatures the pellets showed significant weight loss after baking. The weight loss was between 4 and 11 mg at 650°C and 2-3 mg at 450°C. After exposure to the flowing gas environment for up to 1400 h at 450°C, the Li_2O pellets showed slight weight gain. The pellets exposed to the gas environment at 650°C indicate larger weight losses than those at 550°C.

In summary, only Li_2O was found to react with structural materials at 550°C to form corrosion scales. Thicknesses of the total scale and internal penetration were similar for Type 316 stainless steel and ferritic alloy HT9. Increasing H_2O content in the helium carrier gas increased corrosion. However, the corrosion rate decreased with time, indicating that corrosion may saturate at longer exposure times. Significant Li_2O mass transfer (weight loss) was observed at 550°C in flowing helium containing 93 and 1 ppm H_2O. Similar tests showed weight gain at 450°C and larger weight losses at 650°C. Further tests of this topic are warranted.

6.3.3 Irradiation Experiments

Four solid breeder irradiation experiments (TULIP, FUBR-1A, TRIO-1, and VOM-15H) are covered in this section. TULIP (Section 6.3.3.1) and FUBR-1A (Section 6.3.3.2) are sealed capsule experiments; TRIO-1 (Section 6.3.3.3) and VOM-15H (Section 6.3.3.4) are in-situ tritium recovery experiments. Discussions of the experimental results will focus on the tritium, helium, and swelling behavior in Li_2O and γ-$LiAlO_2$. Behavior differences noted under sealed capsule and in-situ environments will be summarized in Section 6.3.3.5.

6.3.3.1 TULIP

TULIP is a sealed capsule, fast-neutron irradiation experiment on relatively large grain diameter (40-50 μm), high-density (~89% TD) Li_2O.[6.3-87] The experiment was conducted in EBR-II over a rather narrow range of irradiation temperatures (608-625°C to ~3 at $\%^6Li$ burnup). Four Li_2O breeder elements, clad with either a Ti-modified 316 stainless steel or a 35% Ni alloy, were used. The breeder element design is depicted in Figure 6.3-13.

The irradiation conditions of TULIP and the results of tritium/helium retentions in irradiated Li_2O were previously reported by Porter, et al.[6.3-87,6.3-88] Scanning electron microscopy (SEM) examinations of the Li_2O microstructure were performed by Mattas;[6.3-89] Liu, et al.[6.3-90] provided an interpretation of the relationships between the observed Li_2O microstructure and the measured tritium/helium retentions. Discussions below shall thus highlight results and major conclusions from the above studies.

Table 6.3-5 lists the TULIP irradiation conditions and the measured helium/tritium retentions in the irradiated Li_2O. Eight of a total of 26 Li_2O pellets from selected capsules were chosen for SEM examination. The capsules from which the pellets were taken are identified in Table 6.3-5. In addition to the irradiated pellets, a single unirradiated pellet was also examined.

Figure 6.3-14 shows the SEM pictures of the unirradiated Li_2O archive sample. The fracture surface consists of roughly equal amounts of intergranular and transgranular fracture. The intergranular fracture is shown in Fig. 6.3-14a and 3-14b. The grain size is 40-50 μm in diameter, and the grain boundary surfaces have a nodular appearance. It is not known if this nodular appearance is typical of as-fabricated pellets, since this particular pellet was exposed to atmosphere for several months before being examined. The exposure may have resulted in an increased moisture content in the pellet. The transgranular cleavages (Fig. 6.3-14c and 3-14d) indicate that some porosity exists within the grains. These pores are 5-10 μm in diameter. The intergranular porosity can be identified by the nodular growths on the pore surfaces.

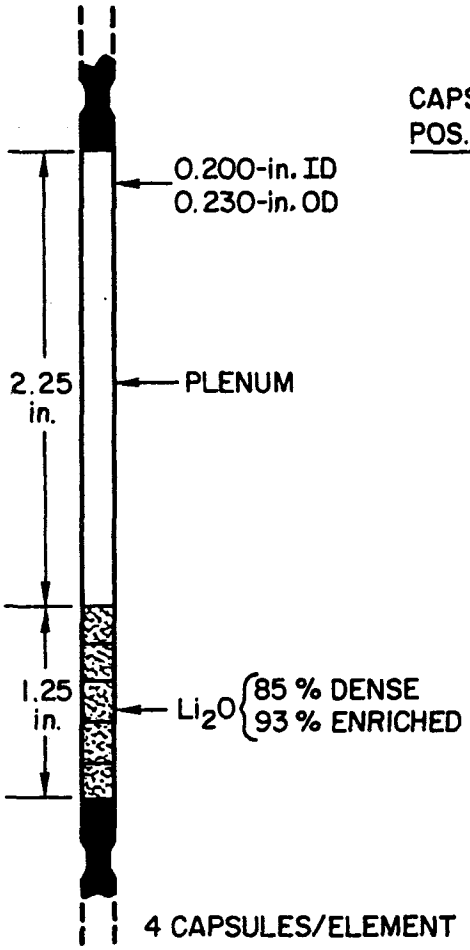
The eight irradiated Li_2O pellets can be grouped together according to their irradiation temperatures and burnups for purposes of microstructure comparisons.[6.3-91] Major findings from the SEM examinations are:

TABLE 6.3-5. Li_2O IRRADIATION CONDITIONS AND TRITIUM/HELIUM RETENTIONS (TULIP)

Element	Position	Batch	Clad	Peak Temp. °C	ϕ/ϕ_{max} [1]	Reaction Rate [2] x 10^{13}/s	Heating Rate [3] x 10^7 W/m^3	Li^6 Bu at%	T/He Production x 10^{20}	T Retained % (wppm)	He Retained % (wppm)	Examined
EA401	1	3 of #1 1 of #3	35% Ni	606	0.55	3.89	5.12	1	3.46	8.1 (140)	71 (1630)	
	2	#3	"	624	0.89	5.53	7.78	1	3.65	6.4 - 7.3 [4] (117 - 133)	63 (1520)	
	3	#2	"	625	1.0	6.08	8.0	1	3.92	5.3 - 6.7 [4] (104 - 131)	51 (1320)	
	4	#2	"	608	0.86	5.48	7.21	1	3.76	8.4 - 9.7 [4] (158 - 182)	53 (1330)	X
EA403	1	#4	Ti Mod 316	606	0.55	3.89	5.12	1	3.64	6.2 (112)	63 (1520)	X
	2	#4	"	624	0.89	5.53	7.28	1	3.59	6.2 - 7.4 [4] (111 - 133)	64 (1530)	X
	3	#4	"	625	1.0	6.08	8.0	1	3.11	7.9 - 8.0 [4] (124)	53 (1100)	X
	4	#4	"	608	0.86	5.48	7.21	1	3.48	50 (870)	45 (1050)	X
EA400	1	#3	35% Ni	606	0.55	3.89	5.12	3	8.82	NA	NA	
	2	#3	"	624	0.89	5.53	7.28	3	11.6	1.3 (75)	9 (704)	
	3	#2	"	625	1.0	6.08	8.0	3	13.8	NA	NA	
	4	#1	"		0.86	5.48	7.21	3	11.4	4.6 (262)	22 (1700)	X
EA404	1	#3	Ti Mod 316	606	0.55	3.89	5.12	3	8.82	NA	NA	
	2	#3	"	624	0.89	5.53	7.28	3	11.2	1.4 (78)	11 (790)	X
	3	#2	"	625	1.0	6.08	8.0	3	13.8	NA	NA	
	4	#1	"	608	0.86	5.48	7.21	3	11.2	6.5 (364)	18 (1350)	X

1. $\phi_{max} = 1.232 \times 10^{15}$ n/cm^2.s, E > 0.1 MeV.
2. Based on average of 5-group neutron fluxes and (n,^{6}Li) reaction cross sections over an energy range of 0.01 to 6.0 MeV.
3. Based on an energy of 4.78 MeV per (n,^{6}Li) reaction.
4. More than one Li_2O pellets dissolved for tritium analysis.

TEST CAPSULE DESIGN



CAPSULE POS.	CLADDING TEMP., °C	MAX. Li_2O TEMP., °C	ϕ/ϕ_{max} (E > 0.1 MeV)
1	557	606	0.55
2	554	624	0.89
3	548	625	1.0
4	538	608	0.86

Figure 6.3-13. Sealed-capsule design used in the TULIP (Li_2O) experiment.

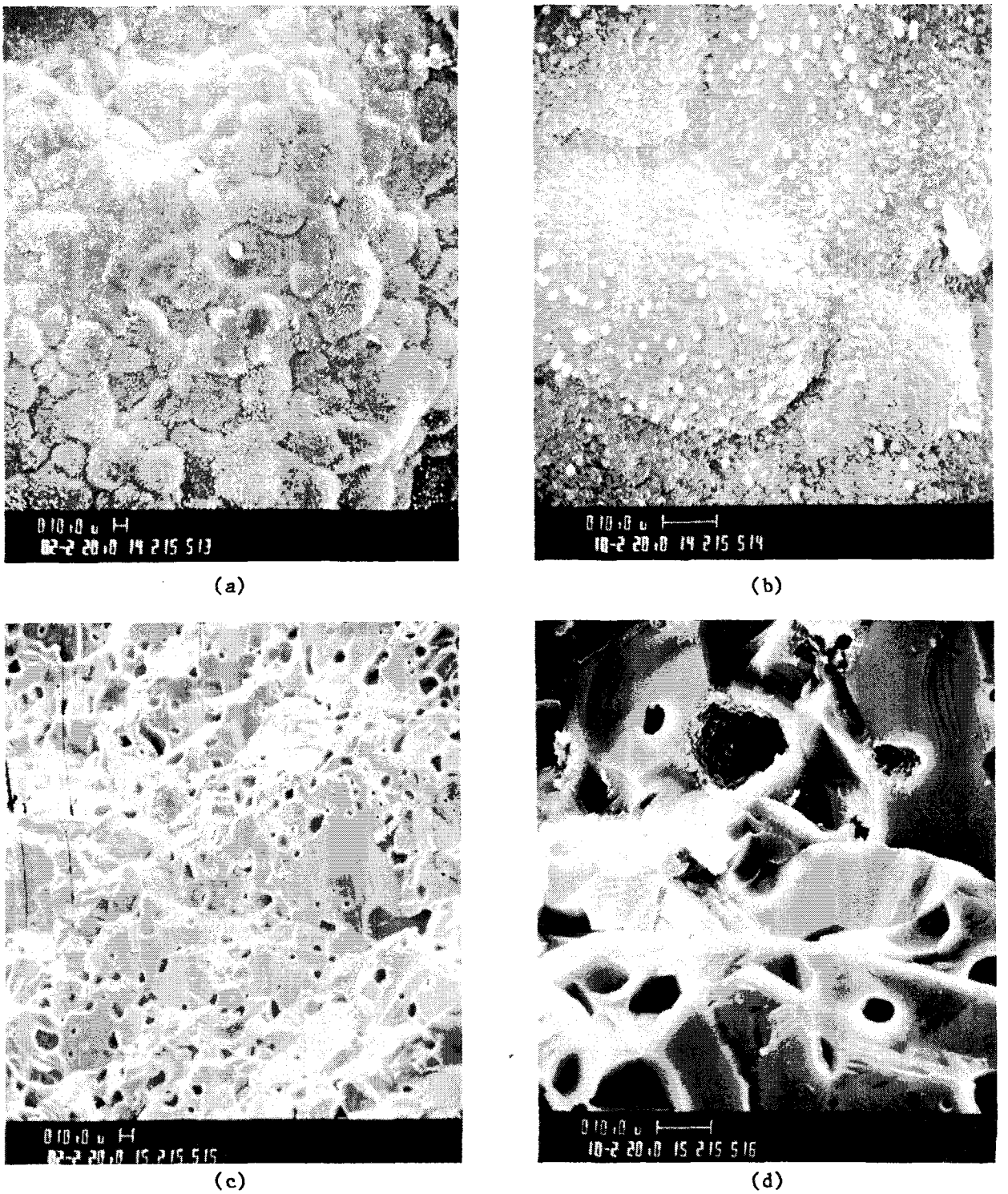


Fig. 6.3-14. Unirradiated Li_2O - (a) intergranular fracture, 200 x, (b) intergranular fracture, 1000 x, (c) transgranular fracture, 200 x, (d) transgranular fracture, 1000 x.

(1) There is significant bubble formation and growth in irradiated Li_2O. Grain growth, on the other hand, has not been observed in the present experiment up to 3 at % burnup. In several instances, the bubbles exhibit a faceted appearance and they have aligned themselves into rows or planes (Fig. 6.3-15)

(2) There is a qualitative correlation between the volume fraction of bubbles within the grains and the amount of retained tritium. The strongest correlation is shown for EA403-4 (Fig. 6.3-16) which retained 50% of the generated tritium. Fabrication batch difference and the lower irradiation temperature may have contributed to the unusually high tritium retention in this Li_2O pellet.

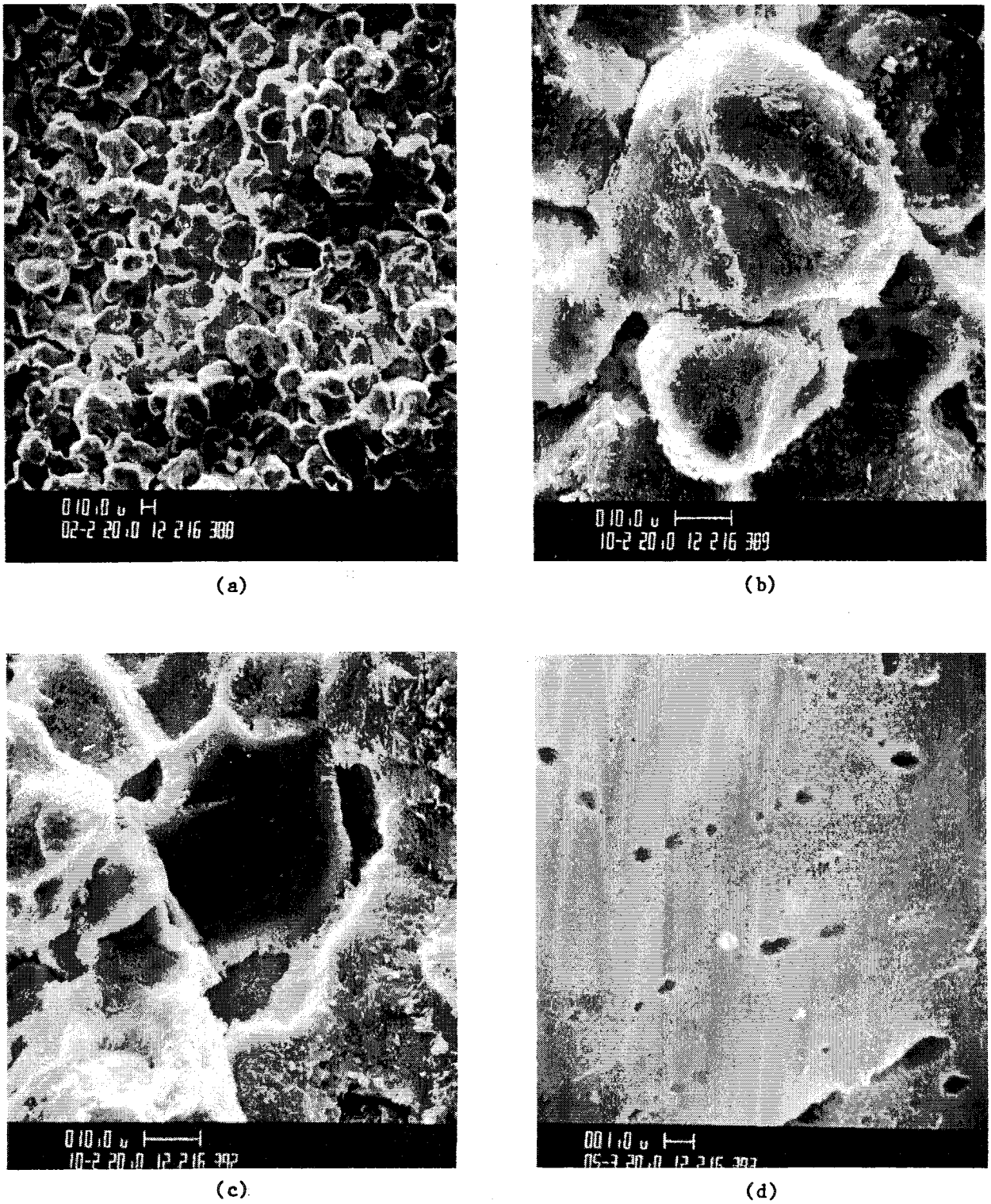
(3) Only in high burnup (~3 at % ^6Li) samples, the aligned bubbles have become interconnected to form pathways through the grains (Figs. 6.3-17, 6.3-18). At 1 at % ^6Li burnup, bubbles were found primarily within grains as separate entities (Figs. 6.3-15, 6.3-16).

Relation Between Microstructure and Tritium/Helium Retentions in Li_2O

Data on percent retention of tritium and helium in Li_2O (Table 6.3-5) are plotted in Figs. 6.3-19 and 6.3-20, respectively. It should be noted that the percent retention represents data normalized to the total amount of tritium/helium generated during irradiation which increases with burnup. Comparison of percent retention data are, therefore, meaningful only at a given burnup level. Translation of these percent retention data into residual tritium/helium concentrations (wppm) in Li_2O has been done; the values are given in Table 6.3-5. These residual concentrations may be related directly to tritium inventory in an Li_2O blanket, 1 wppm tritium is roughly equivalent to 1 kg tritium in a 4000 MW(th) STARFIRE-type blanket.

Also plotted on Figs. 6.3-19 and 6.3-20 are four unpublished data pairs of Porter et al. from another encapsulated Li_2O element that was irradiated at 470°C to ~1 at% ^6Li burnup in EBR-II. Examination of these percent retention data revealed the following patterns:

(1) At 1 at% ^6Li burnup and 608 to 625°C irradiation temperatures, percent tritium retentions are in the range of 5.3 to 9.7% (104-182



(a) (b)

(c) (d)

Fig. 6.3-15. Specimen 403-1 - (a) fracture surface, 200 x, (b) intergranular fracture, 1000 x, (c) transgranular fracture, 1000 x, (d) transgranular fracture, 5000 x.

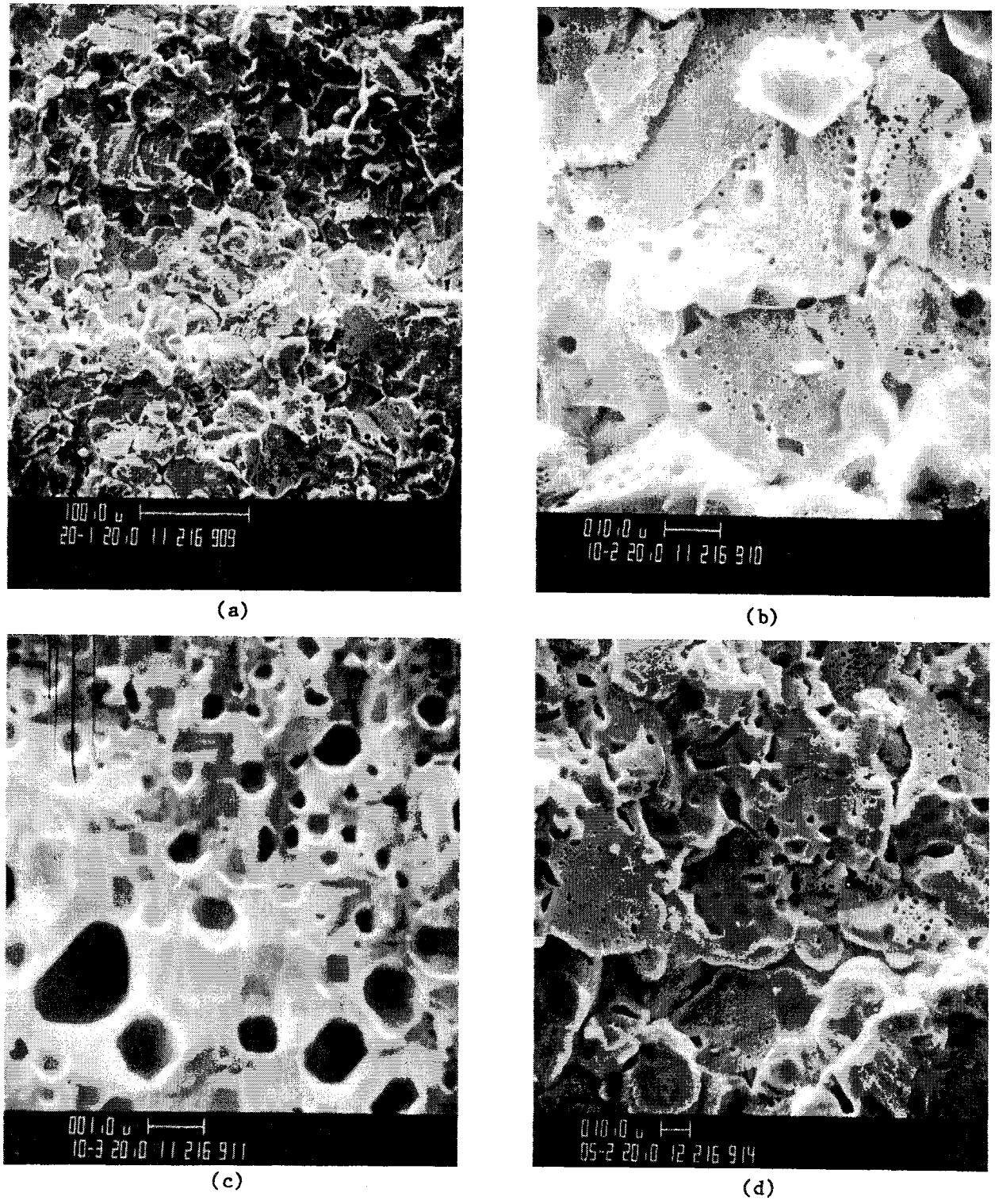


Fig. 6.3-16. Specimen 403-4, (a) fracture surface, 200 x, (b) transgranular fracture showing large bubbles, 1000 x, (c) bubbles showing faceted appearance, 10,000 x, (d) fracture surface showing rows of bubbles, 500 x.

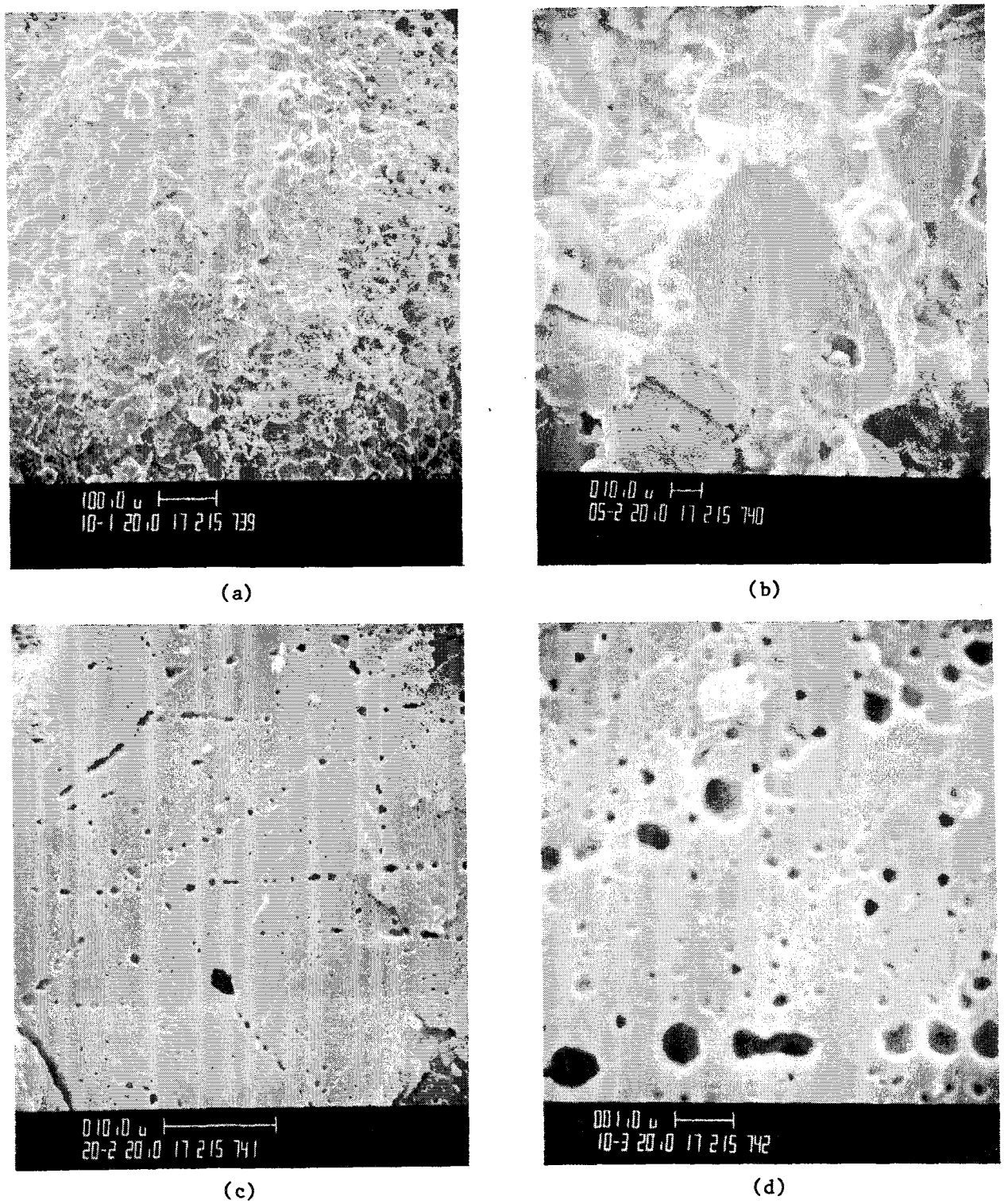
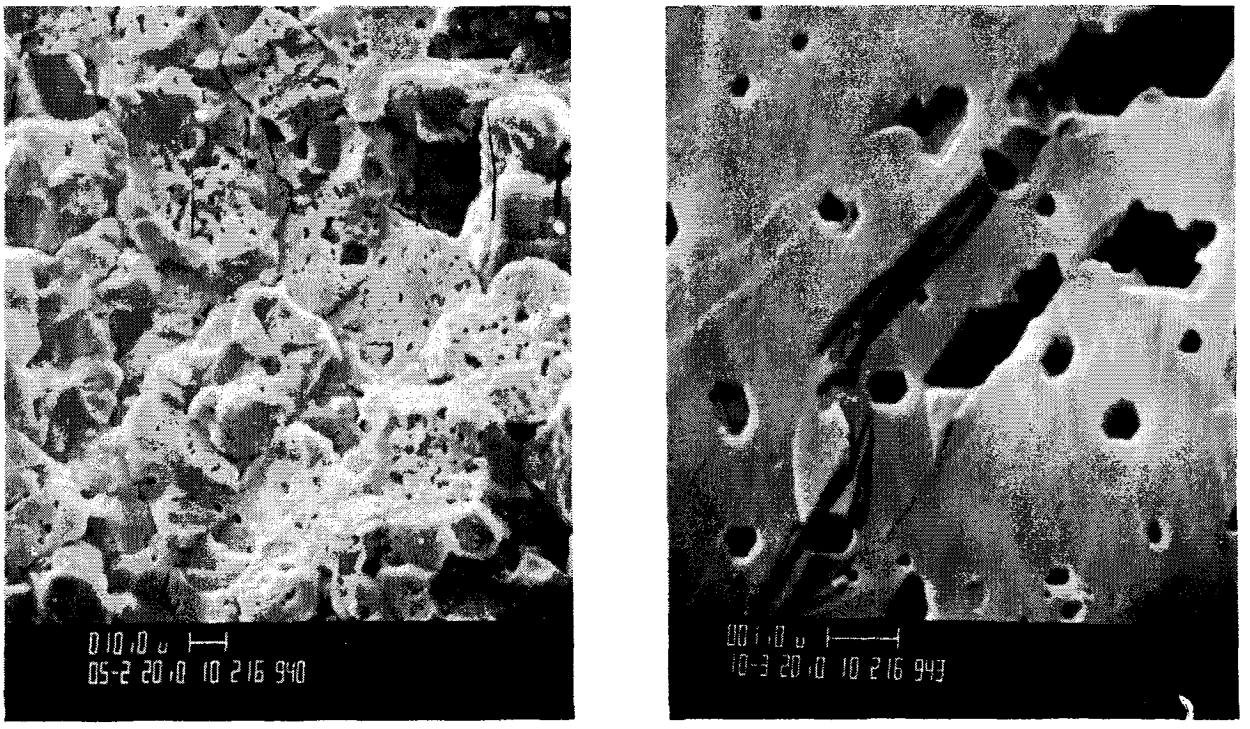


Fig. 6.3-17. Specimen 404-4 - (a) fracture surface, 100 x, (b) middle of (a) showing transgranular fracture, 500 x, (c) middle of (b) showing rows of bubbles, 2000 x, (d) bubbles at 10,000 x.



(a) (b)

Fig. 6.3-18. Specimen 404-2 - (a) fracture surface, 500 x, (b) transgranular fracture showing bubbles, 10,000 x.

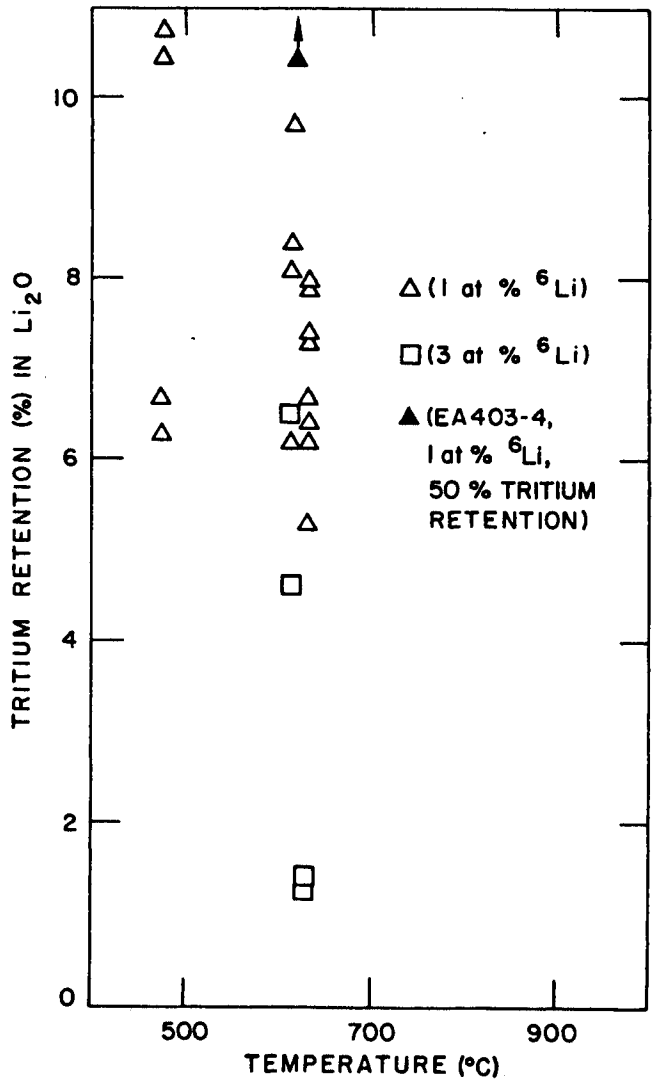


Figure 6.3-19. Percent tritium retention in Li_2O as a function of irradiation temperature and burnup.

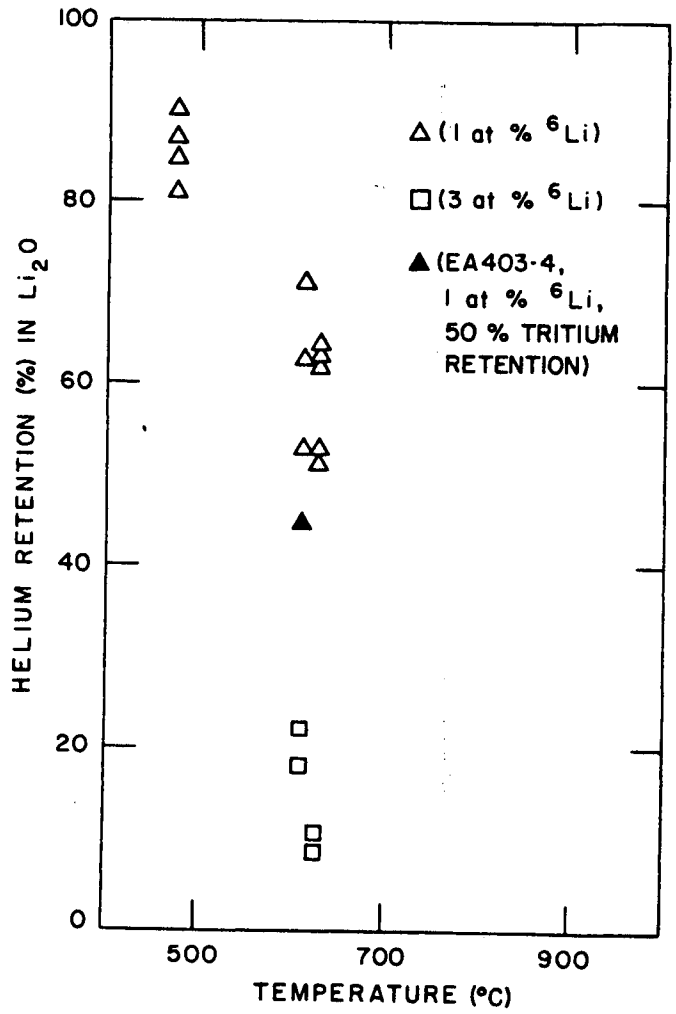


Figure 6.3-20. Percent helium retention in Li_2O as a function of irradiation temperature and burnup.

wppm not including EA403-4), whereas percent helium retentions are in the range of 51 to 71% (1320-1630 wppm).

(2) At 1 at% ^{6}Li burnup but lower irradiation temperature (470°C), percent tritium retentions (6.3 to 10.8%) are slightly higher than those at higher temperatures; percent helium retentions (81-90%), on the other hand, are considerably higher.

(3) At 3 at% ^{6}Li burnup, the tritium retained in the 625°C pellets (~75 wppm) is in the same range as for the 1 at% burnup. This suggests that the inventory has reached a steady-state level. However, at the lower irradiation temperature, the inventory appears to have doubled as the burnup increased. This is somewhat surprising as the two temperatures differ by less than 20°C. Helium retention shows negligible increase with burnup and appears to have saturated.

An estimate for the irradiation temperature uncertainties has been made;[6.3-90] the results showed that the main uncertainty is associated with the heat conduction across the Li_2O/cladding gap. Assuming the gap eventually closes owing to Li_2O swelling (to be discussed later), the Li_2O centerline temperatures (Fig. 6.3-13 insert) may decrease by 24 to 38°C toward the end of irradiation. For purposes of the following discussion, the earlier calculated irradiation temperatures by Porter et al. will be used.

Bearing in mind the batch difference of these Li_2O pellets and the uncertainties in irradiation temperatures, the above data nevertheless indicate rather strong correlations between tritium/helium behavior in Li_2O and the irradiation conditions (temperatures and burnups). With the SEM microstructural examinations given in Figs. 6.3-14 to 6.3-18, and the information on tritium and helium diffusion behavior in Li_2O, the data shown in Figs. 6.3-19 and 6.3-20 may be rationalized as follows:

Recent measurements of tritium diffusivity in single-crystal Li_2O showed tritium diffusion coefficients about 3 orders-of-magnitude higher than previous estimates based on measurements from powdered samples (Section 6.3.2.2). Using a simple spherical grain diffusion model with a grain diameter of 50 μm, one can estimate percent tritium retention from the experimental tritium generation rates and diffusivities. The tritium retentions thus calculated

are all extremely low (< 10^{-4}%), indicating that factors other than tritium lattice diffusion in Li_2O were involved for the observed retention data.

Helium diffusivity in Li_2O has not been measured to permit calculations of percent helium retentions, similar to those done for the tritium. A recent Japanese isochronal annealing experiment[6.3-91] on helium-ion implanted Li_2O showed that below 527°C, helium is hardly released at all from Li_2O during a 30-minute anneal at that temperature. Even at 750°C helium release (during the 30-minute anneal) is only 1/2 of the peak release at 827°C. The drastic change in the helium release behavior (zero to peak release from 527 to 827°C) indicates that helium diffusion in Li_2O should have a rather steep temperature dependence (i.e., high activation energy). If that were the case, it would not be surprising to find high helium retentions (81-90%) in Li_2O irradiated at 470°C.

Discussions of tritium/helium behavior in Li_2O (Figs. 6.3-19 and 3-20) thus far have yet to relate the behavior to the microstructural features noted in Figs. 6.3-14 to 6.3-18. For EA403-4 that retained 50% of the generated tritium, the microstructure shows an unusually high population of large, <u>isolated</u> bubbles within the Li_2O grains. Defect (i.e., helium bubbles) trappings of tritium may have contributed to the observed high tritium retention. In the calculations of percent tritium retentions the tritium diffusivities used were determined from irradiated single-crystal Li_2O samples. Because these samples were lightly irradiated,[6.3-73] they are unlikely to contain a large population of helium bubbles. Possible trapping effects on tritium diffusivity are therefore negligible, with a resultant underestimate of percent tritium retention for cases where numerous helium bubbles were found.

Final observations of the relationships between percent retention data and microstructure are bubble alignments within the Li_2O grains and pathway formation, which were found only in high-burnup (3 at% ^6Li) samples, Figs. 6.3-17 through 6.3-18. The curious feature about bubble alignments is that they occurred within the Li_2O grains effectively as a process for subgrain formation, even though growth of the as-fabricated grains has not been observed in the present experiment. The cause for this phenomenon is not known at present. Migration of helium bubbles to grain boundaries and the formation of interconnected grain-edge tunnels will create easy pathways for

tritium and helium releases. The fact that these bubble alignments and interconnections were found in 3 at% ^{6}Li burnup samples also qualitatively explains the observed low percent tritium and helium retentions, a factor that the previous simple spherical grain diffusion model had not considered.

Implications of Li_2O Microstructural Evolution on Blanket Performance

One of the primary functions of a solid-breeder blanket is to breed and recover tritium for use as fuel in a D-T fusion reactor. Concerns in feasibility, economics, safety, and environment dictate a low blanket tritium inventory. Since helium bubbles do form in Li_2O upon (n,^{6}Li) reactions and their retentions are high at relatively low temperatures (e.g., 470°C), the possibility of helium atoms/bubbles to act as trap sites for tritium seems real, especially when helium atoms/bubbles are isolated and dispersed within the Li_2O grains. Unacceptably high tritium inventory may build up in the colder region of the blanket (i.e., near coolant containing structures and away from the plasma side). The steep temperature dependence of helium behavior in Li_2O (inferred from the short-term isochronal annealing experiments), [6.3-91] and the high percent helium retentions (81-90%) observed at 470°C and 1 at% ^{6}Li burnup indicate that at temperatures around 470°C and below, helium diffusion in Li_2O is likely to be a slow process. If that were the case, the chance of forming interconnected bubble pathways may be remote even at higher burnups.

Other phenomena, such as Li_2O microcracking and swelling, are also closely related to the helium behavior. Transgranular and intergranular microcracks can occur in Li_2O during neutron irradiation; the former due to gas overpressurization in bubbles and the latter due to bubble interconnection on grain boundaries. Both forms of microcrackings will degrade the Li_2O effective thermal conductivity, of which the intrinsic part (lattice) is already low due to irradiation effects (Section 6.3.2.2). A reduced effective thermal conductivity of Li_2O will make blanket design even more challenging because of the relatively tight Li_2O design temperature window (410 to 800°C, Section 6.3.4).

Swelling due to the retained helium bubbles in Li_2O is also undesirable. Mechanical interaction between Li_2O and its containing structure induced by Li_2O swelling needs to be accommodated. Based on post-irradiation plenum

volume measurements, an Li_2O volume increase ($\Delta V/V_o$) of ~7% was reported by Porter et al.[6.3-87] between 1 and 3 at% ^6Li burnups. After 3 at% ^6Li burnup this value (at ~608-625°C) corroborates well with the other reported Li_2O swellings from direct measurements and neutron radiography (Section 6.3.3.2). If a simplifying assumption is made that Li_2O will swell, without constraints, at a rate of 2.3% $\Delta V/V_o$/at% ^6Li burnup, large volumetric swelling will result upon extrapolation to the blanket goal burnup. The extrapolated swellings, if realistic, can induce large Li_2O/structure mechanical interaction causing either unacceptable structure deformation or premature failure. Increasing the structure thickness may be a solution, but the approach will degrade the blanket tritium breeding ratio owing to the decreased/increased volume fractions of Li_2O/structure. A potentially large penalty on blanket performance is therefore associated with Li_2O swelling, which has its microstructural origin in helium behavior.

Finally, it should be emphasized that the Li_2O experiment discussed in this section is a sealed capsule test, i.e., without a helium purge stream. Current solid breeder blanket designs (Chapters 8 and 9) all require helium purge channels for in-situ tritium recovery. Preliminary information from the VOM-15H in-situ experiment (Section 6.3.3.4) indicated a strong role of purge chemistry on tritium recovery. The form of the recovered species (i.e., HT, HTO, T_2O) also exerts significant impacts on tritium containment. While tritium recovery from Li_2O may differ greatly with and without the purge chemistry factor, the diffusional steps through which tritium migrates to the Li_2O surface should be identical under both conditions. Helium bubble trapping, bubble alignment, grain-edge tunnel formation, microcracking, and swelling are all phenomena occurring either within the Li_2O grains or along grain boundaries. They are thus expected to be operative in a blanket environment.

6.3.3.2 FUBR-1A

FUBR-1A is a sealed-capsule, fast-neutron irradiation experiment on four solid breeders (Li_2O, γ-$LiAlO_2$, Li_4SiO_4, and Li_2ZrO_3) conducted by Hanford Engineering Development Laboratory.[6.3-92] All solid breeder pellets were fabricated by hot pressing (Section 6.3.1) to obtain relatively small grain sizes (Table 6.3-3) with a reference density of 85% TD. The experiment was conducted in EBR-II at three irradiation temperatures (500, 700, and 900°C) to

three levels of ^{6}Li burnups (~1, 2 and 3% or ~3, 6, and 9 x 10^{20} captures/cm^3). Preliminary information from post-irradiation examination has been presented by G. Hollenberg at various times during the BCSS project period; these will be summarized below with emphasis on Li_2O and γ-$LiAlO_2$.

Cracking appears prevalent in all solid breeders during the FUBR-1A irradiation. Photographic pictures showed that the cracks are predominantly macrocracks in the radial and axial directions of the pellets. The pattern strongly suggests thermal-stress induced cracking due to temperature gradients in the breeders. Similar cracks have been observed in Li_2O in the TULIP experiment (Section 6.3.3.1).

Figure 6.3-21 shows the results of grain diameter measurements after ~ 1 at% ^{6}Li burnup. Among the three breeders examined, γ-$LiAlO_2$ showed no grain growth after being irradiated at 500-900°C for ~ 2400 h. The grains in Li_2O, on the other hand, grew substantially at 700°C and more so at 900°C. These in-reactor grain growth data are qualitatively consistent with the data obtained from the out-of-reactor thermal stability tests (Section 6.3.1). After 8 h at 900°C γ-$LiAlO_2$ was found to be stable, whereas Li_2O experienced a 10-fold increase in grain size.

Figure 6.3-22 shows the percent tritium retentions in three solid breeders after ~ 1 at% ^{6}Li burnup (~ 3 x 10^{20} captures/cm^3) as a function of the irradiation temperature.(6.3-93) Tritium retention decreases with increasing temperature for both Li_2O and γ-$LiAlO_2$ owing to enhanced diffusion. However, the temperature sensitivity of the latter is apparently stronger, as indicated by the slopes of the connecting data points. This temperature sensitivity is also qualitatively supported by the activation energies of tritium diffusion in γ-$LiAlO_2$ and Li_2O, the former has a higher activation energy (Section 6.3.2.2). Another point worth noting for Li_2O is that despite significant grain growths at 700 and 900°C, the percent tritium retentions are lower than that at 500°C for which the Li_2O grains remained essentially as-fabricated. Ratios of the tritium retentions do not scale as the square of the grain size according to the spherical grain diffusion model (to be given in Section 6.3.4.1). One reason for this lack of grain size sensitivity is the enhanced tritium diffusivities at high temperatures. As mentioned in Section 6.3.2.2, the latest tritium diffusivity data obtained from single-crystal Li_2O specimens are ~ 3 orders-of-magntitude higher than

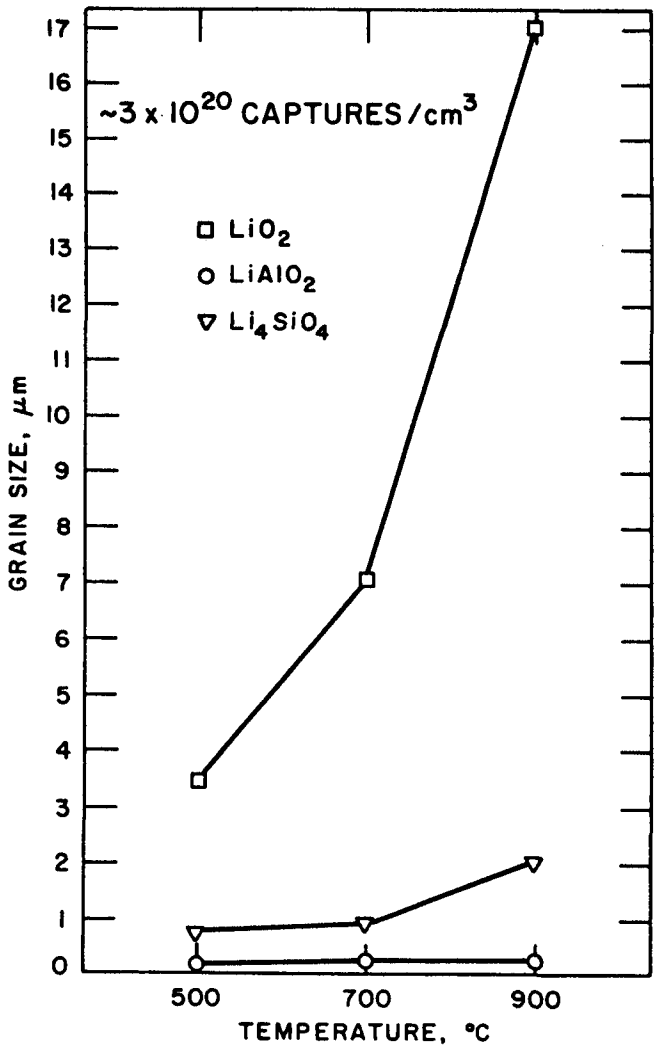


Figure 6.3-21. Post-irradiation grain growth measurements of lithium ceramics (G. W. Hollenberg, HEDL).

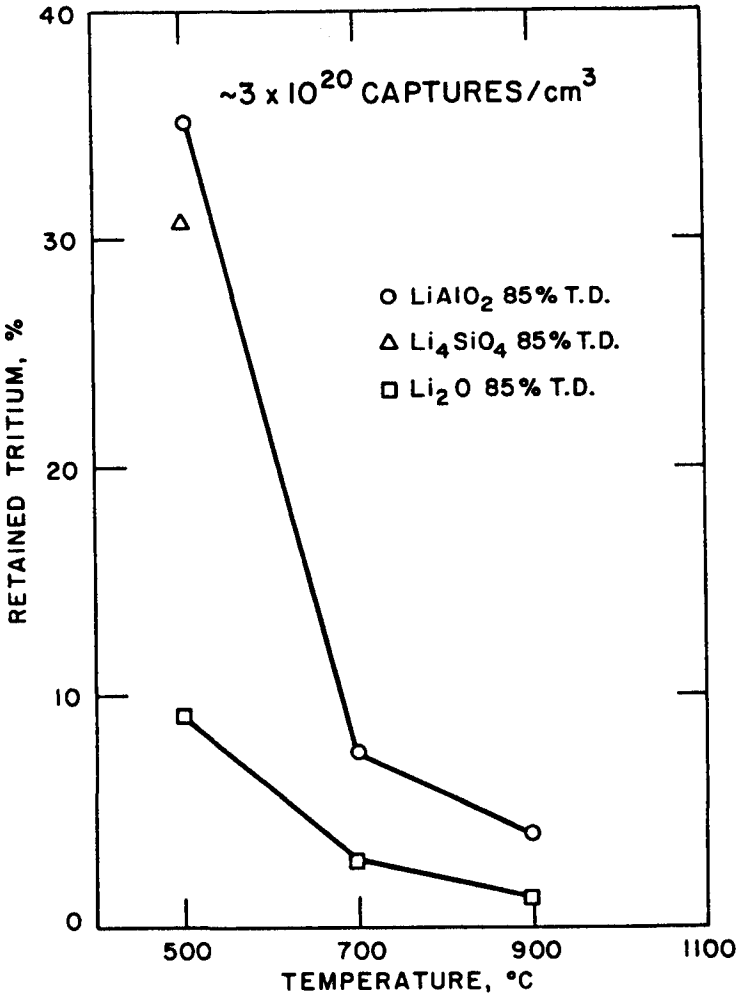


Figure 6.3-22. Percent tritium retention in Li_2O, γ-$LiAlO_2$, and Li_4SiO_4 irradiated in the FUBR-1A experiment in EBR-II (from Ref. 6.3-93).

the previous results. Using the single-crystal tritium diffusivity will in fact give very low tritium retentions (< 10^{-4}%) in Li_2O, in contrast to the measured values of 1 and 9.5% (9 and 79 wppm) at 900 and 500°C, respectively. Although the irradiation temperatures differ, the FUBR-1A tritium retentions in Li_2O at 500 and 900°C also appear consistent with those in TULIP after 1 at% ^6Li burnup at 608-625°C (Fig. 6.3-19).

Figure 6.3-23 shows the percent helium retentions in three solid breeders after ~ 1 at% ^6Li burnup as a function of the irradiation temperature.(6.3-94) The Li_2O helium retentions at 500 and 700°C are again consistent wiht the bulk of the TULIP data at 608-625°C after 1 at% ^6Li burnup (Fig. 6.3-20). Based on microstructure examinations performed for the Li_2O specimens from TULIP, helium bubbles are likely to be found in the FUBR-1A Li_2O pellets irradiated at 500 and 700°C. However, this remains to be confirmed.

While defect trapping of tritium by helium bubbles (Section 6.3.3.1) may contribute to the relatively high measured tritium retentions in Li_2O, the case is apparently different for γ-$LiAlO_2$ which retains very little of the irradiation-produced helium. In contrast to Li_2O, the helium retention data of γ-$LiAlO_2$ show almost no temperature sensitivity as if helium release is an athermal process. The cause for the low helium retention in γ-$LiAlO_2$ and the apparent athermal behavior is not known at present.

Figure 6.3-24 shows the diametral swelling of solid breeders after ~ 1 at% ^6Li burnup as a function of the irradiation temperature. All ternary breeders exhibited much lower diametral swelling than that of Li_2O. As discussed previously for the TULIP experiment, the cause of swelling is believed to be the helium bubbles formed during irradiation and retained in the breeder. For γ-$LiAlO_2$ the very low diametral swelling is thus consistent with the low helium retentions (Fig. 6.3-23). The high helium retentions in Li_2O (Fig. 6.3-23), on the other hand, should manifest themselves into higher swellings if helium exists in Li_2O primarily as gas bubbles. The Li_2O diametral swelling results in Fig. 6.3-24 lend qualitative support for the relationship between helium retention and swelling; microstructure examination is needed to ascertain the helium bubble morphology at different irradiation temperatures.

Another indirect evidence for the helium-swelling relationship in Li_2O can be inferred from Fig. 6.3-25. The figure shows the Li_2O diametral swelling as a function of the irradiation temperature and burnup. Although the

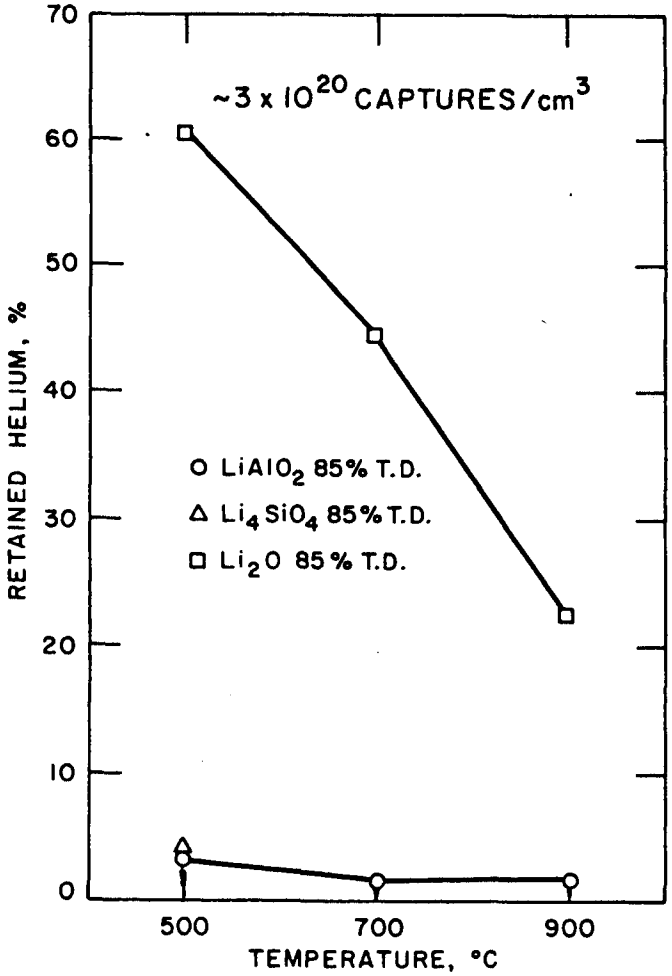


Figure 6.3-23. Percent helium retention in Li_2O, $LiAlO_2$ and Li_4SiO_4 irradiated in the FUBR-1A experiment in EBR-II (from Ref. 6.3-93).

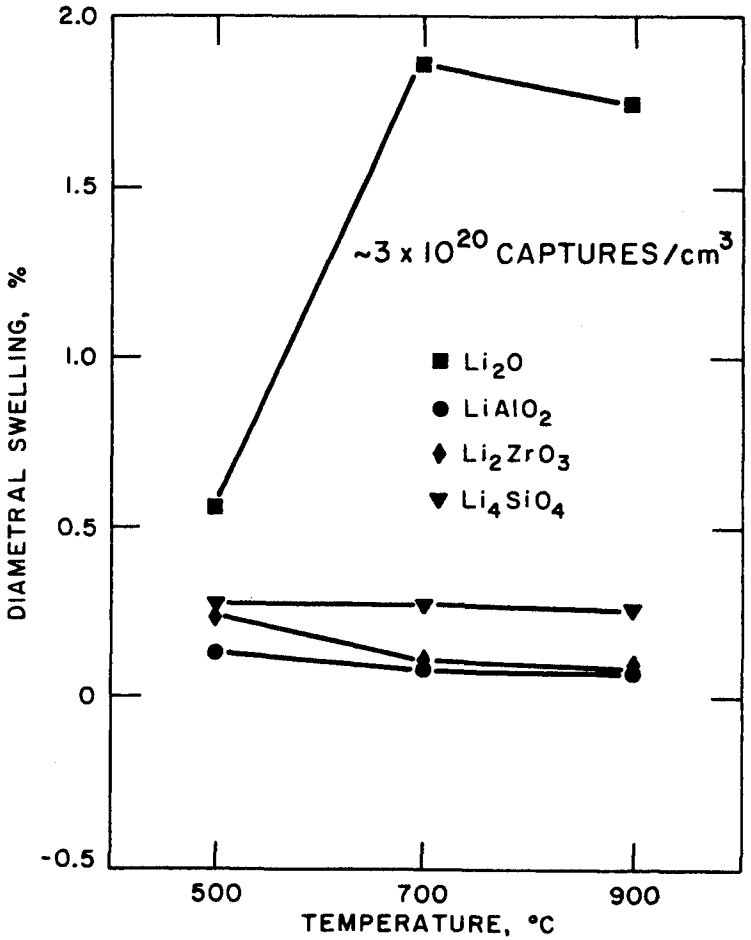


Figure 6.3-24. Irradiation-induced swelling in lithium ceramics (G. W. Hollenberg, HEDL).

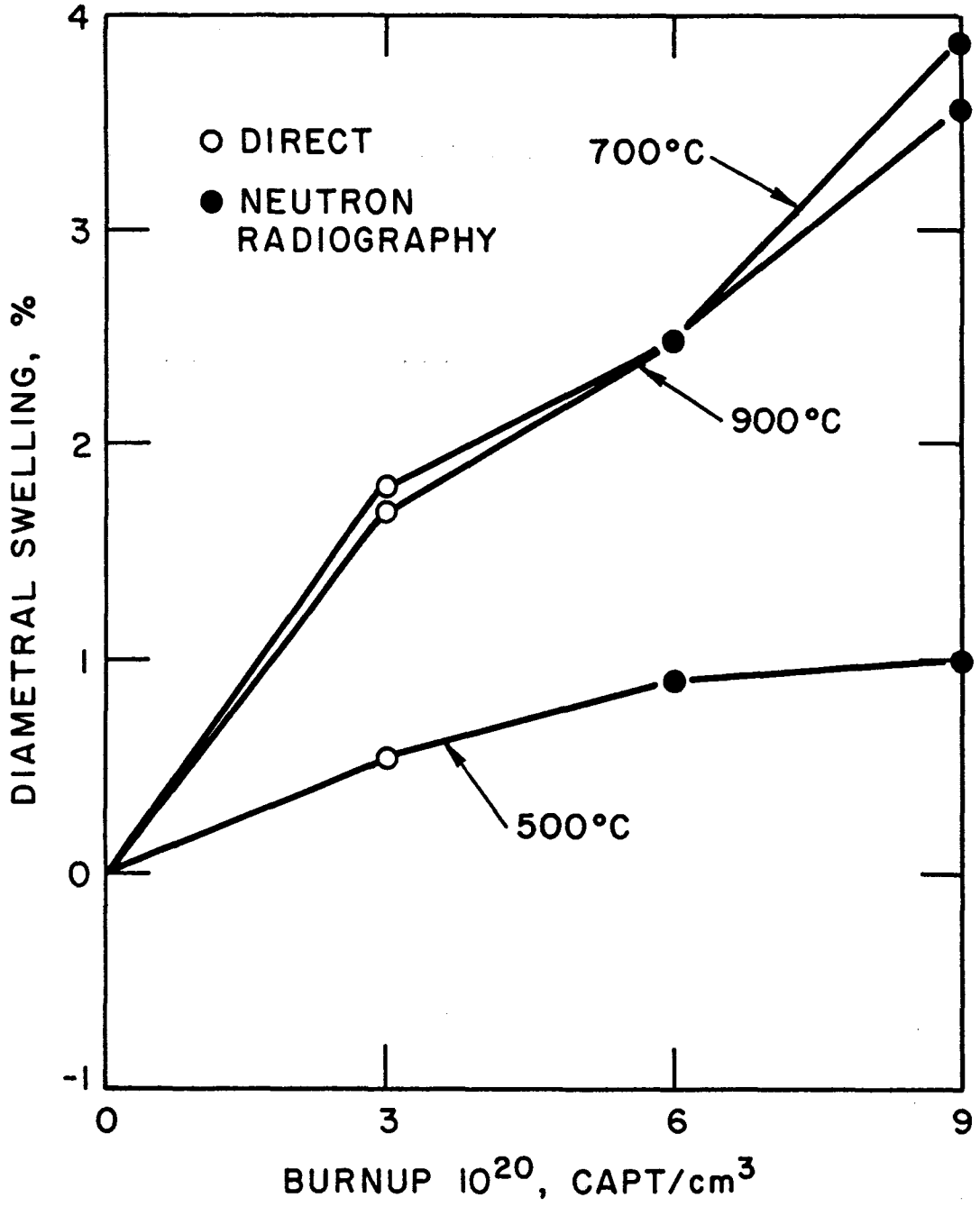


Figure 6.3-25. Irradiation-induced swelling in Li_2O as a function of burnup (G. W. Hollenberg, HEDL).

results obtained from neutron radiography are less precise than those obtained from direct measurements, the trends show increasing diametral swelling with increasing burnup at all three irradiation temperatures. The burnup dependence of Li_2O swelling can be rationalized with the continuing generation by helium in Li_2O by the capture reaction (or burnup) of ^6Li.

It has been noted in the TULIP experiment (Section 6.3.3.2) that a volumetric swelling ($\Delta V/V_o \simeq 7\%$) of Li_2O occurred between 1 and 3 at% burnups. Assuming isotropic swelling gives a diametral swelling of ~ 2.3%, which is slightly higher than the FUBR-1A results at 700 and 900°C. Comparison of the Li_2O tritium/helium retention results and swelling in FUBR-1A and TULIP thus showed that the data from these two sealed-capsule experiments are essentially consistent. Previous discussions of Li_2O/structure mechanical interaction due to Li_2O swelling and purge chemistry effects are also valid for FUBR-1A; they will not be repeated here.

6.3.3.3 TRIO-1

TRIO-1 is the first in-situ tritium recovery experiment on γ-$LiAlO_2$ conducted in the Oak Ridge Research Reactor (ORR) by Argonne National Laboratory.(6.3-94) The experiment used sintered (~65% TD) γ-$LiAlO_2$ pellets depleted in ^6Li (0.55%) with a tailored bimodal breeder microstructure (i.e., 0.2 μm-diameter grains in particles of ~50 μm diameter). The capsule design is shown in Fig. 6.3-26. The γ-$LiAlO_2$ pellets are in the form of hollow cylinders enclosed in an inner capsule, which is separated from the outer capsule by a gas filled gap. The gap provides a resistance to heat flow, and temperature control is achieved by varying the He/Ar ratio in the flowing gap gas. The sweep gas flows down through the center of the capsule, back up through the annulus between the inner tube and the inside surface of the breeder pellets, and out to the gas analysis system. Temperature is monitored by thermocouples located on the inside and outside surfaces of the breeder pellets. Neutron flux is monitored by self-powered neutron detectors wrapped around the outside of the capsule. In addition, dosimetry wires are placed in the center of the capsule and on the outside of the capsule assembly.

The controlled experimental variables are the average (nominal) breeder temperatures (400-700°C), sweep-gas flow rates (30, 100, and 300 cc/min), and the sweep-gas composition (100% He, 0.1% H_2 + He, 1% H_2 + He, and 0.2% O_2 +

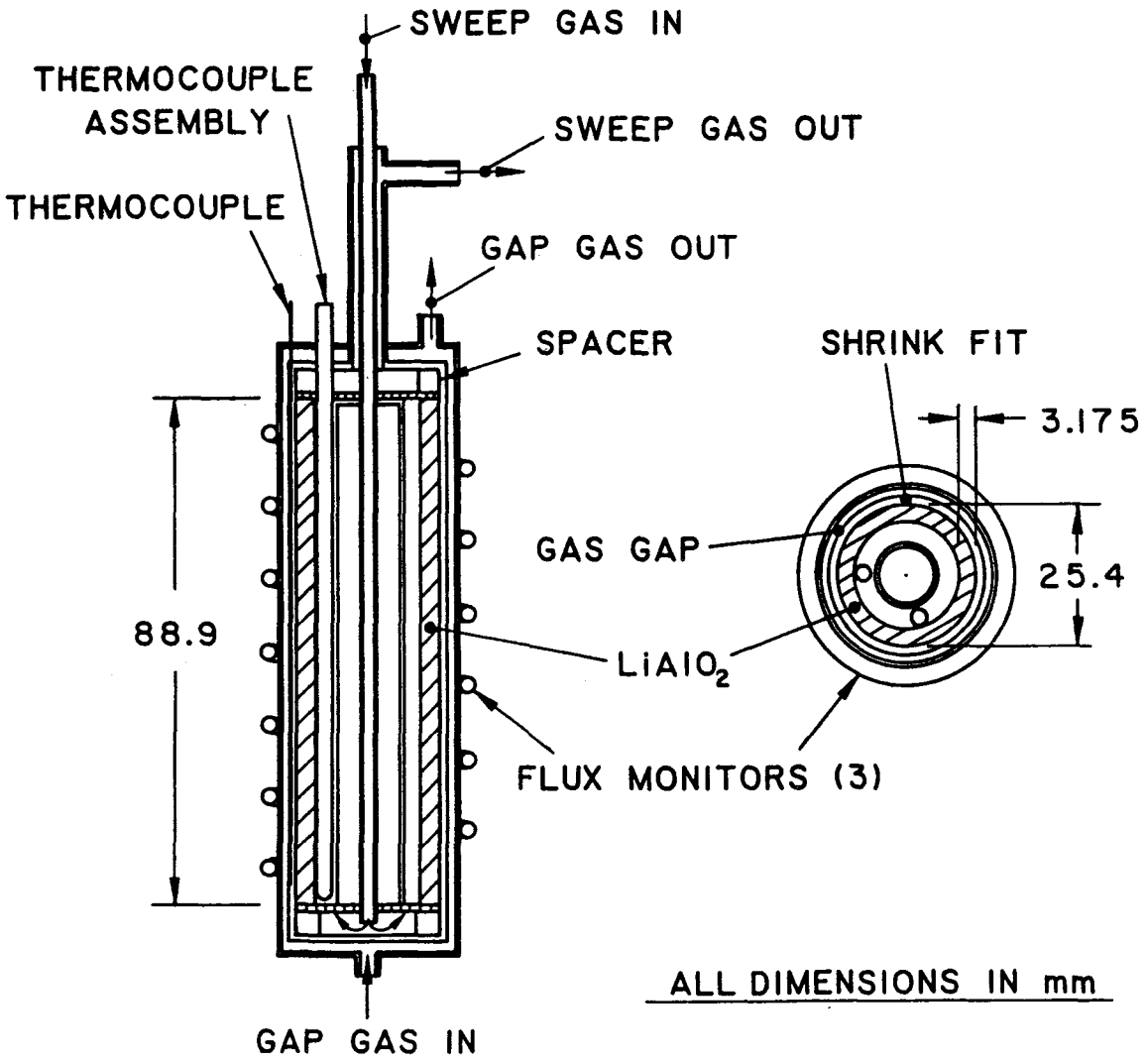


Figure 6.3-26. Capsule design used in the TRIO-1 in-situ tritium recovery experiment on γ-$LiAlO_2$.

He). Specific conditions for the 33 runs of the experiment are summarized in Table 6.3-6 which totaled up to ~2120 h in ORR with a ^{6}Li burnup of 0.18%.

Experimental results from the first nine runs (Table 6.3-6) are shown in Fig. 6.3-27. The dark line represents the response of the tritium monitor which senses the molecular (HT + T_2) tritium level. The dotted line represents an estimate of the tritium generation rate. The small barred circles represent integral tritium which was measured in scintillation traps. The results are representative of those obtained in all 33 runs. Individual results are discussed below.

When the breeder assembly was exposed to neutron at low power (3-30 kW and up to 12 MW), a measurable response was noted in the tritium monitors. Breeder temperatures at these low power levels were 30-200°C. Tritium diffusion would be very slow at these low temperatures. Consequently it was estimated that ~5% of the tritium generated during the low-temperature irradiation was released by recoil.

The tritium release rate at a nominal 600°C with a sweep-gas composition of He/0.1% H_2 appeared to reach steady-state within a few hours. Changes in temperatures (from low to high and vice versa) and/or sweep-gas composition (from 0.1% H_2 to 1 and 0% H_2, etc.) introduced either positive or negative transient spikes into the system (Fig. 6.3-27). Increasing temperatures (while holding the sweep gas composition constant) resulted in positive spikes, whereas decreasing temperatures resulted in negative spikes. Reducing hydrogen content (from 0.1% to 0% H_2) in the sweep gas (while holding the temperature constant) resulted in a negative spike (Run 9), whereas increasing hydrogen content (from 0.1% to 1% H_2) resulted in a positive spike (Run 3). The times required for these transient spikes to settle back to the steady-state values vary substantially, from a few hours at 700°C (Run 2), ~3 days at 550°C (Run 4), to more than 5 days at 650°C after hydrogen was removed from the sweep gas (Run 9). The effects of both temperature and sweep-gas composition on tritium release are thus apparent.

Detailed run-to-run tritium inventory results for TRIO-1 are given in Ref. 6.3-94. As will be discussed in Section 6.3.4.1, the data from the first eight runs and the last seven runs provided an excellent fit to a steady-state diffusion model. These runs represent conditions which were favorable for tritium release - namely, 0.1 % H_2 added to the sweep gas stream. It is in-

TABLE 6.3-6. TEMPERATURE AND SWEEP GAS COMPOSITIONS FOR THE TRIO-1 EXPERIMENT

Run No.	Time (Days)	Nominal[a] Temperature (°C)	Changes in Nominal Sweep Gas Composition
1	2	600	---[b]
2	2	700	---
3	1	700	He/1.0% H_2
4	5	550	---
5	2	500	---
6	1	550	---
7	3	600	---
8	2	650	---
9	6	650	100% He
10	1	400	100% He
11	1	500	100% He
12	4	550	100% He
13	5	600	100% He
14	2	700	100% He
15	1	700	---
16	1	700	300 cc/min
17	3	700	30 cc/min
18	1	700	---
19	1	650	---
20	4	650	He/0.2% O_2
21	2	650	---
22	1	600	---
23	3	550	---
24	1	600	---
25	2	500	---
26	3	550	---
27	7	525	---
28	7	500	---
29	3	480	300 cc/min
30	4	480	---
31	2	500	---
32	2	550	---
33	3	650	---

[a]Average temperature on west side. Coldest temperature is 100° lower, hottest temperature is approximately 50° higher.

[b]Dotted lines refer to standard sweep gas composition (i.e., He/0.1% H_2, 100 cc/min).

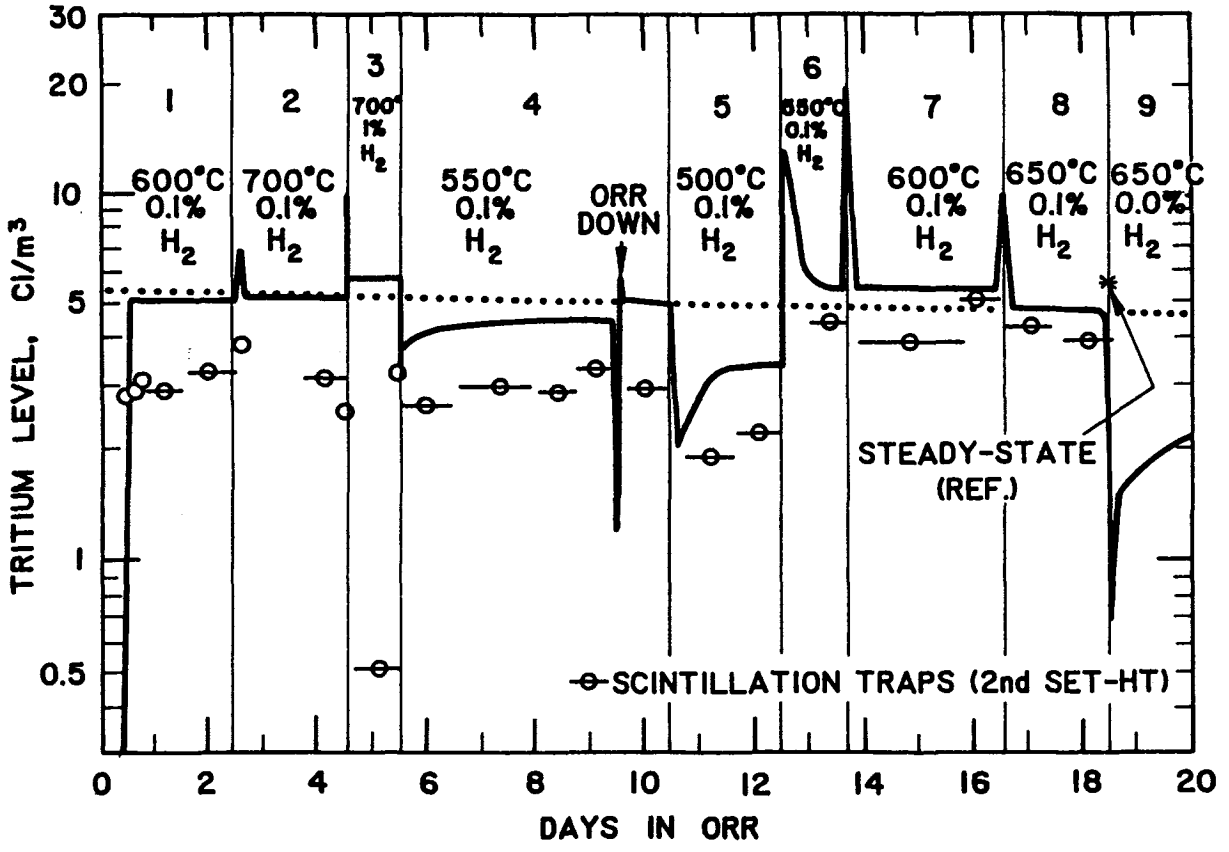


Figure 6.3-27. Tritium release results from γ-$LiAlO_2$ in the first nine runs of the TRIO-1 experiment.

ferred that, when hydrogen is added, surface release is enhanced but intragranular diffusion is not appreciably changed. Under these conditions intragranular diffusion is the rate-limiting step for tritium release, and the inventory data can thus be used to derive an apparent tritium diffusivity.

For runs 9-27, it is assumed that the inventory is a sum of two components, I_d - the diffusive inventory and I_s - the effective surface (includes solubility) inventory. The derived tritium diffusivity from runs 1-8 and 28-33 was used to calculate diffusive inventories for runs 9-27. Each surface inventory (I_s) was taken to be the total inventory minus the diffusive inventory (I_d). The results are also given in Ref. 6.3-94.

Certain trends appear from the above two sets of results. For runs 1-8, the surface inventory term is negligible because the inventories are ascribed to intragranular diffusion. This set of runs had hydrogen added to the sweep gas, generally 0.1 % or a thousand-fold excess with respect to tritium. Runs 9-14 had no hydrogen added to the sweep gas stream (the actual hydrogen concentration was about 3 ppm, or about three times the tritium level). For this set of runs the surface inventory increases from a negligible quantity to about one curie (2.4 wppm).

Runs 15-19 represent a return to "standard" conditions, namely hydrogen was again added to the sweep gas, but with three different flow rates (300, 30, and 100 cc/min) however. The calculated diffusive inventories for this set of runs do not appear to account for all the tritium, which is 0.6 Ci (1.4 wppm). However, the uncertainty in tritium inventory for these runs is estimated to be 0.5 Ci (1.2 wppm). Therefore, it cannot be concluded that the surface inventory is significantly large for these runs.

Run 20 had 0.2 % oxygen added to the sweep gas. Very little tritium was evolved during this run, and the retention was more than 2 Curies when the run was ended. Given the temperature, the diffusive inventory is calculated to be negligible in comparison to the total inventory. Furthermore, this excess inventory of about 2 Ci (4.6 wppm) persisted for many runs after run 20 was completed - even though hydrogen was added thereafter. In addition, a large amount (about 1.5 Ci or 3.5 wppm) of HTO (tritium in the condensible form) was released in runs 25-29, about a month after run 20 was ended. About two Curies of tritium were retained either in the breeder material or somewhere else in the system for an extended period of time as a result of the addition

of oxygen. As pointed out elsewhere[6.3-94], it appeared that there were small HTO spikes which consistently occurred about one day after large HT spikes. It is inferred that the response time of the system to a release of HTO from the breeder is about one day. Therefore, the two Curies of excess tritium is ascribed to be associated with either the surface or the bulk of the γ-$LiAlO_2$ breeder material.

The last six runs appear to be diffusion controlled; total tritium inventories in these runs are essentially equal to the calculated tritium diffusive inventories.

In relating the above tritium inventory results to those in a blanket, it is useful to note that both the tritium generation rate and the mass of breeder material in a 4000-MW(th) fusion reactor are just about ten million times those in the TRIO-1 experiment. Since one kg of tritium is ten million curies, the inventories listed in Ci for TRIO-1 would translate to inventories in BCSS in units of kg under comparable operating conditions (e.g., temperatures and purge chemistry).

The predominant form of tritium evolved during the TRIO-1 experiment was HT, the non-condensible form. Prior to the experiment, the expectation was that the oxide breeder would give rise to the oxide form of tritium. The issue has serious implications for blanket design because the permeation rates for HT are much greater than for HTO, and tritium loss rates by permeation could become high. A number of possible rationales for this observation exist, including kinetic and thermodynamic arguments. These will be discussed later.

The data on tritium permeation through the primary cladding were translated into permeation rates in units of curies per day. The resultant permeation rates are illustrated in Fig. 6.3-28. The data appear to follow a definite pattern. The first few runs for which permeation data were obtained (runs 4-8) all show high rates in comparison with the rest of the data. It is noted that run 2 was at 700°C with 0.1 % H_2 and run 3 was at 700°C with 1% H_2 in the sweep gas. The steel temperature was about 650°C for these two runs. The conditions of these runs may reduce oxide layers on the surface of the steel cladding. The next several runs were without hydrogen addition to the sweep gas. The breeder material tends to interact with the cladding, forming an oxide film. Thus, the permeation rate is reduced. Runs 16-18 represent

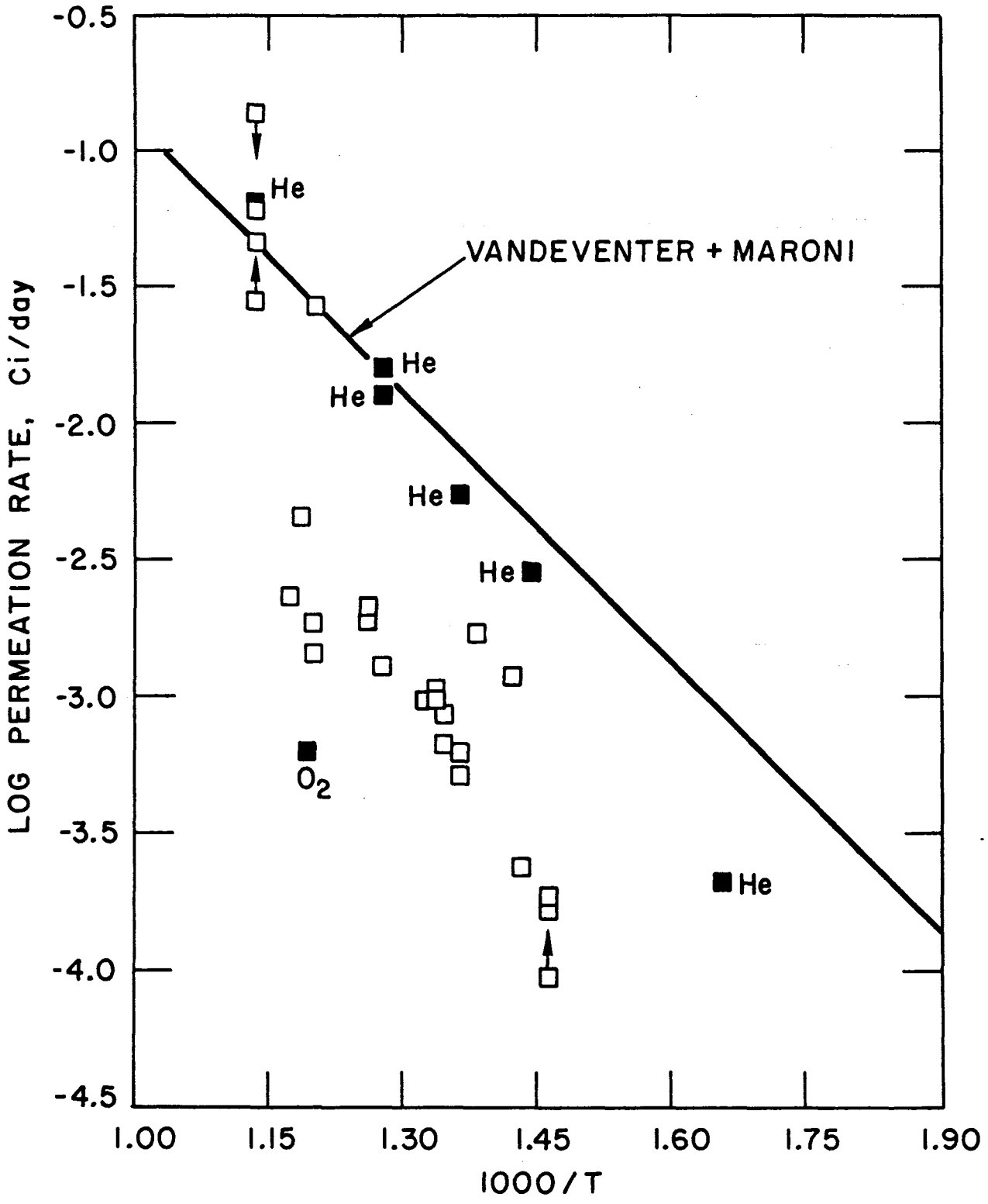


Figure 6.3-28. Tritium permeation from 304 stainless steel cladding in TRIO-1.

0.1 % H_2 in the sweep gas. Since run 17 is at a low sweep gas flow rate, the tritium partial pressure is relatively high, so is the permeation rate. On the other hand, run 16 is correspondingly reduced, owing to a high sweep gas flow rate. Run 20 had oxygen added to the sweep gas. Following this run, the permeation rates are still lower. Runs 21-33 are at the lower part of Fig. 6.3-28. For purposes of reference, a permeation curve for austinitic stainless steel[6.3-95] is also shown. The absolute vertical position of the curve is somewhat arbitrary, but the slope corresponds to reported data. The final set of runs appears to agree reasonably well with this line. This last set of data provides a simulation of permeation through steel having an oxidized surface. It approximates the situation in a fusion reactor blanket because with time the breeder will tend to corrode the surfaces of the cladding and form an oxide film. Since permeation is proportional to the area-to-thickness ratio, the equivalent permeation in a fusion reactor blanket can be estimated. The area-to-thickness ratio for a BCSS water-cooled, 4000-MW(th) blanket is greater than that in TRIO-1 by a factor of 6.3×10^6. Extrapolating the data to an approximate cladding temperature of 320°C results in an estimated permeation into the water coolant of ~1000 Ci/day.

The most significant results in the area of heat transfer in TRIO-1 were the in-pile measurement of thermal conductivity of the lithium aluminate. These data are plotted in Figure 6.3-29. The large open circles represent the data for the first few experimental runs. The dots represent the later runs. The estimated precision is < 10 %. The data show no significant changes in thermal conductivity as a result of increased irradiation. It is inferred that, for the temperature range of interest, limited radiation damage (equivalent to about two months in a fusion reactor) does not significantly affect thermal conductivity.

Impurities in γ-$LiAlO_2$ (Section 6.3.1) resulted in the generation of measurable quantities of a number of volatile radionuclides during radiation. The levels measured showed significant temperature dependence, but the data were not adequate to calculate release rates. Chemical analysis including neutron activation was performed prior to irradiation. In addition, the irradiated material was analysed by gamma spectrometry. These data will provide guidance to calculations of BCSS blanket activation and waste management (Section 6.12).

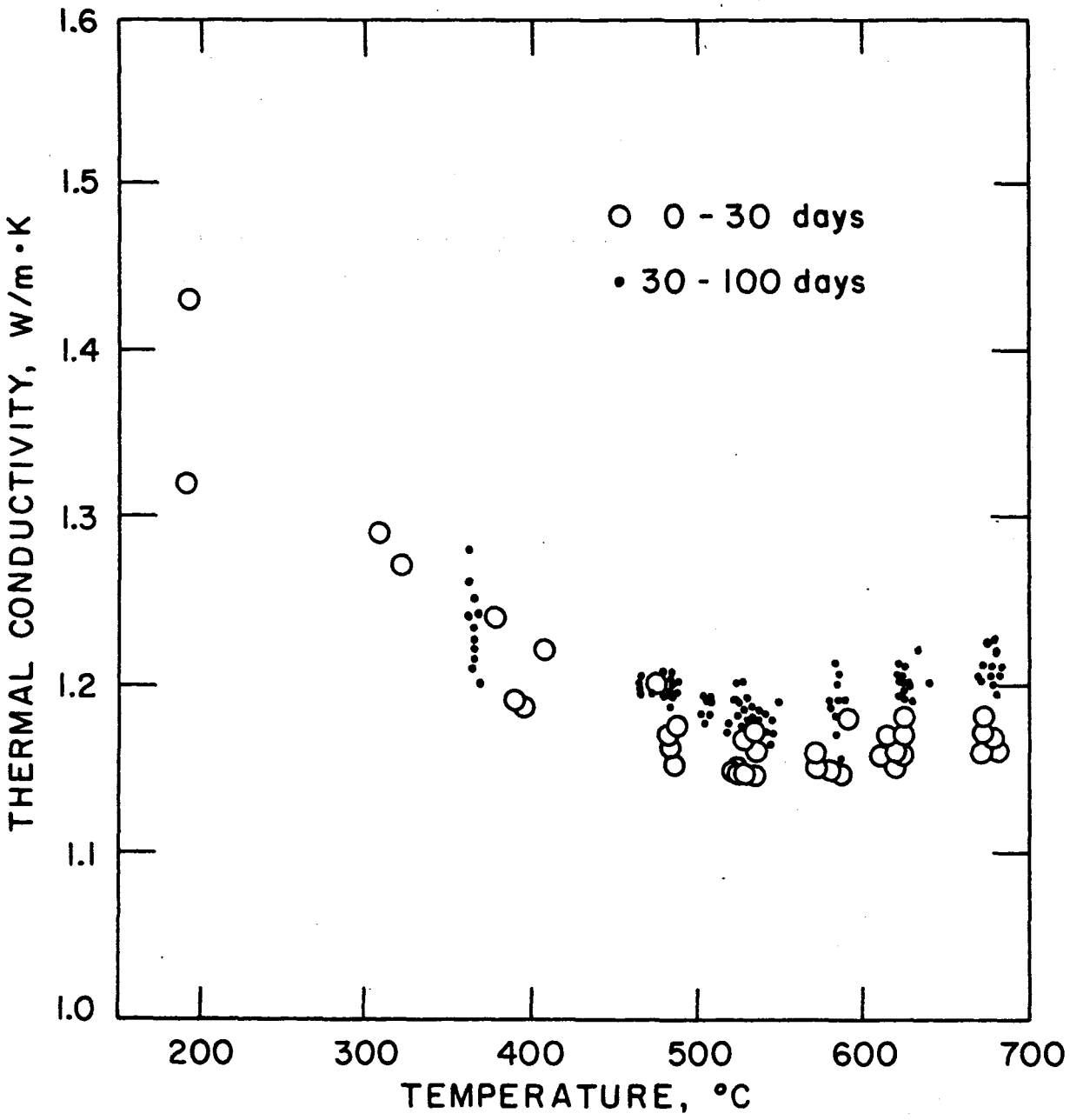


Figure 6.3-29. Thermal conductivity data of γ-$LiAlO_2$ from the TRIO experiment.

Tritium Diffusivity and Radiation Damage

As mentioned previously, an apparent tritium diffusivity in γ-$LiAlO_2$ has been derived from the TRIO-1 tritium inventory data at the beginning and end runs of the experiment. The controlling mechanism for tritium transport was assumed to be intragranular diffusion; surface desorption was assumed uninhibited in these runs because of the addition of 0.1% H_2 in the helium sweep gas. The relatively high activation energy (35 kcal/mole) of the apparent tritium diffusivity also gives qualitative support that intragranular diffusion is the governing process, as other processes such as surface desorption and/or grain-boundary diffusion should have a much weaker temperature dependence (hence lower activation energies if they dominate). Comparison of the apparent tritium diffusivity derived from the TRIO-1 data and other reported values showed considerably discrepancies (Section 6.3.2.2). However, the lack of precise information of grain size in these other studies made meaningful comparisons difficult.

It is possible that a material such as lithium aluminate could show a wide range of diffusivities, owing to impurities (Section 6.3.1) and solid-state effects (Section 6.3.2.2). The diffusivity could also be affected by the oxygen vacancy concentration in solid breeders. Since low oxygen potentials tend to form more vacancies, diffusivity could be enhanced. Conversely, when oxygen potential is high (e.g., run 20) defect content is reduced and diffusion may be correspondingly reduced. However, this possibility cannot be quantitatively resolved with the TRIO-1 results.

Earlier in discussions of the TULIP and FUBR-1A experiments (Sections 6.3.3.1 and 6.3.3.2), the possibility of tritium trapping by helium bubbles was raised for Li_2O. Both microstructural examinations (Figs. 6.3-14 through 6.3-18) and the strong correlation between tritium/helium retention results suggest irradiation-induced trapping of tritium. Furthermore, the calculated tritium diffusive inventories fell far below the measured residual tritium in Li_2O after irradiation. For γ-$LiAlO_2$, in the TRIO-1 experiment at least, radiation damage and tritium trapping did not appear to have occurred to any significant degree. The tritium inventory data for the first 8 runs (beginning of irradiation) and the last 6 runs (end of irradiation) fit a single tritium diffusivity equation. Had there been significant irradiation-induced tritium trapping, one would expect a change in slope of the apparent tritium

diffusivity toward the end of irradiation. Since this had not been observed, it is concluded, therefore, that for the limited conditions and burnups of the experiment, trapping is not a significant contributor to tritium inventory at the temperatures tested. The lack of radiation damage in γ-$LiAlO_2$ under the TRIO-1 irradiation conditions is also partially supported by the thermal conductivity results. However, it cannot be conclusively established whether the lattice phonon conductivity of γ-$LiAlO_2$ had been unduly degraded because of the preponderance of interconnected porosity (35%) in the specimens (Section 6.3.2.2).

Purge Chemistry and Surface Effects

As mentioned before, hydrogen addition of 0.1 %, a thousandfold excess, appears to enhance tritium release rates and reduce tritium inventories associated with the surface. A simple argument based on isotopic swamping of surface sites[6.3-94] could account for the reduction in tritium inventory when hydrogen was added. Another evidence for purge chemistry effects is also noted in Fig. 6.3-27. In run 3, the hydrogen content was increased from 0.1 % to 1 %. The HT release curve showed a positive spike followed by a very rapid return to equilibrium. The time constant is on the order of ten minutes. This rapid response is not characteristic of processes in the bulk of the solid such as intragranular diffusion. Rather, it appears to be a surface process, which is much more rapid.

For run 20, oxygen was added and very little tritium came out. Following a return to 0.1% H_2 addition, run 21 showed a large positive peak, followed by a return to steady state. The release curve for run 21 does not show a different response than other similar runs(e.g., run 33). Thus, although tritium retention is higher for run 21, the release kinetics does not appear to be affected. The excess tritium, perhaps in the oxide form, does not seem to inhibit release rates of the rest of the tritium. If this excess tritium is on the surface, it does not seem to be affecting surface release rates.

Finally, it should be noted that in the TRIO-1 runs, the cladding temperature was rather high, the tube on the inside was hotter than the breeder material and the cladding was near the temperature at the colder surface of the breeder. In the γ-$LiAlO_2$/H_2O/HT9/Be blanket (Chapter 9) the temperature of the steel structural material is considerably lower (~320°C). In this case,

the effect of the cladding as a reducing agent will be much less. In addition, if the cladding is oxidized before use with an oxide layer on the steel, the steel may not participate in the equilibrium. Under this circumstance, the fraction of the condensible form could be considerably larger.

6.3.3.4 VOM-15H

VOM-15H is an in-situ tritium recovery experiment for Li_2O conducted by the Japan Atomic Energy Research Institute (JAERI).[6.3-96] VOM-15H is the third JAERI experiment in a helium sweep-gas environment also the first experiment in which Li_2O was subjected to relatively high irradiation temperatures (480-760°C) and achieved a relatively high burnup (0.24 at% ^6Li) compared to those of the first two JAERI experiments. Sintered (86% dense) Li_2O pellets were used with an average grain size of <10 μm and a ^6Li content of 7.4%. The experiment was conducted in the Japan Research Reactor (JRR-2) over a period of 990 hrs. During irradiation the sweep gas was either dry helium, or helium/1% H_2, flowing at a rate of 100 cm^3-STP/min.

Post-test dimensional and microstructural information for VOM-15H are not yet available. Macrocracks in Li_2O were observed, however, and these cracks are generally parallel to the heat transfer directions (i.e., radial and axial) of the pellets. Given the fact that the Li_2O pellets in VOM-15H went through four reactor cycles and numerous temperature changes during the experiment, it is not surprising to find these Li_2O macrocracks; they were most likely induced by thermal stresses generated during the reactor/temperature cycles.

As one might expect from the nature of the in-situ tritium recovery experiment, most of the preliminary data reported for VOM-15H are on tritium. Major differences between VOM-15H and the sealed-capsule experiment (FUBR-1A) discussed in Section 6.3.3.2 are the presence of helium purge stream (with varying purge chemistry from dry helium to 1% H_2 addition) in VOM-15H, and the temperature variations during irradiation. Changes in either purge chemistry or irradiation temperature introduced transients into the system, which are noticeable in VOM-15H due to online tritium monitoring. For example, Fig. 6.3-30 shows the tritium fractional release rate as a function of time following changes of the sweep-gas composition. Negative and positive spikes in the tritium fractional release are noted; the 1% H_2 addition to

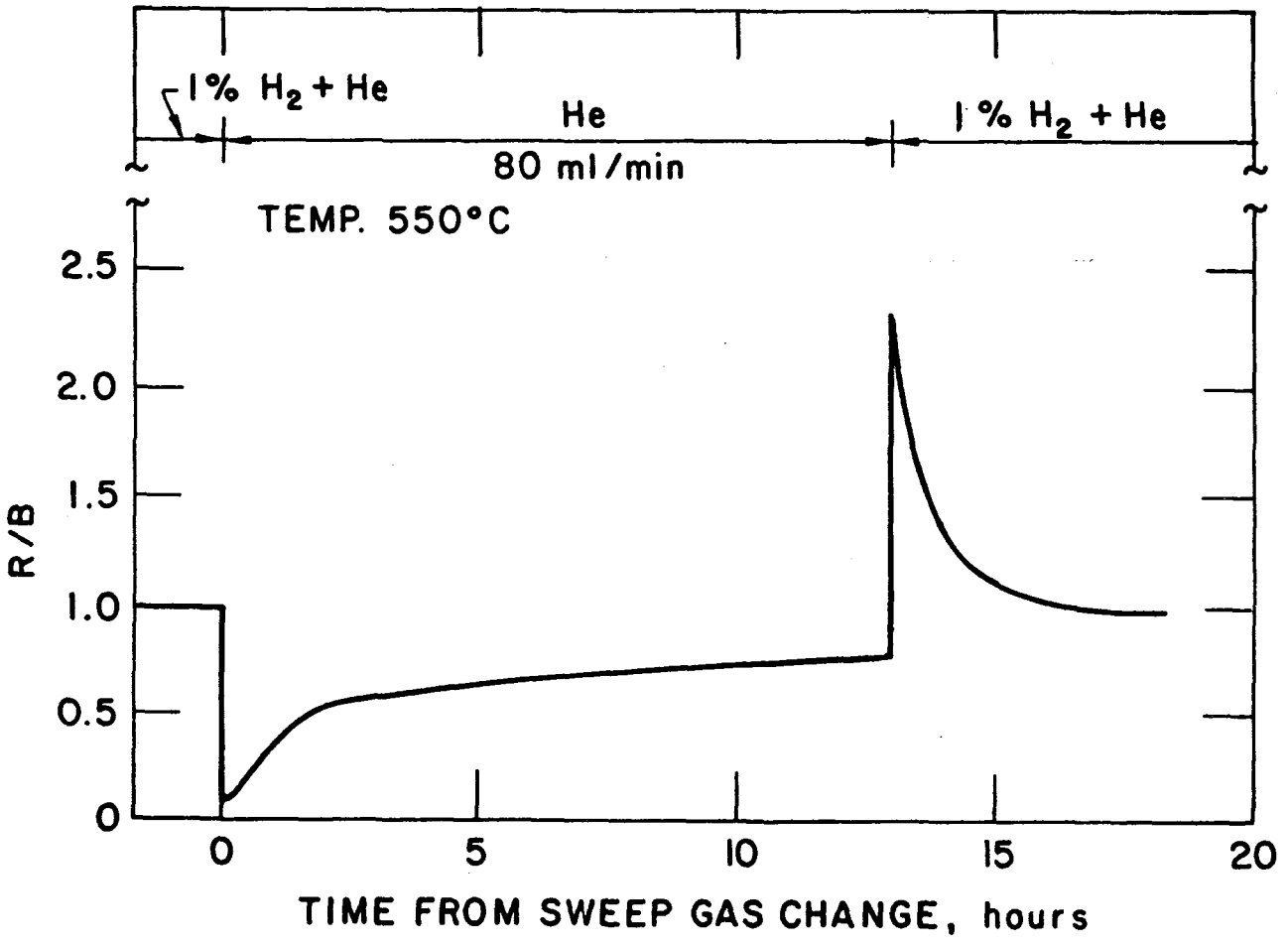


Figure 6.3-30. Effect of purge gas composition on fractional tritium release (R/B) from Li_2O in the VOM-15H experiment (from Ref. 6.3-96).

helium apparently enhanced tritium release. In general, depending upon the experimental condition (i.e., from low to high temperature and vice versa, or from dry helium to He/1% H_2 and vice versa), different lengths of times were required for these transients to die out and settle back to the steady state values. Similar types of transient behavior have also been observed in the TRIO-1 experiment.(6.3-94) The transient settling times and their dependence on test conditions are relevant to determining the burn-dwell time requirements of a fusion device for testing of solid breeder tritium recovery.(6.3-97)

Differences of tritium behavior in Li_2O under purge flow environment and sealed capsule condition can be contrasted by the amount of residual tritium measured in Li_2O. For VOM-15 the reported values are 0.5-0.9 wppm, which were measured after a final short-period (~20 hrs) irradiation at 710-760°C in the 4th (and final) reactor cycle of the experiment. These values are significantly lower than the FUBR-1A results obtained after 1 at% ^6Li burnup, i.e., 22 and 9 wppm of tritium in Li_2O, respectively, at comparable (700°C) and higher (900°C) irradiation temperatures. Since the starting grain sizes and densities are comparable in VOM-15H and FUBR-1A, and since substantial grain growth occurred in FUBR-1A at 700°C and more so at 900°C (Fig. 6.3-21), one might suspect that the higher FUBR-1A tritium retentions may result from the larger grain sizes and their effects on tritium lattice diffusion. However, calculations (Section 6.3.4.1) using the Li_2O single-cystal tritium diffusivity showed that the higher temperatues more than compensate for the larger grain sizes, and that even for Li_2O with average grain diameters of 14 and 34 μm, the steady-state tritium diffusive inventories at 700 and 900°C are still low, i.e., 1.3 and 1.1 x 10^{-4} wppm, respectively, compared to the FUBR-1A data. The spherical-grain diffusion model employed for the above calculations assumes a perfect-sink (i.e., zero tritium concentration) condition at the grain surface. Such an idealization is obviously questionable when the surface kinetics of tritium plays a dominant role in the overall tritium release process. For Li_2O (and γ-$LiAlO_2$ in Section 6.3.3.3), experimental evidence strongly suggested the important role of the tritium surface kinetics.

Perhaps the more interesting results in VOM-15H are the low-temperature (<550°C) tritium behavior. Figure 6.3-31 shows a marked decrease of the steady-state total tritium concentration in the recovery system at 480°C, compared to the near-flat concentrations at temperatures above 550°C. The

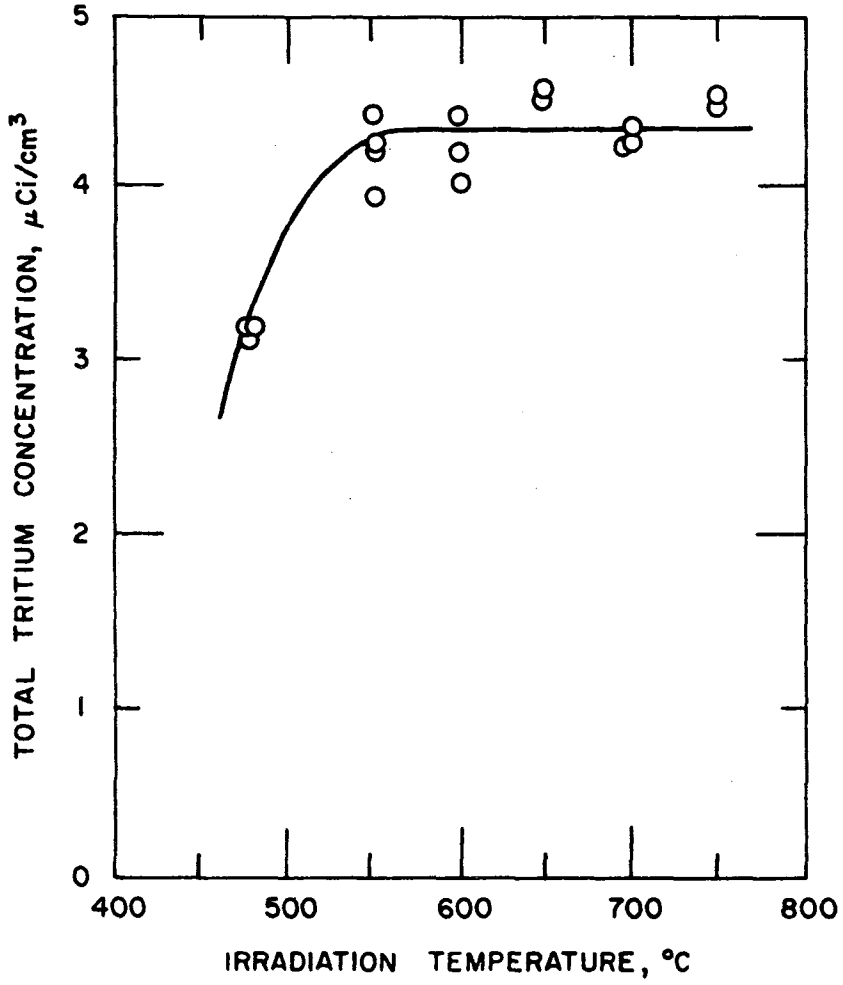


Figure 6.3-31. Temperature dependence of tritium release from Li_2O pellets in VOM-15H (from Ref. 6.3-96).

ratio of total tritium concentrations at 480 and >550°C is 0.74, a significant portion (~26%) of tritium is thus tied up either in Li_2O or in other parts of the system. In the TULIP experiment (Section 6.3.3.1) a marked increase of tritium retentions in Li_2O were also noted at 470°C after 1 at% ^6Li burnup, compared to the high-temperature (608-625°C) values (Fig. 6.3-19). This result could have been caused by three factors, i.e., limited tritium lattice diffusion (low temperature and defect trapping), surface hangups, and LiOT formation. Kurasawa et al[6.3-96] attributed the cause entirely to the last factor, however. If H_2 were added to the helium purge stream during the low-temperature irradiation, isotopic exchange is likley to enable the release of surface tritium, but the other two factors must still be considered.

Figure 6.3-32 shows that the ratio of gaseous tritium, HT/(HT + HTO) measured downstream, varies between 0.1 and 0.2 during the last three of the four reactor cycles of the experiment. However, Kurasawa et al[6.3-96] indicated that the ratio (or the HT fraction) at the capsule outlet was significantly higher (~90%). Isotopic exchange reaction, $HT(g) + H_2O(g) \rightleftarrows HTO(g) + H_2(g)$, enhanced by the catalytic reactivity of the surface of the stainless steel pipe (heated to 110°C), and the passage of gas through a ~10 m pipe are thought to be responsible for the higher fraction of the oxidized form downstream.

Kurasawa et al[6.3-96] also estimated the amount of Li_2O material transfer in the helium sweep-gas flow based on LiOH(T) decomposition. The amount of Li_2O mass transfer during four cycles of irradiation (990 hrs) was less than 0.3 wt% which extrapolates to an Li_2O mass transfer of 2.65 wt% per year. This mass transfer rate is in reasonable agreement with that (3.2 wt%/y) obtained in the out-of-reactor tests (Section 6.3.2.4).

6.3.3.5 Sealed Capsule Versus In-Situ Experiments

Table 6.3-7 summarizes the tritium retention results obtained from the four irradiation experiments on Li_2O and γ- $LiAlO_2$. For both materials the residual tritium (in wppm) are significnatly lower in the purge flow experiments (VOM-15H and TRIO-1) than those in the sealed capsule experiments (TULIP and FUBR-1A). If literal translation were made of the residual tritium retentions in the sealed capsule experiments, the steady-state tritium inventories in a 4000 MW(th) STARFIRE-size blanket would become unacceptably high. Simi-

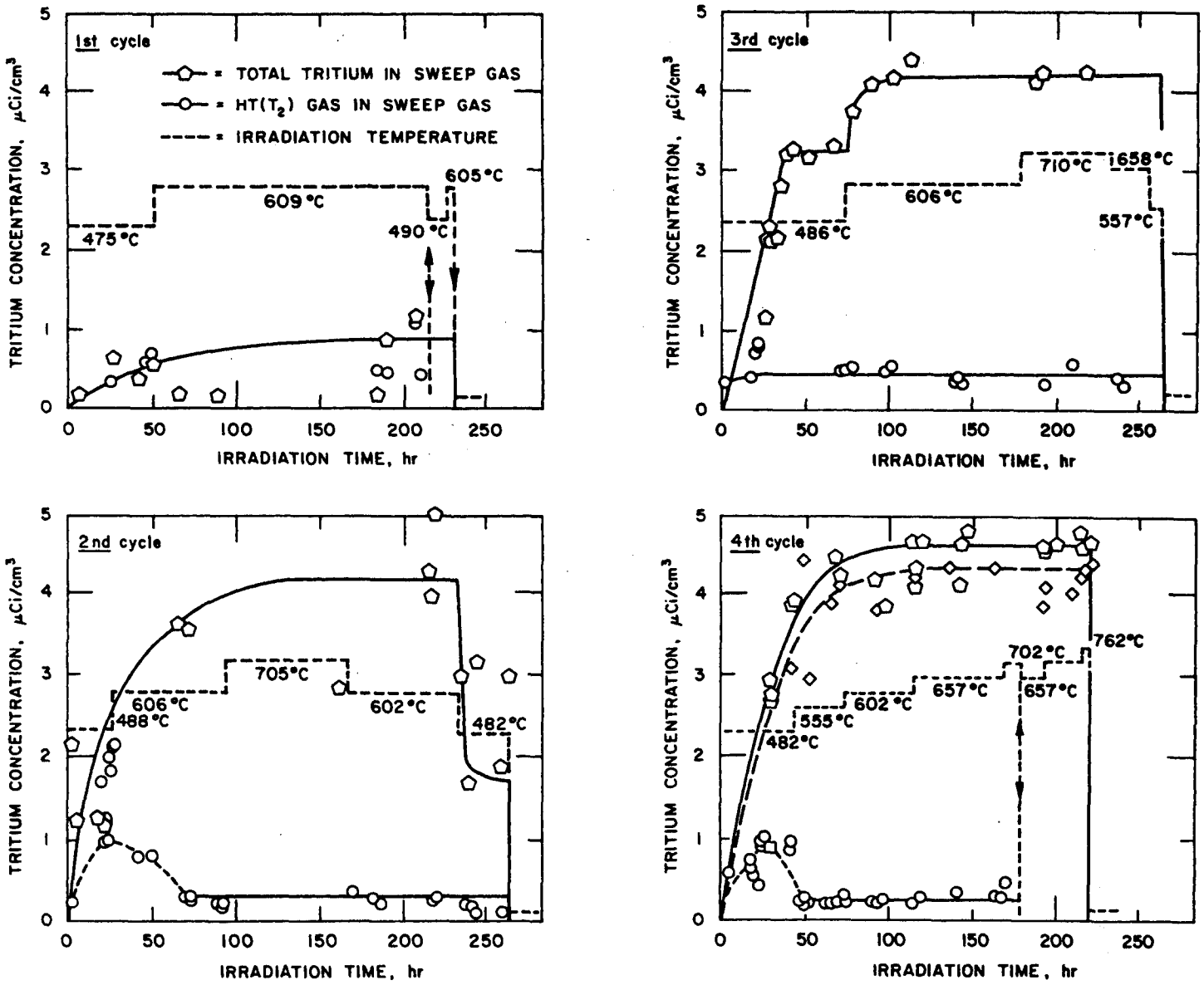


Figure 6.3-32. Tritium release data obtained during the four reactor cycles of the VOM-15H experiment (from Ref. 6.3-96).

TABLE 6.3-7. SUMMARY OF TRITIUM RETENTION IN FOUR SOLID BREEDER IRRADIATION EXPERIMENTS

Experiment	Density (% TD)	Grain-Size (μm)	Temperature (°C)	^{6}Li Burnup (at.%)	Retained Tritium	
					%	wppm
Li_2O						
TULIP/EBR-II	85-89	40-50	608	1	<9.7[a]	<182
(Sealed Capsule)	85-89	40-50	625	1	<8	<124
	85-89	40-50	608	3	<6.5	<364
	85-89	40-50	625	3	<1.4	<78
	85-89	40-50	470	1	<10.8	<259
FUBR-1A/EBR-II	85	4	500	1	9	79
(Sealed Capsule)	85	7	700	1	2.5	22
	85	7	900	1	1	9
VOM-15H/JRR-2	86	<10	750	0.23	0.1-0.2	0.5-0.9
(In-Situ)						
γ-$LiAlO_2$						
FUBR-1A/EBR-II	85	<1	500	1	35	235
(Sealed Capsule)	85	<1	700	1	8	54
	85	<1	900	1	4	27
TRIO-1	65	0.2	650	0.18	0.003	<0.1
(In-Situ)						

[a]EA403-4 retained 50% tritium and 45% helium generated during EBR-II irradiation.

lar translation of the residual tritium retentions from in-situ experiments, on the other hand, will result in levels of blanket tritium inventories that are acceptable. Since in-situ tritium recovery is a requirement for all solid breeder blankets (Chapters 8, 9 and 10), the information generated from the in-situ experiments is apparently much closer to what might have been obtained under the actual blanket operating conditions.

Although not shown in Table 6.3-7, the presence of purge gas and the on-line data collection system in the in-situ experiments provided the most valuable data on tritium release behavior that cannot be obtained otherwise. Because of the online data collection, the cause-effect relationships (such as the temperature and/or purge chemistry effects on tritium recovery) can be established which are extremely useful to aid future solid breeder blanket designs.

Sealed-capsule experiments provide an effective means for screening potential solid breeder candidates. Such experiments are particularly useful during the early stage of solid breeder development. Thus in FUBR-1A the irradiation behavior of four solid breeders can be compared under closely similar conditions, and that of the sphere-pac breeders can be examined for early problem identification (if any) in the FUBR-1B experiment.[6.3-98] Other useful information generated by the sealed-capsule experiments are breeder microstructural evolution and swelling.

In summary, sealed-capsule and in-situ experiments on solid breeders are complimentary in nature. Both types of experiments have their unique test objectives. Sealed-capsule experiments are ideal for breeder materials screening; they also provide the baseline information from which purge chemistry and surface effects on tritium release can be assessed. When the choice of breeder candidates narrows down, in-situ experiments must be performed to establish the engineering feasibility of in-situ tritium recovery. In-situ experiments are rich in information content because of online data collection, which also make them suitable for obtaining mechanistic understanding of the solid breeder behavior.

6.3.4 Design Guidelines

Design guidelines for solid breeders have been updated from those given in the Interim BCSS report.[6.3-3] Significant changes were made for all sol-

id breeder materials, most notably for Li_2O and γ-$LiAlO_2$. Changes in design guidelines for these two materials resulted largely from the availability of recent irradiation data (Section 6.3.3) and from the modeling work performed (Section 6.3.4). Current guidelines are consistent with data from various ex- and in-reactor materials studies. However, long-term fluence (>2.8 MW yr/m^2) effects on these guidelines remain to be investigated.

Table 6.3-8 shows the design guidelines adopted by the BCSS project that include selected properties and operating temperature ranges for eight solid breeders. Bases for these design guidelines are summarized in the footnotes of the table. Additional comments are given in the following.

Melting Point

These values are identical to those given in Ref. 6.3-3.

Lithium Density

These values are identical to those given in Ref. 6.3-3.

Thermal Conductivity

Except for Li_2O and γ-$LiAlO_2$, the thermal conductivity values given for the other solid breeders were estimated at 1000 K for unirradiated, 85%-dense sintered products. The value for Li_8ZrO_6 is based on the data of Hollenberg,[6.3-93] corrected for porosity effects.

Two kinds of thermal conductivities, k for sintered product and k_{eff} for sphere-pac system, were estimated for Li_2O and γ-$LiAlO_2$ at 1000 K, assuming radiation damage saturates at a fusion neutron fluence of 2.8 MW yr/m^2. Experimental data bases, estimation procedures and models used for the k and k_{eff} estimations were described in detail in a separate publication;[6.3-53] they will not be repeated here. Temperature- and pressure-dependent thermal conductivity curves are given in Figs. 6.3-5 through 6.3-8 of Section 6.3.2.2.

For the sphere-pac solid breeders (Li_2O and γ-$LiAlO_2$), it is assumed that the sphere-pac is made of high-density (~100% TD) particles with three sizes (30, 300, and 1200 μm diameters); the helium fill gas is assumed at 1 atm pressure. The values of k_{eff} will change when the sphere-pac system deviates from the above description (e.g., changing particle densities and/or sizes).

TABLE 6.3-8. BCSS DESIGN GUIDELINES

Parameters: Properties and Operating Temperature Ranges for Solid Breeders
Value(s):

VALUES FOR CANDIDATE SOLID BREEDER MATERIALS[a]

Breeder	MP, °C	ρ Li, g/cm^3	k,[b] W/m-K	T_{min},[e] °C	T_{max},[g] °C	ΔT, °C	Grain[i] Dia., μm
Li_2O	1433	0.93	2.5[c] 1.27[d]	410[f]	800[h]	390	3.0[j]
γ-$LiAlO_2$	1610	0.28	1.6[c] 1.1[d]	350	1000	650	0.2
Li_8ZrO_6	1295	0.68	1.8	350	760	410	2.0
Li_5AlO_4	1047	0.61	2.3	350	600	250	--
Li_2SiO_3	1200	0.36	1.5	410	700	290	--
Li_4SiO_4	1250	0.54	1.5	320	730	410	2.0
Li_2ZrO_3	1616	0.33	1.3	400	970	570	2.0
Li_2TiO_3	1550	0.33	2.0	400	930	530	--

[a]Estimates based on limited unirradiated and irradiated data (solid breeders, other ceramic materials).

[b]Unless otherwise noted, values are estimated for unirradiated, sintered materials of 85% theoretical density at 1000°K.

[c]Estimated for 85%-dense, sintered material at 1000°K after 0.7-2.8 MW yr/m^2 fusion neutron fluence.

[d]Estimated for 87% solid packing fraction, sphere-pac material made of high-density (~100% TD) particles with three sizes (30, 300, and 1200 μm diameters) at 1000°K (1 atm He pressure) and after 0.7-2.8 MW yr/m^2 fusion neutron fluence.

[e]Unless otherwise noted, values are estimated based on diffusive inventory considerations (i.e., maximum tolerable blanket tritium inventory ≤10 kg). T_{min} depends strongly on grain size and tritium diffusivity. Experimental information on the latter two are available only for Li_2O and γ-$LiAlO_2$. Possible radiation-induced defect trapping of tritium is not included.

[f]Based on solubility consideration (i.e., formation of LiOH/LiOT separate phases at a T_2O partial pressure of 160 Pa). T_{min} may be higher (500°C) according to the Japanese Li_2O in-situ tritium recovery experiment (VOM-15).

[g]Unless otherwise noted, values are based on short-term (<0.25 MW yr/m^2 thermal and radiation-enhanced sintering considerations for 85%-dense materials. T_{max} = 0.66 T_m, where T_m is the absolute melting point. T_{max} may be less than 0.66 T_m for high fluence (burnup) conditions.

[h]Based on high-temperature mass transfer (LiOT/LiOH) considerations; T_{max} also satisfies the sintering rule g.

[i]Based on the smallest grain diameters with existing fabrication technology.

[j]Grain growth occurred during irradiation (FUBR-1A) at temperatures >500°C.

Changing the helium fill-gas pressure will also change k_{eff}. However, the fill-gas pressure effects on k_{eff} appear to saturate at pressures above 6 atm.

Lower Temperature Limit (T_{min})

Except for Li_2O, the values of T_{min} were determined from tritium diffusive inventory considerations. Except for γ-$LiAlO_2$, the T_{min} values for the other solid breeders are the same as those given before.(6.3-3) These values are subjected to considerable uncertainties because precise values for tritium diffusivity and grain size are not known. Tritium diffusive inventories in Li_2O and γ-$LiAlO_2$ were calculated based on either the single-crystal or the apparent tritium diffusivities, the minimum as-fabricated grain sizes, the BCSS blanket configurations and their prescribed operating conditions (i.e., tritium production rates, temperatures, and temperature gradients), and a maximum blanket tritium diffusive inventory of 10 kg. Tritium diffusive inventory in the Li_2O blanket was found to be non-limiting at 410°C, whereas that for the γ-$LiAlO_2$ blankets resulted in a T_{min} of 350°C. Possible irradiation-induced defect trapping of tritium(6.3-90) has not been included in the estimates of T_{min}, which appears to be more important for Li_2O than for γ-$LiAlO_2$ (Section 6.3-3). Irradiation-induced trapping of tritium, if significant, can be expected to raise T_{min} from the present estimates.

The value of T_{min} for Li_2O was determined from solubility (i.e., formation of LiOH/LiOT separate phases) which depends on the H_2O (or T_2O) partial pressure.(6.3-2) Current estimate is based on a H_2O (or T_2O) partial pressure of 40 Pa, assuming the reaction $Li_2O + H_2O \rightleftarrows 2LiOH$. T_{min} may be higher (i.e., ~500°C) according to data from the Japanese in-situ tritium recovery experiment (VOM-15H, Section 6.3.3.4).

Upper Temperature Limit (T_{max})

Except for Li_2O, the values of T_{max} were estimated based on considerations of short-term (<0.25 MW yr/m^2) thermal and irradiation-enhanced sintering of the 85%-dense materials. T_{max} was obtained as 0.66 T_m, where T_m is the absolute melting point. At higher fluences (>0.25 MW yr/m^2) T_{max} may be less than 0.66 T_m and more close to 0.6 T_m, because sintering depends upon both

temperature and time at temperature. The 0.6 T_m behavior was found to be the temperature at which equiaxed grain growth occurred in UO_2.[6.3-99]

The value of T_{max} (800°C) for Li_2O is based on high-temperature mass transfer (vaporization) consideration[6.3-3] which also satisfies the 0.66 T_m rule. The low burnup OG-5 irradiation experiment[6.3-100] (<0.25 MW yr/m^2) of 70%-dense Li_2O showed significant pore closure (sintering) at temperatures above 850°C, whereas most pores remained open at temperatures below 750°C. Ex-reactor thermal stability tests,[6.3-101] on the other hand, showed that the cold-pressed and sintered (77% TD) Li_2O densified to ~86% TD after 1500 hrs at 800°C, whereas no densification occurred after 1200 h at 700°C. Densification has not been observed in the hot-pressed (85% TD) Li_2O pellets in the FUBR-1A experiment after either 2400 or 7200 hrs at 500, 700, and 900°C; swelling occurred, instead (Section 6.3.3.2).

The value of T_{max} (1000°C) for γ-$LiAlO_2$ is based solely on sintering consideration. Thermal stability tests of hot-pressed (85% TD) γ-$LiAlO_2$ showed no densification after 8 hrs at 900°C (Section 6.3.1), whereas some sintering occurred in cold-pressed and sintered (80% TD) γ-$LiAlO_2$ after 60 hrs at 1000°C.[6.3-100] The OG-5 irradiation experiment[6.3-100] (<0.25 MW yr/m^2) of 80% TD cold-pressed and sintered γ-$LiAlO_2$ indicated no pore closure below 950°C; however, crumbling occurred in specimens that were irradiated above 950°C. The hot-pressed (85% TD) γ-$LiAlO_2$ pellets in FUBR-1A were found to be stable up to 900°C after 7200 h of irradiation. Neither densification nor swelling occurred. Currently there is no data to assess the T_{max} for sphere-pac γ-$LiAlO_2$. Other than the temperature dependence, sintering of spherical particles also depends upon the particle size and the time at temperature. The smaller particles are more susceptible to sintering, as pointed out in Section 6.3.1.

Temperature Window, ΔT

These values were simply obtained as $T_{max} - T_{min}$; they are almost entirely different (except for Li_2O) from those given in Ref. 6.3-3 due to changes made for T_{max} and T_{min}.

Grain Diameter

The smallest grain diameters that can be fabricated from existing technology (Section 6.3.1) were specified in this column. Grain diameters must be given in order to define the lower temperature limit (T_{min}). For the high-density (~100% TD) particles used for the sphere-pac breeders, fabrication technology remains to demonstrate that fine grains of 0.2 μm-average diameter can be formed in particles of 30, 300, 1200 μm diameters. Otherwise, tritium diffusive inventory in γ-$LiAlO_2$ will be a serious problem.

Small grain size in Li_2O is not as critical as that in γ-$LiAlO_2$ because of the much higher tritium diffusivity in Li_2O (Section 6.3.2.2). Substantial grain growth in the Li_2O has been observed in FUBR-1A (6.3.3.2) at irradiation temperatures as low as 700°C. Although grain growth had not caused the expected sharp increase in Li_2O tritium retention (i.e., owing to the enhanced diffusivity at high temperatures), the helium-bubble induced swelling, on the other hand, may increase with increasing grain size. Both helium and tritium diffusions in the Li_2O lattice will be hampered by the larger grain size, but the effects on helium are likely to be greater, especially at intermediate temperatures (500-600°C). Grain growth had not been observed in the hot-pressed (85% TD) γ-$LiAlO_2$ pellets in FUBR-1A up to 900°C and after 7200 h of irradiation.

In summary, the current design guidelines for solid breeders are consistent with all the existing ex- and in-reactor experimental data and model calculations. Most uncertainties in these guidelines are related to either the sphere-pac system and/or the long-term fluence effects. The R&D work recommended in the preceding sections should help to define more realistic operating limits for these solid breeders.

6.3.5 Modeling

Significant work on solid breeder behavior modeling has been done during the BCSS project period in areas of steady-state tritium inventory (Section 6.3.5.1), transient tritium response (Section 6.3.5.2), tritium permeation, leakage, and containment (Section 6.3.5.3), physical integrity and gap conductance (Section 6.3.5.4), and solid-breeder/structure mechanical interaction (Section 6.3.5.5). Other modeling work not included in this section are theoretical estimates of solid-breeder thermal conductivities with and without

irradiation effects,[6.3-53] and the theoretical thermodynamic calculations of the oxygen activity effects (Sections 6.3.2.1 and 6.3.3.3). In many instances, the physics-based models have provided useful insights to the governing mechanisms of solid breeder behavior, assisted in the interpretation of experimental data, and generated results for blanket design evaluations. Physical modeling will remain useful in guiding future solid breeder experimental and design efforts.

6.3.5.1 Steady-State Tritium Inventory

In this subsection, models are presented for predicting the steady-state tritium inventory in the BCSS solid breeder blankets. This information is needed in order to perform a safety analysis for each of the blanket concepts.

Conceptually, the steady-state inventory (I) is divided into components in the ceramic breeder (I_b) -- including the interconnected porosity and purge stream, the metal structure (I_m), and the coolant (I_c):

$$I = I_b + I_m + I_c \ . \qquad [6.3\text{-}8]$$

As the breeder contains the largest component of inventory, it is further subdivided into retained tritium due to bulk diffusion (I_d), solubility (I_s), surface adsorption (I_a), and porosity-percolation/purge-stream-convection (I_p):

$$I_b = I_d + I_s + I_a + I_p \ . \qquad [6.3\text{-}9]$$

Diffusive Inventory (I_d)

After tritium is bred in the breeder, the initial process in tritium transport is bulk diffusion from the interior of the solid-breeder grains to the grain boundaries. Tritium is generated within the grain matrix at a rate per unit volume $\dot{g}$. Assuming a spherical, isothermal grain of radius r_g and temperature T, the intragranular diffusive inventory (assuming zero concentration at grain boundaries) is given by the classical formula[6.3-70]

$$I_g = \tau \dot{g} V_g \ , \qquad [6.3\text{-}10]$$

where

τ = the mean residency time in s
= $(r_g^2/15\ D)$

r_g = the grain radius in cm

D = the diffusion coefficient in cm^2/s
= $D_o \exp(-Q/RT)$

D_o = a pre-exponential factor for the diffusion coefficient

Q = the apparent activation energy for diffusion in kcal/mol

R = 1.986×10^{-3} kcal/mol • K

T = temperature in K

$\dot{g}$ = tritium generation rate in g/s • cm^3

and

V_g = $(4/3)\ \pi\ r_g^3$ = grain volume in cm^3.

In applying Eq. [6.3-10] to the whole blanket, care must be taken to properly account for the large variations in temperature and generation rate across the blanket. To simplify the analysis, the blanket is divided into unit cells. The two unit cells of practical interest in this study are the hollow cylinder and the plate (see Fig. 6.3-33). Integrating Eq. [6.3-10] over one unit cell gives

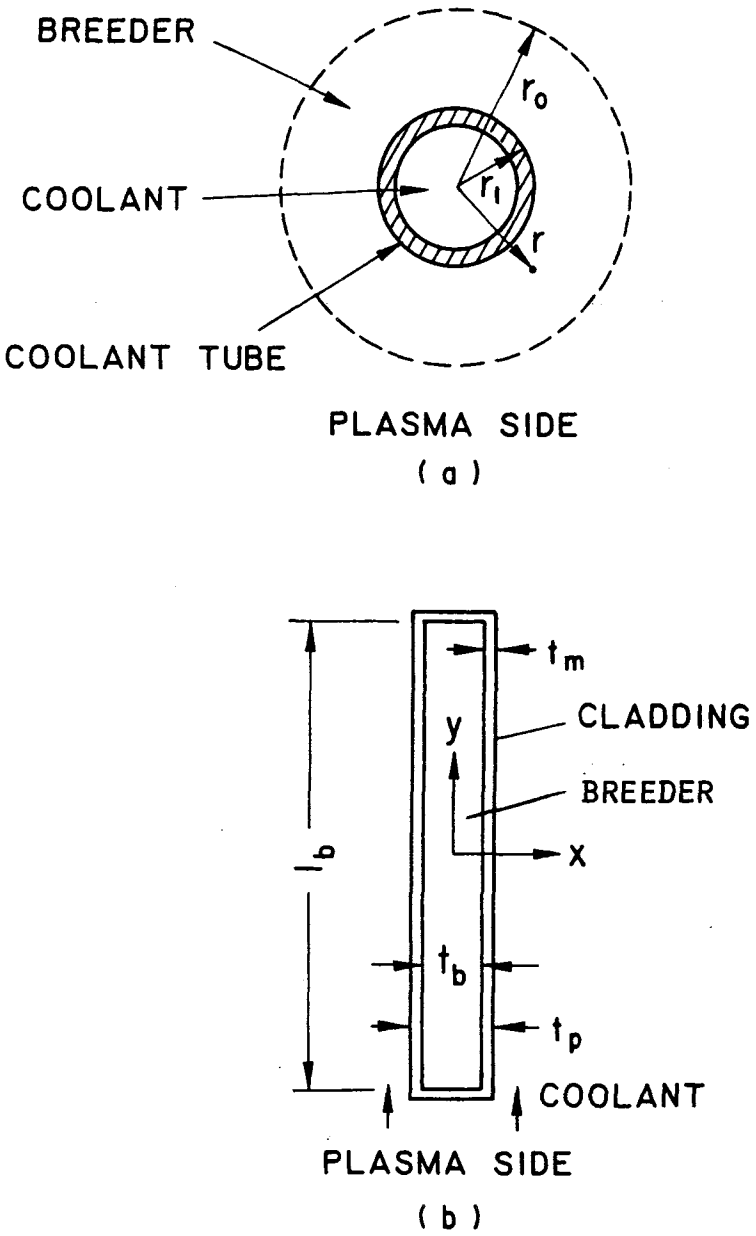


Figure 6.3-33. Representative cross-sections of unit cells for cylindrical and plate geometries. Purge stream channels are not shown.

$$I_{cell} = \int_{V_{cell}} \tau \dot{g}(1 - \varepsilon)\, dV \,, \qquad [6.3\text{-}11]$$

where

V_{cell} = the breeder volume in a unit cell

ε = the breeder porosity fraction

and

$$dV = \begin{cases} rdrd\theta dz \text{ for the cylinder} \\ dxdydz \text{ for the plate.} \end{cases}$$

The total tritium diffusive inventory in the blanket can then be found by summing over the unit cells, each employing the local temperature and tritium generation rate as appropriate:

$$I_d = \sum_{i=1}^{N} (I_{cell})_i \,. \qquad [6.3\text{-}12]$$

The application of Eqs. [6.3-11] and [6.3-12] to the BCSS blankets of interest is cumbersome. A number of simplifying assumptions have been employed to generate a model which allows calculations to be performed for scoping studies and blanket comparisons. The first assumption is that variations in temperature and generation rate in the z direction for both cylindrical and plate unit cells are negligible. The second assumption is that the generation rate is constant in the x-direction for the plate and in the r and θ directions for the cylinder. The motivation for this approximation with regard to the generation rate is that the inventory varies linearly with the generation

rate. The assumptions on temperature variation are less stringent because the inventory varies in a highly nonlinear fashion with respect to temperature.

Using the above assumptions, Eq. [6.3-12] can be rewritten for the plate as

$$(I_d)_{plate} = \dot{G}_p \int_{-1/2}^{1/2} h(\xi) \left\{ \int_o^1 \tau(\eta,\xi)\, d\eta \right\} d\xi \,, \qquad [6.3\text{-}13]$$

where

$\dot{G}_p$ = the generation rate in g/s for the plate

ξ = the normalized position (y/ℓ_b) along the coolant path

$h(\xi) = \dot{g}(\xi)/\bar{\dot{g}}$ = the normalized tritium production rate along the coolant path direction

η = the normalized position ($2x/t_b$) in the plate thickness direction

$$\tau(\eta,\xi) = (r_g^2/15\ D_o) \exp\left(\frac{Q}{RT}\right)$$

and

$$T = T(\eta,\xi) \,.$$

If an exponential function is used to characterize the variation of generation rate with ξ, then

$$\dot{g}(\xi) = \dot{g}_{max} \exp\left[-\alpha(\xi + 1/2)\right] \,,$$

$$\bar{\dot{g}} = \int_{-1/2}^{1/2} \dot{g}(\xi)\, d\xi = (\dot{g}_{max}/\alpha)[1 - \exp(-\alpha)] ,$$

and

$$\dot{g}(\xi)/\bar{\dot{g}} = \frac{\alpha \exp[-\alpha(\xi + 1/2)]}{1 - \exp(-\alpha)} , \qquad [6.3\text{-}14]$$

where $\dot{g}_{max}$ and $\bar{\dot{g}}$ are the maximum and average tritium generation rates in the blanket, respectively, and α is a nondimensional distance characteristic of the exponential. Similarly, if the heating rate has the same exponential dependence, then the temperature dependence on ξ and η can be expressed in an explicit form for constant geometry and material properties as

$$T(\eta,\xi) = T_{in} + (\bar{q}_p\, V_p/\dot{m}\, C_p) \frac{1 - \exp[-\alpha(\xi + 1/2)]}{1 - \exp(-\alpha)}$$

$$+ (\bar{q}_p\, t_p/2)\left(1/h_c + t_m/k_m\right) \frac{\alpha \exp[-\alpha(\xi + 1/2)]}{1 - \exp(-\alpha)}$$

$$+ (\bar{q}_b\, t_b/2)[1/h_{gap} + (t_b/4k_b)(1-\eta^2)]\alpha \frac{\exp[-\alpha(\xi + 1/2]}{1 - \exp(-\alpha)} ,$$

[6.3-15]

where

T_{in} = the coolant inlet temperature

$\bar{q}_p$ = the average volumetric heating rate in the plate

V_p = the volume of the plate

$\dot{m}$ = the coolant mass flow rate associated with one plate

C_p = the coolant specific heat

t_p = the plate thickness

h_c = the coolant-cladding heat transfer coefficient

t_m = the cladding thickness

k_m = the average thermal conductivity of the cladding

$\bar{q}_b$ = the average volumetric heat generation rate within the breeder

t_b = the breeder thickness

h_{gap} = the breeder-cladding gap conductance

and

k_b = the average breeder conductivity.

From a practical viewpoint, the only explicit integration performed in Eq. [6.3-13] is in the η direction. The integration in the ξ direction is approximated by subdividing the plate into a number of axial sections, each with assumed constant heat and tritium generation rates. The inventories from these sections are then summed to approximate the inventory in a single plate.

In the case of the cylinder, a more convenient approximation to Eqs. [6.3-11] and [6.3-12] can be obtained because the cylindrical unit cell extends only a small fraction across the blanket thickness, whereas the plate extends across the whole thickness. Equation [6.3-11] can be rewritten for this case as

$$(I_d)_{cyl} = [r_g^2/15\ D(\bar{T})] \cdot f \cdot \hat{G}_{cyl}, \qquad [6.3\text{-}16]$$

where

$D(\overline{T})$ = the diffusion coefficient evaluated at the volume-averaged cell temperature

$\dot{G}_{cyl}$ = the tritium generation rate of the cell

$$f = (\beta - 1)^{-1} \int_1^{\beta} \exp\left[(Q/R\overline{T})\ (\overline{T}/T - 1)\right] d\eta \qquad [6.3\text{-}17]$$

$\eta = r^2/r_i^2$

$\beta = r_o^2/r_i^2$

r_o = the cell outer radius

r_i = the cell inner radius

r = an arbitrary radial position within the cell

$\overline{T}$ = the cell averaged temperature

T = a local temperature within the cell.

For the assumed case of radial heat flow from r_o to r_i, the average and local temperatures are given by

$$\overline{T} = T_{min} + \Delta T \left\{\frac{(1 - \beta^{-1})^{-2}\ (\ell n\ \beta - 1 + \beta^{-1}) - 1/2}{(1 - \beta^{-1})^{-1}\ \ell n\ \beta - 1}\right\}, \qquad [6.3\text{-}18]$$

$$T = T_{min} + \Delta T \left\{\frac{(1-\beta^{-1})^{-1}\ \ell n\ \eta - (\beta-1)^{-1}\ (\eta-1)}{(1 - \beta^{-1})^{-1}\ \ell n\ \beta - 1}\right\}, \qquad [6.3\text{-}19]$$

where

T_{min} = the minimum cell temperature (at r_i)

and

$\Delta T = T_{max} - T_{min}$ = the radial temperature drop across the cell.

Summing Eq. [6.3-16] over the unit cells in the blanket gives

$$I_d = \dot{G} \left(r_g^2/15\right) \left\{ \sum_{i=1}^{N} \left[D(\bar{T}_i)\right]^{-1} f_i \left(\dot{G}_{cyl}\right)_i / \dot{G} \right\} \qquad [6.3\text{-}20]$$

where

$\dot{G}$ = the total tritium generation rate within the blanket in g/s.

A further simplication of Eq. [6.3-20] is possible by considering an "average" unit cell to characterize the whole blanket. If it is assumed that the whole blanket is operating at the volume-averaged heat generation $(\bar{q}_b)$ and tritium generation $(\dot{\bar{g}})$ rates, then the cell size is defined implicitly by:

$$(\beta - 1) \left[\left(1 - \beta^{-1}\right)^{-1} \ell n\, \beta - 1\right] \leq \frac{4\, \bar{k}_b\, \Delta T}{\bar{q}_b\, r_i^2}, \qquad [6.3\text{-}21]$$

and Eq. [6.3-20] simplifies to

$$I_d = \left[r_g^2/15\; D(\bar{T})\right] f\, \dot{G}\ . \qquad [6.3\text{-}22]$$

Equation [6.3-22] has been compared to Eq. [6.3-20] for an extreme case of an $LiAlO_2/H_2O$/HT9/Be blanket with very steep gradients in q_b and $\dot{g}$. The inventory from Eq. [6.3-22] was only 14% lower than that obtained by using the more

detailed formula of Eq. [6.3-20]. Figure 6.3-34 shows the results of the detailed calculation which yielded an inventory of 9.1 kg. Equation [6.3-22] gave 7.8 kg. Thus, Eq. [6.3-22] is recommended for the blanket-outside-of-tube designs.

A critical parameter in the equations for diffusive inventory is the diffusion coefficient. A review of the literature reveals a wide range of values for the diffusion coefficients for Li_2O and γ-$LiAlO_2$ depending on impurity levels within the sample, concentrations of water vapor in the sample and the atmosphere surrounding the sample, the rate limiting phenomena (e.g., bulk diffusion, grain boundary diffusion, solubility, surface adsorption, etc.), and the experimentor's method for correlating and interpreting the data. A comprehensive review of the data (prior to 1982) for Li_2O is contained in Ref. 6.3-3 and summarized in Fig. 6.3-10, along with the latest single-crystal results of Guggi et al.[6.3-73]. The use of single crystals eliminated the uncertainties associated with polycrystalline materials regarding the grain boundary effects. The crystals were irradiated at low temperature in a dry atmosphere and then subjected to postirradiation anneals in a dry helium atmosphere. The released tritium species was transported to a Zn-reductor bed and mixed with methane for counting purposes. Guggi, et al's results for the diffusion coefficient of tritium in Li_2O in the temperature range of 575 to 925°C are summarized by[6.3-73]

$$\ell n \left(D/cm^2\ s^{-1}\right) = - \left(5.93 \pm 0.48\right) - \left(19.52 \pm 1.01\right) \text{ kcal/RT}, \quad [6.3\text{-}23]$$

where the ± numbers refer to three standard deviations.

As no comparable experiment has been performed on single crystal γ-$LiAlO_2$, a number of different experiments were reviewed and compared with the apparent diffusivities calculated from the TRIO-1 data. As mentioned in Section 6.3.3.3, the TRIO-1 data for runs 1-8 and 28-33 were analyzed to determine a bulk diffusion coefficient for tritium diffusion in γ-$LiAlO_2$. These runs were chosen because they exhibited characteristics of a bulk-diffusion-dominated transport mechanism. The sweep gas for all of these runs contained at least 0.1% H_2 which would tend to minimize the inventory

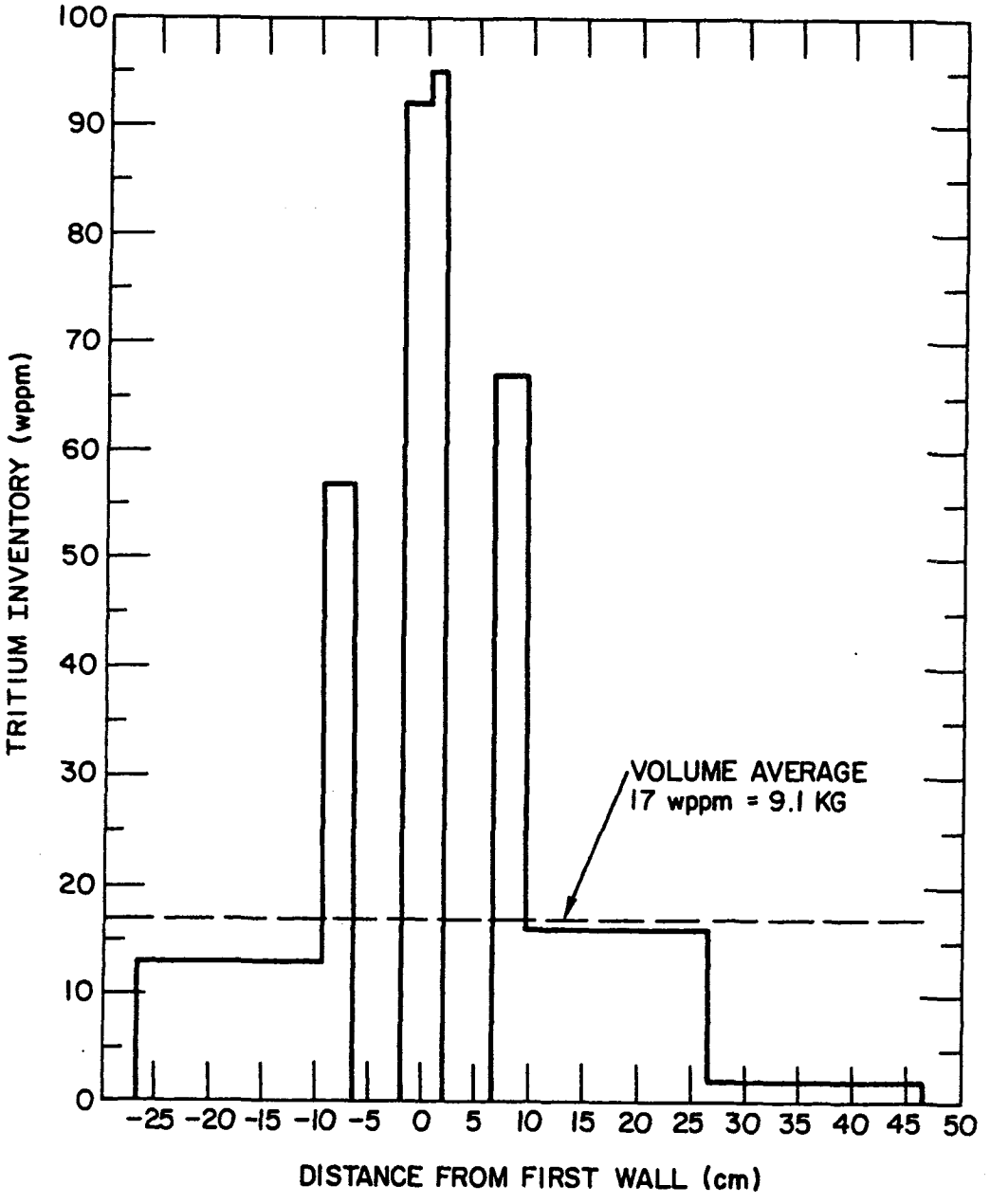


Figure 6.3-34. Distribution of tritium concentration in the BCSS (LOBE-2B) γ-$LiAlO_2$/Be/H_2O/HT9 blanket for the case of 0.1% H_2 added to the purge stream (T_{max} = 950°C, T_{min} = 360°C, G = 866 g/day, r_g = 0.1 μm).

associated with surface adsorption. Equation [6.3-22] was inverted to solve for $D(\overline{T})$ as a function of the measured temperatures, the pre-irradiation grain size, the calculated generated rates and the inventory measured directly for run 33 and deduced from release measurements for the other runs. Figure 6.3-35 shows the results for diffusion coefficient as a function of volume-averaged temperature. The results (which include a one-standard-deviation uncertainty estimated in I_d and $\dot{G}$) are summarized by:

$$\ell n \left(D/cm^2\ s^{-1}\right) = \left(-13.7 \pm 2.3\right) - \left(35.8 \pm 3.9\right) \text{ kcal/RT.} \qquad [6.3\text{-}24]$$

For the purposes of comparison to other investigators' results, a ±30% uncertainty is assumed for the grain size. Statistically including this in Eq. [6.3-24] gives:

$$\ell n \left(D/cm^2\ s^{-1}\right) = \left(-13.7 \pm 1.8\right) - \left(35.8 \pm 3.9\right) \text{ kcal/RT.} \qquad [6.3\text{-}25]$$

Equation [6.3-25] has been compared to the results of Yunker[6.3-103] and of Wiswall and Wirsing[6.3-102] in Fig. 6.3-36. Given that no uncertainty is included in the data of these authors, the agreement among the experimental results appears adequate.

Design calculations have been performed for the γ-$LiAlO_2$ and Li_2O blanket designs (Chapters 8 and 9). Equations [6.3-21], [6.3-22], and [6.3-24] were used for the γ-$LiAlO_2$ design. The inputs for the case were $\dot{G}$ = 866 g/day, T_{max} = 1000°C, r_g = 0.1 μm, $\bar{q}_b$ = 18 W/cm^3, r_i = 0.650 cm, and $\bar{k}_b$ = 1.1 W/m • K. Figure 6.3-37 shows the predicted diffusive inventory as a function of the minimum blanket temperature (T_{min}). The sensitivity of I_d to T_{min} is clearly demonstrated in this figure. At a minimum blanket temperature of 335°C, the diffusive inventory is estimated to be ~2 to ~10 kg with a nominal value of 4.5 kg. An increase of only 15°C in T_{min} results in a 50% decrease in inventory.

The diffusive inventory of Li_2O is expected to be orders of magnitude

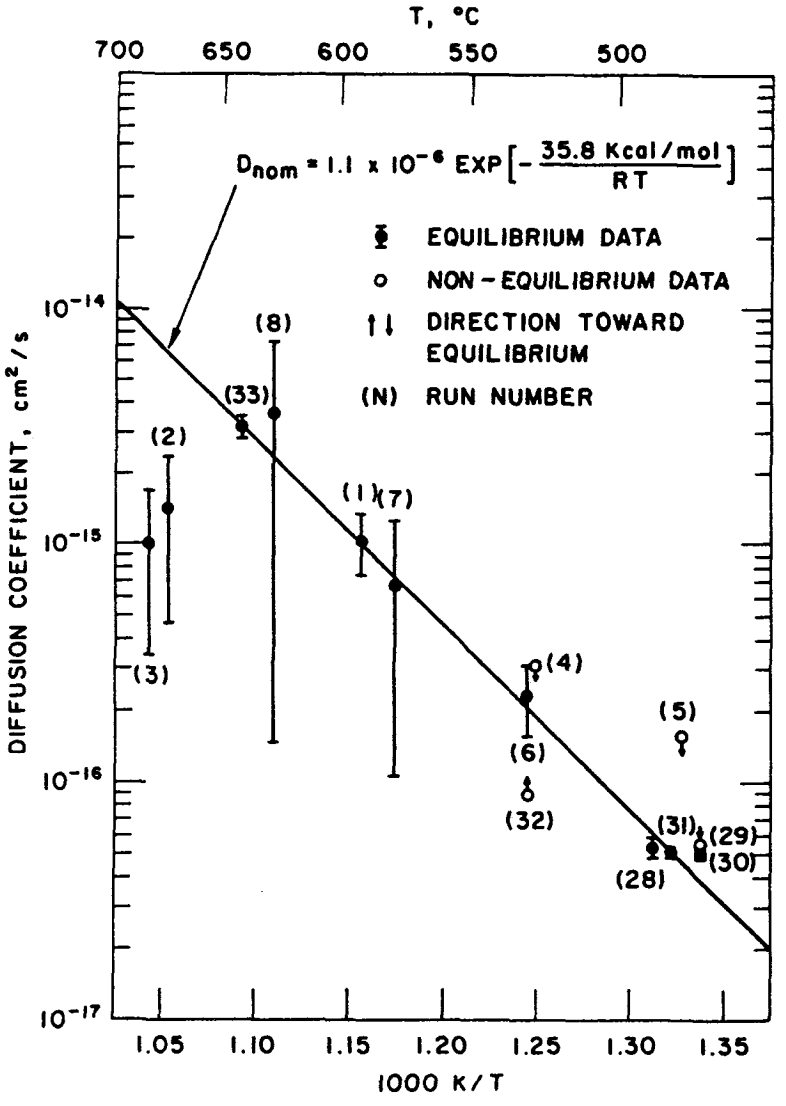


Figure 6.3-35. Diffusion coefficient for tritium in $LiAlO_2$ determined from selected TRIO runs in which intragranular diffusion appeared to be the rate limiting phenomenon in tritium transport. The one-sigma bands are based on uncertainties in the experimental generation rate ($\dot{G}$) and inventory (I).

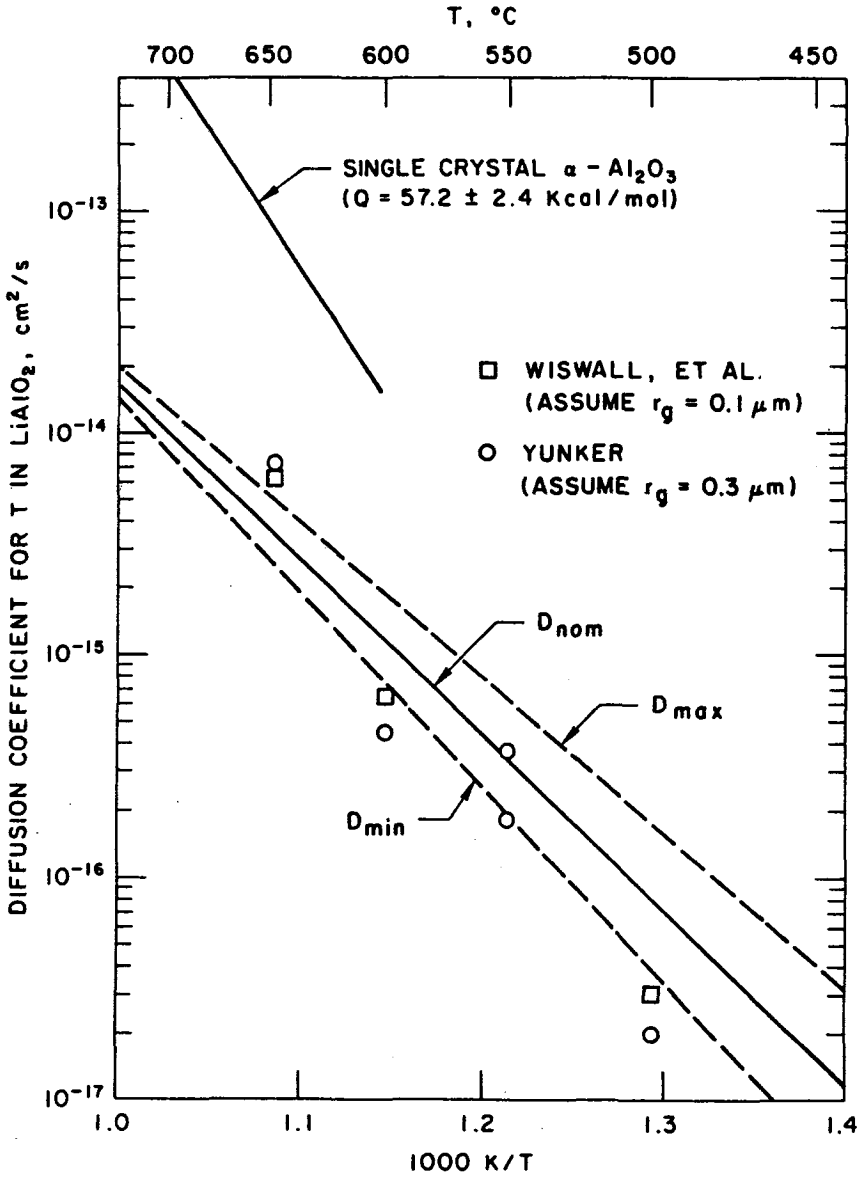


Figure 6.3-36. Comparison of selected data for tritium diffusion in γ-$LiAlO_2$ with the TRIO-1 correlation (includes uncertainties in grain size, inventory, and generation rate).

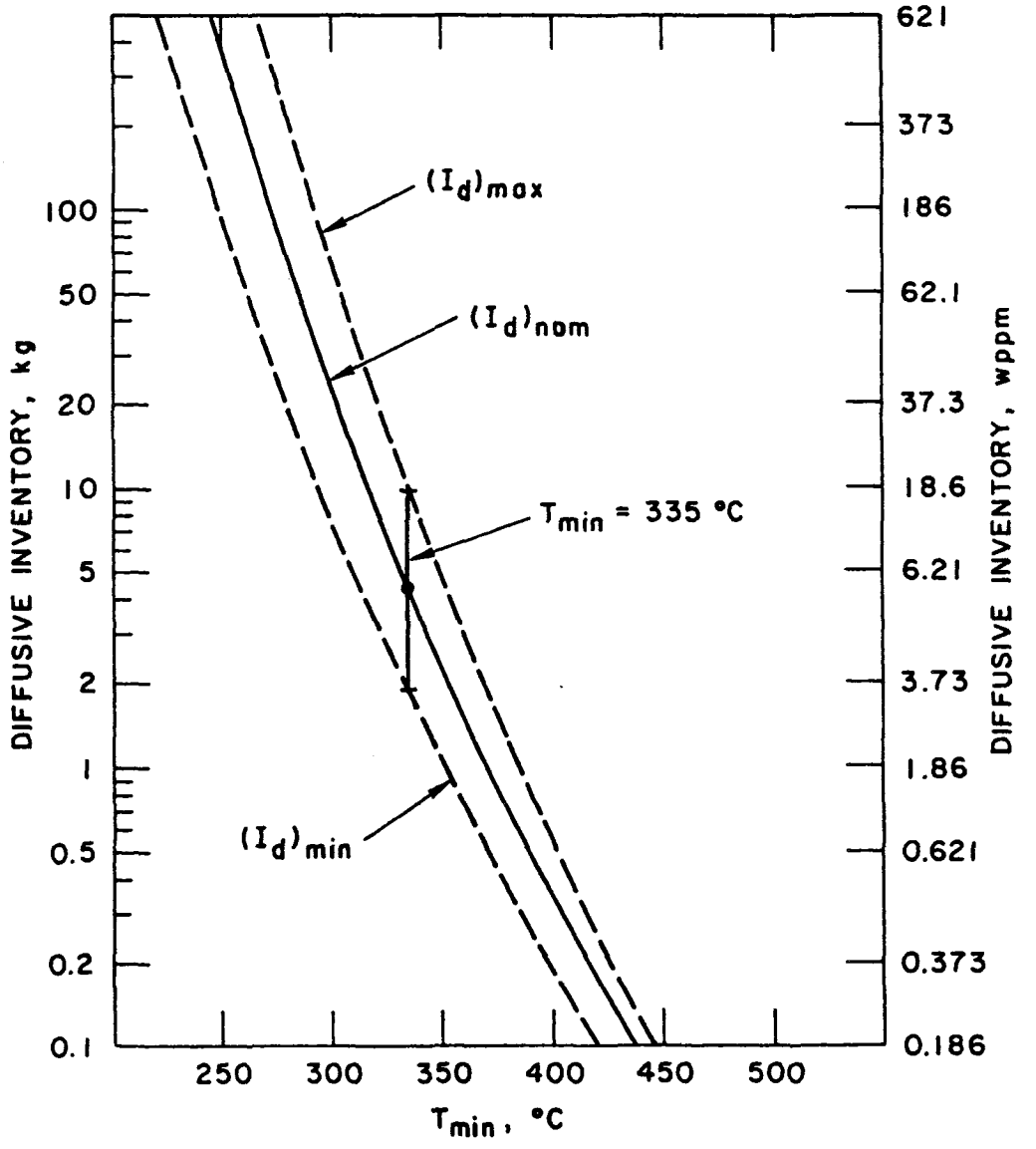


Figure 6.3-37. Predicted diffusive inventory in the BCSS γ-$LiAlO_2$/Be/H_2O/HT9 design as a function of T_{min} for T_{max} = 1000°C, $\dot{G}$ = 866 g/day and r_g = 0.1 μm.

lower than for γ-$LiAlO_2$ because of the high diffusivity of this material. An upper bound on I_d has been calculated for conditions similar to those for γ-$LiAlO_2$, but with a grain radius of 10 μm and a minimum temperature of 500°C. The whole Li_2O plate was assumed to operate at 500°C which gave an upper bound $I_d \sim 1$ g.

Solubility (I_s)

The solubility of hydrogen isotopes and water vapor in Li_2O has been reviewed in Section 6.3.2.2. In order to compare the solubility inventory to the diffusive inventory for Li_2O, calculations were performed for $P_{T_2O} = 2$ Pa, T = 500°C, and 500 mg of Li_2O. This temperature and pressure combination resulted in a mole fraction of LiOT in Li_2O of 2×10^{-7}. Converting this number to wppm of tritium in Li_2O and total tritium in grams gives I_s = 0.02 wppm = 10 g. Thus, under these conditions, the solubility inventory is about 10 times the diffusive inventory for Li_2O. Low solubility inventory in γ-$LiAlO_2$ was estimated in earlier thermodynamic calculations.[6.3-1] The presence of metal oxide (e.g., $LiAl_5O_8$) due to burnup could affect the phase equilibrium relationship, hence the tritium solubility. However, the magnitude of the burnup effects is highly uncertain. For the BCSS design calculations, the solubility of tritium in γ-$LiAlO_2$ is assumed to be negligible compared to the diffusive inventory.

Surface Adsorption

Adsorption could hold up tritium on the solid breeder surfaces (e.g., pore/solid surface area), thereby affecting the tritium inventory. As the work to investigate the mechanisms (chemisorption and/or physiosorption) associated with the surface effects has just begun (Section 6.3.2.2), the approach taken in this subsection is to examine the experimental results in TRIO-1 for which the tritium solubility in γ-$LiAlO_2$ is assumed negligible and the empirical observations of surface effects are available due to purge chemistry variation.

As mentioned before, the tritium inventories from the TRIO-1 runs 1-8 and 28-33 were used to determine the apparent tritium diffusivity in γ-$LiAlO_2$ (Fig. 6.3-35). These runs contained 0.1% - 1% hydrogen in the helium sweep gas and tritium inventories are typically low due to possible isotopic swamp-

ing. Tritium release is assumed uninhibited by surface adsorption; bulk diffusion follows as the rate limiting step for these runs. However, after run 8, the hydrogen was removed from the sweep gas causing an instantaneous depression in the tritium release rate and an increase in tritium inventory. Figure 6.3-38 shows the difference between the measured inventories (I) and the calculated diffusive inventories for runs 8-29. This difference $I-I_d$ is attributed to surface adsorption in this discussion although other interpretations are certaintly possible. Run 9 lasted 144 hours accumulating an excess inventory of ~2 ± 1 wppm of tritium. While a steady-state diffusive inventory had been achieved during run 8 at the same temperature, run 9 did not reach a steady-state release rate. Runs 10 and 11 were at low temperatures and of short duration (~24 h). As the diffusive inventory clearly did not reach steady state, no useful information with regard to excess inventory could be obtained. Run 12 was at high enough temperature for a long enough period of time to establish steady-state diffusion. The excess inventory was ~4 ± 1 wppm. It is anticipated that if overall steady-state had been achieved, the excess inventory would have been higher. Runs 13 and 14 appeared to come to equilibrium (i.e., release rate equal to generation rate). The combined inventory for these runs was ~3 ± 2 wppm.

After run 14, the 0.1% H_2 was again added to the sweep gas. Because of the large uncertainty in the "measured" inventory for these runs, it is difficult to estimate the excess inventory. The results show 1.5 ± 1.3 wppm. Based on the concept of surface desorption/adsorption proposed here, one would expect the excess inventory to approach zero once hydrogen was readmitted to the system. Runs 15-19 neither support nor contradict this concept.

After run 19, the hydrogen was again removed and 0.2% O_2 was added to the sweep gas. The temperature was also decreased to ~350°C. Both effects caused a significant depression in the release rate. The temperature was later increased to ~640°C over a period of 120 hours, but the system still did not come to equilibrium. As noted in Section 6.3.3.3, if T_2O or HTO was generated during this stage, it was not released from the system until about a month later during runs 27-30. The excess inventory reached 5 ± 1 wppm during run 20 and held fairly constant (even with the addition of hydrogen) until run 28.

While purge chemistry effects on tritium release clearly need more experimental work and modeling, a surface adsorption inventory of I_a = 3 ± 2 wppm is used for γ-$LiAlO_2$ blankets with pure helium for a purge gas. Based on

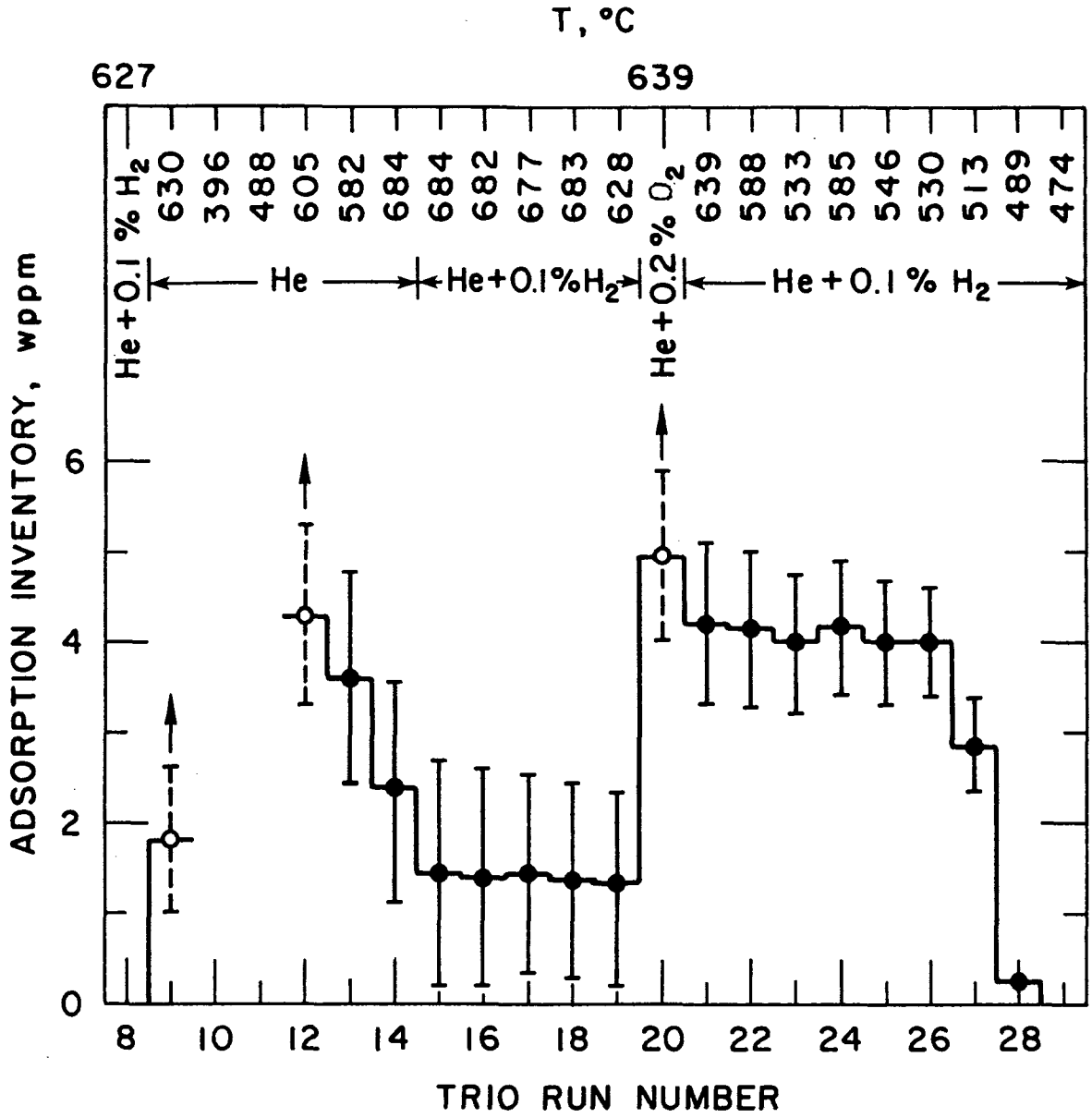


Figure 6.3-38. Estimation of "surface-adsorption" inventory for TRIO-1 runs 9-27 as a function of purge stream chemistry and average γ-$LiAlO_2$ temperature.

TRIO runs 1-8 and 28-33, $I_a = 0$ if the above design adds 0.1% H_2 to the purge gas.

The Japanese in-situ experiment (VOM-15H) demonstrated that Li_2O is also sensitive to purge chemistry similar to that observed in TRIO-1. Figure 6.3-30 shows the release rate to generation rate fraction as a function of time for two sweep gas conditions. With the temperature held constant, the release rate decreases by a factor of ~10 when hydrogen is removed from the sweep gas. Addition of the hydrogen after 13 hours causes a burst release. However, without further experimental controls, it is very difficult to determine whether the excess tritium is associated with solubility effects, surface effects, or artifacts of the metal piping in the system (Section 6.3.3.4).

To further explore the degree to which γ-$LiAlO_2$ and Li_2O behave similarly with respect to environment, the results of the FUBR-1A 100-day (~1 at% ^6Li burnup) irradiations are examined. Both the γ-$LiAlO_2$ and the Li_2O capsules are analyzed with the equation:

$$I_a + I_s = I - I_d \ , \qquad [6.3\text{-}26]$$

where

I is measured inventory

I_d is the calculated diffusive inventory

and

$I_a + I_s$ is the excess inventory.

Figure 6.3-39 shows the excess tritium inventory for the two solid breeders. Except for γ-$LiAlO_2$ at low temperature, the calculated diffusive inventory was negligible compared to the measured inventory. Even for the low-temperature γ-$LiAlO_2$ case, the calculated inventory was only ~10% of the measured inventory. Curve fitting of the temperature dependence of $I-I_d$ showed that the apparent activation energies for both Li_2O and γ-$LiAlO_2$ are in

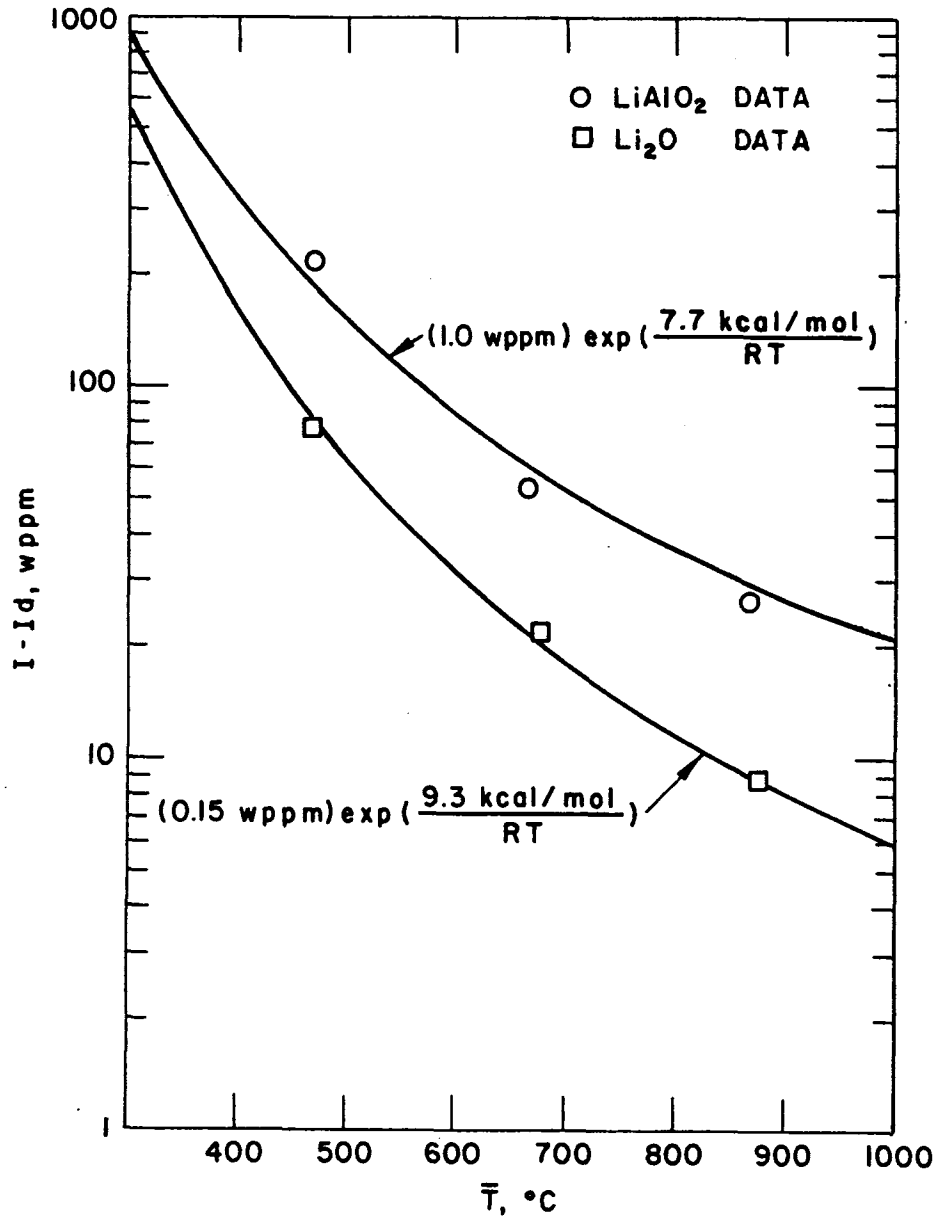


Figure 6.3-39. Measured tritium inventory in the FUBR-1A experiment (105 FPD) minus the calculated diffusive inventory.

the range of 8-9 kcal/mole, which is consistent with a surface desorption phenomenon. While the results shown in Fig. 6.3-39 may raise more questions than they answer (especially when compared to the TRIO-1 results in Fig. 6.3-38), it appears that Li_2O and $LiAlO_2$ behave in a comparable manner with regard to excess inventory due to a surface adsorption mechanism. For design calculations, the same surface adsorption inventory (3 ± 2 wppm) for γ-$LiAlO_2$ is also used for Li_2O with a pure helium purge gas.

Porosity/Purge Stream Transport

The build-up of tritium partial pressure in the interconnected porosity and the purge stream has received a great deal of attention in the past[6.3-104,6.3-2] because of solubility concerns and permeation into the primary coolant. The results of earlier modeling efforts are summarized in the following.

If it is assumed that the partial pressures of the released tritium and helium are small compared to the ambient pressure of the purge stream, then the transport of tritium through the interconnected porosity is dominated by gas diffusion. For a cylindrical unit cell with the purge tube located next to the coolant tube, an expression can be derived for the maximum and average tritium partial pressure in the interconnected porosity

$$P_A = (P_A)_i + \frac{(1/\varepsilon - 1)\, R\, \bar{T}\, \dot{g}_A\, r_i^2\, f(\beta)}{4\, W_A\, D_e(\bar{T})} \quad , \qquad [6.3\text{-}27]$$

where

A = the tritium species (e.g., HT, T_2, HTO, T_2O) desorbed from the pore/solid surface

$(P_A)_i$ = the partial pressure of A in the purge stream (see Section 6.3.5.3)

ε = interconnected porosity fraction

R = the universal gas constant

$\bar{T}$ = the average temperature in the porosity

$\dot{g}_A$ = the generation rate of species A per unit of 100% dense solid volume

r_i = the inner radius of the unit cell

W_A = the molecular weight of species A

$f(\beta) = \beta \ln \beta - \beta + 1$ for maximum P_A
$= \left(1 - \beta^{-1}\right)^{-1} \ln \beta - 1$ for average P_A

$\beta = r_o^2/r_i^2$

r_o = the unit cell outer radius

$D_e(\bar{T})$ = the effective diffusion coefficient for tritium species A in He evaluated at the average cell temperature.

The expression for D_e depends on the ratio of mean free path for molecular collisions (λ) and the average pore radius (r_p). For $\lambda/r_p > 10$, Knudsen diffusion dominates and the diffusion of A is independent of the presence of the helium(6.3-105)

$$D_e = D_{KA}/\tau \quad \text{for} \quad \lambda/r_p > 10 \ , \qquad [6.3\text{-}28]$$

where

τ = tortuousity $(1/\varepsilon < \tau < 2/\varepsilon)$

$D_{KA} = (2\ r_p/3)\ [8\ RT/\pi\ W_A]^{1/2}$.

At the other extreme, i.e., $\lambda/r_p < 0.1$, ordinary molecular diffusion dominates the transport process and D_e is independent of the pore radius[6.3-106]

$$D_e = D_{AB}/\tau \quad \text{for} \quad \lambda/r_p < 0.1 \ , \qquad [6.3\text{-}29]$$

where

$D_{AB} = (C/P)\ T^n$

P = total pressure in atmosphere

T = temperature in °K

C = 4.6×10^{-5} $cm^2/s \cdot atm$ for HT

= 4.2×10^{-5} $cm^2/s \cdot atm$ for T_2

= 3.6×10^{-6} $cm^2/s \cdot atm$ for HTO

= 3.5×10^{-6} $cm^2/s \cdot atm$ for T_2O

n = 1.823 for HT and T_2

= 2.334 for HTO and T_2O.

In the transition region between Knudsen diffusion and ordinary diffusion, the following effective diffusion coefficient is recommended[6.3-105]

$$D_e = \left[\tau\left(1/D_{KA} + 1/D_{AB}\right)\right]^{-1} \quad \text{for } 0.1 < \lambda/r_p < 10 \ . \qquad [6.3\text{-}30]$$

Equation [6.3-27] with auxilliary Eqs. [6.3-28] through [6.3-30] has been used for the BCSS design calculations. While a number of simplifying assumptions were invoked in deriving these equations (e.g., isothermal unit cell),

the estimated error associated with these assumptions is less than ±20%. This error is acceptable in light of the factor of 2 uncertainty in the tortuousity factor τ. A relationship similar in form to Eq. [6.3-27] can be derived for the plate geometry.

For a variety of tailored microstructure (e.g., sphere-pac, bimodal pore structure, monolithic structure with average pore radii >5 μm), the rise in tritium partial pressure across a unit cell is <1 Pa. The one exception to this is the draw salt γ-$LiAlO_2$ design in which the tritium purge is at the back of the blanket. The path length for this case is ~50 cm leading to considerably higher tritium partial pressures within the breeder.

6.3.5.2 Transient Tritium Response

In addition to the safety implications of the steady-state inventory, the time it takes to establish a steady state release rate is of interest in determining the acceptable minimum blanket temperature for a given tritium breeding ratio. It is difficult to estimate the transient response of a blanket system because of the multitude of phenomena which affect tritium release. However, for the γ-$LiAlO_2$ blankets with hydrogen added to the purge stream, it has been shown that bulk diffusion is the rate-limiting phenomenon. Using classical solutions to the diffusion equation[6.3-109], one can derive the following relationships for tritium response to an instantaneous reactor start up

$$\dot{R}/G = 1 - (6/\pi^2) \sum_{n=1}^{\infty} (1/n^2) (\beta - 1)^{-1} \int_1^{\beta} \exp(-n^2\pi^2 t/\tau) d\eta , \qquad [6.3\text{-}31]$$

and

$$I/I_{ss} = 1 - (90/\pi^4) \sum_{n=1}^{\infty} (1/n^4) \int_1^{\beta} \tau \exp(-n^2\pi^2 t/\tau) d\eta / \int_1^{\beta} \tau \, d\eta , \qquad [6.3\text{-}32]$$

where

$\dot{R}$ = the tritium release rate

$\dot{G}$ = the tritium production rate

$\beta = r_o^2/r_i^2$

r_i, r_o = the average unit cell inner and outer radius, respectively

$\eta = r^2/r_i^2$

$\tau = \left(r_g^2/D_o\right) \exp\left(Q/RT\right)$

$T = T(\eta)$

I = inventory

$$I_{ss} = \left(\dot{G}/15\right)\left(\beta - 1\right)^{-1} \int_1^{\beta} \tau d\eta$$

and

t = time.

Table 6.3-9 shows the times it takes the release rate fraction $\left(\dot{R}/\dot{G}\right)$ to reach 67.4% (mean residency time) and 99% as a function of minimum temperature for a maximum temperature of 1000°C in a typical water cooled γ-$LiAlO_2$ blanket. Figure 6.3-40 shows $\left(\dot{R}/\dot{G}\right)$ and (I/I_{ss}) as functions of time (in MWy/m^2) for a minimum temperature of 350°C and a maximum temperature of 1000°C with a grain diameter of 0.2 μm.

From Table 6.3-9, it can be seen that the time to reach 67.4% of the release rate fraction is very short (~1 minute) and relatively insensitive to the minimum blanket temperature in the range of 300 to 600°C. This results from the fact that for the above design, a much larger fraction of the γ-$LiAlO_2$ is at a temperature closer to T_{max} than to T_{min}. However, the time it takes the breeder to achieve 99% of the steady-state release rate is much longer and highly sensitive to T_{min}. For example, at a minimum blanket temperature of 350°C, $\tau_{99} \sim 2$ months. The lag in the systems response is due to

the fact the colder grains near the coolant tube wall release very little tritium during the times of interest.

TABLE 6.3-9. TIMES TO REACH 67.4% AND 99% OF THE STEADY-STATE RELEASE RATE AS A FUNCTION OF MINIMUM BLANKET TEMPERATURE FOR A WATER-COOLED γ-$LiAlO_2$ BLANKET WITH A MAXIMUM TEMPERATURE OF 1000°C

T_{min} °C	$\tau_{67.4}$(s) Min	Nom	Max	τ_{99}(s) Min	Nom	Max
600	15.5	29.2	55.4	4.50×10^3	5.22×10^3	6.05×10^3
550	17.9	33.7	62.8	1.43×10^4	1.45×10^4	1.50×10^4
500	21.2	38.9	71.3	4.16×10^4	4.67×10^4	5.27×10^4
450	24.6	44.6	81.0	1.35×10^5	1.77×10^5	2.35×10^5
400	29.0	51.5	91.8	5.22×10^5	8.53×10^5	1.34×10^6
375	31.7	55.4	97.8	1.11×10^6	1.98×10^6	3.41×10^6
350	34.8	59.4	104	2.57×10^6	4.87×10^6	9.67×10^6
325	37.8	64.4	112	6.16×10^6	1.33×10^7	2.74×10^7
300	41.0	69.5	119	1.53×10^7	3.71×10^7	9.3×10^7

The results in Fig. 6.3-40 are even more surprising. While a 99% release rate is achieved for the reference case in ~2 months, the inventory is only ~41% of its steady-state value. It takes the inventory ~6 months to achieve 67.4% of its steady-state value and ~4 years to achieve 99% of its steady-state value. The lag is due to the result that even when the blanket as a whole is releasing 99^+% of the tritium generated, the small fraction retained is being retained in the colder region. It takes a long time for this region to build up an inventory of several kilograms.

As radioactive decay of the tritium was not included in the analysis and as the BCSS γ-$LiAlO_2$ blanket does not achieve 99% of its inventory until the end of life for the blanket module, the steady-state inventory formulas proposed for γ-$LiAlO_2$ in the previous sections represent conservative upper bounds for scoping calculations. Thus, the lag in system response represents a penalty with regard to breeding ratio requirements and a benefit with regard to safety issues.

For the Li_2O blanket designs, bulk diffusion response is much more rapid than it is for the γ-$LiAlO_2$ designs because the diffusion coefficient is orders of magnitude higher for Li_2O. Comparing the two systems at their lowest

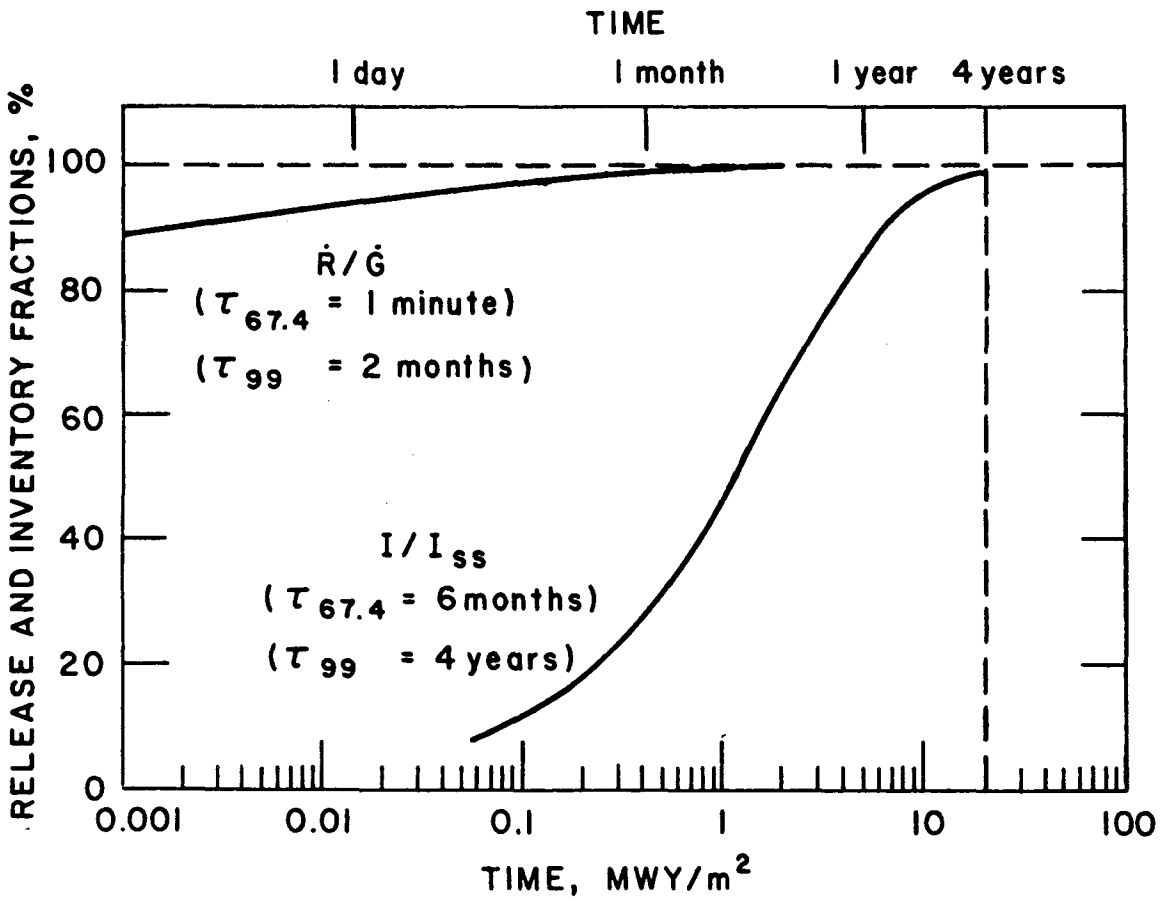


Figure 6.3-40. Tritium response to an instantaneous reactor startup for the $LiAlO_2/H_2O$/Be/HT-9 design with T_{min} = 350°C and T_{max} = 1000°C. Assumed grain diameter is 0.2 μm.

operating temperatures (500°C for Li_2O and 350°C for γ-$LiAlO_2$) and their respective grain sizes (20 μm for Li_2O and 0.2 μm for $LiAlO_2$), the ratio of their time constants for release rate is $(\tau_{0.99})_{Li_2O}/(\tau_{0.99})_{LiAlO_2} \sim 10^{-6}$. However, the tritium inventory for Li_2O appears to be dominated by the mechanisms of surface adsorption and solubility. A better understanding of these phenomena is needed before transient response times can be calculated.

The previous discussion of response times ignored the issues of microstructural changes (e.g., grain growth and sintering), irradiation damage, and compositional changes due to lithium burnup. All of these processes have their own characteristic times which will affect, to some extent, the tritium release rate and inventory buildup in the system. These mechanisms need to be explored in more detail (particularly for Li_2O) in order to evaluate the tritium response over the lifetime of the blanket.

6.3.5.3 Tritium Permeation, Leakage, and Containment

Solubility, intragranular diffusion, porous diffusion, and surface kinetics of tritium in solid breeders were discussed in the preceding section with emphasis on the steady-state blanket tritium inventories. Tritium leakage into the blanket primary coolant loop is another concern that has economic as well as safety ramifications. Analysis of tritium leakage into the primary coolant loop entails modeling of tritium permeation through structural materials (i.e., cladding or coolant tubes made of HT9); the scientific principles involved parallel those considered for the first wall tritium containment (Section 6.6).

Governing equations for tritium permeation through structural materials will be given in this section. Specification of a maximum tritium leakage rate into the coolant allows the calculation of a limiting tritium partial pressure in the purge channel, from which derives a limiting purge-gas volumetric flow rate and an associated pressure drop. Tritium partial pressure, purge-gas volumetric flow rate, and pressure drop are thus closely related parameters in the blanket helium purge channels. By the same token, tritium permeation (or leakage) is closely related to blanket purge flow design and purge chemistry.

and f is the friction factor depending on the Reynolds number ($R_e \equiv 2\, r_h\, V\rho/\mu$, μ is the gas viscosity) and surface roughness.

With simplifying assumptions of incompressible flow (i.e., ρ constant) and constant properties, direct integration of Eq. [6.3-37] over the purge channel length L gives the pressure drop, viz.,

$$\Delta P_f = - f\rho v^2 L/(4 g_c r_h) \quad . \qquad [6.3\text{-}38]$$

The average linear velocity (v) in Eqs. [6.3-37] and [6.3-38] is related to the volumetric flow rate $(\dot{V})$ in Eq. [6.3-36] via

$$v = \dot{V}/S, \qquad [6.3\text{-}39]$$

where S is the cross-sectional flow area of the purge channels.

Equations [6.3-33] to [6.3-39] provide the set of equations for tritium permeation and purge flow design calculations. Purge chemistry (Sections 6.3.2.1, 6.3.3.3, and 6.3.3.4) largely determines the type (or types) of tritium species in the purge stream and how the equations are to be used. Permeability of tritium species in the structural materials is evidently a key material parameter; structural thickness, purge channel geometry, temperature, and tritium production rate are determined by particular blanket design and operating conditions. The remaining portion of the section will explore the effects of these parameters on the tritium leakage rate. High payoff R&D areas in reducing tritium permeation should become apparent from the parametric study.

Materials, Design, and Operating Parameters

Permeability

Few data exist for tritium permeation through structural materials. However, data of hydrogen permeation through materials are quite extensive. In a

recent literature review (Section 6.6), Hassanein and Sze of ANL surveyed the permeation data of hydrogen and its isotopes through iron and three other steel alloys (chromium ferritic steels, austenitic steels, and high-temperature steel alloys). Assuming applicability of the Richardson equation (Eq. [6.3.33]), Hassanein and Sze of ANL recommended the following correlation for tritium permeability in HT9 (based on data of chromium ferritic steels):

$$P_m = 2.69 \times 10^{-3} \exp\left(-11100/RT\right) \quad , \qquad [6.3\text{-}40]$$

where P_m is in units of $cm^3(STP)/cm \cdot s \cdot atm^{1/2}$, and the HT9 surface is assumed to be relatively clean (i.e., no oxide layers). Inspection of the scattered data shows that they deviate from Eq. [6.3-40] by ~ ±50%.

More significant to the hydrogen (tritium) permeation through bare metal alloys is the effect of oxide layers, either preformed or formed in-situ on the metal surface. One group of data on high-temperature steel alloys showed permeation impeding factors as high as 500 at 650°C for Incoloy 802 (Section 6.6). Impeding factors for other alloys varied over a wide range to as low as 5 for In586 at 650°C. Oxide layer effects on hydrogen permeation through HT9 have <u>not</u> been experimentally investigated. For conservatism a range of impeding factors (1-100) will be assumed. In later calculations, these impeding factors are simply used to reduce P_m in Eq. [6.3-40] before it is substituted into Eq. [6.3-35]. Also, since the assumed range of the oxide impeding factors more than embodies the correlation uncertainties (±50%) of the bare-alloy permeability, no separate consideration of the latter uncertainties is judged necessary.

<u>Blanket Design Parameters</u>

Structural thickness, purge channel configuration and geometry vary among the different solid-breeder blanket designs (Chapters 8, 9, and 10). Purge channel location is the only feature shared by these blanket designs, which is adjacent to the primary coolant and in the relatively cold region of the breeder. For purposes of parametric calculations, design features pertaining to the γ-$LiAlO_2$/HT9/H_2O/Be blanket (Chapter 9) will be used. The relevant

parameters are given in Table 6.3-10. When considering the oxide layer effect on tritium permeability, it should be noted that each of the assumed impeding factors (1 to 100) is multiplied by 3 in the calculations. The factor of 3 comes from the assumption that equally effective oxide layers form on 3 of the 4 surfaces of the double-walled coolant tube (DWT); no oxide layer is assumed to form on the surface facing solid breeder because of the intentional addition of hydrogen in the purge.

Blanket Operating Parameters

Structural temperature (Eq. [6.3-40]), purge channel temperature and tritium production rate (Eq. [6.3-36]) also vary among the different solid-breeder blanket designs (Chapter 8, 9, and 10). The structural and the purge channel temperatures in the Li_2O/HT9/He blanket are ~150°C higher than those of the γ-$LiAlO_2$/HT9/H_2O/Be blanket. The latter structural temperatures vary from the coolant inlet end to outlet; they are only slightly higher than the coolant temperatures (280-320°C), however. The purge channel temperature in the γ-$LiAlO_2$/HT9/H_2O/Be blanket is designed to be ~350°C.

Tritium production rates in the γ-$LiAlO_2$/HT9/H_2O/Be blanket can be found in Chapter 9, which vary within the blanket as a function of the distance from plasma as well as the local environment (i.e., the presence/absence of Be neutron multipliers). Subsequent calculations use an average unit cell (midway across the blanket depth) to represent the entire blanket. The cell is also assumed to have reached steady-state conditions such that the average tritium production rate in the solid breeder is equal to the tritium arrival rate at the purge channel. The assumption seems reasonable since the steady-state tritium inventory in such a unit cell has been shown to be relatively small with hydrogen addition (Sections 6.3.3.3 and 6.3.4.1).

Purge Chemistry

Purge chemistry effects on solid-breeder tritium recovery have already been discussed in the sections on thermodynamic/chemical properties (Section 6.3.2.1) and on irradiation experiments, TRIO-1 and VOM-15H (Section 6.3.3). While considerable amount of work has been done for Li_2O in ellucidating the importance of oxygen activity, many issues remain to be resolved through future experimentation. Comparable theoretical investigation has <u>not</u> been con-

TABLE 6.3.10 SOLID BREEDER BLANKET DESIGN PARAMETERS USED IN TRITIUM PERMEATION AND PURGE FLOW DESIGN CALCULATIONS

Parameters	Values
Structural Material	HT9/DWT
Structure Thickness (mm)	1.5, thickness of each wall of DWT is 0.75
Total Structural Surface Area Exposed to Purge (m^2)	1.74×10^4
Average Structure Temperature (°C)	335
Purge Channel Cross Sectional Area (cm^2)	0.283
Average Purge Channel Length (m)	4
Average Purge Temperature (°C)	350
Number of Unit Cells	1.202×10^5

ducted for γ-$LiAlO_2$, although similar significance of the oxygen activity effects is expected. For the in-situ tritium recovery experiments of γ-$LiAlO_2$ and Li_2O, hydrogen addition to the helium purge enhanced tritium recovery substantially in both TRIO-1 and VOM-15H. The TRIO-1 tritium recovery exceeded 99% with 0.1% hydrogen addition. Current specification for the purge chemistry of the γ-$LiAlO_2$/HT9/H_2O/Be blanket is 0.01% (or 100 ppm) hydrogen addition to the helium purge, derived essentially from the TRIO-1 results without consideration of the oxygen activity factor. With 100 ppm hydrogen addition, the recovered tritium species is also assumed to be primarily HT, again based on the TRIO-1 data.

For tritium leakage calculations, several different conditions may exist depending on the purge stream chemistry. In the case of no hydrogen addition to the purge stream, the probable tritium species are T_2 and T_2O. If the predominant species is T_2 (e.g., 99%), then Eqs. [6.3-35 through 6.3-39] may be used directly where $\dot{n}$ is interpreted as the total arrival rate of tritium. If the predominant species is T_2O (e.g., 99%) which is assumed not to permeate

through the coolant tube, then the production rate in Eq. [6.3-36] is reduced accordingly (e.g., by a factor of 100). However, as all of the solid breeder designers have elected to add 100 wppm hydrogen to the helium purge stream, some modification of Eqs. [6.3-35] through [6.3-39] is required to reflect the isotope swamping effect. Based on TRIO-1 results, this situation produces tritium primarily in the form of HT. Equation [6.3-35] is modified to separate out the permeation of the two hydrogen isotopes:

$$(P_{HT} + P_{H_2}) \leq [(\dot{m}_T + \dot{m}_H)t/P_m A]^2 \qquad [6.3\text{-}41]$$

Equation [6.3-41] is indeterminate. However, the 100 wppm of H_2 in the purge corresponds to P_{H_2} = 20 Pa for a 1 atm (1.01×10^5 Pa) helium purge stream. Under these conditions, it is reasonable for all of the solid breeder designs (except the nitrate salt cooled $LiAlO_2$ blanket which contains a high tritium partial pressure) to assume that $P_{HT}/P_{H_2} << 1$. Equation [6.3-41] is thus rewritten in the following form to allow simplification under these conditions:

$$P_{H_2}(1 + P_{HT}/P_{H_2}) \leq \left(\frac{\dot{m}_{H_2}\, t}{P_m A}\right)^2 (1 + \dot{m}_{HT}/\dot{m}_{H_2})^2 \quad . \qquad [6.3\text{-}42]$$

Using the assumptions $P_{HT}/P_{H_2} << 1$ and $\dot{m}_{HT}/\dot{m}_{H_2} << 1$, we have

$$P_{H_2} \doteq (\dot{m}_{H_2}\, t/P_m A)^2 \qquad [6.3\text{-}43]$$

and

$$P_{HT} \leq 2\sqrt{P_{H_2}}\, \dot{m}_{HT}\, t/P_m A \quad , \qquad [6.3\text{-}44]$$

where

$$\dot{m}_{HT} = 1.33\ \dot{m}_T \quad .$$

The effects of isotope swamping can be seen clearly from Eq. [6.3-44]. As the partial pressure of H_2 is increased, the allowable partial pressure of HT is increased for a fixed $\dot{m}_T$.

Results and Discussion

For the case of a pure helium purge stream, Eq. [6.3-35] (with the input in Table 6.3-10 and a tritium generation rate of 890 g/day) becomes

$$P_{T_2} \leq \left(1.87 \times 10^{-11}\ \text{Pa}\right) \left(\frac{B_f\ \dot{m}_\ell}{\text{Ci/day}}\right)^2 \quad , \qquad [6.3\text{-}45]$$

where B_f is the total barrier factor for the coolant tube (e.g., B_f = the number of oxidized surfaces times the impedance factor (IF) for one surface). For a leakage rate of 100 Ci/day, the range of limiting T_2 partial pressures in the purge varies from 1.9×10^{-7} Pa for $B_f = 1$ (clean walls) to 0.017 Pa for $B_f = 300$ (three oxide surfaces and IF = 100). It is doubtful that any realistic designs could achieve such limits for reasonable purge flow conditions. The corresponding purge volumetric flow rate is obtained by combining Eqs. [6.3-45] with Eq. [6.3-36] to give

$$\dot{V} = \left(4.74 \times 10^{14}\ \ell/\text{s}\right) \left(\frac{\text{Ci/day}}{B_f\ \dot{m}_\ell}\right)^2 \left(\frac{1}{1 + P_{T_2O}/P_{T_2}}\right) \quad . \qquad [6.3\text{-}46]$$

For $B_f = 300$, $\dot{m}_\ell = 100$ Ci/day, and $P_{T_2O}/P_{T_2} = 0.01$, $\dot{V} = 5.2 \times 10^5$ ℓ/s which corresponds to 150 m/s linear velocity. However, for $B_f = 300$ and either $\dot{m}_\ell$ = 1000 Ci/day or $P_{T_2O}/P_{t_2} = 99$, $\dot{V} = 5.2 \times 10^3$ ℓ/s and v = 1.5 m/s.

The above calculations were performed assuming that the helium purge stream contained no added hydrogen. The effect of isotope swamping will now

be examined. For the design case of 100 wppm protium in the helium purge stream and a helium purge stream pressure of 1 atm at 350°C, the hydrogen partial pressure entering the blanket is 2×10^{-4} atm (20.3 Pa). Substituting this partial pressure into Eq. [6.3-44] gives

$$P_{HT} < (5.2 \times 10^{-5} \text{ Pa}) \left(\frac{B_f \dot{m}_\ell}{\text{Ci/day}}\right) \quad . \qquad [6.3\text{-}47]$$

For a limit of 100 Ci/day and a barrier factor of 1 to 300, the range of limiting HT partial pressures is from 5.2×10^{-3} Pa to 1.6 Pa. Figure 6.3.-41 shows the relationship between the limiting partial pressure of HT in the purge and the leakage rate with the barrier factor as a parameter. In the figure, IF refers to the oxide impedance factor for a single surface.. The total barrier fctor for the double-walled tube is assumed to be B_f=3IF.

The limiting purge volumetric flow rate corresponding to Eq. [6.3-46] is

$$\dot{V} > (3.5 \times 10^{8} \text{ ℓ/s}) \left(\frac{\text{Ci/day}}{B_f \dot{m}_\ell}\right) \quad , \qquad [6.3\text{-}48]$$

if it is assumed (conservatively) that no HTO is formed. $\dot{V}$ is plotted as a function of $\dot{m}_\ell$ with IF as a parameter in Fig. 6.3-42. For the reference case of $\dot{m}_\ell$ = 100 Ci/day and IF = 100 (B_f = 300), the minimum volumetric flow rate is 1.2×10^{4} ℓ/s which corresponds to 3.5 m/s linear velocity.

The corresponding pressure drops can be derived from Eq. [6.3-38]. For the case of no protium added to the purge, the pressure drop is given as

$$\Delta P = 1.7 \times 10^{12} \text{ Pa} \left(\frac{\text{Ci/day}}{B_f \dot{m}_\ell}\right)^2 \left(\frac{1}{1 + P_{T_2O}/P_{T_2}}\right) \quad . \qquad [6.3\text{-}49]$$

For the case of isotopic swamping with protium,

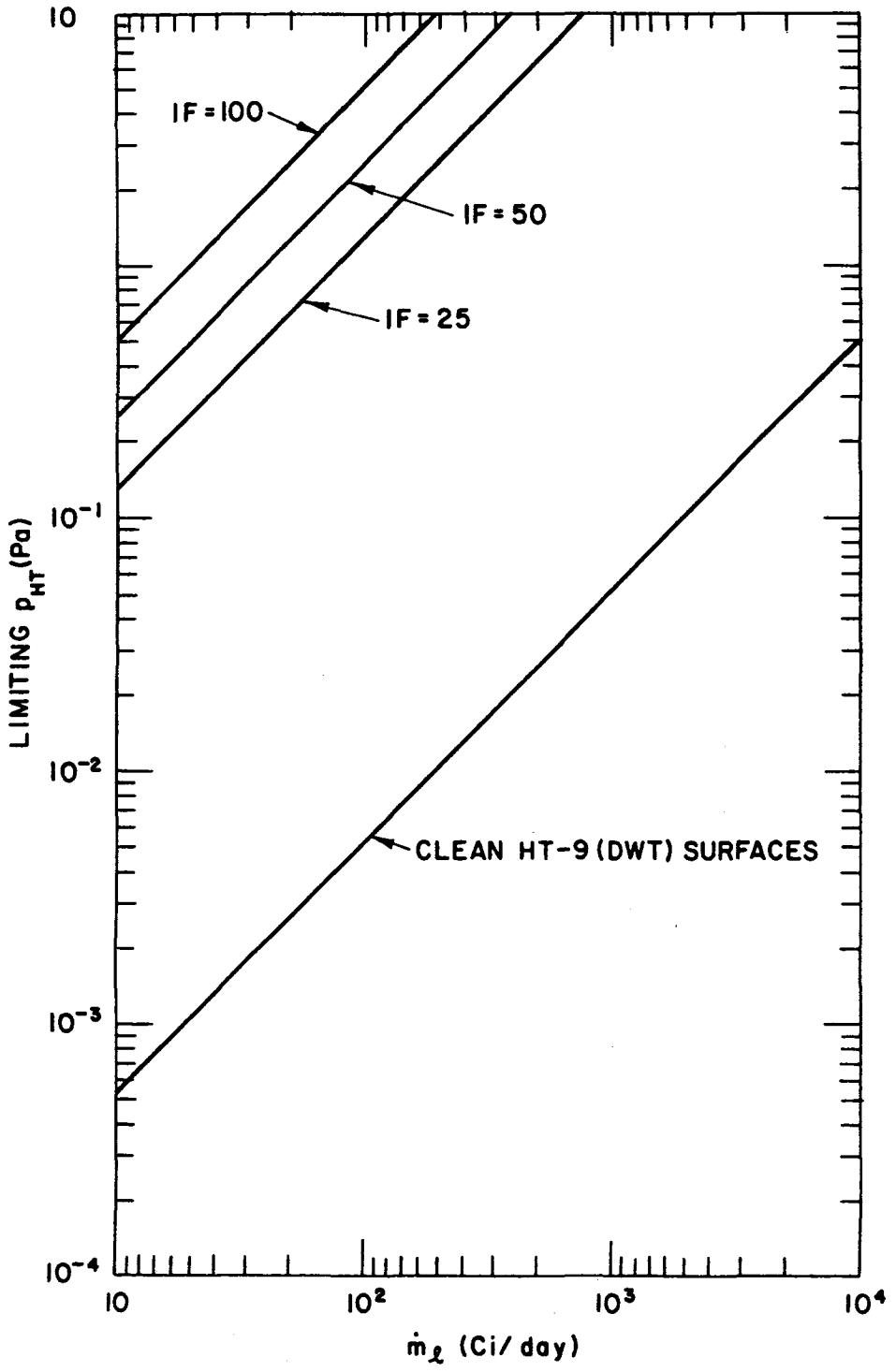


Figure 6.3-41. Limiting tritium partial pressure in the purge channel plotted as a function of maximum tritium leakage rate ($\dot{m}_\ell$) into the primary coolant loop (γ-$LiAlO_2/H_2O$/HT9/Be blanket).

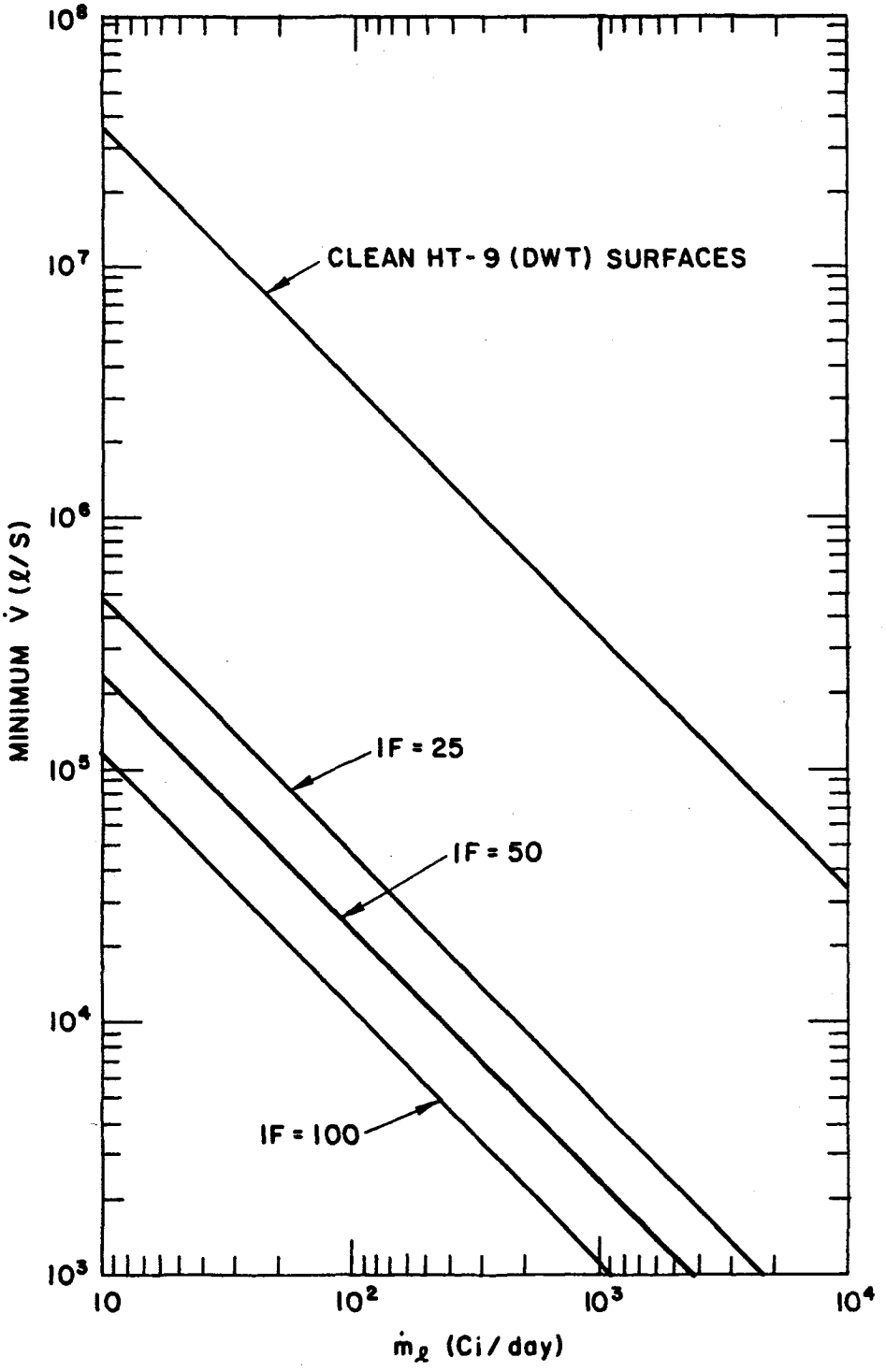


Figure 6.3-42. Limiting volumetric gas flow rate in the purge channel plotted as a function of maximum tritium leakage rate ($\dot{m}_\ell$) into the primary coolant loop (γ-$LiAlO_2/H_2O$/HT9/Be blanket).

$$\Delta P = 1.2 \times 10^7 \text{ Pa } \left(\frac{\text{Ci/day}}{B_f \dot{m}_\ell}\right) \quad . \qquad [6.3\text{-}50]$$

From Eq. [6.3-49], it can be seen that for $\dot{m}_\ell$ = 100 Ci/day and P_{T_2O}/P_{T_2} = 0.01, the pressure drop is inordinately large (1.7×10^8 Pa for B_f = 1 and 1.9×10^3 Pa for B_f = 300). The comparable results from Eq. [6.3-50] with protium swamping are 1.2×10^5 Pa for B_f = 1 and 400 Pa for B_f = 300. Figure 6.3-43 shows ΔP for the isotopic swamping case (Eq. [6.3-50]) as a function of $\dot{m}_\ell$ with the barrier factor as a parameter.

In summary, tritium permeation and leakage into the blanket primary coolant loop should be regarded as part of the overall tritium containment problem (including first wall tritium permeation and other sources). The modeling and the parametric study showed clear advantage for the development of tritium permeation barriers in reducing tritium leakage. A high-priority R&D item should thus be development of effective tritium permeation barriers. Positive results in this area are also likely to help understanding and alleviating general problems in tritium handling and containment.

Research and development activities for understanding the purge chemistry effects are also highly recommended based on tritium leakage consideration. The importance of this area has been emphasized before regarding solid-breeder tritium inventory and recovery (Sections 6.3.2.1 and 6.3.3).

6.3.5.4 Physical Integrity and Gap Conductance

Physical integrity (cracking) and gap conductance are phenomena of generic importance to the performance/lifetime evaluation of solid breeder blankets. Modeling of these two phenomena have been reported in the interim BCSS report;[6.3-3] they are updated for the current solid breeder blankets.

Physical Integrity

Previous thermal stress analyses[6.3-2,6.3-110] showed that for STARFIRE and DEMO blankets employing monolithic blocks of γ-$LiAlO_2$ and Li_2O, the temperature-gradient induced thermal stresses can reach very high magnitudes, well beyond the estimated solid breeder fracture strengths. The same analyses also showed that for thin disc geometry (instead of long cylinder) thermal stresses can be reduced somewhat, but the propensity for cracking is still

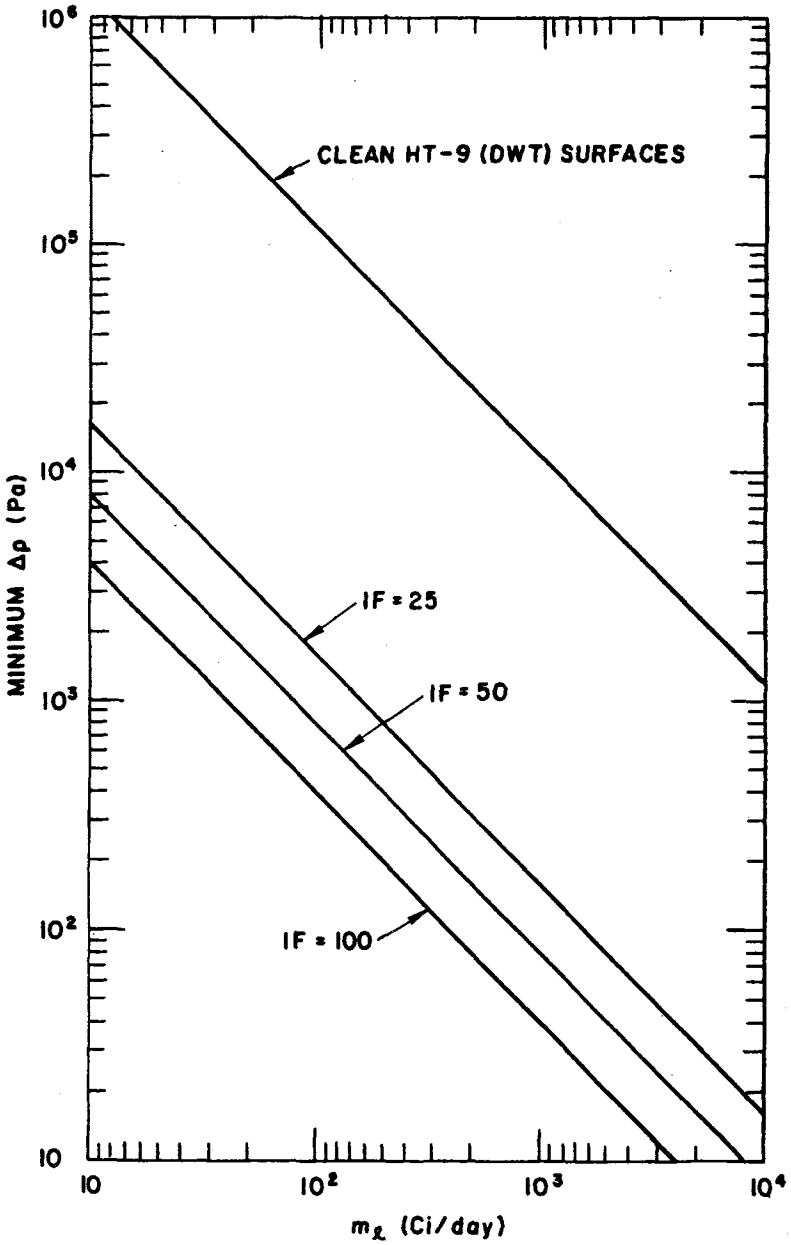


Figure 6.3-43. Purge channel pressure drop (Δp) plotted as a function of maximum tritium leakage rate ($\dot{m}_\ell$) into the primary coolant loop (γ-$LiAlO_2/H_2O$/HT9/Be blanket).

very high. Since cracking and the resulting cracked fragment relocation create problems in controlling the gap between solid breeder and its surrounding structural material, several potential design and materials solutions (i.e., solid breeder segmentation, ceramic/metal metallurgical bonding, and solid breeder dispersion toughening) were suggested as possible means to overcome the problem. The principle behind one of these solutions, breeder segmentation, has since been employed for the BCSS water and draw-salt cooled blankets using the sphere-pac γ-$LiAlO_2$. Sphere-pac breeders can be regarded as a form of precracking. Because the spherical particles are small (<1200 μm in diameter), the temperature gradient (hence thermal stresses) in the particles should be insufficient to cause further cracking. Uncertainty in the breeder/structure interface conductance is thus lowered because of the decreasing likelihood of breeder relocation. Fabrication, thermal conductivity, and sintering are the potential concerns for sphere-pac breeders as pointed out in Sections 6.3.1 and 6.3.2.

Among the BCSS solid breeder blankets, the helium-cooled designs (Chapter 8) employ sintered (80% TD) Li_2O and γ-$LiAlO_2$ breeders enclosed in a relatively thin (0.25 mm thickness) HT9 cladding of a rectangular plate geometry. The plate orientation in the blanket module is that the long direction of the plate coincides with the radial direction of the reactor, which is also the flow direction of the helium coolant. Assuming heat transfer within the solid breeder in the long direction of the plate is small, previous analysis[6.3-3] developed for a plate-like or beam-like geometry can be used to calculate thermal stresses in solid breeders and to assess the propensity of cracking.

Two types of criteria for determining the solid breeder thickness were derived in the previous work. The first criterion, based on considerations of heat transfer and temperature limits, resulted in

$$h^2 \leq \frac{2k}{Q} \Delta T \quad , \qquad [6.3\text{-}51]$$

where

h = half-thickness of the solid breeder plate or beam

k = thermal conductivity of solid breeder (assumed constant and evaluated at the breeder volume averaged temperature)

Q = volumetric nuclear heating rate in the solid breeder

and

$\Delta T = T_{max} - T_{min}$ (T_{max} and T_{min} are the upper and lower temperature limits for solid breeders defined in Section 6.3.4), or

$\Delta T = T_{CL} - T_s$ (T_{CL} and T_s are the breeder plate centerline and surface temperatures, respectively).

The second criterion, based on thermal stress-induced cracking, gave[6.3-3]

$$h^2 < \frac{3(1-\nu)\,k}{\alpha\,Q}\left(\frac{\sigma_f}{E}\right) \quad , \qquad [6.3.52]$$

for plate-like breeder, and

$$h^2 < \frac{3k}{\alpha\,Q}\left(\frac{\sigma_f}{E}\right) \quad , \qquad [6.3.53]$$

for beam-like breeder, where α, E, and ν are, respectively, the thermal expansion coefficient, Young's modulus and Poisson's ratio of solid breeders and σ_f is the breeder tensile fracture strength.

Table 6.3-11 lists the values of materials properties, the breeder plate dimensions, and the helium-cooled blanket operating conditions (Chapter 8) used for the thermal stress and cracking analysis. Thermal conductivity and thermal expansion are those for the unirradiated, sintered materials (Section 6.3.2.2); all mechanical properties (Young's modulus, Poisson's ratio, and tensile fracture strength) are estimated based on data of other ceramic mate-

rials. For Li_2O these estimates can be found in Ref. 6.3-3; those for γ-$LiAlO_2$ were based on data of Al_2O_3.[6.3-111]

Three average nuclear heating rates, each representative of a separate region in the blanket are considered. Region 1 has the highest nuclear heating rate ($Q = 47\ W/cm^3$) and is taken near the first wall. Region 2 is taken within the blanket where nuclear heating is 25% of that in Region 1. Region 3 is taken near the shield region where the nuclear heating rate is 4% of the maximum value.

Table 6.3-12 gives the solid-breeder plate and beam thickness requirements established from the temperature window (ΔT) and fracture strength (σ_f) constraints, Eqs. [6.3-41] through [6.3-43]. The temperature windows are taken to be $\Delta T = 390°C$ for Li_2O and $\Delta T = 650°C$ for γ-$LiAlO_2$ in all three regions of the respective blankets.

The salient features in Table 6.3-12 can be summarized as follows:

a. Between the two criteria for sizing the solid breeder plate or beam thickness, the fracture strength (σ_f) criterion always results in smaller half-thickness (h) than that from the temperature window (ΔT) criterion. To avoid cracking, the plate or beam thickness should be determined from the σ_f criterion, which, if satisfied, automatically satisfies the temperature-window constraint.

b. Had the temperature windows ($\Delta T = 390°C$ for Li_2O and 650°C for γ-$LiAlO_2$) been fully utilized in the helium-cooled solid-breeder blanket designs (Chapter 8), thermal-stress-induced cracking is likely to occur in both breeders. The σ_f criterion gives breeder half-thicknesses that are lower than those shown in Table 6.3-11. Using the breeder surface and centerline temperatures given in Table 6.3-11 and the breeder half-thicknesses of 0.55 and 0.45 cm, the calculated maximum tensile stresses in Li_2O and γ-$LiAlO_2$ are 259 and 784 MPa, respectively, for plate geometry; 194 and 603 MPa, respectively, for beam geometry. These stresses are all much greater than the estimated tensile fracture strengths of Li_2O and γ-$LiAlO_2$.

TABLE 6.3-11. INPUT VALUES ASSUMED FOR THERMAL STRESS/CRACKING ANALYSIS OF PLATE- OR BEAM-LIKE SOLID BREEDERS

Material/Geometry/Operating Parameters	Li_2O	γ-$LiAlO_2$
Thermal Conductivity, k (W/m °C)	3.9	2.0
Thermal Expansion Coefficient, α (/°C)	2.935×10^{-5}	1.196×10^{-5}
Young's Modulus, E (MPa)	54.4×10^{3}	230×10^{3}
Poisson's Ratio, ν	0.25	0.23
Tensile Fracture Strength, σ_f (MPa)	48.3	72.8
Breeder Plate on Beam Half-Thickness (cm)	0.55	0.45
Volumetric Nuclear Heating Rate, Q (W/cm^3)		
Near First Wall	47.0	65.0
Midway of Blanket Depth	11.8	16.3
Rear of Blanket	1.9	2.6
Breeder Plate or Beam Temperatures Near First Wall (°C)		
Breeder Surface	510	520
Breeder Centerline	773	866

TABLE 6.3-12. PLATE- AND BEAM-TYPE SOLID BREEDER HALF-THICKNESS (h) REQUIREMENTS

	Li_2O Half-thickness, h (cm) Region			γ-$LiAlO_2$ Half-thickness, h (cm) Region		
	1	2	3	1	2	3
ΔT criterion	0.80	1.61	4.0	0.63	1.26	3.16
σ_f criterion (plate)	0.24	0.47	1.18	0.14	0.27	0.69
σ_f criterion (beam)	0.27	0.55	1.36	0.16	0.31	0.78

It should be emphasized that the thickness requirements given in Table 6.3-12 and the cracking analysis depend on the assumed materials properties values. Except for the thermal conductivity and thermal expansion coefficient which are based on the solid breeder data, the other mechanical properties are all estimates subjected to considerable uncertainties (Section 6.3.2.3). Experimental investigation of solid breeder elastic and fracture properties is required to provide the basic information needs.

Gap Conductance

Thermal conductance (h_I) across the interface of solid breeder and structural materials (i.e., cladding, coolant tubes) is an important issue for solid breeder blankets, especially those breeders (e.g., Li_2O) with tight operating temperature windows. Gap conductance variation during blanket operation is a major source for the uncertainties in breeder temperatures, which must be controlled for reasons of tritium recovery/inventory, blanket thermal/mechanical performance, etc.

A general approach was taken in the earlier study[6.3-3] to develop a theoretical model for the overall conductance of a helium-filled gap. Heat transfer across the gap is assumed to take place via three parallel processes, i.e., conduction through gas phase, radiative heat transport, and solid-solid contact conduction. The last process is active only when the gap is closed which enables contact conduction at the surface asperities.

At typical solid breeder and structural temperatures during blanket operation, radiative heat transport across the gap should be small and hence ignored in the previous work. The model for contact conductance was not developed in detail because of its dependence on the solid breeder/structure interface pressure. Reliable solid breeder mechanical properties data (non-existent) are required to assess this interface pressure. For the gas-phase conductance, h_g, the appropriate equations are

$$h_g = \frac{k_g}{d + g_1 + g_2} \quad , \qquad [6.3\text{-}54]$$

for two flat plates (1 and 2) separated by a distance d, and

$$h_g = \frac{k_g}{r_1 \left(\log \frac{r_2}{r_1} + \frac{g_1}{r_1} + \frac{g_2}{r_2}\right)} , \qquad [6.3\text{-}55]$$

for two coaxial cylinders of radii $r_1 < r_2$, where k_g is the thermal conductivity of the gas in the gap, g_1 and g_2 are the temperature jump distances of surfaces 1 and 2 respectively.

Assuming the gap is filled with helium, the experimental helium thermal conductivity correlation of Gandhi and Saxena[6.3-112] can be used, viz.,

$$k_g = 3.366 \times 10^{-3} \, T^{0.668} \quad W/m\text{-}K. \qquad [6.3\text{-}56]$$

This experimental helium thermal conductivity correlation was found to be in good agreement with the kinetic theory model (±5%) over the temperature range (573-773 K) of interest.[6.3-3]

From kinetic theory considerations,[6.3-113] the temperature jump distance g can be written as

$$g_i = 3.501 \times 10^{-7} \left(\frac{2-a}{a}\right)_i \quad m \ , \qquad [6.3\text{-}57]$$

where i denotes surface i and g_i is, therefore, a property of both the solid surface and the helium gas.

If all the gas molecules behave like elastic spheres and have random direction of motion, it can be shown that[6.3-113]

$$a = \frac{2 \, m_1 \, m_2}{(m_1 + m_2)^2} \ , \qquad [6.3\text{-}58]$$

where m_1 and m_2 are the masses of gas and wall molecules, respectively. Strictly speaking, Eq. [6.3-58] applies only when the kinetic energy of trans-

lation is considered, and if each gas molecule strikes the surface only once before returning into the gas.

Denoting the mass of helium gas as m_1 and the mass of solid breeders or structural material (assumed to be Fe) as m_2 obtains

$$a_1\ (He/Li_2O) = 0.208 \text{ and } a_1\ (He/\gamma\text{-}LiAlO_2) = 0.108;$$

$$a_2\ (He/Fe) = 0.125, \qquad [6.3\text{-}59]$$

from which the temperature jump distances given by Eq. [6.3-47] can be calculated:

$$g_1\ (He/Li_2O) = 3.016 \times 10^{-6} \text{ m and } g_1\ (He/\gamma\text{-}LiAlO_2) = 6.148 \times 10^{-6} \text{ m};$$

$$g_2\ (He/Fe) = 5.252 \times 10^{-6} \text{ m}. \qquad [6.3\text{-}60]$$

For a gap interface in a solid breeder blanket, the initial gap, d_o, is generally known or can be estimated. Difficulty arises in the determination of the gap size (d) during blanket operation. Since d is the distance between the two adjacent boundaries of the solid breeder and structural materials, any change in the boundary locations (either or both) will change d accordingly. Processes affecting the boundary locations during blanket operation include: (1) differential thermal expansion between solid breeder and structural materials, (2) solid breeder cracking and cracked fragment relocation, (3) solid breeder densification due to thermal/radiation-enhanced sintering, (4) solid breeder thermal and radiation-enhanced creep, (5) solid breeder radiation-induced swelling, and (6) time-dependent deformation, i.e., creep and swelling of the structural materials. Since each of these processes is driven by temperature and stress in the solid breeder as well as in the structural materials, and since temperature and stress are in part determined by $h_g \simeq k_g/d$, the problem is clearly of an iterative nature requiring integrated thermal and mechanical analysis. Such an analysis is currently not feasible. Instead,

explicit design equations of h_g are derived below based on Eqs. [6.3-44] through [6.3-50].

When the gap is large, i.e., $d \gg g_1 + g_2$, the effect of the temperature jump distances on h_g is negligible compared to that of d. Equation [6.3-44] then becomes

$$h_g = 3.366 \times 10^{-3} \frac{T^{0.668}}{d} \quad W/m^2\text{-}K \quad . \qquad [6.3\text{-}61]$$

For very small d, i.e., on the order of surface roughness, Eq. [6.3-54] becomes

$$h_g = \frac{3.366 \times 10^{-3} T^{0.668}}{d_m + 8.268 \times 10^{-6}} \quad W/m^2\text{-}K \quad , \qquad [6.3.62]$$

where d_m is the root-mean-square roughness of the two surfaces given by

$$d_m = [(d_1^2 + d_2^2)/2]^{1/2} \quad , \qquad [6.3\text{-}63]$$

and d_1 and d_2 are the roughnesses of surfaces 1 and 2, respectively. For numerical calculations, d_1 and d_2 are assumed to be 10^{-7} m, which are on the same order of magnitude as those used in the fission-reactor fuel element modeling. Equation [6.3-62], hence, becomes

$$h_g^{max} = 4.022 \times 10^2 T^{0.668} \quad W/m^2\text{-}K \quad , \qquad [6.3\text{-}64]$$

which gives an upper bound for h_g as a function of temperature.

Figure 6.3-44 shows the variation of h_g as a function of temperature for d = 1, 2, 3 and 4 mm. Over the range of interface temperatures (573-773 K) of

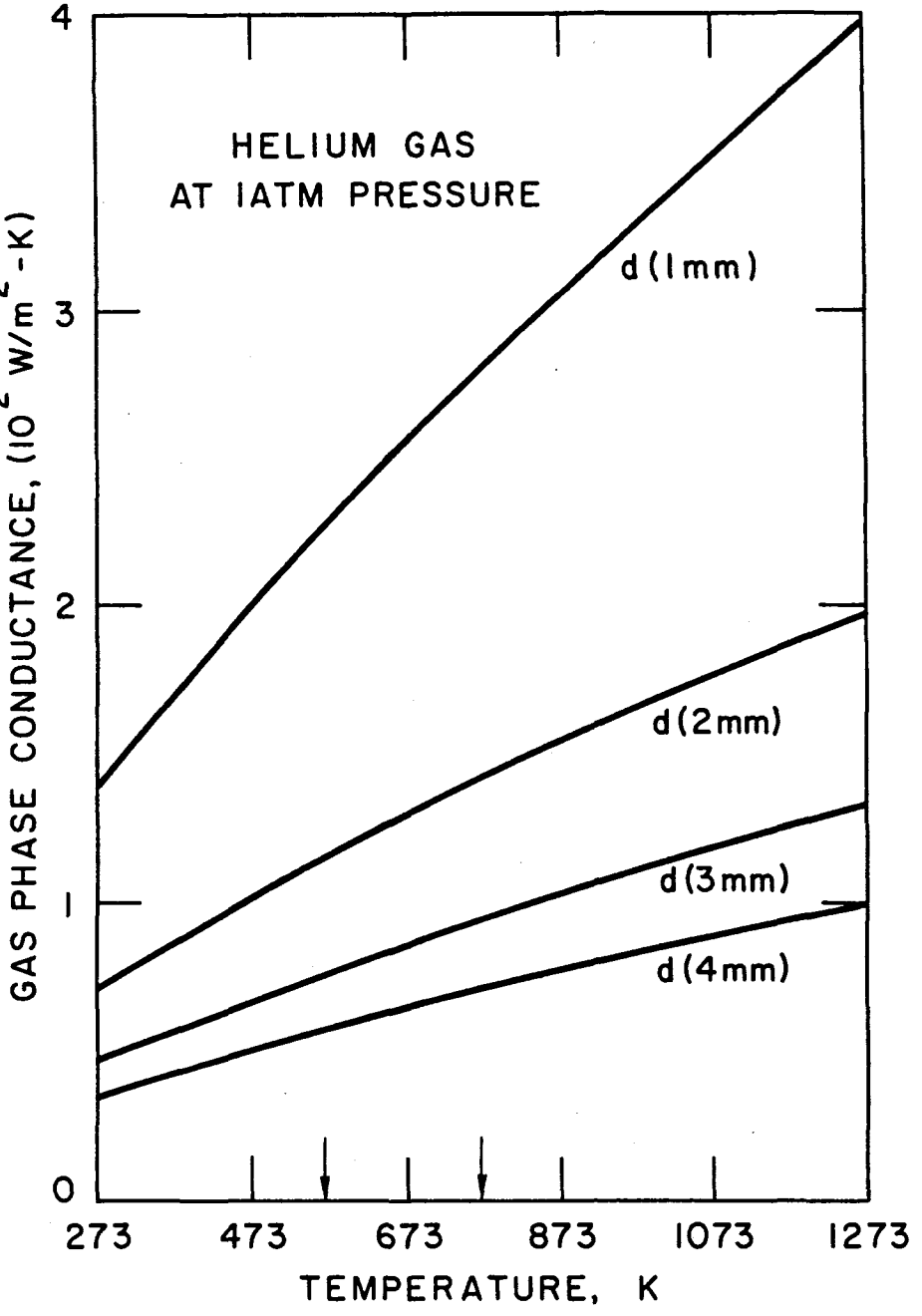


Figure 6.3-44. Variation of gas-phase conductance with temperature and gap size d.

interest during blanket operation, the average h_g are ~ 260, 130, 87, and 65 W/m^2-K, respectively, for d = 1, 2, 3 and 4 x 10^{-3} m. For the same heat flux (q") at the solid breeder surface, the temperature drop (ΔT) will double for doubling gap size according to $\Delta T = q"/h_g$. Assuming the coolant conditions remain the same, the solid breeder temperature must increase substantially.

The other extreme case for h_g as a function of temperature is displayed in Fig. 6.3-45 based on Eq. [6.3-64]. Over the interface temperature of interest, h_g^{max} is ~ 3.12 x 10^4 W/m^2-K. This would be close to the maximum h_g during blanket operation.

Verification of the gas-phase conductance model developed in this section against the ex-reactor experimental data found good agreement for relatively large gaps.(6.3-3) This is to be expected since the gas-phase conductance dominates under such conditions and depends primarily on the helium-gas thermal conductivity. The main uncertainty in the gas-phase conductance model is associated with small gaps where heat transfer under rarefied-gas conditions become important. Data of accommodation coefficients of helium and solid breeders are required.

6.3.5.5 Solid-Breeder/Structure Mechanical Interaction

Solid-breeder/structure mechanical interaction (BSMI) during blanket operation is a potential failure model which could cause premature module replacement and safety and environmental concerns. Failure mode here is defined in general terms to mean the loss of blanket functional capability, thus including physical fracture and/or excessive deformation of the breeder containment structural material.

BSMI loadings in a fusion reactor blanket can arise from several sources: differential thermal expansion between solid breeders and structural materials, irradiation-induced swelling in solid breeders, and localized mechanical interaction in regions near solid-breeder cracks and interfaces. All three phenomena have been described previously (Sections 6.3.2.3, 6.3.3, 6.3.5.4); the experimental data indicate substantial difference among solid breeders. A brief synopsis below of the driving forces for BSMI will show that the Li_2O blanket is probably most susceptible to BMSI, especially for designs utilizing thin breeder-containment structure without any gaps.

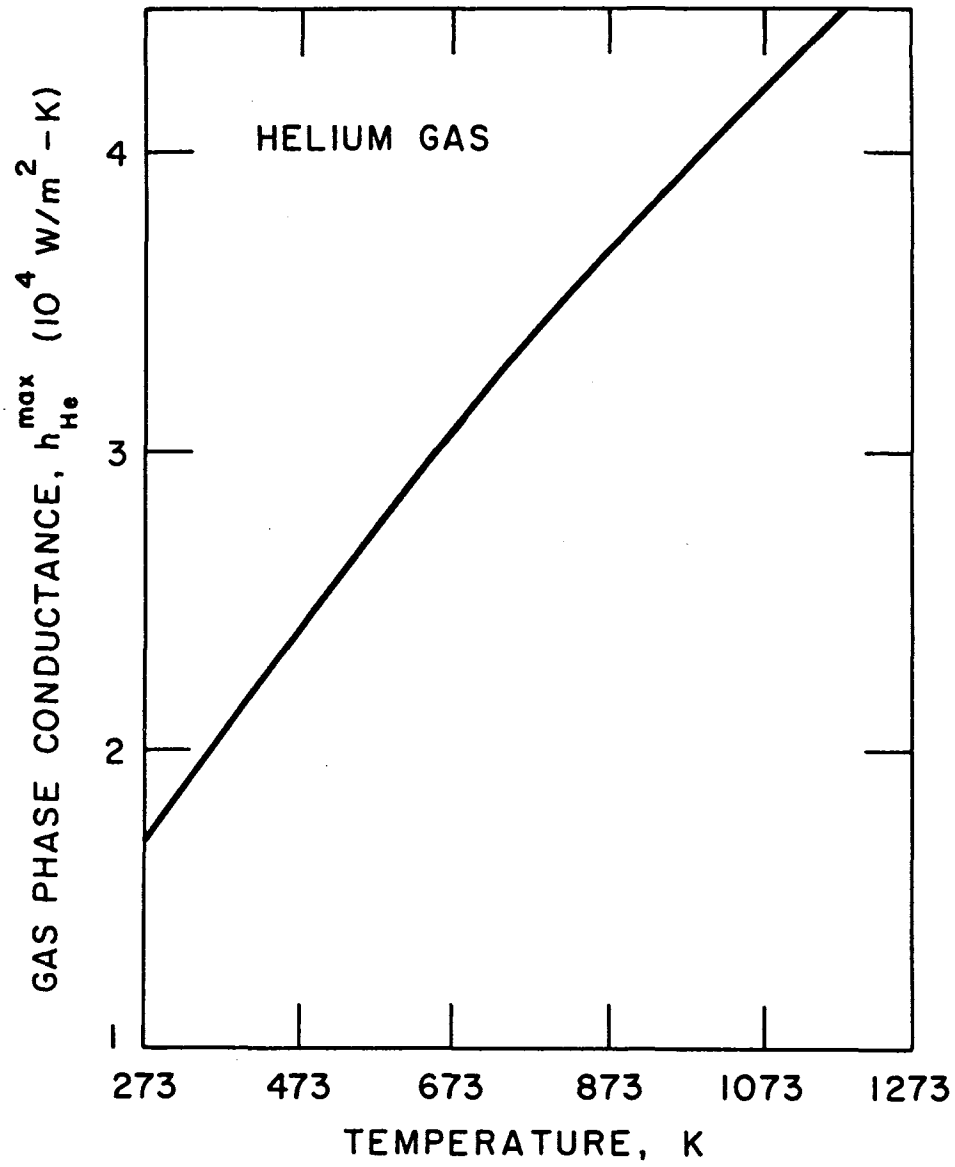


Figure 6.3-45. Variation of maximum gas-phase conductance (d=0) with temperature.

Driving Forces for BSMI

The magnitude of breeder/structure differential thermal expansion can be obtained from Fig. 6.3-9, which shows the length change ($\Delta L/L_o$) due to thermal expansion for solid breeders and for two structural materials, PCA and HT9. The differential thermal expansion strain ($\Delta\varepsilon_{DTE}$) can be defined as

$$\Delta\varepsilon_{DTE} = \left(\overline{\alpha\Delta T}\right)_b - \left(\overline{\alpha\Delta T}\right)_s$$

$$\simeq \alpha_b \left(\overline{\Delta T}\right)_b - \alpha_s \left(\overline{\Delta T}\right)_s , \qquad [6.3\text{-}65]$$

where α is the thermal expansion coefficient, $\Delta T = T_i - T_o$ (i = b or s), T_o is the reference room temperature, subscripts b and s denote solid breeder and structure, respectively, and the bars denote that the terms underneath are volume-averaged quantities. Among the solid breeders, Li_2O has the largest thermal expansion above that of HT9, hence the largest $\Delta\varepsilon_{DTE}$. Two ternary solid breeders (γ-$LiAlO_2$ and Li_2ZrO_3) have lower thermal expansion than that of HT9. Differential thermal expansion for these ternary ceramics, therefore, should be minimal.

Thus far significant irradiation-induced swelling has only been observed in Li_2O, not in γ-$LiAlO_2$ or other ternary breeders. The observed Li_2O swelling, at least during the early stages of the experiments (Section 6.3.3), may be described as unconstrained swelling. In those experiments the gaps between the Li_2O pellets and cladding can accommodate the initial swelling without developing significant BSMI. However, depending on the initial clearance between Li_2O and the surrounding structural material in the blanket design, BSMI due to swelling may soon develop at an estimated unconstrained Li_2O swelling rate of 2.3% $\Delta V/V_o$/at% ^6Li burnup (Section 6.3.3.1).

The Li_2O/He/HT9 blanket module (Chapter 8) consists of radially oriented Li_2O plates (sintered product, 80% TD) clad with thin sheets (0.25 mm thickness) of HT9. Helium coolant at 50 atm pressure enters the module through a flow distribution channel, passes the first-wall region, then flows radially outward between the breeder plates. Flow gap spacing (1 mm width) is provided

by wires wrapped around the exterior of the HT9 cladding. Tritium recovery from the Li_2O plates is achieved by a low-pressure (1 atm) helium stream flowing through grooved paths on the surface of the Li_2O plates. Several advantages were mentioned with regard to this design: (1) Since the cladding is thin and subjected to a net gas pressure differential of 49 atm, the cladding is expected to collapse onto Li_2O early during blanket operation. This will greatly reduce the uncertainty in the Li_2O/HT9 interface conductance (Section 6.3.5.4), hence the uncertainty in the Li_2O temperatures. (2) In the event of a loss of coolant pressure, the gas pressure (1 atm) inside the plates will not be high enough to rupture the cladding. (3) It is claimed that the coolant pressure of 50 atm will be sufficient to clamp the cladding against breeder swelling during blanket operation.

An elastic analysis is performed below to estimate the interface pressure due to BSMI and the associated cladding stresses in the Li_2O/HT9 plate design. For simplicity the analysis drew an analogy for the contact pressure between a misfitting shaft-and-hub assembly or the so called "shrink-fit pressure". Since the assumed cylindrical geometry for the shaft and hub is more effective for pressure containment than the rectangular plate geometry, any problem noted in the shaft-and-hub case is expected to be worse in the plate case.

Assume that the radius of the shaft in the unstressed condition is larger than the inner radius of the hub by an amount δ. After assembly a pressure p is produced between the hub and the shaft. The magnitude of p is found from the condition that the increase in the inner radius of the hub plus the decrease in the shaft radius must be equal to δ, i.e.,

$$\frac{bp}{E_2}\left(\frac{b^2 + c^2}{c^2 - b^2} + \nu_2\right) + \frac{bp}{E_1}\left(1 - \nu_1\right) = \delta, \qquad [6.3.66]$$

where b and c are the inner and outer radii, respectively, of the hub, E_1, E_2 and ν_1, ν_2 are the Young's moduli and Poisson's ratio of the shaft and hub, respectively.

Rearranging Eq. [6.3-66] gives

$$p = \frac{\delta}{b}/\left[\frac{1}{E_2}\left(\frac{b^2 + c^2}{c^2 - b^2} + \nu_2\right) + \frac{1}{E_1}(1 - \nu_1)\right]. \qquad [6.3\text{-}67]$$

The mismatch δ in Eqs. [6.3-66] and [6.3-67] can result from the differential thermal expansion between Li_2O and HT9 and/or from the Li_2O swelling. For the following calculations, the shaft is assumed to be Li_2O with b=5.5 mm (half thickness of the plate) and the hub is HT9 with c=5.75 mm.

Mechanical properties (E_1 and ν_1) for Li_2O are the same as those shown in Table 6.3-11; those (E_2, ν_2) of HT9 are evaluated at 500°C from the following correlations:(6.3-114)

$$E_2\ (\text{MPa}) = 2.137 \times 10^5 - 102.74 \times T\ (°C)$$
$$E_2 = 1.62 \times 10^5\ \text{MPa at } 500°C$$
$$\nu_2 = 0.29.$$

Since b is the shaft radius (or plate half-thickness), the quantity (δ/b) is the mismatch strain at the breeder/structure interface. The interface pressure can be calculated directly for a given δ/b, after which the cladding stresses can be obtained via thin-shell approximation:

$$\sigma_r = -p$$

$$\sigma_\theta = p\,\frac{b}{t}$$

$$\sigma_z = p\,\frac{b}{2t}$$

$$\sigma_e = 1/\sqrt{2}\ p\left[\left(1 - \frac{b}{t}\right)^2 + \left(\frac{b}{2t}\right)^2 + \left(\frac{b}{2t} - 1\right)^2\right]^{1/2}, \qquad [6.3.68]$$

where σ_r, σ_θ, σ_z are the principal stresses in the radial, circumferential, and axial directions of the cladding, respectively, and σ_e is the cladding equivalent stress.

Table 6.3-13 lists the interface pressures (p'), circumferential stresses (σ_θ) and equivalent stresses (σ_e) in the HT9 cladding obtained at three values of δ/b. The interface pressure p' is calculated as p from Eq. [6.3-67] and subtracted from it 50 atm (~ 5 MPa), the counteracting pressure from the helium coolant.

TABLE 6.3-13 INTERFACE PRESSURE AND CLADDING STRESSES DUE TO Li_2O/HT9 MECHANICAL INTERACTION (SHRINK-FIT ANALOGY)

Mismatch Strain, δ/b (%)	p' (MPa)	σ_θ (MPa)	σ_e (MPa)
2	124.4	2737	2262
1	59.7	1313	1086
0.5	27.4	603	498

Except for the case of δ/b = 0.5%, the cladding stress levels are all much higher than the ultimate tensile strength of HT9 (540 MPa at 500°C).[6.3-114] One would, therefore, expect almost an instantaneous cladding rupture if the mismatch strain of > 1% develops and both Li_2O and HT9 behave elastically. For δ/b = 0.5% the cladding equivalent stress is above the yield strength of HT9 (450 MPa at 500°C);[6.3-114] hence favoring cladding plastic deformation. Figure 6.3-9 shows that the thermal expansions of Li_2O and HT9 at 500°C differ by ~ 0.8%. Unconstrained Li_2O diametral swelling up to 3.3% has been noted in the FUBR-1A experiment (Section 6.3.3.2). These experimentally observed results more than envelop the assumed δ/b ranges in the above calculations.

The above analysis assumed that both Li_2O and HT9 behave elastically. With Li_2O swelling gradually increasing during blanket operation, the magnitude of the interface pressure will also be affected by the plastic flow properties of Li_2O. Some credits may be taken for Li_2O hot pressing into the available internal pore spaces in the high temperature region of the Li_2O plates. However, a geometrical limit must be imposed on hot pressing beyond which elimination of breeder internal porosity is no longer possible. An optimistic limit for the sintered Li_2O at 80% TD would be 6.7% in linear dimen-

sion assuming isotropic hot pressing. A considerably lower limit (~ 3%) may be reached sooner when the major fraction of pores become closed pores. In either case, the amount of swelling strains that hot pressing can accommodate at Li_2O/HT9 interface will be further reduced because hot pressing in Li_2O is not expected near the low-temperature (500°C) region of the plate.

The above analysis, though simplified in nature, illustrates that BSMI can be a serious problem for the Li_2O/HT9 plate design. Even in cylindrical geometry, the thin HT9 cladding cannot sustain much interface pressure without yielding and undergoing large deformation which usually precedes fracture. Plate bending and stress concentrations near the unsupported areas over the Li_2O grooves will considerably worsen the situation. In the design of the Li_2O/He/HT9 blanket (Chapter 8), a swelling tolerant plate design was introduced to accommodate up to 10% $\Delta V/V$ swelling. More detailed structural analysis is needed to verify the effectiveness of such a design which requires mechanical properties of Li_2O.

REFERENCES FOR SECTION 6.3

6.3-1 C. Baker et al., Argonne National Laboratory report, ANL/FPP-80-1, 1980.

6.3-2 M. Abdou et al., Argonne National Laboratory report, ANL/FPP-82-1, 1982.

6.3-3 M. Abdou et al., Argonne National Laboratory report, ANL/FPP-83-1, 1983.

6.3-4 D. L. Smith et al., USA Contribution to INTOR Nuclear Data Base Assessment-Group H, ETR-INTOR/DIS/NUC-2, May 1984.

6.3-5 L. Yang et al., J. Nucl. Mater. 103 (1981) 585.

6.3-6 TFTR Lithium Blanket Module (LBM) Program, Preliminary Design Report, GA Technologies, GA-A16616, December 1981.

6.3-7 R. M. Arons et al., J. Nucl. Mater. 103 (1981) 573.

6.3-8 R. B. Poeppel, Argonne National Laboratory, unpublished work.

6.3-9 T. Takahashi and T. Kikuchi, JAERI-M7518 (1978).

6.3-10 L. N. Wilson and G. W. Hollenberg, Fifth Annual Progress Report on Special Purpose Materials for Magnetically Confined Fusion Reactors, DOE-ER-0113/2, October 1983.

6.3-11 T. Takahashi and T. Kikuchi, J. Nucl. Mater. 91 (1980) 610.

6.3-12 "Gel-Sphere-Pac Fuel for Thermal Reactors - Assessment of Fabrication Technology and Irradiation Performance," ORNL-5469, November 1979.

6.3-13 Sol-Gel Processes for Ceramic Nuclear Fuels, (Proc. Panel Sponsored by IAEA, Vienna, May 6-10, 1968), International Atomic Energy Agency, Vienna, 1968.

6.3-14 R. G. Wymer and A. L. Lotts, Co-chairman, Symposium on Sol-Gel Processes and Reactor Fuel Cycles, (Proc. Symposium Sponsored by ORNL, Gatlinburg, TN, May 4-7, 1970), CONF-700502.

6.3-15 Sol-Gel Processes for Fuel Fabrication, (Proc. Panel Organized by IAEA, Vienna, May 21-24, 1973), IAEA-161, International Atomic Energy Agency, Vienna, 1974.

6.3-16 A. L. Lotts, Comp., Fast Breeder Reactor Oxide Fuels Development - Final Report, ORNL-49-1 (November 1973).

6.3-17 J. P. Moore et al., Oak Ridge National Laboratory report, ORNL/TM-8196, June 1982.

6.3-18 W. D. Kingery et al., Introduction to Ceramics, 2nd Ed., John Wiley & Sons, 1976.

6.3-19 J. N. Anno and H. H. Boeing, Methods of Producing Porous Lithium Oxide, U.S. Patent 4,221,775, September 1980.

6.3-20 Y. Naruse et al., Japan/U.S. Workshop on Blanket Design/Technology, JAERI, February 27-29, 1984.

6.3-21 JANAF Thermochemical Tables, 2nd ed., D. R. Stull and H. Prophet, project directors, NSRDS-NBS37, June 1971. Revisions and supplements for selected species have been issued at various times since this edition.

6.3-22 M. Tetenbaum, A. K. Fischer, and C. E. Johnson, to be published in Nuclear Technology/Fusion.

6.3-23 M. Tetenbaum and C. E. Johnson, to be published in J. Nucl. Mat.

6.3-24 N. W. Gregory and R. H. Mohr, J. Am. Chem. Soc. 77(1955)2142.

6.3-25 J. H. Norman and G. R. Hightower, J. Nucl. Mater. 122 & 123(1984)913-920.

6.3-26 M. Tetenbaum, High Temperature Sci., 7 (1975)37.

6.3-27 H. Katsuta, et al., J. Nucl. Mat. 116(1983)244.

6.3-28 H. R. Ihle and C. H. Wu, Proc. Third Topical Meeting on Fusion Reactor Materials, Albuquerque, NM, September 1983.

6.3-29 D. White, et al., J. Chem. Phys. 39(1963)2463.

6.3-30 D. L. Hildenbrand, J. Chem. Phys. 57(1972)4556.

6.3-31 J. Berkowitz, et al., J. Phys. Chem. 63(1959)644.

6.3-32 J. Berkowitz, et al., J. Chem. Phys. 33(1960)533.

6.3-33 H. Kimura, et al., J. Nucl. Mat. 92(1980)221.

6.3-34 H. Kudo, et al., J. Nucl. Mat. 78(1978)380.

6.3-35 H. R. Ihle, et al., J. Nucl. Mat. 78(1978)380.

6.3-36 C. H. Wu, et al., J. Chem. Phys. 70(1979)1815.

6.3-37 Y. Ikeda, et al., J. Nucl. Sci. Tech. 17(1980)650.

6.3-38 Y. Ikeda, et al., J. Nucl. Mat. 97(1981)47.

6.3-39 A. F. Venero and E. F. Westrum, Jr., J. Chem. Thermo. 7(1975)693.

6.3-40 A. K. Fischer, Argonne National Laboratory, unpublished work.

6.3-41 H. Nakagawa, et al., J. Nucl. Mat. 102(1981)292.

6.3-42 M. A. Matveev, et al., Inorganic Materials 1(1965)1301 (translation from Russian).

6.3-43 A. Neubert and D. Guggi, J. Chem. Thermo. 10(1978)297.

6.3-44 D. J. Suiter, McDonnell Douglas Astronautics Company, MDC E2677, June 1983.

6.3-45 S. W. Tam and Y. Y. Liu, to be published.

6.3-46 J. M. Ziman, "Electrons and Phonons," Oxford University Press, London (1968).

6.3-47 G. A. Slack, "Solid State Physics," Ed. H. Ehrenreich, F. Seitz and D. Turnbull, Academic Press, New York, Vol. 34, p. 1(1979).

6.3-48 A. Auerbach and P. B. Allen, Phy. Rev. B 29 (1984) 2884.

6.3-49 G. A. Slack and P. Anderson, Phys. Rev. B 26 (1982) 1873.

6.3-50 S. W. Tam, L. Leibowitz, Y. Y. Liu, R. Bloomquist, and C. E. Johnson, submitted to the International Conference on Fusion Materials, Tokyo, Japan, December 1984.

6.3-51 G. W. Hollenberg, "Thermal Properties of Lithium Ceramics for Fusion Applications," presented at the 84th Annual Meeting of the Am. Cer. Soc., Cincinnati, Ohio, May 3-5, 1982.

6.3-52 L. Leibowitz and R. Bloomquist, private communication.

6.3-53 Y. Y. Liu and S. W. Tam, Argonne National Laboratory Report, ANL/FPP/TM-184, July 1984, to be published.

6.3-54 R. Clemmer, Argonne National Laboratory, personal communication.

6.3-55 H. L. Johnston and T. W. Bauer, J. Am. Chem. Soc., 73, (1951) 1119-1122.

6.3-56 T. Tanifuji, K. Shiozawa, and S. Nasu, J. Nucl. Mater., 78 (1978) 422-424.

6.3-57 I. Barin and O. Knacke, Thermochemical Properties of Inorganic Substances, Springer-Verlag, Berlin, (1973) p. 416.

6.3-58 H. Shomate and A. J. Cohen, J. Am. Chem. Soc., 77 (1955) 285-286.

6.3-59 E. N. Rodigina and K. Z. Gomelskii, Russ. J. Phys. Chem., 35 (1961) 898-901.

6.3-60 W. E. Gurwell, Battelle Pacific Northwest Laboratory, BNWL-CC-464, 1-21 (1966).

6.3-61 T. Kurasawa, T. Takahashi, K. Noda, H. Kakeshita, S. Nasu, and H. Watanabe, J. Nucl. Mater., 107 (1982) 334-336.

6.3-62 F. A. Hummel, J. Am. Cer. Soc., 34 (8) (1951) 235-239.

6.3-63 N. Soga, J. Am. Cer. Soc., 47 (1964) 468-469.

6.3-64 H. P. Kirchner, K. M. Merz, and H. T. Smyth, U. S. Bureau Ordinance, CAL-PI-1273-M-4, Vol. 2 (1959) 1-43.

6.3-65 R. T. Girard, C. T. Sims, and H. R. Wisely, General Electric Company, U. S. Patent #3, 397, 080 (1968).

6.3-66 H. Kudo and K. Okuno, J. Nucl. Mat., 101 (1981) 38-43.

6.3-67 K. Okuno and H. Kudo, Proc. Fall Meeting of Atomic Energy Soc. of Japan, F-17 (1981).

6.3-68 S. Nasu, H. Kudo, K. Shiozawa, T. Takashashi, T. Kurasawa, M. Tachiki, and K. Tanaka, J. Nucl. Mat., 68 (1977) 261-264.

6.3-69 V. G. Vasilev, S. R. Borisov, N. N. Riazantseva, and A. A. Vashman, U.S./USSR Workshop on Engineering and Economic Problems of ETF, Moscow and Leningrad (USSR), September 1979.

6.3-70 K. Okula, D. K. Sze, "Tritium Recovery from Solid Breeders: Implication of the Existing Data," UWFDR-351, presented at the ANS Conf. on Tritium Technology in Fission, Fusion and Isotopic Applications, April 29-May 1, 1980, Dayton, OH.

6.3-71 J. Shearer, S. W. Tam, and C. E. Johnson, "Tritium Diffusion in Lithium Oxide Solid Breeder Materials," presented at the ANS meeting, June 1983, Detroit, MI.

6.3-72 D. Guggi, H. R. Ihle, and U. Kurz, Proc. 9th Symposium on Fusion Technology, Grarmisch-Partinkirchen (FRG), June 1976, p. 337-344.

6.3-73 D. Guggi, H. R. Ihle, D. Bruning, U. Kurz, S. Nasu, K. Noda, and T. Tanifuji, J. Nucl. Mat., 18 (1983) 100-108.

6.3-74 R. Wiswall and E. Wirsing, BNL-50748 (1977).

6.3-75 H. Katsuta, S. Konishi, and H. Yoshida, Proc. Fall Meeting of Atomic Energy Soc. of Japan, F-16 (1981).

6.3-76 D. Guggi, H. Ihle, A. Neubert, and R. Wofle, in Radiation Effects and Tritium Technology for Fusion Reactors, CONF-750989, Vol. III (March 1976) p. 416-432.

6.3-77 R. Clemmer and M. Billone, Argonne National Laboratory, personal communication, 1984.

6.3-78 R. W. Werner, et al., Lawrence Livermore National Laboratory Report, UCID-19609, November 1982, p. 5-14.

6.3-79 ANL Memo, Y. Y. Liu to R. Nygren, April 13, 1984, "Thermal Stresses and Cracking of γ-$LiAlO_2$ in the Microwave Heating Experiment".

6.3-80 L. Yang, GA Technologies Inc., personal communication.

6.3-81 G. W. Hollenberg, Hanford Engineering Development Laboratory, personal communication.

6.3-82 O. K. Chopra and D. L. Smith, Oak Ridge National Laboratory Report, DOE/ER-0045/7, 1981, pp. 321-327.

6.3-83 O. K. Chopra and D. L. Smith, Oak Ridge National Laboratory Report, DOE/ER-0045/8, 1982, pp. 507-513.

6.3-84 O. K. Chopra and D. L. Smith, Oak Ridge National Laboratory Report, DOE/ER-0045/9, 1982, pp. 323-338.

6.3-85 O. K. Chopra and D. L. Smith, Oak Ridge National Laboratory Report, DOE/ER-0045/10, 1983, pp. 204-208.

6.3-86 O. K. Chopra and D. L. Smith, Alloy Development for Irradiation Performance: Semiannual Progress Report for the Period Ending September 30, 1983, to be published.

6.3-87 D. L. Porter, et al., Argonne National Laboratory Report, ANL/FPP/TM-167, Dec. 1982.

6.3-88 D. L. Porter, et al., J. Nucl. Mater., in press.

6.3-89 R. F. Mattas, "Li_2O Examination," ANL Internal Memo, March 9, 1984.

6.3-90 Y. Y. Liu, R.F. Mattas, and D. L. Porter, submitted to 1st Inter. Conf. on Fusion Reactor Materials, Tokyo, Japan, Dec. 3-6, 1984.

6.3-91 K. Noda, et al., submitted to J. Nucl. Mater.

6.3-92 G. W. Hollenberg, Hanford Engineering Development Laboratory Report, TC-2022, August, 1981.

6.3-93 G. W. Hollenberg, 6th Annual Progress Report on Special Purpose Materials for Magnetically Confined Fusion Reactors, to be published.

6.3-94 R. G. Clemmer et al., "The TRIO Experiment," to be published as an Argonne National Laboratory Report.

6.3-95 E. H. VanDeventer and V. A. Maroni, J. Nucl. Mater. 92, 103-111 (1980).

6.3-96 T. Kurasawa et al., Japanese contributions to Disciplinary Group-Nuclear, INTOR Workshop Phase 2A, January 1984.

6.3-97 M. Abdou et al., Fusion Integrated Nuclear Experimental Strategy Study Efforts (FINESSE), to be published as an UCLA report.

6.3-98 G. W. Hollenberg, Hanford Engineering Development Laboratory, personal communication.

6.3-99 D. R. Olander, TID-26711-P1, 1976, p. 278.

6.3-100 L. Yang et al., J. Nucl. Mater., 103 & 104 (1981) 585.

6.3-101 A. R. Veca et al., Nucl. Tech./Fusion, Vol. 4, No. 2, Part 3, September 1978, p. 757.

6.3-102 R. H. Wiswall and E. Wirsing, BNL-50748 (1977).

6.3-103 W. Yunker, "Continuous Extraction of Tritium from Irradiated Lithium Aluminate," Hanford Engineering Development Laboratory, TC-1745 (1980).

6.3-104 D. L. Smith, R. G. Clemmer, V. Z. Jankus, and J. Rest, "Analysis of In-Situ Tritium Recovery from Solid Fusion-Reactor Blankets," Procs. of the Fourth ANS Topical Meeting on the Technology of Controlled Nuclear Fusion, King of Prussia, PA (October 14-17, 1980).

6.3-105 N. Wakao, S. Otani, and J. M. Smith, AIChE Journal, 11 (1964) 439-445.

6.3-106 R. B. Bird, W. E. Stewart, and E. N. Lightfoot, Transport Phenomena, J. Wiley and Sons, Inc., New York (1960) 505.

6.3-107 H. S. Carslaw and J. C. Jaeger, Conduction of Heat in Solids, Oxford Univ. Press, London (1959).

6.3-108 O. W. Richardson, Phil Magazine, Series VI.7, 266 (1904).

6.3-109 W. H. McAdams, Heat Transmission, 3rd Ed., Mcgraw-Hill, 1954, Chapter 6.

6.3-110 Y. Y. Liu, Argonne National Laboratory, unpublished work.

6.3-111 Z. E. Campbell, High-Temperature Technology, John Wiley & Sons, 1956, p. 46.

6.3-112 J. M. Gandhi and S. C. Saxena, J. Chem. and Engng. Data, 13, 3 (1968).

6.3-113 E. H. Kennard, Kinetic Theory of Gases, McGraw-Hill, 1938.

6.3-114 Alloy Properties Databook, Hanford Engineering Development Laboratory, TC-293, Rev. 4, January 1980.

BLANKET COMPARISON AND SELECTION STUDY

SECTION 6.4 - LIQUID BREEDER MATERIALS

SECTION 6.4

TABLE OF CONTENTS

PAGE NO.

6.4 Liquid Breeder Materials.....6.4-1
6.4.1 Lithium Properties.....6.4-1
6.4.2 Lithium-Lead Properties.....6.4-3
6.4.3 FLIBE Properties.....6.4-12
6.4.3.1 Thermophysical Properties.....6.4-12
6.4.3.2 High-Temperature Stability.....6.4-14
6.4.3.3 Corrosion Properties.....6.4-16
6.4.3.4 Tritium Chemistry.....6.4-17
REFERENCES.....6.4-19

LIST OF FIGURES FOR SECTION 6.4

FIG. NO.	TITLE	PAGE NO.
6.4-1	Vapor pressure of lithium as a function of temperature	6.4-2
6.4-2	Phase diagram of LiPb	6.4-6
6.4-3	Sievert's constants for solutions of hydrogen isotopes in liquid LiPb alloys	6.4-6
6.4-4	Activity coefficients for Li and Pb	6.4-8
6.4-5	Density and thermal expansion coefficient of LiPb at liquidus temperature	6.4-10
6.4-6	Electrical conductivity of LiPb	6.4-10
6.4-7	Electrical resistance of LiPb at 800°C	6.4-11
6.4-8	Specific heat (Cp) of 17Li-83Pb as a function of temperature	6.4-11
6.4-9	Density of FLIBE (47% LiF-53% BeF_2) as a function of temperature	6.4-13
6.4-10	Density of FLIBE (66.7% LiF-33.3% BeF_2) as a function of temperature	6.4-13
6.4-11	Viscosity of FLIBE (45% LiF-55% BeF_2) as a function of temperature	6.4-15
6.4-12	Viscosity of FLIBE (66.7% LiF-33.3% BeF_2) as a function of temperature	6.4-15
6.4-13	Equilibrium concentrations of TF and T_2 in the mixture of 2 LiF · BeF_2 at 600°C	6.4-18

REFERENCES 6.4-19

LIST OF TABLES FOR SECTION 6.4

TABLE NO.	TITLE	PAGE NO.
6.4-1	GENERAL PROPERTIES OF LITHIUM	6.4-1
6.4-2	LITHIUM PROPERTIES AT SELECTIVE TEMPERATURES	6.4-3
6.4-3	ANALYTICAL CORRELATIONS FOR THE VARIOUS LITHIUM PROPERTIES	6.4-4
6.4-4	MATERIALS PROPERTIES AVAILABLE FOR 17Li-83Pb	6.4-5
6.4-5	MATERIALS PROPERTIES NOT AVAILABLE FOR 17Li-83Pb	6.4-5
6.4-6	THERMODYNAMIC PROPERTIES OF 17Li-83Pb	6.4-9
6.4-7	PHYSICAL PROPERTIES OF FLIBE SALTS (REFS. 6.4-22 AND 6.4-23)	6.4-14

6.4 Liquid Breeder Materials

Three liquid breeder materials, lithium (Li), lithium-lead (17Li-83Pb), and FLIBE ($LiF-BeF_2$), are included in this section. Among them properties assessment had been done for liquid Li and 17Li-83Pb in the Interim BCSS Report.[6.4-1] A summary of that assessment is given in Sections 6.4.1 and 6.4.2 with emphasis on the remaining data needs. Section 6.4.3 covers FLIBE and includes topics on thermophysical properties, high-temperature stability, corrosion properties, and tritium chemistry. Compatibility (corrosion) of liquid Li and 17Li-83Pb with structural materials is not included in this section; its assessment can be found in Section 6.2. Finally design related issues of the liquid breeder blankets can be found in Chapter 7.

6.4.1 Lithium Properties

Table 6.4-1 lists certain general properties of lithium. There are some questions regarding the exact values of the melting and boiling temperatures, and of the heat of fusion, but the differences among the quoted values[6.4-2,6.4-3] are small.

TABLE 6.4-1. GENERAL PROPERTIES OF LITHIUM

Symbol	Li
Atomic Number	3
Atomic Weight	6.941 a.m.u.
Isotopes/Abundance	^6Li/7.5%, ^7Li/92.5%
Crystal Structure	bcc
Cubic Edge Length of Unit	0.351 nm
Molar Volume	13.1 cm^3/gm mole
Melting Point	180.54°C
Boiling Point	1347°C
Heat of Fusion	432.1 kJ/kg
Heat of Vaporization	19595 kJ/kg

Table 6.4-2 lists values of enthalpy, heat capacity, thermal conductivity, electrical resistivity, surface tension, viscosity, and density of lithium at selective temperatures. Figure 6.4-1 shows the vapor pressure of lithium as a function of temperature. Most of these values are based on the set of Li properties submitted for incorporation into the Materials Handbook for Fusion Energy Systems.[6.4-4] Reference 6.4-2 contains discussions of these proper-

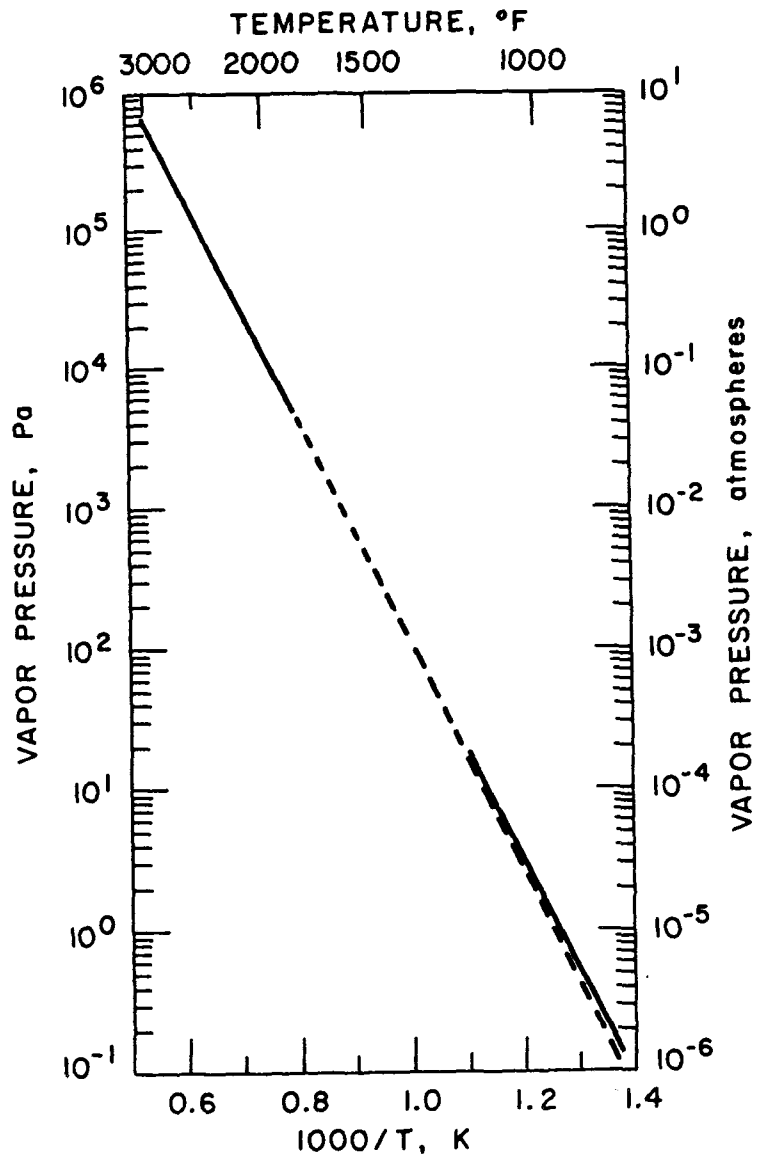


Figure 6.4-1. Vapor pressure of lithium as a function of temperature.

ties which should be consulted for further information. The analytical correlations that can be used to compute the various properties at other temperatures are given in Table 6.4-3. Notice that the correlations for enthalpy and specific heat have been changed from those given in Ref. 6.4-1. The earlier correlations for lithium enthalpy exhibit a discontinuity at 650°C; they are not consistent with the specific heat correlations which must obey $C_p = dH_T/dT$. These inconsistencies have been resolved by using the correlations suggested by Mansteller.(6.4-5)

TABLE 6.4-2. LITHIUM PROPERTIES AT SELECTIVE TEMPERATURES

Properties	Temperature (°C)			
	200	350	500	650
Enthalpy (MJ/kg)	0.52	1.16	1.79	2.42
Heat Capacity (kJ/kg-K)	4.36	4.24	4.17	4.16
Thermal Conductivity (W/m-K)	44.0	46.8	49.6	52.4
Electrical Resistivity (μΩ-cm)	27.3	31.1	35.3	39.5
Surface Tension (dynes/cm)	397	373	350	325
Viscosity (centipoise)	0.57	0.41	0.32	0.27
Density (kg/m^3)	515	500	485	470

In summary, it appears that a rather complete set of liquid lithium properties is now available for fusion blanket design applications.

6.4.2 17Li-83Pb Properties

There is a general lack of materials properties data of 17Li-83Pb. Those material properties which have been measured are listed In Table 6.4-4. The

TABLE 6.4-3. ANALYTICAL CORRELATIONS FOR THE VARIOUS LITHIUM PROPERTIES

Property	Equation[a]
Specific Heat C_p, kJ/kg-K	$C_p = 4.5302 - 8.382 \times 10^{-4}\ T$; $180.54 < T < 420°C$ $C_p = 4.20755 - 7.33 \times 10^{-5}\ T$; $420 < T < 900°C$
Enthalpy H_T, kJ/kg	$H_T = -372 + 4.5302\ T - 4.191 \times 10^{-4}\ T^2$; $180.54 < T < 420°C$ $H_T = -303.86 + 4.20755\ T - 3.615 \times 10^{-5}\ T^2$; $420 < T < 900°C$
Thermal Conductivity kW/m-K	$k = 40.1246 + 1.9037 \times 10^{-2}\ (T - 273)$; $473 < T < 1373$ K
Electrical Resistivity ρ, $\mu\Omega$-cm	$\rho = 21.934 + 2.598 \times 10^{-2}\ T + 2.581 \times 10^{-6}\ T^2 - 1.89 \times 10^{-9}\ T^3$; $200 < T < 1430°C$
Surface Tension σ, dynes/cm	$\sigma = 0.16\ (3550 - T) - 95$; $473 < T < 1673$ K
Viscosity η, Centipose	$\log_{10} \eta = 1.4936 - 0.7368 \log_{10} T + 109.95/T$; $453 < T < 1473$ K $\log_{10} \eta = 726.07/T - 1.338$; $973 < T < 1473$ K
Vapor Pressure P, Atmospheres	$\log_{10} P = 4.8831 - 7877.9/T$; T in K
Density d, kg/m^3	$d = 535.2 - 0.101 \times T$; $200 < T < 1600°C$

[a]The temperature unit in each equation should be consistent with the unit given for the associated temperature range.

properties which have not been measured are listed in Table 6.4-5. Previous assessment[6.4-1] of the available data is summarized below.

The phase diagram of LiPb has been well established and is shown in Fig. 6.4-2.[6.4-6] The melting points of LiPb and 17Li-83Pb were confirmed by different workers.[6.4-7,6.4-8] The accuracy of the phase diagram and, therefore, the melting temperatures of LiPb in various composition appear to be reasonable.

There were basically three different measurements on the Sievert's constant of LiPb.[6.4-9 - 6.4-11] The results from Veleckis and Wu appear to be in good agreement and are shown in Fig. 6.4-3. The results from Ref. 6.4-11 were measured at a hydrogen concentration that is judged to be too high.

TABLE 6.4-4. MATERIAL PROPERTIES AVAILABLE FOR LiPb

- Phase Diagram
- Sievert's Constant
- Lithium Activity
- Density
- Thermal Expansion Coefficient
- Electrical Conductivity
- Vapor Pressure
- Neutronic Data
- Specific Heat <300°C
- ΔH of Melting

TABLE 6.4-5. MATERIAL PROPERTIES NOT AVAILABLE FOR LiPb (DESIGN VALUES BASED ON Pb PROPERTIES)

- Thermal Conductivity
- Viscosity
- Specific Heat >300°C
- Solubility of (Fe, Ni, etc.)
- Diffusivity
- ΔH of Reaction with Water
- ΔH of Reaction with Air

The activity of lithium in the LiPb system has been measured by Knudsen diffusion mass spectrometry at 750 K. The activity was reported to continuously decrease from 4.0×10^{-3} to 2×10^{-5} as the lithium composition decreases from 61 to 5 atom per cent.[6.4-12 - 6.4-15] The activity of

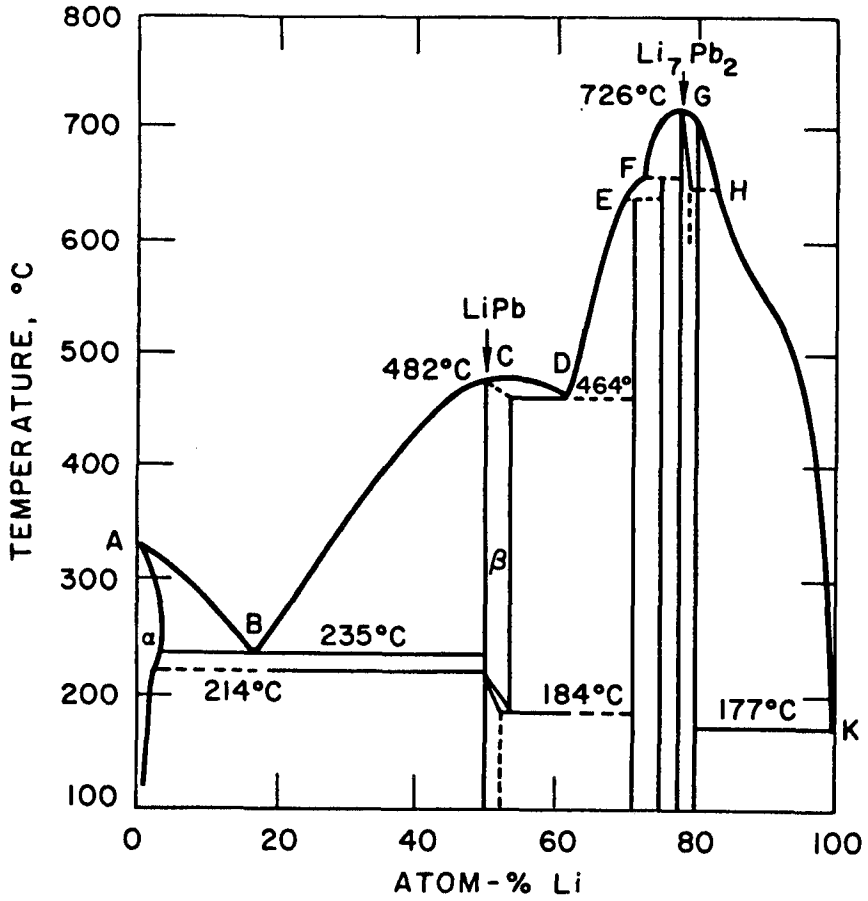


Figure 6.4-2. Phase diagram of LiPb.

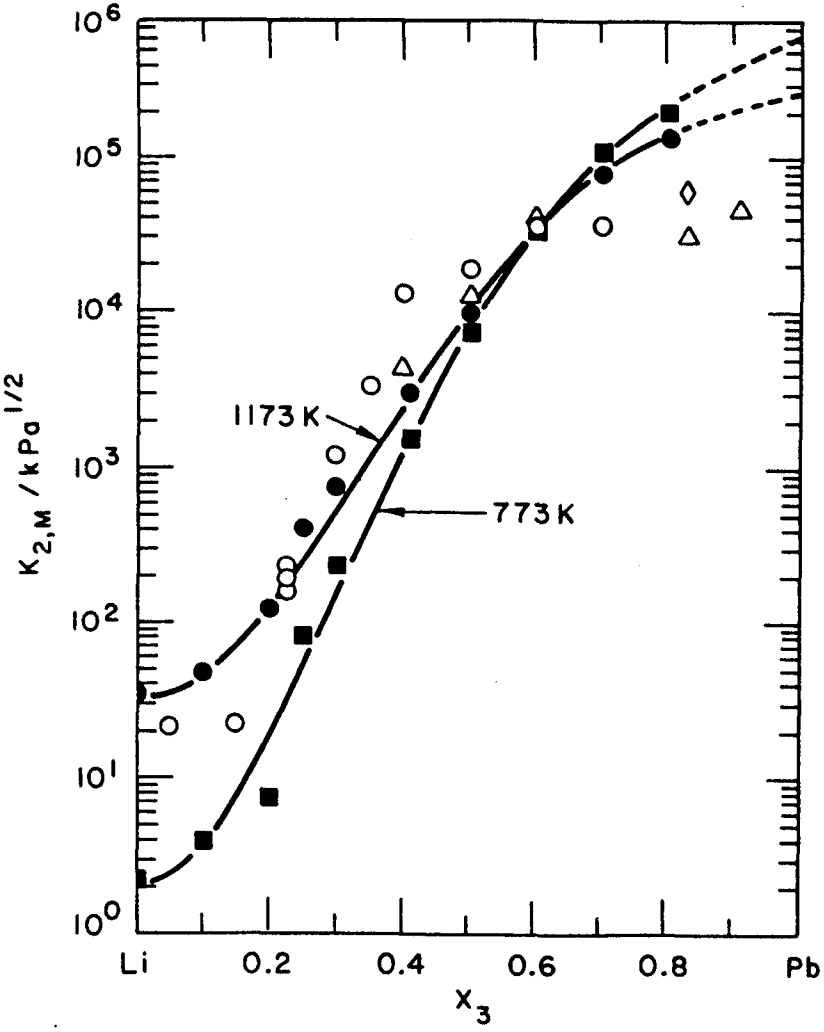


Figure 6.4-3. Sievert's constants for solutions of hydrogen isotopes in liquid LiPb alloys.

lithium (a_{Li}) in 17Li-83Pb can be represented in the following form as a function of the absolute temperature,[6.4-16] i.e.,

$$\ln a_{Li} = -6960/T + 0.0245 \quad . \qquad [6.4\text{-}1]$$

Thus, the lithium activity in 17Li-83Pb is estimated to be about 1×10^{-4} at 750 K. This is an extremely low value, four orders of magnitude lower than that of pure lithium, and it is reasonable to expect that the chemical reactivity of lithium and related safety concerns will be markedly reduced. The chemistry in many respects may be expected to be more similar to that of lead than of lithium. However, the thermodynamic stability of lithium compounds with non-metallic elements (e.g., H, O, N, etc.) is very high and despite the low activity, lithium effects can be significant. The activity of lead can be calculated from the activity of lithium by using the Gibbs-Duhem equation.[6.4-13] A typical curve of activity coefficient of LiPb is reproduced from Ref. 6.4-14 and shown in Fig. 6.4-4. Since $P_n = (rx)P_o = aP_o$ in which

P_n is partial pressure of the material

r is the activity coefficient

x is the mole fraction

a is the activity

P_o is the pressure of the pure material,

the partial pressure of lithium and lead can be calculated from the information of activity. Furthermore, on the lead rich end of the phase diagram, the vapor phase is dominated by lead and, as a first approximation, the vapor pressure of LiPb can be taken the same as that of lead.

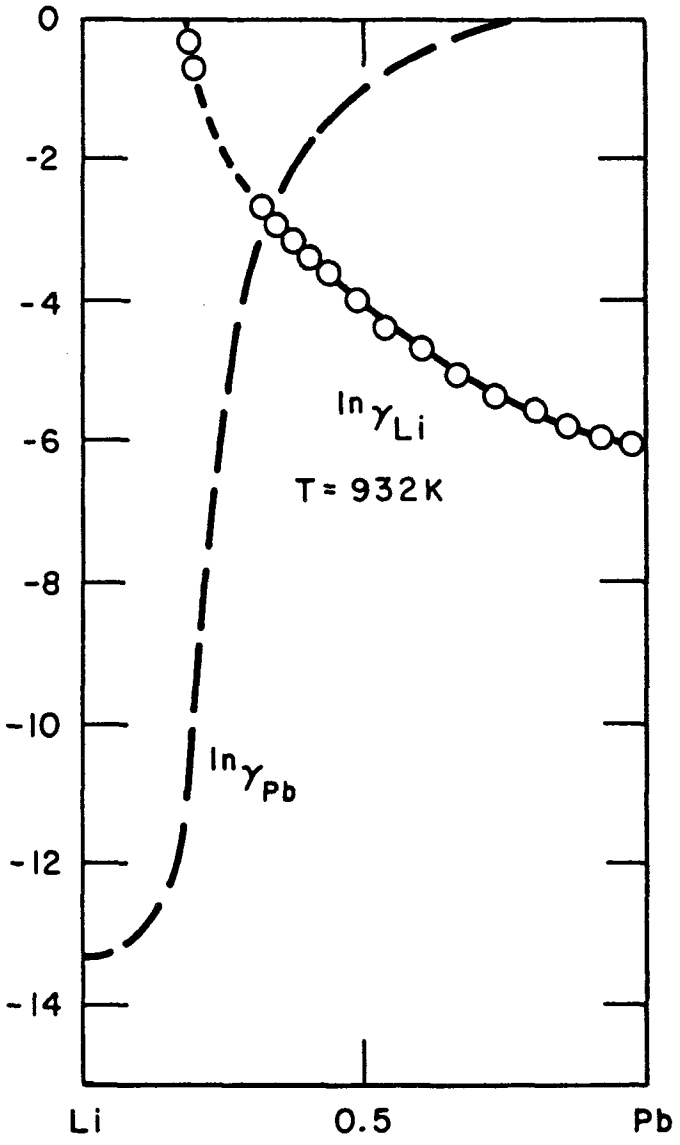


Figure 6.4-4. Activity coefficients for Li and Pb.

The density and thermal expansion coefficient of liquid LiPb has been measured[6.4-17] and the data are shown in Fig. 6.4-5. The results appear to be accurate. The density of solid LiPb has also been reported.[6.4-6]

The electrical conductivity of solid LiPb[6.4-6] and the electrical resistivity of liquid LiPb[6.4-18] have been reported as shown in Figs. 6.4-6 and 6.4-7. The data accuracy is uncertain.

The specific heat at constant pressure (C_p), enthalpy (ΔH), and entropy (ΔS) of 17Li-83Pb have been measured[6.4-19] and listed in Table 6.4-6 as a function of temperature. The latent heat of fusion obtained from these data is 29.59 J/g. The variation of specific heat with temperature is also shown in Fig. 6.4-8.

TABLE 6.4-6. THERMODYNAMIC PROPERTIES OF 17Li-83Pb

T(K)	C_p(J/g K)	ΔH (J/g)	ΔS (J/g K)
298.15	0.1372	0.00	0.0000
313.15	0.1369	2.06	0.0072
333.15	0.1432	4.88	0.0160
353.15	0.1473	7.79	0.0244
373.15	0.1519	10.79	0.0326
393.15	0.1569	13.87	0.0407
413.15	0.1625	17.05	0.0486
433.15	0.1685	20.36	0.0564
453.15	0.1750	23.82	0.0642
473.15	0.1820	27.47	0.0719
493.15	0.1895	31.36	0.0796
507.90	0.1953	34.40	0.0843
507.90	0.2504	63.99	0.1426
513.15	0.2438	65.32	0.1455
533.15	0.2172	70.07	0.1542
553.15	0.1886	74.18	0.1616
573.15	0.1580	77.45	0.1677

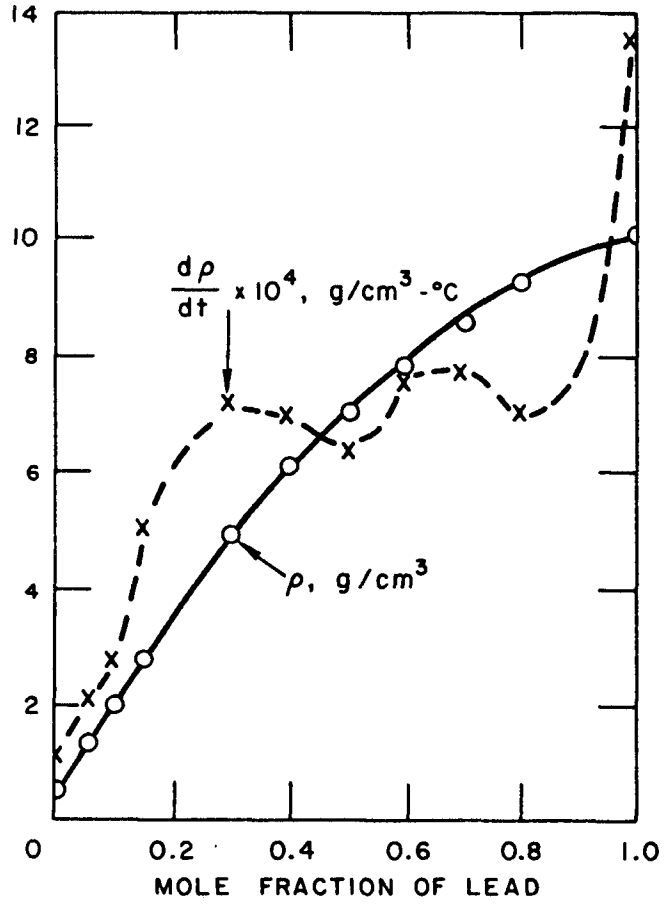


Figure 6.4-5. Density and thermal expansion coefficient of LiPb at liquidus temperature.

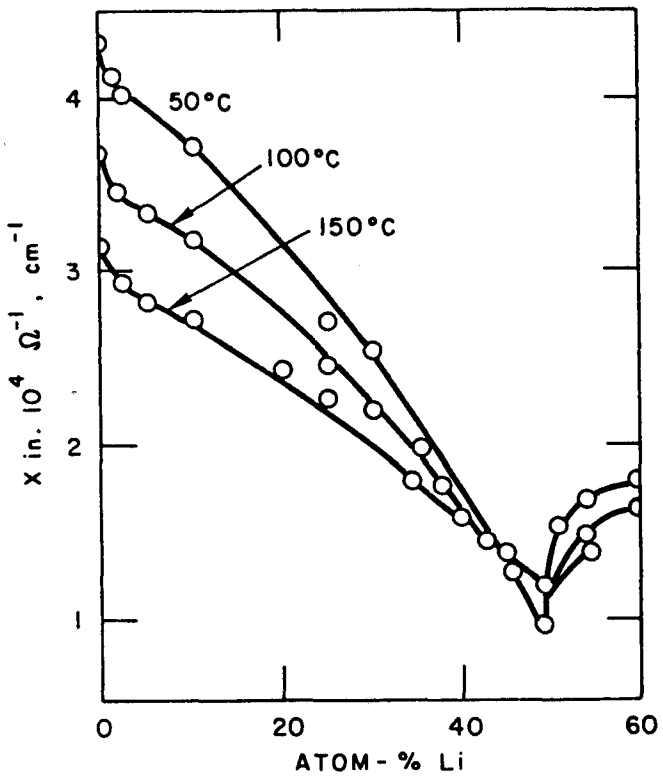


Figure 6.4-6. Electrical conductivity of LiPb.

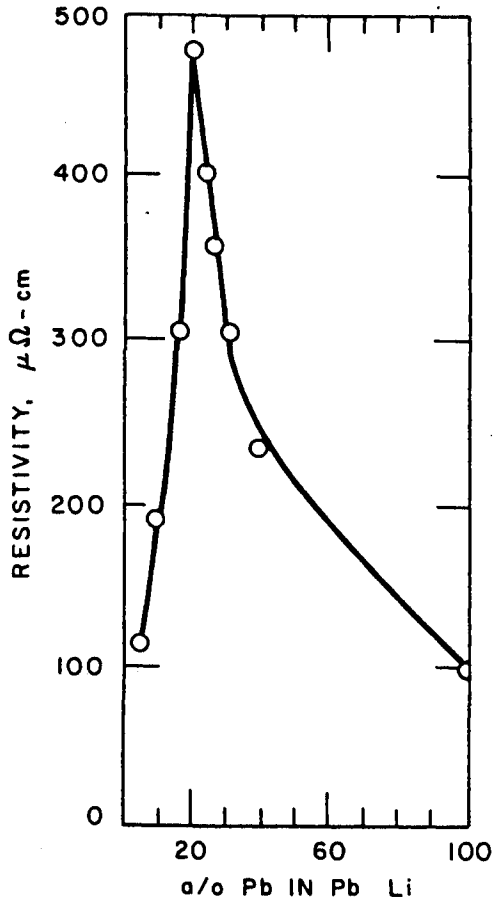


Figure 6.4-7. Electrical resistance of LiPb at 800°C.

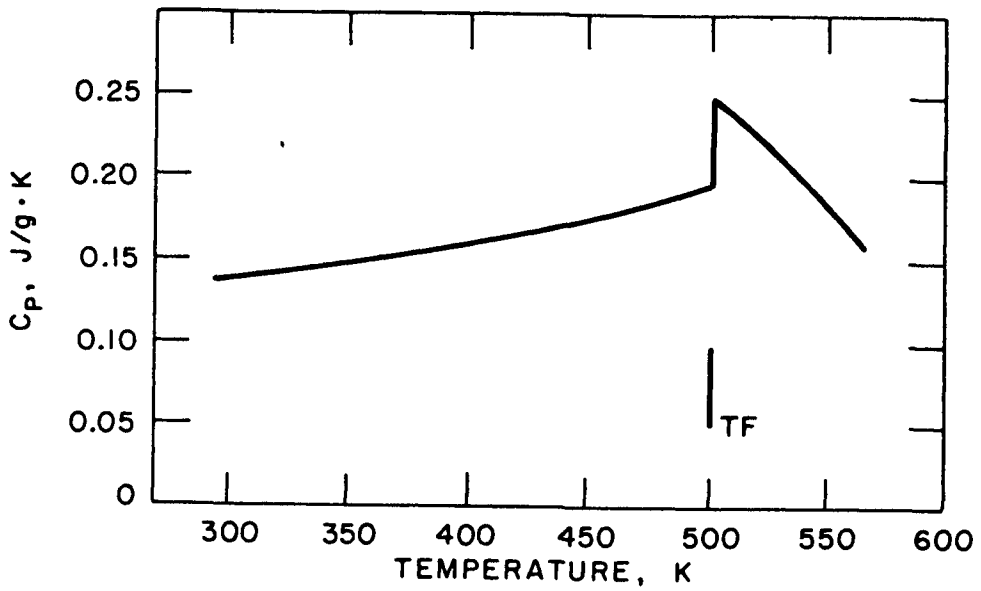


Figure 6.4-8. Specific heat (Cp) of 17Li-83Pb as a function of temperature.

In summary, the material properties data base of 17Li-83Pb has been built up over the past two years. However, much of the important information (Table 6.4-5) is still unavailable. The accuracies of the available data, with a few exceptions, are uncertain.

6.4.3 FLIBE Properties

$LiF-BeF_2$ salt mixtures (FLIBE) have several attractive properties:

- relatively noncorrosive,
- chemically stable in air and water environments,
- low vapor pressure, and
- small density change on melting.

The disadvantages relative to current fusion reactor concepts include:

- relatively high melting point (>360°C), and
- the possibility of magnetic field induced galvanic corrosion.

The minimum liquidus temperature in the $LiF-BeF_2$ system is 363°C and occurs at 53 mole % BeF_2. The 66% LiF-34% BeF_2 mixture, which was used in the Molten Salt Reactor Experiment (MSRE), solidfies at 460°C forming the compound $2LiF \cdot BeF_2$. The principal impurities in this salt are[6.4-20] Cr (<19 wppm), Fe (<166 wppm), and Ni(<26 wppm).

6.4.3.1 Thermophysical Properties

Density-temperature curves for the 53% (Fig. 6.4-9) and 34% BeF_2 (Fig. 6.4-10) mixtures were based on experimental data for the liquid

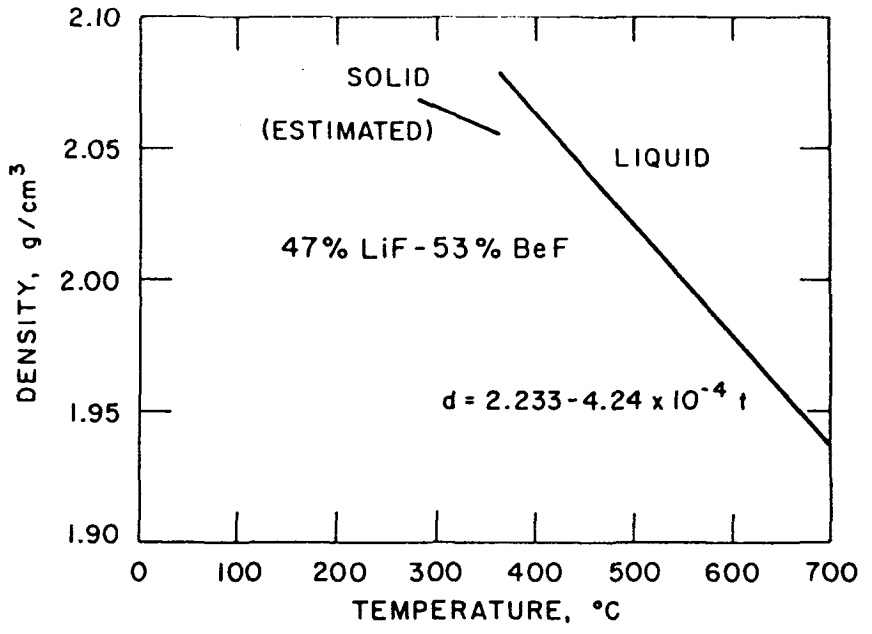


Figure 6.4-9. Density of FLIBE (47% LiF-53% BeF_2) as a function of temperature.

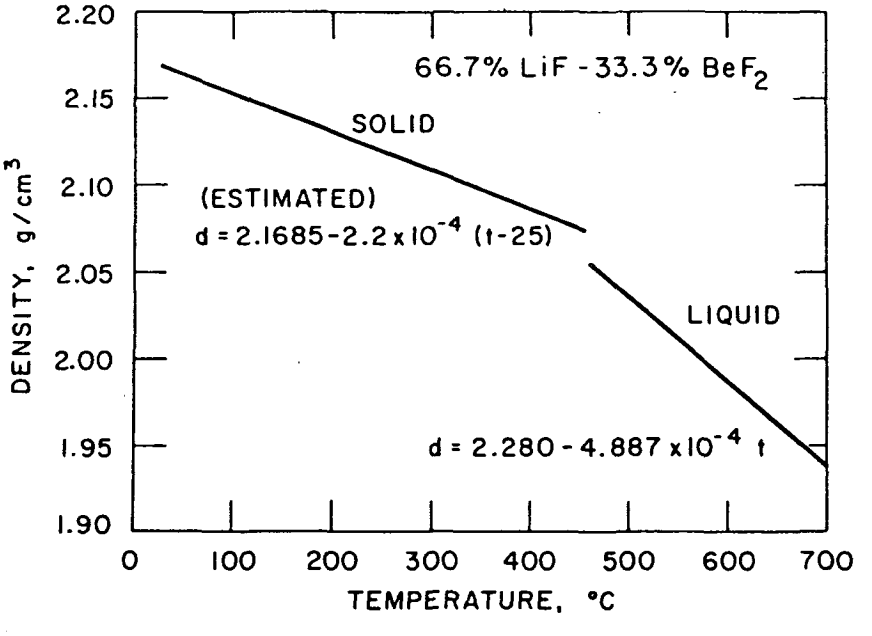


Figure 6.4-10. Density of FLIBE (66.7% LiF-33.3% BeF_2) as a function of temperature.

state[6.4-21,6.4-22] and assumed (1) the expansion coefficient of crystalline (solid) $2LiF \cdot BeF_2$ is the same as crystalline LiF (1×10^{-4}/°C), and (2) the density of solid 53% BeF_2-47% LiF is the sum of the densities of 70% $2LiF-BeF_2$ and 30% BeF_2. The viscosities of the two reference $LiF-BeF_2$ salt mixtures[6.4-22] are plotted against temperature in Figs. 6.4-11 and 6.4-12. Additional thermophysical properties are listed in Table 6.4-7.

TABLE 6.4-7. PHYSICAL PROPERTIES OF FLIBE SALTS (REFS. 6.4-23 AND 6.4-24)

Composition - Li:Be (mole %)		47-53	66-34
Melting Point (°C)		363	460
Specific Conductance K (Ω^{-1} cm^{-1})			
Temperature (°C)	400	0.27	---
	500	0.61	1.55
	600	1.02	2.14
	700	1.49	2.73
Heat Capacity, C_p (J/g°C)		2.35	2.38
Thermal Conductivity, λ (W/m°C)		0.8	1.0
Heat of Fusion (J/g)		480	448
Surface Tension (N/m)			
Temperature (°C)	600	---	0.2

6.4.3.2 High-Temperature Stability

UF_4-containing mixtures of $LiF-BeF_2$ have operated under heat transfer conditions for extended periods up to 1000°C with no evidence of chemical or physical degradation. Extended operation in high radiation fields has resulted in no measurable gas buildup or other evidence of radiolytic decomposition. Because of the high binding energy, the electric potential required to dissociate pure $2LiF \cdot BeF_2$ is high relative to other molten salts. For

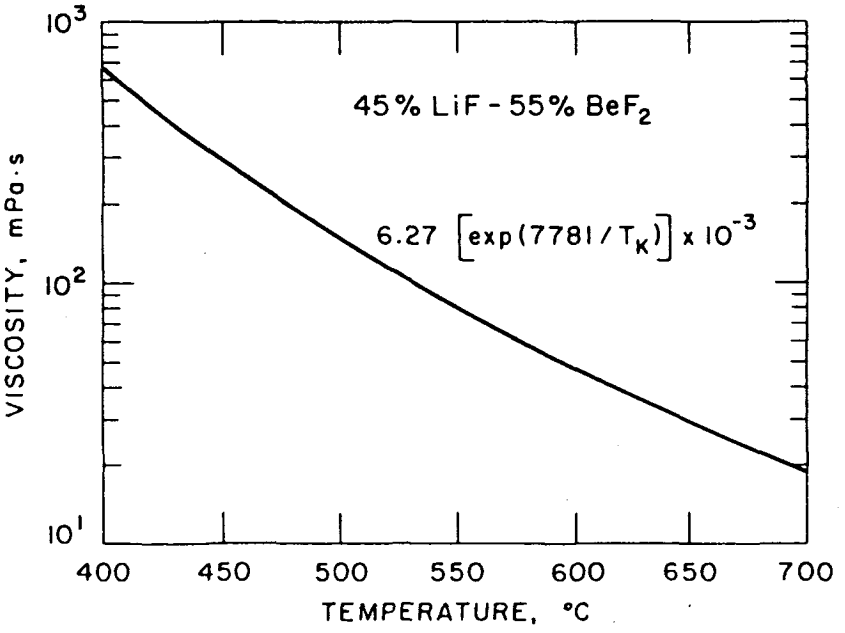


Figure 6.4-11. Viscosity of FLIBE (45% LiF-55% BeF_2) as a function of temperature.

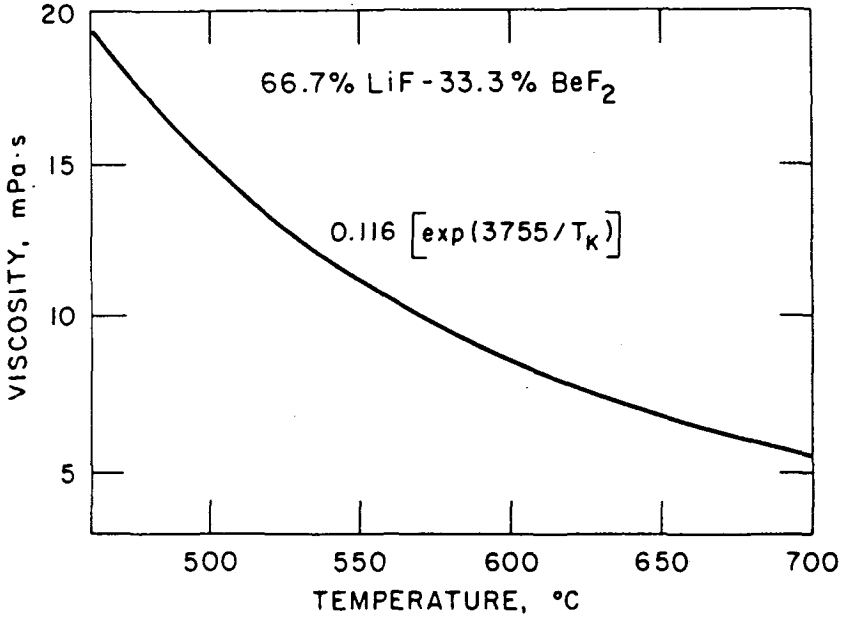


Figure 6.4-12. Viscosity of FLIBE (66.7% LiF-33.3% BeF_2) as a function of temperature.

example, at 600°C, to reduce the salt to beryllium metal and fluorine at 1 atm requires a potential of 4.72 volts, and to reduce LiF to lithium metal and fluorine at 1 atm requires 5.55 volts. However, impurity cations such as Fe^{2+} and Ni^{2+} can be reduced at potentials as low as 2.5 volts.

6.4.3.3 Corrosion Properties

The corrosion of austenitic or ferritic stainless steel by relatively pure LiF-BeF_2 mixtures occurs by selective removal of chromium from hot-leg surfaces and chromium deposition at cooler surfaces. The mass transfer of chromium results from reaction with trace contaminants normally present in the salt. Using the salt purification practices developed for the Molten Salt Reactor Experiment (MSRE), corrosion rates of 316 stainless loops containing the 2LiF-BeF_2 mixture under heat transfer conditions at 650°C average about 8 μm/year. Although relatively low, such rates would begin to degrade the mechanical properties of thinner blanket module sections after approximately one year.(6.4-25) However, these rates can be lowered significantly by (1) chemically buffering the salt and (2) reducing the chromium concentration of the steel. For example, by periodically contacting the salt with a beryllium rod, the corrosion rate of 316 stainless steel at 650°C was reduced from 8 to 2 μm/year.(6.4-26) Alloys low in chromium have been developed specifically for molten fluoride salt containment. Hastelloy N, the alloy adopted for the MSRE, showed no measurable corrosion by 2LiF • BeF_2 in four years of reactor operation. Such alloys can be used effectively outside regions of high neutron fluence at temperatures well above 700°C. Ferritic (Cr-Mo) alloys are also relatively corrosion resistant providing chromium levels are kept below ~10 wt %. For example, a maraging steel (12%Ni-5%Cr-3%Mo-balFe) tested in the MSRE fuel salt for 5700 h at 662°C had a corrosion rate 1/2 that of 304L stainless steel at the same loop position.(6.4-25)

Charge separation produced by movement of ionic substances across magnetic field lines can affect both the free energy change and kinetics of corrosion reactions. The magnitude of charge separation (Lorentz forces) in molten salts is a function of the piping cross section and flow velocity. Thus, the effect of magnetic fields on corrosion cannot be quantitatively assessed without a definitive blanket design, but the problem can be minimized

by developing low impedance flow channels and maintaining low flow rates perpendicular to field lines.

6.4.4.4 Tritium Chemistry

Tritium can be contained in FLIBE both in the reduced form, as T_2, and in the oxidized state, as TF. At equilibrium the concentration of TF is directly proportional to the fluoride ion activity and to the half power of the T_2 pressure. Using the concentration of doubly-oxidized iron in the salt as an index of the fluoride ion activity, Fig. 6.4-13 shows the relative concentrations of T_2 and TF at equilibrium at 600°C in the mixture $2LiF \cdot BeF_2$. At a tritium pressure of 1 atm, the maximum concentration of TF (T^+) that can be contained in $2LiF \cdot BeF_2$ in equilibrium with an iron-based alloy is approximately 10^{-5} mole fraction. The corresponding T_2 concentration is approximately 10^{-6} mole fraction. Under more reducing (less corrosive) conditions (i.e., $\sim 10^{-5}$ mole fraction Fe^{++}) the maximum TF concentration (mole fraction) reduces to approximately 10^{-7} at a tritium pressure of 1 atm and to approximately 10^{-10} at a 1 millitorr (1.3×10^{-6} atm) tritium pressure. The corresponding mole fractions of dissolved T_2 are 10^{-6} and 10^{-12}, respectively. (The UF_4/UF_3 ratio maintained in the MSRE translates to a 10^{-3} mole fraction of Fe^{++}.) These extremely low concentrations emphasize the low solubility of tritium in FLIBE and the need to rapidly process tritium from the salt to avoid high T_2 pressures.

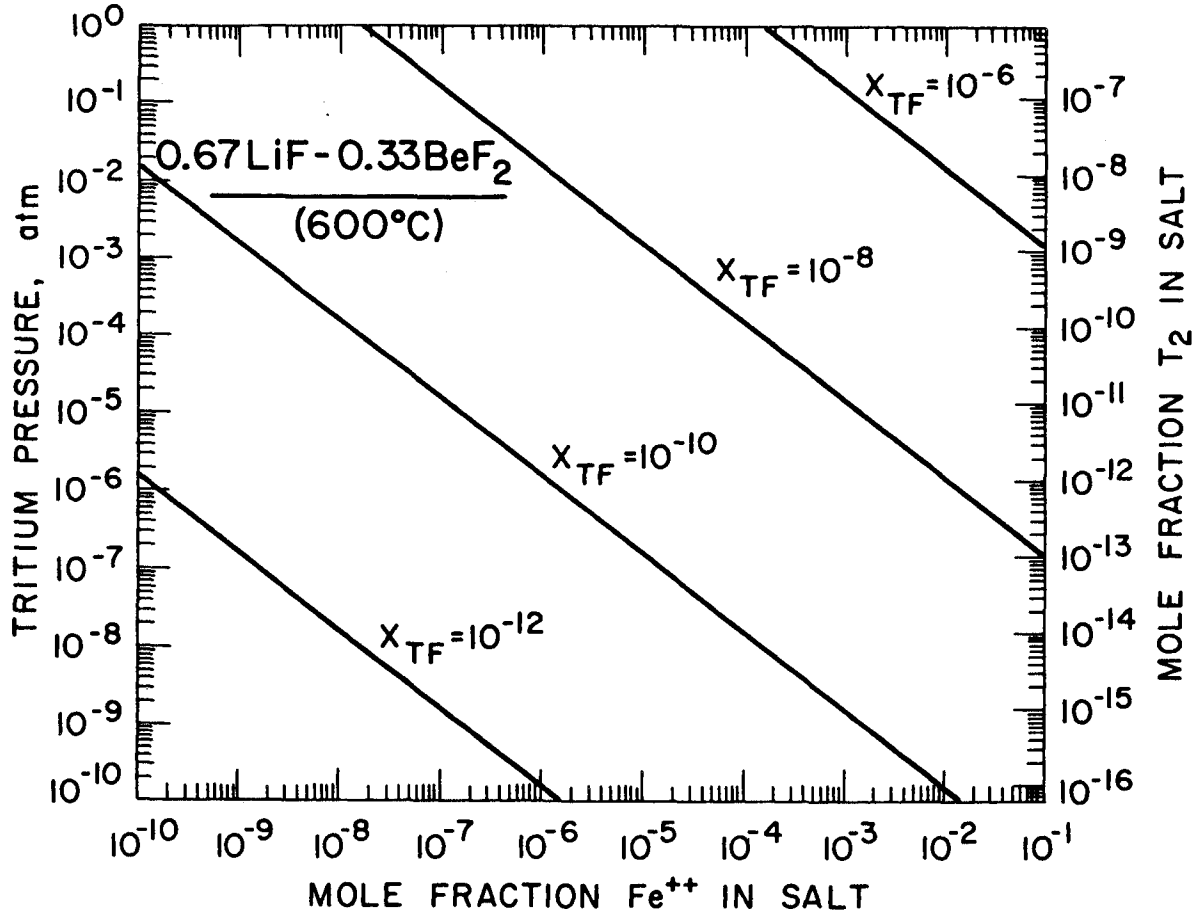


Figure 6.4-13. Equilibrium concentrations of TF and T_2 in the mixture of $2LiF \cdot BeF_2$ at 600°C.

REFERENCES FOR SECTION 6.4

6.4-1 M. Abdou et al., Argonne National Laboratory Report, ANL/FPP-83-1, Vol. 1, Chap. V, October 1983.

6.4-2 D. W. Jeppson et al., Hanford Engineering Development Laboratory Report, HEDL-TME-78-15, UC-20, April 1978.

6.4-3 Letter, D. L. Smith (ANL) to J. W. Davis (MDAC), February 8, 1983.

6.4-4 Materials Handbook for Fusion Energy Systems, Department of Energy Report, DOE/TIC-10122, April 1980.

6.4-5 J. W. Mansteller, Alkali Metal Handling and System Operating Techniques, p. 221.

6.4-6 G. Grube and H. Klaiber, Z. Electrochem 40, 745 (1934).

6.4-7 N. A. Frigerio and L. L. LaVoy, "The Preparation and Properties of LiPb, A Novel Material for Shields and Collinators," Nuclear Technology, 10, p. 322, March 1971.

6.4-8 V. Coen, Ispra, Italy, private communication.

6.4-9 E. Veleckis, ANL, private communication.

6.4-10 C. H. Wu and A. J. Blair, "A Study of the Interaction of Tritium with Liquid 17Li-83Pb," Proceedings of 12th Symposium on the Fusion Technology, Julich, Germany, September 1982.

6.4-11 G. Pieriui et al., "Tritium Recovery from 17Li-83Pb," Proceedings of the 12th Symposium on the Fusion Technology, Julich, Germany, September 1982.

6.4-12 H. Ihle, A. Neubert and C. H. Wu, "The Activity of Lithium, and the Solubility of Deuterium, in Liquid-Lead Alloys," EURATOM Conf., 9th Symp. on Fusion Technology, September 1978, Ispra, Italy.

6.4-13 M. L. Saboungi, J. Marr, and M. Blander, "Thermodynamic Properties of a Quasi-Ionic Alloy from Electromotive Force Measurements - The LiPb System," J. Chem. Phys. 68 (1978), 1375-1384.

6.4-14 A. I. Demidov, A. G. Morachevskii, and L. N. Gerasimenko, "Thermodynamic Properties of Liquid Lithium-Lead Alloys," Sov. Electrochem. 9 (1973), 813-814.

6.4-15 S. P. Yatsenko and E. A. Saltykova, "Thermodynamic Properties of Liquid Lithium-Lead Alloys," Russ. J. Phys. Chem. 50 (1976), 1278.

6.4-16 M. Ortman, University of Wisconsin, private communication.

6.4-17 H. Ruppersburg and W. Speicher, Z. Naturforsch A 31A, 47 (1976).

SECTION 6.5

TABLE OF CONTENTS

PAGE NO.

6.5 Special Materials.....6.5-1
6.5.1 Neutron Mutipliers (Be Only).....6.5-1
6.5.1.1 Trace Impurities.....6.5-2
6.5.1.2 Irradiation Effects.....6.5-2
6.5.1.3 Fabrication and Recycling Technology.....6.5-7
6.5.1.4 Design Considerations.....6.5-13
6.5.2 Electrical Insulators.....6.5-16
6.5.2.1 Candidate Materials.....6.5-18
6.5.2.2 Fabrication Technology.....6.5-18
6.5.2.3 Insulator/Liquid-Metal Compatibility.....6.5-19
6.5.2.4 Irradiation Effects.....6.5-20
6.5.3 Nitrate Salt.....6.5-21
6.5.3.1 Thermophysical Properties.....6.5-22
6.5.3.2 Thermal Stability.....6.5-23
6.5.3.3 Radiation Stability.....6.5-27
6.5.3.4 MHD Effects.....6.5-29
6.5.3.5 Tritium Chemistry.....6.5-31
6.5.3.6 Handling.....6.5-31
6.5.3.7 Corrosion Properties.....6.5-32
REFERENCES.....6.5-36

LIST OF FIGURES FOR SECTION 6.5

FIG. NO.	TITLE	PAGE NO.
6.5-1	Beryllium annual fabrication cost as a function of pebble size	6.5-12
6.5-2	Effective thermal conductivity of a mixture of sphere-pac γ-$LiAlO_2$ and Be	6.5-15
6.5-3	Bare beryllium rod design for the Li_2O/He/Be/HT9 blanket	6.5-17
6.5-4	Density of draw salt as a function of temperature	6.5-24
6.5-5	Electrical conductivity of draw salt as a function of temperature	6.5-24
6.5-6	Viscosity of draw salt as a function of temperature	6.5-25
6.5-7	Heat capacity of draw salt as a function of temperature	6.5-25
6.5-8	Thermal conductivity of draw salt as a function of temperature	6.5-26
6.5-9	Initial rates of weight loss of $NaNO_3$ and KNO_3 in vacuum (Ref. 6.5-19)	6.5-28
6.5-10	Potential/pO^{2-} diagram at 600 K	6.5-30
6.5-11	Stability diagram for iron in fused salt at 600 K	6.5-34

LIST OF TABLES FOR SECTION 6.5

TABLE NO.	TITLE	PAGE NO.
6.5-1	REACTION RATES (REACTIONS/MW FUSION-S) IN URANIUM AND THORIUM IMPURITIES IN BERYLLIUM	6.5-2
6.5-2	SCREENING TESTS FOR INSULATOR COATING EVALUATION	6.5-20
6.5-3	SELECTED DRAW SALT PROPERTIES AT 500°C	6.5-23
6.5-4	EQUILIBRIUM CONSTANT FOR THE OXIDATION OF NITRITE TO NITRATE (REF. 6.5-18)	6.5-27

6.5 Special Materials

Subsections in 6.5 include three topics: neutron multipliers (Section 6.5.1), low-voltage electrical insulators (Section 6.5.2), and nitrate salts (Section 6.5.3). The first two subjects were covered in the BCSS interim report[6.5-1]; only updates/additions will be given, with emphasis on areas which have not been addressed adequately before. For neutron multipliers, only beryllium is treated in more depth. Trace impurities in Be are specified in Section 6.5.1.1 which are used in the activation/waste management analysis (Section 6.12). Irradiation effects on Be, most notably swelling caused by retained helium gas bubbles, are discussed along with oxidation and tritium retention (Section 6.5.1.2). Since beryllium is resource limited, recycling technology of irradiated Be (Section 6.5.1.3) is a key area that needs to be addressed. Finally, design considerations for incorporating beryllium into the BCSS blankets are discussed. These include γ-$LiAlO_2$/H_2O/Be, γ-$LiAlO_2$/DS/Be, γ-$LiAlO_2$/He/Be, and FLIBE/He/Be.

Low-voltage electrical insulators for reducing MHD effects in liquid-metal cooled blanket concepts are evaluated in Section 6.5.2. Fabrication technology (Section 6.5.2.2), insulator/liquid-metal compatibility (Section 6.5.2.3), and irradiation effects (Section 6.5.2.4) are assessed for several candidate materials.

Section 6.5.3 covers nitrate salt which is used as coolant for the BCSS salt-cooled blanket concepts (Chapter 10). Topics included are thermophysical properties (Section 6.5.3.1), thermal stability (Section 6.5.3.2), radiation stability (Section 6.5.3.3), MHD effects (Section 6.5.3.4), tritium chemistry (Section 6.3.5.5), handling (Section 6.3.5.6), and corrosion properties (Section 6.3.5.7).

Research and development (R&D) assessment for the three special materials is done at the end of each subsection. Based on this assessment, a summary of R&D needs and priorities is given in Chapter 4.

6.5.1 Neutron Multipliers (Be Only)

The use of beryllium as neutron multiplier for a solid breeder blanket has been discussed in the STARFIRE report.[6.5-2] Aside from its neutronic properties, beryllium was chosen as the reference neutron multiplier for

STARFIRE because it combines the lowest density with the highest specific heat and thermal conductivity of all the candidate materials. The two main concerns for beryllium are the irradiatin-induced swelling and resource limitation. Both concerns will be discussed below, along with trace impurities and design considerations.

6.5.1.1 Trace Impurities

The impurities in beryllium vary with different ore sources and different processing. Impurity contents used in the activation analysis of Be (Section 6.12) are typical, but they are in general specification maxima rather than actual assays. The beryllium produced from the U.S. ores typically contains 0.007 w/o and 0.0002 w/o of uranium and thorium, respectively. Lee of LLNL has computed the neutron-impurity reactions expected for a 20 cm Be zone. The results are given in Table 6.5-1. These represent concerning concentrations that are 2 to 3 orders of magnitude below the level of waste management or remote handling.

TABLE 6.5-1 REACTION RATES (REACTIONS/MW FUSION-S) IN URANIUM AND THORIUM IMPURITIES IN BERYLLIUM

Reaction	U-235	U-238	TH
(n,fiss)	2.5×10^{12}	1.8×10^{12}	1.6×10^{11}
(n,2n)	3.9×10^{9}	1.2×10^{12}	4.6×10^{11}
(n,γ)	8.9×10^{11}	2.0×10^{14}	2.2×10^{13}

6.5.1.2 Irradiation Effects

Both helium and tritium are generated in beryllium via the following reactions with neutron:(6.5-3)

(n,2n) - threshold energy 2.7 MeV

$$n + {}^{9}Be \rightarrow n + n + {}^{8}Be \begin{array}{l} \nearrow \\ \searrow \end{array} \begin{array}{l} , \\ 2\,{}^{4}He + 94 \pm 1.3 \text{ keV} \end{array} \quad \begin{array}{l} \\ <2 \times 10^{-15} \text{ s} \end{array} \qquad [6.5\text{-}1]$$

(n,α) - threshold energy 0.71 MeV

$$n + {}^{9}Be \rightarrow {}^{4}He + {}^{6}He \quad . \qquad [6.5\text{-}2]$$
$$\beta^- \downarrow \; 0.85 \pm 0.02 \text{ s}$$
$$^{6}Li$$

The ^{6}Li then captures low-energy neutrons via

$$n + {}^{6}Li \rightarrow {}^{4}He + {}^{3}T \quad , \qquad [6.5\text{-}3]$$
$$\beta^- \downarrow \; 12.5 \text{ yr}$$
$$^{3}He$$

and the latter ^{3}He isotope has a thermal neutron cross section of 5400 b with the (n,p) reaction,

$$n + {}^{3}He \rightarrow {}^{3}T + p \quad . \qquad [6.5\text{-}4]$$

In its use as a neutron multiplier in solid breeder blankets, beryllium is generally not perceived as a load bearing material. Various forms (e.g., slabs, spheres, pebbles, rods) of beryllium have been proposed for incorporation into solid breeder blankets, with or without structural containment. The key issue regarding beryllium performance is the irradiation-induced swelling caused by retained helium gas bubbles. If a containment structure is used with adequate internal volume (~30%) provided for swelling accommodation, there would be no loss of beryllium functional capability even in the event of massive swelling and/or loss of physical integrity (i.e., via cracking). A containment/Be-slab (70% TD) approach was recommended for STARFIRE,[6.5-2] as well as in the interim BCSS report.[6.5-1] Remaining issues for this approach are to choose from a sealed versus a vented containment, irradiation temperature limits, and cooling requirement. The latter design has a potential for high-temperature (up to 800°C) capability; swelling will also be less than the geometrical limit (~33% $\Delta V/V_o$) because helium release is enhanced at high temperatures. With a vented design, excessive helium gas pressure cannot buildup within the containment. Thus, the possibility of a containment failure due to gas overpressure is also remote.

As will be shown later in this section, bare beryllium spheres, rods, and pebbles (balls) have been proposed for four BCSS blanket designs, three involve γ-$LiAlO_2$ and one uses FLIBE as breeders. The apparent change in design

philosophy (i.e., from a contained structure to bare) focuses the issue on beryllium physical integrity. Regardless of blanket design specifics, there seems little doubt that in order for beryllium to be an effective neutron multiplier, it should remain at the designated location in the blanket module. The loss of physical integrity of beryllium via swelling and/or cracking is likely to obliterate that requirement, an apparently highly undesirable event.

Beryllium is a hexagonal closed pack metal with very good thermal conductivity. Consequently, beryllium is unlikely to crack owing to thermal stresses. However, the internal stresses generated by crystalline anisotropic swelling, coupled with irradiation embrittlement, may be largely responsible for the observed fractures of the low-temperature (< 120°C) irradiated beryllium reflectors.[6.5-4] The anisotropic swelling will depend strongly on texture, being worse for extruded materials.

Without specification of blanket operating scenarios, beryllium swelling cannot be accurately predicted because of the complex dependency of swelling on fluence, temperature, and helium bubble morphology. Volumetric swelling of beryllium can vary from 5 to 33% $\Delta V/V_o$, depending upon whether it contains enough helium (fluence dependent), and whether helium bubbles chiefly reside along grain boundaries or within grains. Under relatively high-temperature (>650°C) irradiation, for example, helium atoms/bubbles can migrate more easily to grain boundaries (due to enhanced helium diffusivity with increasing temperature); they will eventually form interconnected grain-edge tunnels to vent the gases. Intergranular grain-boundary bubble behavior will dominate in this case, with a swelling less than 5-12% ($\Delta V/V_o$). Overall swelling cannot exceed these values because the driving force for swelling (i.e., helium gases) is lost after grain-edge tunnel formation.

Under low-temperature (<650°C) irradiation, helium atom diffusion will be relatively slow so that bubbles tend to stay within grains and remain small, isolated and dispersed. Intragranular bubble behavior will dominate in this case and swelling should have an approximately linear fluence dependence. However, if temperature excursions occur during blanket operation such that the helium-containing beryllium experiences rapid overheating, massive swelling (up to 33% $\Delta V/V_o$) can develop similar to those observed in the post-irradiation annealing experiments.[6.5-5] Swelling will cease at ~33% $\Delta V/V_o$, at which point the bubbles within grains will grow to touch one another to

form interconnected porosities. Once these interconnected porosities form within grains (as opposed to along grain boundaries), gas is vented and swelling stops.

Both inter- and large intragranular helium-induced swelling weaken the beryllium metal. Mechanical loads and/or coolant-induced flow vibrations may induce fracture of bare beryllium when it experiences grain boundary swelling of 5-12% $\Delta V/V_o$ and/or grain matrix swelling of 33% $\Delta V/V_o$. The allowance of a 30% internal porosity in the containment/Be-slab (70% TD) approach may be conservative (i.e., too much internal volume is provided) for low temperature irradiation under normal blanket operating conditions. However, the conservatism can be justified in view of the uncertain blanket operating scenarios (namely temperature transients or accidents). For high-temperature irradiation, 15% internal porosity is probably more than adequate to accommodate grain boundary swelling.

Besides swelling, three other considerations, vaporization, oxidation, and tritium release are also necessary in selecting an upper irradiation temperature limit for beryllium. Vapor-phase mass transfer of beryllium may become unacceptable (>0.1 mm/yr) at temperatures greater than 800°C;[6.5-6] massive "breakaway" oxidation was found to occur at 850°C in an CO_2 environment.[6.5-7] Below 650°C, on the other hand, the oxides formed on either unirradiated or irradiated beryllium appeared to be protective because they are denser (i.e., smaller molecular volume) than the substrate beryllium metal.

Diffusion of tritium in beryllium is generally slow compared to other materials under normal temperatures.[6.5-8] Tritium release from beryllium may be greatly enhanced, however, upon forming interconnected porosities, either along grain boundaries or within grains. The released tritium in this case represented an extra source that should be factored into blanket tritium recovery/containment considerations.

The above discussions indicate the complex dependencies of beryllium swelling/oxidation/tritium behavior on fluence, temperature, helium bubble morphology, and blanket operating scenarios. Blanket operating scenarios must be factored into design consideration of beryllium neutron multipliers. For bare beryllium designs, grain boundary or matrix swelling is undesirable because they weaken the beryllium metal. Fracture of the weakened bare beryl-

lium can occur under external loads that normally would not produce fracture. Furthermore, bare beryllium fracture caused by anisotropic swelling is another possibility. In this regard, a frequently used term "differential swelling induced stresses" needs clarification. This term is often applied to emphasize the significance of beryllium swelling, yet the supporting argument is really of questionable nature. Very often a thermal-stress analogy was used to obtain stresses in beryllium by equivalence of differential swelling to differential thermal expansion, i.e., gradient induced stresses from the compatibility requirement. The analogy is inadequate when one considers the nature of the two differentials; thermal expansion results from an increase (due to thermal vibrations) of atomic lattice spacings which are continuous and long range, whereas swelling results from helium gas bubbles that are dispersed in grains and along grain boundaries. The bubble spacings must be much larger than the atomic lattice dimension, and the associated stresses are most likely short range, balancing the surface tension and pressures inside gas bubbles on the one hand, and limited by the beryllium matrix flow stress on the other. The situation is very different from the compatibility stresses generated from a temperature gradient.

In summary, the predominant concerns of irradiation effects on beryllium are mainly helium-bubble induced swelling and the issue of physical integrity. Both cannot be dissociated from blanket operating scenarios. For the containment/Be-slab (70% TD) approach, beryllium physical integrity is not an issue, nor is swelling. If a vented design is chosen, the approach also has higher temperature (>650, <800°C) capability with several associated advantages. For bare beryllium (spheres, rods, and pebbles) exposed in an environment containing oxygen below 650°C, protective oxide layers are expected to form on the surface. Swelling is also expected to be less (under normal blanket operating conditions) if helium bubbles are dispersed in grains and do not grow. Should there be a temperature excursion (resulting from loss of coolant flow, for example), large matrix swelling can occur. Concurrent with this massive swelling is a massive "breakaway" oxidation which has been experimentally observed above 850°C in an CO_2 environment. Designers using bare beryllium as neutron multipliers thus need to take account of the possibility of loss of beryllium physical integrity and its consequent relocation. Some of these concerns will be addressed in the design considerations for various blanket concepts in Section 6.5.1.4.

The following information is required for beryllium as part of the R&D needs for solid breeder blanket design and performance evaluation: (1) fabrication (powder metallurgy to reduce preferred orientation, i.e., texture, high- versus low-density beryllium spheres with controlled grain size and porosity); (2) helium diffusivity as a function of temperature and porosity; (3) oxidation and compatibility; (4) irradiation damage as a function of fluence, temperature, and as-fabricated microstructure; (5) post-irradiation mechanical properties.

6.5.1.3 Fabrication and Recycling Technology

In this section the technology required to produce and recycle beryllium pebbles for a fusion blanket is described. Fabrication of other forms (e.g., rods) of beryllium is a proven technology in the aerospace industry that does not require separate discussion (except for the fabrication issues noted at the end of Section 6.5.1.2). For the beryllium pebbles, a production process is proposed below with a cost estimate and an assessment of the process development issues. The beryllium pebble lifetime considerations are discussed in Refs. 6.5-9 and 6.5-10. The lifetime of the beryllium pebbles is presently quite uncertain (two years assumed in this analysis, which is equivalent to $7 MWy/m^2$), but is, to a large extent, dependent upon the fabricated properties described below.

Requirements

Each beryllium pebble is a solid sphere of 1 cm diameter weighing 0.96g. The pebbles occupy a blanket zone of 20 cm thickness. The mass of beryllium calculated in Section 8.10.1.2 is 96 Tonnes for the tokamak and 110 Tonnes for the tandem mirror reactors. Therefore, a nominal mass of 100 Tonnes requires about 100 million pebbles for the initial inventory. For an assumed average pebble lifetime of two calendar years, the annual throughput of the beryllium fabrication/recycling plant will be 50×10^6 pebbles/yr or 50 MT/yr. However, with efficient recycle, the actual beryllium requirement associated with beryllium pebble remanufacture might be 1-10% or 0.5-5 MT/yr.

Currently, the only source of Be metal in the free world is Brush Wellman. $Be(OH)_2$ is produced at a Brush Wellman mill in Delta, Utah. The Be source is a bertrandite ore which contains ~4 lbs of Be/ton. In 1982, the

mill produced approximately 270 MT of Be/yr. Brush Wellman plans to increase production by about 60% using ore (40-50 lb of Be/ton) from China to satisfy the projected needs for BeO and CuBe alloys.

In 1982, Brush Wellman converted ~27 MT/yr Be from the mill in Delta to Be metal in a plant at Elmore, Ohio. The maximum capacity of the metal production capability of the plant is estimated to be ~115 MT/yr.

Recognizing the current Be production capability, it is of interest to consider Brush's capability to expand capacity. To produce one entire beryllium inventory during a four year period (i.e., for the first commercial sized fusion plant), a beryllium requirement of 50 MT/yr would not require Brush to expand operations. For follow-on plants, Brush would have to expand operations as follows:

1. Develop a source of high grade ore (perhaps from China).

2. Expand the mill at Delta.

3. Increase the metal production capability at Elmore.

It is quite clear that the beryllium production capacity would have to be carefully coordinated with fusion blanket development to assure that a supply bottleneck does not occur.

Fabrication Process

The proposed Be pebble fabrication process involves the development of an automated line which will include operations such as cold pressing, vacuum sintering, hot forging to full density, and vacuum annealing. Brush currently uses the first three steps of this process to produce aircraft brake segments - the only difference is that the process is manually operated because current Be powder is not free flowing and, therefore, not amenable to automated operations. In order to automate this process, a free flowing Be powder is required.

The brake parts produced by Brush have properties as good or better than those given in the following:

Ultimate tensile strength	276 MPa
Yield strength	207 MPa
Elongation (%)	1

Use of a free flowing Be powder as starting materials is not expected to degrade these mechanical properties. In fact, use of some of the current Brush manufacturing processes is expected to increase both the tensile strength and elongation.

The equipment needed for production of spherical beryllium pebbles is simple: mechanical presses and powder feeders to make cold pressed compacts, automated vacuum sintering furnaces for pressureless sintering, mechanical presses for hot sizing the sintered compacts, and automated vacuum furances for annealing the forged compact.

The recycling of irradiated Be can be accomplished by vacuum melting of the hot pebbles and using an automated atomization process (modeled after the Brush Wellman process) to re-manufacture the beryllium powder prior to cold pressing. The possibility of removing the helium gas in the irradiated Be by vacuum heating is not excluded. This would result in about 30% volumetric swelling. The enlarged Be pebbles might then be pressed back into size. The entire recycling process will require provision for sheilding and remote maintainability. In addition, hooding requirements as per OSHA limits ($2\mu g/m^3$) must be maintained to limit airborne contamination. A beryllium decontamination step (e.g., electro-refining) is not assumed, but might simplify the shielding and remoting requirements.

Given a two year beryllium lifetime, and assuming an automated plant is operating 24 hours/day, 7 days/week, and 85% of the time with no rejects, the required Be pebble production rate must be 110 balls per minute. While this is a very high production rate for Be parts, it is very low for some powder metal industries (e.g., Ta capacitor manufacturers produce thousands of parts/minute). The beryllium reprocessing line is estimated to lose 7-10% of the beryllium througput, so a small feedstream is required. With a free flowing Be powder, the losses might be reduced below 1%.

As an alternative to fully densed Be, lower density parts can be made by

cold pressing and sintering. If the parts are sintered to 90% of the theoretical density, they are predicted to have 70-80% of their full-density thermal conductivity. Some 90% dense Be parts made in this manner have been tested at LLNL. These were characterized with respect to mechanical properties, porosity, etc. It is likely that the lower density parts can better accommodate irradiation-induced swelling, and consequently, possesses longer life.

Process Cost Estimate

The beryllium fabrication process components and their estimated direct costs were developed in the 1982 tandem mirror fusion breeder design study.[6.5-9] These costs, corrected for inflation to 1984 dollars, are listed below

	Process Components	Direct Cost ($M)
8	Presses with feeders	3.4
4	Sintering furnaces	1.7
4	Sizing presses	1.7
4	Annealing furnaces	1.7
4	Milling machines	1.7
	Transfer line	2.5
12	Inspection lines	4.8
	Air handling, filter, etc.	4.3
	Subtotal	21.8
	Remoting (100%)	21.8
	TOTAL	$43.6 M

The above equipment is sufficient to produce or recycle 18 million, 3 cm diameter pebbles per year, or the entire beryllium inventory of the 1982 fusion breeder in two years. The cost attributed to remoting the process is a guess pending further design work. The inspection line cost shown above anticipates that an inspection test assembly performing a relatively simple mechanical operation (e.g., a compression test) could be developed to test 1 pebble per 15 second interval for a capital cost of $400,000. Approximately 12 such assemblies could be required to inspect 18×10^6 pebbles/yr.

The above costs were adapted to the present FLIBE blanket requirements (i.e., 50 million, 1 cm diameter pebbles per year) by scaling the component costs with throughput and the characteristics parameters of the pebble (i.e., diameter, area, or volume) which drive the magnitude of a specific process and/or cost. For example, the amount of beryllium makeup and the cost of volumetric furances is assumed to scale directly with the pebble volume at a fixed process rate (pebbles/yr). Similarly, the costs of pressing, air handling systems, and plant staff (assumed to be 2 $M/yr for the 1982 blanket requirements) are assumed to scale as the pebble area at a fixed process rate. The cost of transfer lines is assumed to scale as the pebble diameter, and the cost of inspection is assumed to scale directly as the process rate (pebbles/yr). For the updated analysis, the cost of the milling machines (which would scale as the pebble diameter) was deleted as the pebbles for the molten salt blankets do not have the cut groove of the Be/Th snap ring design of Ref. 6.5-9.

The cost of beryllium fabrication as a function of the blanket pebble inventory (I in grams), lifetime (L in years), and radius (r in cm) is estimated to be

$$C(\$M/yr) = 0.13 \frac{I}{L}\left[0.221 + \frac{0.184}{r} + \frac{0.054}{r^2} + \frac{0.153}{r^3}\right] \quad . \qquad [6.5\text{-}5]$$

Figure 6.5-1 shows the annual beryllium fabrication cost as a function of pebble radius. The estimated cost assumes a total capital cost of 1.8 times the direct cost, a capital carrying charge of 15%/yr and includes a makeup of 7% of the beryllium throughput at 350 $/kg. If the beryllium loss during fabrication can be reduced from 7% to 1%, the leading term of the sum in Eq. [6.5-5] is reduced from 0.221 to 0.059. For the molten salt blanket (I = 100MT, L = 2 yr, r = 0.5 cm), the annual cost becomes 13 $M/yr. This relatively large cost represents roughly 5% of the overall annual cost. It is dominated by inspection and would be reduced to less than ~$5M/yr if the inspection lines can be eliminated.

Development Issues

The only special equipment needed for the beryllium fabrication/recycling process line is the air handling system needed to contain the Be powder. The

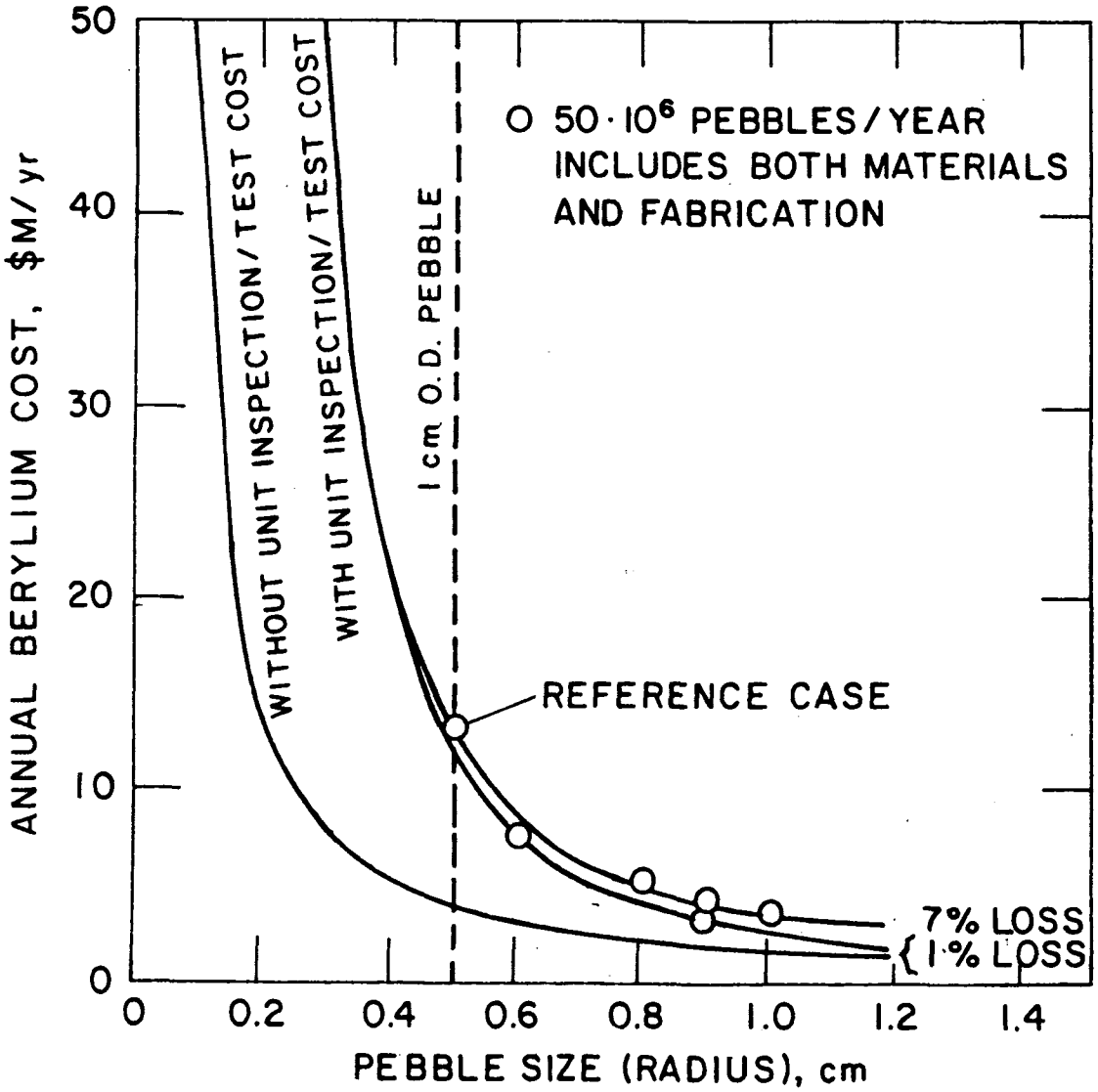


Figure 6.5-1. Beryllium annual fabrication cost as a function of pebble size.

die life should be comparable to other powder metallurgy products (500,000-1,000,000 parts/die with punches redressed every ~500,000 parts). Production of a free flowing Be powder suitable for automated operations requies further development. This might be achieved by a new powder manufacturing technique at Brush Wellman (spherical powder) or by the use of binders which can be totally removed during a bake-out prior to sintering.

Development of a pressing technique for uniformly dense spheres which can be pressureless sintered to 90-95% of theoretical density is also required. The pressed spheres must be strong enough to permit automated handling. An efficient inspection/test capability may need to be developed if an adequate process reliability cannot be achieved. The technology for remoting the fabrication process is expected to be straightforward, but further study is required.

6.5.1.4 Design Considerations

To mitigate the intense nuclear heating (~150 W/cc) near the beryllium multiplier zone in the γ-$LiAlO_2$/H_2O/Be/HT9 blanket, current sphere-pac γ-$LiAlO_2$/H_2O/HT9 design seeks a solution by dispersing beryllium spherical particles within the sphere-pac γ-$LiAlO_2$ region. Neutronics calculations (Section 6.10, Chapter 9) showed that the approach is effective when the volume fraction of γ-$LiAlO_2$ in the γ-$LiAlO_2$/Be zone is small (i.e., <0.1), thus requiring a relatively thick (~20 cm) γ-$LiAlO_2$/Be zone. Within this zone, Be is the major constituent and γ-$LiAlO_2$ the minor constituent.

For purposes of retaining high sphere-particle packing fraction and for good mixing among Be and γ-$LiAlO_2$, the same spherical particle sizes for both materials should be used, i.e., 30, 300, and 1200 μm diameters, with particle densities close to 100%. Since the diameters of these spheres are relatively small, the average diffusion path lengths for helium are 15, 150, and 600 μm to the particle surfaces. With submicron grains in these particles, the diffusion paths will be further reduced so that Be swelling should not be a major problem. However, similar to that discussed for the sphere-pac breeder fabrication (Section 6.3.1), the above statement presupposes successful fabrication of submicron grained Be spherical particles. Whether or not this will be the case remains to be demonstrated.

In the event that high-density submicron grained spherical particles cannot be easily manufactured, spherical particles of lower density (~70% TD) with interconnected porosity are favored for swelling accommodation. The interconnected porosity provides easy escape routes for helium and tritium; the release of the former reduces the driving force for swelling, the release of the latter can be handled by the blanket tritium recovery/containment systems. Neither of these two releases cause major concerns, except for the possible loss of physical integrity of the beryllium spheres.[1] Compared to bare beryllium rods in the γ-$LiAlO_2$/He/HT9 design (to be discussed later), the physical integrity issue of sphere-pac Be is of less importance because even after particle breakup, the broken particles cannot relocate far before being stopped by the surrounding spherical particles. Chances of a complete pulverization of Be spheres into very fine powders seem remote.

Estimates have been made for the effective thermal conductivity (k_{eff}) of a mixture of sphere-pac Be/γ-$LiAlO_2$. The curves shown in Fig. 6.4-2 are plotted at three helium fill-gas pressures (1, 2, and 6 atm), all at 1000 K, as a function of Be volume fraction in the mixture zone. These curves also correspond to irradiated values after 0.5 - 2.0 $\times$ 10^{26} n/m^2 (0.7 - 2.8 MW yr/m^2) fast fluence. With regard to neutron irradiation effects on k_{eff}, a 25% reduction is assumed for lattice conductivity of γ-$LiAlO_2$ at 400 K (Section 6.3.2.2), whereas no reduction is taken for Be because conduction in metals is mainly by electrons which should be affected little by irradiation.

For purposes of design calculations, it is recommended that the irradiation temperature for the sphere-pac Be/γ-$LiAlO_2$ mixture zone be kept below 650°C under normal blanket operating conditions. Thermal hydraulic design for this zone should use the recommended effective thermal conductivities given in Fig. 6.5-2.

The γ-$LiAlO_2$/DS/Be/HT9 design also uses a mixture of sphere-pac γ-$LiAlO_2$ and Be. The above design considerations for the water-cooled γ-$LiAlO_2$ blanket are, therefore, entirely applicable.

The γ-$LiAlO_2$/He/Be/HT9 designs for tokamak and tandem mirror reactors are illustrated in Figs. 8.6-1 and 8.6-2, resepctively. In order to provide adequate tritium breeding, bare beryllium rods are placed in front of the γ-$LiAlO_2$ region for neutron multiplication.

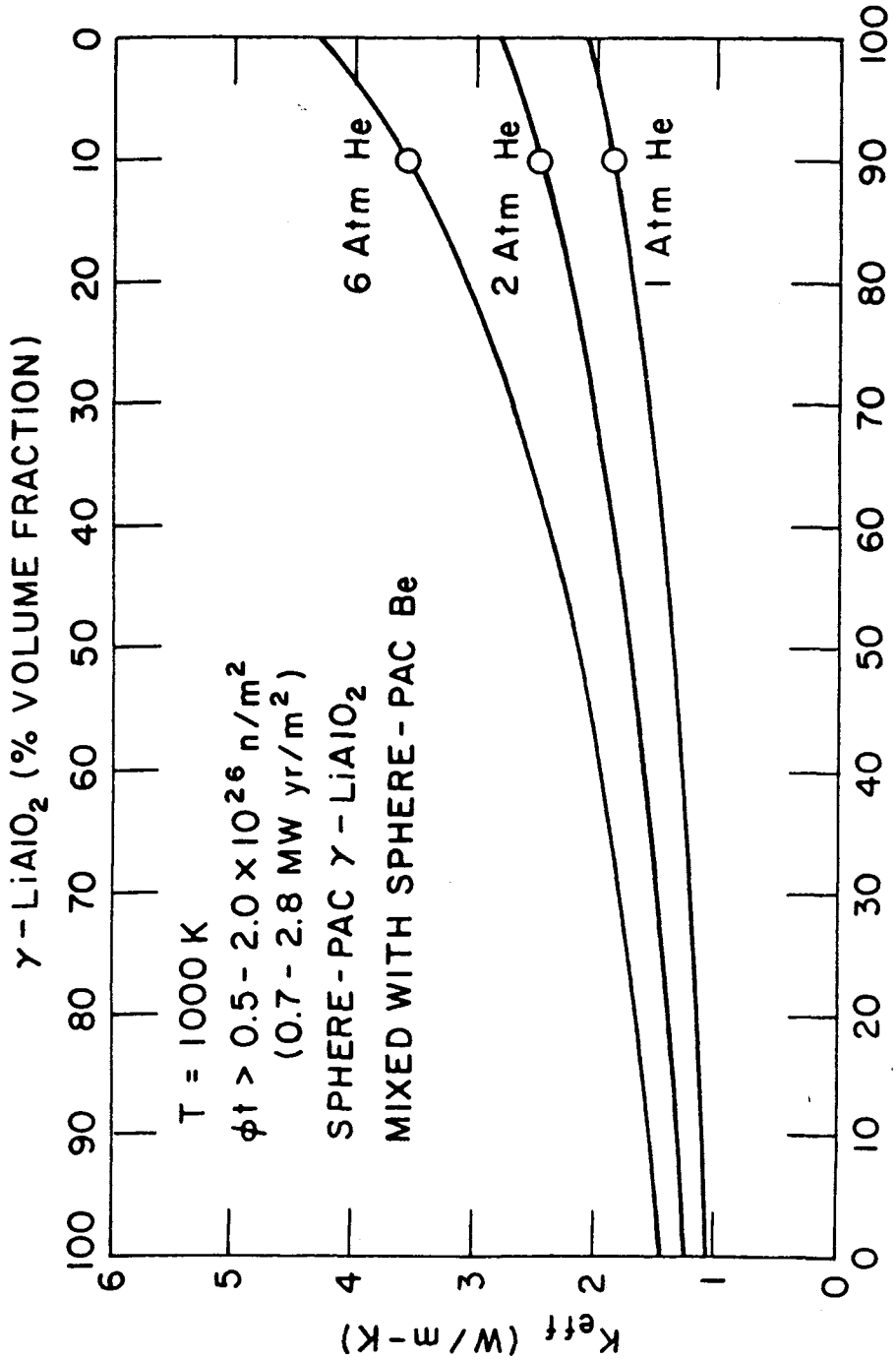


Figure 6.5-2. Effective thermal conductivity of a mixture of sphere-pac γ-$LiAlO_2$ and Be.

Figure 6.5-3 shows that the bare beryllium rods are supported by plates with partially flanged holes. The lower view of the figure shows a plot of the temperature gradient, which is fairly small across a 2 cm diameter beryllium rod having a maximum of 10°C from center which is plotted on the same view. The rods are held as shown in the upper view, and gross swelling is allowed to slide out. The support points are arranged such that the differential swelling, which produces a circular curve in the unrestrained bar, gives an equal deflection of the bar toward and away from the plasma. The swelling component, which is seen as the curvature in the swelling plot, is averaged by the curvature and a residuum of 0.03% strain is left. Thus, assuming no creep, a stress of 82.7 MPa (12,000 psi) is induced, versus a yield of 207 MPa (30,000 psi). Rods further away from the plasma see progressively less movement as shown in the center view. Although it has been stated that the above bare beryllium rod assembly is an acceptable design, the analysis is subjected to uncertainties of irradiation-induced swelling dilation and creep effects. Should the beryllium rod lose its physical integrity, such as the spallation and chips found for the low-temperature (< 120°C) irradiated beryllium reflectors,[6.5-4] the potential consequence could be coolant flow blockage and blanket temperature hot spots.

The FLIBE/He/Be design (Chapter 7) uses 1 cm diameter beryllium pebbles for neutron multiplication. The diameter of these pebbles is chosen such that they would not result in bridging (hence causing flow blockage) between the FLIBE containing tubes. Concerns for physical integrity and swelling of the bare beryllium pebbles are similar to those of the beryllium spheres used for the γ-$LiAlO_2/H_2O$/Be/HT9 blanket. No separate discussion is, therefore, needed.

6.5.2 Electrical Insulators

Magnetohydrodynamic (MHD) pressure losses are an important consideration in the design of liquid metal cooled blankets. Both MHD experiment and theory indicate that the pressure losses would be significantly reduced if high electrical resistance structural walls were used in the design. Two possible methods of achieving this benefit have been considered.[6.5-1] The first utilizes a thin insulator film on the surface of the conducting wall. Compatibility and stability of the insulator in contact with the liquid metal is a

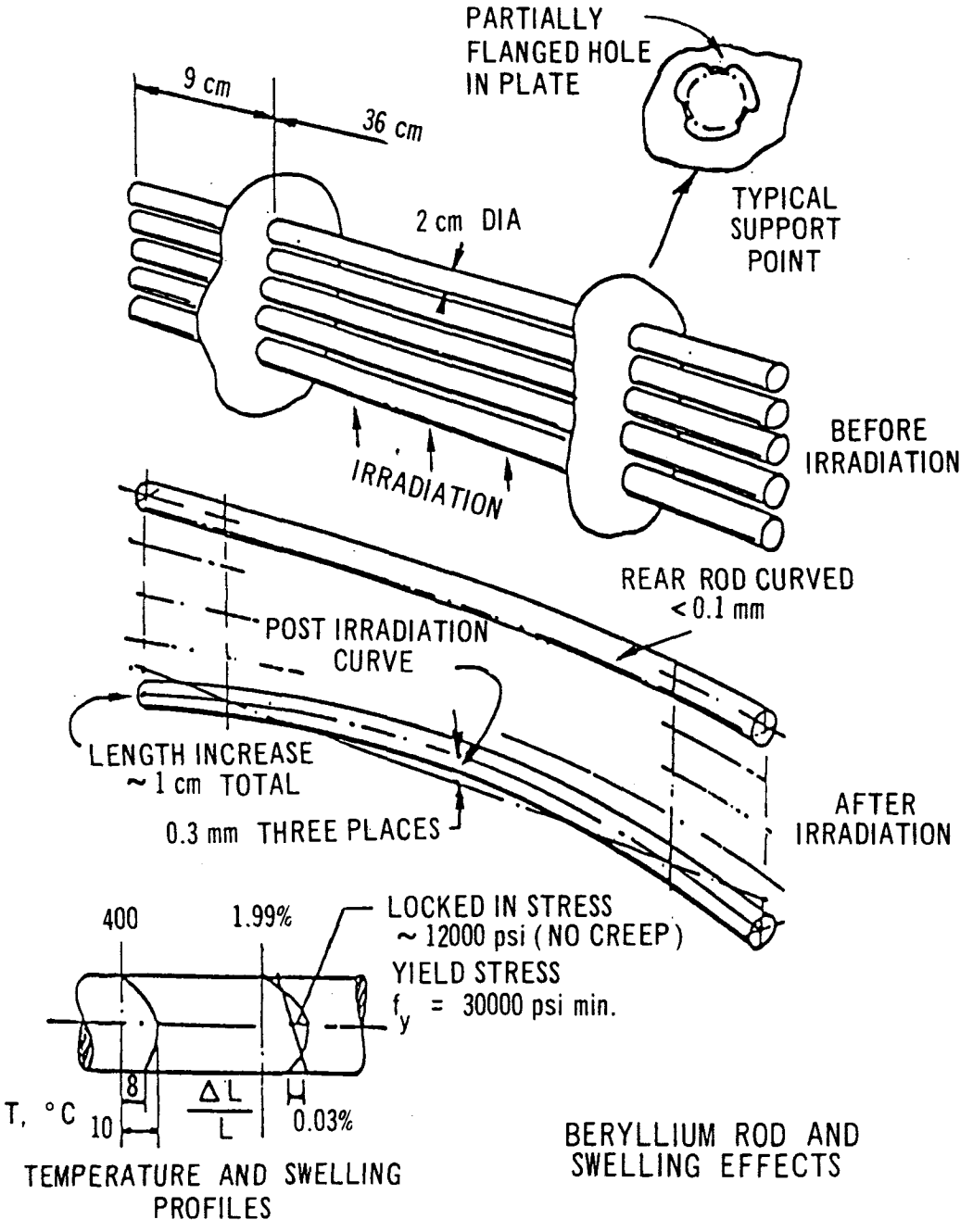


Figure 6.5-3. Bare beryllium rod design for the Li_2O/He/Be/HT9 blanket.

major concern. The second consists of a laminated structure with a thin metallic layer over an insulator layer on the wall. In this case the insulator is protected from the corrosive effects of the liquid metal coolant. However, the corrosion and mechanical integrity of the thin metal clad become more critical. In both cases radiation effects are critical, particularly for the insulator. Only low voltage (<1 volt) insulators are required in these liquid-metal blanket applications. Blanket operating temperatures (up to 550°C for PCA and HT9, 750°C for vanadium alloy) also dictate the use of inorganic insulators (i.e., dielectric solids), since plastics generally do not meet the temperature requirement. Candidate materials, fabrication technology, insulator/liquid-breeder compatibility, and radiation effects are the four subjects covered in this section.

6.5.2.1 Candidate Materials

Attempts have been made to identify possible candidate insulator materials for liquid breeder blanket application. Both oxides and nitrides have been considered. Selected nitrides e.g., TiN, ZrN, and AlN, are predicted to be thermodynamically stable in liquid lithium and Li-Pb alloy. However, the electrical resistivities of nitrides as a class are probably not sufficiently high to provide significant benefits.

Selected oxides may be acceptable for this application. Yttrium oxide (Y_2O_3) is currently being evaluated as a potential candidate. Alternate oxides that are possible candidates include scandium oxide (Sc_2O_3), calcium oxide (CaO), and spinels (e.g., $MgAl_2O_4$). Much more effort is required to fully evaluate these and any other potential candidates.

6.5.2.2 Fabrication Technology

Between the two insulator design concepts, the insulator film in direct contact with liquid breeder appears more attractive from the fabrication viewpoint. Laminated (or sandwiched) structure requires two ceramic/metal interfaces, whereas the film requires only one. If a thin film can be applied to structural surfaces that proves both electrical and corrosion resistant during blanket operation, there is an added advantage in reducing liquid-metal corrosion of the substrate metals. An associated advantage from this is the potential for higher blanket operating temperatures and higher energy conversion

efficiency. Potential payoffs in thin insulator for liquid-metal blankets are, therefore, large enough to warrant the R&D effort.

Development of protective coatings for metals date back to the turn of the century. By 1967 coating technology had advanced to a stage that various metals, organics and inorganics have all been used with a considerable amount of field experience.(6.5-11) The inorganics (i.e., ceramics, refractories) often found their use in severe environments (e.g., liners for rocket nozzles, coatings for turbine blades, etc.) with the presence of high temperatures, chemical reactions, and particle impingements.

A survey of the high-temperature coating fabrication methods showed more than a dozen possibilities: electrodeposition, electrophoresis, spraying, brushing, troweling, cementation, fluidized bed, hot dipping, vapor deposition, and various combinations thereof. Specific coating requirements and cost will dictate choice of the most suitable fabrication method for blanket insulators. Fabrication feasibility does not appear to be an issue. Typical screening tests for high-temperature coating evaluations are summarized in Table 6.5-1. Selected proof tests combining several service parameters into test conditions may also be conducted.

6.5.2.3 Insulator/Liquid-Metal Compatibility

Among the oxide insulator candidates, preliminary work is being performed for Y_2O_3. Yttrium oxide is one of the few oxides that are stable in low-oxygen lithium. Yttrium has been used as a getter for nonmetallic elements in experimental lithium loops.(6.5-12) Exposure of yttrium to relatively high purity lithium (400-600°C) results in a uniform adherent oxide film.(6.5-12) Preliminary measurements indicate that this film is highly resistive (ρ of the order of 10^8-10^9 Ω-cm).(6.5-13) In order to be effective for the proposed application it is generally conceded that a self-healing coating is required. Microcracks formed during thermal cycling, e.g., startup/shutdown, could severely degrade the effectiveness of the coating unless it would reform during operation. Typical oxygen concentrations in lithium are probably adequate for this purpose. An important concern regarding the use of yttrium is its high affinity for hydrogen (tritium). A minimal amount of yttrium should be used. Incorporating yttrium into a thin surface region of the structural alloy may be sufficient to provide the desired insulating properties.

Insulator/liquid-metal compatibility testings on other candidate insulators ($MgAl_2O_4$, SC_2O_3, CaO, etc.) in flowing Li and Li-Pb are being planned for comparison with Y_2O_3 and data base establishment.

TABLE 6.5-2. SCREENING TESTS FOR INSULATOR COATING EVALUATION

Test	Factors Evaluated
Bend Tests	Coating adhesion, ductility.
Tensile Tests	Effect of coating or processing on base material strength; ductility; elongation.
Microhardness Traverse	Cross-sectional hardness of coating and substrate; effect of processing on substrate ductility.
Thermal Cycling Sustained Load Test in Air or Static Oxidation	Effect of coating on ductility of substrate; effect of substrate creep on the coating integrity; thermal shock resistance; oxidation resistance.
Metallography	Substrate/coating structure; coating thickness; bond characteristics; detection of inclusions.
X-ray Diffraction Electron Microprobe	Coating processing/composition dependence

6.5.2.4 Radiation Effects

Radiation effects on electrical insulators should include both neutrons and gamma photons. While neutron effects enter mainly into displacement damage and dimensional stability (i.e., swelling), gamma photons are likely to affect electrons in the insulator materials by photoelectric absorption, compton scattering, and production of electron-positron pairs. Dose rates could be important in addition to doses.

Substantial fast-neutron irradiation data exist on dieletrical materials such as MgO, Al_2O_3, and others (including limited data on Y_2O_3, Y_2O_3-1% ZrO_2, and $MgAl_2O_4$).[6.5-14] A review article on radiation damage in crystalline insulators was given by Matzke[6.5-15] covering both materials and physics aspects of radiation damage in insulators. The latter knowledge is particu-

larly useful in guiding the selection of candidate insulators. Among the various materials studied for a fast fluence of up to 2×10^{26} n/cm^2 (equivalent to 2.8 MW•yr/m^2 fusion neutron fluence), Y_2O_3 exhibited a swelling ($\Delta V/V_o$) less than 0.5%. The swellings of Al_2O_3 and $MgAl_2O_4$ are >3 and ~0% $\Delta V/V_o$, respectively. Post-irradiation thermal diffusivity measurements showed a ~50% reduction from the unirradiated values for Y_2O_3-1% ZrO_2, MgO, and Al_2O_3, whereas no reduction was noted for $MgAl_2O_4$. Transmission electron microscopy[6.5-16] of Al_2O_3 and $MgAl_2O_4$ showed that in Al_2O_3; unfaulted interstitial dislocation loops can easily be formed leading to a bias for precipitation of interstitials, thus leaving vacancies to form cavities (i.e., cause for swelling). Achieving the stoichiometric ratio of vacancies for cavities in $MgAl_2O_4$ would be more difficult than Al_2O_3, fewer interstitial loops form because of the difficult loop nucleation condition. Existing loops remain faulted, thus acting as less effective sinks for interstitials (i.e., less or no swelling).

In summary, the development of a low-voltage, thin-film electrical insulators for liquid-metal blankets is highly advantageous when suitable film insulators can be found that are resistant to both corrosion and radiation damage. A survey of thin film (coating) technology showed that several processes (i.e., plasma spraying, vapor depositions, etc.) may be used either directly or modified for metal surface coatings. Preliminary laboratory experiment has been initiated to study the corrosion of Y_2O_3 in a flowing Li-Pb loop. Similar work is being planned on other candidate materials ($MgAl_2O_4$, etc.). Initial laboratory corrosion tests will allow screening of candidate insulators, following which a mock-up test in an electromagnetic field (but without radiation) will permit assessment of the effectiveness of thin-film insulator in reducing the MHD pressure losses. Radiation damage studies are also recommended, particularly with regard to gamma-photon/neutron irradiations, temperatures, dose rate and dose effects. Theoretical calculations of gamma dose rates in a fusion liquid-metal blanket environment are also necessary to guide the experimental effort.

6.5.3 Nitrate Salt Properties

Molten salts based on $NaNO_3$-KNO_3 and $NaNO_3$-$NaNO_2$-KNO_3 have been used for many years as high temperature coolants, process heating fluids, and constant

temperature (heat treating) baths. Measured against the relevant coolant requirements for fusion energy devices, molten nitrate mixtures offer the following important advantages:

- Reasonable melting points (140 - 220°C)
- Relatively noncorrosive (up to 600°C)
- "Infinite sink" for tritium
- Chemically stable in air and water environments
- Heat transfer coefficient comparable to water.

Against the same requirements, however, there are important disadvantages and unknowns:

- Explosive in contact with reducible substances
- N^{14} $^{n}{}_{1}p$ C^{14}
- Moderately volatile above 450°C
- May be subjected to decomposition (and galvanic corrosion) in magnetic fields.

6.5.3.1 Thermophysical Properties

Selected physical properties of $NaNO_3$-KNO_3 mixtures were tabulated by Janz et al. in 1979.(6.5-17) Useful data on heat capacity, surface tension, specific conductance, ionic diffusivity, thermal conductivity, viscosity, and density are available from this tabulation up to a maximum temperature of 450°C. More recent studies were conducted under the auspices of Sandia National Laboratory to measure the thermophysical properties of draw salt (50% $NaNO_3$-50% KNO_3) up to 600°C.(6.5-18) Properties included heat capacity, viscosity, surface tension, and density. Expeirmental and estimated values for density, electrical conductivity, viscosity, heat capacity, and thermal

conductivity are presented graphically in Figs. 6.5-4 through 6.5-8, and values at 400°C are tabulated in Table 6.5-2. The principal impurities in nitrate salt are:

Cr	800 wppm
Ni	10
Fe	50
Mo	10
Nb	1
Co	<<1

The 1 wppm of Nb will give the dominant activation and hence effort to remove it should be made.

TABLE 6.5-3. SELECTED DRAW SALT PROPERTIES AT 400°C

Density (kg/m^3)	1840
Thermal Conductivity (W/m°C)	0.52
Viscosity (m • Pas)	1.8
Heat Capacity (J/kg°C)	1605
Electrical Conductivity (1/ohm • cm)	1.04

6.5.3.2 Thermal Stability

The mechanisms and rates of thermal decomposition of nitrate salt melts have been investigated at Sandia National Laboratories.[6.5-19,6.5-20] The decomposition reaction

$$NO_3^- \rightleftarrows NO_2^- + 1/2\, O_2 \qquad [6.5\text{-}6]$$

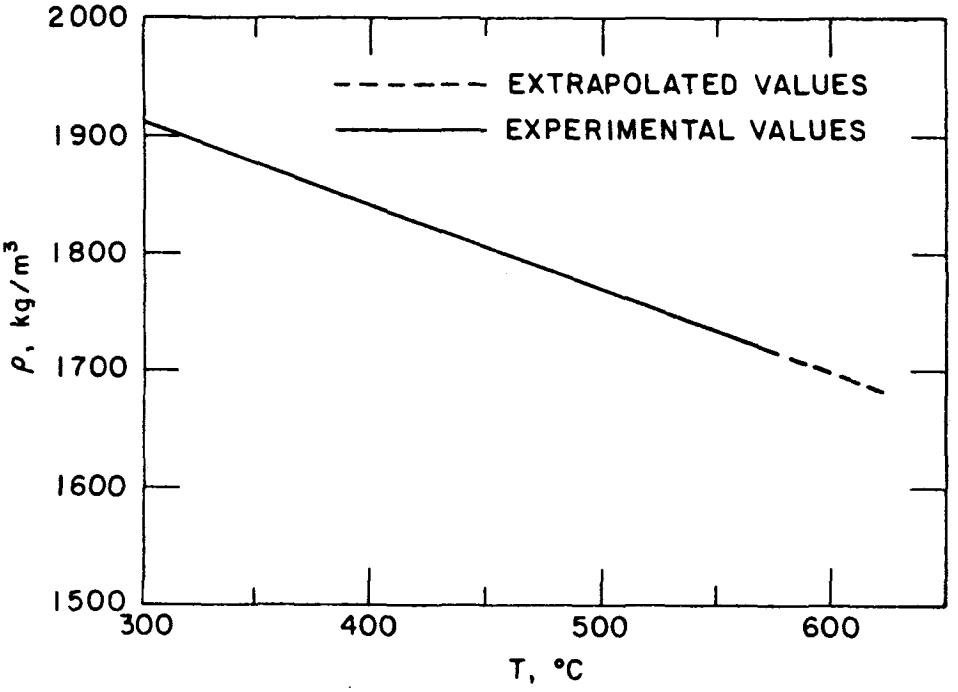


Figure 6.5-4. Density of draw salt as a function of temperature.

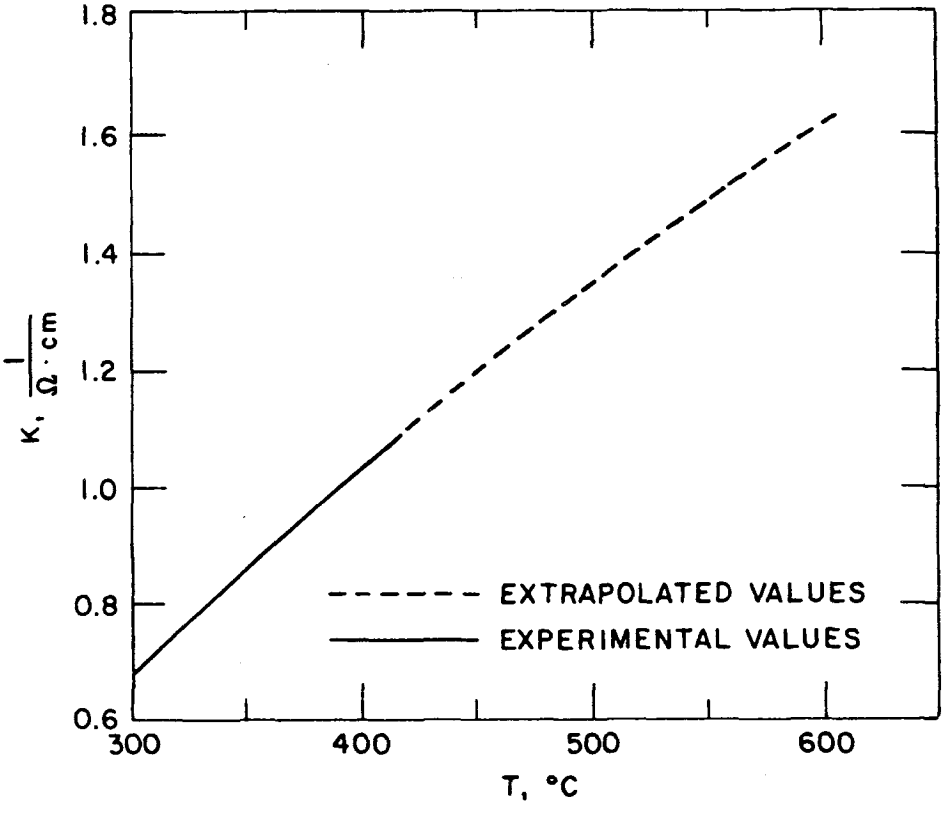


Figure 6.5-5. Electrical conductivity of draw salt as a function of temperature.

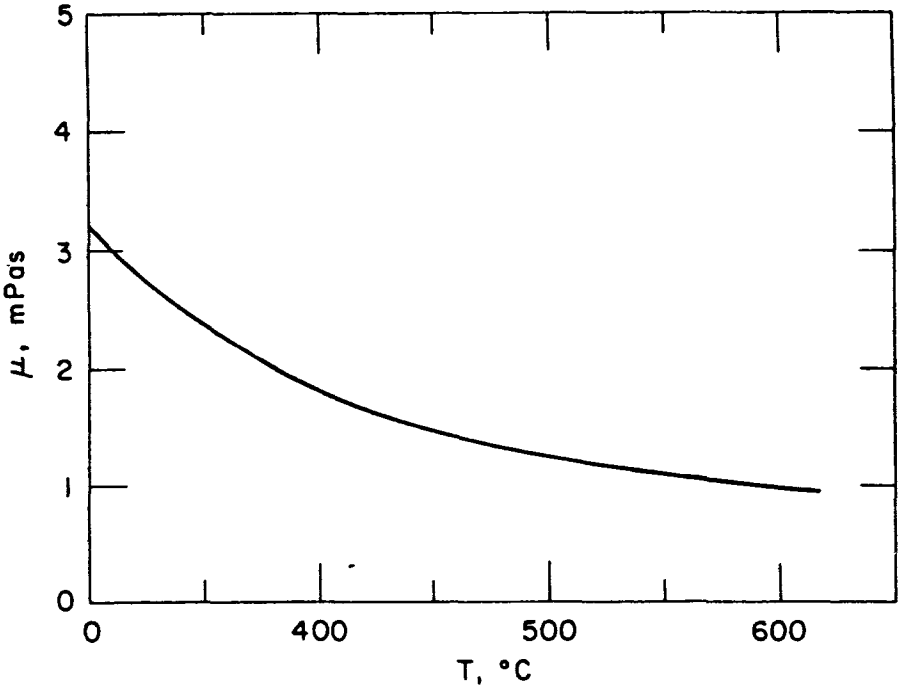


Figure 6.5-6. Viscosity of draw salt as a function of temperature.

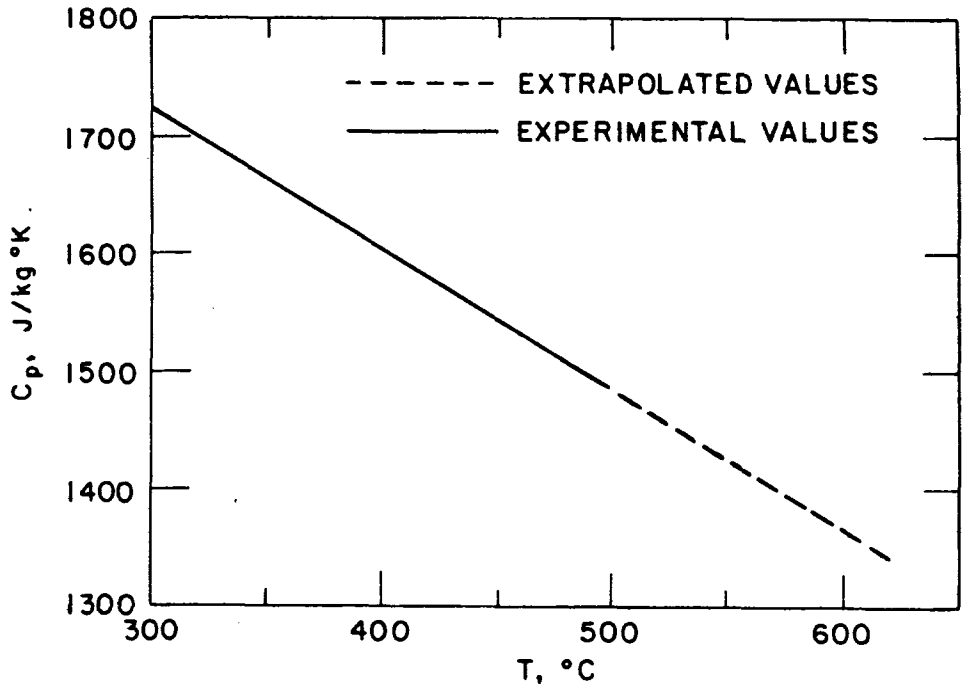


Figure 6.5-7. Heat capacity of draw salt as a function of temperature.

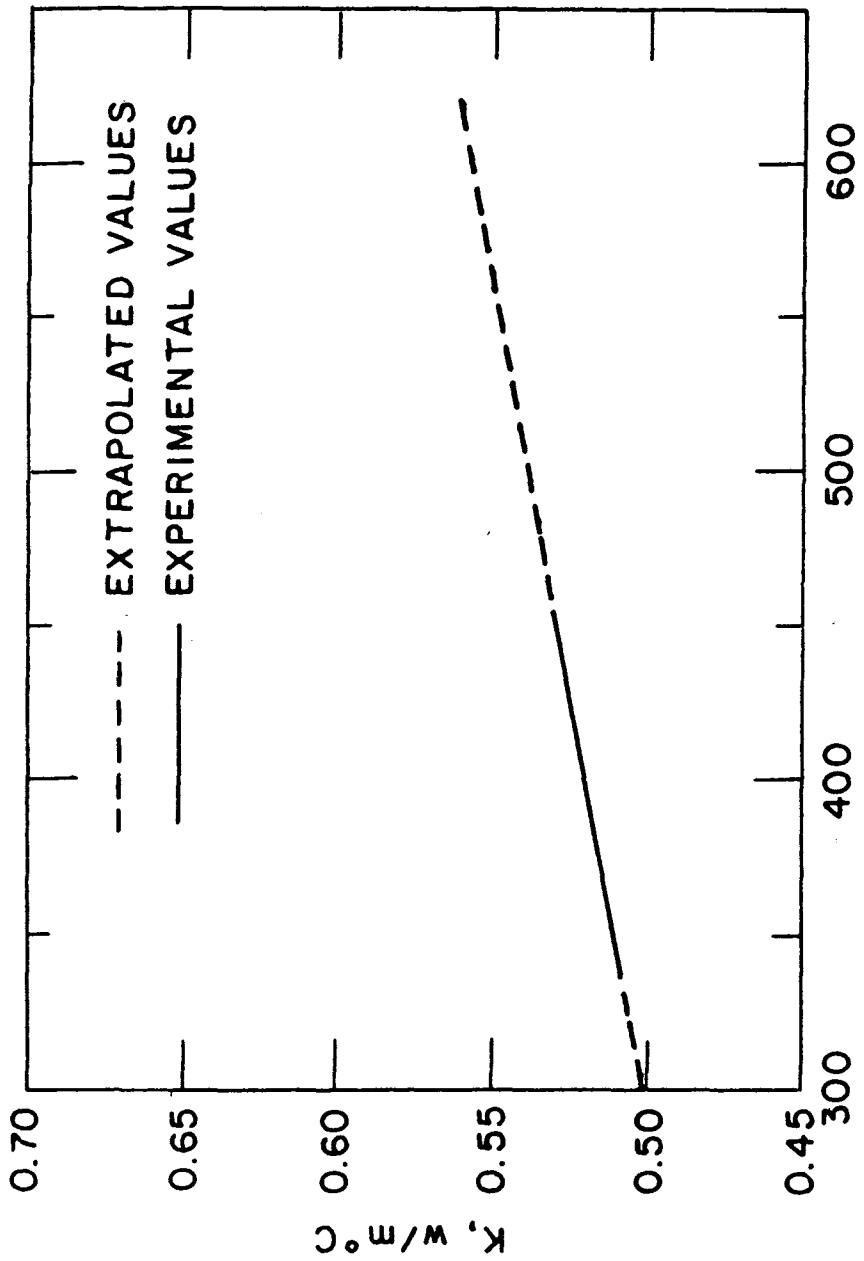


Figure 6.5-8. Thermal conductivity of draw salt as a function of temperature.

dominates over the 500 to 600°C temperature range. Values of the equilibrium constants (for the reverse reaction) are listed in Table 6.5-4. Decomposition rates in vacuum for KNO_3 and $NaNO_3$, respectively, are plotted in Fig. 6.5-9. Decomposition occurs principally by the evolution of nitrogen, nitric oxide, and oxygen, although evidence of direct vaporization is inferred by the observation of $NaNO_3$ and KNO_3 deposits in colder regions of the vacuum system.

TABLE 6.5-4. EQUILIBRIUM CONSTANT FOR THE OXIDATION OF NITRITE TO NITRATE (REF. 6.5-18)

T (°C)	k_{eq} ($atm^{-1/2}$)
500	100.0
550	40.3
600	18.6
620	12.5

These data indicate that thermal decomposition could require some makeup and chemical reprocessing of draw salt in a fusion reactor given the proposed operating times and temperatures. However, draw salt has been circulated in closed loops at ORNL at 600°C for over four years without makeup and with decomposition product gases building up to no more than 50 kPa (7 psig). With respect to cover gas chemistry, SNL reports (Ref. 6.5-18, p. 20) that air is nearly optimal from the standpoint of nitrate stability and discourages the use of pure nitrogen, oxygen, or inert gas.

6.5.3.3 Radiation Stability

Data on the stability of nitrate salts under neutron and gamma radiation are extremely limited. A Co^{60} source was used by Breon et al. at ANL(6.5-21) to irradiate both HTS (nitrite-containing) and draw salt at 530°C. During an integrated exposure of 0.8×10^9 R (at a flux of 3×10^6 R/h), no gaseous decomposition products could be detected in a helium sweep gas over the molten salts. These results indicate no major effect of irradiation on salt decomposition. However, the inability of the experiments to detect thermally-

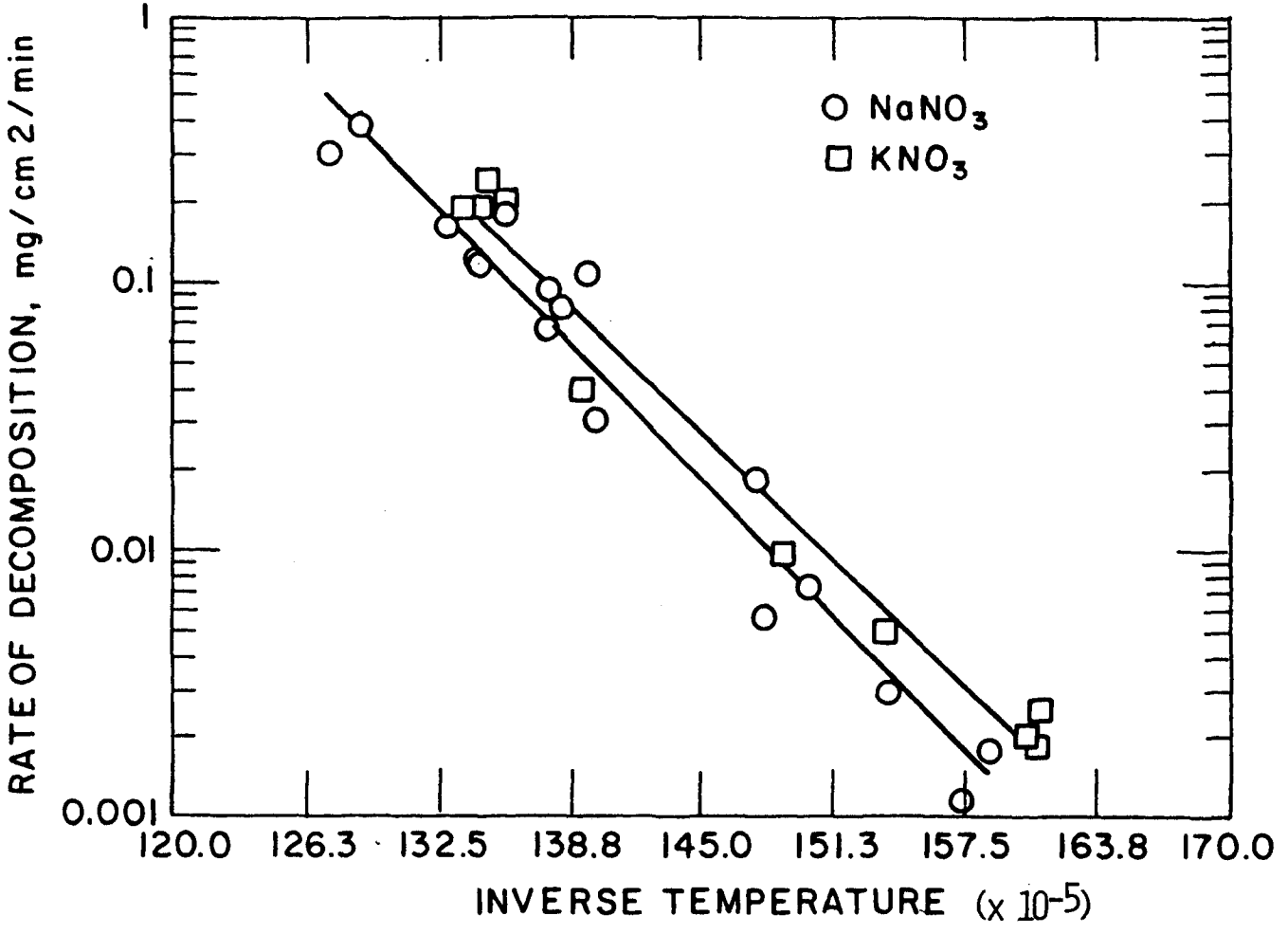


Figure 6.5-9. Initial rates of weight loss of $NaNO_3$ and KNO_3 in vacuum (Ref. 6.5-19).

produced decomposition gases does cast some doubt as to the ultimate sensitivity of the analytical techniques. In any case, more experiments at higher fluxes and fluences will be required to gauge the stability of the salts under the simultaneous effects of high temperature and radiation fields.

6.5.3.4 MHD Effects

In addition to radiolytic and thermal decomposition considerations, electrolytic effects are also relevant if molten salts are moved through strong magnetic fields. Based on the Gibb's free energy of pure $NaNO_3$ and KNO_3, the electric potential required to reduce pure draw salt to its elements (i.e., pure sodium, N_2, and O_2 at 1 atm) is approximately 3 volts. However, the introduction of impurities (such as transmutation and corrosion products, tritium, and atmospheric contaminants) will provide a number of alternate paths for electrolytic decomposition. Figure 6.5-10 records the equilibrium potentials for a number of half-cell reactions that can serve either as cathodic or anodic reactions leading to salt decomposition. The abscissa of this diagram indicates the tendency of the salt to donate oxygen ions to (or accept oxygen ions from) any oxygen-containing species dissolved in the melt. The parameter pO^{2-} is defined as the negative log of oxygen ion activity and is, in effect, a measure of the Lewis acidity of the melt. Note that at a pO^{2-} level of approximately 11, which corresponds to the oxygen ion activity of a neutral (pure) salt, the external potential required to trigger any complementary anode/cathode set of reactions (at low NO or NO_2 activities) is on the order of 1.5 volts (or higher if not under standard state conditions). These voltages appear sufficiently high that electrolytic decomposition could be avoided even in a tokamak reactor, providing duct sizes and salt velocities are kept to reasonable magnitudes. However, salt chemistry becomes of vital concern, since voltages required for electrolytic decomposition decrease significantly as pO^{2-} increases. This point is discussed more fully in Section 6.5.3.7 on corrosion.

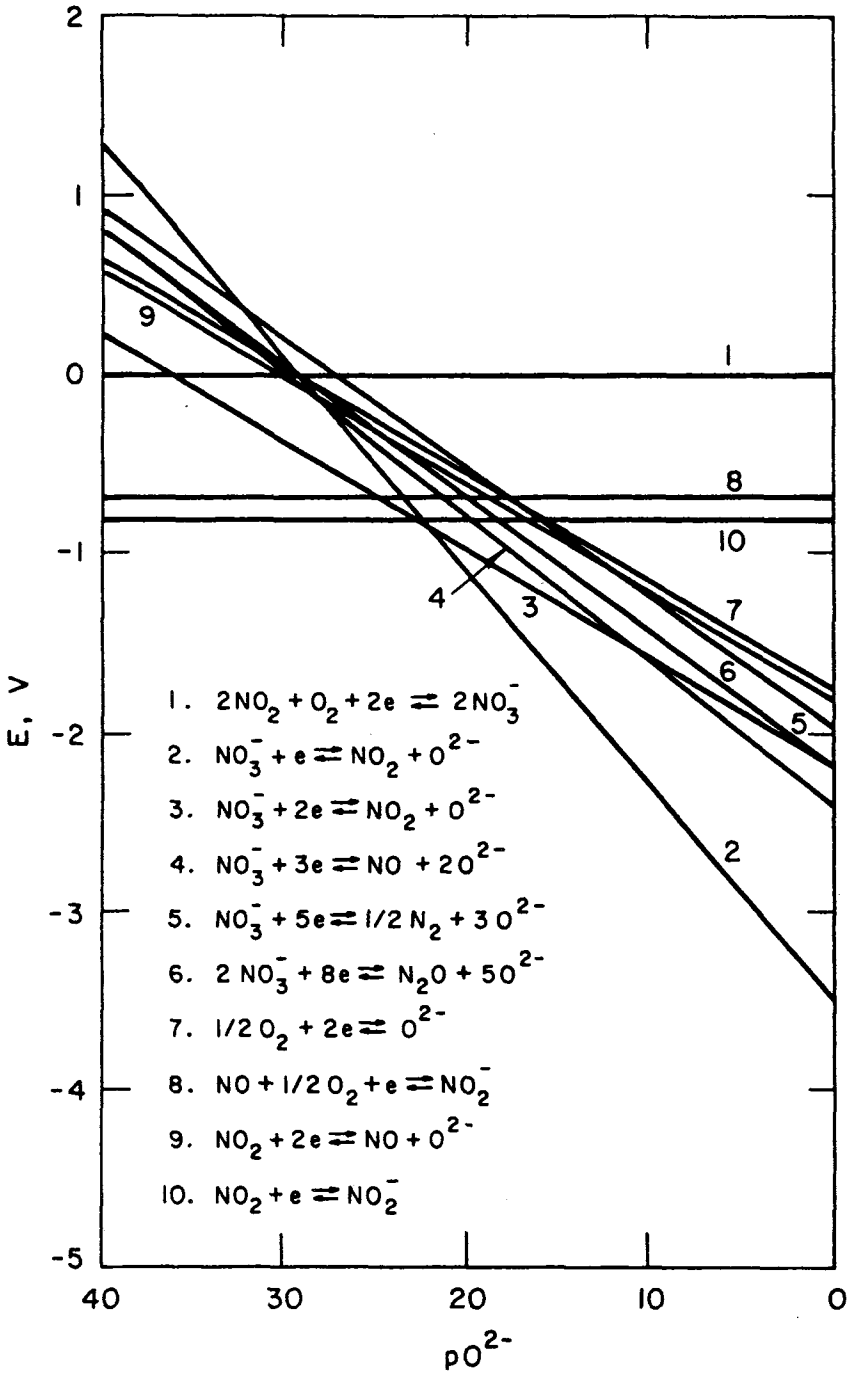


Figure 6.5-10. Potential/pO^{2-} diagram at 600 K.

6.5.3.5 Tritium Chemistry

Experimental and thermodynamic data indicate that H_2O is extremely stable in molten alkali nitrates[6.5-22] and does not chemically decompose except in highly basic melts or possibly in the presence of CO_2 impurities. Thus, any incoming hydrogen or tritium gases should be rapidly oxidized and retained as dissolved H_2O (T_2O) through the reaction

$$2\ H + NO_3^- \rightarrow NO_2^- + H_2O(d) \quad . \qquad [6.5\text{-}7]$$

The reaction $H_2O + O^{2-} \rightarrow 2\ OH^-$ could also become important at high O^{2-} activities (highly basic conditions).

The solubility-pressure relationship for H_2O in draw salt has been experimentally determined[6.5-23] between 227 and 294°C at pressures from 5 to 30 torr. The results subscribe to the equation

$$\log_{10} C/P = -6.72 + 1.845 \times 10^3\ T^{-1} \quad , \qquad [6.5\text{-}8]$$

where C = mol H_2O/kg salt, P = torr, and T = °K. Displacement of dissolved water by inert gas stripping is effective in the case of sodium nitrate and potassium nitrate but less effective for lithium nitrate. Thus, in assessing the replacement of potassium or sodium with lithium to effect tritium breeding, it will be necessary to determine whether salt mixtures carrying lithium nitrate behave reversibly with respect to the dissolution and evolution of water. The kinetics of water removal from draw salt using dry argon were recently examined by White and Twardoch,[6.5-22] who found that water could be dissolved and removed reversibly and rapidly between 200 and 600°C without evidence of chemical reaction products.

6.5.3.6 Handling

With any molten salt, the expansion occurring on thawing is an important design consideration, given the possibility of inadvertant salt freeze-ups.

The volume expansion of $NaNO_3$-KNO_3 on melting, $(V_l-V_s)/V_s$, is listed in Ref. 6.5-17 (page 407) as 4.6(±0.6)%. (No dependence on composition is noted. However, since $NaNO_3$ + KNO_3 form a complete series of solid solutions, it is probable that the expansion from solid to liquid is nearly the same for all compositions.) If, as the datum suggests, the volume expansion approaches 5%, blanket designs will either have to guarantee a free surface from which to start thawing or be willing to accept blanket module replacement in the event of an accidental freeze-up.

Nitrates are strong oxidants. Explosive reactions are possible if nitrates contact pyrophoric materials. Based on the manufacturer's standard practice procedures,(6.5-23 - 6.5-25) nitrate salts should not be allowed to contact carbonaceous materials (organic and cellusoic compounds, petroleum coke, carbon, etc.), aluminum alloys, or magnesium alloys. Thus, lithium, sodium, and possibly lead-lithium must be considered potentially dangerous in contact with draw salt. However, graphite and beryllium appear to be acceptable under most accident conditions. A series of tests was conducted(6.5-26) at LLNL which showed a very slow reaction between draw salt and a 4.6-mm-diam graphite rod at 500°C and no measurable reaction between the salt and a 0.36-mm beryllium wire at 540°C.

6.5.3.7 Corrosion Properties

An adequate corrosion data base now exists for the design of nonnuclear heat transfer systems up to 600°C. Corrosion studies have shown essentially equivalent corrosion behavior of alloy 800 and type 300 series stainless steels in draw salt at 400 to 600°C. However, alloy 800 has been selected as the reference material for solar thermal energy systems based on its superior high temperature strength. Corrosion properties of Cr-Mo steels (specifically 2-1/4 Cr-1 Mo) appear adequate for service to at least 500°C and, if aluminized, to approximately 600°C.

The only corrosion effect observable in heat transfer systems of these materials is the formation of a duplex spinel/magnetite oxide film and an uptake of oxidized chromium (+6) by the molten salt. There is no measurable thermal gradient mass transfer up to 600°C, and oxide films have resisted spalling up to 600°C in virtually all tests for times in excess of three years. For non-nuclear applications, a corrosion allowance of 13 μm/year

appears adequate up to 600°C.[6.5-27] Operation above this temperature is not realistic because of salt decomposition and steeply increasing corrosion rates.

In the case of the proposed fusion application, corrosion mechanisms become more complicated because of galvanic (MHD) affects induced by movement of the salts through magnetic fields. The stability diagram shown in Fig. 6.5-11 is useful for illustrating the MHD problem relative to iron-based alloy systems. (The reference salt is pure $NaNO_3$, not draw salt, but its chemical properties can be considered quite representative of draw salt.) In the absence of any impurity ions, the neutral condition of fused nitrate (at 300°C) is calculated to be at an oxygen ion activity of 2.85×10^{12}, or $pO^{2-} = -\log A_O 2- = 11.5$. This condition is marked by the cross-hatched vertical band in Fig. 6.5-11. At the corrosion potential (i.e., without external polarization), the stability diagram predicts the formation of iron oxides, which will consist mostly of Fe_3O_4 (as shown by the doubly cross-hatched region). There are many possible cathodic reactions which can balance the oxidation reactions of iron. However, the major cathodic reaction at the corrosion potential appears to be $NO_3^- + 2\ e \rightarrow NO_2^- + O^{2-}$.

Based on experiments, when the anodic polarization voltage is increased from the open circuit (corrosion) potential, the oxidation current increases only slightly as the incipient oxides that formed at the corrosion potential (Fe_3O_4) are oxidized to Fe_2O_3. If the anodic polarization voltage is decreased below the corrosion potential, the oxidation reaction will eventually stop as the iron becomes noble. Neither change in polarization voltage would significantly affect the rate of corrosion (assuming the solubility of Fe_2O_3 in fused nitrate is not significantly more than the solubility of Fe_3O_4).

However, if the "acidity" of the salt is increased by decreasing the oxide ion concentration (i.e., increasing pO^{2-}), the effect of external polarization on corrosion becomes more insidious. In Fig. 6.5-11 it is seen that the phase stability ranges for oxide films on iron do not extend to high pO^{2-} values. Above a pO^{2-} of approximately 25, increasing the polarization voltage above the open circuit (corrosion) potential leads to the formation of Fe^{2+} and Fe^{3+} ions, a condition which portends catastrophically high corrosion rates.

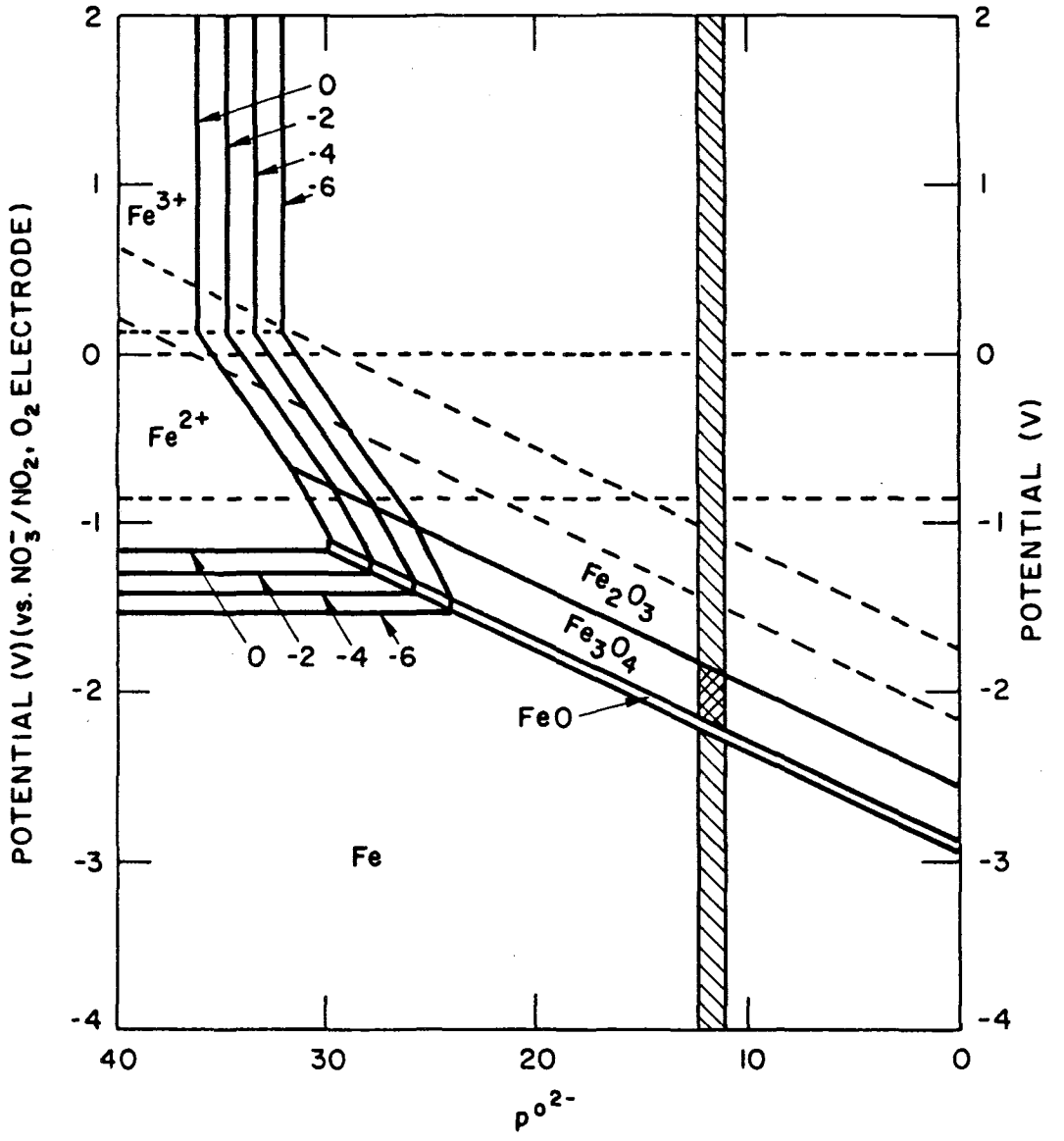


Figure 6.5-11. Stability diagram for iron in fused salt at 600 K.

In summary, the degree of which external polarization (MHD-induced voltages) will affect corrosion rates will depend on whether the "acidity" (pO^{2-} level) of the salt can be maintained near that of the impurity-free salt. The buildup of corrosion and transmutation products, the levels of residual CO_2 and H_2O impurities, and the entry of reductants such as H_2 and T_2 become fundamentally important in predicting MHD effects, since they affect the acidity of the salt. Thus, an analysis of MHD effects becomes possible only when the steady-state composition of the salt can be predicted. Solutions to the MHD problem can be approached (1) by restricting the magnitude of magnetically-induced voltages (e.g., duct size and salt velocity) and (2) by controlling salt chemistry (pO^{2-}). The MHD problem appears to be more a design issue than a feasibility issue; nevertheless, it is one of the more important unknowns in evaluating fused nitrates for fusion applications.

REFERENCES FOR SECTION 6.5

6.5-1 M. A. Abdou et al., Blanket Comparison and Selection Study, Interim Report, ANL/FPP-83-1, October 1983.

6.5-2 C. Baker, et al., "STARFIRE - A Commercial Tokamak Fusion Power Plant Study," Argonne National Laboratory Report, ANL/FPP-80-1, September 1980.

6.5-3 G. E. Darwin and J. H. Buddery, Beryllium, Academic Press, 1960, Chapter 11.

6.5-4 E. H. Smith, et al., Proc. Symp on Materials Performance in Operating Nuclear Systems, eds. M. S. Wechsler and W. H. Smith, Ames Lab., Iowa State University, Ames, Iowa, August 28-30, 1973, p. 41.

6.5-5 J. B. Rich, et al., J. Nucl. Mater. 1(1959) 96-105.

6.5-6 M. Abdou, et al., Impurity Control and First Wall Engineering, FED-INTOR/ICFW/82-17, 1982.

6.5-7 M. J. Bennett, et al., J. Nucl. Mater. 17(1965) 60-72.

6.5-8 S. A. Steward, Lawrence Livermore National Laboratory Report, UCRL-53441, August 1983.

6.5-9 D. H. Berwald et al., "Fission-Suppressed Hybrid Reaction -- The Fusion Breeder," Lawrence Livermore National Laboratory Report, UCID-19638 (1982).

6.5-10 J. Beeston et al., "Beryllium Lifetime Assessment for the Reference Tandem Mirror Fusion Breeder," in press, contact author at EG&G/Idaho.

6.5-11 R. M. Burns and W. W. Bradley, Protective Coatings for Metals, 3rd Ed., Reinhold Publishing Co., 1967.

6.5-12 D. L. Smith, et al., 2nd Inter. Conf. on Liquid Metals in Energy Production, Richland, WA, April, 1980, p. 2-72.

6.5-13 D. L. Smith, Argonne National Laboratory, personal communication.

6.5-14 F. W. Clinard, Jr., J. Nucl. Mater., 85&86(1979)393-404.

6.5-15 Hj. Matzke, Radiation Effects, Vol. 64 (1982) p. 3-33.

6.5-16 G. F. Hurley and F. W. Clinard, DOE/ET-0095 (1979).

6.5-17 G. J. Janz et al., Physical Properties Data Compilations Relevant to Energy Strorage, NSRDS-NBS61, Part II, National Bureau of Standards, April 1979.

6.5-18 R. W. Mar et al., Progress Report, Molten Nitrate Salt Technology Development, SAND 82-8220, Sandia National Laboratory, April 1982, pp. 10-15.

6.5-19 C. M. Kramer and Z. A. Munir, "Thermal Decomposition of $NaNO_3$ and KNO_3," Proceedings of the Third International Symposium on Molten Salts, The Electrochemical Society, Inc., Proceedings Volume 81-9, pp. 494-505, 1980.

6.5-20 R. W. Carling et al., Molten Nitrate Salt Technology Development Status Report, SAND 80-8052, Sandia National Laboratory, pp. 59-77, March 1981.

6.5-21 S. R. Breon et al., Gamma Irradiation of Nitrate-Based Salts, ANL/FPP/TM-129, Argonne National Laboratory, March 1980.

6.5-22 P. G. Zambonin, V. L. Cardetta, and G. Signorile, "Solubility and Detection of Water in the (Na,K)NO Eutectic Melt," J. Electroanal. Chem., 28 (1970), 237-243.

6.5-23 H. P. Voznick and V. W. Uhl, "Molten Salt Baths for Heat Transfer," Chemical Engineering, May 27, 1963, pp. 132-133.

6.5-24 Potential Hazards in Molten Salt Baths for Heat Treatment of Metals, National Board Fire Underwriters Research Report No. 2, 1954.

6.5-25 L. Bretherwick, Handbook of Reactive Chemical Hazards, Butterworths Co., London, 1975.

6.5-26 Interdepartmental Letter, F. Helm to R. Moir, "Compatibility Testing of Wood, Graphite, and Beryllium with Molten Draw Salt," March 15, 1984, Lawrence Livermore National Laboratory.

6.5-27 P. F. Tortorelli and J. H. DeVan, Thermal Convection Loop Study of the Corrosion of Fe-Ni-Cr Alloys by Molten NaNO -KNO, ORNL/TM-8298, Oak Ridge National Laboratory, December 1982.

BLANKET COMPARISON AND SELECTION STUDY

SECTION 6.6 - TRITIUM CONTAINMENT

SECTION 6.6

TABLE OF CONTENTS

PAGE NO.

6.6 Tritium Containment....6.6-1

6.6.1 Introduction....6.6-1

6.6.2 Release of Tritium from Solid Breeders....6.6-3

6.6.2.1 Introduction....6.6-3

6.6.2.2 Results from Post-Irradiation Extraction Experiments....6.6-4

6.6.2.3 Results from In-Situ Experiments....6.6-4

6.6.2.4 Recommended Criterion from the Evaluation of Tritium Leakage....6.6-6

6.6.3 Oxidation of Tritium in a Double-Walled Heat Exchanger Tube....6.6-7

6.6.4 Tritium Permeation....6.6-14

6.6.4.1 Tritium Permeation and Inventory in First Wall....6.6-14

6.6.4.2 Tritium Permeation in HT-9....6.6-19

6.6.5 Isotopes Effect....6.6-19

6.6.6 Tritium Release Guidelines....6.6-23

6.6.7 Conclusions and Summary....6.6-23

REFERENCES....6.6-31

LIST OF FIGURES FOR SECTION 6.6

FIGURE NO.	TITLE	PAGE NO.
6.6-1	The effect of temperature on the fraction of tritium leaving the heat exchanger via the helium purge stream. (Constant total purge stream pressure	6.6-10
6.6-2	Percentage of tritium converted to HTO as a function of the helium purge stream mass flow rate. (Constant total purge stream pressure.)	6.6-10
6.6-3	Fraction of tritium entering the heat exchanger which leaves via the helium purge stream. Curves shown are for various partial pressures of tritium in the liquid metal. (Constant total purge stream pressure.)	6.6-11
6.6-4	The effect of oxide barriers on the fraction of tritium leaving the heat exchanger via the helium purge stream. (Constant total purge stream pressure.)	6.6-11
6.6-5	Tritium permeation into the coolant as a function of years of operation	6.6-15
6.6-6	Permeation of hydrogen in HT-9 ferritic steel	6.6-20
6.6-7	Breeding blanket recovery system	6.6-24

LIST OF TABLES FOR SECTION 6.6

TABLE NO.	TITLE	PAGE NO.
6.6-1	CONCENTRATION REDUCTION FACTOR REQUIRED BETWEEN THE BREEDING MATERIAL AND BEFORE THE LAST BARRIER TO STEAM	6.6-3
6.6-2	DISTRIBUTION OF TRITIATED SPECIES RELEASED FROM NEUTRON IRRADIATED LITHIUM COMPOUNDS ON HEATING UNDER VACUUM	6.6-5
6.6-3	VALUES FOR PARAMETERS USED TO SOLVE EQUATION [6.6-1]	6.6-9
6.6-4	TRITIUM PERMEATION AND INVENTORY FOR PCA TOKAMAK FIRST WALL	6.6-16
6.6-5	TRITIUM PERMEATION AND INVENTORY FOR PCA AND VANADIUM FOR BOTH TOKAMAK AND TANDEM MIRROR REACTOR CONCEPTS	6.6-18
6.6-6	TRITIUM CALCULATION SUMMARIES FOR TOKAMAK DESIGNS	6.6-27
6.6-7	TRITIUM CALCULATION SUMMARIES FOR TMR DESIGNS	6.6-29

6.6 Tritium Containment

6.6.1 Introduction

Tritium containment in a D-T fusion reactor blanket and coolant system has been a much concerned problem. However, very little engineering work has been done to critically evaluate the seriousness of the problem. To prevent tritium leakage to the steam side, either one or both of the following assumptions were made in past studies.

1. Tritium can be oxidized rapidly into oxide form after which it will be taken out of the permeation considerations.

2. A diffusion barrier is available, mostly oxide barrier, which will reduce the permeation by a factor of 100 to 1000.

However, some recent experimental results have shown that the assumptions may not be valid. In particular, it has been shown that the kinetics of tritium oxidation is slow, with or without gamma radiation.[6.6-1] It has also been shown with limited experimental results converting tritium into oxide form will reduce permeation only if extreme care is taken to insure that no reducing surfaces are available.[6.6-2] As far as the diffusion barrier is concerned, the mechanism of resistance is not clear. Therefore, it is difficult, if possible at all, to extrapolate the experimental results to the reactor region.

A special task group was formed to study this problem. The goal of the task group is not to try to define the severity of the problem for each design. Rather, it tries to review the existing experimental results available and to define a set of ground rules which will form a common basis for each particular design group to resolve their particular problem. Due to the scarcity of the information, and often contradiction nature of the existing information, it has to be pointed out that the set of ground rules is judged to be most reasonable by the special task group. The purpose of defining the ground rules is for each team has the common basis to go through the exercise

to assess the problem. It is, by no means, try to imply that this set of ground rules should be used for the future study in its entirity. Both theoretical modeling and experimental results will be required to assess the validity of the ground rules.

The severity of the tritium containment can be shown by a simple calculation. Assuming the steam generator has the following set of parameters:

Temperature = 450°C

Area = 2.5×10^4 m^2

Allowable tritium leakage rate = 10 curie/day

Oxide barrier factor = 100

$$\text{Permeability of T in HT-9} = .46 \frac{\text{mol } T_2 - \text{mm}}{D \cdot m^2 - \text{atm}^{1/2}}$$

It can be shown that the allowable tritium partial pressure before the last structural barrier to the steam is 2.1×10^{-7} Pa. If this partial pressure is to exist in 1 atm purge gas, the tritium concentration is 2.1×10^{-6} appm.

Table 6.6-1 shows the typical tritium partial pressure in the blanket for different design, and the corresponding concentration reduction factor required between the breeding material and the steam generator. With the exception of lithium blanket, the severity of the problem is obvious.

By making some reasonable assumptions, the effort required to keep the tritium leakage rate of the steam side to ~10 curie/day can be estimated. For a solid breeder, helium purge and helium coolant blanket, the cleanup system for the primary coolant has to be ~99% efficient. The key assumption here is that tritium diffused out from the solid breeder is 100% in elementary form. For a 17Li-83Pb cooled blanket with a Na intermediate loop, 36 kg/d of hydrogen would have to be added to the sodium for isotope dilution purpose. Therefore, 3.2×10^5 kg/y of NaH would have to be recovered from the cold trap. For a double-walled steam generator, the purge gas flow rate in the gap is to be 1.5×10^7 liter/sec, which corresponding to a linear velocity of 6×10^4 m/sec. The key assumption here is that no oxidation occurs in the gap.

From these calculations, it becomes clear that tritium containment may be a critical problem, especially if the leakage rate is limited to 10 curie/day. This section will try to define the source term, the transport mechanism and the allowable sink for the tritium leakage calculations.

TABLE 6.6-1. CONCENTRATION REDUCTION FACTOR REQUIRED BETWEEN THE BREEDING MATERIAL AND BEFORE THE LAST BARRIER TO STEAM

	Typical Operating Pressure	Concentration Reduction Factor (To Reach 2.1×10^{-7} Pa)
LiPb	1.3×10^{-2} Pa	6×10^{4}
Li	9×10^{-9} Pa	---
Solid Breeders	.73 Pa[a] to $.73 \times 10^{-4}$ Pa	3.5×10^{6} to 350

[a] If $V_{purge} = 10^{4}$ liter/sec and all T in T_2, $\Delta P = .73$ Pa/Pass, or $P \geq .73$ Pa.
If $V_{purge} = 10^{6}$ liter/sec and 1% T in T_2, $\Delta P = .73 \times 10^{-4}$ Pa/Pass, or $P \geq .73 \times 10^{-4}$ Pa.
(For tritium production rate of 600 g/day.)

6.6.2 Release of Tritium from Solid Breeders

6.6.2.1 Introduction

For the solid breeder blanket designs, it is important to know the behavior of the bred tritium in order to predict tritium migration and inventory in the respective blankets. To investigate this behavior, two types of experiments have been performed. They are the post-irradiation out-of-pile extraction experiments and the in-situ extraction experiments. The former one considers the chemical behavior of the tritium species, the kinetics of tritium release as a function of temperature and the species of the released tritium. The latter experiments, which are more relevant to fusion reactor conditions, consider similar tritium behavior with the additional information of the effects of tritium release under in-situ reactor environments, including radiation effects, and the impact of hydrogen, oxygen, or moisture addition into

the helium purge stream. From the consideration of tritium leakage, it is important to know the species of tritium release from solid breeders (T_2 versus T_2O). More importantly, the in-situ release experiments allow the equilibrium to be studied where tritium production is balanced by release and inventory has reached a steady-state. Results from the post-irradiation extraction experiments are summarized in this section. Results of the American TRIO-1 and the Japanese VOM-15H in-situ experiments are summarized in Section 6.6.2.2 and discussed in more detail in Section 6.4.3.

6.6.2.2 Results from Post-Irradiation Extraction Experiments

Experiments were performed on the out-of-pile removal of tritium from neutron-irradiated solid breeder compounds under different neutron fluence levels and at different extraction temperatures.[6.6-3,-4,-5] Table 6.6-2 summarizes the distribution of tritium species from neutron irradiated lithium compounds on heating under vacuum. It can be noted that at the temperature range of interest, very little tritium is retained in the target material. It is indicated in Table 6.6-2 that for solid breeder compounds that contain oxygen, >87% of the tritium species is released in condensable form (HTO) and >93% is released in condensable form from Li_2O. Even though the experimental results are very consistent for out-of-pile experiments, they do not necessarily indicate what would happen under in-situ conditions when tritium is continuously extracted from a purge stream of helium in a radiation environment.

6.6.2.3 Results from In-Situ Experiments

When comparing the results of the out-of-pile experiments to the in-situ $LiAlO_2$ TRIO-1[6.6-6] experiment, it is interesting to find that most of the tritium released from the latter experiment was observed to be in noncondensable form (HT), as discussed in detail in Section 6.4.3.3. It is possible that this is due to the very high H_2 content (0.1%) of the TRIO purge gas that was used. Although pure helium and He + O_2 were subsequently also used, the initial tests may have saturated the system with H_2. On the other hand, results from the Japanese Li_2O VOM-15H[6.6-7] in-situ experiment indicate that ~90% of the tritium gathered from the ionization chamber is in condensable form (HTO). It should be noted that the ionization chamber is located 8 m away from the purge gas outlet. It is also observed that the relatively high moisture content (50 appm) in the helium purge gas may be due to moisture

TABLE 6.6-2. DISTRIBUTION OF TRITIATED SPECIES RELEASED FROM NEUTRON IRRADIATED LITHIUM COMPOUNDS ON HEATING UNDER VACUUM[a]

Compounds	Neutron Fluence ($\#/cm^2$)	Isochronal Heating (°C)	Distribution of Tritiated Species (%)				
			HT	HTO	CH_3T	C_2H_{2n-1} (n=1,2)	Retained in Target
LiH	3.0×10^{15}	100-750	99.4	0.3	0.3	<0.1	0.1
Li_2C_2	3.0×10^{15}	200-700	95.9	1.2	0.4	2.6	---[b]
LiAl	3.0×10^{16}	200-800	93.2	5.3	1.2	<0.1	0.3
Li (1 wt %)-Al	3.6×10^{17}	200-750	44.5	53.7	1.8	<0.1	<0.1
LiOH	3.6×10^{16}	100-600	0.3	99.4	0.1	0.2	<0.1
Li_2O	5.4×10^{15}	at 600	0.4	99.1	0.3	0.1	0.1
Li_2O	3.6×10^{16}	100-600	0.9	98.0	0.9	0.1	0.1
Li_2O	8.1×10^{16}	at 600	1.8	97.6	0.4	0.1	0.1
Li_2O	8.9×10^{17}	at 600	5.6	93.5	0.7	0.1	0.1
Li_2CO_3	3.6×10^{16}	100-600	1.7	96.9	0.3	1.0	0.1
$LiAlO_2$	3.0×10^{15}	200-750	8.1	87.1	1.2	3.6	---[b]
Li_2SiO_3	3.0×10^{15}	200-750	2.5	97.1	0.4	---[b]	---[b]

[a]Data extracted from References 6.6-3 through 6.6-5.

[b]Lower than detection limit <0.1.

absorbed on the wall of the piping. This potentially makes the exchange reaction,

$$HT(g) + H_2O \rightleftarrows HTO + H_2(g)$$

important. Therefore, the fraction of tritium in noncondensible form near the source may be very different from that in the ionization chamber. This observation can have important impact in the control of tritium release. More experiments will be performed to quantify further the species of tritium release from Li_2O.

6.6.2.4 Recommended Criterion for the Evaluation of Tritium Leakage

Considering the limited experimental data from in-situ release of tritium from solid breeders, it is impossible to specify with certainty the form of tritium release from Li_2O or from $LiAlO_2$. To define a guideline for tritium leakage calculation, it was recommended that the possibility of tritium release of 1% and 100% in noncondensable form should be considered. This criterion is recommended for design comparison only. Potentially, any design or future experiment that can indicate a drastic reduction in the noncondensable form of tritium to <<1% will contribute significantly to the reduction of tritium leakage. The addition of excess oxygen to the helium purge stream should push the thermodynamics of the $2T_2O \rightleftarrows 2T_2 + O_2$ reaction very strongly toward T_2O (equilibrium $T_2O/(T_2 + T_2O) \sim 10^{11}$), but the form of tritium release from the solid breeder, and the kinetics of the $2T_2 + O_2 \rightarrow 2T_2O$ reaction are not presently known. Carefully controlled in-situ experiments are clearly needed.

6.6.3 Oxidation of Tritium in a Double-Walled Heat Exchanger Tube

One concept considered in maintaining low tritium leakage rates from the primary coolant to the secondary coolant involves the use of double walled heat exchanger tubes. In this concept, a helium purge stream which contains a small amount of oxygen, flows through the double wall space. Tritium permeates into this space from the primary coolant and after it gets there, one of three things happens to it. It can cross the double wall space and then permeate into the secondary coolant. Or, it can be carried out of the heat exchanger segment as tritium (T_2) in the helium purge stream. Finally, it can be oxidized either homogeneously or heterogeneously to T_2O.

To determine the feasibility of the double walled heat exchanger concept, a mathematical model was developed to keep track of tritium inventory. More specifically, knowing the partial pressure of tritium in the primary coolant, the model keeps track of: how much tritium permeates into the double wall space and into the secondary coolant; and, how much is carried out of the heat exchanger by the helium purge stream as tritium or HTO. This latter point involves a consideration of the oxidation kinetics of tritium to HTO. Both heterogeneous oxidation i.e., oxidation at the wall and homogeneous oxidation, i.e., oxidation in the purge gas, can occur. The differential equation which is derived for this model is,

$$\frac{dp_{T_2}}{dZ} = \frac{4\pi P}{3F}\left(\theta_1 r_1 - \theta_2 r_2\right) - 2K_1\left(r_1 - r_2\right)^2 - K_2\left(r_1 + r_2\right) \qquad [6.6\text{-}1]$$

where p_{T_2} is the partial pressure (atm) of tritium in the helium purge stream, P is the pressure (atm) of the helium purge stream (which was assumed constant for the situations modeled here), F is the mass flow rate (g/sec) of the purge stream, and r_1 and r_2 are the average outer and inner radii (cm) of the outer and inner tubes of the double-walled heat exchanger, respectively. K_1 is a homogeneous oxidation rate factor (g/cm^3-sec) and is given by the following equation,

$$K_1 = 1.029 \times 10^{-4} \frac{g\ T_2}{Curie}\ k_1\ P_{T_2}{}^{\alpha}\ P_{O_2}{}^{\delta} \qquad [6.6\text{-}2]$$

where k_1 is the homogeneous rate constant (curies/sec-cm^3-atm$^{\alpha+\delta}$], P_{T_2}, and P_{O_2} are the partial pressures of tritium and oxygen, respectively, and α and δ are the respective reaction orders for tritium and oxygen. K_2 is the heterogeneous rate factor (g/cm^2-sec) and is given by the following equation,

$$K_2 = 1.029 \times 10^{-4} \frac{gT_2}{Curie} \left(k_2 P_{T_2}^{\alpha'} P_{O_2}^{\beta'}\right) \qquad [6.6\text{-}3]$$

where k_2 is the hetergeneous rate constant (curies/cm^2-sec-atm$^{\alpha'+\beta'}$], P_{T_2} and P_{O_2} are the partial pressures of tritium and oxygen in the double wall space, and α' and β' are the reaction orders with respect to tritium and oxygen respectively. θ_1 and θ_2 are permeation rate factors for the inner and outer tubes of the double-walled heat exchanger, and are given by the following equations,

$$\theta_1 = \frac{\Phi_1}{\delta_1} \left[P_{T_2}^{1/2} - P_{T_{2,sc}}^{1/2}\right] \qquad [6.6\text{-}4]$$

$$\theta_2 = \frac{\Phi_2}{\delta_2} \left[P_{T_{2,pc}}^{1/2} - P_{T_2}^{1/2}\right] \qquad [6.6\text{-}5]$$

where Φ_1 and Φ_2 are the permeabilities of the tube wall material [gm/cm-s-atm$^{0.5}$], δ_1 and δ_2 are the inner and outer tube wall thicknesses (cm), and $P_{T_{2,pc}}$ is the partial pressure of tritium [atm] in the primary coolant, and $p_{T_{2,sc}}$ is the partial pressure of tritium on the steam side.

A solution to Eq. [6.6-1] necessitates the use of a computer code for a number of reasons. First of all, a number of the terms (e.g., permeabilities, rate constants) are functions of temperature, and the temperature of a double-walled heat exchanger tube varies greatly along its length, and to some extent in the radial direction also. Secondly, the permeabilities and rate factor

are also functions of the partial pressure of tritium within the double wall space. This partial pressure may also change along the tube length. Finally, in analyzing the situation, one would like to look at the effects of changing variables like: the partial pressure of tritium in the liquid metal coolant; oxidation kinetics; or, the permeability of the tube walls. This last situation arises when the tube wall material is changed, or when oxide layers are present.

Values for the parameters which were used to solve Eq. [6.6-1] are listed in Table 6.6-3. Only a heterogeneous tritium oxidation rate was considered in the computer solution, as a review of homogeneous oxidation rates[6.6-8, 6.6-9] indicated orders of magnitude lower conversion due to homogeneous reaction than due to heterogeneous reaction. The heterogeneous reaction rate which was used here, was derived from a report by Bixel and Kershner [6.6-10]. A first order dependence on tritium partial pressure and a zero order dependence on oxygen partial pressure were assumed.

TABLE 6.6-3. VALUES FOR PARAMETERS USED TO SOLVE EQUATION [6.6-1]

k_2	heterogeneous rate constant [curies/atm-sec-sq.cm.]		2.4×10^{-2} exp[-7,100/RT]
Φ	permeability of HT-9		6.60×10^{-7} exp[-11,100/RT]
	permeability of PCA [g/cm-s-atm 1/2]		3.30×10^{-6} exp[-15,700/RT]
Oxide Barrier Factors		HT-9	100
		PCA	10

The results of the computer modeling are presented in Figs. 6.6-1 through 6.6-4. Figure 6.6-1 shows a number of different results. First of all, as the helium purge stream mass flow rate increases, the fraction of tritium which permeates across the outer wall of the heat exchanger and which leaves via the purge stream also increases to the point where approximately 90% of the entering tritium leaves in this way. The other 10% permeates through to the secondary coolant. The reason for this behavior is due to the lower partial pressure of tritium which develops in the double wall space as the helium

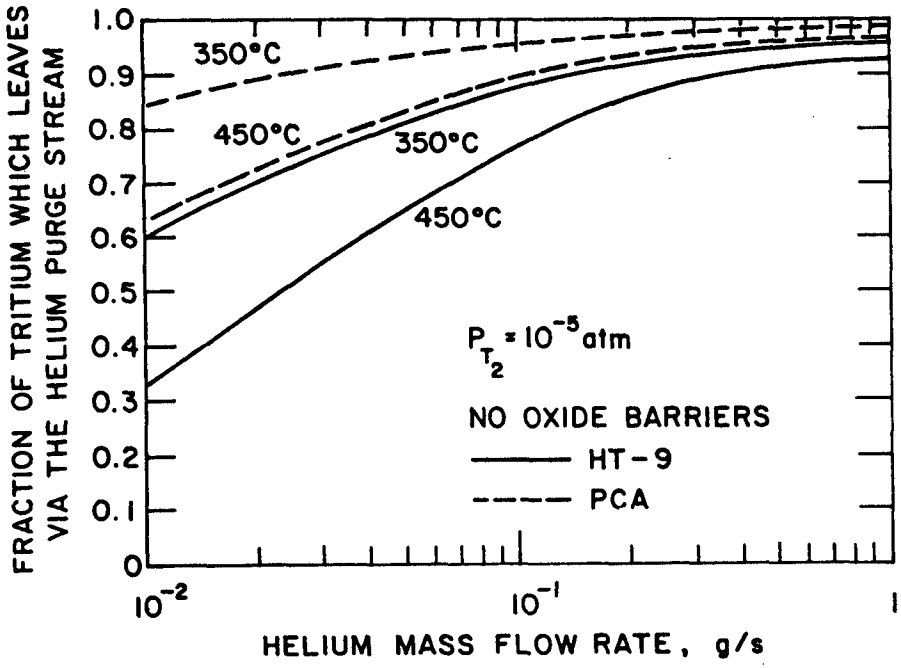


Figure 6.6-1. The effect of temperature on the fraction of tritium leaving the heat exchanger via the helium purge stream. (Constant total purge stream pressure.)

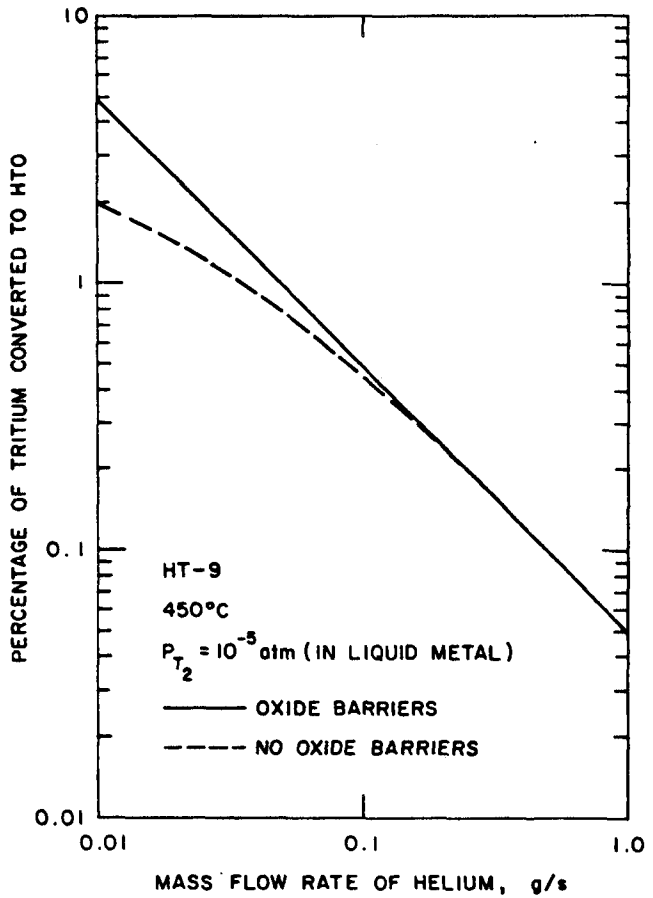


Figure 6.6-2. Percentage of tritium converted to HTO as a function of the helium purge stream mass flow rate. (Constant total purge stream pressure.)

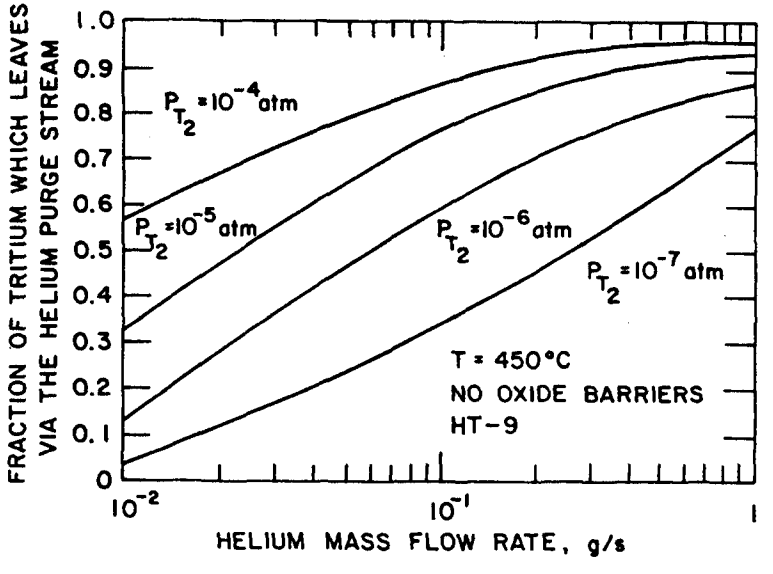


Figure 6.6-3. Fraction of tritium entering the heat exchanger which leaves via the helium purge stream. Curves shown are for various partial pressures of tritium in the liquid metal. (Constant total purge stream pressure.)

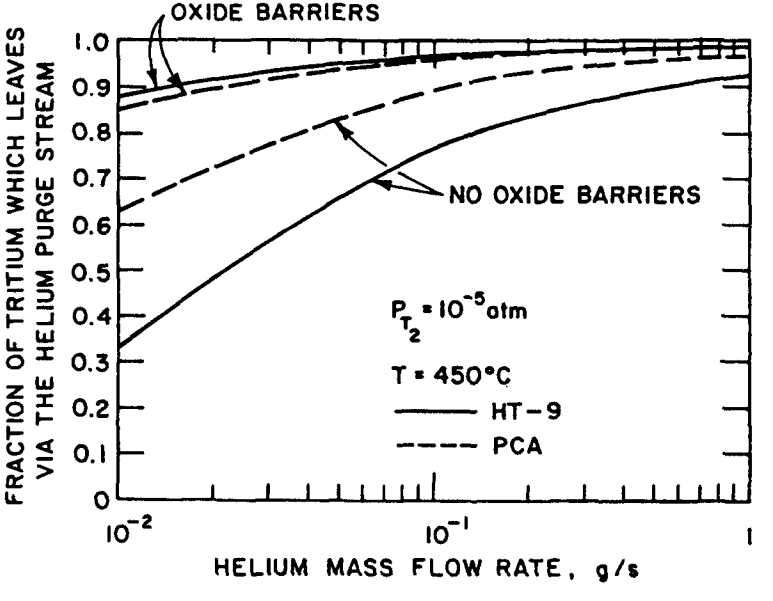


Figure 6.6-4. The effect of oxide barriers on the fraction of tritium leaving the heat exchanger via the helium purge stream. (Constant total purge stream pressure.)

purge stream volumetric flow rate increases. The permeation rate into the secondary coolant is a function of the tritium partial pressure in the double wall gap. Since the tritium permeation rate from the primary coolant side into this gap remains fairly constant, the tritium concentration within the gap becomes more dilute, i.e., its partial pressure decreases with increasing helium flow rate. This causes the decrease in tritium permeation to the secondary coolant. As will be pointed out later, the tritium in the exit stream exists primarily as T_2 rather than T_2O.

A second result illustrated by Fig. 6.6-1 is that an increase in temperature leads to less tritium being carried out in the purge stream, i.e., more tritium leaks into the secondary coolant. Both the permeation rate and the oxidation rate increase with increasing temperature. Apparently, the permeation rate increase with temperature overshadows any kinetic rate increase, as can be seen in the different activation energies shown in Table 6.6-3.

In Fig. 6.6-2, results are shown which indicate that only a small fraction of tritium is oxidized to HTO. The oxidized fraction increases as the helium purge stream flow rate decreases indicating that the longer residence time at low purge stream flow rates increases conversion. Unfortunately, as shown in Fig. 6.6-1, these longer residence times also increase the fraction of tritium which permeates into the secondary coolant.

Figure 6.6-3 shows the effect of different tritium partial pressures in the liquid metal coolant on the fraction of tritium which leaves the heat exchanger tube via the helium purge stream. For a given helium purge stream flow rate, a lower partial pressure of tritium in the primary coolant gives a lower fraction of tritium leaving via the helium purge stream.

The effectiveness of oxide barriers in reducing the amount of tritium which permeates to the secondary coolant is illustrated in Fig. 6.6-4. Oxide barriers, at low helium mass flow rates, substantially increase the fraction of tritium which is retained in the helium purge stream. The effect is greater for HT-9 than it is for PCA.

In light of the fact that heterogenous tritium oxidation does not contribute much in the way of reducing tritium permeation into the secondary coolant, oxide barriers appear to hold the most promise for controlling tritium leakage in a double-walled heat exchanger. Of the amount of tritium which

enters the heat exchanger 85 to 98% could, according to the model, be recovered in the purge stream. One phenomenon that may be used to increase tritium recovery is the temperature dependence of the permeation rate. Because of this temperature dependence, more tritium will permeate in the hot side of the heat exchanger than in the cold side. If one could somehow, perhaps with a novel double-walled heat exchanger design, recover the tritium in the hot side, then one could cut down on the tritium residence time and thus reduce permeation.

6.6.4 Tritium Permeation

6.6.4.1 Tritium Permeation and Inventory in First Wall

Tritium permeation into the coolant and inventory in the first wall are important issues for D-T fusion reactors. High concentrations of tritium in the near surface region of the first wall can be reached by implantation of the charge-exchange neutral flux with a relatively slow recombination rate of these atoms into molecules at the surface. This large concentration of dissolved tritium near the surface results in a concentration gradient through the wall that causes the tritium to diffuse into the bulk and consequently to the coolant of the first wall.

Calculations are presented for two different structures of the first wall, i.e., a PCA first wall and a vanadium first wall for both tokamak and tandem mirror reactors. The models and the code used for these calculations are described elsewhere.[6.6-11] In these models the time-dependent diffusion equation with an implanted source is solved numerically. The boundary condition on both sides of the wall is assumed to be characterized by a recombination constant with a factor α, the molecular sticking coefficient, being taken to be a measure of surface cleanliness. Since the degree of surface cleanliness depends on many parameters like surface composition, presence of oxides, radiation damage, etc. α cannot be uniquely defined, instead, it has to be measured for each particular conditions and environments. The results for tritium permeation into the coolant and tritium inventory in first wall are shown to be strongly dependent on the value of α chosen for both surfaces of the wall. It has been generally assumed that higher values of α (i.e., $\alpha = 1$ or 0.5) represents a relatively clean surface while low values of α ($\alpha < 10^{-3}$) represents a relatively non-clean surface.

The tritium permeation and inventory as a function of number of years in operation for a PCA tokamak first wall are shown in Fig. 6.6-5 and Table 6.6-4. The area of the first wall is 780 m^2 with a tritium flux to the wall of about 1.28×10^{16} particles/cm^2 sec at 100 eV. The back surface temperature (T_b) is estimated to be 330°C while the front wall temperature (T_F) varies from 595°C in first year of operation to about 450°C at the fourth year of operation. This is due to the thinning of the first wall caused by surface erosion of 1 mm/yr. In this calculation α_b i.e., the back surface recombi-

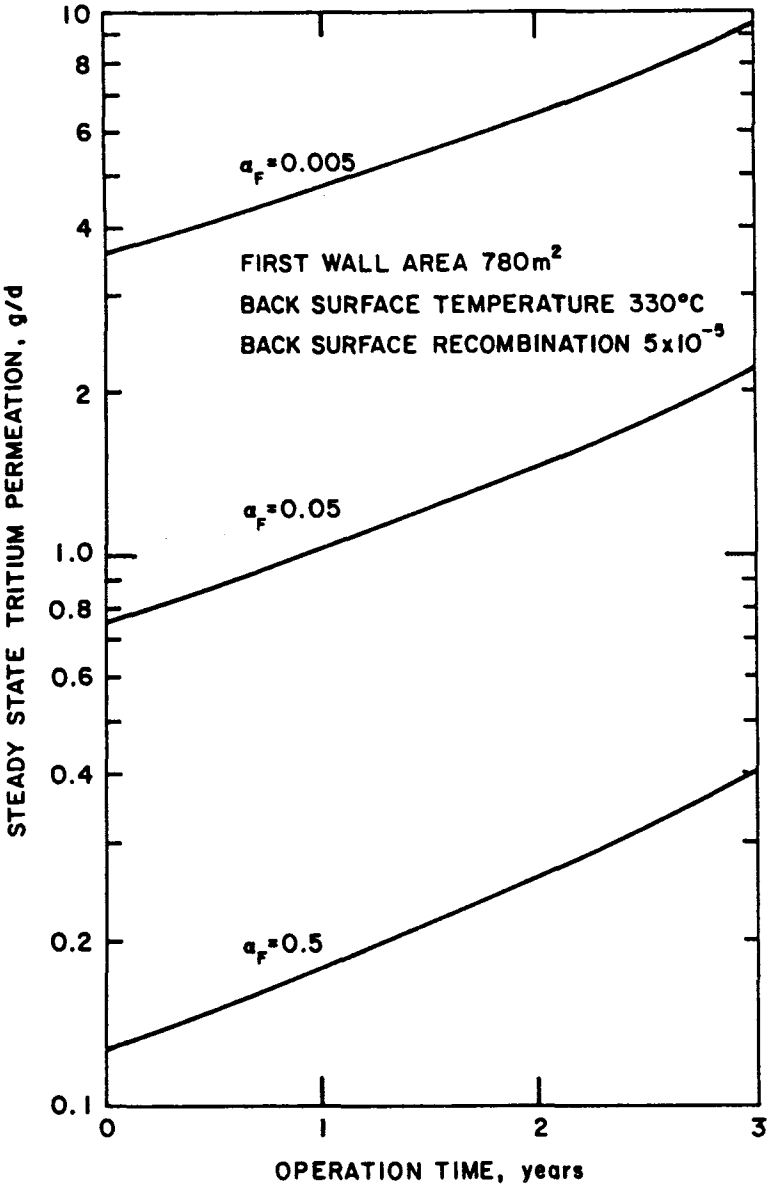


Figure 6.6-5. Tritium permeation into the coolant as a function of years of operation.

TABLE 6.6-4. TRITIUM PERMEATION AND INVENTORY FOR PCA TOKAMAK FIRST WALL

Tritium flux to the wall = 1.28×10^{16} particles/cm^2 sec
First wall area = 780 m^2
Back surface recombination coefficient (α_b) = 5×10^{-5}
Back surface temperature (T_b) = 330°C

Years of Operation	Wall Thickness (mm)	Front Wall Temperature (°C)	α_F = 0.5†		α_F = 0.05†		α_F = 0.005†	
			† (g/d)	I (g)	† (g/d)	I (g)	† (g/d)	I (g)
0	6.	595	0.13	18.7	0.77	56.7	3.67	171.1
1	5.	545	0.18	18.4	1.0	55.2	4.82	165.4
2	4.	500	0.26	17.4	1.44	51.7	6.47	153.6
3	3.	450	0.40	16.1	2.16	47.	9.3	138.2

†d_F = front surface recombination coefficient.
† = permeation rate to the coolant (g/d).
I = tritium inventory in first wall (g).

nation coefficient, is assumed to be 5×10^{-5} (to take into account the effect of an oxide layer existing as a result of the water cooled first wall). The front surface recombination coefficients i.e., α_F is varied from $\alpha_F = 0.5$ (relatively clean) to $\alpha_F = 0.005$ (relatively non-clean), with $\alpha_F = 0.5$ as a reference case. It can be seen from Fig. 6.6-5 that the permeation rate is strongly dependent on the surface recombination coefficients. Lower values of α_F results in higher permeation rates to the coolant and larger tritium inventories in the first wall as shown in Table 6.6-4. This inventory is due to the mobile tritium atoms in the bulk since no neutron induced traps are expected at these high temperatures. It can also be seen that the rate of tritium permeation to the coolant increases as the operation time of the reactor continues. This is mainly because of the wall erosion (1 mm/yr is assumed) which results in a smaller temperature difference across the first wall that drives more tritium to diffuse towards the coolant. On the other hand, the tritium inventory in the wall decreases slightly as the operation time of the reactor continues. This is mainly due to two factors. The first is the wall thinning which reduces the inventory and the second factor which is slightly less dominant, is the lower temperature difference which increases the diffusive inventory.

The tritium permeation and inventories for PCA and vanadium first wall for both tokamak and tandem mirror reactor concepts are shown in Table 6.6-5. Since the vanadium alloy wall is used with liquid lithium coolant it is assumed that there is no oxide layer at the back surface of the wall. This means that the back surface recombination coefficient α_b is high and it is assumed in this case that $\alpha_b = \alpha_F = 1$. This results in a much higher tritium permeation rate (more than 3 orders of magnitude) from the vanadium wall to the liquid lithium coolant than those associated with PCA structure and water coolant for the conditions shown in Table 6.6-5. The significance of these results will depend on both the efficiency and the economics of the tritium extraction unit in the liquid lithium coolant loop.

The study of tritium permeation and inventory in the first wall of the reactor indicates a strong dependancy on the surface conditions of the wall. Accurate characterization of the surface conditions in an actual reactor environment require in situ experimental work to study all the parameters that can contribute to the recombination coefficient. The numbers shown in this study

TABLE 6.6-5. TRITIUM PERMEATION AND INVENTORY FOR PCA AND VANADIUM FOR BOTH TOKAMAK AND TANDEM MIRROR REACTOR CONCEPTS

First Wall Structure	Design Specifications	Tokamak	Tandem Mirror
Vanadium	Tritium flux to the wall $\left(\frac{\#}{cm^2 \cdot sec}\right)$	1.28×10^{16}	1.5×10^{15}
	First wall thickness (mm)	6	2
	Area of first wall (m^2)	780	490
	Front surface temperature (°C)	600	500
	Back surface temperature (°C)	400	500
	Front surface recombination (α_F)	1	1
	Back surface recombination (α_b)	1	1
	Tritium permeation (g/d)	168	162
	Inventory in first wall (g)	5.6	0.65
PCA	Tritium flux to the wall $\left(\frac{\#}{cm^2 \cdot sec}\right)$	1.28×10^{16}	1.5×10^{15}
	First wall thickness (mm)	6	3
	Area of first wall (m^2)	780	490
	Front surface temperature (°C)	595	450
	Back surface temperature (°C)	330	450
	Front surface recombination (α_F)	0.5	0.5
	Back surface recombination (α_b)	5×10^{-5}	5×10^{-5}
	Tritium permeation (g/d)	0.13	0.19
	Inventory in first wall (g)	18.7	3.7

for tritium permeation and inventory should only be looked at on a relative basis for different reactor designs and not on absolute values to judge a specific reactor or a blanket concept.

6.6.4.2 Tritium Permeation in HT-9

Data for hydrogen and its isotope permeation in steel alloys has been extensively reviewed in Ref. 6.6-12. Figure 6.6-6 shows the recommended permeability of tritium in HT-9 ferritic steel as a function of temperature. This recommended permeability is for "clean" surface condition and can be represented by:

$$P_m = \frac{4.66 \times 10^{-3}}{\sqrt{3}} \exp\left(-11100 \text{ "cal/mol"}/RT\right) \frac{CCS\ (S.T.P.)}{CM \cdot S \cdot atm^{1/2}} \qquad [6.6\text{-}6]$$

It is well known that oxide and other containment films on the surface can strongly impede hydrogen permeation. So it is recommended as given in Ref. 6.6-12 that for in situ process oxide layer at temperature around 500°C that the permeability given above be reduced by a factor of 20 to 100 to take into effect the oxide resistance to hydrogen permeation at the surface. The reference value used in BCSS calculation was 100.

6.6.5 Isotopes Effect

The effect of isotopes on tritium permeation was first summarized by Hickman.(6.6-13) For a classical permeation case, the tritium has to be dissociated to atomic form, of which the surface will absorb. The dissociation relationship is:

$$T_2 \rightleftarrows 2T \qquad [6.6\text{-}7]$$

therefore,

$$[T] = k\, P_{T_2}^{1/2} . \qquad [6.6\text{-}8]$$

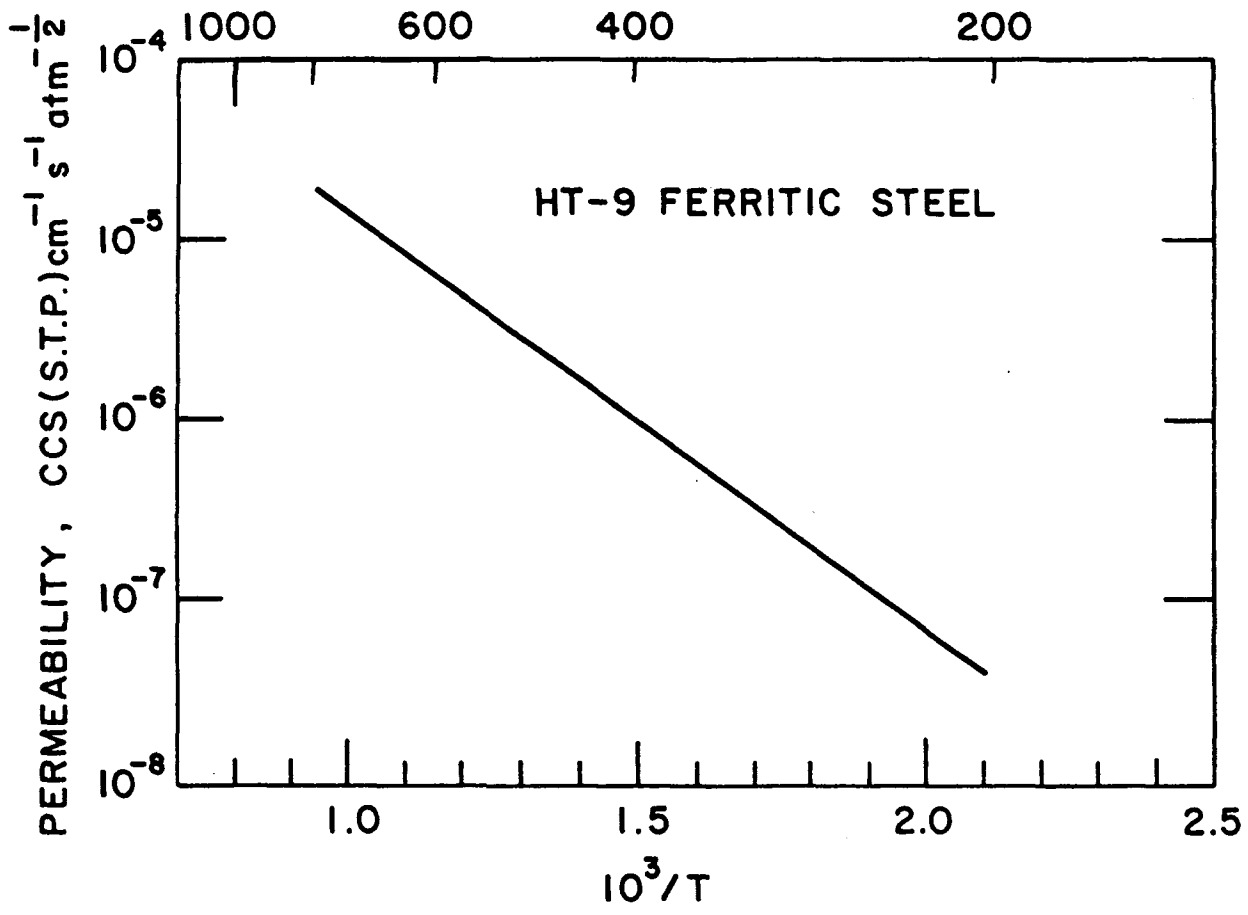


Figure 6.6-6. Permeation of hydrogen in HT-9 ferritic steel.

This is the reason of the square root pressure depending on the classical permeation relationship, or

$$\dot{M} = DS\left[\left(P_{T_2}^{1/2}\right)_1 - \left(P_{T_2}^{1/2}\right)_2\right] \qquad [6.6\text{-}9]$$

in which

D is the diffusivity of tritium in structure,

S is the solubility,

$\left(P_{T_2}\right)_1$ is the upstream tritium partial pressure,

$\left(P_{T_2}\right)_2$ is the downstream tritium partial pressure,

$\dot{M}$ is the permeation rate.

The square root dependency greatly increase the driving force of tritium permeation at low partial pressure.

If hydrogen is added to the system and $P_{H_2} >> P_{T_2}$, the situation can be very different. For this case, it can be assumed that all T will exist in the HT form, and for tritium to permeate, HT had dissociated by

$$HT \underset{\leftarrow}{\overset{\rightarrow}{\rightleftharpoons}} H + T \qquad [6.6\text{-}10]$$

However, H is controlled by the following relationship

$$H_2 \underset{\leftarrow}{\overset{\rightarrow}{\rightleftharpoons}} 2H \qquad [6.6\text{-}11]$$

and

$$[H] = K(P_{H_2})^{1/2} \qquad [6.6\text{-}12]$$

Since

$$[H]\ [T] = K^2\ P_{HT} \qquad [6.6\text{-}13]$$

Therefore

$$[T] = K\ P_{HT}/(P_{H_2})^{1/2} \qquad [6.6\text{-}14]$$

and

$$\dot{M} = DS\ [(P_{HT}/(P_{H_2})^{1/2})_1 - (P_{HT}/(P_{H_2})^{1/2})_2] \qquad [6.6\text{-}15]$$

It is interesting to note that by the addition of H_2, the functional relationship of the permeation changes from $P_{T_2}{}^{1/2}$ dependent of Eq. [6.6-9], to P_{HT} linear dependent of Eq. [6.6-15]. If 1 Pa pressure hydrogen is added to the system, the allowable HT pressure at the steam generator is 4.5×10^{-4} Pa, instead of 2.1×10^{-7} Pa for the case with no hydrogen. This increasing of allowable pressure by a factor of 10^3 will be very valuable in the system design.

It has been proved theoretically that, as the partial pressure of T_2 decreased, the permeation relationship will start to deviate from the classical permeation relationship and, ultimately, to a linear dependency. Theory cannot predict at what pressure this deviation will start to occur. Experiments claimed that the linear dependency has been observed.(6.6-14) But is is

not clear whether this linear dependency is caused by the background hydrogen partial pressure, or caused only by the reduction of tritium partial pressure. In a recent article,[6.6-15] Stover observed that the square root dependency is valid down to 10^{-6} Pa hydrogen pressure. The isotope effects, as described here, will have a major impact on the reactor design. In addition, to reduce the tritium permeation, it will also reduce purge gas volumetric flow rate, tritium inventory in both structure and breeding material. Although theoretically the model should be correct, it has not been verified experimentally. The importance of this effect should be clear, since almost all of the design R=1 have adopted this technique to reduce the tritium leakage to acceptable level.

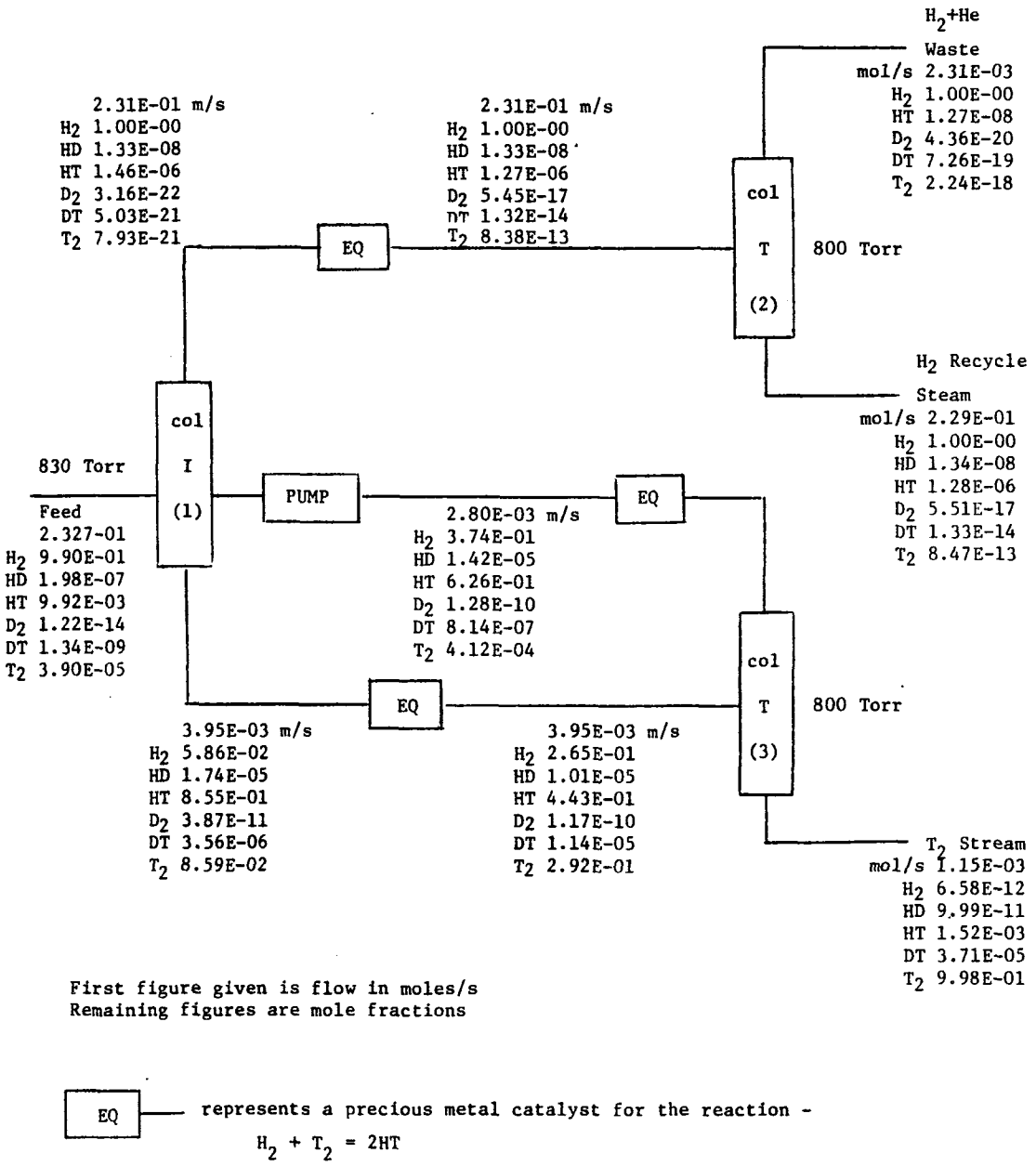
The flow diagram of the isotope separation system to separate the tritium from the hydrogen is shown on Fig. 6.6-7.[6.6-16] The capital cost of the system is estimated to be <10 million dollars and is not a major economics factor.

6.6.6 Tritium Release Guidelines

Any design guidance or limits on tritium effluents from a fusion facility are necessarily speculative. It is not known what future standards might exist. Ideally, the eventual standards will themselves be a function of the cost versus benefit of controlling tritium releases. For purposes of this study, designers needed some guidance concerning what level of releases is "good" and what level is "bad". Based on a regulatory limit of 10 mrem/yr to the maximum individual, which equals the present proposed U.S. EPA standard, a 100 m stack height, and a 500 m site boundary, it was found that atmospheric tritium releases must be kept below 200 Ci/day, without leaving any of the dose limit for non-tritium exposure. Assuming that 75 percent of the tritium getting into the steam side is released atmospherically, allotting some of the 10 mrem/yr for non-tritium exposure, and setting the design limit lower than the regulatory limit, implies a design limit of 10-100 Ci/day through the steam generator. CANDU reactors would meet these various guidelines. Further details can be found in Subsection 5.4.4.3.1.

6.6.7 Conclusions and Summary

From the study of the special task group, the following values are recommended as a common basis ground rule for each design concept:



First figure given is flow in moles/s
Remaining figures are mole fractions

EQ — represents a precious metal catalyst for the reaction -

$$H_2 + T_2 = 2HT$$

Figure 6.6-7. Breeding blanket recovery system.

1. Permeability of T_2 in PCA (316 SS) is

$$P_m = \frac{2.33 \times 10^{-2}}{\sqrt{3}} \exp(-15700/RT) \quad \frac{CC\ (S.T.P.)}{cm - sec - atm^{1/2}} \cdot$$

2. Permeability of T_2 in HT-9 is

$$P_m = \frac{4.66 \times 10^{-3}}{\sqrt{3}} \exp(-11100/RT) \quad \frac{CC\ (S.T.P)}{cm - sec - atm^{1/2}} \cdot$$

3. Oxide barrier factor for PCA is 3-10, reference value is 10.

4. Oxide barrier factor for HT-9 is 20 ~ 100, reference value is 100.

5. Appropriate design limit for tritium leakage rate at steam generation is 10 ~ 100 Ci/day.

6. Based on the existing experimental results, it is not possible to determine the form of tritium released from solid breeders. It is recommended that two cases be studied:

   a. 100% of tritium is in the elementary form.
   b. 1% of tritium is in the elementary form.

It should be emphasized that this set of conditions has been chosen based on the judgement of the group. The results from literature are far from consistent to each other.

Detailed calculations for blanket tritium systems of each blanket concept have been carried out, as summarized in Table 6.6-6 and 6.6-7 for tokamak and TMR respectively. It appears that the blankets can be divided into four categories from tritium containment considerations.

1. Self-cooled lithium blanket. No major problem is anticipated in this type of design. The high tritium solubility results a very low tritium partial pressure and therefore, the problem is to recover the tritium at an acceptable inventory, not in tritium containment.

2. He-cooled lithium blanket. Moderate effort may be required for tritium containment. The source of the tritium is from the plasma, not the breeding material.

3. Solid breeders and 17Li-83Pb self-cooled blankets. Major effort is required for tritium containment. By using combined effects of oxide barrier and isotope swamping, tritium leakage can be limited to an acceptable level. The calculation is very sensitive to the parameters used and the seriousness of the problem may increase or decrease significantly by the new experimental results to be obtained in the future. The possible deviation of the permeation relationship to P_{T_2} linear dependent is not included because it is not possible to determine at what pressure this deviation will occur. The problem may not exist if the deviation occurs at a high T_2 pressure.

4. The FLIBE blanket. The problem here is critical. Since tritium in FLIBE obeys Henry's law, instead of Sievert's law, the solubility is very low. The tritium partial pressure over the breeding material on the reference design is 2600 Pa, which requires two metallic diffusion barriers, each much more effective than the oxide, as well as an oxide barrier on one of the metallic barriers, to reduce the tritium leakage rate. A major R&D program will be required to assess the possibility and the reliability of the diffusion barrier under the environemnt to be expected before the feasibility of the blanket can be assessed.

TABLE 6.6-6. TRITIUM CALCULATION SUMMARIES FOR TOKAMAK DESIGNS

	Production g/day	Breeder T_2 Pressure Pa	First Wall to Breeder g/d	Purge to Coolant g/d	First Wall to Coolant g/d	Coolant T_2 Pressure Pa	First Wall Inventory g	Blanket Structure Inventory g
$LiAlO_2$[a] NS/HT-9 Be	924	263	---	NA	.22	NA	18.7	42

Li/Li V	953	8.6×10^{-9}	168	---	---	---	5.6	.5
Li_2O/He HT-9	828	.69	---	.64	.22	3.6×10^{-4}	18.7	1.1
$LiAlO_2$ He/HT-9 Be	823	.75	---	2.23	.22	1.3×10^{-3}	18.7	1.2
Li/He HT-9	866	1.2×10^{-7}	---	---	.22	9.8×10^{-7}	18.7	7×10^{-2}
FLIBE/He[b] HT-9/Be	846	2600	---	113	.22	.19	18.7	189
$LiAlO_2/H_2O$ HT-9/Be	869	2.2	---	.01	.22	6×10^{-6}	18.7	9.3

[a]Consistent information was not available.

[b]A W coating is required in the blanket and an Al coating is required in the steam generator. System was designed at lower thermal power and scaled to the higher thermal power for both tokamak and TMR designs.

TABLE 6.6-6. TRITIUM CALCULATION SUMMARIES FOR TOKAMAK DESIGNS (CONTINUED)

	Purge Inventory g	Coolant Inventory g	Breeding Material Inventory g	Leakage to Na Curie/d	Leakage to H_2O Curie/d	T to[a] Coolant from Be g/d	H_2 Added in Purge g/d	Σ H_2 Pressure Maximum Pa	Maximum H[b] Concentration wppm
$LiAlO_2$[c] NS/HT-9 Be	.4	900	2000	---	NA	---	added	NA	NA

Li/Li V	---	---	490	300	3	---	---	8.6×10^{-9}	.15
Li_2O/He HT-9	10.5	3.3×10^{-5}	134	---	44	---	9×10^{4}	250	.6
$LiAlO_2$ He/HT-9 Be	1.0	1.1×10^{-5}	38	---	44	9	9×10^{4}	250	.6
Li/He HT-9	---	6×10^{-7}	330	---	16	---	---	1.2×10^{-7}	.5
FLIBE/He[d] HT-9/Be	---	---	.5	---	260	9	---	2600	1.5
$LiAlO_2/H_2O$ HT-9/Be	.03	53	2300	---	2	---	5.5×10^{3} (10 Pa in H_2O)[e]	42	.5

[a]Tritium generated in Be was not included in evaluation because the problem was uncovered too late for system design.

[b]Maximum total hydrogen isotopes concentration in structure, either due to implantation or due to solubility.

[c]Consistent information was not available.

[d]A W coating is required in the blanket and an Al coating is required in the steam generator. System was designed at lower thermal power and scaled to the higher thermal power for both tokamak and TMR designs.

[e]10 Pa of hydrogen over pressure in the primary coolant was assumed and T/H ratio in the gas phase was assumed to be equal to T/H ratio in water.

TABLE 6.6-7. TRITIUM CALCULATION SUMMARIES FOR TMR DESIGNS

	Production g/day	Breeder T_2 Pressure Pa	First Wall to Breeder g/d	Purge to Coolant g/d	First Wall to Coolant g/d	Coolant T_2 Pressure Pa	First Wall Inventory g	Blanket Structure Inventory g
$LiAlO_2$[a] NS/HT-9 Be	619	263	---	NA	.2	NA	3.7	29
Li/Li HT-9	564	8.6×10^{-9}	.2	---	---	---	3.7	2×10^{-2}
LiPb/LiPb V	569	1.3×10^{-4}	162	---	---	---	.65	5
Li/Li V	573	8.6×10^{-9}	162	---	---	---	.65	.47
Li_2O/He HT-9	550	.78	---	.65	.2	6.4×10^{-4}	3.7	1.0
$LiAlO_2$ He/HT-9 Be	554	.84	---	2.31	.2	1.9×10^{-3}	3.7	.8
Li/He HT-9	558	1.1×10^{-7}	---	---	.2	7.8×10^{-7}	3.7	7×10^{-2}
FLIBE/He[b] HT-9/Be	622	2600	---	83	.2	.14	3.7	139
$LiAlO_2/H_2O$ HT-9/Be	586	2.2	---	.01	.2	6×10^{-6}	3.7	9.3

[a]Consistent information was not available.

[b]A W coating is required in the blanket and an Al coating is required in the steam generator. System was designed at lower thermal power and scaled to the higher thermal power for both tokamak and TMR designs.

TABLE 6.6-7. TRITIUM CALCULATION SUMMARIES FOR TMR DESIGNS (CONTINUED)

	Purge Inventory g	Coolant Inventory g	Breeding Material Inventory g	Leakage to Na Curie/d	Leakage to H_2O Curie/d	T to[a] Coolant from Be g/d	H_2 Added in Purge g/d	Σ H_2 Pressure Maximum Pa	Maximum H[b] Concentration wppm
$LiAlO_2$ NS/HT-9 Be	2	500	250	---	NA	---	added	NA	NA
Li/Li HT-9	---	---	336	200	2	---	---	8.6×10^{-9}	.3
LiPb/LiPb V	.02	---	.1	---	10	---	4.2×10^{4}	.3	10
Li/Li V	---	---	336	200	2	---	---	8.6×10^{-9}	.3
Li_2O/He HT-9	.7	3.8×10^{-5}	131	---	41	---	5.6×10^{4}	238	.6
$LiAlO_2$ He/HT-9 Be	.7	1.3×10^{-4}	24	---	28	6	5.7×10^{4}	256	.6
Li/He HT-9	---	6×10^{-7}	233	---	10	---	---	1.1×10^{-7}	.3
FLIBE/He[d] HT-9/Be	---	---	0.4	---	191	6	---	2600	1.5
$LiAlO_2/H_2O$ HT-9/Be	.03	53	1500	---	2	---	3.7×10^{3} (10 Pa in H_2O)[e]	42	.5

[a]Tritium generated in Be was not included in evaluation because the problem was uncovered too late for system design.

[b]Maximum total hydrogen isotopes concentration in structure, either due to implantation or due to solubility.

[c]Consistent information was not available.

[d]A W coating is required in the blanket and an Al coating is required in the steam generator. System was designed at lower thermal power and scaled to the higher thermal power for both tokamak and TMR designs.

[e]10 Pa of hydrogen over pressure in the primary coolant was assumed and T/H ratio in the gas phase was assumed to be equal to T/H ratio in water.

REFERENCES FOR SECTION 6.6

6.6-1 C. E. Easterly and M. R. Bennett, "Radiation Catalyzed Conversion of Tritium Gas to Tritiated Water," Nuclear Technology/Fusion, 4, 2, p. 116 (1983).

6.6-2 G. R. Longhurst, "Gamma Radiation Effects on Tritium Permeation Through Stainless Steel, "Nuclear Technology/Fusion, 4, 2, p. 681 (1983).

6.6-3 S. Nasu et al., "A Preliminary In-Pile Test of Tritium Release from Li_2O Pellets," JAERI-memo 9276 (1980).

6.6-4 H. Kudo e tla., "Chemical Behaviors of Tritium Produced by $^6Li(n,\alpha)T$ Reaction in Li_2O," J. Igorg. Nucl. Chem., Vol. 40, pp. 363-367, Pergamon Press, 1978.

6.6-5 K. Tanaka et al., "Tritium Recovery of the Fusion Reactor of Lithium Oxide Blanket," Int. Conf. Rad. Effect & Tritium Technology for Fusion Reactors, CONF 750989 (1975).

6.6-6 R. G. Clemmer et al., "The TRIO Experiment," to be published as an Argonne National Laboratory Report.

6.6-7 T. Kurasawa et al., "In-Pile Test of Tritium Recovery from Lithium Oxide - Tritium Release Behavior," JAERI-M 84-087 (May 1984).

6.6-8 P. J. Papagiannakopoulos and C. E. Easterly, "Mechanism of HTO Formation in Gaseous Tritium Mixtures," Int. J. of Chem. Kin. 14, (1982), pp. 77-90.

6.6-9 C. E. Easterly and M. R. Bennett, "Radiation Catalyzed Conversion of Tritium Gas to Tritiated Water," Nucl. Tech./Fusion, 4, (September 1983), pp. 116-120.

6.6-10 J. C. Bixel and C. J. Kershner, "A Study of Catalytic Oxidation and Oxide Adsorption for the Removal of Tritium from Air," Proc. 2nd Environmental Protection Conference, WASH-1332, U.S. AEC (1974).

6.6-11 M. I. Baskes, "Diffuse 83," Report No. SAND83-8231, June 1983.

6.6-12 A. M. Hassanein and D. K. Sze, "Data Base Assessment and Recommendation Values for Hydrogen Permeation Through Steel Alloys," ANL/FPP/TM-186.

6.6-13 R. G. Hickman, "Some Problems Associated with Tritium in Fusion Reactors," Technology of Controlled Thermonuclear Fusion Experiments and the Engineering Aspects of Fusion Reactors," Austin, Texas, November 1972.

6.6-14 A. S. Zarchy and R. C. Axtmann, J. Nucl. Mater. 79(1979)110.

SECTION 6.7

TABLE OF CONTENTS

PAGE NO.

6.7 Structural Analysis.....6.7-1

6.7.1 Load Definition.....6.7-1

6.7.2 Design Criteria.....6.7-2

6.7.2.1 Classification of Stresses.....6.7-2

6.7.2.2 Stress Allowables.....6.7-3

6.7.2.3 Crack Growth Life.....6.7-14

6.7.3 Comparison of PCA, HT-9 and V-15Cr-5Ti as Structural Materials.....6.7-21

6.7.4 R&D Requirements for Structural Design and Analysis.....6.7-29

LIST OF FIGURES FOR SECTION 6.7

FIGURE NO.	TITLE	PAGE NO.
6.7-1	Allowable primary stresses for HT-9 (normalized and tempered) as a function of fluence and temperature. Dashed lines indicate allowable primary stress based on thermal creep	6.7-8
6.7-2	Allowable primary stress for V-15Cr-5Ti (strain hardened) as a function of fluence and temperature. Dashed lines indicate allowable primary stress based on thermal creep	6.7-9
6.7-3	Allowable primary stress of PCA (25 CW) as a function of fluence and temperature. Dashed lines indicate allowable primary stress based on thermal creep	6.7-10
6.7-4	Bilinear damage diagram for computing creep fatigue life	6.7-15
6.7-5	Modelling of a grooved wall by a stepped beam	6.7-15
6.7-6	Variation of stress concentration factors with thickness ratio for a grooved plate	6.7-18
6.7-7	Variation of crack driving force (ΔK) with crack length in a HT-9 plate of thickness 10 mm subjected to a temperature gradient of 300°C	6.7-20
6.7-8	Variation of maximum stress intensity factor with temperature gradients and thickness of the wall. Dashed lines correspond to a width of the solid part of the groove ℓ_2 = 2 cm	6.7-20
6.7-9	Fatigue crack growth life of a grooved plate (HT-9) of 5 mm thickness. Dashed lines correspond to a width of the solid part of the groove ℓ_2 = 2 cm	6.7-22
6.7-10	Fatigue crack growth life of a grooved plate (HT-9) of 7.5 mm thickness. Dashed lines correspond to a width of the solid part of the groove ℓ_2 = 2 cm	6.7-22
6.7-11	Fatigue crack growth life of a grooved plate of thickness 10 mm. Dashed lines correspond to a width of the solid part of the groove ℓ_2 = 2 cm	6.7-23
6.7-12	Comparison of thermal stress factor (η) of three candidate blanket materials	6.7-25

6.7-13 Variation of maximum allowable surface heat flux as a function of film temperature drop, first wall thickness and coolant outlet temperature for a solid plate first wall made of PCA, HT-9 and V-15Cr-5Ti.....6.7-27

6.7-14 Variation of maximum allowable surface heat flux (based on fatigue crack growth) as a function of total wall thickness and film temperature drop for a grooved first wall made of PCA, HT-9 and V-15Cr-5Ti.....6.7-28

LIST OF TABLES FOR SECTION 6.7

TABLE NO.	TITLE	PAGE NO.
6.7-1	SCHEDULE OF CYCLES PER YEAR	6.7-3
6.7-2	ALLOWABLE STRESSES FOR PCA (25% CW)	6.7-5
6.7-3	ALLOWABLE STRESSES FOR HT-9 (NORMALIZED AND TEMPERED)	6.7-6
6.7-4	ALLOWABLE STRESSES FOR V-15Cr-5Ti (STRAIN HARDENED)	6.7-7
6.7-5	ALLOWABLE PRIMARY STRESSES FOR VARIOUS SERVICE LEVELS	6.7-13
6.7-6	ALLOWABLE PRIMARY PLUS SECONDARY STRESS RANGE FOR VARIOUS SERVICE LEVELS	6.7-13

6.7 Structural Analysis

Structural analysis of a fusion reactor blanket involves a three-step process. First, the geometric configuration of the blanket is determined by interactions with other disciplines such as neutronics, heat transfer, etc. by an iterative procedure. The next step involves the definitions of loads. Loadings considered in the present study are those due to coolant pressure, temperature gradients due to surface and volumetric heat fluxes, electromagnetic body forces due to disruptions, inertia body forces due to earthquakes and dead weight, and body forces in ferritic steel structures due to magnetostatic interaction. After conducting the appropriate stress analyses using the given loading on the defined structures, the final step involves comparing and ensuring that the computed stresses fall within allowables, i.e., satisfy Design Criteria.

The first item, geometric configuration for the various concepts, has been discussed in detail in other sections of this report. The other two items will be discussed here briefly. Three candidate blanket materials, PCA, HT-9, and V-15Cr-5Ti are compared as structural materials. Finally, a prioritized list of R&D needs for structural design and analysis is presented.

6.7.1 Load Definition

Loadings on the blanket can be categorized, following the American Society of Mechanical Engineers (ASME) Boiler and Pressure Vessels Code, Section III into three levels. Level A service loadings are any loadings arising from system startup, operation in the design power range, hot standby and system shutdown. Level B loadings are deviations from Level A loadings which are frequent enough that design should include a capability to withstand these loadings without operational impairment. These events include any abnormal incidents not resulting in a forced outage and also forced outages for which the corrective action does not include any repair of mechanical damage. Finally, Level C loadings are deviations from Level A loading which require shutdown for correction of the loading or repair of damage in the system. These conditions have a low probability of occurrence but are involved to provide assurance that no gross loss of structural integrity will result due to damage developed in the system. Stresses due to different level loadings, in general, may have different allowables.

Loadings due to coolant pressure (Level A), surface and volumetric heat fluxes (Level A) with accompanying heat transfer analyses, and electromagnetic forces (Level B) on the first wall due to disruptions have been discussed in details for the various design concepts in their respective sections. Magnetostatic forces (Level A) on the first wall made of ferritic steel generate negligible stresses in the first wall itself. However, global analyses of the complete blanket together with the supports are needed to fully evaluate the impact of these loadings. Although such analyses have not been carried out for most design concepts, it is expected that supports for the blankets can be judiciously provided to keep these stresses manageable.

As an initial check for earthquake loading (Level B), all blankets evaluated by the BCSS were examined to determine whether they would survive a Zone II earthquake with ground accelerations of .09g vertical and .13g horizontal in any two orthogonal directions applied simultaneously. Two alternative procedures of conducting the earthquake analysis were considered. First, a detailed structural dynamics analysis may be carried out. An alternative approach is to use, simply but more conservatively, an equivalent static analysis with applied acceleration of 4.4g in all three directions simultaneously. In all cases the second alternative has been followed. However, as in the case of disruption loading, a global analysis of the blanket, which is needed to fully evaluate the effects of earthquake loading on the blanket, has not been carried out for most designs.

The schedule of cycles needed to conduct the fatigue and creep-fatigue analysis is given in Table 6.7-1. For present purposes, one disruption per thousand shots for the pulsed Tokamak and nominally one per year for the steady state Tokamak and Mirror have been assumed.

6.7.2 Design Criteria

6.7.2.1 Classification of Stresses

Stresses are categorized into three classes - Primary, Secondary, and Peak. Primary stresses are developed in response to an applied load and are necessary to satisfy equilibrium of forces. The basic characteristic of a primary stress is that it is not self-limiting. Secondary stresses are developed in response to constraint of adjacent material or by the self constraint

TABLE 6.7-1. SCHEDULE OF CYCLES PER YEAR

	Startup[a] and Shutdown	Disruptions[b]	Pulses
Steady State Mirror	12	1	0
Steady State Tokamak	12	1	0
Pulsed Tokamak	12	2-3	2500[c]

[a]Typical of power plants.

[b]Disruptions assumed to occur once a year except for pulsed tokamak design where it is assumed to occur once every thousand pulses.

[c]Based on 10^4 s burn time and 80% availability.

of the structure. A basic characteristic of secondary stress is that it is self-limiting. Minor distortion can satisfy the conditions which give rise to the stresses and failure from one application of the load is not expected. Peak stresses are additive to primary and secondary stresses by reason of local discontinuity or local thermal stress including effects of stress concentrations. Examples of primary stress are those due to coolant pressure, earthquake, electromagnetic body forces and magnetostatic body forces. Examples of secondary stress are those due to temperature gradients, swelling gradients and bending stress at a gross structural discontinuity. Examples of peak stress include stress at a local structural discontinuity, thermal stresses which result from a complete suppression of differential expansion and thus cause no significant distortion. Note that although the stress due to suppression of swelling has been classified as secondary stress it is qualitatively different from thermal stress in that small distortion of the structure does not relieve the source of the stress.

6.7.2.2 Stress Allowables

The allowable primary and secondary stresses for the BCSS blanket designs have been based on the procedures followed in the ASME Boiler and Pressure Vessels code (Section III), code Case N47 with some modifications in order to account for the high radiation environments in the first wall area.

Primary Stess Limits. The allowable primary membrane stress (S_{mt}) for Level A service loading is the lesser of two quantities, S_m or S_t,where S_m is the least of the following four quantities:

2/3 S_y at T (0.9 S_y for austenitic stainless steels)
2/3 S_y at R.T.
1/3 S_u at T
1/3 S_u at R.T.

where T is the operating temperature, R.T. is room temperature and S_y and S_u are the minimum yield and ultimate strengths respectively. The detrimental effects of radiation fluence on the yield and ultimate strengths, if any, are taken into account.

Similarly S_t is the least of the following three quantities:

67% minimum stress to cause stress rupture in time t
80% minimum stress to beginning of tertiary creep in time t
100% minimum stress to cause 1% thermal creep in time t

Since radiation induced creep is considered to be nondamaging, in general, allowable stresses need not be determined by the radiation creep strain. However, significant amounts of radiation induced creep strain will be generated in the first wall region and designers have the option of considering these effects in either of two ways. First, the allowable stress may be determined by restricting the radiation induced creep strain to 5%, in which case the allowable stresses may be read directly off Tables 6.7-2 through 6.7-4 for PCA, HT-9 and V-15CR-5Ti respectively. To use these tables the designer has to determine the allowable stress corresponding to the design life and temperature from the left half of the tables, and a similar number corresponding to the design fluence and temperature from the right half of the tables, then take the lesser of the two. Both the temperature and the fluence should be thickness averaged values. Alternatively designers could calculate the deformation produced by radiation induced creep and ascertain that the computed deformation is within acceptable limit. Since constitutive equations for radiation induced creep are not easily accessible, Figs. 6.7-1 through

TABLE 6.7-2. ALLOWABLE STRESSES FOR PCA (25% CW)

Temperature (°C)	Unirradiated (< 10 DPA)					Irradiated (> 10 DPA)			
	S_m (MPA)	S_{mt}[a] (MPA)				S_m[a] (MPA)	S_{mt}[c] (MPA)		
		10^4 h	2×10^4 h	3×10^4 h	5×10^4		50 dpa	75 dpa	100 dpa
100	225	225	225	225	225	225	225	185	140
200	208	208	208	208	208	208	208	185	140
300	205	205	205	205	205	205	205	185	140
400	205	205	205	205	205	205	205	155	115
500	205	205	205	205	205	190	190	135	100
550	195	195	195	190	175	175	170	115	85

[a]These S_m values may be increased by 10%.

[b]For $t < 2.8 \times 10^4$ h, $S_{mt} = S_m$ (unirradiated).

[c]For DPA < 50, $S_{mt} = S_m$ (irradiated) based on a maximum strain limit of 5%.

TABLE 6.7-3. ALLOWABLE STRESSES FOR HT-9 (NORMALIZED AND TEMPERED)

Temperature (°C)	Unirradiated					Irradiated			
	S_m (MPA)	S_{mt} (MPA)				S_m (MPA)	S_{mt}[a] (MPA)		
		10^4 h	3×10^4 h	10×10^4 h	30×10^4 h		50 dpa	75 dpa	100 dpa	150 dpa
20	250	250	250	250	250	250	235	198	163	125
200	220	220	220	220	220	220	220	198	163	125
300	210	210	210	210	210	210	210	198	163	125
400	200	200	200	200	200	200	200	198	163	125
500	175	160	150	140	125	175	175	175	163	125
550	160	110	90	80	75	160	160	160	150	115

[a]For DPA < 50, $S_{mt} = S_m$ (irradiated), based on a maximum strain limit of 5%.

TABLE 6.7-4. ALLOWABLE STRESSES FOR V-15Cr-5Ti (STRAIN HARDENED)

Temperature (°C)	Unirradiated (< 10 dpa)					Irradiated (> 10 dpa)				
	S_m[a] (MPA)	S_{mt} (MPA)				S_m[a] (MPA)	S_{mt} (MPA)			
		10^4 h	2×10^4 h	3×10^4 h	5×10^4 h		100 dpa	150 dpa	200 dpa	250 dpa
20	275	275	275	275	275	275	165	125	105	90
200	250	250	250	250	250	250	165	125	105	90
300	240	240	240	240	240	240	165	125	105	90
400	230	230	230	230	230	230	165	125	105	90
500	220	220	220	220	220	220	165	125	105	90
600	235	235	235	235	235	235	165	125	105	90
650	235	235	235	235	235	235	165	125	105	90
700	235	230	190	175	155	235	165	125	105	90
750	230	160	125	115	85	230	155	115	95	80

[a]Since these S_m values are based on average values of S_u from a single heat of material rather than true minimums determined from a number of heats of materials, they are equal to 1/3 S_u and not 1.1/3 S_u.

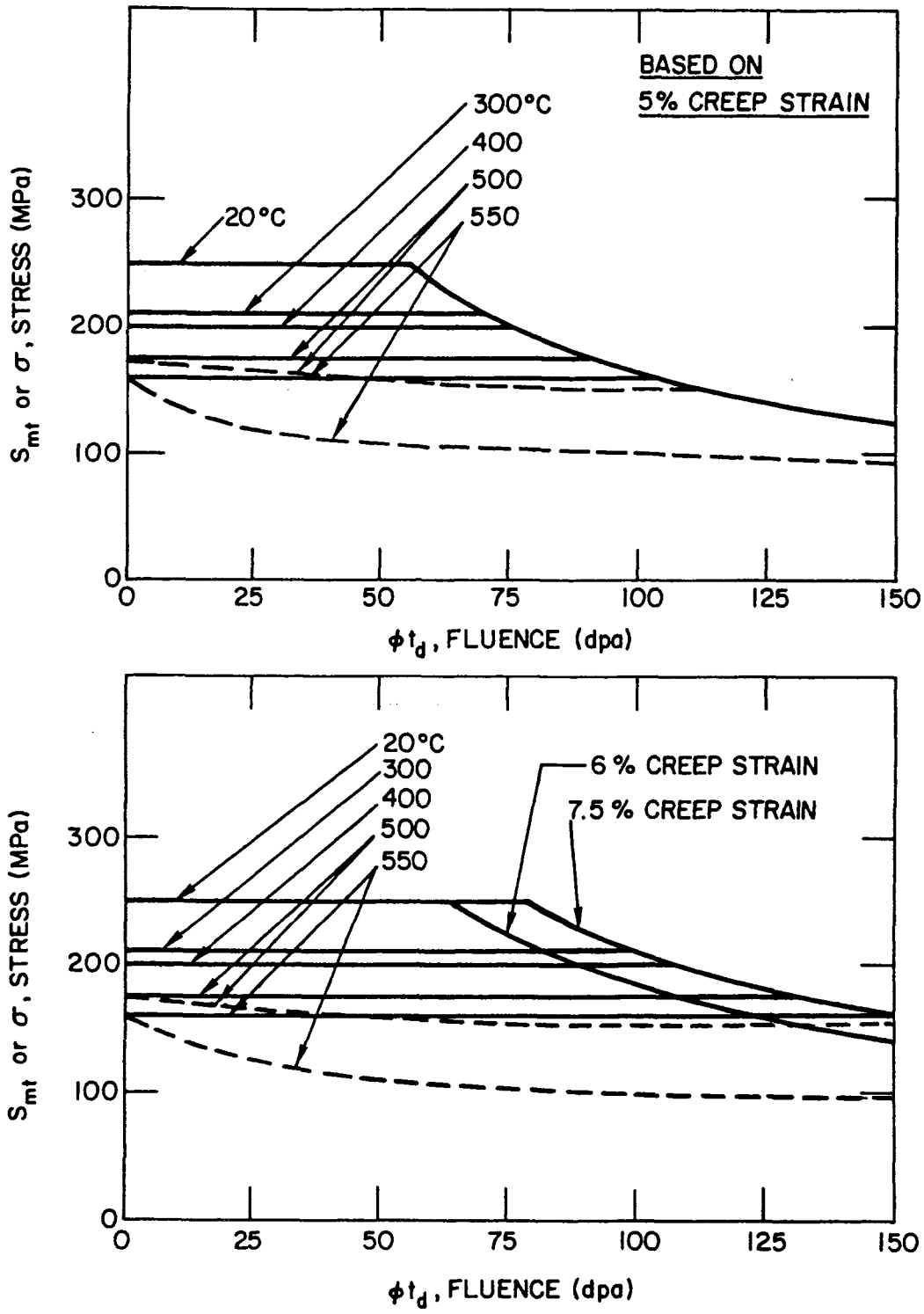


Figure 6.7-1. Allowable primary stresses for HT-9 (normalized and tempered) as a function of fluence and temperature. Dashed lines indicate allowable primary stress based on thermal creep.

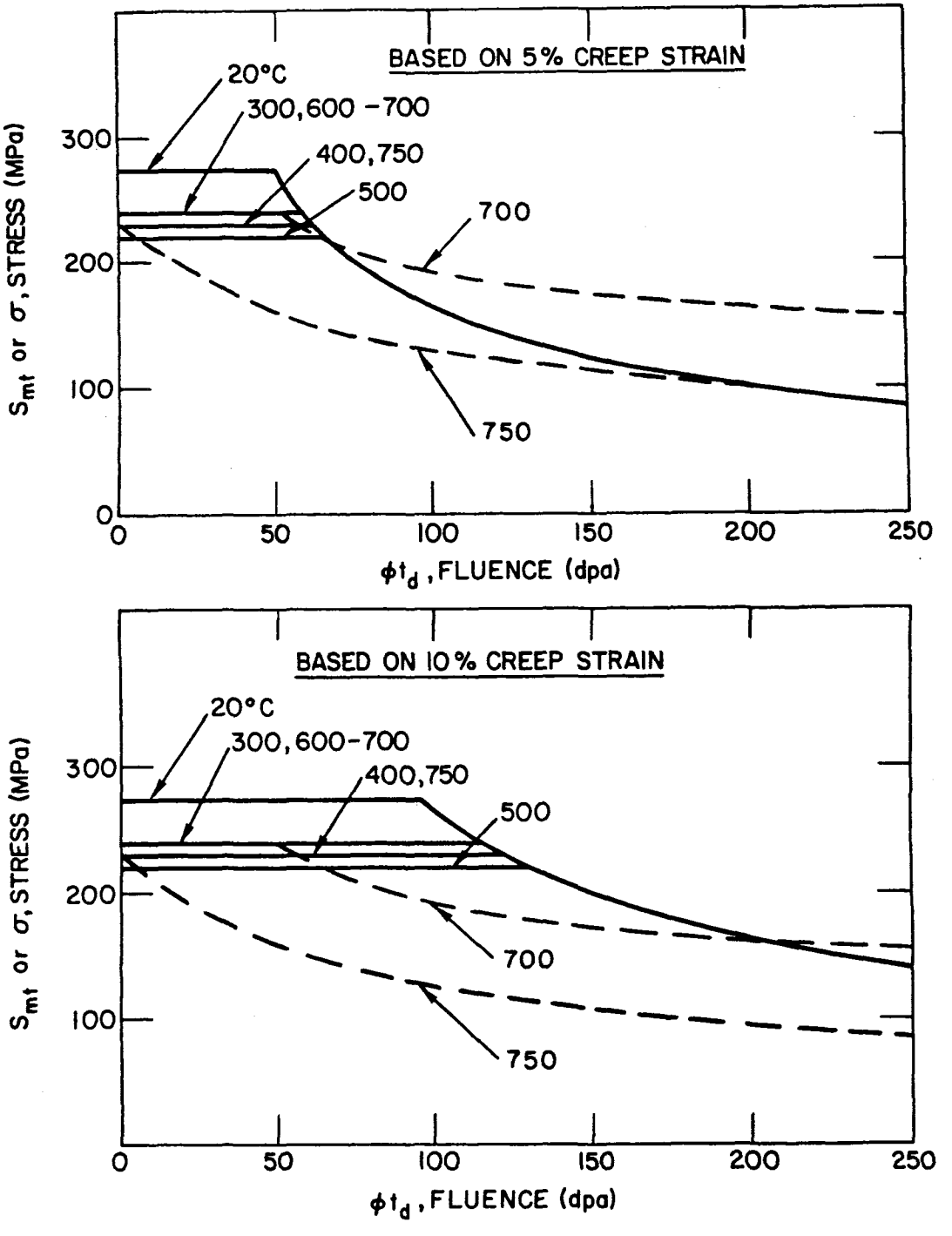


Figure 6.7-2. Allowable primary stress for V-15Cr-5Ti (strain hardened) as a function of fluence and temperature. Dashed lines indicate allowable primary stress based on thermal creep.

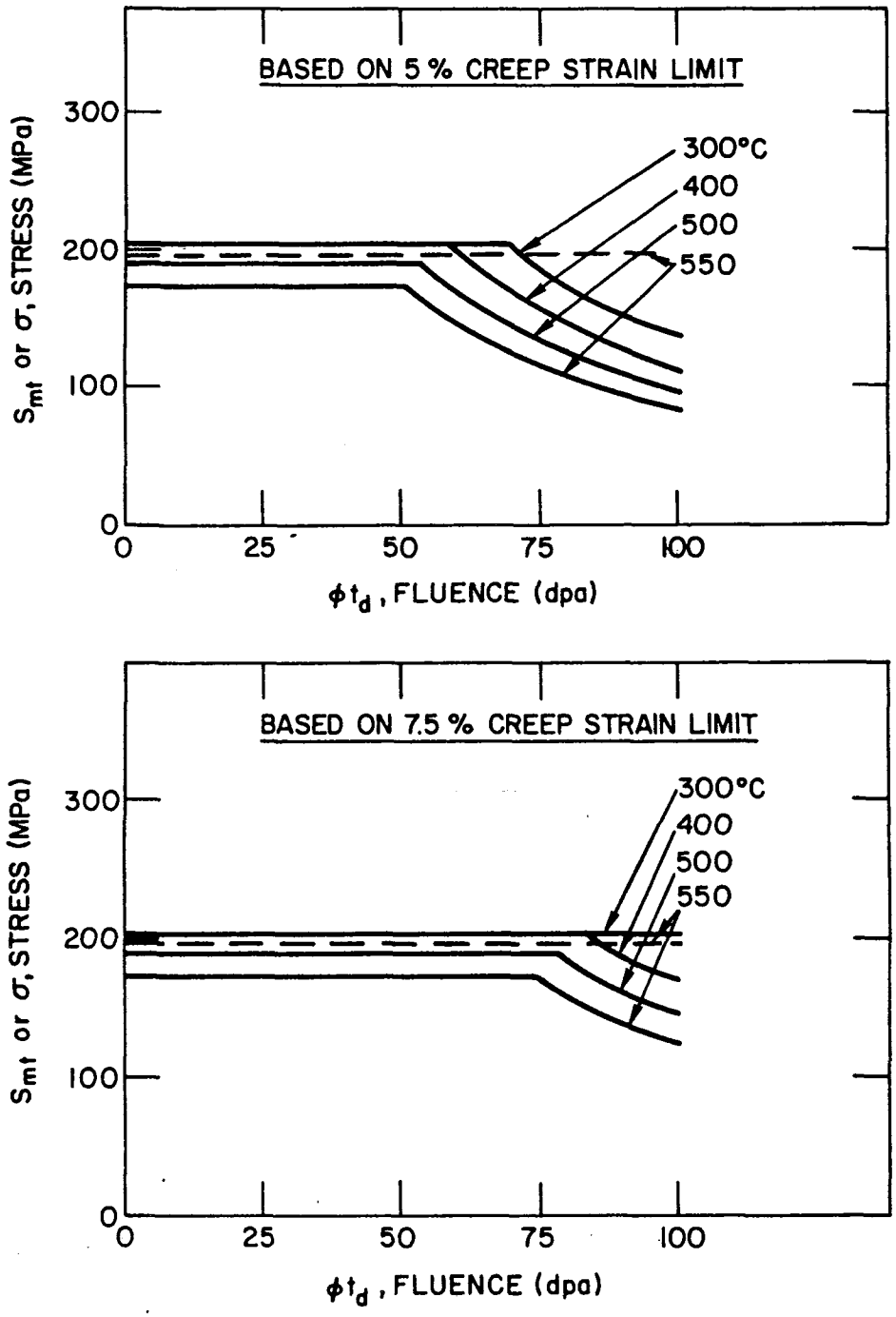


Figure 6.7-3. Allowable primary stress of PCA (25 CW) as a function of fluence and temperature. Dashed lines indicate allowable primary stress based on thermal creep.

vided for the three materials indicating the allowable stresses corresponding to various strain and fluence values at the end of life. If strain limits higher than 5% are used, the primary stresses should be calculated based on the deformed geometry rather than the undeformed geometry of the blanket. Figures 6.7-1 through 6.7-3 also indicate, by dashed lines, allowable primary stresses (S_{mt}) based on thermal creep assuming a neutron flux of 50 dpa/10^4 h. Note that for temperatures above 500°C, thermal creep determines the allowable primary stress for HT-9. Consequently, the allowable primary stress cannot be increased by increasing the end-of-life radiation (150 dpa) induced creep strain beyond 5% for a temperature of 550°C and 6% for a temperature of 500°C. For a similar reason, the allowable primary stress for V-15Cr-5Ti cannot be increased by increasing the permissible radiation (250 dpa) induced creep strain beyond 5% for a temperature of 750°C and about 10% for a temperature of 700°C. On the other hand, because of its relatively high thermal creep strength, the allowable primary stress of PCA (25% CW) can be significantly increased by increasing the maximum permissible radiation (100 dpa) induced creep strain beyond 5% at all temperatures. In no case can the allowable primary stress exceed S_m.

For variable stress histories the primary membrane stress history may be divided into a number of approximately constant stress segments and the following sum computed

$$D = \sum_{i=1}^{n} \left(\frac{\phi t}{\phi t_d}\right)_i \qquad [6.7\text{-}1]$$

where

ϕt = fluence accumulated in segment i

ϕt_d = allowable fluence at the stress and temperature in segment i obtained from Figs. 6.7-1 through 6.7-3.

The maximum value of D has been restricted to be 1. This procedure will allow the designers to exceed the allowable stresses for part of life provided the design stresses are less than the allowable stresses by corresponding amounts

at a different part of life. A similar sum based on time rather than fluence should also be computed for the thermal creep part of the history.

The allowable primary membrane (P_L) plus bending (P_B) stress for Level A service loading has been limited to:

$$P_L + P_B < KS_m$$

$$P_L + P_B < K_t S_t$$

where for solid rectangular sections K=1.5, and K_t=1.25. Since the linear stress distribution through the thickness is not altered by radiation induced creep, K_t in above should be set equal to 1 whenever S_t is controlled by radiation induced creep rather than by thermal creep.

Primary Plus Secondary Stress Limit. In order to prevent "low temperature type" ratchetting and open hysteresis loop from occuring and ensure shakedown to elastic action, the primary plus secondary stress limit for Level A service loading has been set equal to $3S_m$. The effect of radiation induced creep on this type of ratchetting, unknown at this time, may be a potential problem for all first wall designs and needs further research. This effect has been ignored in all designs.

Level B and Level C Stress Limits. Allowable stress limits for Level B and Level C together with Level A are summarized in Tables 6.7-5 through 6.7-6. Note that the allowable stresses are the same for Level A and Level B loadings, whereas, slightly higher stresses are allowed for Level C loadings.

Fatigue and Creep-Fatigue (Level A, Level B, and Level C). In accordance with the procedures in Section III, Code Case N47 of the ASME Code, fatigue damage (D_F) has been computed from the total effective strain range and the maximum temperature in the cycle. The factor of safety used is 2 on strain range or 20 on life, whichever provides the smaller allowable life.

TABLE 6.7-5. ALLOWABLE PRIMARY STRESSES FOR VARIOUS SERVICE LEVELS

Service Level	Allowable Primary Stress
A	$P_m \leq S_{mt}$ $P_L + P_B \leq 1.5\ S_m$ $P_L + P_B \leq K_t S_t$
B	Same as Level A
C	$P_m \leq 1.2\ S_m$ $P_m \leq S_t$ $P_L + P_B \leq 1.8\ S_m$ $P_L + P_B \leq K_t S_t$

Note:. For rectangular sections $K_t = 1.25$. However, if S_t is controlled by radiation induced creep, $K_t = 1$.

TABLE 6.7-6. ALLOWABLE PRIMARY PLUS SECONDARY STRESS RANGE FOR VARIOUS SERVICE LEVELS

Service Level	Allowable Primary Stress
A	$P_L + P_B + Q \leq 3\ S_m$
B	Same as Level A
C	No Limit

Considering a typical cycle for the BCSS designs it can be shown that irradiation induced creep will relax out the thermal stress shortly after start-up so that the thermal creep damage (D_C) can be based only on the primary stress, membrane and bending, at the appropriate temperature and time provided the following condition is satisfied:.

$$3S_m\ (\text{hot}) - S_y\ (\text{cold}) < 2(P_L + P_B)$$

where S_m(hot) represents the S_m value corresponding to the hot temperature of the cycle, and S_y(cold) represents the yield strength corresponding to the cold temperature of the cycle. Otherwise the creep damage due to thermal stresses will have to be considered. Since irradiation induced creep is considered to be nondamaging, creep damage is computed from minimum thermal stress rupture plots of the material (unirradiated) using a time fraction damage rule as in Code Case N47 of the ASME Code. However, advantage may be taken of the additional stress relaxation due to irradiation induced creep.

The fatigue and creep damages are added linearly as in Code Case N47 of Section III and the sum limited by the bilinear damage diagram shown in Fig. 6.7-4. Figure 6.7-4 is the damage diagram for the austenitic stainless steels given in Code Case N47. Since such a diagram is not currently available for the ferritic steels and the vanadium alloys, the same diagram has been used for all three materials.

6.7.2.3 Crack Growth Life

Crack growth life has been ignored in all smooth wall designs. However, since most designs have used a grooved first wall in order to reduce high thermal stresses, the grooved first wall has been designed for crack growth by using the following simplified analysis.

Grooved Wall Analysis. The grooved wall has been modelled as a stepped beam shown in Fig. 6.7-5 where the full thickness h_2 is replaced by an effective thickness $h_{2_{eff}}$. If a linear temperature gradient $\frac{dT}{dy}$ is imposed on the unconstrained beam, it will deform at a constant curvature so that slope at the free end is given by $\alpha \frac{dT}{dy} (\ell_1 + \ell_2)$ and the stress everywhere is zero. However, because of symmetry, the slope at the free end must be zero. This can be achieved by applying the end bending moments M as shown in the Fig. 6.7-5. Note that, because of symmetry, there can be no resultant shear force at the ends. A simple calculation taking into account that the structure is a plate rather than a beam gives the following expression for M:

$$M = \frac{E\alpha}{12(1-\nu)} \frac{dT}{dy} \frac{\ell_1 + \ell_2}{\frac{\ell_1}{h_1^3} + \frac{\ell_2}{\beta^3 h_2^3}} \qquad [6.7\text{-}2]$$

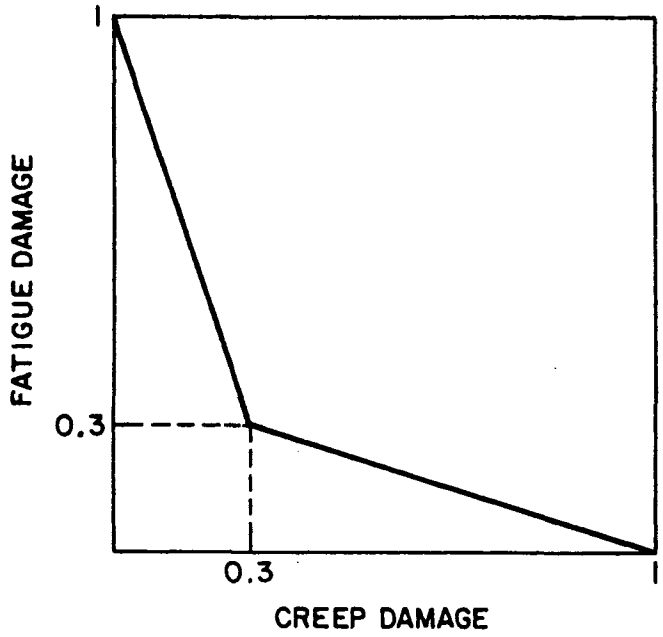


Figure 6.7-4. Bilinear damage diagram for computing creep fatigue life.

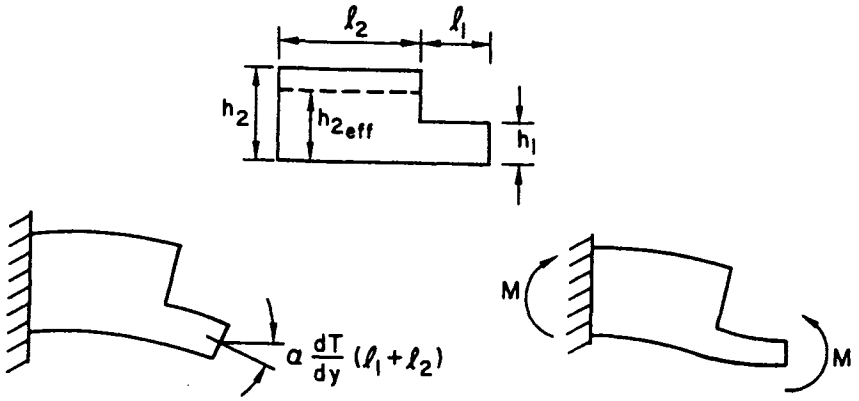


Figure 6.7-5. Modelling of a grooved wall by a stepped beam.

where

α = Coefficient of thermal expansion

$\beta = h_{2_{eff}}/h_2$

E = Elastic modulus

ν = Poissons ratio.

The maximum bending stress in the thin bar is then given by:

$$\sigma_{max} = \frac{6M}{h_1^2} = \frac{E\alpha}{2(1-\nu)} \frac{dT}{dy} h_1 \frac{\ell_1 + \ell_2}{\ell_1 + \ell_2/(\beta h_2/h_1)^3} \qquad [6.7\text{-}3]$$

Let K_T be the equivalent stress concentration factor needed to obtain the maximum stress in a grooved plate stress from the maximum stress in a smooth plate (h_1). Since the maximum stress in a smooth bar of thickness h_1 due to the same temperature gradient is given by:

$$\sigma_{max} = \frac{E\alpha}{2(1-\nu)} \frac{dT}{dy} h_1 \qquad [6.7\text{-}4]$$

the stress concentration factor is given by:

$$K_T = \frac{\ell_1 + \ell_2}{\ell_1 + \ell_2/(\beta h_2/h_1)^3} \qquad [6.7\text{-}5]$$

An alternative stress concentration factor defined on the basis of the maximum stress in a smooth bar of thickness h_2 is given by:

$$K_T' = \frac{K_T h_1}{h_2} \qquad [6.7\text{-}6]$$

Both stress concentration factors are dependent on the value of β. Figure 6.7-6 shows that by choosing the following functional form for β:

$$\beta = \frac{h_1}{h_2}\left[2 - \frac{h_1}{h_2}\right] \qquad [6.7\text{-}7]$$

the stress concentration factors obtained at McDonnell Douglas Astronautics Company (MDAC) by Finite Element Methods can be reasonably approximated by the current simple model. This form for β does not take into account the effects of ℓ_2/h_2. Consequently, the present model is applicable to geometries considered by MDAC, i.e., $1 < \ell_2/h_2 < 3$. Also note that the alternate stress concentration factor $K_T' > 1$ so that the maximum stress in the thick plate cannot be reduced by grooving. However, grooving does remove the location of the maximum stress from one of high temperature to one of much lower temperature. Equation [6.7-7] predicts that the maximum value of $h_{2_{eff}}$ corresponding to $h_2 \to \infty$ is $2h_1$.

A crack growth analysis of the grooved plate is carried out by the following conservative approach, replacing the groove by a crack of length $(h_2 - h_1)$. In addition to the linear temperature gradient assume there is a uniform temperature rise (ΔT_i), the deformation due to which is completely constrained. Thus the beam is subjected to an axial load as well as a bending moment. Although initially these loads are compressive, with passage of time they will be relaxed out by radiation induced creep and reappear as tensile stress when the reactor is turned off. For the present we assume that the beam is subjected to an axial load P and bending moment M which collectively produce a crack driving force ΔK. Initially P, M, and ΔK are given by:

$$P = \frac{E\alpha\, h_1}{(1-\nu)}\left[\Delta T_i + \frac{1}{2}\frac{dT}{dy}\, h_1\right] \qquad [6.7\text{-}8]$$

$$M = K_T M_o - \frac{1}{2} P(h_2 - h_1) \qquad [6.7\text{-}9]$$

where

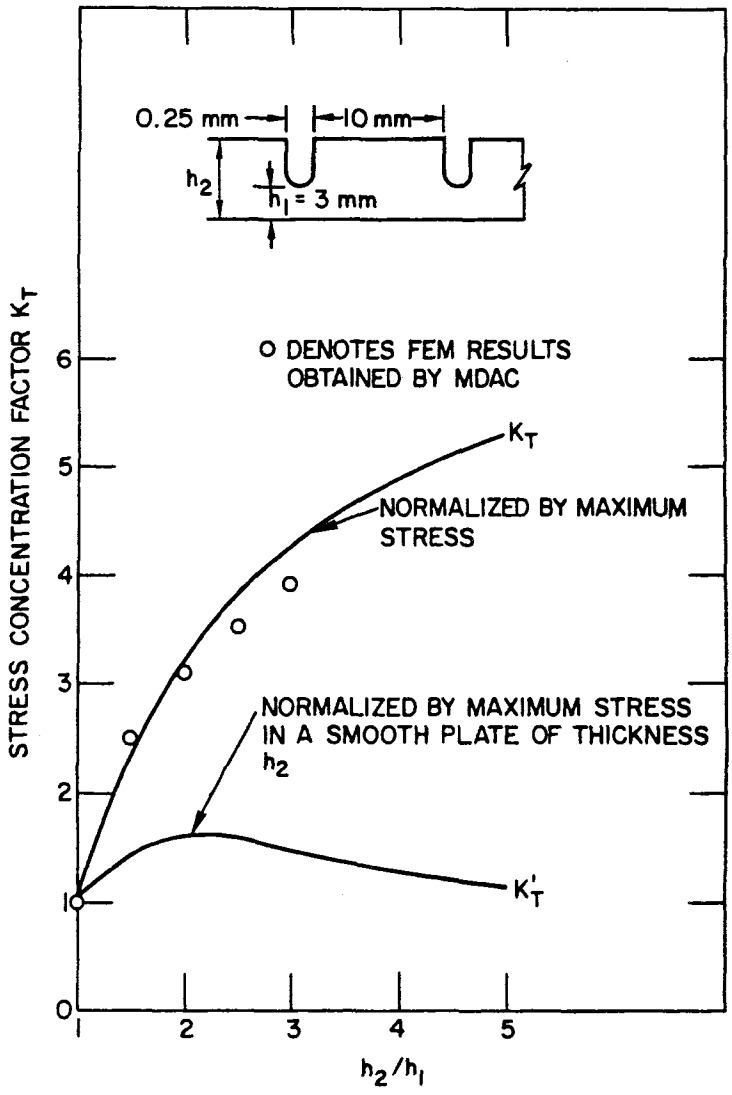


Figure 6.7-6. Variation of stress concentration factors with thickness ratio for a grooved plate.

$$M_o = \frac{E\alpha}{12(1-\nu)} \frac{dT}{dy} h_1^3$$

and K_T is given by Eq. [6.7-5].

$$\Delta K = \left[F_p(a/h_2)P(3h_2-2h_1) + F_M(a/h_2)\,6M\right] \frac{\sqrt{\pi a}}{h_1\sqrt{h_1 h_2}} \qquad [6.7\text{-}10]$$

The parameters F_p and F_M can be obtained from G. Sih's Handbook for Stress Intensity Factors. As the crack grows to a current length a, h_1 in above equations is replaced by $(h_2 - a)$. Crack growth data for HT-9 and PCA as a function of ΔK has been obtained from the Nuclear Systems Materials Handbook. Cycles to failure due to crack growth is given by:

$$N_f = \int_{h_2-h_1}^{a_f} \frac{da}{da/dN} \qquad [6.7\text{-}11]$$

where

$$\frac{da}{dN} = f(\Delta K)$$

N_f is the cycles to failure and a_f is the final crack size assumed conservatively to correspond to the crack tip location at the midwall of the solid section of the first wall.

An interesting result shown in Fig. 6.7-7 is the variation of the crack driving force as a function of the crack length for a given thermal loading. The driving force ΔK reaches a maximum before decreasing with increasing crack length. For the deep grooves that are considered in this study the driving force always decreases with increasing crack length. Figure 6.7-8 shows the variation of the maximum K as a function of the temperature gradient through the wall (ΔT) and the temperature difference ΔT_i between the first wall at the coolant interface and the temperature T_B of the bulk of the blanket at the

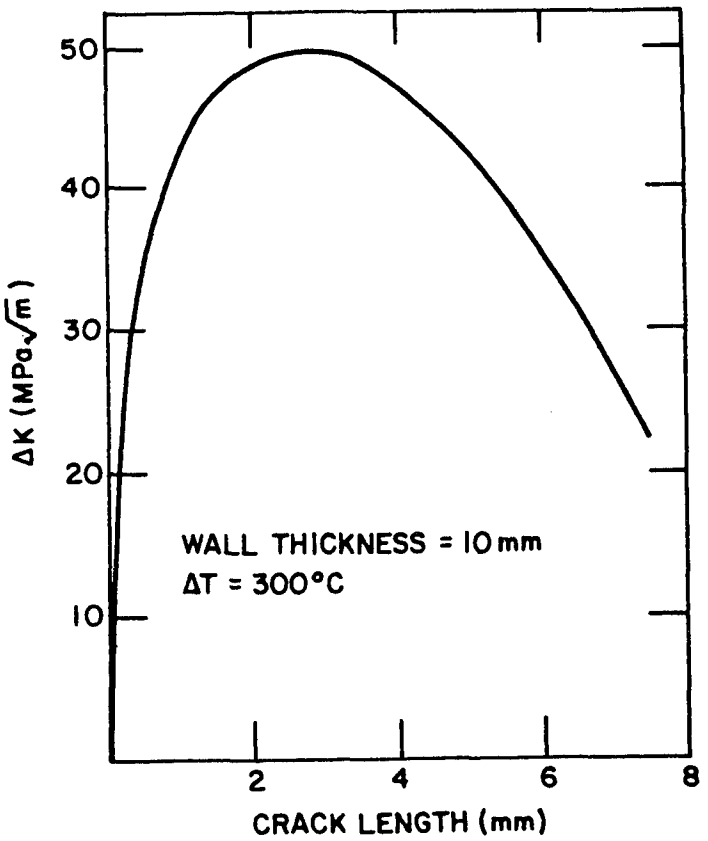


Fig. 6.7-7. Variation of crack driving force (ΔK) with crack length in a HT-9 plate of thickness 10 mm subjected to a temperature gradient of 300°C.

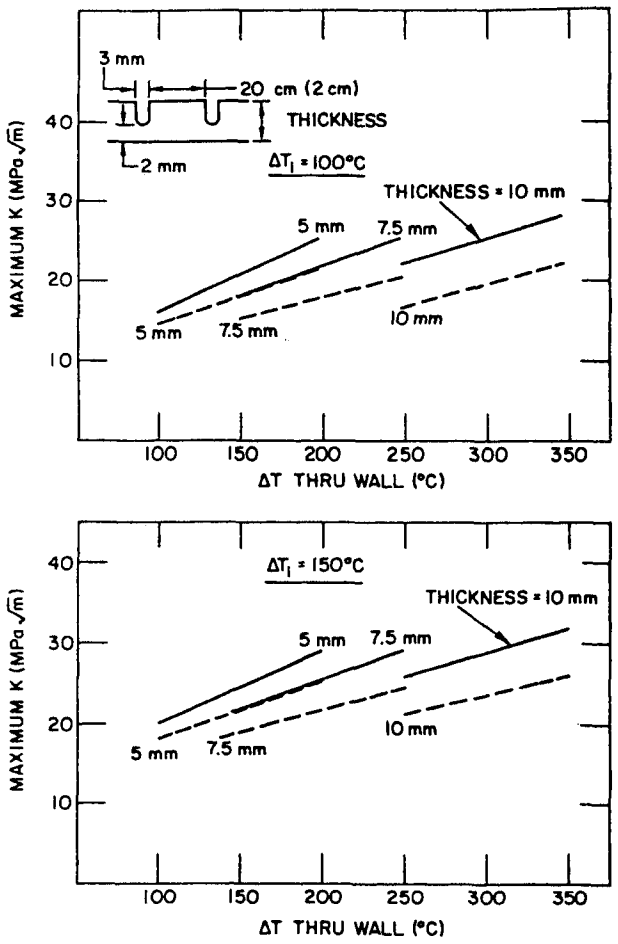


Fig. 6.7-8. Variation of maximum stress intensity factor with temperature gradients and thickness of the wall. Dashed lines correspond to a width of the solid part of the groove ℓ_2 = 2 cm.

back (which may in some cases equal the bulk temperature of the coolant of the first wall). The solid portion of the first wall is assumed to be 2 mm thick in all cases. The maximum temperature of the first wall is given by:

$$T_{max} = T_B + \Delta T_i + \Delta T \qquad [6.7\text{-}12]$$

It must be assured in designs that the K_{max} given in Fig. 6.7-8 is less than the material critical stress intensity factor K_{IC}, which in all cases will be reduced from its nominal value due to radiation effects.

The crack growth lives of a grooved first wall (HT-9) as functions of the temperature gradient (ΔT) through the first wall and ΔT_i, for three wall thicknesses are given in Figs. 6.7-9 through 6.7-11. The solid and the dashed lines in these figures correspond to a groove spacing of 20 cm and 2 cm respectively. A factor of safety of 4 on life has to be applied to these numbers for design purposes. Since crack growth data for vanadium alloys are not currently available, these figures have also been used for computing lives of blankets made of vanadium alloys.

Although grooves may be profitably used to remove the region of highest stress from one at the highest temperature to one at a much lower temperature, the stresses between the grooves are not negligible. However, the grooved regions of the wall are exempted from the maximum metal temperature criterion because cracking or removal of metal from the plasma side of the first wall reduces the crack driving force for the cracks that are assumed to initiate from the roots of the grooves. Also, the grooved thickness is not considered for containing the coolant pressure. The grooved geometry has not been optimized in the present study. A detailed R&D effort involving both testing and analysis will be needed before the grooved first wall can become a viable option.

6.7.3 Comparison of PCA, HT-9 and V-15Cr-5Ti as Structural Materials

Three candidate materials for potential application to fusion reactor blankets are PCA, HT-9 and V-15Cr-5Ti. As first wall materials they will be subjected to high thermal stress due to surface and volumetric heat fluxes. A

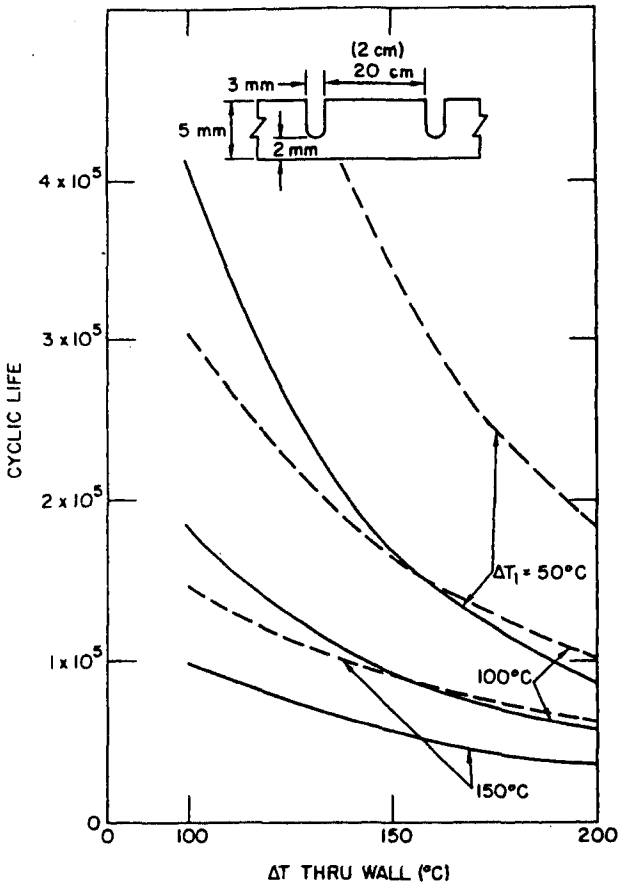


Fig. 6.7-9. Fatigue crack growth life of a grooved plate (HT-9) of 5 mm thickness. Dashed lines correspond to a width of the solid part of the groove ℓ_2 = 2 cm.

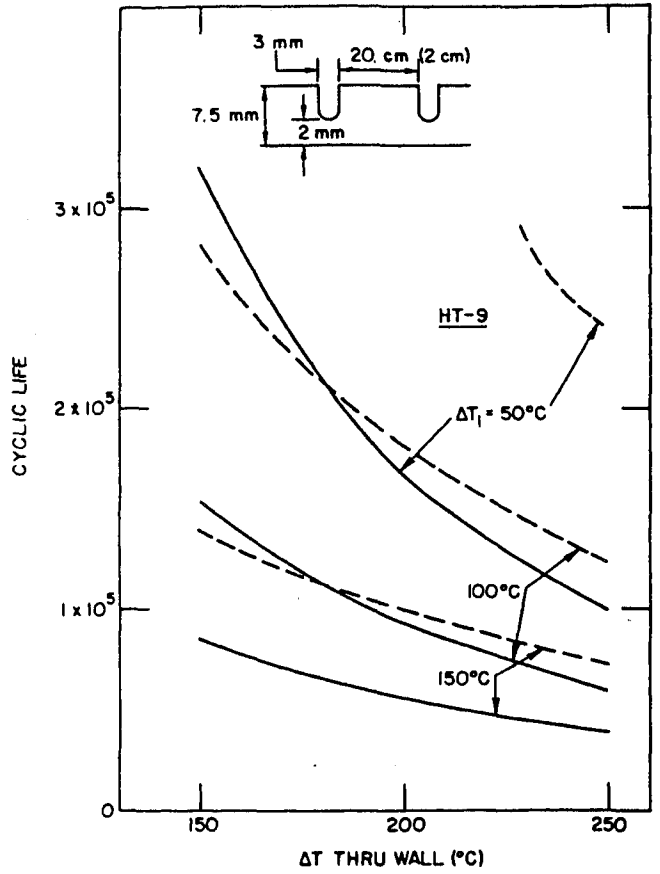


Fig. 6.7-10. Fatigue crack growth life of a grooved plate (HT-9) of 7.5 mm thickness. Dashed lines correspond to a width of the solid part of the groove ℓ_2 = 2 cm.

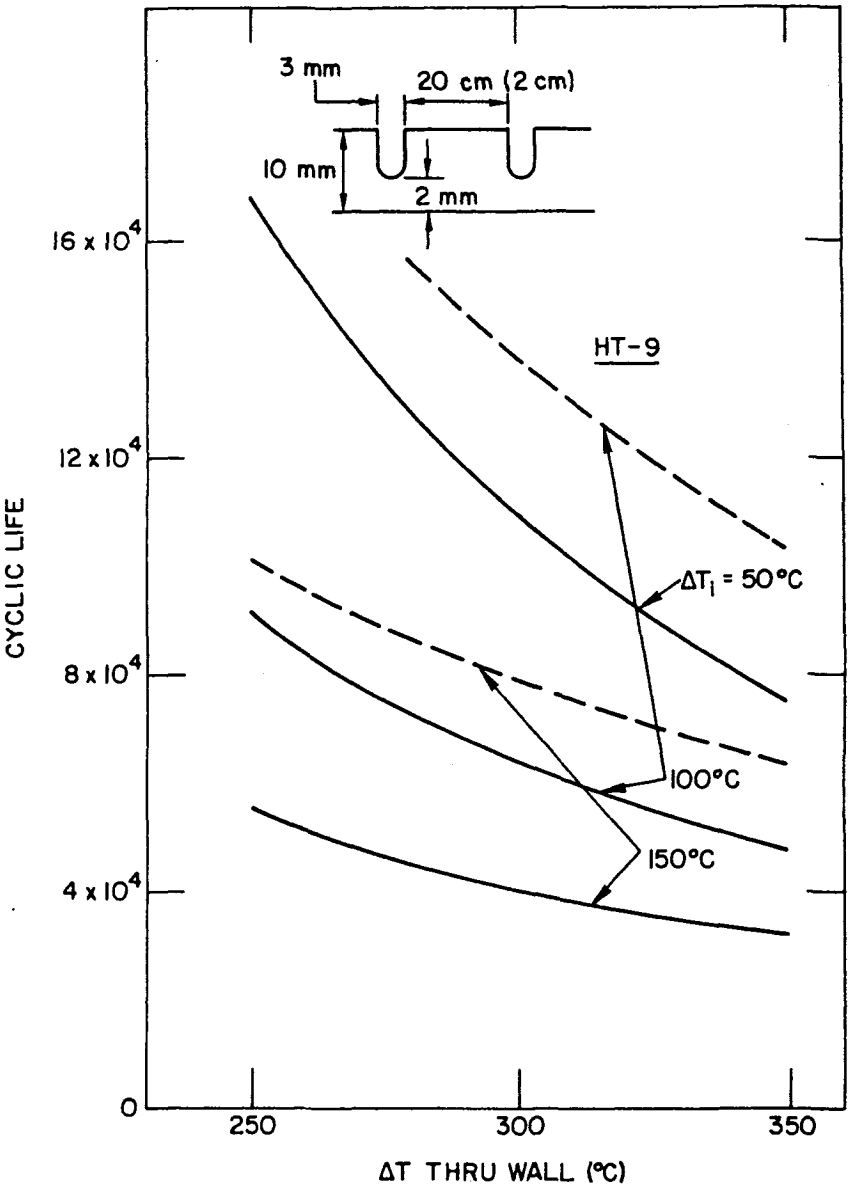


Figure 6.7-11. Fatigue crack growth life of a grooved plate of thickness 10 mm. Dashed lines correspond to a width of the solid part of the groove ℓ_2 = 2 cm.

convenient measure for the resistance of a material is the thermal stress factor, defined as

$$\eta = \frac{(1-\nu)kS_u}{E\alpha} \qquad [6.7\text{-}13]$$

where E = Modulus of elasticity (MPa)

α = Coefficient of thermal expansion (/K)

ν = Poissons ratio

k = Thermal conductivity (W/M/K)

S_u = Ultimate tensile strength (MPa)

The thermal stress factor η may be considered as the maximum allowable surface heat flux in MW/m^2 on a 1 mm thick plate which is constrained from deforming. The larger the factor η of a material the higher the surface heat flux the material can sustain. Figure 6.7-12 shows the factor η as a function of temperature for the three materials. Because of its low coefficient of thermal expansion and high thermal conductivity V-15Cr-5Ti has the largest value of η, followed by HT-9 and PCA. In contrast to the other materials the thermal stress factor for HT-9 drops off significantly with temperature so that at their maximum temperature limit of 550°C HT-9 is only slightly superior to PCA whereas at lower temperatures it is significantly stronger than PCA.

Of course the thermal stress factor is only one indicator of material performance. It ignores effects due to bulk heating, fatigue strengths, etc. of the materials which unfortunately are design dependent and are not easily quantifiable. For the present purpose of comparing the three materials it will be assumed that the first wall has the geometry of a flat plate which is constrained from deforming by the rest of the blanket which is at the same temperature as the average coolant temperature. Also, the film temperature drop from the first wall to the bulk coolant will be treated as a parameter. The bulk nuclear heating rate for the three materials are chosen to correspond to those existing in the reference design of the liquid metal cooled Tokamak reactor. The maximum allowable surface heat flux is computed by restricting the maximum temperature of the first wall at the plasma side to the allowables

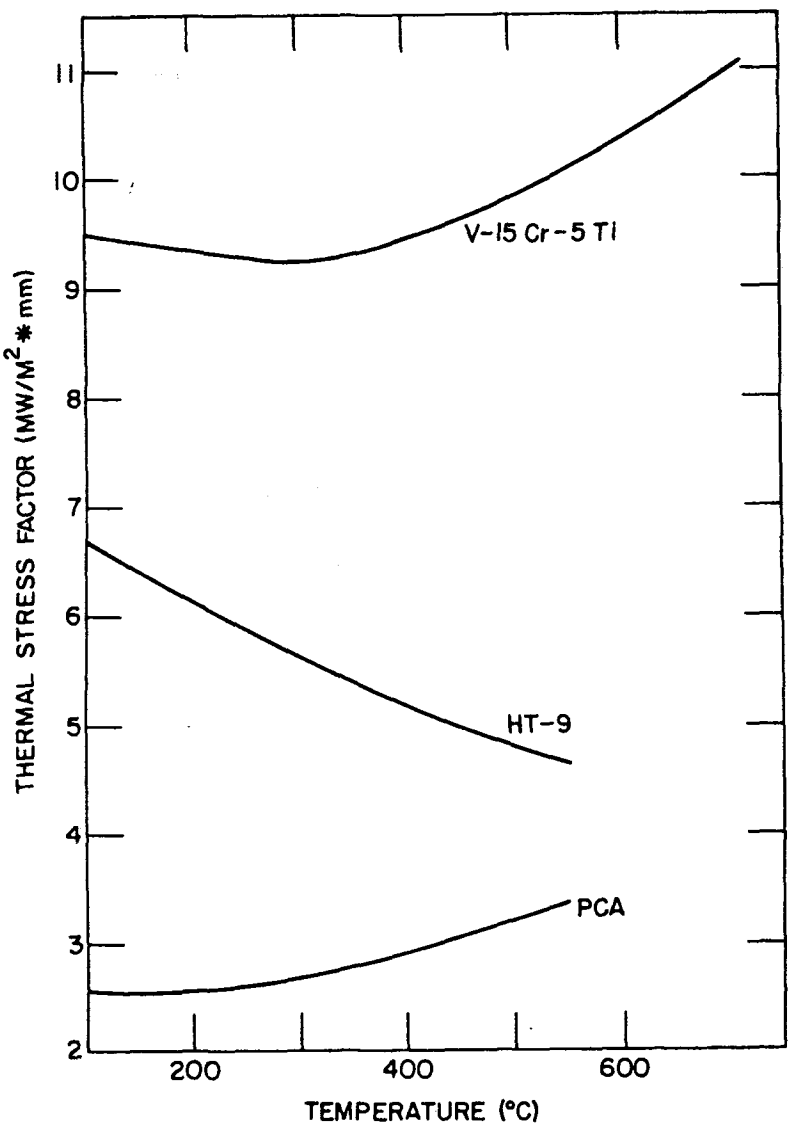


Figure 6.7-12. Comparison of thermal stress factor (η) of three candidate blanket materials.

given in Section 5.1, and also by limiting the maximum thermal stress to the ultimate tensile strength. Figure 6.7-13 shows a plot of the maximum allowable surface heat fluxes as functions of wall thickness, and film temperature drop for the three materials, assuming that the first wall is a solid plate. The allowable surface heat fluxes are plotted for four coolant outlet temperatures. It is evident from these figures that V-15Cr-5Ti is by far the strongest of the three and that HT-9 is only slightly stronger than PCA. However, it appears that for realistic values of local coolant temperatures (300-400°C for PCA and HT-9 and 550°C for V-15Cr-5Ti) none of the materials can sustain a surface heat flux of 1 MW/m^2 unless the thickness is reduced to less than 5 mm.

A potential solution to the high thermal stress and temperature in the first wall is orthogonal grooving of the first wall in the plasma side as discussed in Section 6.7.2.3. Again, for comparison purposes a grooved plate with a solid thickness of 2 mm is considered. The maximum surface heat flux is computed by limiting the temperature at the root of the groove to the material allowables, the nominal thermal stress at the root of the groove to 3 S_m (for these materials ultimate tensile strength), and the design fatigue crack growth life of the wall (assuming the grooves to be starter cracks and using the equivalent thickness approach described in Section 6.7.2.3) to be 10,000 cycles. No restriction is put on the maximum temperature at the plasma side of the wall. Since crack growth data for V-15Cr-5Ti are not available, they are assumed to be the same as that of HT-9. If fatigue data of smooth specimens are any indication of crack growth life in a relative sense then this assumption is not unreasonable and is probably conservative. Figure 6.7-14 shows the maximum allowable surface heat fluxes as functions of wall thickness and film temperature drop. As before, V-15Cr-5Ti appears to be the most resistant to cyclic thermal stresses of the three materials. Because of its superior fatigue properties, HT-9 can sustain higher surface heat flux than PCA. Also noted in the figure (within brackets) are the temperature drop through the first wall. In order to obtain the maximum temperature of the first wall, the average coolant outlet temperature and the film temperature drop have to be added to these. If the existing material maximum temperature limits are relaxed by 200°C then V-15Cr-5Ti can sustain a heat aflux of 1 MW/m^2 up to a thickness of about 9 mm, and HT-9 can sustain the same heat load up to a thickness of about 7 mm. Although PCA can, under the relaxed condi-

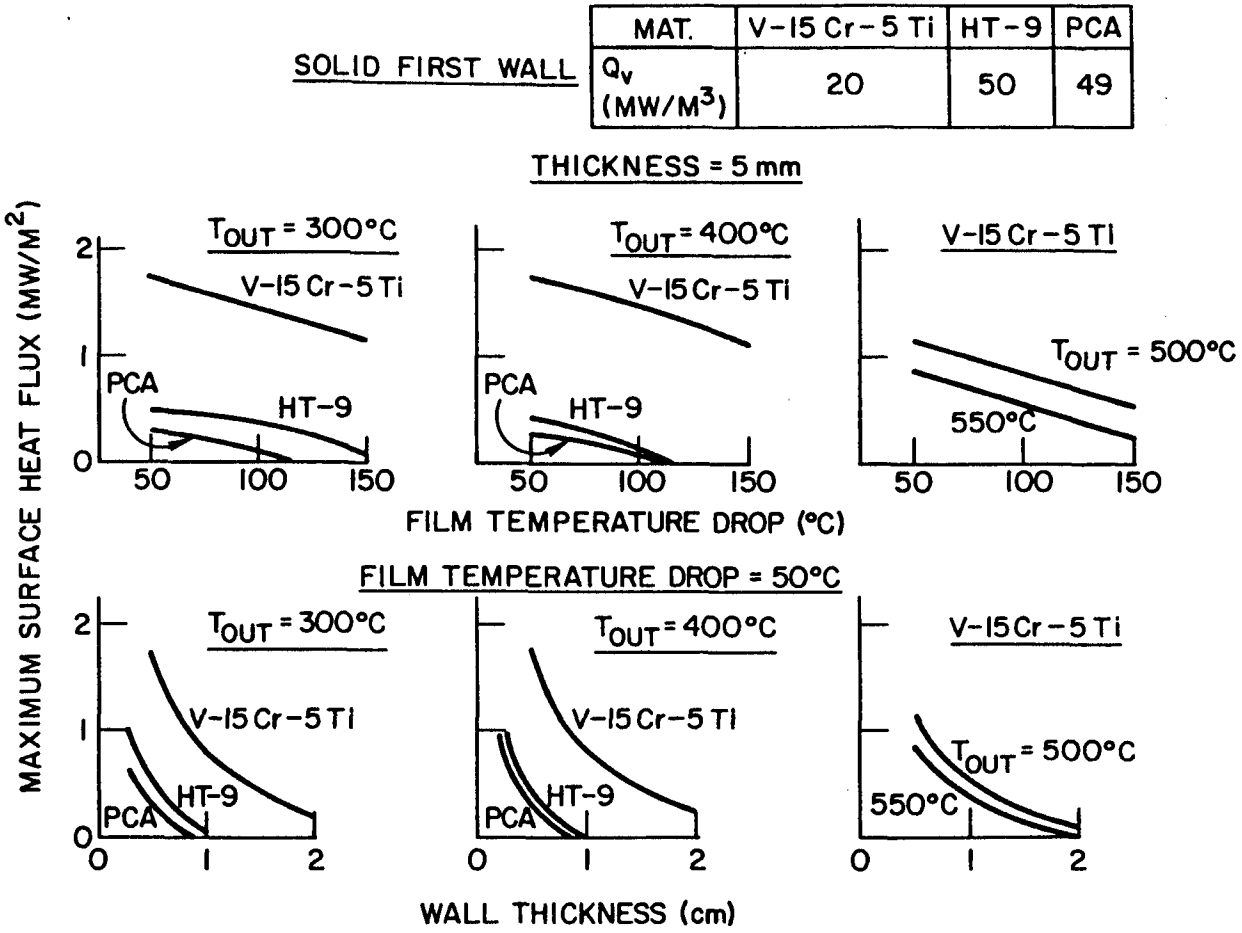


Figure 6.7-13. Variation of maximum allowable surface heat flux as a function of film temperature drop, first wall thickness and coolant outlet temperature for a solid plate first wall made of PCA, HT-9 and V-15Cr-5Ti.

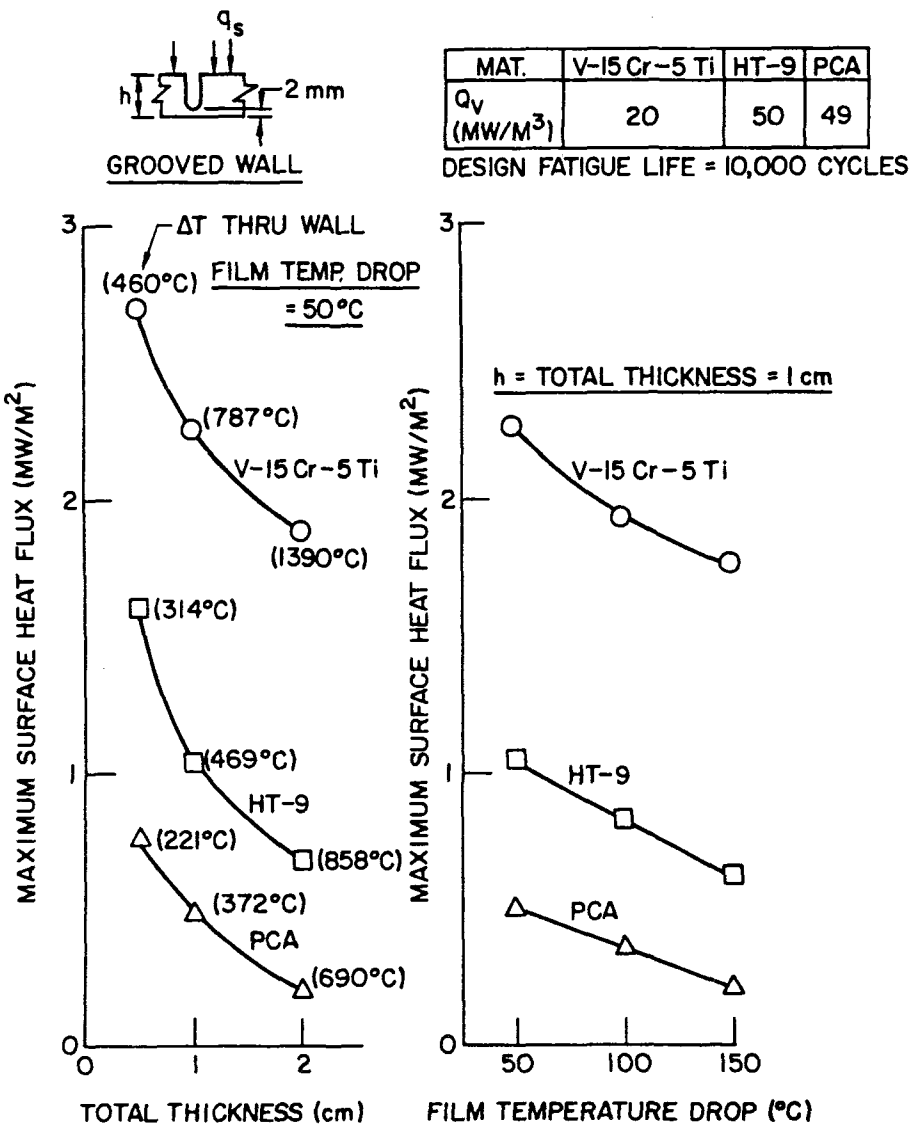


Figure 6.7-14. Variation of maximum allowable surface heat flux (based on fatigue crack growth) as a function of total wall thickness and film temperature drop for a grooved first wall made of PCA, HT-9 and V-15Cr-5Ti.

tion, sustain a surface heat flux of 1 MW/m^2 up to a thickness of 5 mm, it would fail to meet the fatigue life requirement as is evident from Fig. 6.7-14. Thus a grooved first wall made of PCA could withstand a surface heat flux of 1 MW/m^2 up to a thickness of 5 mm but with reduced design fatigue life. However, there may be other factors, such as achieving economical power cycle efficiency levels, etc. which may reduce the useful range of thickness or surface heat flux capability of PCA. Finally, HT-9 is considerably more resistant to radiation induced creep deformation than PCA as is evident in Tables 6.7-2 and 6.7-3, and Figs. 6.7-1 through 6.7-3. However, this high resistance to radiation induced creep strain cannot be taken advantage of to boost the allowable primary stress of HT-9 at temperatures above 500°C, because its thermal creep properties are degraded rapidly beyond 500°C so that the allowable primary stress becomes controlled by thermal creep properties rather than by its superior radiation creep properties.

6.7.4 R&D Requirements for Structural Design and Analysis

Structural design of any complex system such as a fusion reactor is the result of a number of successive interations of design involving interactions with various other disciplines such as Materials, Physics, Fluid Mechanics, Fabrication, etc. As a result, R&D requirements for structural design in fusion reactor technology may be broadly divided into two categories: a) those that are directly related to structural design and/or design methodology (for example, geometrical optimization of the grooved first wall, development of design criteria, etc.), and b) those that are not directly related to structural design but nonetheless have significant impact on it (for example, deformation and damage due to irradiation induced creep and swelling, Magnetohydrodynamics (MHD) pressure drop, etc.). Although such a distinction seems natural, in reality most structural design issues are not as clear cut and tend to have various degrees of overlap with other disciplines.

The following is a brief summary of items that have emerged from the BCSS program and which, according to the BCSS Task Force on Stress Analysis, represents outstanding problems in structural design that must be addressed in future R&D studies in order that the concepts studied in this program and rated R=1 by the Project can become viable options. The items have been prioritized

viewpoint issues whose resolution more than any others will either determine the feasibility or significantly increase the attractiveness of any concept or concepts. Priority B signifies those issues whose resolution will be necessary before structural design of any concept or concepts can be completed.

1. Grooved First Wall Design (Priority A)

All tokamak concepts studied under the BCSS program will require some form of stress relief in the first wall in order to withstand the high surface heat flux (>=1 MW/m^2). Preliminary analyses using unsophisticated models have shown that providing orthogonal grooves on the first wall may be a potential solution to both the high thermal stress and high temperature problems in the plasma side of the first wall. However, many issues are still unresolved. For example, in spite of the grooves the stresses are not zero in the grooved part of the first wall. What should be the maximum allowable temperature in such a case? What is the true stress concentration factor for the groove and how can it be optimized by choosing the groove geometry adequately? What are the implications of loss of ductility due to irradiation effects on the allowable stresses and fatigue life of a grooved wall? These are some of the questions that need be answered before grooving of the first wall can become a viable option. In the opinion of the Task Force members, most of these issues can be resolved by carrying out a two-year combined analytical/experimental R&D program. The experiments should be performed on a representative structural material whose ductility has been artificially reduced by appropriate thermo-mechanical treatment.

2. Poloidal and Toroidal Growth of First Wall (Priority A)

All blanket designs with integral first walls will have to accommodate significant toroidal and poloidal growths due to irradiation-induced creep and swelling, temperature differential between the front and the back of the blanket and pressure-induced stress. If unconstrained, these growths could become excessive and interfere with the operation of the reactor. If fully constrained, large stresses with the accompanying possibility of creep buckling will be generated in the first wall. Therefore, an optimum constraint on the first wall by the rest of the blanket needs to be determined. A corrugated first wall has been proposed by GA as a means of reducing the toroidal stress due to

differential swelling and temperature. Detailed inelastic stress analyses are needed to determine if such a design is acceptable, particularly for an embrittled material, and, if so, what minimum ductility is needed to make such a design workable. Similarly, ratchetting due to thermal cycling in the presence of a primary stress and irradiation-induced creep is a possibility that has been recognized in the BCSS program but not been analyzed. This could potentially pose a serious problem in any blanket design and should be carefully analyzed. In the opinion of the Task Force members these issues should be addressed in a future analytical R&D program. Since much of the material properties data needed to carry out such analyses are not currently available, the analyses should be conducted in a parametric fashion and should provide guidance as to what minimum properties (e.g., ductility, creep rate, strength, etc.) are needed to meet the design objectives. Simple in-reactor structural tests to validate design procedures have to be carried out in the future. Such tests might include pressurized cylinders which are constrained by a material having vastly different radiation creep and swelling properties.

3. Creep, Fatigue and Creep-Fatigue of Structural Materials (Priority A)

The first wall of all tokamak reactors (including the so-called steady-state tokamak reactors) will be subjected to cyclic thermal stresses and, consequently, to low cycle fatigue. Further, they will operate in a temperature regime where thermal creep in addition to radiation induced creep will be an important mode of damage and deformation. The combined effects of fatigue, thermal creep and radiation induced creep on material fracture are largely unknown. The materials of interest are the base structural alloys as well as weld materials and heat affected zones. Because of its potential impact on life of the first wall, generation of relevant data in fatigue and creep-fatigue together with development of techniques for predicting life under fusion environment should receive a high priority and will require a multi-year R&D effort. The levels of thermal stress and temperature being considerably lower, creep fatigue may not be a problem for TMR first walls.

4. Environmental Effects on Mechanical Properties (Priority A)

Mechanical properties of structural materials bear a uniquely important relationship to structural analysis since all design calculations depend

critically on these properties. Structural design analyses use a variety of mechanical properties such as yield strength, ultimate strength, fatigue strength, fatigue crack growth rate, creep-fatigue interaction, thermal conductivity, etc. all of which are affected to various degrees by the unique environment in a fusion reactor. At present most analyses use in-air data. The effects of irradiation, representative of fusion reactors, on these properties are largely unknown and represent one of the greatest uncertainties in the design analyses. The reduction of thermal conductivity of the solid breeder because of cracking can conceivably lead to breeder melting and deserves further research. The effects of coolants such as lithium, lithium-lead, helium, etc. on the various mechanical properties are also largely unknown. Another feature unique to pulsed tokamak reactors is the cycling nature of operation which is quite different from any of the fission reactor operation. Virtually no data currently exist that indicate what the effects are of such temperature cycling on the fatigue crack initiation and propagation lives. The task force strongly recommends a multi-year R&D program on materials to generate these data.

5. MHD Effects (Priority A)

MHD pressure drop in liquid metal cooled fusion reactors represents a source of large primary stress in the blanket structure. It is, in a sense, unique in that the stresses cannot be reduced by increasing the wall thickness, because increasing the wall thickness also increases the pressure drop proportionately. Some clever engineering has been used in the liquid metal cooled blanket design under the BCSS program in order to get around this problem. However, the margin of safety against uncertainties in pressure drop calculations is not large. Similarly, uncertainties exist in the effects of MHD on the heat transfer characteristics of the first wall; this may have important repercussions on the thermal stress. The task force feels that MHD effects have serious impacts on the structural design of the liquid metal cooled designs and strongly recommends conducting the necessary R&D in order to reduce the uncertainties in MHD calculations.

6. Design Criteria Development (Priority B)

The task force believes that the development of design criteria for fusion technology is extremely important but that such a development should evolve gradually by consensus amongst designers in the fusion community. To this end the task force recommends setting up a national group consisting of members from various projects of the national fusion and fission programs. The aim of this group should be to determine the failure consequences and safety requirements for the various concepts and to define the objectives of the design criteria. Most fusion design studies to date have used the ASME Code rules developed specifically for the Liquid Metal Fast Breeder Reactor (LMFBR). If in the opinion of the national group the failure consequences of a fusion reactor are far less severe than those of an LMFBR, then the safety factors used in the ASME Code should be relaxed for fusion applications. In addition, new rules have to be developed to handle the intense radiation field the first wall and the blanket structure are subjected to. Although the RDT standards developed for the LMFBR core may serve as guides, they have to be modified in order to take into account the unique environment of a fusion reactor.

7. Minimum Practical Wall Thickness (Priority B)

To reduce thermal stresses, most designs in the BCSS program have used very small thicknesses (~2 mm) for the first wall at the end of life. Although the ASME Code does not require a minimum wall thickness as long as the stresses satisfy the code criteria, there should be a practical lower limit for wall thickness based on fabrication considerations as well as to guard against non-uniform erosion. A study should be undertaken to determine a realistic minimum wall thickness.

8. Load Definition (Priority B)

To carry out a structural design analysis, the designer has to have a knowledge of the loads acting on the structure. MHD pressure drop is one such load and its importance has already been discussed. Plasma disruption represents another source for primary stress and needs adequate definition with respect to both its magnitude and frequency of occurence. In a similar fashion, magnetostatic force on blankets made of HT-9 is a source of primary stress.

Although preliminary calculations by GA have shown that these stresses are manageable by proper design of the blanket, there are uncertainties in the calculations of the magnetostatic forces near free edges. All these issues have direct bearing on the structural design of blankets and need to be resolved by adequate R&D programs.

9. Fracture Mechanics of Short Cracks (Priority B)

Although linear elastic fracture mechanics of relatively long cracks is firmly established such is not the case for short cracks, particularly when the crack growth is in the thickness direction of a thin plate. However, the latter situation is of interest in the design of the first wall of a fusion reactor, because short cracks will very likely initiate in the plasma side of the first wall as a result of plasma disruptions. Recent results have shown that short cracks grow faster than linear elastic fracture mechanics would predict. Further, because of creep, non-linear fracture mechanics will have to be employed. The task force feels that an R&D effort should be launched to develop fracture mechanics of short cracks for fusion application.

BLANKET COMPARISON AND SELECTION STUDY

SECTION 6.8 - TRITIUM BREEDING REQUIREMENTS AND UNCERTAINTIES

SECTION 6.8

TABLE OF CONTENTS

PAGE NO.

6.8 Tritium Breeding Requirements and Uncertainties.....6.8-1
6.8.1 Introduction.....6.8-1
6.8.2 Definition of the Problem.....6.8-1
6.8.3 Model for Required TBR.....6.8-4
6.8.4 Calculations of Required Breeding Ratio.....6.8-13
6.8.4.1 Base Case.....6.8-13
6.8.4.2 Sensitivity to Single Parameter Variation.....6.8-16
6.8.4.3 Sensitivity to Variations in Two Parameters.....6.8-24
6.8.5 Uncertainties in System Definition.....6.8-33
6.8.5.1 Introduction.....6.8-33
6.8.5.2 Geometrical Description of the Standard Model.....6.8-38
6.8.5.3 Calculational Method.....6.8-39
6.8.5.4 Results of Uncertainty Analysis.....6.8-39
6.8.5.5 Variation in Blanket Material Composition.....6.8-51
6.8.6 Uncertainties in Nuclear Data.....6.8-60
6.8.6.1 Introduction.....6.8-60
6.8.6.2 Theoretical Background for the Cross-Section Sensitivity/Uncertainty Analysis.....6.8-62
6.8.6.3 Blanket Concepts Considered for the Analysis and the Calculational Procedures.....6.8-64
6.8.6.4 Calculation Results.....6.8-67
6.8.6.5 Comparison of the Uncertainty Analysis Results to Results from the Non-Statistical Treatment.....6.8-93
6.8.6.6 Estimates for the Uncertainty in the Tritium Breeding Ratio for Other Blanket Concepts.....6.8-97
6.8.6.7 Conclusions on Nuclear Data Uncertainty.....6.8-100
REFERENCES.....6.8-102

LIST OF FIGURES FOR SECTION 6-8

FIGURE NO.	TITLE	PAGE NO.
6.8-1	Schematic model of the fuel cycle for a DT fusion reactor used in the present work	6.8-5
6.8-2	Tritium inventory variation with time for the base case parameter values, using $\beta = 0.05$ and $t_d = 5$ y	6.8-17
6.8-3	Tritium inventory variation with time for the base case parameter values except $\beta = 0.1$ and $t_d = 10$ y	6.8-18
6.8-4	Variation of the required tritium breeding ratio with key parameters. The horizontal axis is x/x_{ref}, where x_{ref} is the value of the parameter in the reference base case shown in Table 6.8-1	6.8-21
6.8-5	Required breeding ratio as a function of the tritium fractional burnup in the plasma at several values for the number of days of fuel reserve (t_r)	6.8-23
6.8-6	TBR sensitivity analysis of Base Case 1 with tritium fractional burnup continuously varied and each of the other parameters fixed at one-tenth and at ten times its reference value	6.8-27
6.8-7	TBR sensitivity analysis of Base Case 1 with tritium doubling time continuously varied and each of the other parameters fixed at one-tenth and at ten times its reference value	6.8-28
6.8-8	TBR sensitivity analysis of Base Case 1 with days of tritium reserve continuously varied and each of the other parameters fixed at one-tenth and at ten times its reference value	6.8-29
6.8-9	TBR sensitivity analysis of Base Case 1 with tritium fractional nonradioactive loss in plasma exhaust processing system continuously varied and each of the other parameters fixed at one-tenth and at ten times its reference value	6.8-30
6.8-10	TBR sensitivity analysis of Base Case 1 with tritium residence time in plasma exhaust processing system continuously varied and each of the other parameters fixed at one-tenth and at ten times its reference value	6.8-31
6.8-11	TBR sensitivity analysis of Base Case 1 with tritium residence time in blanket continuously varied and each of the other parameters fixed at one-tenth and at ten times its reference value	6.8-32

6.8-12 A vertical cross section of the reference reactor system for tokamaks.....6.8-35

6.8-13 A cross section of the reference limiter design.....6.8-37

6.8-14 Schematic of the Li_2O/He/FS blanket design.....6.8-50

6.8-15 The relative sensitivity profile for the Pb(n,2n) cross section in the LiPb/LiPb/PCA blanket integrated over the system.....6.8-77

6.8-16 The relative sensitivity profile for the Fe(n, inelastic) cross section in the LiPb/LiP/PCA blanket integrated over the system.....6.8-78

6.8-17 The relative sensitivity profile for the Fe(n, elastic) cross section in the Li_2O/He/PCA blanket integrated over the system.....6.8-79

6.8-18 The direct and indirect part of the relative sensitivity profile for the $^6Li(n,\alpha)t$ cross section in the LiPb/LiPb/PCA blanket integrated over the system.....6.8-81

6.8-19 The net relative sensitivity profile for the $^6Li(n,\alpha)t$ cross section in the LiPb/LiPb/PCA blanket integrated over the system.....6.8-82

6.8-20 The neutron spectrum in the middle of the breeding zone of the LiPb/LiPb/PCA and the Li_2O/He/PCA blankets.....6.8-83

6.8-21 The correlation matrix and relative standard deviation for the ^6Li (MAT = 1303) and reaction $(n,\alpha)t$ (MT = 105).....6.8-86

6.8-22 The correlation matrix and relative standard deviation for the Pb (MAT = 1382) and reaction (n,2n') (MT = 16).....6.8-87

6.8-23 The correlation matrix for beryllium (MAT = 104) for the inelastic level (MT = 52).....6.8-88

LIST OF TABLES FOR SECTION 6.8

TABLE NO.	TITLE	PAGE NO.
6.8-1	BASE CASE PARAMETER DEFINITIONS AND VALUES	6.8-14
6.8-2	REQUIRED TRITIUM BREEDING RATIO (Λ) FOR FOUR CASES	6.8-15
6.8-3	SUMMARY OF VARIATION OF THE REQUIRED BREEDING RATIO WITH A SINGLE CHANGE IN EACH OF THE REFERENCE PARAMETERS	6.8-19
6.8-4	EFFECT ON THE REQUIRED TRITIUM BREEDING RATIO (Λ) DUE TO SIMULTANEOUS VARIATION IN TWO PARAMETERS IN THE REFERENCE BASE CASE	6.8-25
6.8-5	MATERIAL CONFIGURATION OF REFERENCE CALCULATION	6.8-36
6.8-6	MATERIAL COMPOSITION	6.8-40
6.8-7	TRITIUM BREEDING RATIO WITH FULL BLANKET COVERAGE	6.8-42
6.8-8	CONTRIBUTION TO TRITIUM PRODUCTION FROM EACH BLANKET SECTOR	6.8-43
6.8-9	IMPACT OF NON-BREEDING INBOARD BLANKET ON TBR	6.8-45
6.8-10	IMPACT OF LIMITER DESIGN ON TBR	6.8-47
6.8-11	IMPACT OF RF-WAVEGUIDE DESIGN ON TBR	6.8-49
6.8-12	IMPACT OF HOMOGENIZATION OF BREEDING ZONE ON TBR	6.8-52
6.8-13	DESCRIPTION OF BLANKET MODEL FOR ANALYSIS ON VARIATION IN MATERIAL COMPOSITION	6.8-53
6.8-14	EFFECT OF CHANGE IN FIRST WALL THICKNESS ON TRITIUM BREEDING RATIO	6.8-55
6.8-15	EFFECT OF VOLUME FRACTION CHANGE OF STRUCTURE IN BLANKET 1 ON TRITIUM BREEDING RATIO	6.8-57
6.8-16	EFFECT OF VOLUME FRACTION CHANGE OF STRUCTURE IN BLANKET 2 ON TRITIUM BREEDING RATIO	6.8-58
6.8-17	EFFECT OF VOLUME FRACTION CHANGE OF STRUCTURE THROUGHOUT BLANKET ON TRITIUM BREEDING RATIO	6.8-59
6.8-18	EFFECT OF Li_2O DENSITY FACTOR CHANGE IN BLANKET 1 ON TRITIUM BREEDING RATIO	6.8-61

6.8-19 MATERIAL COMPOSITION ON DIMENSIONS FOR THE FOUR BLANKET CONCEPTS CONSIDERED FOR THE CROSS-SECTION SENSITIVITY/UNCERTAINTY ANALYSIS.....6.8-65

6.8-20 TRITIUM BREEDING RATIO FROM ^{6}Li (T_6), FROM ^{7}Li(T_7), AND THE TOTAL BREEDING RATIO IN THE FOUR BLANKET CONCEPTS.....6.8-66

6.8-21 THE TRITIUM BREEDING RATIO IN THE FLIBE/He/FS/Be BLANKET USING THREE DIFFERENT EVALUATIONS FOR THE BERYLLIUM CROSS-SECTIONS.....6.8-70

6.8-22 THE TRITIUM BREEDING RATIO IN THE $LiAlO_2/H_2O$/FS/Be BLANKET USING THREE DIFFERENT EVALUATIONS FOR THE BERYLLIUM CROSS-SECTIONS.....6.8-71

6.8-23 THE INTEGRATED RELATIVE SENSITIVITY COEFFICIENT, $S_{\Sigma_x}^{T_6}$, FOR THE TRITIUM BREEDING RATIO FROM ^{6}Li DUE TO A 1% INCREASE IN THE VARIOUS PARTIAL CROSS-SECTIONS OF MATERIALS PRESENT IN FOUR BLANKET CONCEPTS.....6.8-74

6.8-24 THE INTEGRATED RELATIVE SENSITIVITY COEFFICIENT, $S_{\Sigma_x}^{T_7}$, FOR THE TRITIUM BREEDING RATIO FROM ^{7}Li DUE TO A 1% INCREASE IN THE VARIOUS PARTIAL CROSS-SECTIONS OF MATERIALS PRESENT IN THE FOUR BLANKET CONCEPTS.....6.8-75

6.8-25 THE RELATIVE VARIANCE AND RELATIVE STANDARD DIVIATION IN TRITIUM BREEDING RATIO FROM ^{6}Li, ^{7}Li AND THE TOTAL BREEDING RATIO DUE TO CROSS SECTION UNCERTAINTIES OF VARIOUS MATERIALS IN Li_2O/HELIUM-COOLED BLANKET.....6.8-89

6.8-26 THE RELATIVE VARIANCE AND THE RELATIVE STANDARD DEVIATION, RSD, IN THE TRITIUM BREEDING FROM ^{6}Li, ^{7}Li, AND THE TOTAL TRITIUM BREEDING RATIO DUE TO CROSS-SECTION UNCERTAINTIES OF VARIOUS MATERIALS IN THE LiPb, $LiAlO_2$ AND THE FLIBE BLANKET.....6.8-90

6.8-27 PERCENTAGE (%) CONTRIBUTION FROM EACH BLANKET CONSTITUENT TO THE UNCERTAINTY IN TRITIUM BREEDING FROM ^{6}Li, $\Delta R_{^{7}Li}/R_{^{7}Li}$ IN THE FOUR BLANKET CONCEPTS CONSIDERED IN THE ANALYSIS.....6.8-92

6.8-28 ERROR ESTIMATES FOR VARIOUS PARTIAL CROSS SECTIONS (AS OBTAINED FROM LITERATURE).....6.8-94

6.8-29 MAXIMUM EXPECTED ERROR IN TRITIUM BREEDING (Li_2O HELIUM-COOLED BLANKET).....6.8-95

6.8-30 ESTIMATES OF THE UNCERTAINTY IN TBR DUE TO UNCERTAINTY IN NUCLEAR DATA BASE IN FOUR BLANKET CONCEPTS.....6.8-98

6.8-31 ESTIMATE OF THE UNCERTAINTY ASSOCIATED WITH TRITIUM BREEDING RATIO $\Delta_D = \Delta T/T$, IN VARIOUS BLANKET CONCEPTS DUE TO UNCERTAINTIES ASSOCIATED WITH NUCLEAR DATA BASE.....6.8-99

6.8 Tritium Breeding Requirements and Uncertainties

6.8.1. Introduction

A self-sustaining fusion reactor operated on the D-T fuel cycle must breed tritium. In all fusion reactor design concepts, tritium is produced in a lithium-containing blanket that circumscribes the plasma. Attaining fuel self-sufficiency is a critical goal for fusion as one of a very limited number of options for a renewable energy source. Therefore, careful evaluation of the conditions for attaining self-sufficiency is necessary in order to define the selection criteria for design concepts and the range of acceptable performance parameters and to prudently plan the R&D programs.

In this work, we attempt to addresss many of the technical problems associated with attaining fuel self-sufficiency in D-T fusion reactors. The problems are found to be far more complex than can be inferred from simple calculations of the tritium breeding ratio. Attaining fuel self-sufficiency is strongly dependent on many reactor plasma physics and technology components performance parameters, many of which are presently subject to large uncertainties. These uncertainties result in a large variation in the required tritium breeding ratio. On the other hand, the maximum tritium breeding ratio achievable with present blanket concepts is limited and its prediction suffers from uncertainties in neutronics calculations. In this work, we analyze the uncertainties in both the required and achievable tritium breeding ratios. This analysis is then extended to compare the risks of various candidate blanket concepts and to define the range of acceptable plasma and engineering components performance parameters necessary to enhance the potential for success in attaining fuel self-sufficiency in future D-T fusion reactors.

6.8.2 Definition of the Problem

The tritium breeding ratio (TBR or Λ) is defined as

$$\Lambda = \dot{N}^{+}/\dot{N}^{-} \qquad (6.8\text{-}1)$$

where $\dot{N}^{+}$ is the rate of tritium production in the system (normally the blanket) and $\dot{N}^{-}$ is the rate of burning tritium in the plasma. The required tritium breeding ratio (Λ_r) in a self-sustained fusion power economy must

exceed unity by a margin, G, to: 1) compensate for losses and radioactive decay of tritium during the period between production and use, 2) supply inventory for startup of other fusion reactors, and 3) provide hold-up inventory which accounts for the time delay between production and use as well as reserve storage.

We show later that G is a function of many reactor parameters as well as the doubling time, t_d. Many of these reactor parameters vary from one design to another; and for a given design the prediction of some of these parameters is subject to uncertainties. For example, the required tritium breeding ratio increases rapidly as the tritium inventory, I, in the reactor increases. The total inventory, I, includes the tritium inventory in the blanket, fueling and exhaust systems, other reactor components, and the storage inventory for use in off-normal conditions and to start up a new reactor. The magnitude of tritium inventory retained in the blanket is uncertain by about an order of magnitude for some concepts. The tritium flow rate into the plasma is inversely proportional to the tritium fractional burnup which might vary from 0.01 to 0.5 reflecting present inventories.

We write Λ_r as

$$\Lambda_r = 1 + G_o + \Delta_G \qquad (6.8\text{-}2)$$

where G_o is the doubling time margin for a reference conceptual design based on a given estimate of its performance parameters, and where Δ_G is the uncertainty in estimating the required breeding ratio $(1+G_o)$.

The achievable tritium breeding ratio, Λ_a, is also a function of the reactor design with particularly strong dependence on the blanket design concept. There are two problems in providing a precise evaluation of Λ_a:

1. Uncertainties in System Definition
   Fusion reactor design concepts are in an evolving process. The choices for many of the design features, materials and technology options have not been made. The achievable tritium breeding ratio is strongly dependent on many of these choices.

2. Inaccuracies in Prediction
   For a well specified reactor system, the prediction of the achievable

breeding ratio is subject to uncertainties. These are due to approximations or errors in the various elements of the calculations, e.g., in basic nuclear data, data representation, calculational methods, and geometric representation.

Therefore, we write the achievable tritium breeding ratio, Λ_a, as:

$$\Lambda_a = \Lambda_c - \sqrt{\Delta_s^2 + \Delta_p^2} \qquad (6.8\text{-}3)$$

where

Λ_c = tritium breeding ratio calculated for a specified blanket in a specified reactor system

Δ_s = uncertainty associated with system definition, i.e. the changes in Λ_c due to changes in the reference system.

Δ_p = uncertainty in predicting the breeding ratio (Λ_c) for the specified system due to nuclear data uncertainties, numerical approximations, etc.

The condition to attain self sufficiency can then be written as:

$$\Lambda_a > \Lambda_r \qquad (6.8\text{-}4)$$

In comparing blanket concepts as well as plasma and technology choices for future fusion reactors one needs a "figure of merit." One such figure of merit is:

$$\varepsilon = [\Lambda_c - (1+G_o)] - \sqrt{\Delta_G^2 + \Delta_s^2 + \Delta_p^2} \qquad (6.8\text{-}5)$$

The larger ε is, the higher is the probability that the D-T fuel self-sufficiency condition will be met, i.e. higher values of ε represent a lower degree of risk in not satisfying the fuel self sufficiency requirements. An alternative figure of merit is:

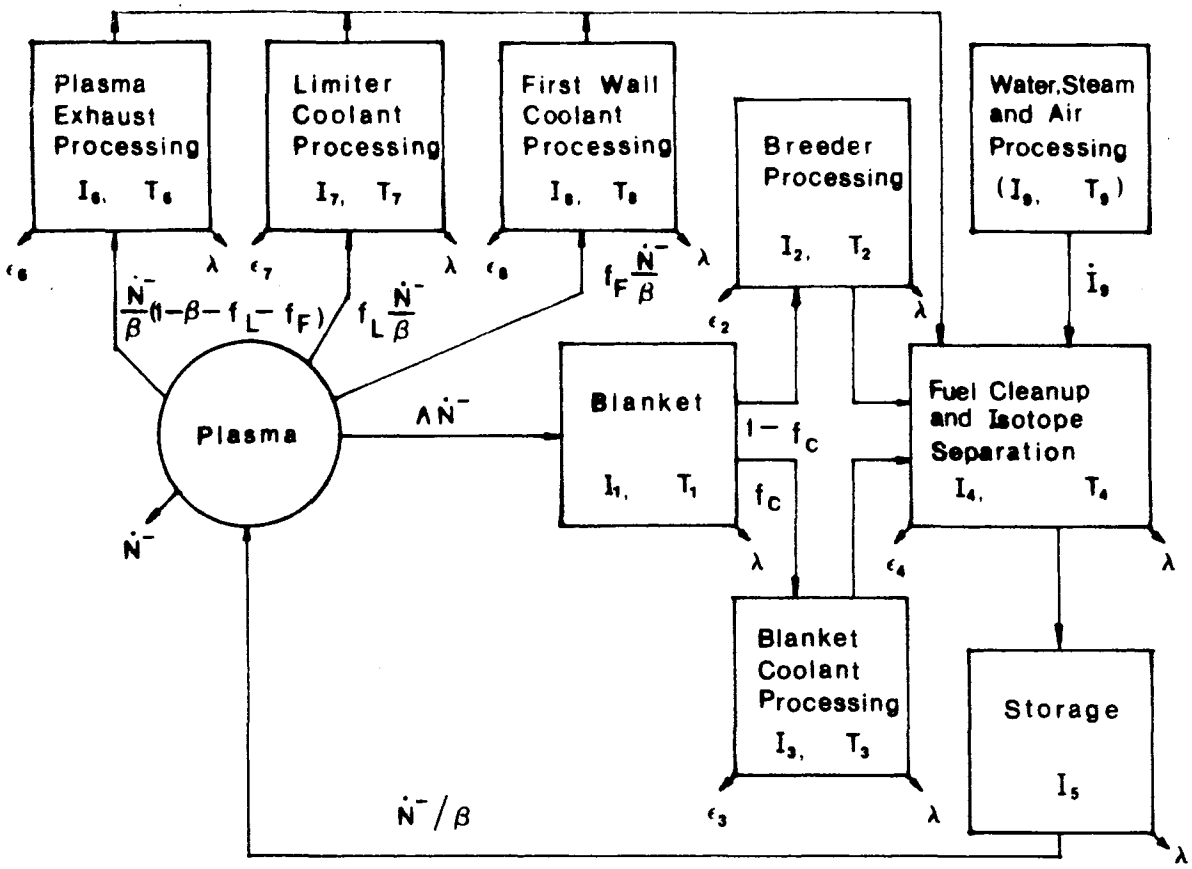
$$F = \frac{\Lambda_c - (1+G_o)}{\sqrt{\Delta_G^2 + \Delta_s^2 + \Delta_p^2}} \qquad (6.8\text{-}6)$$

A thorough statistical treatment of the fuel self sufficiency problem is not intended here, although it represents an excellent area for future research. Our effort in this area resulted in an expression that modifies the Δ's in the above formulas by a mix of partial derivatives of G_o and Λ_c with regard to many of the reactor system parameters. Our present knowledge of the fusion system does not permit reasonable evaluation of the more complex expression. Therefore, we maintain in this work the above simple expressions as they are more amenable to evaluation and they help provide insight into those parameters that have the largest impact on fuel self sufficiency.

Using expressions (5) or (6) the problem reduces to evaluating Λ_c, G_o, Δ_G, Δ_s and Δ_p. The evaluation of Λ_c involves three-dimensional calculation of the breeding ratio in a detailed reference design, and is the subject of another section in this report. The following subsections provide an attempt to evaluate the other quantities.

6.8.3 Model for Required TBR

An analytic model was developed to describe the characteristic parameters of the various elements of the tritium cycle as a tool for evaluating the tritium breeding requirements. The basis for the model is shown schematically in Fig. 6.8-1 which describes the tritium flow through the various components of a fusion reactor system. In previous work, Carre, et al,[6.8-1] Abdou,[6.8-2] and Jung[3] reported models for deriving the tritium breeding requirement. We have found Carre's model to be the most versatile as a starting point for this work. We have expanded on Carre's original model to include the first wall and limiter coolant processing and the fuel clean-up system. The first step in developing the model was to write down a set of differential equations that relate the time-dependent tritium inventories in the various components of Fig. 6.8-1 to their operating parameters. These equations were then solved analytically to derive explicit expressions for the functional dependence of the tritium inventories. We then derived an exact expression for the required tritium breeding ratio as a function of the doubling time and the tritium cycle operating parameters. A computer program was also written and used for evaluating the dependence of the required breeding ratio on the key physics and technology parameters for fusion reactors.



Λ : tritium breeding ratio

$\dot{N}^-$: tritium burn rate in the plasma

I_i : tritium inventory in compartment i

T_i : mean residence time of tritium in comparment i

ϵ_i : nonradioactive loss of tritium in comparment i

λ : tritium decay constant

β : tritium fractional burnup in the plasma

f_i : tritium fractional leakage to compartment i

I_9 : constant flow rate of tritium recovered from waste, steam, and air processing units

Figure 6.8-1 Schematic model of the fuel cycle for a DT fusion reactor used in the present work.

The tritium permeation pathway via the in-vessel components, was separated in this model from tritium permeation to the blanket coolant. In general, the limiter (or divertor) is bombarded directly by the high flux of hydrogen ions, while the first wall is exposed to a relatively modest flux of charge-exchange neutrals. Furthermore, it is possible that different coolants and their specific processing methods are used for the blanket, the first wall, and the limiters.[6.8-4] Therefore, the first wall coolant processing and the limiter coolant processing subsystems were considered individually. Radiation effects on tritium permeation and retention in the in-vessel components have not been explicitly accounted for but they can still be examined through adjustments in the present model parameters.

Two modes of tritium loss are accounted for in the model: radioactive decay in each but the plasma compartment, and the continuous nonradioactive losses in all processing compartments. The waste, steam and air processing units in the fuel cycle scenario of the STARFIRE[6.8-5] and ANL-DEMO[6.8-6] designs are modelled here as a single compartment. Since the waste processing unit is defined to recover tritium from the wastes (continuous nonradioactive losses) in other tritium recovery compartments, the initial one-time tritium loss such as the exchange of tritium with hydrogen and tritium sorption on all surfaces in the system are not included. During normal reactor operation or maintenance, it is required that tritium losses to the waste, steam and air are small. Therefore, a small constant tritium flow rate in Fig. 6.8-1 ($\dot{I}_9$ = 0.01 g/d) returned from this compartment is used in the model.

The residence times of tritium in all compartments are assumed to be constants although this is unlikely to be accurate during start-up or in fractional power operation. Although the residence time in the blanket is assumed to be a constant value, it has been treated as a function of time before the tritium inventory in the blanket reaches equilibrium.

The governing equation for the tritium inventory, I, in each compartment (with compartment # and parameters as defined in Fig. 6.8-1) is written as:

Blanket (#1)

$$\frac{dI_1}{dt} = \Lambda\dot{N}^- - \frac{I_1}{T_1} - \lambda I_1 \qquad (6.8\text{-}7)$$

Breeder processing (#2)

$$\frac{dI_2}{dt} = (1-f_c)\frac{I_1}{T_1} - (1 + \varepsilon_2)\frac{I_2}{T_2} - \lambda I_2 \qquad (6.8\text{-}8)$$

Blanket coolant processing (#3)

$$\frac{dI_3}{dt} = f_c \frac{I_1}{T_1} - (1+\varepsilon_3) \frac{I_3}{T_3} - \lambda I_3 \qquad (6.8\text{-}9)$$

Fuel cleanup and isotope separation (#4)

$$\frac{dI_4}{dt} = \frac{I_2}{T_2} + \frac{I_3}{T_3} + \frac{I_6}{T_6} + \frac{I_7}{T_7} + \dot{I}_9 - (1 + \varepsilon_4)\frac{I_4}{T_4} - \lambda I_4 \qquad (6.8\text{-}10)$$

Storage and fueling (#5)

$$\frac{dI_5}{dt} = \frac{I_4}{T_4} - \frac{\dot{\bar{N}}}{\beta} - \lambda I_5 \qquad (6.8\text{-}11)$$

Plasma exhaust processing (#6)

$$\frac{dI_6}{dt} = \frac{\dot{\bar{N}}}{\beta}(1 - \beta - f_L - f_F) - (1 + \varepsilon_6)\frac{I_6}{T_6} - \lambda I_6 \qquad (6.8\text{-}12)$$

Limiter coolant processing (#7)

$$\frac{dI_7}{dt} = f_L \frac{\dot{\bar{N}}}{\beta} - (1 + \varepsilon_7)\frac{I_7}{T_7} - \lambda I_7 \qquad (6.8\text{-}13)$$

First wall coolant processing (#8)

$$\frac{dI_8}{dt} = f_F \frac{\dot{\bar{N}}}{\beta} - (1 + \varepsilon_8) \frac{I_8}{T_8} - \lambda I_8 \qquad (6.8\text{-}14)$$

Following Fig. 6.8-1, the effective residence time for each compartment, τ_i, is defined by letting

$$\frac{1}{\tau_i} = \begin{cases} \frac{1}{T_i} + \lambda \quad , & i = 1 \\ \lambda \quad , & i = 5 \\ \frac{1 + \varepsilon_i}{T_i} + \lambda, & i = 2,3,4,6,7,8 \end{cases} . \qquad (6.8\text{-}15)$$

The exact solutions for the time dependent compartment inventories, I_i, were derived and they are expressed as:

Blanket

$$I_1(t) = I_{1\infty}\left(1 - e^{-\frac{t}{\tau_1}}\right) \tag{6.8-16}$$

Breeder processing

$$I_2(t) = I_{2\infty}\left(1 + \frac{\tau_1}{\tau_2 - \tau_1} e^{-\frac{t}{\tau_1}} + \frac{\tau_2}{\tau_1 - \tau_2} e^{-\frac{t}{\tau_2}}\right) \tag{6.8-17}$$

Blanket coolant processing

$$I_3(t) = I_{3\infty}\left(1 + \frac{\tau_1}{\tau_3 - \tau_1} e^{-\frac{t}{\tau_1}} + \frac{\tau_3}{\tau_1 - \tau_3} e^{-\frac{t}{\tau_3}}\right) \tag{6.8-18}$$

Fuel cleanup and isotope separation

$$\begin{aligned} I_4(t) = {} & \sum_{i=2,3} I_{i\infty} \frac{\tau_4}{T_i} \left[1 - \frac{\tau_1^2}{(\tau_i - \tau_1)(\tau_4 - \tau_1)} e^{-\frac{t}{\tau_1}} - \frac{\tau_i^2}{(\tau_1 - \tau_i)(\tau_4 - \tau_i)} e^{-\frac{t}{\tau_i}}\right. \\ & \left. - \frac{\tau_4^2}{(\tau_1 - \tau_4)(\tau_i - \tau_4)} e^{-\frac{t}{\tau_4}}\right] \\ & + \sum_{j=6,7,8} I_{j\infty} \frac{\tau_4}{T_j} \left[1 + \frac{\tau_4}{\tau_j - \tau_4} e^{-\frac{t}{\tau_4}} + \frac{\tau_j}{\tau_4 - \tau_j} e^{-\frac{t}{\tau_j}}\right] \\ & + \dot{I}_9 \tau_4 \left(1 - e^{-\frac{t}{\tau_4}}\right) \end{aligned} \tag{6.8-19}$$

Storage and fueling

$$I_5(t) = I_5^o e^{-\frac{t}{\tau_5}}$$

$$+ \sum_{i=2,3} \{ I_{i\infty} \frac{\tau_4\tau_5}{T_i T_4} [1 + \frac{\tau_1^3}{(\tau_i-\tau_1)(\tau_4-\tau_1)(\tau_5-\tau_1)} e^{-\frac{t}{\tau_1}}$$

$$+ \frac{\tau_i^3}{(\tau_1-\tau_i)(\tau_4-\tau_i)(\tau_5-\tau_i)} e^{-\frac{t}{\tau_i}} + \frac{\tau_4^3}{(\tau_1-\tau_4)(\tau_i-\tau_4)(\tau_5-\tau_4)} e^{-\frac{t}{\tau_4}}$$

$$+ \frac{\tau_5^3}{(\tau_1-\tau_5)(\tau_i-\tau_5)(\tau_4-\tau_5)} e^{-\frac{t}{\tau_5}}] \}$$

$$+ \sum_{j=6,7,8} \{ I_{j\infty} \frac{\tau_4\tau_5}{T_j T_4} [1 - \frac{\tau_4^2}{(\tau_j-\tau_4)(\tau_5-\tau_4)} e^{-\frac{t}{\tau_4}}$$

$$- \frac{\tau_5^2}{(\tau_j-\tau_4)(\tau_4-\tau_5)} e^{-\frac{t}{\tau_5}} - \frac{\tau_j^2}{(\tau_4-\tau_j)(\tau_5-\tau_j)} e^{-\frac{t}{\tau_j}}] \}$$

$$+ \dot{I}_9 \frac{\tau_4\tau_5}{T_4} [1 + \frac{\tau_4}{\tau_5-\tau_4} e^{-\frac{t}{\tau_4}} + \frac{\tau_5}{\tau_4-\tau_5} e^{-\frac{t}{\tau_5}}]$$

$$- \frac{\dot{N}\tau_5}{\beta} (1-e^{-\frac{t}{\tau_5}}) \qquad (6.8\text{-}20)$$

Plasma exhaust processing

$$I_6(t) = I_{6\infty}(1-e^{-\frac{t}{\tau_6}}) \qquad (6.8\text{-}21)$$

Limiter coolant processing

$$I_7(t) = I_{7\infty}(1-e^{-\frac{t}{\tau_7}}) \tag{6.8-22}$$

First wall coolant processing

$$I_8(t) = I_{8\infty}(1-e^{-\frac{t}{\tau_8}}) \tag{6.8-23}$$

where $$I_{1\infty} = \Lambda\dot{N}^{-}\tau_1 \tag{6.8-24}$$

$$I_{2\infty}=(1-f_c)\frac{\Lambda\dot{N}^{-}\tau_2\tau_1}{T_1} = \Lambda\cdot I_{2\Lambda} \tag{6.8-25}$$

$$I_{3\infty}=f_c\frac{\Lambda\dot{N}^{-}\tau_3\tau_1}{T_1} = \Lambda\cdot I_{3\Lambda} \tag{6.8-26}$$

$$I_{4\infty}=\tau_4\Big(\sum_{\substack{i=2\\ i\neq4,5}}^{8}\frac{I_{i\infty}}{T_i} + \dot{I}_9\Big) \tag{6.8-27}$$

$$I_{5\infty} = \tau_5\Big[\frac{\tau_4}{T_4}\Big(\sum_{\substack{i=2\\ i\neq4,5}}^{8}\frac{I_{i\infty}}{T_i} + \dot{I}_9\Big) - \frac{\dot{N}^{-}}{\beta}\Big] \tag{6.8-28}$$

$$= \tau_5\Big(\frac{I_{4\infty}}{T_4} - \frac{\dot{N}^{-}}{\beta}\Big)$$

$$I_{6\infty} = (1-\beta-f_L-f_F)\frac{\dot{N}^{-}\tau_6}{\beta} \tag{6.8-29}$$

$$I_{7\infty} = f_L\frac{\dot{N}^{-}\tau_7}{\beta} \tag{6.8-30}$$

$$I_{8\infty} = f_F\frac{\dot{N}^{-}\tau_8}{\beta} \tag{6.8-31}$$

In this model, we have incorporated the flexibility to specify a minimum tritium inventory reserve. This reserve quantity is to allow continued reactor operation during operational interruption of any part of the tritium cycle. The most demanding system on the reserve inventory is the plasma exhaust processing system, which is calculated in the model as a function of the number of days (t_r) required to supply fuel to the plasma while the plasma exhaust processing system is not operational. The tritium flow rate to the plasma is inversely proportional to the tritium fractional burnup in the plasma. For low fractional burnup, this reserve quantity, or minimum inventory turns out to be one of the more important parameters in establishing the required TBR.

The required initial start-up inventory was set equal to this reserve or minimum quantity plus the sum of equilibrium inventories for each model of the reactor compartments. The initial inventory is defined to be in the storage compartment with all other compartments inventory initially set equal to zero.

The doubling time is defined as the time when the storage inventory reaches a value equaling the sum of the initial inventory, I_5^o, and the minimum inventory, I_5^m. Expressing these concepts in terms of the above equations in order to obtain the doubling time, t_d, we set the inventory in the storage unit, #5, equal to:

$$I_5(t_d) = I_5^m + I_5^o \qquad (6.8\text{-}32)$$

Thus, at $t = t_d$, the tritium storage inventory must equal the minimum storage inventory, I_5^m, required to sustain operation plus the initial storage inventory, I_5^o, required to start operation of a second reactor. Since different definitions of the doubling time have been used in the literature, a doubling time defined as the time for storage inventory equal to two times the initial inventory has also been evaluated, as shown shortly, but this case is considered unnecessarily restrictive over the minimum requirements.

The value of the minimum inventory is not readily accessible by analytic solution owing to the complicated expression for storage inventory as a function of time. The minimum inventory was calculated numerically by evaluating the storage inventory as a function of time using Eq. (20). With

I_5^m and I_5^o known, their sum [by Eq.(32)] is set equal to $I_5(t_d)$ given in Eq. (20). The dependence of Eq. (20) on tritium breeding ratio, denoted Λ, is related explicitly in Eqs. (25) and (26). By substituting these expressions (25) and (26) into Eq. (20), and rearranging, we get an explicit expression for TBR = $\Lambda(t_d)$:

$$\Lambda(t_d) = \{[I_5^m + I_5^o(1-e^{-\frac{t_d}{\tau_5}})] - \dot{I}_9 \frac{\tau_4\tau_5}{T_4}\left[1 + \frac{\tau_4}{\tau_5-\tau_4}e^{-\frac{t_d}{\tau_4}} + \frac{\tau_5}{\tau_4-\tau_5}e^{-\frac{t_d}{\tau_5}}\right]$$

$$+ \frac{\dot{\bar{N}}\tau_5}{\beta}(1-e^{-\frac{t_d}{\tau_5}}) - \sum_{j=6,7,8} I_{j\infty}\frac{\tau_4\tau_5}{T_jT_4}\left[1 - \frac{\tau_4^2 e^{-\frac{t_d}{\tau_4}}}{(\tau_j-\tau_4)(\tau_5-\tau_4)}\right.$$

$$\left. - \frac{\tau_5^2 e^{-\frac{t_d}{\tau_5}}}{(\tau_j-\tau_5)(\tau_4-\tau_5)} - \frac{\tau_j^2 e^{-\frac{t_d}{\tau_j}}}{(\tau_4-\tau_j)(\tau_5-\tau_j)}\right]\}$$

$$+ \{\sum_{i=2,3}\{I_{i\Lambda}\frac{\tau_4\tau_5}{T_iT_4}\left[1 + \frac{\tau_1^3 e^{-\frac{t_d}{\tau_1}}}{(\tau_i-\tau_1)(\tau_4-\tau_1)(\tau_5-\tau_1)}\right.$$

$$+ \frac{\tau_i^3 e^{-\frac{t_d}{\tau_i}}}{(\tau_1-\tau_i)(\tau_4-\tau_i)(\tau_5-\tau_i)} + \frac{\tau_4^3 e^{-\frac{t_d}{\tau_4}}}{(\tau_1-\tau_4)(\tau_i-\tau_4)(\tau_5-\tau_4)}$$

$$\left. + \frac{\tau_5^3 e^{-\frac{t_d}{\tau_5}}}{(\tau_1-\tau_5)(\tau_i-\tau_5)(\tau_4-\tau_5)}\right]\} \qquad (6.8\text{-}33)$$

It is important to keep in mind that the storage unit minimum inventory, I_5^m, cannot be set independently, rather it is a function of the initial inventory and other system parameters. For practical convenience we have omitted an analytic expression for I_5^m, which was determined numerically more easily with a short computer program.

After Λ is calculated, the initial inventory is recalculated to check against the initial inventory which was originally estimated using an assumed Λ value. Because initial inventory is weakly dependent upon Λ , the original guess and final value for initial inventory were found to be always in good agreement (<1% difference) and so an iterative calculation of Λ was generally not necessary.

6.8.4. Calculations of Required Breeding Ratio

6.8.4.1 Base Case

Parameter values were selected for a base (reference) case to represent the most probable or expected values in the tritium cycle. These values define the Base Case for the calculation of $1 + G_o$ and are listed in Table 6.8-1. By selecting a negligible loss fraction, ($f_c = 0.01$), to the coolant, the base case applies equally well to a liquid metal blanket or to a solid breeder provided that tritium permeation from the solid breeder to the coolant is kept very low, e.g., by use of tritium permeation barriers. The blanket residence time, T_1, in the reference case is 10 d which results in an equilibrium blanket tritium inventory of ~ 5 kg. This is consistent with present estimates for solid breeder blankets but it is somewhat higher than representative values for liquid metals. However, since the TBR varies only slightly with lower T_1, as shown later, the reference case applies to a typical liquid metal breeder as well. The selection of a tritium burn fraction equal to 0.05 or 5% is considered to be equally valid for a tokamak or for a tandem mirror design in light of present uncertainties with both confinement concepts. The three coolant processing units had a residence time of 100 days set that long to account for slow recovery processes expected in coolants. It can be much longer in the case of water. In the reference case reported here the loss fraction from the fuel cleanup unit was set to zero, and the residence time set very short (≤0.1d) to simulate hold-up in the separate compartments and a rapid channeling of tritium through the fuel cleanup unit and into storage

In Table 6.8-2, the results of the required TBR, Λ, are shown for the base case along with that for three other cases. All cases have similar parameter values except for the doubling time, burn fraction, and the inventory condition used to define the doubling time. In the base case (case

Table 6.8-1. Base Case Parameter Definitions and Values

Parameter (X)	Base Case Value (X_{ref})
Tritium Consumption (Burn in Plasma) ($\dot{N}^-$)	0.5 kg/day
Doubling Time (t_d)	5 yr
Tritium Fractional Burnup in Plasma (β)	5%
Number of Days of Reserve for Plasma Fueling (t_r)	2 days
Non-Radioactive Loss (Chemical Tie-up in Radioactive Waste, Etc.) in:	
Breeder Processing (ε_2)	0.1%
Blanket Coolant Processing (ε_3)	0.1%
Fuel Cleanup and Isotope Separation Units (ε_4)	0.0
Plasma Exhaust Processing (ε_6)	0.1%
Limiter Coolant Processing (ε_7)	0.1%
First Wall Coolant Processing (ε_8)	0.1%
Tritium Mean Residence Time in:	
Blanket (T_1)	10 days
Breeder Processing (T_2)	1 day
Blanket Coolant Processing (T_3)	100 days
Fuel Cleanup and Isotope Separation Units (T_4)	0.1 days
Plasma Exhaust Processing (T_6)	1 day
Limiter Coolant Processing (T_7)	100 days
First Wall Coolant Processing (T_8)	100 days
Tritium Fractional Leakage from:	
Breeder to Blanket Coolant Processing (f_c)	1%
Plasma to Limiter Coolant Processing (f_L)	0.01%
Plasma to First Wall Coolant Processing (f_F)	0.01%
Constant tritium Flow Returned from the Waste, Steam, and Air Processing ($\dot{I}_9$)	0.01g/day

Table 6.8-2. Required Tritium Breeding Ratio (Λ) for Four Cases

Case	Doubling Time Condition*	Doubling Time (t_d)	Tritium Fractional Burnup (β)	Initial Inventory (Kg-^{3}He)	Minimum Inventory (Kg-^{3}He)	Λ
1 (Base Case)	$I_5 = I_5^o + I_5^m$	5 yr	0.05	35.5	21.4	1.08
2	$I_5 = 2*I_5^o$	5 yr	0.05	35.6	21.4	1.10
3	$I_5 = I_5^o + I_5^m$	10 yr	0.1	20.2	11.5	1.03
4	$I_5 = 2*I_5^o$	10 yr	0.1	20.3	11.5	1.04

*Expressed in terms of the storage unit inventory, I_5, its initial inventory, I_5^o and its minimum inventory, I_5^m.

1), Λ is calculated as 1.08. If the definition of doubling time (t_d) is changed to be that at which the storage inventory is twice the initial inventory (i.e., $I_5 = 2I_5^o$), then Λ increases to 1.10. However, the definition in the base case (i.e., $I_5 = I_5^o + I_5^m$ at t_d) is more consistent with that in the power industry and is used throughout the rest of this work. Case 3 is similar to case 1 except that the doubling time and the fractional burnup (β) in the plasma are changed from 5 yr and 5% to 10 yr and 10%, respectively. This increase in t_d and β reduces Λ to 1.03. The effect of using the alternative definition for t_d in case 3 is shown in Table 6.8-2.

The time variation of the inventories by subsystem are shown for cases 1 and 3 described above in Figs. 6.8-2 and 6.8-3, respectively. As noted from the figures the tritium inventory in the plasma exhaust processing subsystem remains constant after the first two days. Thereafter, because of its short residence time in that subsystem, the tritium inventory is constant at its equilibrium value. The storage inventory decreases as tritium initially is injected into the plasma and burnt but it increases slowly then rapidly as the tritium inventories in the other subsystems build up and reach their saturation levels. We have found that the minimum inventory occurs about 30 days post-start-up. It is noted from Fig. 6.8-3 for case 3 that a larger burn fraction causes the plasma exhaust processing inventory to be less than the blanket inventory. Blanket inventory variations will then appear more significant.

Case 1 above, together with the definition of the doubling time as the time when storage inventory equals the sum of the initial and minimum inventories was selected as the base case for subsequent analysis of TBR sensitivity and uncertainty. For this base case Λ is found to be 1.08, i.e., the breeding margin, G_o, is 0.08.

6.8.4.2. Sensitivity to Single Parameter Variation

The sensitivity of TBR to each of the parameters of the fuel cycle was examined over a range from one tenth to ten times the base case reference value. Table 6.8-3 shows the required breeding ratio, Λ , at the endpoints of these variations, i.e., at $x = x_{ref}/10$ and $x = 10\ x_{ref}$, where x_{ref} is the value of the parameter in the reference base case described in the previous subsection. The rate of change in TBR due to variations in each parameter,

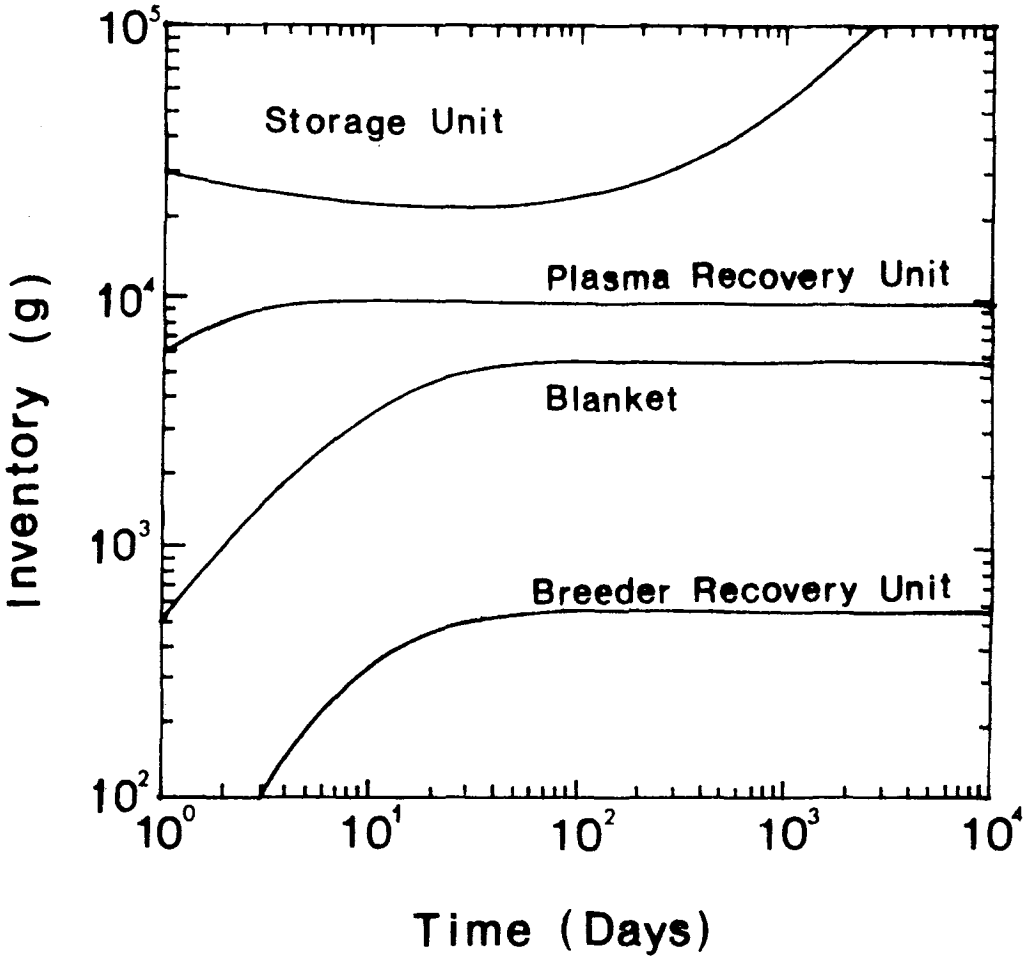


Figure 6.8-2 Tritium inventory variation with time for the base case parameter values, using $\beta = 0.05$ and $t_d = 5$ yr.

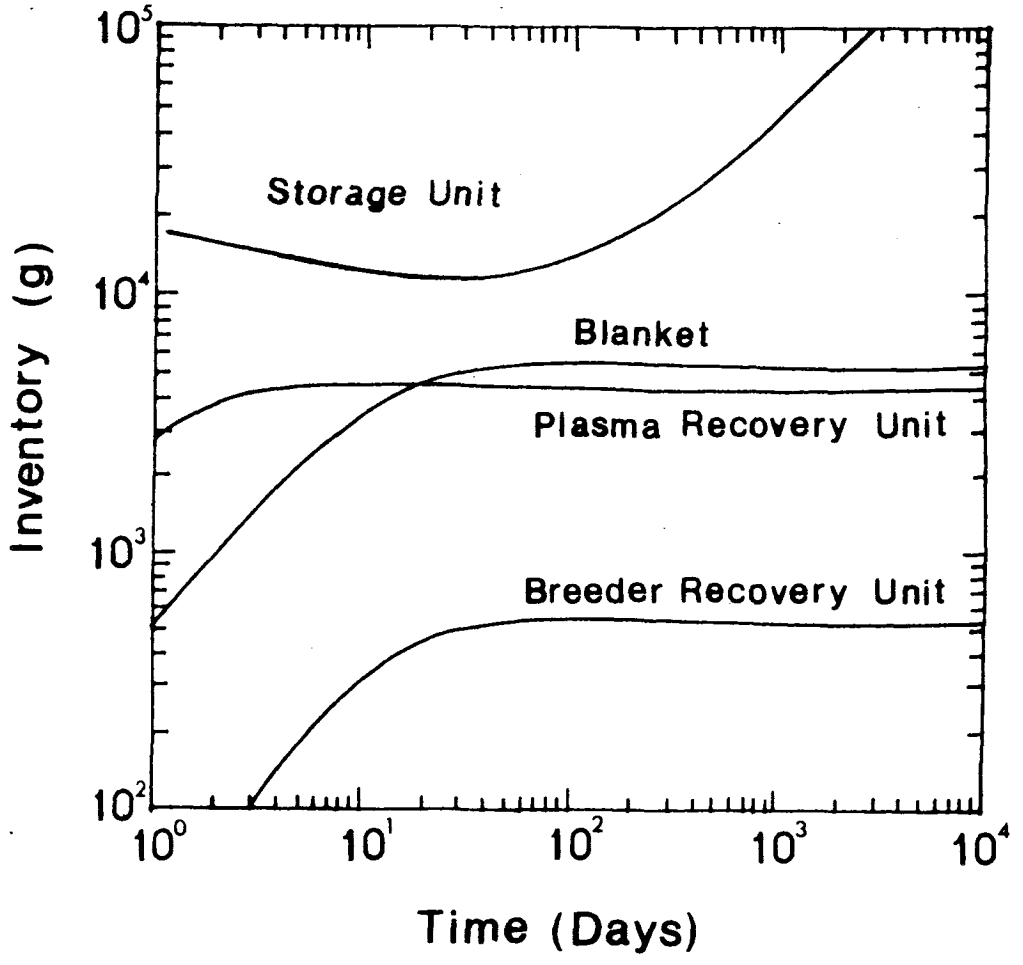


Figure 6.8-3 Tritium inventory variation with time for the base case parameter values except $\beta = 0.1$ and $t_d = 10$ y.

Table 6.8-3. Summary of Variation of the Required Breeding Ratio with a Single Change in Each of the Reference Parameters

Parameter (X)	TBR for		Absolute Slope of Λ	Percentage of Total Slope
	$(X_{ref}/10)$	$(X_{ref} \cdot 10)$		
$\dot{N}^-$	1.08(0.0%)*	1.08(0.0%)*	0.0001	0.1
t_d	1.53(41.7%)	1.04(-3.7%)	0.0534	24.0
β	1.70(57.4%)	1.02(-5.6%)	0.0863	38.8
t_r	1.05(-2.8%)	1.37(26.8%)	0.0322	14.5
ε_2	1.08(0.0%)	1.09(0.9%)	0.0011	0.5
ε_3	1.08(0.0%)	1.08(0.0%)	0.0000	0.0
ε_6	1.06(-1.8%)	1.25(15.7%)	0.0192	8.6
ε_7	1.08(0.0%)	1.08(0.0%)	0.0000	0.0
ε_8	1.08(0.0%)	1.08(0.0%)	0.0000	0.0
T_1	1.07(-0.9%)	1.19(10.2%)	0.0096	4.3
T_2	1.08(0.0%)	1.09(0.9%)	0.0009	0.4
T_3	1.08(0.0%)	1.09(0.9%)	0.0015	0.7
T_4	1.08(0.0%)	1.10(1.9%)	0.0009	0.4
T_6	1.06(-1.8%)	1.22(13.0%)	0.0153	6.9
T_7	1.08(0.0%)	1.08(0.0%)	0.0002	0.1
T_8	1.08(0.0%)	1.08(0.0%)	0.0002	0.1
f_c	1.08(0.0%)	1.09(0.9%)	0.0014	0.6
f_L	1.08(0.0%)	1.08(0.0%)	0.0004	0.2
f_F	1.08(0.0%)	1.08(0.0%)	0.0004	0.2
			$\sum$ = 0.2231	$\sum$ = 100.0

* Values in parenthesis represent the relative change of TBR with respect to a reference TBR of 1.08.

was evaluated as the slope of the TBR curve at the parameters' normalized reference value and this slope $(\partial TBR/\partial(x/x_{ref}))$ is also shown in the table. The parameter slopes are summed and the percentage of total slope, or percent of the total TBR slope at the base case values which is attributable to each parameter is calculated as shown in the last column. This column can be interpreted as the percent of the total variation in the base case due to each parameter for a small change in all the independent variables simultaneously. These values also give a relative measure of the importance of the various parameters to the required TBR in the base case. For example, the results in the table show that the number of days of fuel reserve, i.e. t_r, is twice as important as the mean residence time in the plasma exhaust processing system, i.e. T_6, in terms of changes in TBR due to changes in the reference values. The percentages of the total slope for t_r and T_6 are 14.5 and 6.9, respectively.

Based on extreme TBR values within this range of parameter variations and on the slope of the TBR sensitivity curve at the parameter reference value, six parameters can be identified as significantly affecting the expected TBR over that range. These parameters have an absolute slope of the TBR sensitivity curve at the base case condition of equal to or greater than 0.01, as seen in Table 6.8-3. This represents a 1% variation in TBR resulting per unit change in the reference case parameter value. These six parameters were selected for further study as they accounted for over 97% of the total variation in TBR at the base case values. None of the other parameters contributed more than about 0.7% to the total variation. In order of their significance these parameters are: tritium fractional burnup in the plasma, doubling time, number of days of tritium fuel reserve, non-radioactive loss fraction, and mean residence time in the plasma exhaust processing system, and to a lesser extent, the blanket mean residence time. The TBR variation with each of these six parameters is shown in Fig. 6.8-4. Each parameter is varied in the range $0.1 \cdot x_{ref}$ to $10 \cdot x_{ref}$, where x_{ref} is the value of the parameter in the reference case.

The strong dependence of TBR on the fractional burnup and, doubling time has been previously reported, and our results agree closely with those in the literature[6.8-1 to -3]. The number of days of tritium fuel (t_r) reserve are noted here to be very important especially for values greater than the refer-

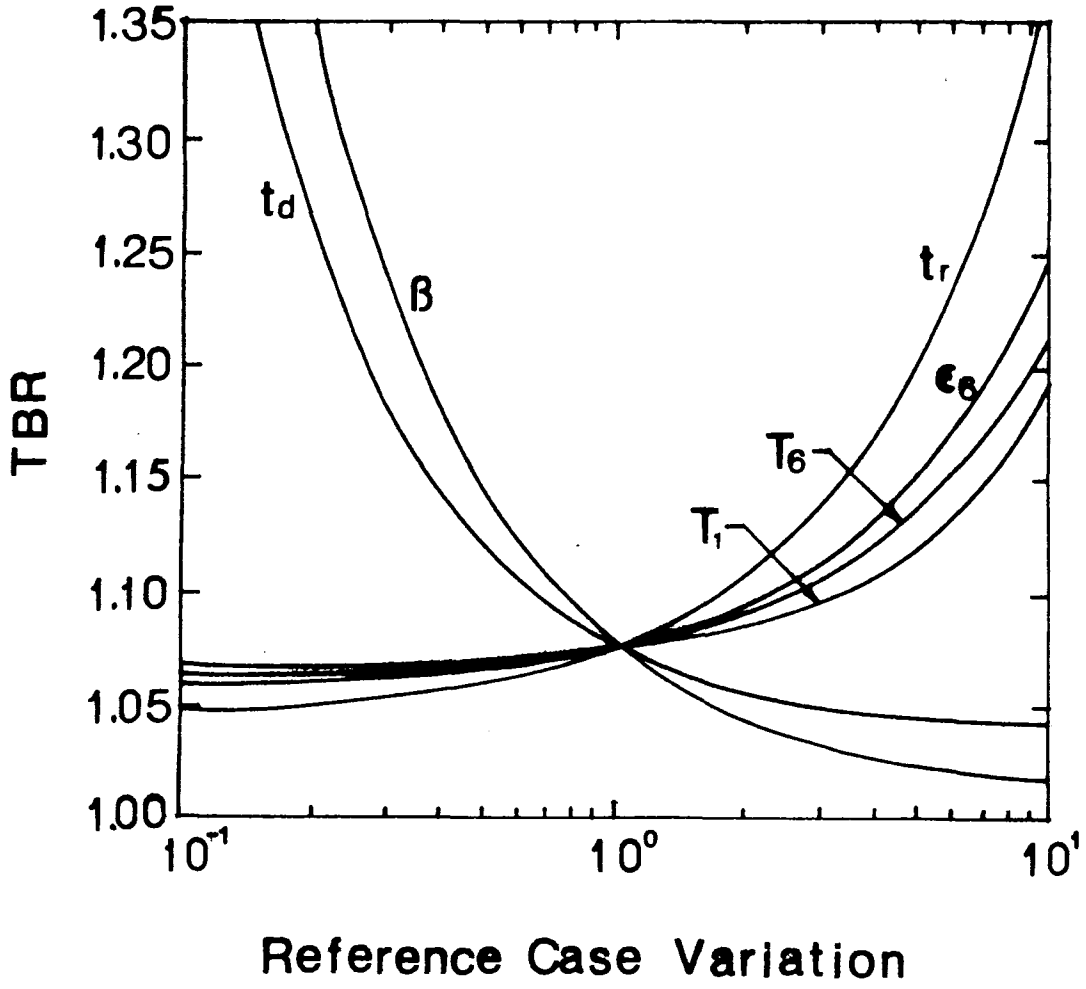


Figure 6.8-4 Variation of the required tritium breeding ratio with key parameters. The horizontal axis is x/x_{ref}, where x_{ref} is the value of the parameter in the reference base case shown in Table 6.8-1.

ence case of two days, due to the resulting large inventory. This has not been previously noted in the literature. Fig. 6.8-5 shows the required tritium breeding ratio as a function of the tritium fractional burnup in the plasma (β) at several values of t_r. The required Λ increases very rapidly as β decreases and t_r increases since the reserve inventory is proportional to t_r and the tritium fueling flow rate to the plasma which is inversely proportional to β . For $\beta > 20\%$, the importance of t_r decreases substantially. For $\beta > 5\%$, t_r up to ~ 3 days can be tolerated if Λ of ~ 1.10 is acceptable. At lower β, it is extremely important that t_r be minimized. This means that the plasma exhaust processing system must be reliable and will require only a short time to repair. The alternative of shutting down the fusion power plant each time there is a failure in the plasma exhaust processing system is likely to be economically unacceptable.

Increasing the blanket inventory significantly increases the required TBR particularly as the inventory exceeds two to three times the reference value of about 5 kg, (corresponding to a mean blanket residence time (T_l) of 10 days) as shown in Fig. 6.8-4. This could become a significant concern for a solid breeder undergoing chronic radiation damage with possible subsequent increases in tritium residence time and inventory.

Reactor subsystem which were modelled because of reported potential tritium permeation problems[6.8-7,-8] included the first wall and limiter (or divertor) coolant systems. In the reference case, the tritium fractional leakage into the first wall and limiter coolant processing compartments were fixed at 0.01% which is equivalent to an incoming tritium flow rate of 1 g/day. This value is consistent with recent estimates of tritium permeation[6.8-7,-8] but there are very large uncertainties in this area. However, as the fractional leakage into the first wall was increased by an order of magnitude (to 10 g/day), less than one percent change in the required TBR was observed. Even in the case of long residence times (100 days) representing a possibly slow tritium separation process from a water coolant, these subsystems held negligibly small inventories and thus they had negligible impact on the expected TBR. Obviously, much higher tritium permeation rates on retention inventories in the in-vessel components can significantly increase the required TBR but the safety and economic implications of such higher rates are too large to be acceptable.[6.8-8]

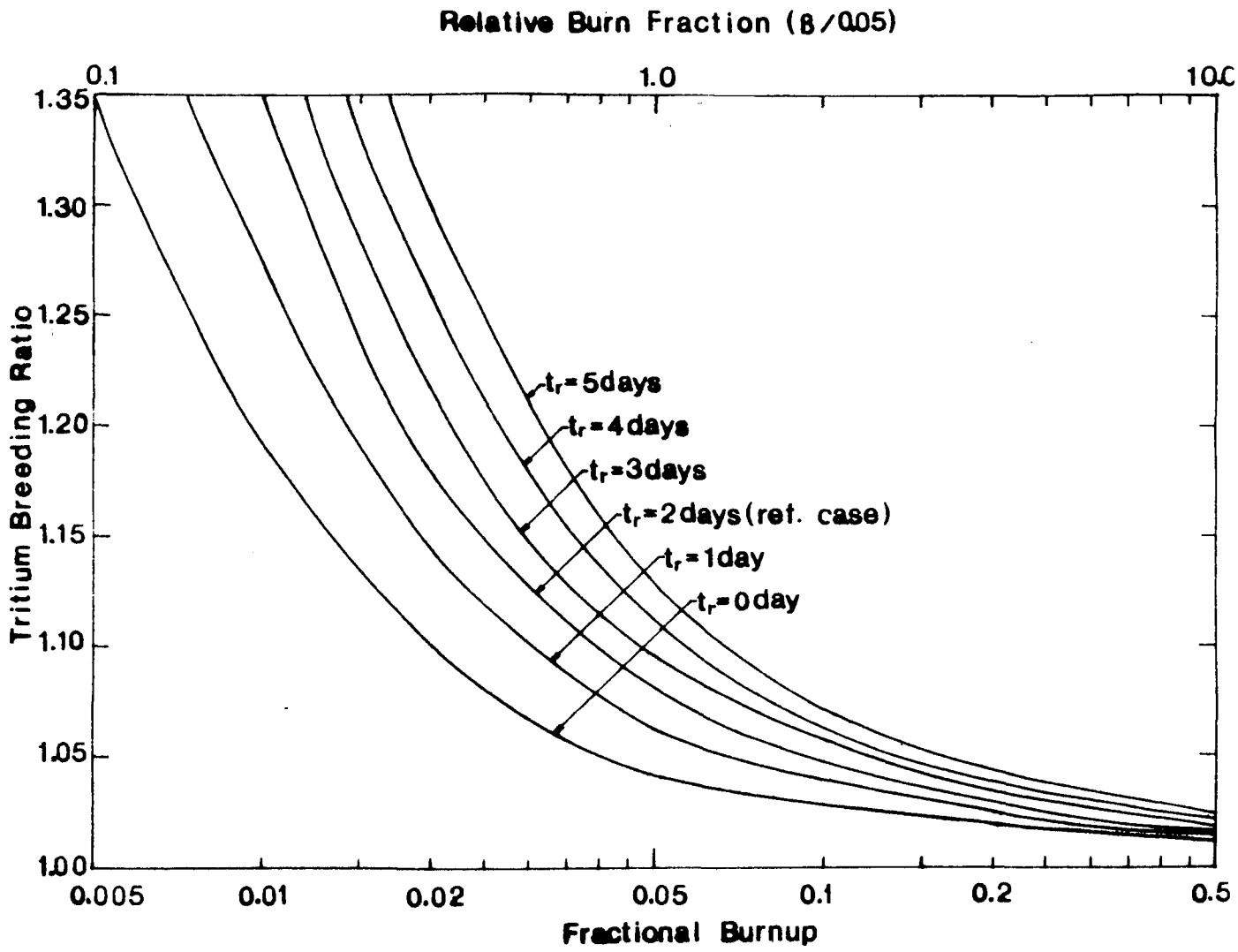


Figure 6.8-5 Required breeding ratio as a function of the tritium fractional burnup in the plasma at several values for the number of days of fuel reserve (t_r).

6.8.4.3. Sensitivity to Variations in Two Parameters

Some effort was made to examine the effect on the required breeding ratio of varying two parameters simultaneously. The combined effect is non-linear and would have to be calculated separately for each combination of parameters. With one parameter (called floated parameter) continuously varied from one tenth to ten times of its base case reference value and the second parameter fixed at one tenth and then at ten times of its reference value, the ranges of the TBR's for these two varied parameters were calculated. The six most important parameters discussed before were examined.

Table 6.8-4 lists the required TBR values (Λ) for the two parameters varied from one tenth to ten times their reference values in the base case 1. One of the worst cases found is when the doubling time is short (0.5 year) and the tritium residence time in the blanket is long (100 days), then, as shown in the table, the required TBR value can be unrealistic, as large as several hundred. The long tritium residence time in blanket means that a large equilibrium tritium inventory is held up in the blanket. The initial storage tritium inventory is thus increased by this large equilibrium blanket tritium inventory. In order to meet such a high initial tritium storage requirement within a very short period, a large tritium production rate, and therefore large Λ must be required. The best case (Λ = 1.01) can be found when the tritium fractional burnup is high (0.5) and either the doubling time is long (50 years), the tritium reserve fuel time is short (0.2 d) or the blanket residence time is short (1 d). Since a long doubling time may be an impractical constraint in fusion power economy, the alternatives to obtaining a small required TBR must be seriously considered as goals for fusion R&D. Such goals include attaining high tritium fractional burnup in the plasma through selection, design and development of the impurity control and exhaust system, minimizing the tritium inventory in all reactor components, particularly the blanket and developing reliable and efficient tritium processing systems. If the tritium fractional burnup and doubling time are kept at the reference values, then a lower TBR requirement may be obtained by decreasing any one or two of the remaining four most important parameters simultaneously.

The required breeding ratios for the first parameter continuously varied with each of the second parameters at the reference and at the two extreme

Table 6.8-4. Effect on the Required Tritium Breeding Ratio (Λ) due to Simultaneous Variation in Two Parameters in the Reference Base Case (Λ = 1.08 for the Reference Case)

Floated Parameter		Second Parameter											
		T_1(day)		T_6(day)		ε_6		t_r(day)		t_d(year)		β	
		1	100	0.1	10	0.0001	0.01	0.2	20	0.5	50	0.005	0.5
β	0.5	1.01	1.11	1.02	1.02	1.02	1.02	1.01	1.04	1.14	1.01	-	1.02
	0.005	1.68	1.90	1.56	3.16	1.52	3.49	1.41	4.57	5.38	1.40	1.70	-
t_d	50	1.04	1.08	1.04	1.10	1.03	1.21	1.03	1.16	-	1.04		
	0.5	1.40	>100	1.42	2.90	1.52	1.72	1.29	3.93	1.54	-		
t_r	20	1.35	1.53	1.35	1.51	1.35	1.54	-	1.37				
	0.2	1.04	1.15	1.04	1.19	1.03	1.22	1.05	-				
ε_6	0.01	1.24	1.37	1.24	1.39	-	1.25						
	0.0001	1.05	1.17	1.05	1.20	1.06	-						
T_6	10	1.21	1.35	-	1.22								
	0.1	1.06	1.17	1.06	-								
T_1	100	-	1.19										
	1	1.07	-										

values are depicted in Figs. 6.8-6 to 6.8-11. In each of these figures, the x-axis is the ratio of the new value of the first parameter to its reference value. The Y-axis is for the required breeding ratio (Λ_r). Several curves are displayed in each figure, with each curve for a specified value of the second parameter. Besides obtaining the required TBR within certain ranges, these figures can be used as reference maps in tradeoff analysis. Several examples explaining the results of the figures are given in the following.

If the achievable tritium fractional burnup of a fusion reactor is assumed to be no more than 0.1, then as seen from Fig. 6.8-6 the required TBR varies from 1.02 to 1.32 depending on the value of the other parameters. From Fig. 6.8-7, if the tritium fractional nonradioactive loss in the plasma exhaust processing system (ε_6) is no less than 0.01, no matter how the tritium doubling time is changed the required TBR is always no less than 1.21. But, from Fig. 6.8-9, there is one possible way to obtain a TBR as low as 1.03 when $\varepsilon_6 > 0.01$, which is attaining a high tritium fractional burnup.

As an example of trade-off considerations, suppose that the maximum achievable TBR for a fusion reactor is 1.05 and the days of tritium fuel reserve cannot be less than one day, then as seen from Fig. 6.8-8, several alternatives can be considered: designing the tritium residence time in the plasma exhaust processing subsystem at no more than 0.1 day, decreasing the tritium fractional nonradioactive loss to less than 0.0001, increasing the tritium doubling time to more than about 15 years, or raising the fractional burnup to no less than about 0.1 whichever is achievable. Note that the examples shown above changed only two parameters in the reference case at one time. Changing more than two parameters simultaneously can provide additional perspective on the required TBR. However, such variations are so large that they must be considered only for specific cases.

In the parameter sensitivity study, the efficiencies of the recovery unit processes were examined and the plasma exhaust processing loss fraction was seen to significantly affect the resultant TBR value as shown in Fig. 6.8-9. For example, as a worst case, setting the plasma recovery loss fraction, ε_6 equal to 0.02 results in a required TBR of 1.47. In Fig. 6.8-6, the importance of ε_6 increases rapidly at lower fractional burnup. This emphasizes the need to achieve very high efficiencies in the tritium processing subsystems, particularly that of the plasma exhaust.

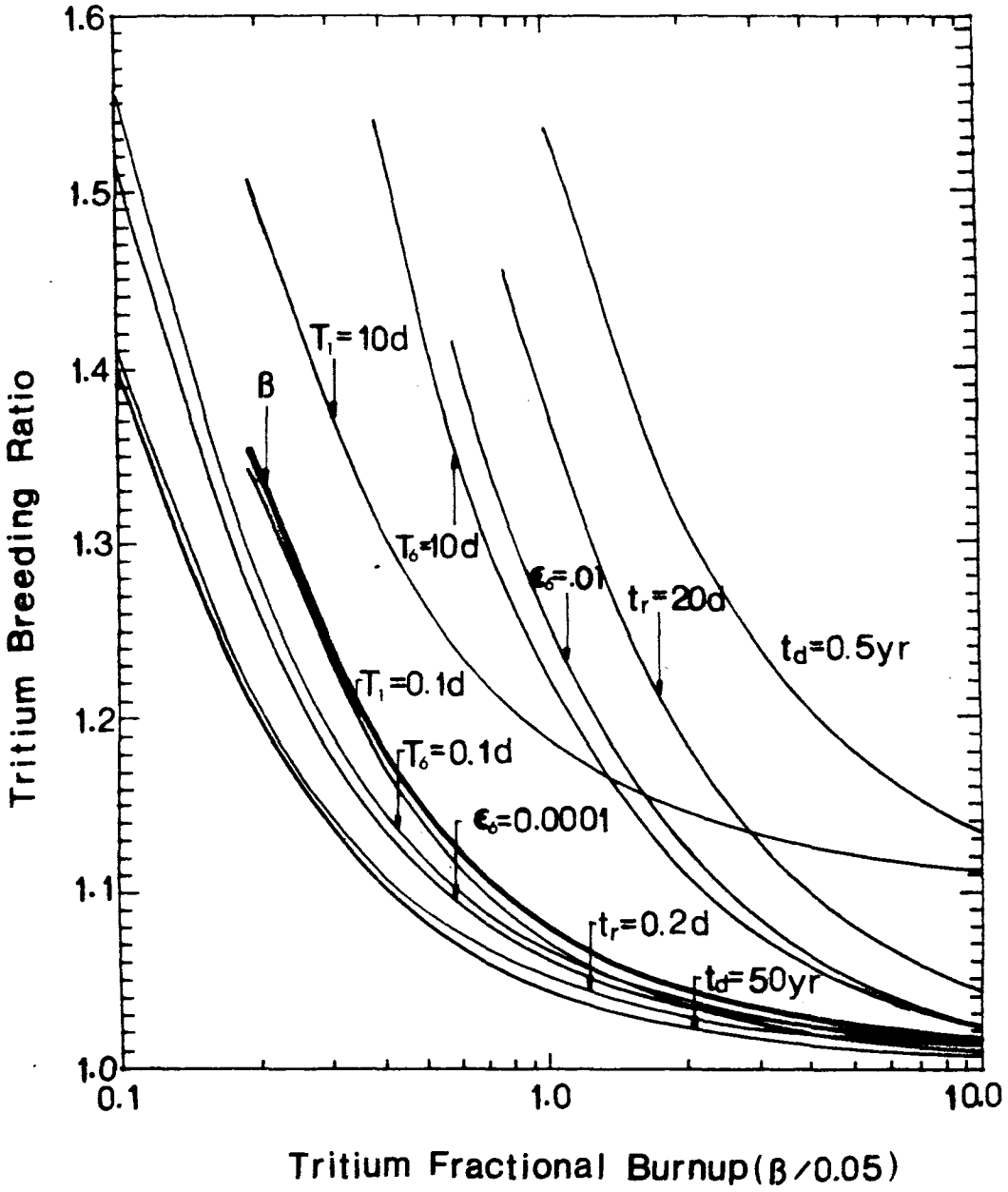


Figure 6.8-6 TBR sensitivity analysis of Base Case 1 with tritium fractional burnup continuously varied and each of the other parameters fixed at one-tenth and at ten times its reference value.

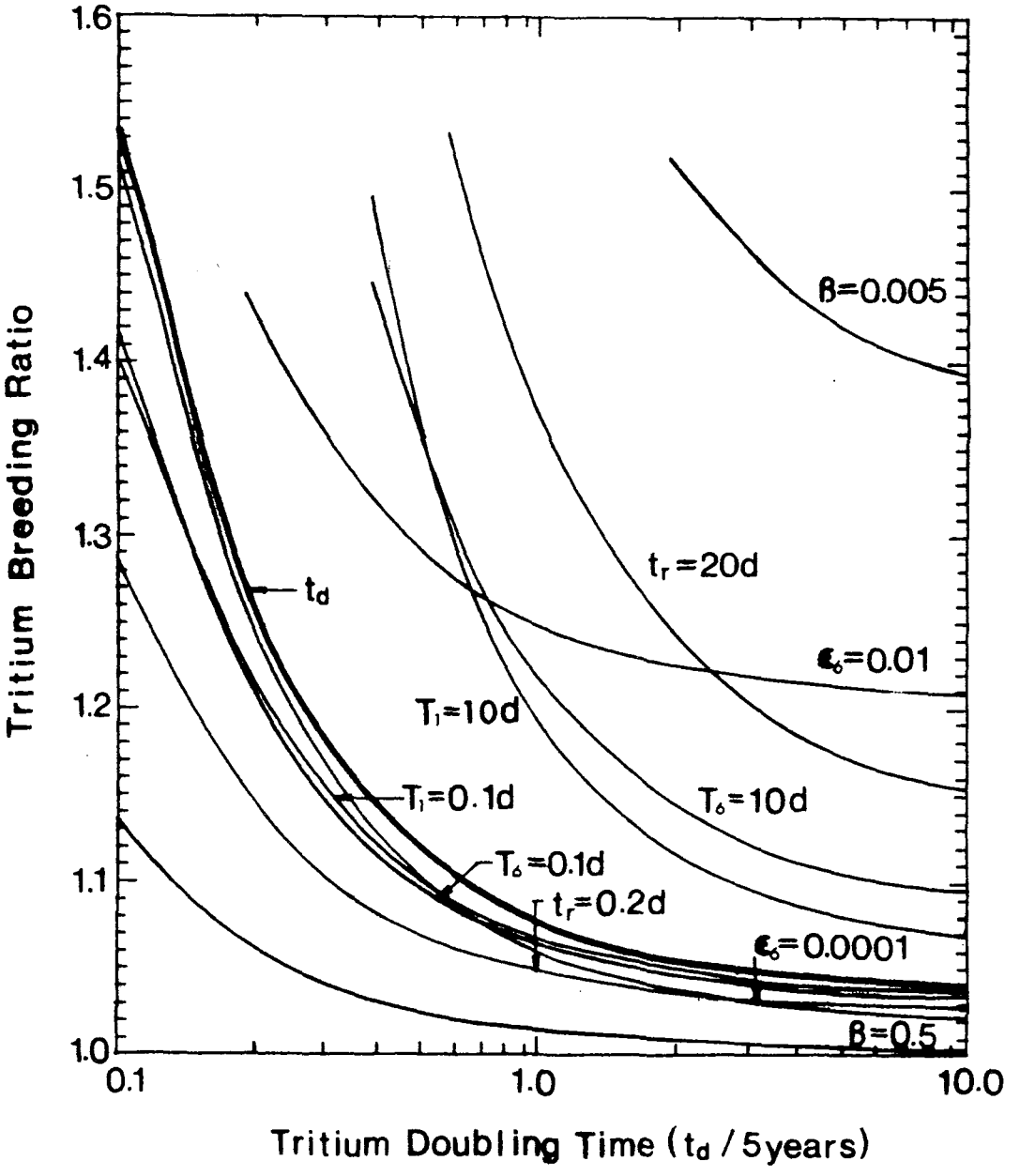


Figure 6.8-7 TBR sensitivity analysis of Base Case 1 with tritium doubling time continuously varied and each of the other parameters fixed at one-tenth and at ten times its reference value.

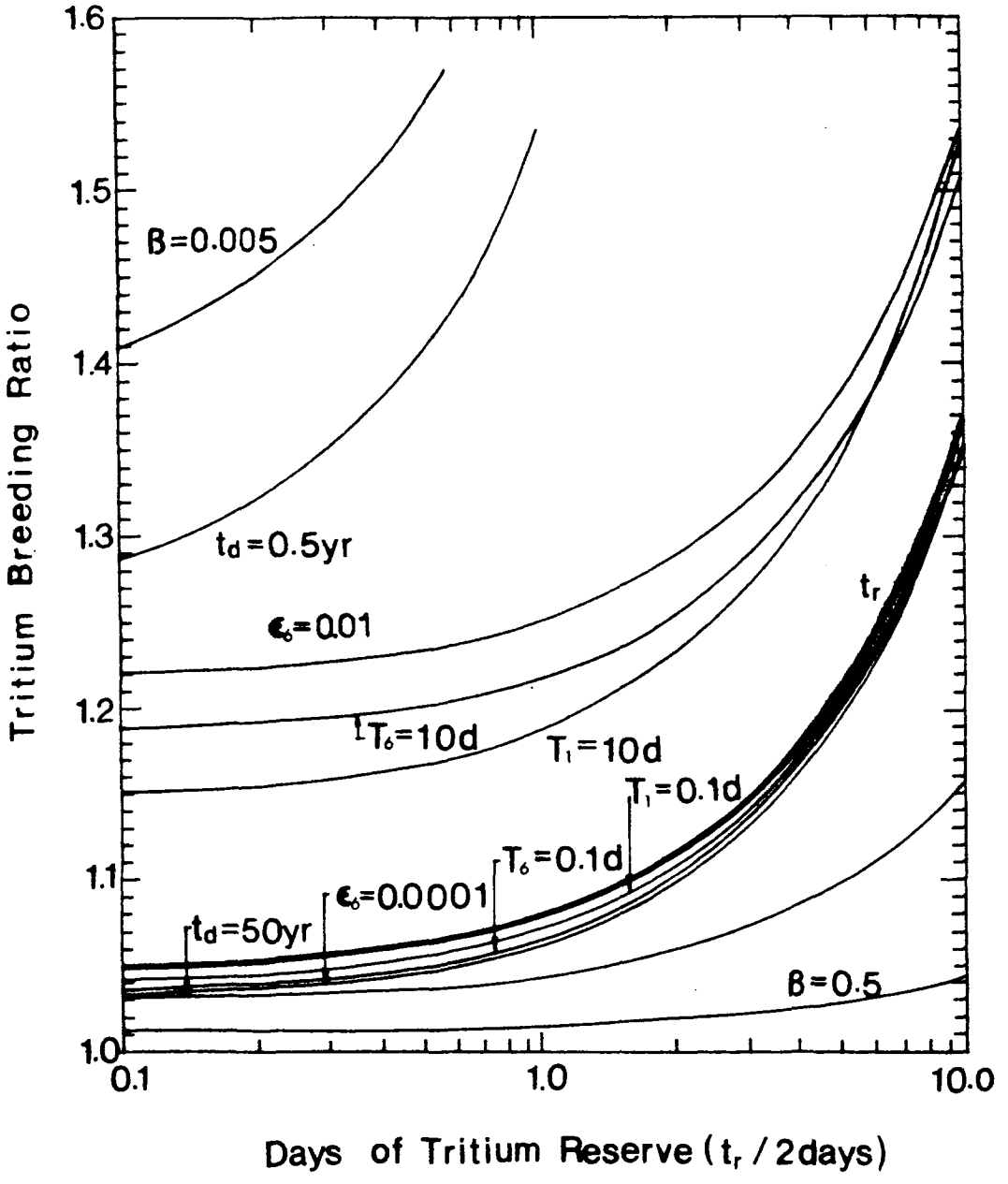


Figure 6.8-8 TBR sensitivity analysis of Base Case 1 with days of tritium reserve continuously varied and each of the other parameters fixed at one-tenth and at ten times its reference value.

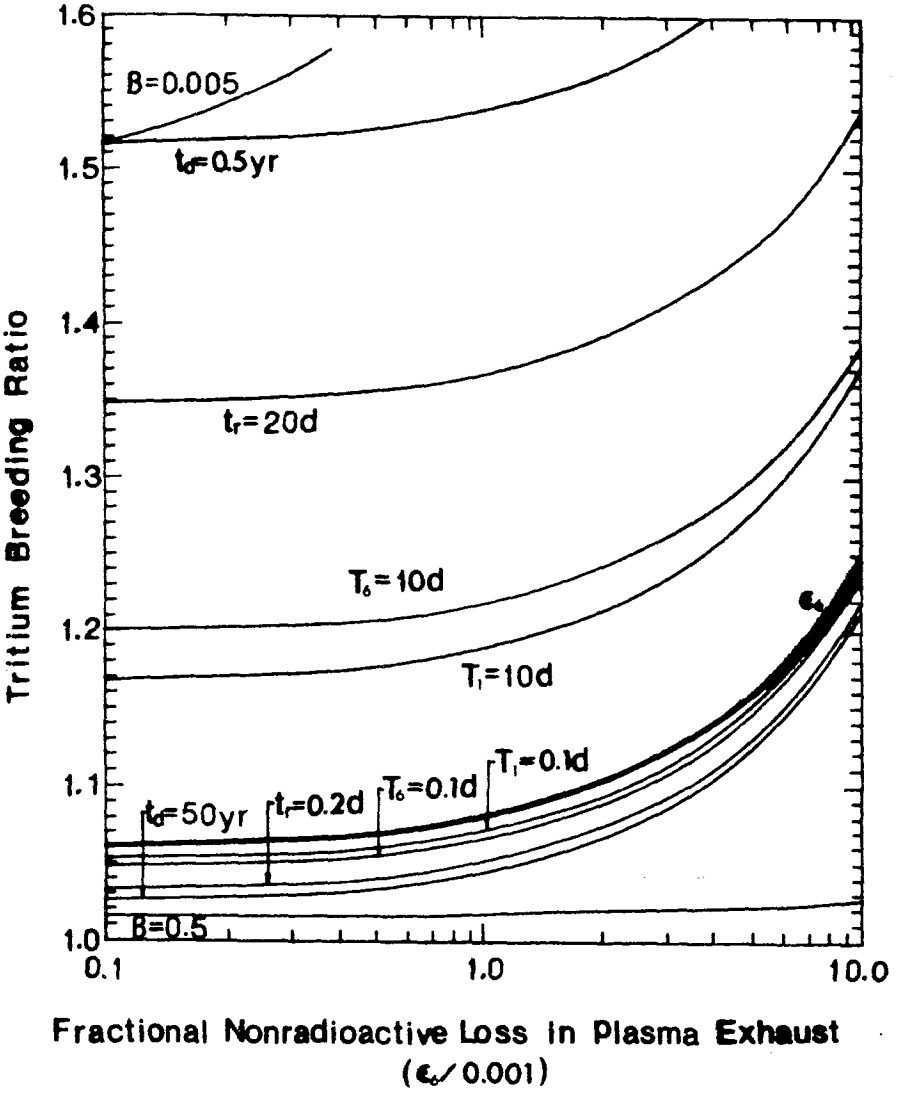


Figure 6.8-9 TBR sensitivity analysis of Base Case 1 with tritium fractional nonradioactive loss in plasma exhaust processing system continuously varied and each of the other parameters fixed at one-tenth and at ten times its reference value.

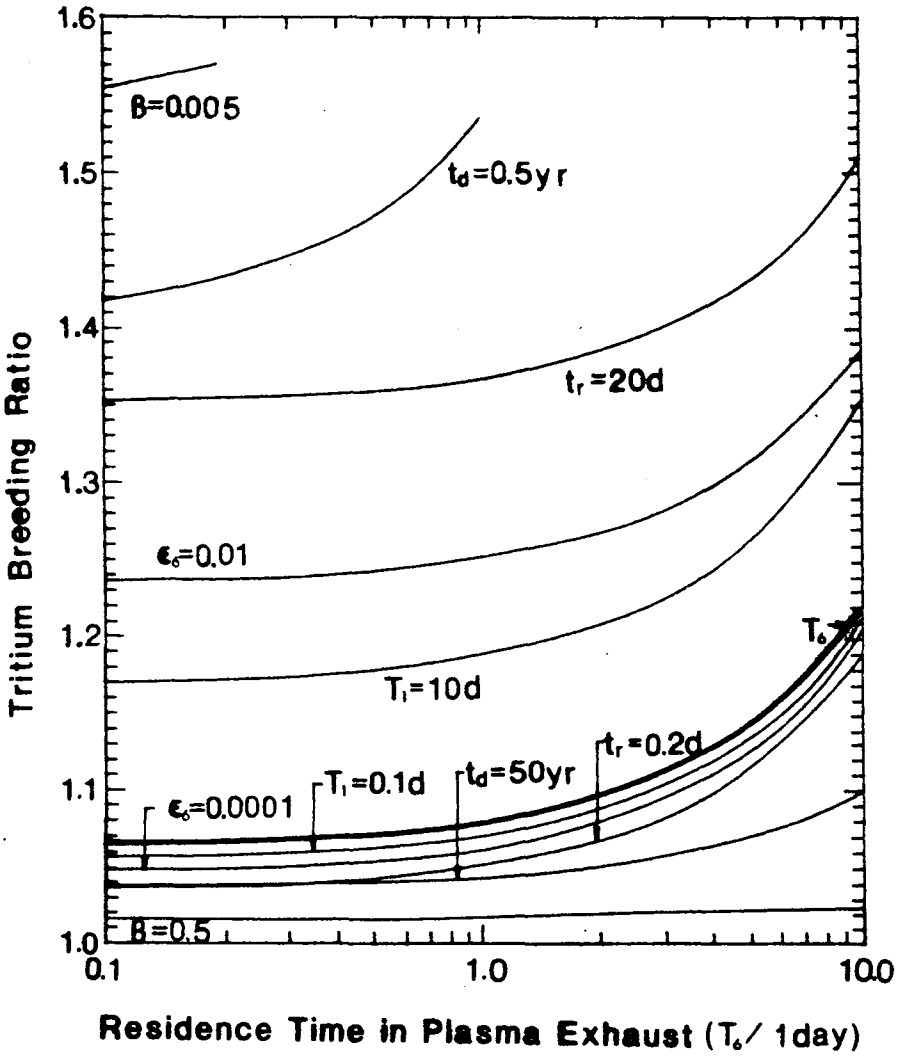


Figure 6.8-10 TBR sensitivity analysis of Base Case 1 with tritium residence time in plasma exhaust processing system continuously varied and each of the other parameters fixed at one-tenth and at ten times its reference value.

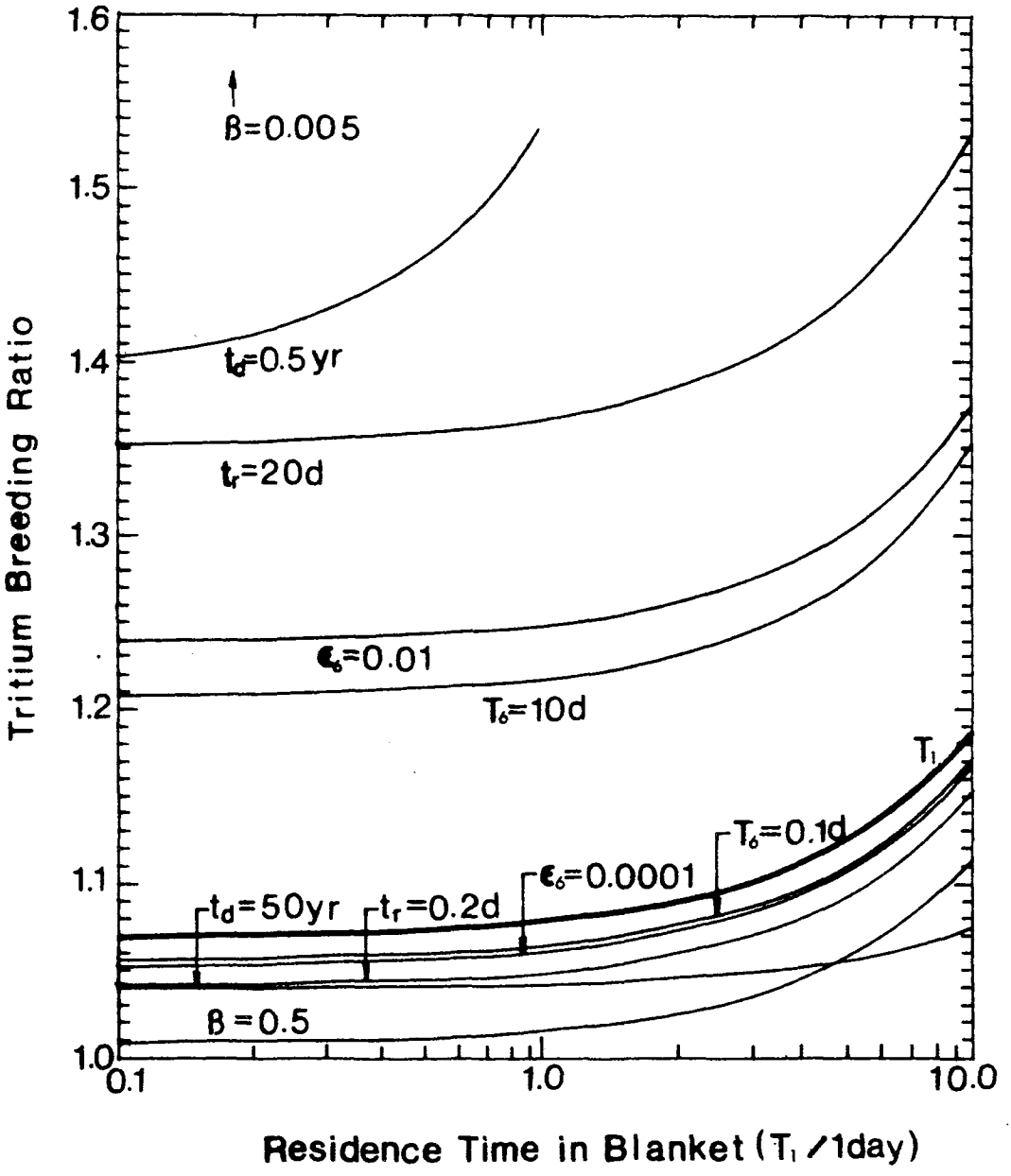


Figure 6.8-11 TBR sensitivity analysis of Base Case 1 with tritium residence time in blanket continuously varied and each of the other parameters fixed at one-tenth and at ten times its reference value.

Another problem arises in the recovery of tritium from the solid breeder where the tritium in the He purge gas may contain some fraction of tritiated water and other additives or a large fraction of the bred tritium permeates to the coolant. This tritium may need to be cycled through a long term recovery process which will significantly change the kinetics of the system. This possiblity could be considered by setting the fraction of bred tritium which is transported to the coolant, f_c, (or therefore the long recovery process) equal to a large fraction, e.g., 50%. This value of transport fraction to the coolant was examined in the study, and changed the base case reference value of the required TBR from 1.08 up to about 1.13 at f_c = 50%. This could be a very critical increase for breeders which have limited achievable breeding ratio.

The model assumed that tritium in the storage unit was lost only by radioactive decay. A real system may need occasional replacement of the uranium beds, may leak, and is subject to rare accidents involving tritium loss (which may be considered as a time averaged value in a simple analysis). This was examined briefly for the base case by adding a loss pathway in the model from the tritium storage compartment which allowed for a constant loss fraction, proportional to the stored quantity. It was found that the required TBR did not increase significantly above the Base Case value of 1.08 until the loss fraction was increased to about one part per one thousand, where the TBR required is about 1.13. The required TBR increases rapidly for greater loss fractions from storage. But it appears that with existing technology a realistic storage loss can easily achieve a loss of under 1 part per thousand.

6.8.5 Uncertainties in System Definition

6.8.5.1 Introduction

In previous sections, we indicated the large uncertainties in estimating the required breeding ratio due to uncertainties in defining the relevant parameters, e.g., tritium inventories in the fuel cycle. This section attempts to examine those uncertainties in the definition of a fusion reactor system that leads to uncertainties in estimating the achievable breeding ratio.

The uncertainties in the fusion system definition that impact the achievable tritium breeding ratio (Λ_a) can be classified into two types, the first relates to the first wall/blanket and the second to the rest of the reactor. There are a diversity of blanket concepts that involve different combinations of breeder, coolant, multiplier and structure. These concepts have different breeding potential that can be calculated for a specified blanket. However, even for a given first-wall blanket concept there are uncertainties associated with the ability to make precise specifications of configuration details, amount and distribution of breeder, structure, coolant and coolant manifolds. For example, future data on radiation effects on the thermophysical properties and temperature window may require change in our present conceptual design as to the volume percentages of the structure, coolant and breeder, which will affect the breeding ratio.

For a given first wall/blanket the TBR is affected by many of the reactor features that are presently uncertain. Examples are:

1. Technology choices for major components, e.g., limiter vs. divertor for impurity control and neutral beam vs. rf for auxiliary heating.

2. For a given technology choice (e.g., limiter) there remains uncertainties as to the choice of materials and geometry and size of plates and penetrations all of which affect TBR.

3. Presence of yet undefined, or poorly defined, components, e.g., penetrations for diagnostics and fueling.

4. Possible need for components to satisfy yet undefined, or poorly defined, requirements, e.g., passive copper coils may need[6.8-7] to be placed inside a tokamak blanket for plasma stabilization, and there may be a need for neutronically significant sector to sector electrical joints.[6.8-6]

The procedure adopted here is: (1) to estimate the obtainable tritium breeding ratio for a given blanket concept in a specified reference reactor system, e.g. STARFIRE[6.8-5] for tokamaks or MARS for mirrors,[6.8-9] and (2) to estimate the changes in TBR for the given blanket due to variations in the reference reactor system. These changes can be combined to make an estimate of Δ_s, the uncertainty in the achievable breeding ratio due to uncertainties in the system definition.

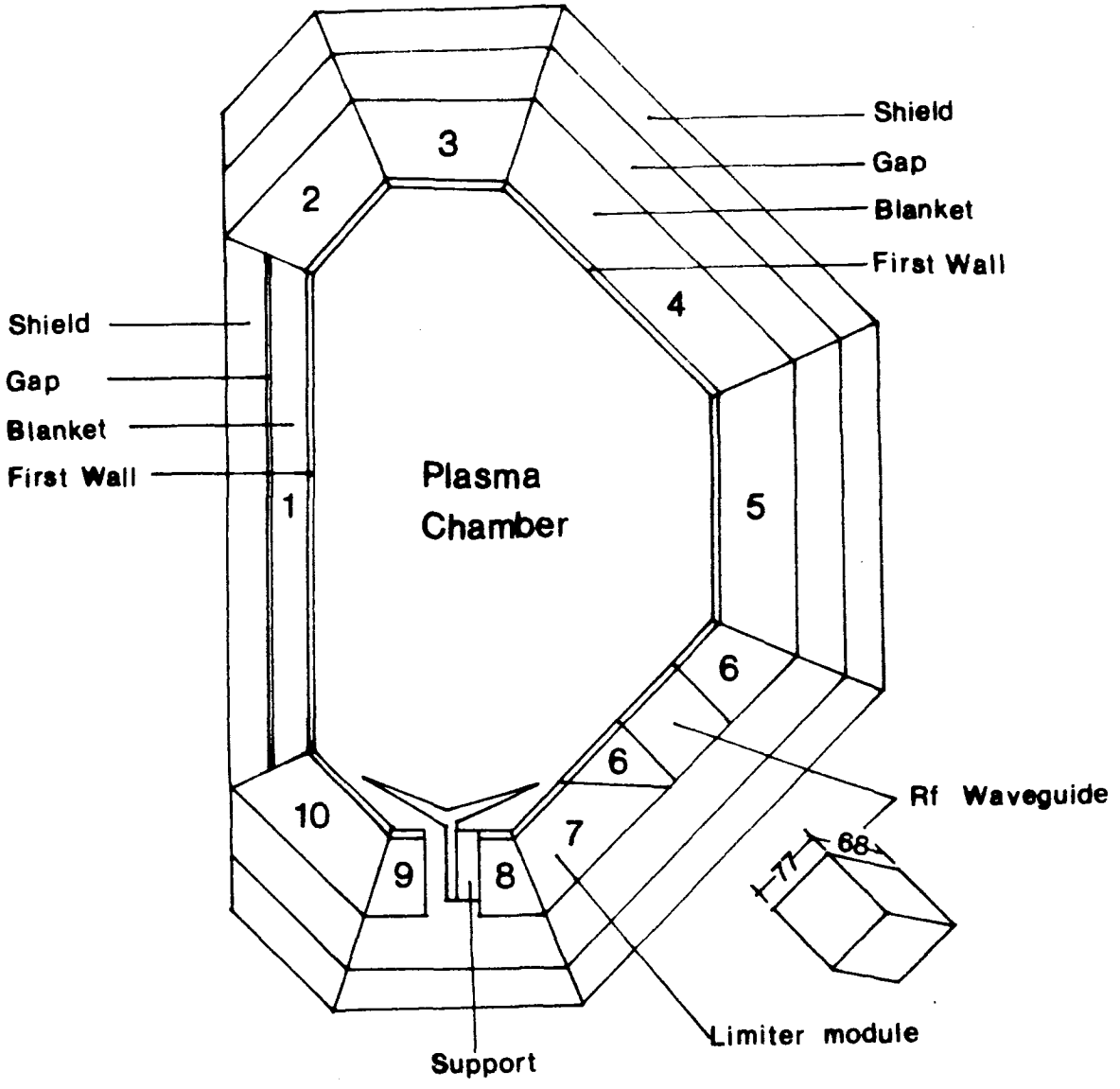


Figure 6.8-12 A vertical cross section of the reference reactor system for tokamaks.

Table 6.8-5. Material Configuration of Reference Calculation

I. Blanket		
Inboard	FW	6 cm (0.117 HT-9)
	Blanket 1	12 cm (0.079 HT-9, 0.806 Li_2O)
	Blanket 2	12 cm (0.286 HT-9, 0.625 Li_2O)
	Plenum	11 cm (0.20 HT-9)
	Gap	2 cm
	Shield	50 cm (316 SS)
Outboard	FW	6 cm (0.117 HT-9)
	Blanket 1	45 cm (0.079 HT-9, 0.806 Li_2O)
	Blanket 2	12 cm (0.286 HT-9, 0.625 Li_2O)
	Plenum	22 cm (0.2 HT-9)
	Gap	50 cm
	Shield	50 cm (316 SS)
II. Limiter (71.6 m^2 Area)		
Plate	Coating	1 cm (Be)
(107 cm width)	Coolant Pass.	0.65 cm (0.385 Cu, 0.615 H_2O)
	Structure	1.5-10 cm (Cu)
	Coolant Pass.	0.65 cm (0.385 Cu, 0.615 H_2O)
	Coating	0.2 cm (Be)
Interior support	Coating	0.2 cm (Be)
	Coolant Pass.	0.65 cm (0.385 Cu, 0.615 H_2O)
	Structure	10.3 cm (Cu)
	Coolant Pass.	0.65 cm (0.385 Cu, 0.615 H_2O)
	Coating	0.2 cm (Be)
Duct		57 cm width
Support		22.5 cm width (HT-9)
III. RF Waveguide (77cm x 68cm)*		
Waveguide		85 cm (0.53 PCA, 0.08 H_2O)

*Placed at every 30°.

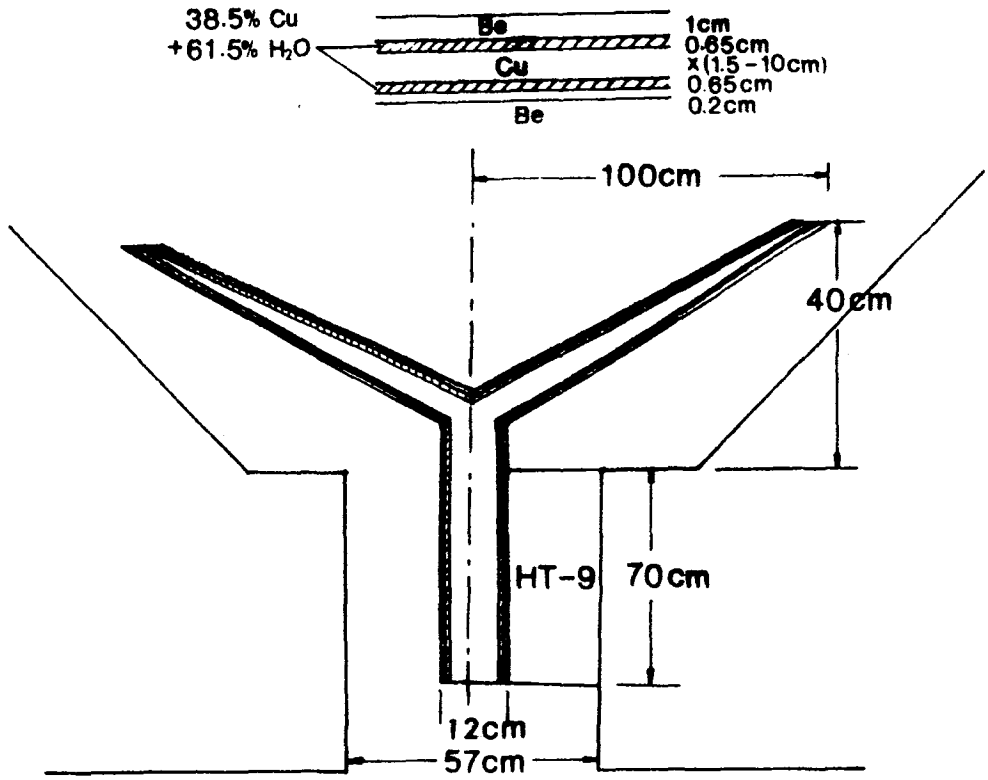


Figure 6.8-13 A cross section of the reference limiter design.

The reference calculations for the top-ranked blanket concepts in the reference reactor systems are provided by Jung[6.8-10] in Sec. 6.10. Below, we provide the results for the sensitivity of TBR to reactor system definition. It is not practically possible, nor is it productive, to consider all types of blankets and all possible system variations. Below we consider only one blanket concept in a given reference reactor design and we examine the effect of a number of key changes in the system definition.

6.8.5.2 Geometrical Description of the Standard Model

The STARFIRE model was utilized as the reference three-dimensional tokamak reactor configuration as shown in Fig. 6.8-12. The Li_2O/He/FS blanket was used as a typical blanket. The material configurations in the outboard and inboard blanket sectors are listed in Table 6.8-5. These configurations are exactly the same as in the reference model of Jung,[6.8-10] except that the 316 stainless steel of 50 cm thickness was assumed here. The selection of the shield material gives less impact on the TBR than other system parameters. The vacuum boundary condition was imposed at the outer surface of the shield in the radiation transport calculation.

A water cooled limiter was assumed at the bottom of the plasma. It was taken from the FED/INTOR Phase 2A study.[6.8-7] The limiter was sustained at the center of the 57 cm wide limiter duct with a HT-9 support material which was fixed to the limiter module (see Fig. 6.8-13). Coolant channels were not considered in the support. Limiter panels extended for 1 m from the center support. They occupied ~ 72 m^2 area, which is ~ 9% of the whole area of the first wall surface. The limiter was assumed to be made of copper, which is the structural material, water coolant and beryllium coating. The thickness of the copper structure in the panels varied from 1.5 cm at the edge to 10 cm at the center. The coolant channel regions were homogenized as shown in Fig. 6.8-13 and in Table 6.8-5 in the radiation transport calculation.

The rf waveguides of the STARFIRE design were employed as representative of the plasma heating and current drive systems. As shown in Fig. 6.8-12, the waveguides were located in the outboard blanket at every 30 degrees along the toroidal direction. The rectangular opening of the waveguide was 77 cm by 68 cm. The waveguide penetrated the outboard blanket straight to the blanket bottom, but beyond this point no additional details were considered. The

material compositions of the waveguide structural materials along with the water coolant were taken from the STARFIRE design. Two different compositions, which were assigned to different parts of the waveguides inside the blanket in the original design, were averaged in this calculation to get the single composition, shown in Table 6.8-5.

The atomic density composition of each material used in this analysis is summarized in Table 6.8-6.

No other type of penetrations such as gaps between blanket sectors and the instrumentation relating to plasma diagnostics was included in the reference model. Contribution to the TBR uncertainty from each of these penetrations will be small, but the total values of all these contributions may not be negligible.

A uniform D-shaped plasma was assumed in the analysis. The uniform plasma distribution tends to give larger TBR values compared to an MHD-shifted distributed plasma.

6.8.5.3 Calculational Method

The MCNP[6.8-11] Monte Carlo code was used in the uncertainty analysis along with the RMCCS[6.8-11] neutron cross section library. The RMCCS library contains pointwise nuclear data based mainly on the ENDF/B-V evaluation,[6.8-12] and partly on the LASL T-2 group evaluation.[6.8-13] In the nuclides listed in Table 6.8-6, ^{7}Li and Fe cross sections were taken from the T-2 group evaluation.[6.8-13] All other nuclear data came from the ENDF/B-V evaluation. The T-2 group evaluation reproduces the secondary neutron spectra from Li more closely to a recent experiment[6.8-14] than the ENDF/B-V does.

6.8.5.4 Results of Uncertainty Analysis

6.8.5.4.1 Full Breeding Coverage Geometry

Calculations were performed in full blanket coverage geometries using a 1-D and the 3-D geometry to serve as a reference against which the effects of system variations can be examined. The 3-D calculation by MCNP considered the inboard and outboard blanket configuration, but it did not account for any penetration. The 1-D calculation was performed using ANISN[6.8-15] for the

Table 6.8-6. Material Composition

		Atom/b-cm
HT-9	Fe	6.855×10^{-2}
	Cr	9.930×10^{-3}
	Ni	3.825×10^{-5}
	Mo	4.680×10^{-4}
	Mn	4.09×10^{-4}
	Si	4.00×10^{-4}
	C	7.48×10^{-4}
Li_2O*	^{7}Li	7.551×10^{-2}
	^{6}Li	6.052×10^{-3}
	O	4.078×10^{-2}
H_2O	H	6.686×10^{-2}
	O	3.343×10^{-2}
Be		1.236×10^{-1}
Cu		8.45×10^{-2}
Ta		5.523×10^{-2}
PCA	Fe	5.486×10^{-2}
	Cr	1.266×10^{-2}
	Ni	1.282×10^{-2}
	Mo	9.793×10^{-4}
	Mn	1.710×10^{-3}
316 SS	Fe	5.462×10^{-2}
	Cr	1.52×10^{-2}
	Ni	1.121×10^{-2}
	Mo	1.401×10^{-3}
	Mn	1.232×10^{-3}
	Si	7.752×10^{-4}
	C	2.286×10^{-4}

*Density is 0.8 of theoretical density (T.D.).

poloidal model of the outboard blanket. The VITAMIN-C 33 and MACKLIB-IV libraries[6.8-16] was used in the ANISN calculation. Results are shown in Table 6.8-7. As the MACKLIB-IV was derived from the ENDF/B-IV library, the 1-D calculation resulted in relatively large value because of the overestimated $^{7}Li(n,n'\alpha)t$ cross-section. A simple way of correction to the results derived using ENDF/B-IV data was made by reducing T_7, the tritium production rate from ^{7}Li, by 15%. This yields a breeding ratio of 1.212. Comparing this value with the 3-D result, the installation of the thinner inboard blanket decreased the TBR by 3%. This reduction is probably underestimated, because the uniformly distributed neutron source assumed more neutrons incident on the outboard blanket than a distributed source with MHD shift does.

6.8.5.4.2 Tritium Production of Each Blanket Sector

Table 6.8-8 shows contributions to the tritium production from each blanket sector, which were obtained for the reference model with penetrations. The sector numbers referred to in the first column of the table correspond to those identified in Fig. 6.8-12.

The first wall of the inboard blanket covers about 20% of the total first wall area. However, the relative contribution of the inboard blanket to the TBR is only 14% as is seen in the table. The difference in the tritium production rate (TPR) between sectors 2 and 10 is due to the shadow effect by the limiter panel which covers about a half of the first wall of sector 10. So the limiter panel affected the TPR in sector 10 by about 20%. The TPR in sectors 8 and 9 was affected by both the limiter panels and the limiter duct. The opening of the limiter duct took 43% of the first wall area of sector 3. Without the shadow effect by the limiter panels, the sum of the tritium production rates in sectors 8 and 9 would be ~ 60% of that in sector 3. Values in the table, however, show that the sum of the two sectors is ~ 30% of the value of sector 3. So the limiter panels decreased the tritium production in sectors 8 and 9 by about 50%.

The area of the rf-waveguide opening is only 4% of the area of the sector 4 first wall. So the main factor which affected the tritium production in sectors 6 and 7, compared to sector 4, would be the shadow effect of the limiter panel. Actually the panel covered sector 7, whose surface area is 20% of the total first wall area of these sectors. The sum of the tritium production of sectors 6 and 7 is about 15% smaller than the sector 4 value.

Table 6.8-7. Tritium Breeding Ratio with Full Blanket Coverage

Geometry	TBR
3-D Geometry* (Outboard/Inboard Different)	1.182
1-D Cylinder** (Outboard representative)	1.264

*MCNP/RMCCS

**ANISN/MACKLIB-IV $T_6 + 0.85\ T_7 \sim 1.212$

Table 6.8-8. Contribution to Tritium Production from Each Blanket Sector

Sector Number	Contribution (%)
1	13.8
2	5.31
3	7.80
4	23.8
5	21.5
6	15.4
7	5.37
8	1.28
9	1.32
10	4.42
	Total 100

6.8.5.4.3 Non-breeding Inboard Blanket

The capital cost of a tokamak is very sensitive to the total thickness, Δ^{i}_{BS}, of the inboard region between the first wall and magnet, which is generally occupied by a blanket and shield. One option to reduce Δ^{i}_{BS}, in order to improve the economics, without violating the magnet radiation protection criteria is to reduce the thickness of or totally eliminate the inboard breeding blanket. However, this reduces the achievable tritium breeding ratio. The reference Li_2O/He/FS blanket design in BCSS employs a thin breeding blanket of 24cm. The impact on the TBR due to the non-breeding inboard blanket was examined by replacing the Li_2O in the inboard blanket with HT-9 in the reference model. The volume ratio of the He coolant was kept the same as in the reference model. By this replacement, the TBR decreased by ~ 8% as shown in Table 6.8-9. The first column in the Table shows the TBR decreasing rate which will be caused by simply neglecting the contribution of the inboard blanket in the reference model calculation. Reflection of low energy neutrons by using HT-9 in the inboard increased the ^{6}Li tritium production in all the blanket sectors except the inboard sector, but this increment did not cancel the decrement caused by replacing the inboard breeder with HT-9.

A neutron multiplying inboard blanket was considered. The breeding material, Li_2O, in the inboard sector was replaced with lead, which is well known as a good neutron multiplier, and the TBR calculation was repeated. The lead drastically increased the ^{6}Li tritium production by more than the decrement of T_6 caused by the removal of the inboard breeder. However, the total TBR was still lower by ~ 2% than the reference value because of the reduction in T_7.

6.8.5.4.4 Uncertainties Relating to Limiter Design

There are considerable uncertainties concerning the impurity control and exhaust system. There are several candidates for the type of the system and many open questions as to the design of any given type. For the limiter, the open issues are the choice and amount of structural and plasma-side materials, the choice of coolant, the size of the limiter blade, the method and material for structural support and the size of the vacuum duct. With reference to Fig. 6.8-12, it is desirable to have a non-breeding material in the region

Table 6.8-9 Impact of Non-Breeding Inboard Blanket on TBR

	No Inboard Breeding (%)	HT-9 Inboard Blanket (%)	Pb Inboard Blanket (%)
T_6	-12.8 (± 2.9)	-5.4 (± 1.2)	+2.9 (± 1.2)
T_7	-15.2 (± 3.1)	-15.8 (± 1.4)	-15.8 (± 1.4)
TBR	-13.8 (± 2.2)	-8.2 (± 1.0)	-2.3 (± 1.0)

Note: Relative deviation from the standard values shown.

indicated as the limiter module. Because the limiter has short life, easy access to replace the limiter is desirable. All of these open issues result in uncertainties in estimating the achievable TBR.

The impact of the non-breeding limiter module on the TBR was examined by the following simple model: the breeding material Li_2O was replaced with HT-9 steel in sectors 7 and 8 (see Fig. 6.8-12), the coolant being kept at the same volume as in the reference model. Results are shown in Table 6.8-10. The adoption of a non-breeding limiter module causes the TBR to drop by as much as 6%, which is significant.

The sensitivity of the TBR to the limiter duct width was analyzed by calculating the TBR for a case in which the width of the duct opening, 57cm in the reference model was doubled. By doubling the duct width, about 3% more area of the total first wall area was taken by the duct. The net decrease in the TBR is about 2% as shown in Table 6.8-10, which is smaller than the fractional area change of the duct opening. This is because of the shadow effect of the limiter panels.

The limiter panels were coated by 1 cm thick Be tile in the reference model. The coating is predicted to be eroded away by physical sputtering during reactor operation. So all the coating may be lost at the end of the short limiter lifetime. Estimation of the TBR uncertainty relating to this effect was done by testing the change in the TBR due to the removal of all the Be coating from the panels. Though the limiter panels covered about 10% of the total first wall area, the absence of the Be coating resulted in only about 1% drop of the TBR (see Table 6.8-10). It affected the T_6 value, but did not affect the T_7, as was expected by the fact that Be is a good neutron multiplier.

As the vacuum region surrounded by the blanket was filled with multi-scattered low energy neutrons, the use of a strong low energy neutron absorber as a limiter coating material would have more severe effect on the TBR than the Be coating did. For the purpose of this analysis, a case in which the Be coating material in the reference model was replaced by Ta which is a candidate limiter material but is known to have large resonance absorption cross sections was calculated. Results are shown in the last column of Table 6.8-10. As expected, the Ta coating affected the T_6 value much stronger than the T_7 value. The total TBR dropped by $\sim$ 4%.

Table 6.8-10. Impact of Limiter Design on TBR

	Non-breeding Limiter Module (%)	Limiter Duct Width (%)	Be Coating (%)	Strong Absorber Coating (%)
T_6	-6.2 (± 1.2)	-2.4 (± 1.2)	-1.6 (± 1.2)	-5.6 (± 1.2)
T_7	-5.8 (±1.4)	-0.6 (± 1.4)	+0.1 (± 1.4)	-0.6 (± 1.4)
TBR	-6.1 (± 1.0)	-1.9 (± 1.0)	-1.1 (± 1.0)	-4.2 (± 1.0)

Note: Relative deviation from the standard values shown.

6.8.5.4.5 Uncertainties Due to Plasma Heating System

The Rf waveguides of the STARFIRE model were assumed in the reference model for the plasma heating as well as for the plasma current drive. To evaluate the TBR uncertainties due to the rf-waveguide design, the fractional change in the TBR value from the reference case was calculated for the following two cases: (1) the area of the waveguide opening at the first wall was doubled, and (2) all the materials inside the waveguide were removed, keeping the increased area of the opening. By case 1, the size effect of the rf-tubes on the TBR value can be tested. The second case will clarify two different things: effect of the structure materials as combined with the result of the case 1, and the effect of void regions.

The results are shown in Table 6.8-11. The rf-waveguides take 0.8% of the total first wall area which is relatively small. The T_7 results of both cases agree with this value within statistical errors. A weak effect of the structure materials is noticeable on the T_6 value as the two T_6 values are compared with each other. But its magnitude is very small as compared to the void region effect which is represented by the second case. Roughly speaking, the magnitude of the void region effect is approximately equal to the ratio of the hole opening area to the whole first wall area.

The STARFIRE design for the rf (lower hybrid) system attempted to minimize the penetrations size and effects. Recent plasma physics and engineering results on plasma heating and current drive indicate that the size of the waveguides may be even larger than what was considered above. Furthermore these results also indicate that systems other than lower hybrid, e.g. ICRH, may have to be used to keep the circulating power requirement reasonable. Systems such as ICRH generally require antennas inside the first wall which would have significantly negative effect on TBR.

6.8.5.4.6 Homogenization Effect of Sector Side Wall

The reference calculation was performed with homogenized material arrangement in the blanket region. The actual blanket, however, is partitioned into many sectors with over 1 cm thick side wall. Monte Carlo analysis was made to assess the uncertainty in the TBR due to these walls. Fig. 6.8-14 shows a heterogeneous geometry model used in this analysis. The geometry is

Table 6.8-11 Impact of Rf-Waveguide Design on TBR

	Double the rf volume (with structure) (%)	Double the rf volume (without structure) (%)
T_6	-1.5 (± 1.2)	-1.2 (± 1.2)
T_7	-1.0 (± 1.4)	-1.2 (± 1.4)
TBR	-1.4 (± 1.0)	-1.2 (± 1.0)

Note: Relative deviation from the standard values shown.

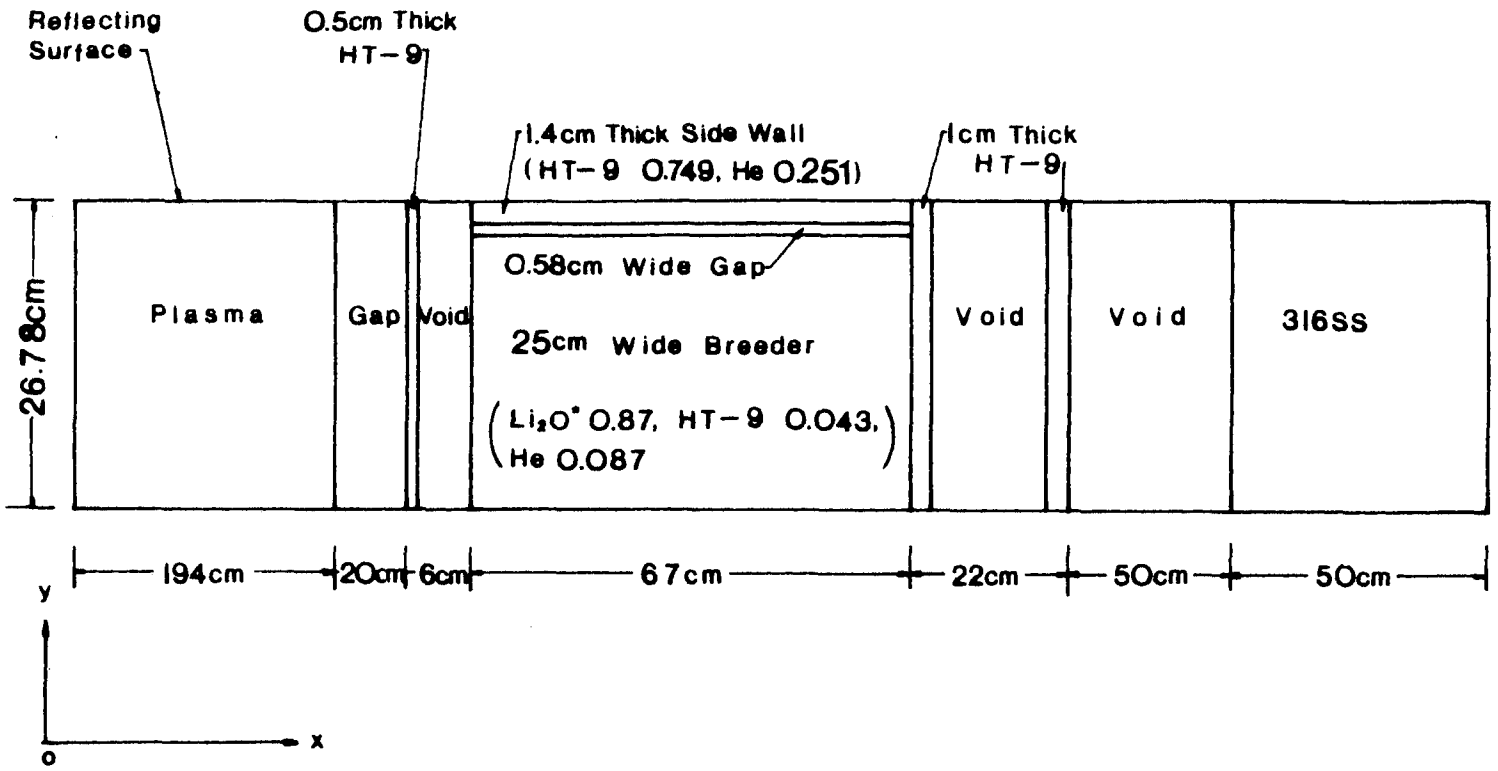


Figure 6.8-14 Schematic of the Li_2O/He/FS blanket design.

defined in x-y coordinates. The thickness of each material region is the same as in the reference outboard model of Table 6.8-5 except that the blanket regions identified as 1 and 2 in Table 6.8-5 were combined into a single 67 cm thick breeding zone. The material composition of the breeder in Fig. 6.8-14 was the result of homogenization over the Li_2O plates, HT-9 clads and He coolant channels of the BCSS design. The thickness of the side wall, which includes coolant channels, and the gap width between the wall and the breeder were determined so that the overall volume ratio of the structural material (HT-9), the breeding material (Li_2O) and the void (or He) may be the same as in blanket region 1 in the reference blanket. A homogeneous geometry model was defined just by homogenizing the three regions, i.e., the breeder, gap and the side wall of Fig. 6.8-14.

The results are summarized in Table 6.8-12. The homogenization seems to have resulted in some degree of overestimation of the TBR, but the degree of its magnitude is within the statistical errors of the Monte Carlo calculations. We may say within the accuracy of the Monte Carlo statistics that the homogenization of the breeding zone including the thick side wall will not result in large uncertainty in the estimated TBR. It probably will not exceed 1.5 ~ 2%.

6.8.5.5. Variation in Blanket Material Composition

In this section we examine the effect of changes in the blanket material composition on the obtainable tritium breeding ratio. The analysis was performed based on one dimensional cylindrical model which represented the outboard blanket. The Li_2O/He/FS design was again adopted for this analysis. Table 6.8-13 shows the material configuration used here for this blanket as shown in the table, the breeder region is divided into two parts, referred to as blanket 1 and blanket 2, that have different material composition. The plasma was assumed to be uniformly distributed. No vacuum gap was considered between the plenum and the shield. The ANISN code with 46 groups (25n + 21γ) and the S_6P_3 approximation were used. The group constants were derived from the VITAMIN-C/MACLIB-IV library.

The problem of interest here is to estimate the impact on the tritium breeding ratio (TBR) of changes in the first wall thickness, the volume fraction of the structure material in the breeder, or the Li_2O density factor.

Table 6.8-12 Impact of Homogenization of Breeding Zone on TBR

Geometry	Tritium Production		
	T_6	T_7	TBR
Homogeneous	0.941	0.355	1.297 (± 0.016)
Heterogeneous	0.929	0.352	1.281 (± 0.016)

Table 6.8-13. Description of Blanket Model for Analysis on Variation in Material Composition

Region	Outer Radius (cm)	Material Composition	
Plasma	194	Vacuum	
Scrape-off	214	Vacuum	
First Wall	220	HT-9	0.117
Blanket 1	265	Li_2O*	0.806
		HT-9	0.079
		He	0.115
Blanket 2	277	Li_2O*	0.625
		HT-9	0.286
		He	0.089
Plenum	299	HT-9	0.2
		He	0.8
Shield	329	316 SS	1.0

*Density: 0.8 of the theoretical density.

The required degree of porosity in Li_2O is presently uncertain as it is dependent on tritium transport, radiation effects and other blanket characteristics that cannot presently be quantified exactly. A direct sensitivity analysis approach was adopted to analyze the problem. For instance, each design parameter such as the first wall thickness was changed by a certain amount, and the direct forward transport calculation was done. Then the obtained TBR was compared to that of the reference case to get the effect of that parameter variation on the TBR.

Effect of First Wall Thickness

The volume fraction of the structure (HT-9) in the first wall is 0.117, while the thickness of the first wall zone is 6cm. Thus, the effective structure thickness is ~ 0.7 cm. To test the effect of the first wall thickness on the TBR value, the reference structure thickness was increased to 1.05 cm or 1.4 cm, i.e., by 50% and 100%, respectively. The results are shown in Table 6.8-14. The reduction in TPR in blanket 2 was twice that in blanket 1 when the first wall thickness is changed. This is because additional scatterings which took place in the thicker first wall attenuated high energy neutrons more than slow neutrons, and this made the depth profile of the tritium production rate in the breeder somewhat steeper. The two cases of the 50% change and the 100% change in the wall thickness show about the same TBR sensitivity, where the sensitivity is defined as the ratio of the relative change in TBR to the relative change in the first wall thickness. So the nonlinearity in the TBR sensitivity was not significant up to the 100% change in the first wall thickness. The sensitivity of the total TBR to the first wall thickness is -0.0244 using the result for the 50% change.

Effect of Structural Material Volume Change in the Breeding Zone

The Li_2O breeder is proposed in the reference design to be packed in 1 cm thick plates which have 0.25 mm thick HT-9 cladding. Future analysis and new data may show that the thickness of the clad is not sufficient, for example, to accomodate excessive Li_2O swelling or to keep tritium permeation to the coolant acceptably low.

The volume fraction of the HT-9 structure in the blanket 1, which was originally 0.079, was increased by 50%, 100% and 300%. The increment of the

Table 6.8-14. Effect of Change in First Wall Thickness on Tritium Breeding Ratio

Thickness (cm)	Blanket 1	Blanket 2	Total
0.7cm (Reference)	1.200	6.389×10^{-2}	1.2639
1.05 (+50%)[a]	1.1863 (-1.14%)[a]	6.222×10^{-2} (-2.61%)	1.2485 (-1.22%)[a]
1.40 (+100%)[a]	1.1734 (-2.22%)[a]	6.062×10^{-2} (-5.12%)[a]	1.2340 (-2.37%)[a]

[a]Relative deviation from the reference values.

structure material was compensated for by the decrease in the Li_2O volume. The reduction rates in the Li_2O volume was 4.9%, 9.8%, and 29.4%, respectively. Results of the TBR calculations are shown in Table 6.8-15 as well as the reference values. The TBR in both blankets 1 and 2 dropped by about the same fraction. The TBR drop in blanket 1 was caused by both the neutron flux depression caused by the increase in the structure volume and the decrease of the Li_2O volume, while in the blanket 2, the TBR was influenced only by the flux depression. The depth profile of the neutron flux became steeper by the increase in the structure volume. The sensitivity of the TBR value to the deviation in the structure volume fraction (and the compensating decrease in the Li_2O volume fraction) was estimated to be -0.050 using the case of 50% change in the structure volume.

Next, the volume fraction of the structure in blanket 2 was increased 25%, or 50%, and to compensate for this increment, the Li_2O volume in the blanket 2 was decreased by 11.4% or 22.9%, respectively. The obtained TBR values are listed in Table 6.8-16. As the volume fraction of the structure was very large in blanket 2 as compared to blanket 1, the impact of the structure increase on the TBR in blanket 2 is pronounced when it is compared to the results in Table 6.8-15. However, the absolute contribution to the total TBR from blanket 2 is relatively small. Moreover, the increased structure in blanket 2 scatters additional neutrons back to blanket 1, so the TBR in blanket 1 was slightly increased. Consequently, the total TBR was only slightly changed.

In another case, the volume fraction of the structure was increased by 50% everywhere in the blanket. The increment of the structure was compensated for by a decrease in the He coolant volume by 6.63% in the first wall and a volume decrease of the Li_2O of 4.9% in blanket 1, and 22.9% in blanket 2. The attained material composition after this variation is shown in the footnote of Table 6.8-17. The calculated results are shown in this Table together with the reference results. The change in the TBR in this case is about the same amount as the sum of the TBR variation observed in the 50% change cases in Table 6.8-14 to 6.8-16. For blanket 1, the sum of the values in Tables 6.8-14 to 6.8-16 is -3.37% which is close to -3.1% obtained in the present case. The sum is -21.2% for blanket 2, which is similar to the -20.3% change obtained in the present case. The TBR sensitivity to the 50% structure increase throughout the blanket is -0.079.

Table 6.8-15. Effect of Volume Fraction Change of Structure in Blanket 1 on Tritium Breeding Ratio

Volume Fraction in Blanket 1	TBR		
	Blanket 1	Blanket 2	Total
HT-9 0.079 (Reference)	1.200	6.389×10^{-2}	1.2639
HT-9 0.1185 (+50%)[a]	1.1703 (-2.47%)[a]	6.220×10^{-2} (-2.65%)[a]	1.2325 (-2.48%)[a]
HT-9 0.158 (+100%)[a]	1.1414 (-4.87%)[a]	6.078×10^{-2} (-4.87%)[a]	1.2022 (-4.88)[a]
HT-9 0.316 (+300%)[a]	1.0268 (-14.43%)[a]	5.744×10^{-2} (-10.1%)[a]	1.0842 (-14.22%)[a]

[a]Relative deviation from the reference values.

Table 6.8-16. Effect of Volume Fraction Change of Structure in Blanket 2 on Tritium Breeding Ratio

Volume Fraction in Blanket 2	TBR		
	Blanket 1	Blanket 2	Total
HT-9 0.286 (Reference)	1.200	6.389×10^{-2}	1.2639
HT-9 0.3575 (+25%)[a]	1.2029 (+0.24%)[a]	5.890×10^{-2} (-7.81%)[a]	1.2618 (-0.17%)[a]
HT-9 0.429 (+50%)[a]	1.2056 (+0.47%)[a]	5.371×10^{-2} (-15.9%)[a]	1.2593 (-0.36%)[a]

[a]Relative deviation from the reference values.

Table 6.8-17. Effect of Volume Fraction Change of Structure throughout Blanket on Tritium Breeding Ratio

Volume Fraction	TBR		
	Blanket 1	Blanket 2	Total
Reference*	1.200	6.389×10^{-2}	1.2639
+50%**	1.1628 (-3.1%)[a]	5.093×10^{-2} (-20.3%)[a]	1.2137 (-3.97%)[a]

Note: * 1st wall: HT-9 0.117, He 0.883
Blanket 1: HT-9 0.079, Li_2O 0.806, He 0.115
Blanket 2: HT-9 0.286, Li_2O 0.625, He 0.089
Plenum: HT-9 0.2, He 0.8

** 1st wall: HT-9 0.1755, He 0.8245
Blanket 1: HT-9 0.1185, Li_2O 0.7665, He 0.115
Blanket 2: HT-9 0.429, Li_2O 0.482, He 0.089
Plenum: HT-9 0.3, He 0.7

[a] Relative deviation from the reference values

Effect of Li_2O Density Factor Change

The assumed Li_2O density factor was 0.8 of the theoretical density in the reference design. However, future experiments on tritium extraction, Li_2O swelling and other performance characteristics may show a need for higher degree of porosity.

The Li_2O density factor in blanket 1 was decreased in two ways: from 0.8 to 0.7 or from 0.8 to 0.6, and the volume fraction of the void was correspondingly increased. The volume of the structure was not changed.

The obtained TBR values are compared with those of the reference case in Table 6.8-18. As the amount of the Li_2O was decreased in blanket 1, the TBR value in blanket 1 decreased. But the decrease rate in the TBR was about one third of the relative variation in the Li_2O density. The reason is that the neutron flux increased everywhere in the breeding zone because the amount of the absorber was decreased. This is also the reason why the TBR in blanket 2 was enhanced drastically. The estimation of the TBR sensitivity to the Li_2O density was done by using the result for the 12.5% decrease case. It was 0.153.

6.8.6 Uncertainties in Nuclear Data

6.8.6.1. Introduction

For a given blanket in a specified reactor system, there are uncertainties in predicting the achievable tritium breeding ratio due to uncertainties in calculational methods, geometrical modeling and nuclear data. There are many sources of uncertainties associated with nuclear data ranging from uncertainties in basic measurements to those introduced in data processing and representation. This section investigates the uncertainties in the achievable tritium breeding ratio (Λ_a) due to uncertainties in basic nuclear data.

Various studies have recently been conducted to assess the impact of neutron cross-section uncertainties on various responses such as tritium breeding,[6.8-17] fissile breeding in a fusion-fission hybrid system,[6.8-18,-19] heating and damage rates,[6.8-20] exposure dose

Table 6.8-18. Effect of Li_2O Density Factor Change in Blanket 1 on Tritium Breeding Ratio

Density Factor in Blanket 1	TBR		
	Blanket 1	Blanket 2	Total
0.8 (Reference)	1.200	6.389×10^{-2}	1.2639
0.7 (-12.5%)[a]	1.1544 (-3.8%)[a]	8.528×10^{-2} (+33.5%)[a]	1.2397 (-1.91%)[a]
0.6 (-25%)[a]	1.0946 (-8.78%)[a]	0.1132 (+77.2%)[a]	1.2078 (-4.44%)[a]

[a]Relative deviation from the reference values.

rate, [6.8-21] etc. However, these studies were limited in their scope since either a particular system was considered and the analysis was performed only for that system[6.8-22] or no statistical treatment for the cross-sections uncertainties propagation was taken into consideration and only rough estimates for cross-section uncertainties were used in the analysis over limited ranges of neutron energy.[6.8-23 to -27]

In the present study rigorous analysis has been conducted to statistically incorporate the present cross-section uncertainties and their correlations to derive an estimate for the range of uncertainty, Δ_D, in the TBR in four of the primary blanket concepts. Moreover, estimates for Δ_D in other concepts have also been assessed based on a combination of the results from the present study and an expert judgement. Since some of the blankets considered utilize beryllium as a neutron multiplier, a serious effort has been devoted to study the impact of various evaluations for the beryllium cross-sections on the TBR.

In Section 6.8.6.2, a brief theoretical background for the methodology used in the sensitivity and the uncertainty analysis is given. Description of the blankets considered along with the calculational procedures and data base are discussed in Section 6.8.6.3. Results for the impact of the various evaluations for the $^{9}Be(n,2n')$ cross-section on the TBR is given in Section 6.8.5.4. Also, we included in this section the results from the sensitivity and the uncertainty analysis. Special effort has been devoted to comparing the uncertainty analysis results to those obtained with published estimates for cross-sections uncertainties where the non-statistical treatment is employed. The results of such a comparison is given in Section 6.8.6.5. Estimates for Δ_D in other blanket concepts is given in Section 6.8.6.6, while we devoted Section 6.8.6.7 to the conclusions and comments regarding nuclear data uncertainties.

6.8.6.2. Theoretical Background for the Cross-Section Sensitivity/Uncertainty Analysis

The statistical variance in the integrated tritium production rate, $R_k \equiv$ TBR, is given by[6.8-18 to -22,-28]

$$\frac{\Delta R_k}{R_k}^2 = \sum_{g,g'} \frac{p^g}{\sigma_{x,k}} \frac{p^{g'}}{\sigma_{y,k}} \mathrm{CORR}\left(\sigma_x^g, \sigma_y^{g'}\right) \mathrm{RSD}\left(\sigma_x^g\right) \mathrm{RSD}\left(\sigma_y^{g'}\right) \qquad (6.8\text{-}34)$$

where Σ_x^g is the neutron interaction cross-section y type x in energy group g, $CORR(\Sigma_x^g, \Sigma_y^{g'})$ is the correlation matrix for the multigroup cross-sections Σ_x^g and $\Sigma_y^{g'}$ and the coefficient $P_{x,k}^g$ is the relative cross-section sensitivity profile of the response R_k due to variation in the cross-section type Σ_x^g at energy group g. This coefficient is defined as the fractional change (%) in the response R_k due to a 1% increase in the cross-section Σ_x^g at neutron group g.

The coefficient $P_{\Sigma_{x,k}}^g$ is system-dependent and its evaluation is straight forward using first-order perturbation theory[6.8-29,-30] and is given by,

$$P_{\Sigma_{x,k}}^g = \frac{\delta R_k/R_k}{\delta\Sigma_x^g/\Sigma_x^g} = -\frac{1}{R_k}\langle\phi_k^*, L_{\Sigma_x}\phi\rangle_g \,, \qquad (6.8\text{-}35)$$

where ϕ and ϕ_k^* denotes the forward and the adjoint angular flux, respectively while L_{Σ_x} is the portion of the Boltzmann transport operator, L, which contains the cross-section Σ_x. In Eq. (35), only the indirect effect of the perturbed cross-section is accounted for. If the response is also evaluated directly from Σ_x, a contribution to $P_{\Sigma_{x,k}}^g$ should be added.

The correlation matrix, $CORR(\Sigma_x^g, \Sigma_y^g)$, represents the correlation between the multigroup cross-section Σ_x^g and Σ_y^g and its elements are independent of the specific blanket under consideration. The $RSD(\Sigma_x^g)$ appearing in Eq. (34) is the relative standard deviation (RSD) of cross-section Σ_x^g and the information required to construct the correlation matrices and the relative standard deviations for various cross-section types are implemented in File 33 of the ENDF/B-V.[6.8-31]

The relative variance in the response R_k given by Eq. (34) is made up of contributions from each material present in a particular blanket. In the uncertainty analysis results given in Section 6.8.5.4 we assume that the uncertainty associated with cross-sections of a particular material is uncorrelated to the uncertainties in the cross-sections of other materials. Thus, $(\Delta R_k/R_k)^2$ given by Eq. (34) is the algebraic sum of the contributions from each material. However, for a particular material the correlations between errors in the cross-sections of that material are considered according to Eq. (34). Furthermore, and to investigate the impact of these correlations, we compare the results obtained from Eq. (1) to the case where $(\Delta R_k/R_k)^2$ is

evaluated from the expression

$$(\Delta R_k/R_k)^2 = \sum_{g\,g'} P^g \; P^{g'} \; \Sigma_{x,k} \; \Sigma_{y,k}$$

$$\text{X CORR}(\Sigma_x^g, \Sigma_y^{g'})\text{RSD}(\Sigma_x^g)\text{RSD}(\Sigma_y^{g'})\delta_{gg'} \quad , \qquad (6.8\text{-}36)$$

where $\delta_{gg'}$=1 when g=g' and zero otherwise. In this formulation, it is assumed that the correlation matrix for the cross-sections Σ_x^g and $\Sigma_y^{g'}$ is filled only through its diagonal and the uncertainties are assumed to be uncorrelated between different energy groups. A more conservative evaluation for the relative variance in the response R_k can be obtained from the expression

$$(\Delta R_k/R_k)^2 = \sum_{gg'} P^g \; P^{g'} \; \Sigma_{x,k} \; \Sigma_{y,k} \; \text{RSD}(\Sigma_x^g)\text{RSD}(\Sigma_y^{g'}) \quad . \qquad (6.8\text{-}37)$$

In this expression, the uncertainties in the cross-sections Σ_x^g and $\Sigma_y^{g'}$ are assumed to be fully correlated over the energy range where such correlation exists (as specified in the error files of ENDF/B-V). In this case the correlation matrice is assumed to be

$$\text{CORR}(\Sigma_x^g, \Sigma_y^{g'}) = \pm 1 \qquad (6.8\text{-}38)$$

and the sign of the correlation depends on whether Σ_x^g and $\Sigma_y^{g'}$ are correlated or anticorrelated over the specified energy range.

6.8.6.3. Blanket Concepts Considered for the Analysis and the Calculational Procedures

The material composition and dimensions for the four blankets under consideration are summarized in Table 6.8-19. These blankets are the Li_2O helium-cooled blanket with PCA structure (Li_2O/He/PCA), the 17Li-83Pb self-cooled blanket (LiPb/LiPb/PCA), the $LiAlO_2$ water-cooled blanket with beryllium multiplier and ferritic steel (FS) structure ($LiAlO_2/H_2O$/FS/Be), and the flibe blanket (Flibe/He/FS/Be).[6.8-32] In Table 6.8-20, the tritium breeding ratio from $^6Li(T_6)$, from $^7Li(T_7)$, and the total breeding ratio (TBR) in these blankets are shown based on a 1-D poloidal-axis calculational model. Note in

Table 6.8-19. Material Composition and Dimensions for the Four Blanket Concepts Considered for the Cross-Section Sensitivity/Uncertainty Analysis

	Li_2O/He/PCA		LiPb/LiPb/PCA	
Zone	Outer Radius (m)	Composition	Outer Radius	Composition
1	2.53	Plasma	1.94	Plasma
2	2.73	Vacuum	2.14	Vacuum
3	2.79	First Wall: 100% PCA (6.6% Dense)	2.15	First Wall: 50% PCA, 50% LiPb (90% ^{6}Li)
4	3.21	Breeding Zone: 6% PCA, 85% Li_2O (density factor 0.8), balance helium	2.75	Breeding Zone: 7.5% PCA, 92.5% LiPb (90% ^{6}Li)
5	3.43	Plenum Zone: 100% PCA (10% dense)	3.05	Reflector: 90% PCA, 10% LiPb (90% ^{6}Li)
6	3.73	Shield: 100% Stainless steel	3.65	Shield: 90% Fe 1422, 10% H_2O
		$LiAlO_2/H_2O$/FS/Be		Flibe/He/FS/Be
1	1.94	Plasma	1.94	Plasma
2	2.14	Vacuum	2.14	Vacuum
3	2.19	First Wall: 32% HT-9, 7% H_2O, 61% Void	2.20	First Wall: 11.7% HT-9
4	2.39	Blanket 1: 19.5% HT-9, 21.5% H_2O, 5% $LiAlO_2$,[a] 45% Be,[b] 9% Void	2.40	Blanket 1: 6% HT-9, 9% Flibe[c] 53% Be[d]
5	2.46	Blanket 2: 12.5% HT-9, 11.5% H_2O, 70% $LiAlO_2$,[a] 6% Void	2.52	Blanket 2: 6% HT-9, 9% Flibe, 75% SiC
6	2.66	Blanket 3: 7% HT-9, 4% H_2O, 84% $LiAlO_2$[a] 5% Void	2.77	Blanket 3: 28% HT-9, 9% Flibe, 53% SiC
7	2.84	Coolant Manifold: 33% HT-9, 67% H_2O	2.99	Plenum: 27% HT-9
8	3.14	Shield: 80% Fe 1422, 20% H_2O	3.29	Shield: 80% Fe 1422, 20% H_2O

[a]Breeder (γ-$LiAlo_2$): 87% Theoretical Density (T.D.), 90% ^{6}Li enrichment
[b]Beryllium: 87% Theoretical Density
[c]Flibe (natural lithium): ^{6}Li: 1.135-3, ^{7}Li: 1.420-2, Be: 1.729-2, F: 4.991-2 abm/b-cm for 100% T.D.
[d]Beryllium: 100% Theoretical Density

Table 6.8-20. Tritium Breeding Ratio from ^{6}Li (T_6), From ^{7}Li(T_7), and the Total Breeding Ratio in the Four Blanket Concepts[a]

Tritium Breeding Ratio	Li_2O/He/PCA	LiPb/LiPb/PCA	$LiAlO_2$/H_2O/FS/Be	Flibe/He/FS/Be
T_6	0.8026	1.5792	1.2489[c]	1.2808[c]
T_7	0.4253	2.640-3[b]	1.999-3[c]	1.079-2[c]
T (total)	1.2279	1.5818	1.2509[c]	1.2916[c]

[a]Based on one-dimensional poloidal-axis calculational model.

[b]Read: 2.64×10^{-3}

[c]Based on the Los Alamos National Laboratory evaluation for beryllium, see text.

particular that the contribution to the total breeding from the $^{7}Li(n,n'\alpha)t$ reactions is generally small in the LiPb, $LiAlO_2$, and the flibe blankets where the neutron spectrum is soft as compared to the Li_2O blanket. In addition, the LiPb blanket has the highest TBR value as compared to other blankets.

To carry out the cross-section sensitivity/uncertainty analysis, the partial cross-sections for each element present in each blanket were generated from the DLC41/VITAMIN-C library[6.8-33] using the AMPX module[6.8-34] and a modified version of the SWANLAKE[6.8-35] sensitivity code was employed to generate the sensitivity profiles, P's in a 1-D geometry. The integrated relative sensitivity coefficient, $S_{\Sigma_x}^{k}$, defined as[6.8-17 to -27]

$$S_{\Sigma_x}^{k} = \sum_{g} P_{\Sigma_{x,k}}^{g} \qquad (6.8\text{-}39)$$

was evaluated for both the responses $R_{6_{Li}} \equiv T_6$ and $R_{7_{Li}} \equiv T_7$ based on a 1% increase in the partial cross-section Σ_x^g at all energy groups.

The correlation matrices and cross-sections relative standard deviations for the elements ^{6}Li, Pb, Fe, Cr, Ni, ^{16}O, F, Al, Si, C, H and Be were generated using the UNCER code (a modified version of the PUFF-2 code).[6.8-26] Although the results shown in Table 6.8-20 are based on the ENDF/B-IV evaluation, the generated correlation are based on the ENDF/B-V evaluation. This is not a point of concern since the correlation matrices are relative in nature.

For ^{7}Li, since only private evaluation for the $^{7}Li(n,\alpha n')t$ cross-section and its covariance exists but not officially released,[36] the cross-sections used in the calculation are those based on the ENDF/B-IV. However, in carrying out the uncertainty analysis, results for the non-statistical treatment (see Section 6.8.5.5.) were used where the $^{7}Li(n, n'\alpha)t$ cross-section was decreased by 15%.

6.8.6.4. Calculation Results

(A) Impact of Various Evaluations for the $^{9}Be(n,2n')$ Cross-Section on the TBR

For the flibe and the $LiAlO_2$ blankets, the TBR has been calculated using three evaluations for the $^{9}Be(n,2n')$ cross-sections: the ENDF/B-IV (Be-IV), the ENDF/B-V (Be-V) and the Los Alamos National Laboratory evaluation (Be-

LANL). The motivation behind comparing the results is that recent studies have indicated that the beryllium (n,2n') cross-section currently supplemented in the ENDF/B-V is in error and results in a different neutron multiplication factor when the experimental and analytical values are compared.[6.8-37,38] The ENDF/B-IV and V evaluations are carried out by Howarton and Perkins[6.8-39] while the latest evaluation for the $^{9}Be(n,2n')$ cross-section was provided by Young and Stewart from LANL.[6.8-40]

As it stands, the ENDF/B-IV and V evalutations are the same where the time-sequential reaction

$$^{9}Be(n,n_1')^{9*}Be(n_2')\ ^{8*}Be,$$

is allowed to be described by up to four time-sequential processes through four $^{9*}Be$ excitation levels of 1.68 MeV, 2.43 MeV, 6.76 MeV, and 11.28 MeV. This inherent difficulty in presenting the $^{9}Be(n,2n')$ cross-section that carried over to the ENDF/B-V evaluation limits the presentation of the $^{9}Be(n,2n')$ measurements by not allowing more than four levels to describe the time-sequential reactions. Recent measurements by Drake, et al.[6.8-37] showed that while the integrated values of the (n,2n') reaction are in good agreement with the ENDF/B-IV evaluation at energies 5.9, 10.1, and 14.2 MeV, the differential cross-section $\sigma(E \rightarrow E',\mu)$ is not. Drake indicated that from about 6-12 MeV the cross-section for excitation of the 2.43 level in $^{9*}Be$ is substantially lower by a factor of 2, i.e., the low-lying states in the $^{9*}Be$ are overemphasized in the ENDF/B-IV (and V) evaluations. This remark has also been indicated by Purser[41] and Basu[38] measurements. In the Basu's work, the measured values of neutron multiplication were found to be ~ 25% lower than the calculated values in a rectangular geometry made of beryllium and surrounding the 14-MeV neutrons.

The recent and unofficial evaluation for the ^{9}Be cross-sections carried out by Young and Stewart[6.8-40] (LANL-1979) has been updated and represented correctly the energy-angle distribution of the secondary neutrons from the $^{9}Be(n,2n')$ reactions. In this evaluation, the $^{9}Be(n,2n')$ reactions which are binned in excitation energy of MT = 51-83 are derived to agree with Drake's evaluation.[6.8-37] The (n,2n') distributions are based on data for a cluster of real levels in $^{9*}Be$ near 2.43 MeV (MT = 52) and 32 excitation

energy bins to represent the (n,2n') continuum.[6.8-40] To be emphasized is that integrating the differential cross-section, $\sigma(E \rightarrow E', \mu)$, over scattering angle in Young's evaluation yields essentially the same values for the total $^{9}Be(n,2n')$ cross-section. It is the energy-angle correlation for the $^{9}Be(n,2n')$ cross-section which has been improved.

The (Be-IV), (Be-V), and (Be-LANL) evaluations described above have been used in the current comparative analysis and the results are summarized in Tables 6.8-21 and 6.8-22 for the flibe and the $LiAlO_2$ blanket, respectively. To minimize sources of difference in the evaluated tritium breeding ratio, we chose to use the ENDT/B-IV data base for other materials present in these blankets. In processing the beryllium data from the (Be-LANL) evaluation, only the levels MT = 51-73 were considered (the levels MT > 73 occur at energies higher than the 14.1 MeV neutron source). A multiplication factor of 2 is used in processing the $^{9}Be(n,2n')$ cross-section from these inelastic levels.

Upon using the (Be-LANL) evaluation, about 4.6% decrease in tritium breeding ratio from ^{6}Li, T_6, and a corresponding decrease of ~ 7.5% in T_7 is obtained in the flibe blanket as compared to the results obtained with the (Be-V) evaluation. In the $LiAlO_2$ blanket, the corresponding decrease in T_6 and T_7 is 1.1 and 2.5%, respectively. However, since the tritium breeding is mostly from ^{6}Li, the overall decrease in the TBR is ~ 4.6 and 1.1% in the flibe and the $LiAlO_2$ blanket, respectively. One also should notice from tables 6.8-21 and 6.8-22 that the contribution to the overall decrease in the TBR is mainly from the front zone of the breeding region (Blanket-1) in both blankets. Simultaneous decrease in both T_6 and T_7 upon using the (Be-LANL) evaluation can only be explained by the decrease in the number of neutrons available for breeding. This becomes apparent when the neutron balance in the blanket with the two evaluations is examined. We have carried out this task for both the flibe and the $LiAlO_2$ blankets using the three evaluations. For the flibe blanket, for example, the following conclusions are drawn:

(a) Neutron multiplication is 2.02, 1.93 and 2.02, with the (Be-V), (Be-LANL) and (Be-IV) evaluation, respectively. This multiplication is solely due to the (n,2n') reactions which is dominated by the contribution from the $^{9}Be(n,2n')$ reaction. This contribution is about 46.4, 44 and 46.3% in the three cases, respectively.

Table 6.8-21. The Tritium Breeding Ratio in the Flibe/He/FS/Be Blanket using Three Different Evaluations for the Beryllium Cross-Sections

Parameter	Be-V Evaluation	Be-LANL Evaluation	% Decrease	Be-IV Evaluation
Tritium Breeding Ratio for $^{6}Li, T_6$				
Blanket-1 zone	9.896-1	9.382-1	5.19	9.704-1
Blanket-2 zone	2.223-1	2.146-1	3.46	2.242-1
Blanket-3 zone	1.296-1	1.280-1	1.23	1.349-1
sub-sum	1.342	1.281	4.55	1.330
Tritium Breeding Ratio for $^{7}Li, T_7$				
Blanket-1 zone	9.865-3	9.068-3	8.08	9.877-3
Blanket-2 zone	1.351-3	1.290-3	4.52	1.380-3
Blanket-3 zone	4.486-4	4.347-4	3.10	4.596-4
sub-sum	1.166-2	1.079-2	7.46	1.172-2
Total Tritium Breeding Ratio, TBR	1.354	1.292	4.58	1.342

Table 6.8-22. The Tritium Breeding Ratio in the $LiAlO_2/H_2O$/FS/Be Blanket using Three Different Evaluations for the Beryllium Cross-Sections

Parameter	Be-V Evaluation	Be-LANL Evaluation	% Decrease	Be-IV Evaluation
Tritium Breeding Ratio for $^6Li, T_6$				
Blanket-1 zone	1.039	1.021	1.73	1.031
Blanket-2 zone	1.427-1	1.451-1	-1.68	1.489-1
Blanket-3 zone	8.125-2	8.330-2	-2.52	8.559-2
sub-sum	1.263	1.249	1.11	1.265
Tritium Breeding Ratio for $^7Li, T_7$				
Blanket-1 zone	6.410-4	6.132-4	4.34	6.413-4
Blanket-2 zone	7.353-4	7.202-4	2.05	7.467-4
Blanket-3 zone	6.737-4	6.662-4	1.11	6.864-4
sub-sum	2.050-3	1.999-3	2.49	2.074-3
Total Tritium Breeding Ratio, TBR	1.265	1.251	1.11	1.267

(b) Most of the neutron absorption reactions are in ^{6}Li. The fraction of the available neutrons contributing to T_6 is about 63.3, 63 and 62.7% in the (Be-V), (Be-LANL) and (Be-IV) case, respectively.

(c) The results from the (Be-IV) evaluation case are essentially the same as the (Be-V) evaluation case since the $^{9}Be(n,2n')$ cross-section is derived in the same manner in both evaluations and are essentially based on the same data and format.

(d) The decrease in the $^{9}Be(n,2n')$ reaction rates upon using the (Be-LANL) evaluation is ~ 9.3% as compared to the $^{9}Be(n,2n')$ reaction rate with the (Be-V) evaluation. However, the decrease in the neutron multiplication is ~ 4.3% which is basically the same amount of decrease in the TBR. The last two conclusions emphasize that the present $^{9}Be(n,2n')$ evaluation in the ENDF/B-V overestimates the neutron multiplication. The ~ 9.3% decrease observed in the $^{9}Be(n,2n')$ reaction rate is due to the difference in the representation of the energy-angle distribution of the secondary neutrons obtained from this reaction rather than from the integrated value for the $^{9}Be(n,2n')$ cross-section. The overestimation in the neutron multiplication of ~ 25% observed by Basu[6.8-38] is due to utilizing beryllium everywhere in his experiment.

It is interesting to explain the decrease in the neutron multiplication although the total $^{9}Be(n,2n')$ cross-section is almost the same in the three evaluations. The energy-angle correlation corrected in the LANL evaluation for the secondary neutrons tends to transport these neutrons in the forward direction and away from the breeding zone (notice that isotropic scattering for the second neutron in the time-sequential reaction was assumed in the ENDF/B-IV and V evaluations). Since the $^{9}Be(n,2n')$ reactions contribute the most to the excess neutrons, the relative amount of neutrons available for further multiplication in the beryllium zone through successive Be(n,2n') reactions decreases especially when we notice that the threshold for the $^{9}Be(n,2n')$ reaction is only ~ 2.4 MeV. Consequently, the total number of neutrons available for breeding decreases and that results in a comparable decrease in the TBR.

We have focused in the above discussion on the impact of various representations for the secondary energy and angular distribution of the $^{9}Be(n,2n')$ cross-section on the TBR in the flibe and the $LiAlO_2$ blanket. One would

expect that the uncertainty in the TBR gets larger when the uncertainty in the secondary energy-angle distribution of similar reactions [e.g., (n,inelastic), (n,3n'), etc.] and in other materials are considered. The example given above for the $^{9}Be(n,2n')$ is based on direct evaluation for the uncertainty in the TBR due to the uncertainty in the secondary neutrons distributions. In addition to this uncertainty, there is another contribution that comes from the uncertainty in the integrated values for the various partial cross-sections. This part is evaluated in the manner described by Eqs. (1-3). Estimates for the impact of this contribution to the total uncertainty in the TBR is given below.

(B) The Cross-Section Sensitivity Analysis Results

The relative integrated sensitivity coefficient $S^{k}_{\Sigma_x}$, given by Eq. (39) has been evaluated for the response $R_{T_6} = T_6$ and $R_{T_7} = T_7$ based on a 1% increase in the partial cross-section Σ^{g}_{x} at all energy for each element presents in the four blankets and the results are summarized in Table 6.8-23 and Table 6.8-24 for $S^{T_6}_{\Sigma_x}$ and $S^{T_7}_{\Sigma_x}$, respectively. The results shown are for those elements whose coefficients are large. From these tables, the following observations can be made.

Tritium Breeding from ^{6}Li, T_6

First, all reaction types that lead to neutron disappearance (e.g., (n,γ), (n,p), (n,d), (n,t)...) have negative sensitivity coefficients as expected since these reactions decrease the number of neutrons available for tritium breeding (both from ^{6}Li and ^{7}Li). The exception is for the case of the $^{6}Li(n,\alpha)t$ reaction which has a positive net coefficient since the direct part (the part that comes from

$$\frac{\delta R_{^6Li}/R_{^6Li}}{\delta\Sigma_x/\Sigma_x} = \frac{1}{R_{T_6}} < \Sigma_{(n,\alpha)}\phi >$$

and has a value of unity) dominates the indirect contribution evaluated from Eq. (35). As a second observation, one notices that all reaction types that lead to neutron multiplication (e.g. (n,2n'), (n,3n'), (n,2n') α) have positive coefficients since the number of neutrons available for tritium breeding increases due to these reactions.

Table 6.8-23 The Integrated Relative Sensitivity Coefficient, $S_{\Sigma_x}^{T_6}$, for the Tritium Breeding Ratio from ^6Li due to a 1% Increase in the Various Partial Cross Sections of Materials Present in Four Blanket Concepts

Cross Section Perturbed	Li_2O/He/PCA			LiPb/LiPb/PCA			$LiAlO_2$/H_2O/FS/Be			Flibe/He/FS/Be		
	^7Li	^6Li	Fe	Pb	^6Li	Fe	Fe	Be	^6Li	Fe	Be	^6Li
(n,elastic)	7.23-2[a]	4.44-3	1.46-2	4.26-2	5.20-3	1.58-2	-7.40-3	-5.24-3	2.21-3	3.29-2	1.34-1	1.09-4
(n,inelastic)	6.55-2	5.81-3	1.97-2	-1.86-2	-9.02-3	-2.24-2	-6.01-2		1.92-3	-3.62-2		-1.23-4
(n,2n′)	2.39-2	5.10-2	1.07-1		6.41-3	5.70-2	2.51-1[c]		1.65-2	4.13-1[c]		
(n,3n′)			7.33-3									
(n,γ)	-4.84-4	-3.49-5	-1.95-2	-2.11-2	-2.67-5	-1.63-2	-5.67-2	-4.61-4	-4.04-5	-1.74-1	-4.14-3	-3.33-5
(n,^{3}He)		-1.94-5		-2.46-5	-7.00-5		-3.39-5					
(n,p)		-1.31-3	-1.46-2		-6.71-4	-1.29-2	-4.37-2	-1.87-5	-5.76-4	-2.19-2	-3.39-5	-2.71-5
(n,t)		-2.32-5		-3.01-5	-8.49-5	-6.72-3		-4.10-5	-1.24-2			
(n,d)	-6.91-3	-1.62-3		-1.83-3	-5.48-3		-2.66-3					
(n,n′p)		5.60-4		-1.50-3	-2.84-3		-1.83-3					
(n,2n′)α	3.20-2	6.11-3		6.69-4		1.67-3			4.04-5			
(n,n′)α		4.07-5		-1.12-4	-2.14-4		-1.34-4					
(n,α)		7.10-2[b]	-4.13-3		7.75-2[b]	-3.97-3	-1.29-2	-3.06-2	3.89-2[b]	-6.40-3	-6.03-2	1.85-1[b]
(n,abs.)	-7.40-3	6.96-2[b]	-3.99-2	-2.11-2	7.68-2[b]	-3.51-2	-1.19-1	-3.78-2	3.83-2[b]	-2.05-1	-7.68-2	1.85-1[b]
(n,total)	1.85-1	8.60-2[b]	4.56-2	1.17-1	7.35-2[b]	-3.51-2	-1.30-1	2.08-1	4.41-2[b]	-1.92-1	4.71-1	1.85-1[b]

[a] Read 7.23×10^{-2}.

[b] Values shown include the direct contribution to the sensitivity coefficient from perturbation in the $^6Li(n,\alpha)t$ cross section.

[c] Sum of contribution from each inelastic level used to represent the $^9Be(n,2n')$ reaction in Be-LANL evaluation.

Table 6.8-24. The Integrated Relative Sensitivity Coefficient, $S_{\gamma_x}^{T_7}$, for the Tritium Breeding Ratio from ^7Li due to a 1% Increase in the Various Partial Cross-Sections of Materials Present in the Four Blanket Concepts

Cross-Section Perturbed	Li_2O/He/PCA			LiPb/LiPb/PCA			$LiAlO_2H_2O$/FS/Be			Flibe/He/FS/Be		
	^7Li	^{16}O	Fe	^7Li	Pb	Fe	^7Li	Fe	Be	^7Li	Be	Fe
(n,elastic)	-7.93-2[a]	-2.36-2	-6.32-4	-3.24-4	-6.30-3	-1.24-3	-3.25-3	-4.65-2	-1.52-1	-2.25-3	-5.68-2	-2.47-3
(n, inelastic)	7.07-1	-1.82-1	-8.61-2	9.99-1[b]	-1.22-1	-6.26-2	9.73-1[b]	-4.34-1		9.99-1[b]		-1.43-1
(n,2n')	-1.83-2		-3.79-2	-1.51-4	-7.08-1	-4.35-2	-3.12-4	-1.88-1	-4.25-1[c]	-4.51-4	-4.12-1[c]	-6.58-2
(n,3n')					-1.00-2							
(n,γ)	-1.10-5	-2.16-6	-2.92-5	-8.18-8	-9.04-5	-2.69-5	-2.29-7	-1.36-4	-1.12-4	-2.77-7	-1.28-4	-4.94-5
(n,^{3}He)			-2.01-5			-2.52-5		-1.02-4				-3.64-5
(n,p)		-1.94-2	-1.37-2			-1.34-2		-6.52-2	-3.96-5		-4.01-5	-2.30-2
(n,t)			-2.41-5		-3.09-5	-1.85-5		-1.23-4	-1.43-2		-1.47-2	-4.40-5
(n,d)	-7.68-3	-6.11-3	-1.66-3	-6.91-5		-1.89-3	-1.24-4	-8.24-3		-1.89-4		-2.88-3
(n,n'p)			-3.04-3			-3.65-3		-1.53-2				-5.40-3
(n,2n')α	-2.44-2			-2.27-4			-3.86-4			-6.02-4		
(n,n')α			-2.19-4			-2.76-4		-1.12-3				-3.97-4
(n,α)		-7.38-2	-4.14-3			-4.15-3		-1.98-2	-1.74-2		-2.21-2	-6.96-3
(n,abs.)	-7.70-3	-9.92-2	-1.96-2	-6.92-5	-9.04-5	-1.95-2	-1.25-4	-9.36-2	-3.19-2	-1.89-4	-3.69-2	-3.30-2
(n,total)	5.77-1[b]	-3.04-1	-1.51-1	9.98-1[b]	-8.46-1	-1.35-1	9.89-1 [b]	-7.92-1	-6.09-1	9.96-1 [b]	-5.06-1	-2.56-1

[a] Read -7.93×10^{-2}

[b] Values shown include the direct contribution to the sensitivity coefficient from perturbation in the $^7Li(n,n'\alpha)t$ cross-section. This cross-section is presented by the ^7Li(n,inelastic) cross-section.

[c] Sum of contribution from each inelastic level used to represent the $^9Be(n,2n')$ reaction in the (Be-LANL) evaluation.

In the LiPb blanket, tritium breeding from ^6Li is more sensitive to variations in the Pb, ^6Li, and Fe in that order. A 1% increase in the total cross-sections of these elements (equivalent to increasing the atomic densities by a 1%) leads to a 0.117, 0.074, and 0.035% change in T_6, respectively. In the Li_2O blanket however, T_6 is most sensitive to ^7Li, ^6Li, and Fe in that order with corresponding coefficients of 0.185, 0.086 and 0.046%, respectively. Because lead is used as a neutron multiplier in the LiPb blanket, variation in the Pb(n,2n') reaction has the largest coefficient as compared to the sensitivity coefficient for other partial reactions of other materials. The profile $P^g_{\Sigma(n,2n)}$ for lead is shown in Fig. 6.8-15 and it is positive at all energies with the largest values occuring at the highest energy group.

It is interesting to notice from Tables 6.8-23 that the (n,inelastic) cross section for all materials has a negative senstivity coefficient in the LiPb blanket while it is positive in the Li_2O blanket. This reaction type, which occurs mainly at high energy, competes with the neutron production from the Pb(n,2n') reaction in the high energy range down to the threshold for the Pb(n,2n') reaction ($\sim$ 7.5 MeV). In this energy range, increasing the (n,inelastic) reactions in the LiPb blanket tends to decrease the Pb(n,2n') reactions and hence the sensitivity profiles have negative values in this energy range as shown in Fig. 6.8-16 as an example. However, below the Pb(n,2n') threshold, the profiles for the (n,inelastic) reactions have positive values since in this case the (n,inelastic) reactions moderate neutron energy to the range where the $^6Li(n,\alpha)t$ cross-section is large and hence more breeding from ^6Li occurs. However, the net coefficient $S^{T_6}_{\Sigma(n,inel)}$ is negative since the negative part of the sensitivity profile above the Pb(n,2n') threshold dominates. Since no multiplier such as lead exists in the Li_2O blanket, the profiles for the (n,inelastic) cross-section are always positive as shown in Fig. 6.8-17 for iron as an example.

The (n,elastic) cross-section has positive coefficient for all elements in the LiPb and the Li_2O blankets. This reaction occurs at all energies but it is more pronounced at low energy. It tends to decrease neutron energy to the range where the $^6Li(n,\alpha)t$ cross-section is large.

One can notice from Table 6.8-23 that variations in the ^7Li cross-section have practically no impact on the tritium breeding from ^6Li in the LiPb

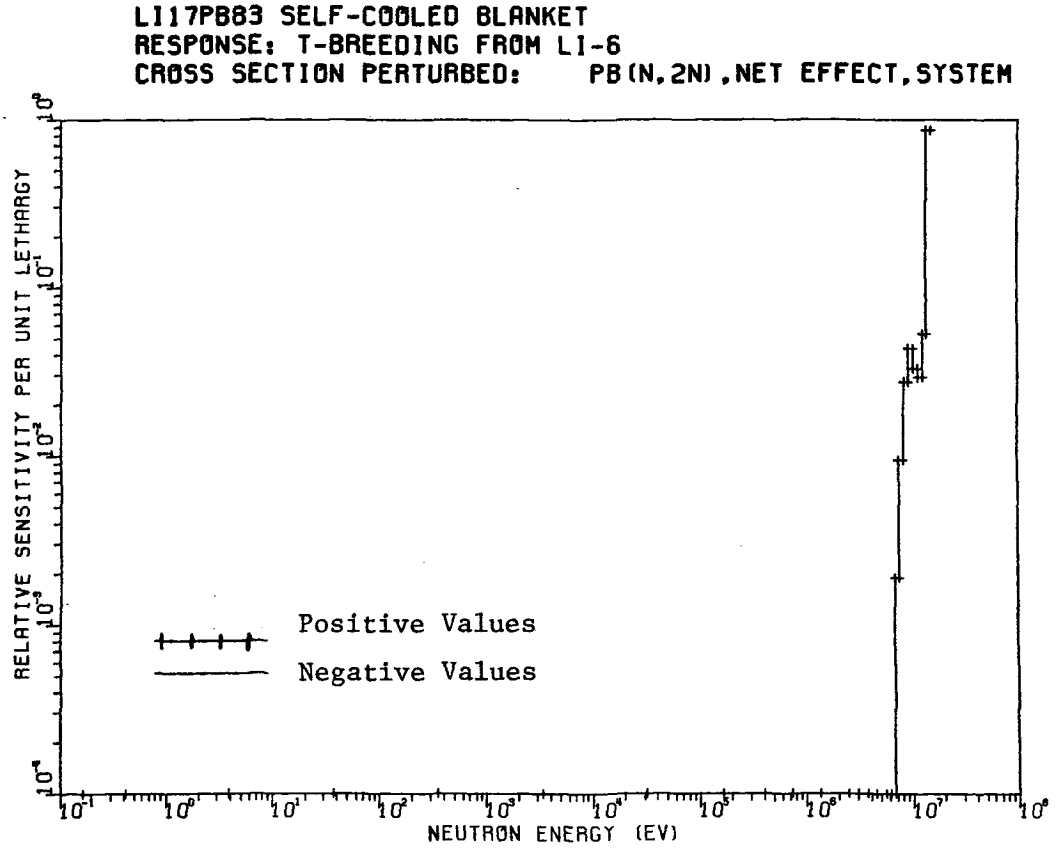


Figure 6.8-15 The relative sensitivity profile for the Pb(n,2n) cross section in the LiPb/LiPb/PCA blanket integrated over the system.

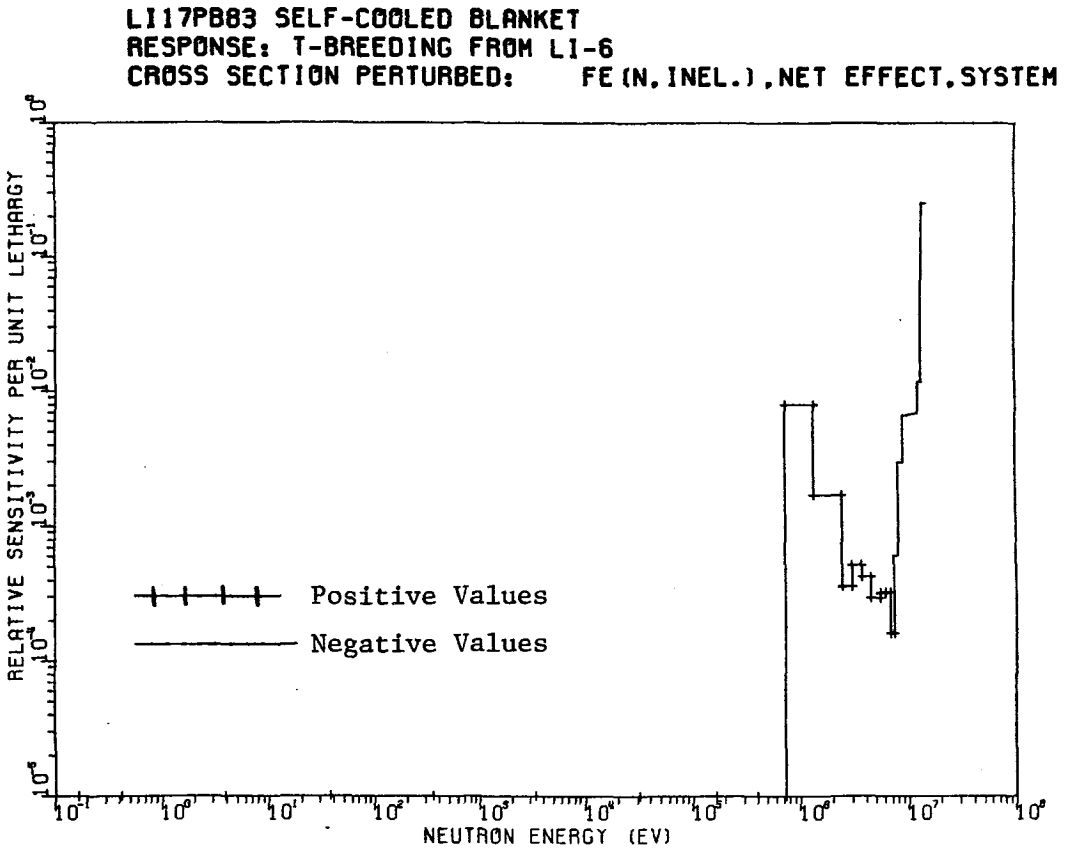


Figure 6.8-16 The relative sensitivity profile for the Fe(n, inelastic) cross section in the LiPb/LiP/PCA blanket integrated over the system.

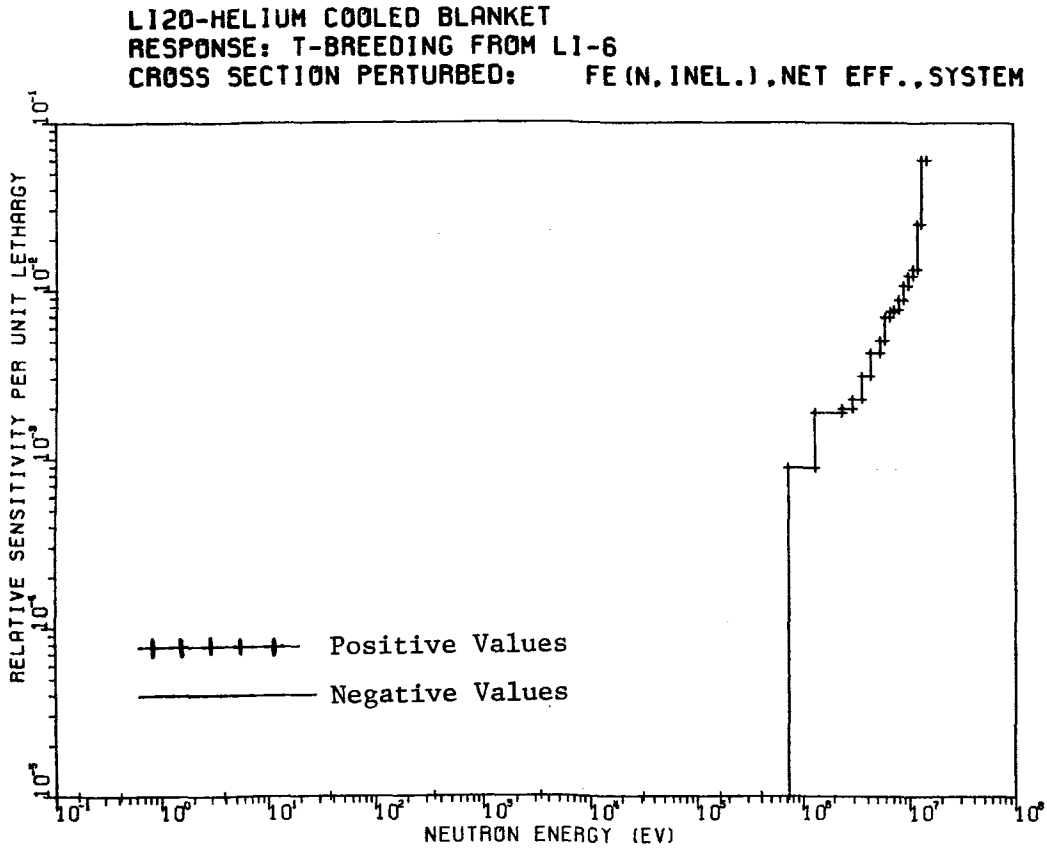


Figure 6.8-17 The relative sensitivity profile for the Fe(n, inelastic) cross section in the Li_2O/He/PCA blanket integrated over the system.

blanket. However, this is not the case in the Li_2O blanket where T_6 is most sensitive to variation in the ^7Li cross-section and in particular to variation in the elastic and the inelastic cross-sections. In addition, the total sensitivity coefficient for ^7Li in the LiPb blanket is about three orders of magnitude lower as compared to corresponding value in the Li_2O blanket. This is due to the fact that ^6Li is 90% enriched in the LiPb blanket whereas natural lithium is employed in the Li_2O blanket.

The direct, indirect and net sensitivity profiles for the $^6Li(n,\alpha)t$ cross section in the LiPb blanket are shown in Figs. 6.8-18 and 6.8-19. Similar profiles were obtained in the Li_2O blanket. The direct part is always positive at all energies and its profile presents the contribution to T_6 from each energy group whereas the indirect part is negative at all energies. In addition, the profiles for the $^6Li(n,\alpha)$ cross-section is larger in the thermal and epithermal range in the Li_2O blanket as compared to the LiPb case. This is due to the fact that the neutron spectrum in the LiPb blanket is lower in this energy range than the corresponding spectrum in the Li_2O blanket. This is shown in Fig. 6.8-20 where the spectrum in the Li_2O blanket is about three orders of magnitude larger in the low energy range than these values found in the LiPb blanket. This is true since the thermal and epithermal fluxes are depressed in the later blanket where 90% enrichment for ^6Li is used. At higher energy (> 1 MeV) the Li_2O blanket exhibits larger values for the spectrum since helium is used as a coolant while the elastic and inelastic scattering processes in lead tend to soften this spectrum in the LiPb blanket.

The results shown in Table 6.8-23 indicate that tritium breeding from ^6Li in the $LiAlO_2$ blanket is most sensitive to variations in the total cross-section of Be, Fe and ^6Li in that order. This is also true in the Flibe blanket with almost the same order of magnitude for the total coefficients. It can also be noticed that increasing the structural material (equivalent to increasing the total cross-section for the structure constituents) leads to a decrease in tritium production for ^6Li. In addition, the cross-section sensitivity coefficient to variation in the total cross section of beryllium has the largest values (0.21% and 0.47% in the $LiAlO_2$ and the flibe blanket, respectively). As it is the case for the Pb(n,2n') cross-section in the LiPb blanket, tritium breeding from ^6Li has the largest sensitivity coefficient for the Be(n,2n') reactions. As cited earlier, the cross-section for this reac-

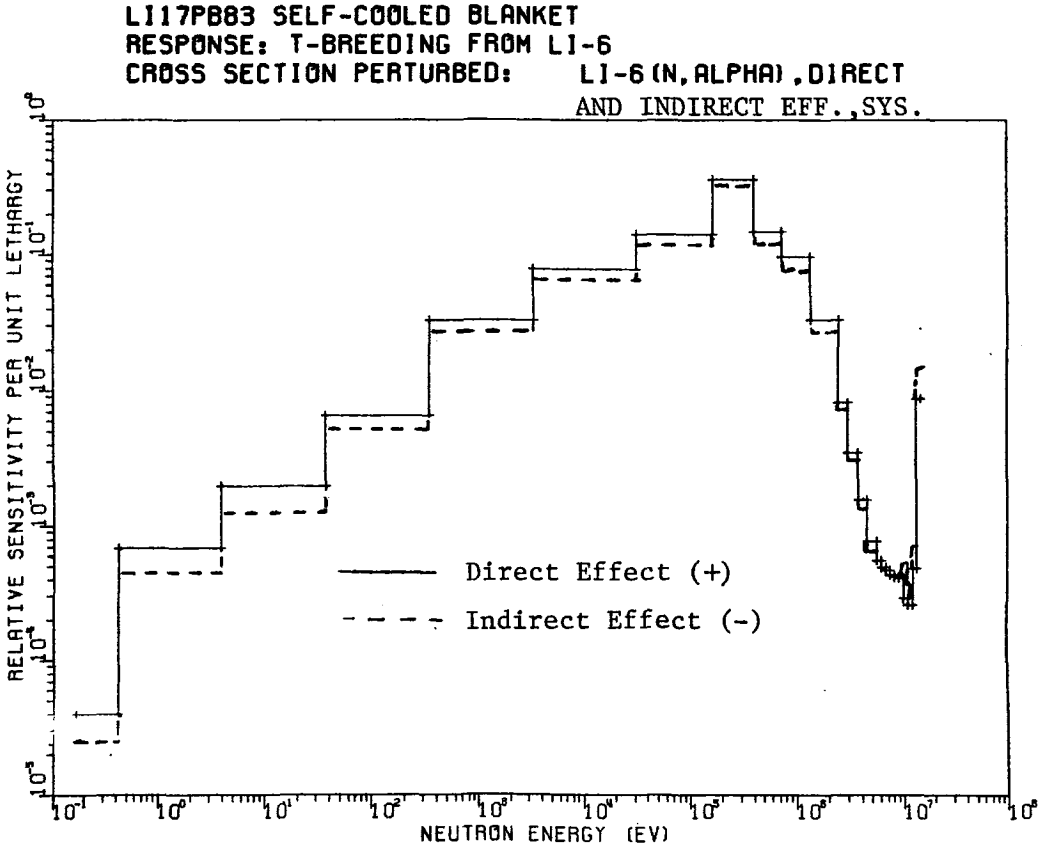


Figure 6.8-18 The direct and indirect part of the relative sensitivity profile for the $^{6}Li(n,\alpha)t$ cross section in the LiPb/LiPb/PCA blanket integrated over the system.

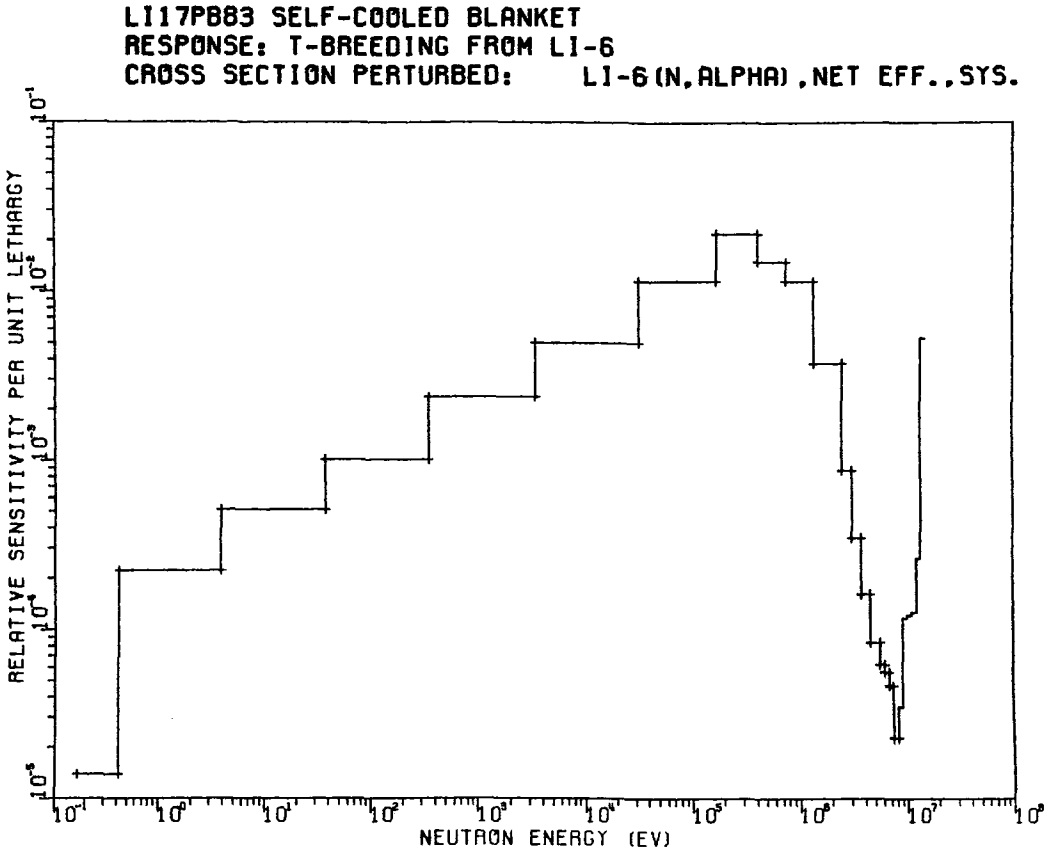


Figure 6.8-19 The net relative sensitivity profile for the $^{6}Li(n,\alpha)t$ cross section in the LiPb/LiPb/PCA blanket integrated over the system.

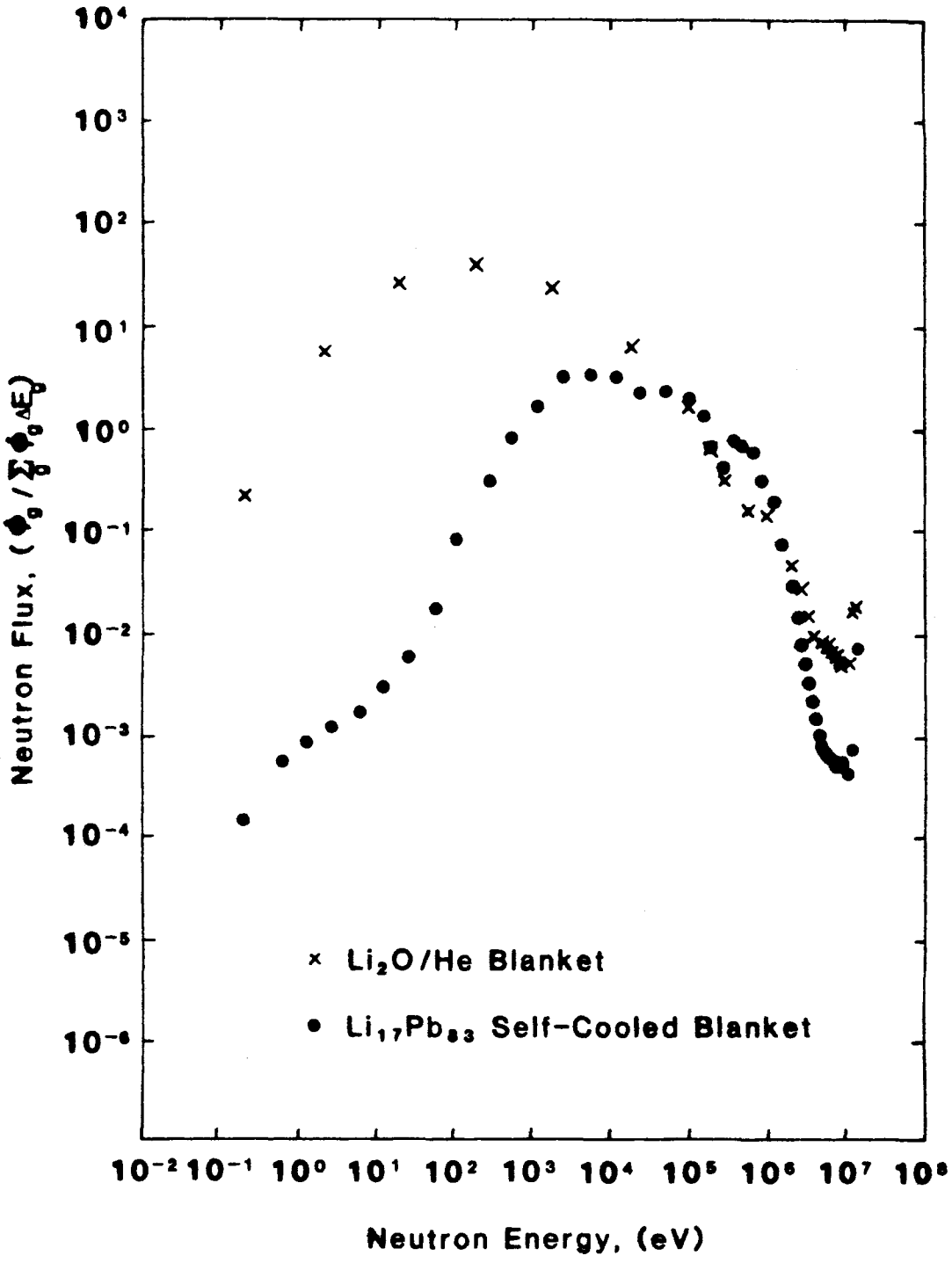


Figure 6.8-20 The neutron spectrum in the middle of the breeding zone of the LiPb/LiPb/PCA and the Li_2O/He/PCA blankets.

tion is constructed from the inelastic levels MT = 51-73 and the coefficient shown in Table 6.8-23 for the Be(n,2n') cross-section is the algebraic summation of the sensitivity coefficient for each inelastic level evaluated individually.

Tritium Breeding from ^{7}Li, T_7

Although tritium breeding from ^{7}Li is much smaller in the LiPb, $LiAlO_2$ and the flibe blankets as compared to the value attainable in the Li_2O blanket (see Table 6.8-20), a parallel analysis was carried out to evaluate the coefficients $S_{\Sigma_x}^{T_7}$, and the results are given in Table 6.8-24.

As general observations drawn from this table one notices that all reactions leading to neutron disappearance have also negative coefficient as it is the case for tritium breeding from ^{6}Li. In addition, all reactions occuring at high energy (e.g. (n,inelastic), (n,n'p), (n,2n')α, etc.) have negative coefficients since increasing these reactions is at the expense of decreasing the $^{7}Li(n,n'\alpha)t$ reaction. In fact, the total sensitivity coefficients are all negative except for the $^{7}Li(n,n'a)t$ cross-section (treated as the inelastic cross-section in the tables shown) which has a positive coefficient, as expected. One also notices that positive variation in the ^{6}Li total cross-section always lead to negative coefficients in all the blankets but the impact is practically negligible as compared to other elements. In addition, increasing the structural materials in three blankets leads to a decrease in T_7 since they exhibit negative sensitivity coefficients. Note also that the largest coefficient is due to variation in the ^{7}Li(n,total) cross-section and the contribution comes mainly from the ^{7}Li(n,inelastic) and the ^{7}Li(n,elastic) cross-sections.

(C) The Cross-Section Uncertainty Analysis Results

To arrive at an estimate for the uncertainty associated with tritium production in the four blankets considered, the P_{Σ_x,T_6}^{g} and P_{Σ_x,T_7}^{g} profiles were coupled with the correlation matrices and the relative standard deviation for the various cross-section types in the manner given by Eqs. (34-37).

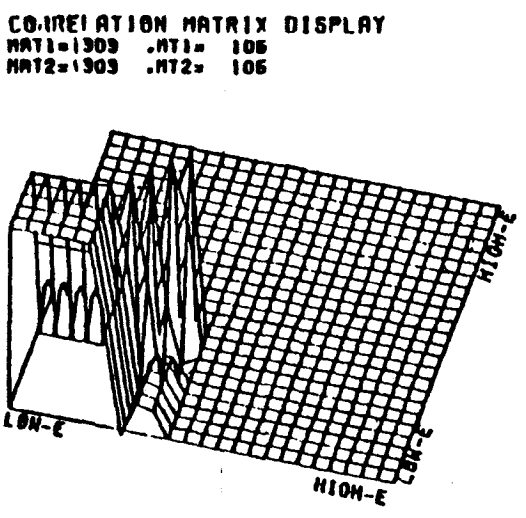
Although tritium breeding from ^{6}Li or ^{7}Li shows high sensitivity to a particular cross-section change, the uncertainty analysis can lead to different conclusions depending on the size of the current uncertainties associated

with various cross-section types. As stated in Section 6.8.5.2, the two expressions given by Eqs. (36) and (37) were used to study the impact of the correlation between cross-section uncertainties on the final results.

Examples of the relative standard deviation (RSD) and the correlation matrices CORR($\sigma_x^g, \sigma_y^{g'}$) are shown in Figs. 6.8-21 and 6.8-22 for the ^{6}Li(n, α)t (MAT = 1303, MT = 105) and the Pb(n,2n') (MAT = 1382, MT = 16). The Pb(n,2n') cross-section has a large RSD of ~ 200%. The maximum RSD in the ^{6}Li(n,α)t cross-section is only ~ 3.6%. Also, shown on Fig. 6.8-23 is the correlation matrix for the inelastic level MT = 52, where the real levels in the (Be-LANL) evaluation for the ^{9}Be(n,2n') cross-section are clustered around 2.43 MeV. The maximum RSD for this level is ~ 24% and occurs near the threshold. For other levels, the RSD varies between 11-19%.

The results for the relative variance and relative standard deviation in the breeding ratio from ^{6}Li and ^{7}Li, individually, are given in Tables 6.8-25 and 6.8-26 for the four blankets. The results shown in Table 6.8-25 for the Li_2O blanket are for the case where the correlation between the cross-section uncertainties is considered according to Eq. (34). Also given in this table are the corresponding results obtained from Eq. (36) and Eq. (37). It is clear from this table that neglecting the correlation that exists between data uncertainties gives smaller variance in both T_6 and T_7 while assuming that the correlation is full (± 1) overestimates these variances. This holds true for the other blankets for which we only show the correlated case in Table 6.8-26.

In the Li_2O blanket the relative standard deviation (RSD) in T_6 and T_7 is 1.2 and 12% respectively. However, the RSD in the total TBR is ~ 5%. Most of the contribution to the variance in T_6 comes from the uncertainties associated with the cross-sections of oxygen (75%), iron (15%), and lithium-7 (3.6%). Notice that the sensitivity analysis reveals different results where T_6 was shown to be more sensitive to variation in the ^{7}Li, ^{6}Li and Fe cross-sections in that order, and least sensitive to variation in the ^{16}O cross-sections. This demonstrates that the current uncertainties in the ^{16}O cross-sections are large. Most of the contribution to the variance in T_7 is from the uncertainties in the ^{7}Li cross-section. This contribution is ~ 96%. As pointed out in Section 6.8.6.3, no error file for ^{7}Li is currently implemented in the ENDF/B-V although non-official data exist. In the present analysis a reduction of ~ 15% in the ^{7}Li(n,inelastic) cross-section was assumed such that the total



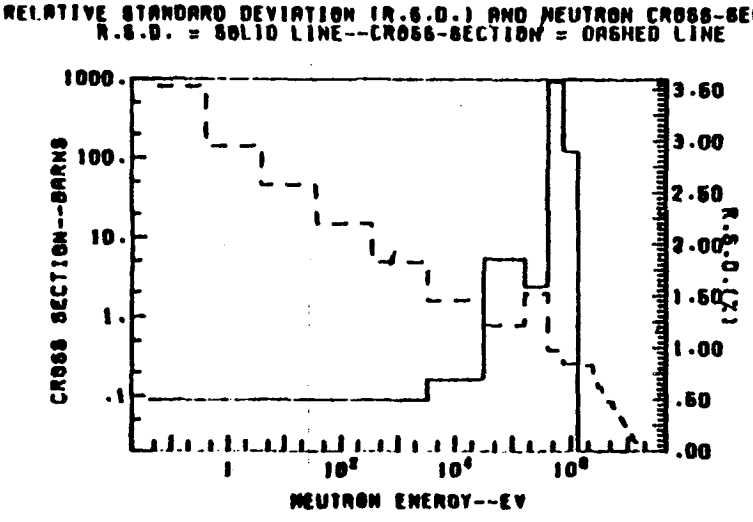
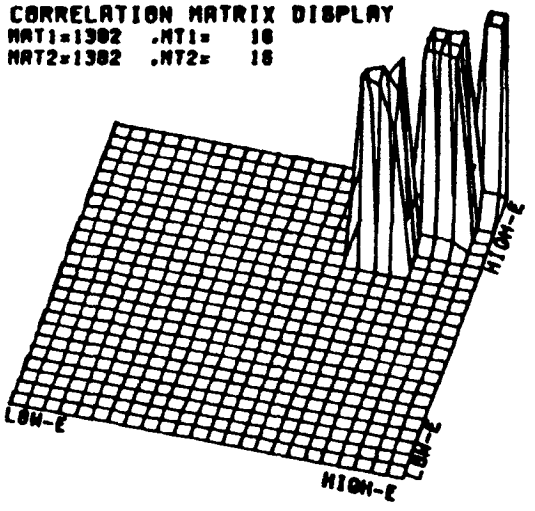


Figure 6.8-21 The correlation matrix and relative standard deviation for the ^{6}Li (MAT = 1303) and reaction (n,α)t (MT = 105).



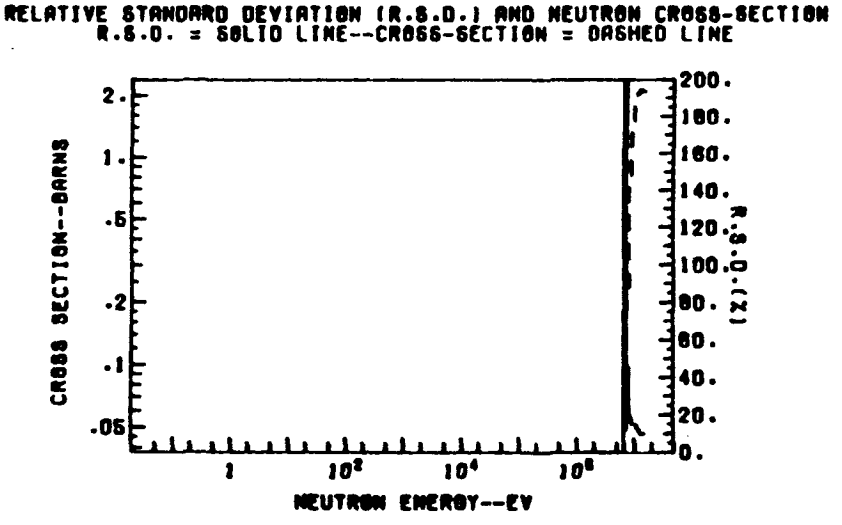


Figure 6.8-22 The correlation matrix and relative standard deviation for the Pb (MAT = 1382) and reaction (n,2n') (MT = 16).

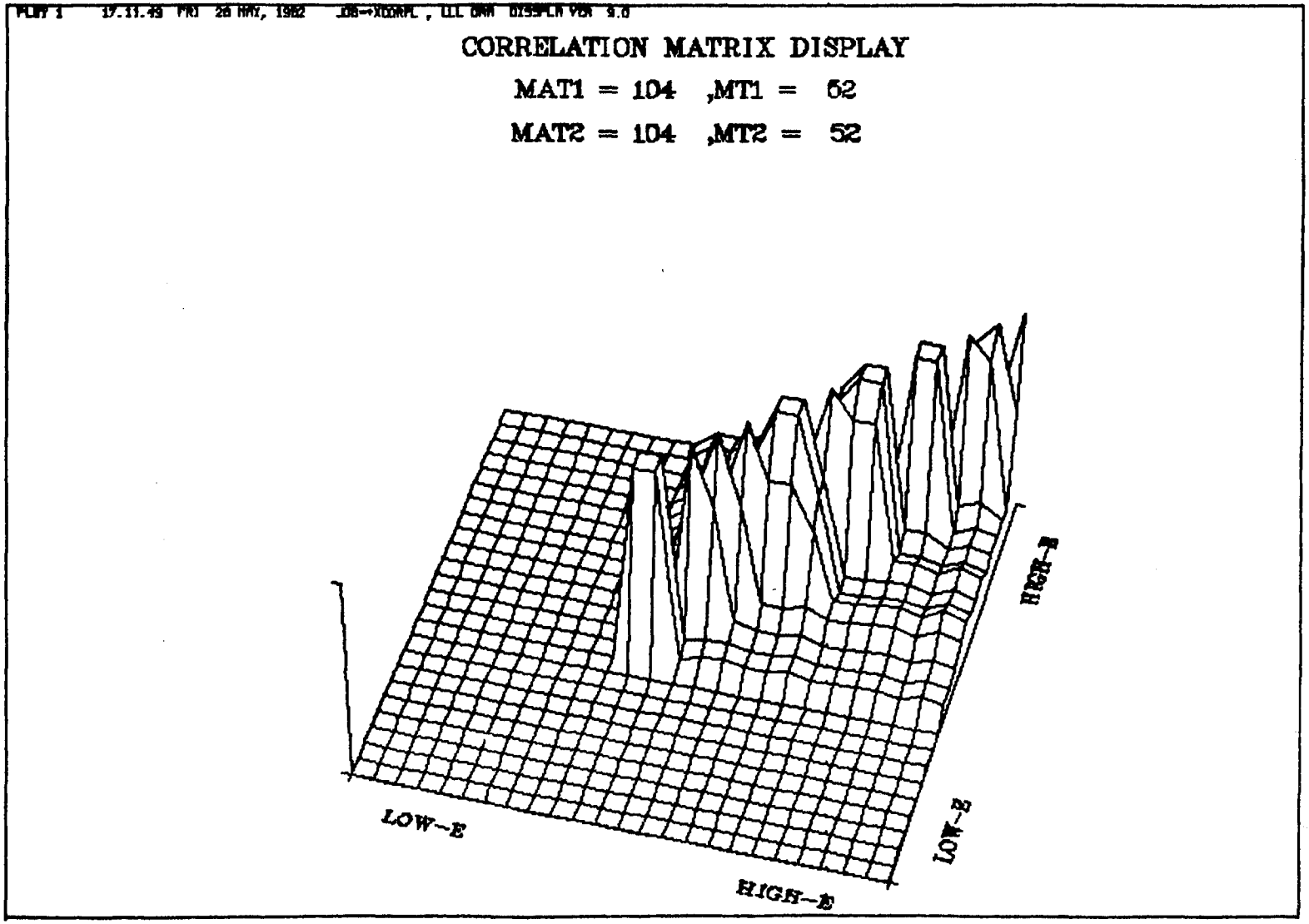


Figure 6.8-23 The correlation matrix for beryllium (MAT = 104) for the inelastic level (MT = 52).

Table 6.8-25 The Relative Variance and Relative Standard Deviation in Tritium Breeding Ratio from ^{6}Li, ^{7}Li and the Total Breeding Ratio due to Cross Section Uncertainties of Various Materials in Li_2O/Helium-Cooled Blanket

	$\left(\Delta R_{^{6}Li}/R_{^{6}Li}\right)^2$			$\left(\Delta R_{^{7}Li}/R_{^{7}Li}\right)^2$		
Material	Correlated	Uncorrelated	Fully Correlated	Correlated	Uncorrelated	Fully Correlated
Lithium-6	2.00-2	7.04-3	3.03-2	0	0	0
Lithium-7[a]	3.61-2	3.61-2	3.61-2	1.39+2	1.39+2	1.39+2
Oxygen	1.03	7.75-1	2.30	4.6	3.76	5.38
Iron	2.00-1	1.41-1	2.69-1	4.63-1	2.19-1	2.32-1
Nickel	4.68-2	1.87-2	5.60-2	9.54-2	4.79-2	1.17-1
Chromium[b]	3.23-2	2.99-2	3.30-2	5.41-1	5.32-1	4.54-1
Relative Variance (Total)	1.37	1.01	2.72	1.45+2	1.44+2	1.45+2
Relative Standard Deviation (%)	1.17	1.00	1.65	1.20+1	1.19+1	1.20+1
Relative Standard Deviation in TBR (correlated case) = ±4.92%[c]						

[a]Error estimates for lithium-7 are considered uncorrelated and are obtained from the non-statistical treatment, see text.

[b]Covariance matrices for chromium are assumed to be the same as those for iron.

[c]Based on the values of T_6 and T_7 shown in Table 6.8-20.

Table 6.8-26. The Relative Variance and the Relative Standard Deviation, RSD, in the Tritium Breeding from ^{6}Li, ^{7}Li, and the Total Tritium Breeding Ratio due to Cross-section Uncertainties of Various Materials in the LiPb, $LiAlO_2$ and the Flibe Blanket[a]

Element	LiPb/LiPb/PCA		$LiAlO_2/H_2O$/FS/Be		Flibe/He/FS/Be	
	Variance in T_6	Variance in T_7	Variance in T_6	Variance in T_7	Variance in T_6	Variance in T_7
Lithium-6	8.19-2	0	1.20-3	0	3.82-2	0
Lithium-7	5.43-4	2.75+2	2.92-6	2.22+2	4.84-4	2.25+2
Oxygen			7.55-2	4.13	9.25-9	1.57-11
Iron	1.19-1	1.73-1	6.94-1	1.47+1	7.99-1	1.34
Nickel	5.14-2	8.62-2	1.49-12	2.79-12	4.09-8	1.27-12
Chromium	1.13-2	8.23-2				
Florine					2.98-1	5.66
Silicon					7.31-2	4.75-1
Carbon					3.76-3	1.76-2
Hydrogen			1.51-3	9.89-2		
Aluminum			1.69-3	6.50-1		
Lead	1.53+1	1.59+1				
Beryllium			3.54	9.30	9.77	9.91
Total Variance	1.56+1	2.41+2	4.31	2.51+2	1.10+1	2.42+2
Relative Standard Deviation, RSD (%)	3.95	1.55+1	2.08	1.58+1	3.31	1.56+1
RSD in the Total TBR (%)	± 3.98		± 2.1		± 3.41	

[a]Values shown are for the "correlated uncertainties" case. The footnotes of Table 6.8-25 apply.

cross-section for ^{7}Li remains the same. This treatment was considered in all the results shown in Tables 6.8-25 through 6.8-27.

In the LiPb blanket, the RSD in T_6 and T_7 is 3.95 and 15.5%, respectively while the RSD in the total TBR is ~ 3.95% since T_7 is insignificant in this case. About 98% contribution to the variance in T_6 comes from the uncertainties associated with the lead cross-section and in particular from the uncertainties in the Pb(n,2n') and Pb(n,3n') cross-sections. The results from the uncertainty analysis is consistent with the results obtained from the sensitivity analysis.

In the $LiAlO_2$ blanket, the RSD in T_6 and T_7 is 2.08 and 15.8% respectively, and the RSD in the total TBR is ~ 2.1%. Most of the contribution to the variance in T_6 is attributed to the uncertainties associated with the beryllium cross-sections and in particular in the current uncertainties in the inelastic levels (MT = 51-73) used to describe the $^{9}Be(n,2n')$ cross-section in the (Be-LANL) evaluation. This contribution is about 82% while a significant contribution (~ 16%) is due to the uncertainties in the iron cross-sections. Note in this case that the contribution from the oxygen cross-section uncertainties is only ~ 1.75% in contrast to the large contribution (75%) in the Li_2O blanket. This shows that results from the sensitivity/uncertainty analysis is highly system-dependent. While the uncertainty in the cross-section of a particular material is acceptable in one system it may not be the case in another system. In addition, the uncertainty analysis shows that the contribution to the RSD in T_6 are more significant from the uncertainties in the ^{9}Be, Fe and ^{16}O cross-section while the sensitivity analysis reveals that T_6 is most sensitive to variations in the Fe, Be and ^{6}Li, in that order. The uncertainties in the cross-sections of Fe and oxygen contribute by ~ 5.9 and 1.7% to the variance in T_7.

In the flibe blanket the RSD in T_6 and T_7 is 3.31 an 15.6%, respectively. The TBR has a relative standard deviation of ~ 3.4%. As it is the case in the $LiAlO_2$ blanket, most of the contribution to the variance in T_6 is due to the uncertainties associated with the $^{9}Be(n,inelastic)$ levels used to derive the $^{9}Be(n,2n')$ cross-section. Although the florine has small cross-section sensitivity coefficient for T_6, the uncertainty analysis shows that the uncertainties associated with the florine cross-sections contribute ~ 3% to the variance in T_6. The same uncertainties contribute ~ 2.3% to variance

Table 6.8-27. Percentage (%) Contribution from Each Blanket Constituent to the Uncertainty in Tritium Breeding from ^{6}Li, $^{\Delta R}6_{Li}/R_{6_{Li}}$, and from ^{7}Li, $^{\Delta R}7_{Li}/R_{7_{Li}}$ in the Four Blanket Concepts Considered in the Analysis

Element	Li_2O/He/PCA		LiPb/LiPb/PCA		$LiAlO_2/H_2O$/FS/Be		Flibe/He/FS/Be	
	Variance in T_6	Variance in T_7	Variance in T_6	Variance in T_7	Variance in T_6	Variance in T_7	Variance in T_6	Variance in T_7
Lithium-6	1.46	~ 0	5.26-1	~ 0	2.78-2	~ 0	3.47-1	~ 0
Lithium-7	3.64	95.86	3.48-3	9.34+1	6.77-5	8.84+1	4.40-3	9.29+1
Oxygen	75.18	3.17	---	---	1.75	1.65	8.41-8	6.49-12
Iron	14.60	3.19-1	7.63-1	7.18-2	1.61+1	5.86	7.26	5.54-1
Nickel	3.42	6.58-2	3.29-1	3.58-2	3.46-11	1.11-12	3.72-7	5.25-13
Chromium	2.36	3.73-1	2.24-2	3.41-2	---	---	---	---
Florine	---	---	---	---	---	---	2.71	2.34
Silicon	---	---	---	---	---	---	6.65-1	1.96-1
Carbon	---	---	---	---	---	---	3.42-2	7.27-3
Hydrogen	---	---	---	---	3.50-2	3.94-2	---	---
Aluminum	---	---	---	---	3.92-2	2.59-1	---	---
Lead	---	---	9.81+1	6.59	---	---	---	---
Beryllium	---	---	---	---	8.21+1	3.71	8.80+1	4.10

in T_7 which is again dominated by the contribution from the uncertainties in the ^7Li cross-sections (93% contribution). A summary of the percentage contribution to variance in T_6 and T_7 is given in Table 6.8-27 for the four blankets considered.

6.8.6.5 Comparison of the Uncertainty Analysis Results to Results from the Non-Statistical Treatment

The results cited in the previous sections are based on the statistical treatment for the uncertainty in the data base and its correlation characterized by the correlation matrices, $CORR(\Sigma_x^g, \Sigma_y^{g'})$. However, in previous studies[6.8-15,-16,-25] the uncertainty in a response, R_k, was derived from the expression

$$\delta R_k/R_k = \sum_g P^g_{\Sigma_x,k} \cdot \frac{\delta\Sigma^g_x}{\Sigma^g_x} \qquad (6.8\text{-}40)$$

In Eq. (40), no correlation between the uncertainty in the cross-section Σ^g_x is considered and estimates for the relative uncertainty $\delta\Sigma_x/\Sigma_x$ is made and is incorporated with the sensitivity profile according to Eq. (40). We have carried out such analysis for the responses T_6 and T_7 in the four blankets. Some estimates for $\delta\Sigma_x/\Sigma_x$ used in this analysis is given in Table 6.8-28 and are obtained from the references cited in the footnote of that table. As stated in these studies, the total cross-section is generally known to have a higher accuracy than the various partial cross-sections. Therefore, it is often more realistic in specifying cross-section error in a given energy range to vary at least two partially compensating cross-sections in such a manner that the total cross-section remains the same. For ^{16}O we included the errors in the ^{16}O(n,total) cross-section and no compensating reactions were considered.

The results of using this non-statistical treatment to arrive at estimates for $\delta R_{6_{Li}}/R_{6_{Li}}$ and $\delta R_{7_{Li}}/R_{7_{Li}}$ are summarized in Table 6.8-29 for the Li_2O blanket. Similar tables were obtained for other blankets (not shown). In Table 6.8-29, the contribution to the uncertainty in T_6 and T_7 from each material is given along with the values obtained from each partial and compensating cross-section. Since the sensitivity profiles for the cross-sections used in the analysis have different signs, error cancellation occurs. The

Table 6.8-28. Error Estimates for Various Partial Cross Sections (as Obtained from Literature)

Element	Cross Section Type Varied	Energy Range (MeV)	Percent Increase in Varied Cross Section (δc)	Cross Section Type Varied to Compensate
^{6}Li[a]	(n,α)t	$<1 \times 10^{-7}$	0.5	(n,total)
		10^{-7}-10^{-2}	1.0	
		10^{-2}-10^{-1}	1.0-2.0	
		10^{-1}-3×10^{-1}	5.0	
		3×10^{-1}-5×10^{-1}	5.0-1.0	
		5×10^{-1}-7×10^{-1}	10-15	(n,elastic)
		7×10^{-1}-1	15	
		1-1.7	15-10	
		1.7-14.1+1	10	
^{7}Li[a]	(n,n′)αt	3-14.1	-15	(n,elastic)
Pb[b]	(n,2n)	7.5-14.1	20	(n,inelastic)
Fe[c]	(n,inelastic)	8-15	25	
Ni[d]	(n,2n′)	8-15	25	
Cr[d]	(n,n′)p	8-15	50	(n,elastic)
	(n,n′)α	8-15	50	
	(n,absorption)	8-15	25	
^{16}O[e]	(n,total)	<0.5	4.0	
		0.5-15	1.0	
	(n,elastic)	<0.5	4.0	
		0.5-4.0	1.0	
		4.0-6.5	3.0	
		6.5-9.5	6.0	
		9.5-12.5	15	
		12.5-15	10	
	(n,inelastic)	6.5-15	30	
	(n,γ)	all energies	14	
	(n,p)	9.5-15	20	
	(n,d)	9.5-12.5	50	
		12.5-15	30	
	(n,α)	2-15	20	

[a]Error estimates are taken from Refs. 25 and 42

[b]Error estimates are assumed.

[c]Error estimates are taken from Ref. 20.

[d]Error estimates for Ni and Cr are considered the same as for Fe. The (n,n′α) reaction is not considered for the Cr.

[e]Error estimates are taken from Ref. 29.

Table 6.8-29. Maximum Expected Error in Tritium Breeding (Li_2O Helium-Cooled Blanket)

Element	Cross Section Type Varied	Compensating Cross Section	$\delta R_{^6Li}/R_{^6Li}$ Cross Section Type Increased	$\delta R_{^6Li}/R_{^6Li}$ Cross Section Type Decreased	$\delta R_{^7Li}/R_{^7Li}$ Cross Section Type Increased	$\delta R_{^7Li}/R_{^7Li}$ Cross Section Type Decreased
Lithium-6	(n,α)t		1.95-1	-1.95-1	-2.92-2	2.92-2
		(n,elastic)	-3.62-2	3.62-2	5.31-2	-5.31-2
		(n,total)	-3.91-2	3.91-2	0.0	0.0
	Maximum δR/R		± 1.20-1		± 2.39-2	
Lithium-7	(n,n´α)t		-9.82-1	9.82-1	-1.06+1	1.06+1
		(n,elastic)	7.92-1	-7.92-1	-1.19	1.19
	Maximum δR/R		± 1.90-1		± 1.18+1	
Oxygen	(n,total)		1.14-1	-1.14-1	-3.04-1	3.04-1
	(n,elastic)[a]		2.30-1	-2.3-1	-1.13-1	1.13-1
	(n,γ)		-5.47-4	5.47-4	-3.03-5	3.03-5
	(n,p)		-3.48-1	3.48-1	-3.87-1	3.87-1
	(n,d)		-1.67-1	1.67-1	-1.86-1	1.86-1
	(n,α)		-1.51	1.51	-1.48	1.48
	(n,inelastic)[a]		1.05	-1.05	-5.45	5.45
	Maximum δR/R		± 3.31		± 7.9	

[a]Cross section varied such that maximum δR/R is estimated.

Table 6.8-29 (continued)

Element	Cross Section Type Varied	Compensating Cross Section Type	$\delta R_{^6Li}/R_{^6Li}$ Cross Section Type Increased	$\delta R_{^6Li}/R_{^6Li}$ Cross Section Type Decreased	$\delta R_{^7Li}/R_{^7Li}$ Cross Section Type Increased	$\delta R_{^7Li}/R_{^7Li}$ Cross Section Type Decreased
Iron	(n,2n)		1.27	-1.27	-9.46-1	9.46-1
	(n,n'α)		2.04-3	-2.04-3	-1.10-2	1.10-2
	(n,n'p)		2.80-2	-2.80-2	-1.52-1	1.52-1
	(n,absorption)		-4.66-1	4.66-1	-4.72-1	4.72-1
	(n,inelastic)		3.25-1	3.25-1	-1.72	1.72
		(n,elastic)	-1.71-1	1.71-1	2.12-2	-2.12-2
	Maximum δR/R		± 9.91-1		± 3.28	
Nickel	(n,2n')		9.47-2	-9.47-2	-7.03-2	7.03-2
	(n,n'p)		1.14-2	-1.14-2	-6.14-2	6.14-2
	(n,absorption)		-3.02-1	3.02-1	-3.03-1	3.72-1
	(n,inelastic)		7.02-2	-7.02-2	-3.72-1	3.72-1
		(n,elastic)	-4.22-2	4.22-2	4.89-3	-4.89-3
	Maximum δR/R		± 1.68-1		± 8.01-1	
Chromium	(n,2n')		2,38-1	-2.38-1	-1.76-1	1.76-1
	(n,n'α)		2.01-4	-2.01-4	-1.17-3	1.17-3
	(n,n'p)		4.54-3	-4.54-3	-2.53-2	2.53-2
	(n,absorption)		-7.97-2	7.97-2	-8.05-2	8.05-2
	(n,inelastic)		4.52-2	-4.52-2	-1.72-1	1.72-1
		(n,elastic)	-3.51-2	3.51-2	3.71-3	-3.71-3
	Maximum δR/R		± 1.73-1		± 4.51-1	
	$\delta R_i/R_i$ (Maximized to $\delta R_{^6Li}$)		± 4.95		±16.79	
	$\delta R_i/R_i$ (Maximized to $\delta R_{^7Li}$)		± 2.62		±24.26	
	$\left(\frac{\delta R_{Li}}{R_{Li}}\right)^a_{max}$		± 8.9% ± 9.8%			

[a] $R_{^6Li}$ = 0.8026, $R_{^7Li}$ = 0.4253, R_{Li} = 1.2279, i = ^{6}Li or ^{7}Li

entry "maximum δR/R" shown in this table for each element either has a positive or negative contribution to the total δR/R. If the contribution to $\delta R_{^6Li}/R_{^6Li}$ from each element are added in one direction (positive or negative) such that the change in $R_{^6Li}$ is maximum, we arrive at the value identified by the entry "$\delta R_{^6Li}/R_{^6Li}$ (maximized to $\delta R_{^6Li}$)" shown in the table. The value for $\delta R_{^7Li}/R_{^7Li}$ in this treatment is consistent with the sign used in maximizing $\delta R_{^6Li}$. Also shown in Table 6.8-29 is the corresponding values when $\delta R_{^7Li}$ is maximized. When the values for T_6 and T_7 are considered, we arrive at the expected deviation in the total TBR given in the last entry of the table for the two cases where $\delta R_{^6Li}$ and $\delta R_{^7Li}$ are maximized individually.

A comparison of the results obtained from both the statistical and non-statistical treatment for cross-sections uncertainties is shown in Table 6.8-30. It is clear from this table that the statistical treatment where the covariance in the cross-section errors are considered tends to decrease the estimate for the uncertainty in the total TBR as compared to the values obtained from the non-statistical treatment. In addition and consistent with the statistical treatment results, the Li_2O blanket exhibits the largest uncertainty in the TBR with a value of ~ 10%. This relatively large value is a point of concern in designing blankets that utilize Li_2O as a breeder since this blanket type has the smallest TBR value as compared to the other blankets. The larger values in the uncertainty in the TBR obtained from the non-statistical treatment can be viewed as conservative estimates although the statistical treatment results are more realistic.

6.8.6.6 Estimates for the Uncertainty in the Tritium Breeding Ratio for Other Blanket Concepts

Estimates for the uncertainty in the TBR, Δ_D, arising from cross-section uncertainties in other blanket concepts are summarized in Table 6.8-31. The blanket concepts shown in this table are those rated to have more plausible features than others. The values cited are based on anticipated estimates as explained in the comments included in that table. As shown, the range of the uncerainty in the TBR due to data base uncertainties is between 2 and 6% in all the blanket concepts considered.

6.8-30. Estimates of the Uncertainty in TBR Due to Uncertainty in Nuclear Data Base in Four Blanket Concepts

Method \ Blanket Concept	Li_2O/He/PCA	LiPb/LiPb/PCA	$LiAlO_2$/H_2O/FS/Be	Flibe/He/FS/Be
<u>Statistical Treatment</u>				
• Errors are correlated	± 4.92%	±3.95%	±2.1%	±3.41%
• Errors are not correlated	± 4.78%	±3.80%	±1.74%	±2.67%
<u>Non-Statistical Treatment</u>				
• $(\delta R_{^6Li}/R_{^6Li})$ maximized	± 9.05%	±4.70%	±6.30%	±7.54%
• $(\delta R_{^7Li}/R_{^7Li})$ maximized	±10.12%	±1.49%	±1.82%	±4.31%

Table 6.8-31. Estimate of the Uncertainty Associated with Tritium Breeding Ratio, $\Delta_D = \Delta T/T$, in Various Blanket Concepts due to Uncertainties Associated with Nuclear Data Base

No.	Blanket Concept	Range of Δ_D (%)	Comments
1	Li_2O/He/PCA	~ 4.9	Based on extensive, detailed cross-section sensitivity/uncertainty analysis. Statistical error propagation was considered. Higher values are obtained with non-statistical cross-section error treatment.
2	LiPb/LiPb/PCA	~ 3.9	See comment on blanket no. 1.
3	$LiAlO_2$/H_2O/FS/Be	~ 2.1	See comment on blanket no. 1.
4	Flibe/He/FS/Be	~ 3.4	See commend on blanket no. 1.
5	Li/Li/V	~ 6	Taken from Ref. 25. In the treatment cited in this reference, no cross-section uncertainty correlation was considered.
6	Li/Li/FS	~ 5.5	Assumed that the uncertainty in TBR is 0.5% less than the Li/Li/V case, since cross-section for ferritic steel constituent (mainly Fe, Ni) is better known than for V.
7	Li/He/FS	~ 5	Assumed same as in the Li/Li/FS blanket less ~ 0.5% due to replacing Li by He coolant.
8	$LiAlO_2$/He/FS/Be	~ 2	Assumed same as in blanket no. 3 less 0.1% due to the contribution from errors associated with H_2O cross section.
9	$LiAlO_2$/DS/FS/Be	~ 1.9	Based on normalizing the contribution to the TBR uncertainty in blanket no. 8 from Be, O, Al, and FS to the weight of these materials in the draw salt (DS) blanket. Contributions from the DS coolant were not considered.
10	LiPb/LiPb/V	~ 4.4	Additional value of 0.5% was added to the uncertainty in TBR of blanket no. 2 for reason explained in comments on blanket no. 6.

6.8.6.7 Conclusions on Nuclear Data Uncertainty

Three out of the four blankets considered in this study utilize a neutron multiplier, lead in the LiPb blanket and beryllium in both the $LiAlO_2$ and the flibe blanket. Consequently, it was found from both the sensitivity and the uncertainty analysis that the uncertainty in tritium breeding from ^6Li (the dominant contributor to the total breeding ratio, TBR, in these three blankets) is due mainly to uncertainties associated with multiplying reactions such as the Pb(n,2n'), Pb(n,3n'), and ^9Be(n,2n') cross-sections.

For the flibe and the $LiAlO_2$ blankets, and aside from the uncertainty associated with the total angle-integrated cross-sections, it was found that upon utilizing the latest evaluation for the ^9Be(n,2n') provided by LANL, a decrease of ~ 4.3% in the TBR is obtained in the flibe blanket as compared to the results with the current ^9Be(n,2n') cross-section implemented in both the ENDF/B-IV and V evaluations. Therefore, improving the representation of the energy-angle distribution for the secondary neutrons in a multiplying reaction can lead to a substantial change in the tritium breeding.

As it has been shown in this study, the uncertainty analysis reveals in some cases different results from the sensitivity analysis. Example of such differences is the case of oxygen. While the sensitivity analysis performed on the Li_2O blanket shows that tritium breeding from ^6Li is least sensitive to variation in the oxygen cross-sections, the uncertainty analysis has revealed that the current uncertainties in the oxygen cross-sections lead to ~ 75% contribution to the variance in T_6. In addition, the same uncertainties in oxygen cross-sections contributed only ~ 2% to the variance in T_6 in the $LiAlO_2$ blanket. This demonstrates that the uncertainty analysis is highly system-dependent.

The present uncertainties in the ^6Li cross-sections seem adequate for predicting the TBR in all the blankets studied. Furthermore, no further improvement is needed in the ^7Li cross-sections except for the case where Li_2O is used as a breeder since the uncertainties in the $^7Li(n,\alpha n')t$ contributes by about 96% to the variance in T_7 in this blanket and almost 50% of the total breeding comes from this reaction. It has also been shown that the Li_2O blanket exhibits the largest uncertainty in tritium breeding (~ 5%) as compared to other blankets. As pointed out earlier, this presents a point of

concern especially because the Li_2O blanket has the lowest TBR values in comparison to the achievable TBR in other blankets.

Considering other blanket concepts, it seems that the uncertainty in tritium production, Δ_D, arising from the uncertainties in nuclear data base is ~ 2 to 6%. Our estimates for Δ_D based on statistical treatment and correlation among uncertainties give smaller results than those obtained from the non-statistical treatment. The values obtained in the later case can be considered as conservative limits.

The uncertainty evaluations given in the present work are limited for two reasons. First, perturbation theory was applied and the results are limited by the limitation inherent in this method.[6.8-30,-43,-44] Second, the uncertainty analysis results are based only on the available data regarding the uncertainty in the total angle-integrated cross-section as currently implemented in the error files of the ENDF/B-V. No error files are presently available for the uncertainty in the angle-energy distribution of the secondary neutrons emitted in neutron producing reactions. Theories and format to incorporate the uncertainties in these secondary distributions within the perturbation theory are currently in progress[45,46]. The results from direct evaluation with a different representation for the $^9Be(n,2n')$ cross-section emphasizes the importance of incorporating such uncertainties.

29. D. E. Bartine, et al., "Radiation-Transport Cross Section Sensitivity Analysis: A General Approach Illustrated for a Na-Fe System," Oak Ridge National Laboratory, ORNL/TM-3944 (1972).

30. S. A. Gerstl and W. M. Stacey, "A Class of Second-Order Approximate Formulation of Deep Penetration Radiation Transport Problems," Nucl. Sci. Eng., 51, 339 (1973).

31. F. G. Perey, "The Data Covariance Files for ENDF/B-V," Oak Ridge National Laboratory, ORNL/TM-5938 (1977).

32. M. A. Abdou, et al., "A Blanket Comparison and Selection Study--Interim Report," Argonne National Laboratory, ANL/FPP-83-1 (1983).

33. "VITAMIN-C: 171 Neutron, 36 Gamma Group Cross Section Library in AMPX Interface Format for Fusion Neutronics Studies," Package DLC-41, ORNL (1978).

34. N. M. Green, et al., "AMPX: A Modular Code System for Generating Coupled Multi-Group Neutron and Gamma Libraries from ENDF/B," Oak Ridge National Laboratory, ORNL/TM-3706 (1976).

35. D. E. Bartine, et al., "SWANLAKE-A Computer Code Utilizing ANISN Transport Calculations for Cross-Section Sensitivity Analysis," Oak Ridge National Laboratory, ORNL/TM-3809 (1973).

36. R. G. Young, private communication, Los Alamos National Laboratory (1980).

37. D. M. Drake, et al, Nucl. Sci. Eng., 63, 401 (1977).

38. T. K. Basu, et al., Nucl. Sci. Eng., 70, 307 (1979).

39. R. T. Howerton and S. T. Perkins, "Evaluated Neutron Interaction and Gamma-Ray Production Cross Section for ^{9}Be for ENDF/B-IV Mat. No. 1289," Lawrence Livermore National Laboratory, UCRL-51603 (1974).

40. R. C. Young and L. Stewart, private communication, Los Alamos National Laboratory (1979)

41. F. O. Purser, private communication, Triangle Universities Nuclear Laboratory (1976).

42. D. Steiner and M. Tobias, "Cross Section Sensitivity of Tritium Breeding in a Fusion Reactor Blanket: Effect of Uncertainties in Cross Sections of ^{6}Li, ^{7}Li, and ^{93}Nb, Nucl. Fusion, 14, 153-163 (1974).

43. M. Embrechts, "Two-Dimensional Cross-Section Sensitivity and Uncertainty Analysis for Fusion Reactor Blankets," Los Alamos National Laboratory, LA-9232-T (1982).

44. T. Wu, and C. W. Maynard, "Higher-Order Sensitivity Theory and Non-Linear Optimization in Fusion Neutronics Studies," University of Wisconsin, UWFDM-402 (1981).

45. S. A. W. Gerstl, "Uncertainty Analysis for Secondary Energy Distributions," Proc. of the Seminar-Workshop on Theory and Application of Sensitivity and Uncertainty Analysis, August 22-24, 1978, Oak Ridge, TN, ORNL/RSIOC-42 (1979). See also, D. W. Muir, "Applied Nuclear Data Research and Development, April 1-June 30, 1977," Los Alamos National Laboratory, LA-6971-PR (1977).

46. M. Youssef, private communication, University of California, Los Angeles (1983).

BLANKET COMPARISON AND SELECTION STUDY

SECTION 6.9

IMPACT OF THE REACTOR DESIGN CHOICES ON THE NEUTRONICS PERFORMANCE OF THE TOKAMAK BLANKET CONCEPTS

SECTION 6.9

TABLE OF CONTENTS

PAGE NO.

6.9 Impact of the Reactor Design Choices on the Neutronics Performance of the Tokamak Blanket Concepts.....6.9-1

6.9.1 Computational Models.....6.9-1

6.9.2 Tritium Breeding and Energy Deposition Analyses.....6.9-7

REFERENCES.....6.9-16

LIST OF FIGURES FOR SECTION 6.9

FIGURE NO.	TITLE	PAGE NO.
6.9-1	Reactor geometrical model with a tritium breeding blanket for the inboard and the outboard sections	6.9-4
6.9-2	Reactor geometrical model with an outboard tritium breeding blanket and an inboard steel blanket	6.9-4
6.9-3	Reactor geometrical model with a tritium breeding blanket for the inboard and the outboard sections and a bottom limiter	6.9-5
6.9-4	Reactor geometrical model with an outboard tritium breeding blanket, and inboard steel blanket and a bottom limiter	6.9-5
6.9-5	Geometrical model for the carbon/copper/ water bottom limiter	6.9-6
6.9-6	Divertor geometrical model	6.9-6

LIST OF TABLES FOR SECTION 6.9

TABLE NO.	TITLE	PAGE NO.
6.9-1	BLANKET PARAMETERS	6.9-2
6.9-2	LIMITER PARAMETERS	6.9-3
6.9-3	DIVERTOR PARAMETERS	6.9-7
6.9-4	BLANKET PERFORMANCE PARAMETERS FROM THE DIFFERENT GEOMETRICAL MODELS WITH A TRITIUM BREEDING CAPABILITY IN THE BOTH REACTOR SECTIONS AND WITHOUT AN IMPURITY CONTROL SYSTEM	6.9-8
6.9-5	IMPACT OF THE INBOARD BLANKET DESIGN AND THE LIMITER OPTION ON THE BLANKET PERFORMANCE	6.9-10
6.9-6	IMPACT OF THE LIMITER MATERIALS ON THE BLANKET PERFORMANCE	6.9-12
6.9-7	IMPACT OF THE IMPURITY CONTROL OPTION ON THE BLANKET PERFORMANCE	6.9-14
6.9-8	IMPACT OF THE NEUTRON SOURCE DISTRIBUTION ON THE BLANKET PERFORMANCE	6.9-15

6.9 Impact of Reactor Design Choices on the Neutronics Performance of Tokamak Blanket Concepts

Several studies were performed to quantify the impact of the impurity control system (limiter or divertor), the material choice for the limiter, the elimination of tritium breeding capability from the inboard section of tokamak reactors, the coolant choice for the nonbreeding inboard blanket, and the neutron source distribution on the neutronics performance of tokamak blanket concepts. A self-cooled liquid metal (lithium or lithium-lead) blanket was considered with a steel (PCA type) structure. Helium or water was the coolant for the non-breeding blanket in the inboard section. The analysis used two limiter blade designs to assess the sensitivity of the limiter design on blanket performance. Two neutron source distributions were used in the calculations to study the impact on the results. The three-dimensional Monte Carlo code MORSE was used for the transport calculations with a 67-multigroup cross section data set. The blanket parameters, the geometrical models, and the results from these studies are discussed in this section.

6.9.1 Computational Models

Two self-cooled liquid metal blanket concepts with different breeder materials were used for this study. The breeder materials are natural liquid lithium and lithium-lead (17Li-83Pb) with 90% lithium-6 enrichment. The PCA steel alloy is the structure and the reflector material. Table 6.9-1 gives the blanket parameters for the inboard and the outboard sections of the reactor. The inboard and the outboard blanket thicknesses are 60 and 90 cm thick, respectively. The breeding blanket has the same composition as the self-cooled liquid lithium reference blanket designed for tokamak reactors. The nonbreeding blanket has a composition of 90% PCA steel and 10% coolant by volume. Water and helium coolants were considered for this blanket. A steel shield behind the blanket was employed to insure correct boundary conditions for the neutrons and photons at the blanket boundary in the transport calculations.

Two limiter blade designs were used in the analysis. The first limiter design has a copper structure material, a water coolant, and a carbon tile, which is judged unsatisfactory for liquid metal blanket concepts but is included here for comparison purposes. The second limiter design uses a

TABLE 6.9-1. BLANKET PARAMETERS

Zone Description	Zone Thickness (cm)	Zone Composition (vol-%)
	Breeding Blanket	
First wall	1	50% PCA, 50% liquid metal[a]
Breeder		
Inboard	40	7.5% PCA, 92.5% liquid metal[a]
Outboard	60	7.5% PCA, 92.5% liquid metal[a]
Reflector		
Inboard	20	90% PCA, 10% liquid metal[a]
Outboard	30	90% PCA, 10% liquid metal[a]
	Nonbreeding Blanket	
Inboard	60	90% PCA, 10% coolant[b]
	Shield	
Inboard/Outboard	--	90% Fe1422 steel alloy, 10% coolant

[a]Natural lithium or 17Li-83Pb with 90% lithium-6 enrichment.
[b]H_2O or helium.

liquid metal coolant with a vanadium (V15Cr5Ti alloy) structure and a beryllium tile. Table 6.9-2 gives the dimensions and the compositions for the two blades. The divertor design uses only a liquid metal plate design shown in Table 6.9-3.

Several geometrical models were developed based on the STARFIRE design. The first geometrical model assumes a tritium breeding blanket for the outboard and the inboard sections of the reactor without an impurity control system as shown in Fig. 6.9-1. The second geomtrical model is similar to the first except a non-breeding blanket is used for the inboard section as shown in Fig. 6.9-2. A bottom limiter was added for both models to study the impact on the blanket performance as shown in Figs. 6.9-3 and 6.9-4. The details of the limiter geometry are shown in Fig. 6.9-5. Also, a single null divertor was used instead of the limiter as shown in Fig. 6.9-6. In addition, two one-

TABLE 6.9-2. LIMITER PARAMETERS

Parameters	First Design	Second Design
Coolant	H_2O	Lithium[a] or 17Li-83Pb[b]
Structural material	Copper	V15Cr5Ti alloy
Tile material	Carbon	Beryllium
Blade width, cm	72	72
Blade thickness, cm	4	6
Duct width, cm	57	57
Blade composition[d]	12.5 mm[c], 100% C 25.0 mm, 50% H_2O, 50% Cu 2.5 mm, 100% C	1.0 mm[c], 100% Be 1.5 mm, 100% V15Cr5Ti alloy 5.0 mm, 80% coolant, 20% V15Cr5Ti alloy 15.0 mm, 100% V15Cr5Ti alloy 5.0 mm, 80% coolant, 20% V15Cr5Ti alloy 1.5 mm, 100% V15Cr5Ti alloy 2.0 mm, 100% Be

[a]Natural lithium.

[b]90% lithium-6 enrichment.

[c]Surface facing the plasma.

[d]Volume percent.

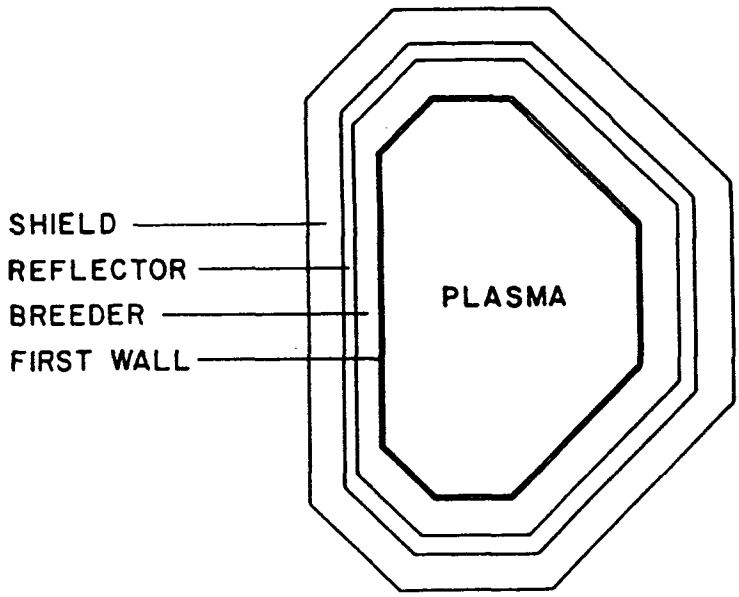


Figure 6.9-1. Reactor geometrical model with a tritium breeding blanket for the inboard and the outboard sections.

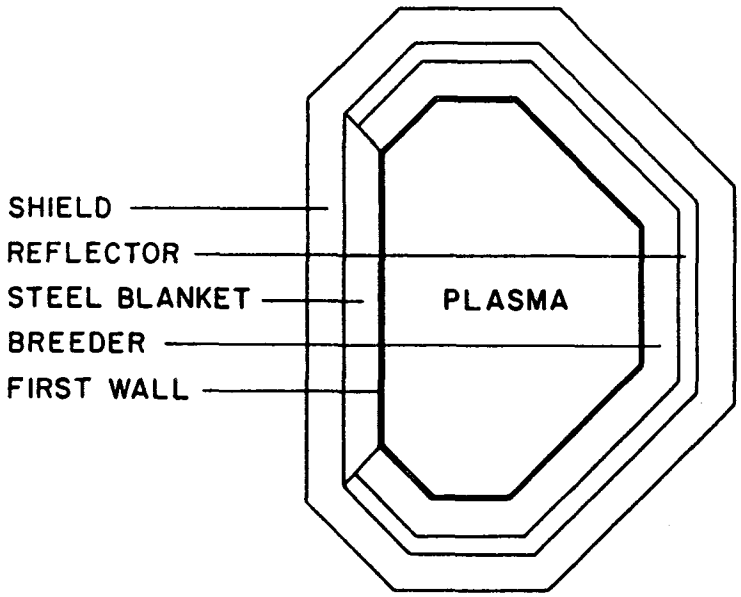


Figure 6.9-2. Reactor geometrical model with an outboard tritium breeding blanket and an inboard steel blanket.

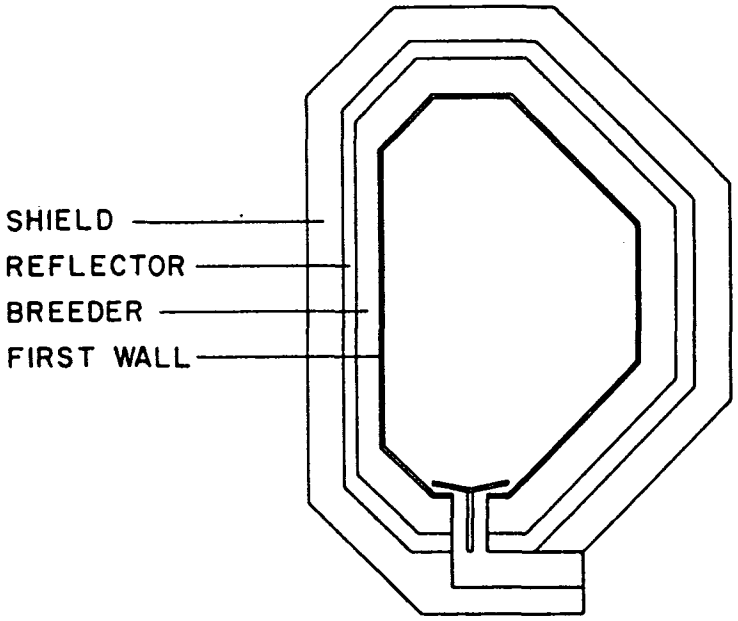


Figure 6.9-3. Reactor geometrical model with a tritium breeding blanket for the inboard and the outboard sections and a bottom limiter.

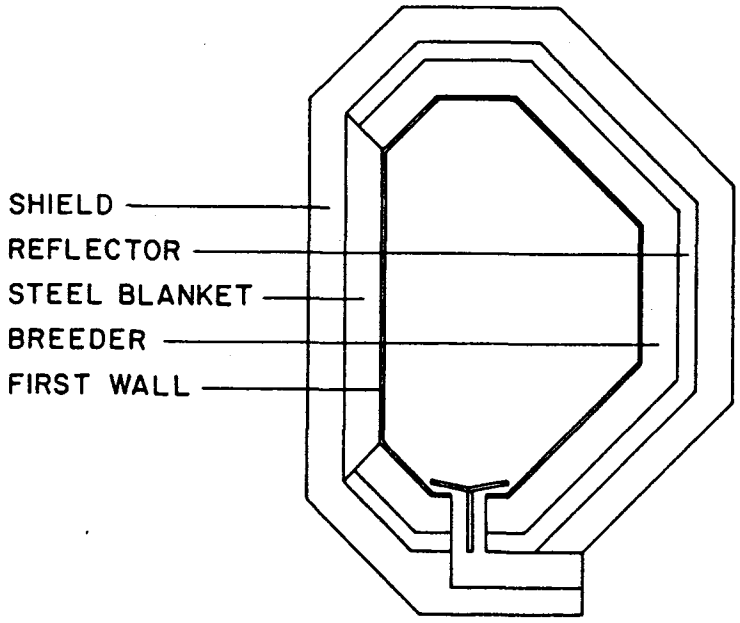


Figure 6.9-4. Reactor geometrical model with an outboard tritium breeding blanket, an inboard steel blanket and a bottom limiter.

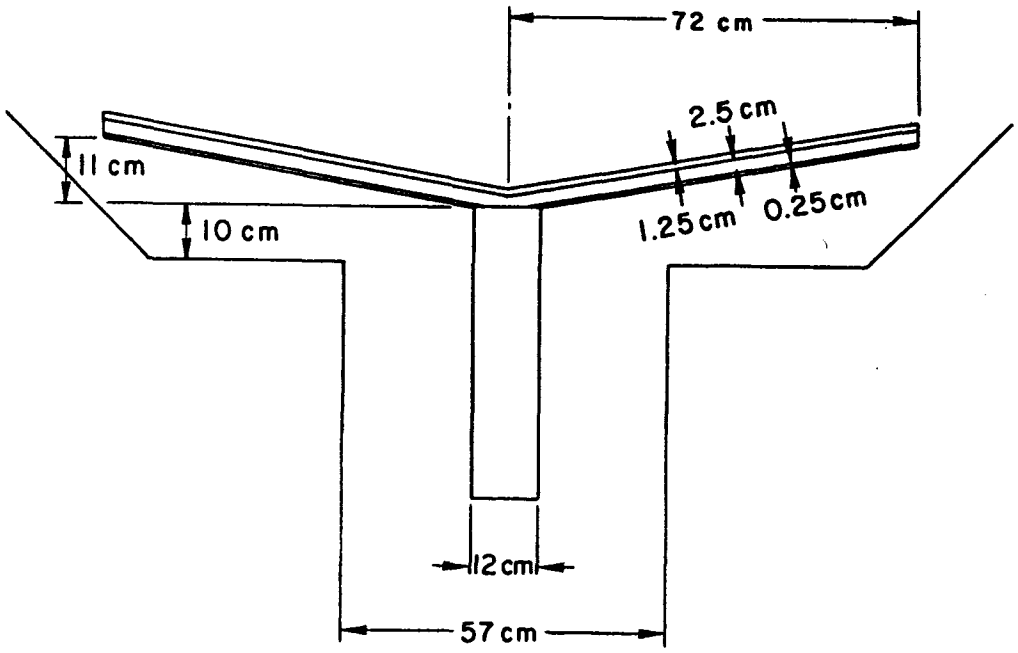


Figure 6.9-5. Geometrical model for the carbon/copper/water bottom limiter.

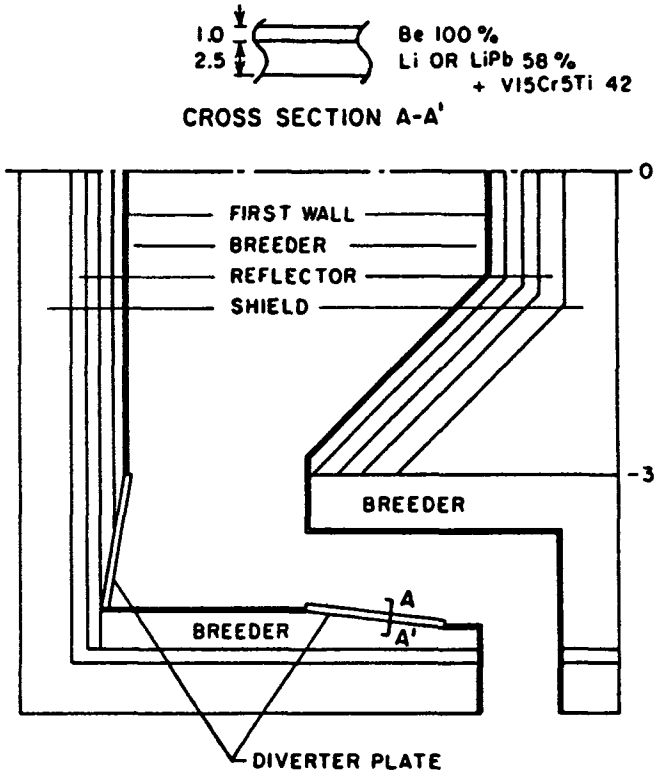


Figure 6.9-6. Divertor geometrical model.

dimensional models were developed to compare the one- and three-dimensional results for the cases with a tritium breeding capability for both blanket sections and without an impurity control system.

The three-dimensional Monte-Carlo code MORSE[6.9-1] was used to perform most of the tranpsort calculations with a P_3 approximation for the scattering cross sections. For the two one-dimensional geometrical models, the discrete ordinates code ANISN[6.9-2] was used instead with P_3S_8 approximations. A 67-coupled group cross-section data library (46 neutron and 21 gamma) based on ENDF/B-IV was employed for these calculations. This data library is based on the VITAMIN-C[6.9-3] and the MACKLIB-IV[6.9-4] libraries.

TABLE 6.9-3. DIVERTOR PARAMETERS

Coolant	Lithium[a] or 17Li-83Pb[b]
Structural material	V15Cr5Ti alloy
Tile material	Beryllium
Blade thickness, cm	3.5
Blade composition[c]	1.0 cm, 100% beryllium 2.5 cm, 58% coolant, 42% V15Cr5Ti alloy

[a]Natural lithium.

[b]90% lithium-6 enrichment.

[c]Volume percent.

6.9.2 Tritium Breeding and Energy Deposition Analyses

The reactor geometrical models without an impurity control system and with a tritium breeding capability in the inboard section were used to calculate the blanket performance parameters. The results from the ANISN calculations show that the poloidal and the toroidal geometrical models predict very similar values for the tritium breeding ratio (TBR) and the blanket energy deposition (BED) as shown in Table 6.9-4.[6.9-5] In fact, the poloidal model does not account for the smaller inboard blanket thickness which causes about a 1% increase in the TBR and about a 1% decrease in the BED. This is due to the increase in the neutron absorption rate in the steel which deposits more

TABLE 6.9-4. BLANKET PERFORMANCE PARAMETERS FROM THE DIFFERENT GEOMETRICAL MODELS WITH A FULL TRITIUM BREEDING BLANKET AND WITHOUT AN IMPURITY CONTROL SYSTEM

	A. Lithium Breeder			
Geometrical model	1-D poloidal	1-D toroidal	1-D toroidal	3-D
Transport code	ANISN	ANISN	ANISN	MORSE
Neutron source distribution	Uniform	Uniform	Peaked	STARFIRE
$^{6}Li(n,\alpha)T$ reaction rate per DTn	0.906	0.909	0.905	0.880
$^{7}Li(n,n'\alpha)T$ reaction rate per DTn[a]	0.470	0.463	0.464	0.479
Tritium breeding ratio	1.376	1.372	1.369	1.359
Blanket energy deposition, MeV/DTn	18.79	18.95	18.89	18.78
Shield energy deposition, MeV/DTn	0.28	0.44	0.43	0.40
	B. Lithium-Lead Breeder			
Geometrical model	1-D poloidal	1-D toroidal	1-D toroidal	3-D
Transport code	ANISN	ANISN	ANISN	MORSE
Neutron source distribution	Uniform	Uniform	Peaked	STARFIRE
$^{6}Li(n,\alpha)T$ reaction rate per DTn	1.648	1.632	1.631	1.606
$^{7}Li(n,n'\alpha)T$ reaction rate per DTn[a]	0.003	0.003	0.003	0.003
Tritium breeding ratio	1.651	1.635	1.633	1.609
Blanket energy deposition, MeV/DTn	17.48	17.67	17.60	17.07
Shield energy deposition, MeV/DTn	0.20	0.39	0.39	0.30

[a]The values are reduced by 15% to account for the change in the ^{7}Li cross sections.

energy than absorption in the lithium. The main difference between the results from both models is in the prediction of the shield energy deposition (SED) as shown in Table 6.9-4. For the reactor under consideration, the poloidal model underestimates the SED by a factor of two relative to the toroidal model and the 3-D model.

Two neutron source distributions, a uniform source and a peaked source at the plasma center, were employed for the ANISN calculations with the toroidal model. The results show that the tritium breeding and the energy deposition are not affected by the change in the neutron source spatial distribution as shown in Table 6.9-4.

A MORSE calculation for the first geometrical model shown in Fig. 6.9-1 with the STARFIRE neutron source distribution was performed to compare with the one-dimensional calculations. The results given in Table 6.9-4 show that the MORSE results are in good agreement with the one-dimensional toroidal results calculated by ANISN. For example, the relative difference in the TBR is 0.7% which is less than the statistical error in the Monte-Carlo calculations. In all of the Monte Carlo calculations, the fractional standard deviations are less than 1.5 and 3% for the TBR and the energy deposition respectively.

Several MORSE calculations were performed to study the change in the TBR and the energy deposition which resulted from the design options selected for the inboard blanket and the impurity control system. Three design options were considered for the inboard blanket. The first option assumes a tritium breeding capability and uses the same materials as the outboard blanket. The other two options have no tritium breeding capability and use He or H_2O as a coolant. Two limiter blade designs were considered in the analysis as shown in Table 6.9-2. The divertor option uses a liquid metal coolant similar to the second limiter design as shown in Table 6.9-3. The results in Table 6.9-5 address the impact of the copper limiter (carbon tile, copper structure, and water coolant) and the different inboard blanket designs on the TBR and the energy deposition in the lithium or the lithium-lead blanket concepts.

The results from the MORSE calculations show that the use of the copper limiter reduces the TBR by 4% and 5% for the lithium and the lithium-lead blanket concepts, respectively. This conclusion is consistent with the previous analysis for a Li_2O blanket performed for FED/INTOR.[6.9-6] Also, the BED is reduced and the SED is increased significantly as shown in Table 6.9-5.

TABLE 6.9-5. IMPACT OF THE INBOARD BLANKET DESIGN AND THE LIMITER OPTION ON THE BLANKET PERFORMANCE

A. Lithium Breeder				
Inboard blanket materials	Li/PCA	Li/PCA	PCA/H_2O	PCA/He
Computational model	3-D/MORSE	3-D/MORSE	3-D/MORSE	3-D/MORSE
Neutron source distribution	STARFIRE	STARFIRE	STARFIRE	STARFIRE
Impurity control option	None	Cu-limiter	Cu-limiter	Cu-limiter
$^6Li(n,\alpha)T$ reaction rate per DTn	0.880	0.852	0.739	0.781
$^7Li(n,n'\alpha)T$ reaction rate per DTn[a]	0.479	0.453	0.389	0.389
Tritium breeding ratio	1.359	1.305	1.123	1.170
Blanket energy deposition, MeV/DTn	18.78	18.02	18.53	18.26
Shield energy deposition, MeV/DTn	0.40	0.51	0.35	0.46
B. Lithium-Lead Breeder				
Inboard blanket materials	17Li-83Pb/PCA	17Li-83Pb/PCA	PCA/H_2O	PCA/He
Computational model	3-D/MORSE	3-D/MORSE	3-D/MORSE	3-D/MORSE
Neutron source distribution	STARFIRE	STARFIRE	STARFIRE	STARFIRE
Impurity control option	None	Cu-limiter	Cu-limiter	Cu limiter
$^6Li(n,\alpha)T$ reaction rate per DTn	1.606	1.522	1.228	1.294
$^7Li(n,n'\alpha)T$ reaction rate per DTn[a]	0.003	0.003	0.002	0.002
Tritium breeding ratio	1.609	1.525	1.230	1.296
Blanket energy deposition, MeV/DTn	17.07	16.65	17.71	17.26
Shield energy deposition, MeV/DTn	0.30	0.43	0.29	0.41

[a]The values are reduced by 15% to account for the change in the ^7Li cross sections.

For both blanket concepts, the inboard blanket was changed and the blanket performance parameters are given in Table 6.9-5. The PCA/H_2O inboard blankets with the copper limiter has the largest impact on the TBR, the reductions are 17% and 24% for the lithium and the lithium-lead blanket concepts, respectively, relative to the full breeding case without the limiter. Comparing both blanket concepts, the lithium-lead blanket has a softer neutron spectrum which makes this blanket concept sensitive to changes in the plasma chamber. For the steel/H_2O inboard blanket and the lithium-lead blanket concept, the reduction in the TBR is proportional to the reduction in the surface area available for the tritium breeding. The BED is increased by about 4% which results from the exothermic absorption of the low energy neutrons in the steel structure and less leakage to the shield. The corresponding impact for the helium coolant case instead of water in the inboard blanket is a factor of two less because the neutron spectrum is harder. For example, the TBR is 1.3 for the reactor with the He cooled inboard blanket compared to 1.23 for water substituting for helium. Also, the helium case has 3% less energy in the blanket and 40% more energy deposited in the shield relative to the water case.

The same observations about the impact of the inboard blanket coolant are valid for to the lithium blanket concept. However, the BED decreases when the lithium is eliminated from the inboard blanket. This is the contrary to the results of the lithium-lead blanket concept. The increase in neutron streaming through the limiter duct is causing this reduction in the BED because of the harder neutron spectrum. The PCA/H_2O inboard blanket increases the BED by 0.5 MeV per DTn and reduces SED by 30% relative to the lithium inboard blanket.

The effect of the limiter design on blanket performance parameters was studied for both blanket concepts as shown in Table 6.9-6. For the lithium blanket concept, the use of a vanadium limiter (beryllium tile, V15Cr5Ti structure, lithium coolant) acts as a neutron multiplier region which cause an increase in the TBR and the BED. In addition, the vanadium alloy has a smaller neutron cross section relative to the copper which also improves the neutron economy. For the lithium-lead blanket concept, the effect of the limiter on the blanket performance is different because it is a thermal blanket with the lead neutron multiplier. The low absorption cross section of the vanadium structure relative to the copper causes an increase in the TBR. However, from

TABLE 6.9-6. IMPACT OF THE LIMITER MATERIALS ON THE BLANKET PERFORMANCE

A. Lithium Breeder				
Inboard blanket materials	Li/PCA	PCA/He	Li/PCA	PCA/He
Computational model	3-D/MORSE	3-D/MORSE	3-D/MORSE	3-D/MORSE
Neutron source distribution	STARFIRE	STARFIRE	STARFIRE	STARFIRE
Limiter structural material	Copper	Copper	V15Cr5Ti	V15Cr5Ti
$^{6}Li(n,\alpha)T$ reaction rate per DTn	0.852	0.781	0.891	0.805
$^{7}Li(n,n'\alpha)$ reaction rate per DTn[a]	0.453	0.389	0.456	0.397
Tritium breeding ratio	1.305	1.170	1.348	1.202
Blanket energy deposition, MeV/DTn	18.02	18.26	18.23	18.34
Shield energy deposition, MeV/DTn	0.51	0.46	0.49	0.39
B. Lithium-Lead Breeder				
Inboard blanket materials	17Li-83Pb/PCA	PCA/He	17Li-83Pb/PCA	PCA/He
Computational model	3-D/MORSE	3-D/MORSE	3-D/MORSE	3-D/MORSE
Neutron source distribution	STARFIRE	STARFIRE	STARFIRED	STARFIRE
Limiter structural material	Copper	Copper	V15Cr5Ti	V15Cr5Ti
$^{6}Li(n,\alpha)T$ reaction rate per DTn	1.522	1.296	1.551	1.334
$^{7}Li(n,n'\alpha)T$ reaction rate per DTn[a]	0.003	0.002	0.003	0.002
Tritium breeding ratio	1.525	1.296	1.554	1.336
Blanket energyb deposition, MeV/DTn	16.65	17.26	16.53	17.07
Shield energy deposition, MeV/DTn	0.43	0.41	0.41	0.38

[a]The values are reduced by 15% to account for the change in the ^{7}Li cross sections.

the energy multiplication point of view, the copper has a higher energy multiplication which leads to a higher BED as shown in Table 6.9-6.

The limiter and the divertor impurity control options with vanadium structure were considered together to compare their effect on both blanket concepts. Table 6.9-7 gives the blanket performance parameters for each impurity control option with different inboard blankets. The results show that the divertor option has a small advantage over the limiter. The TBR is about the same for both options. However, the BED is higher with the divertor because the neutron absorption rate in the vanadium structure is lower. This means more neutrons are absorbed in the steel structure which results in more energy due to the difference in the Q values of both materials. The reactor with a divertor produces about 4% more energy than the limiter case.

Table 6.9-8 gives the blanket performance parameters with the STARFIRE neutron source and a uniform spatial distribution over the same plasma volume. The results from both distributions are the same within the statistical errors of the Monte Carlo calculations which confirms the one-dimensional results discussed before.

TABLE 6.9-7. IMPACT OF THE IMPURITY CONTROL OPTION ON THE BLANKET PERFORMANCE

A. Lithium Breeder				
Inboard blanket materials	Li/PCA	PCA/He	Li/PCA	PCA/He
Computational model	3-D/MORSE	3-D/MORSE	3-D/MORSE	3-D/MORSE
Neutron source distribution	STARFIRE	STARFIRE	STARFIRE	STARFIRE
Impurity control option	Divertor	Divertor	Limiter	Limiter
Divertor or limiter structural material	V15Cr5Ti	V15Cr5Ti	V15Cr5Ti	V15Cr5Ti
$^{6}Li(n,\alpha)T$ reaction rate per DTn	0.877	0.776	0.891	0.805
$^{7}Li(n,n'\alpha)T$ reaction rate per DTn[a]	0.473	0.401	0.456	0.397
Tritium breeding ratio	1.350	1.177	1.347	1.202
Blanket energy deposition, MeV/DTn	18.56	18.93	18.23	18.34
Shield energy deposition, MeV/DTn	0.49	0.34	0.49	0.39
B. Lithium Lead Breeder				
Inboard blanket materials	17Li-83Pb/PCA	PCA/He	17Li-83Pb/PCA	PCA/He
Computational model	3-D/MORSE	3-D/MORSE	3-D/MORSE	3-D/MORSE
Neutron source distribution	STARFIRE	STARFIRE	STARFIRE	STARFIRE
Impurity control option	Divertor	Divertor	Limiter	Limiter
Divertor or limiter structural material	V15Cr5Ti	V15Cr5Ti	V15Cr5Ti	V15Cr5Ti
$^{6}Li(n,\alpha)T$ reaction rate per DTn	1.581	1.320	1.551	1.334
$^{7}Li(n,n'\alpha)T$ reaction rate per DTn[a]	0.002	0.003	0.003	0.002
Tritium breeding ratio	1.584	1.317	1.554	1.336
Blanket energy deposition, MeV/DTn	17.13	17.80	16.53	17.07
Shield energy deposition, MeV/DTn	0.38	0.36	0.41	0.38

aThe values are reduced by 15% to account for the change in the ^{7}Li cross sections.

TABLE 6.9-8. IMPACT OF THE NEUTRON SOURCE DISTRIBUTION ON THE BLANKET PERFORMANCE

A. Lithium Breeder				
Inboard blanket materials	Li/PCA	PCA/He	Li/PCA	PCA/He
Computational model	3-D/MORSE	3-D/MORSE	3-D/MORSE	3-D/MORSE
Neutron source distribution	Uniform	Uniform	STARFIRE	STARFIRE
Limiter structural material	V15Cr5Ti	V15Cr5Ti	V15Cr5Ti	V15Cr5Ti
$^{6}Li(n,\alpha)T$ reaction rate per DTn	0.891	0.827	0.891	0.805
$^{7}Li(n,n'\alpha)T$ reaction rate per DTn[a]	0.445	0.386	0.456	0.397
Tritium breeding ratio	1.336	1.213	1.347	1.202
Blanket energy deposition, MeV/DTn	18.05	18.36	18.23	18.34
Shield energy deposition, MeV/DTn	0.49	0.45	0.49	0.39
B. Lithium-Lead Breeder				
Inboard blanket materials	17Li-83Pb/PCA	PCA/He	17Li-83Pb/PCA	PCA/He
Computational model	3-D/MORSE	3-D/MORSE	3-D/MORSE	3-D/MORSE
Neutron source distribution	Uniform	Uniform	STARFIRE	STARFIRE
Limiter structural material	V15Cr5T	V15Cr5Ti	V15Cr5Ti	V15Cr5Ti
$^{6}Li(n,\alpha)T$ reaction rate per DTn	1.570	1.334	1.551	1.334
$^{7}Li(n,n'\alpha)T$ reaction rate per DTn[a]	0.003	0.002	0.003	0.002
Tritium breeding ratio	1.573	1.336	1.554	1.336
Blanket energy deposition, MeV/DTn	16.59	17.43	16.53	17.07
Shield energy deposition, MeV/DTn	0.47	0.41	0.41	0.38

[a]The values are reduced by 15% to account for the change in the ^{7}Li cross sections.

REFERENCES FOR SECTION 6.9

6.9-1 M. B. Emmett, "The MORSE Monte Carlo Radiation Transport Code System," Oak Ridge National Laboratory, ORNL-4872 (1975).

6.9-2 W. W. Engle, Jr., "A User's Manual for ANISN, A One-Dimensional Discrete Ordinate Code with Anisotropic Scattering," Oak Ridge Gaseous Diffusion Plant, ORGDP-K-1963 (1967).

6.9-3 R. W. Roussin, et al., "The CTR Processed Multigroup Cross Section Library for Neutronics Studies," Oak Ridge National Laboratory, ORNL/RCSIC-37 (1978).

6-9.4 Y. Gohar and M. A. Abdou, "MACKLIB-IV: A Library of Nuclear Response Functions Generated with MACK-IV Computer Program from ENDF/B-IV," Argonne National Laboratory, ANL/FPP/TM-106 (1978).

6.9-5 R. W. Conn, Y. Gohar and C. Y. Maynard," Two-Dimensional Neutron Transport Calculations in a Torus," Transaction of American Nuclear Society, Volume 44, 140 (1983).

6.9-6 Y. Gohard, "Limiter Impact on the Tritium Breeding Ratio in a FED/INTOR Reactor," Trans. Am. Nucl. Soc. 44, 140 (1983).

BLANKET COMPARISON AND SELECTION STUDY

SECTION 6.10 - MULTIDIMENSIONAL NUCLEAR ANALYSIS

SECTION 6.10

TABLE OF CONTENTS

PAGE NO.

6.10 Multidimensional Nuclear Analysis.....6.10-1
6.10.1 General Remarks.....6.10-1
6.10.2 Tritium Breeding and Energy Multiplication.....6.10-8
6.10.2.1 TMR Designs.....6.10-8
6.10.2.2 Tokamak Designs.....6.10-20
REFERENCES.....6.10-33

LIST OF FIGURES FOR SECTION 6.10

FIGURE NO.	TITLE	PAGE NO.
6.10-1	A vertical cross-section of tokamak design	6.10-3
6.10-2	A vertical cross-section of limiter design	6.10-5
6.10-3	System description of the TMR/Li-Li/V15Cr5Ti design	6.10-9
6.10-4	System description of the TMR/Li-Li-HT9 design	6.10-10
6.10-5	System description of the TMR/17Li-83Pb-17Li-83Pb-V15Cr5Ti design	6.10-11
6.10-6	System description of the TMR/γ-$LiAlO_2$/H_2O-HT9-Be design	6.10-12
6.10-7	System description of the TMR/Li-He-HT9 design	6.10-13
6.10-8	System description of the TMR/Li_2O-He-HT9 design	6.10-14
6.10-9	System description of the TMR/γ-$LiAlO_2$-He-HT9-Be design	6.10-15
6.10-10	System description of the TMR/γ-$LiAlO_2$-Draw Salt-HT9-Be design	6.10-16
6.10-11	System description of the TMR/FLIBE-He-HT9-Be design	6.10-17
6.10-12	System description of the tokamak/Li-Li-V15Cr5Ti design	6.10-22
6.10-13	System description of the tokamak/γ-$LiAlO_2$-H_2O-HT9-Be design	6.10-23
6.10-14	System description of the tokamak/Li-He-HT9 design	6.10-24
6.10-15	System description of the tokamak/Li_2O-He-HT9 design	6.10-25
6.10-16	System description of the tokamak/γ-$LiAlO_2$-He-HT9-Be design	6.10-26
6.10-17	System description of the tokamak/γ-$LiAlO_2$-Draw Salt-HT9-Be design	6.10-27
6.10-8	System description of the tokamak/FLIBE-He-HT9-Be design	6.10-28

LIST OF TABLES FOR SECTION 6.10

TABLE NO.	TITLE	PAGE NO.
6.10-1	THE RANK-1 BLANKET DESIGNS ANALYZED	6.10-1
6.10-2	THE CHARACTERISTICS TMR PARAMETERS RELEVANT TO NEUTRONICS ANALYSIS	6.10-2
6.10-3	THE CHARACTERISTIC TOKAMAK PARAMETERS RELEVANT TO NEUTRONICS ANALYSIS	6.10-4
6.10-4	MATERIAL COMPOSITIONS	6.10-7
6.10-5	NUCLEAR PERFORMANCE OF TMR CONCEPTS	6.10-18
6.10-6	A COMPARISON OF TRITIUM BREEDING PERFORMANCE EVALUATED BY MONTE-CARLO AND DISCRETE-ORDINATES METHODS	6.10-19
6.10-7	A COMPARISON OF TRITIUM BREEDING PERFORMANCE BASED ON ENDF/B-IV AND V DATA	6.10-21
6.10-8	NUCLEAR PERFORMANCE OF TOKAMAK CONCEPTS	6.10-29
6.10-9	THE IMPACT OF LIMITER AND RF DESIGNS ON TRITIUM BREEDING FOR TOKAMAK BLANKET DESIGNS	6.10-30
6.10-10	THE IMPACT OF LIMITER/RF DESIGN ON TRITIUM BREEDING FOR THE TOKAMAK/FLIBE-He-HT9-Be DESIGN	6.10-31

6.10 Multidimensional Nuclear Analysis

6.10.1 General Remarks

This section presents the nuclear analysis for the nine TMR designs and seven tokamak designs rated as "Rank-1" in the current BCSS study. These designs include the combinations of breeder, coolant and structural materials presented in Table 6.10-1. All the ternary ceramic designs and the FLIBE designs employ beryllium neutron multipliers in various forms and thicknesses.

TABLE 6.10-1.
THE RANK-1 BLANKET DESIGNS ANALYZED

	Breeder	Coolant	Structure
(A) TMR	Li	Li	V15Cr5Ti
	Li	Li	HT9
	17Li-83Pb	17Li-83Pb	V15Cr5Ti
	Li	He	HT9
	Li_2O	He	HT9
	γ-$LiAlO_2$	He	HT9
	γ-$LiAlO_2$	H_2O	HT9
	γ-$LiAlO_2$	Draw Salt	HT9
	FLIBE	He	HT9
(B) Tokamak	Li	Li	V15Cr5Ti
	Li	He	HT9
	Li_2O	He	HT9
	γ-$LiAlO_2$	He	HT9
	γ-$LiAlO_2$	H_2O	HT9
	γ-$LiAlO_2$	Draw Salt	HT9
	FLIBE	He	HT9

The basic geometrical configurations modeled for the present study are based on the MARS design[6.10-1] for the TMR concepts and on the STARFIRE[6.10-2] design for the tokamak concepts. The characteristic TMR parameters relevant to the neutronics analysis are summarized in Table 6.10-2.

TABLE 6.10-2.
THE CHARACTERISTIC TMR PARAMETERS RELEVANT TO NEUTRONICS ANALYSIS

• Central Cell Length	130 m
• Plasma Radius	0.49 m
• First-Wall Radius	0.60 m
• Fractional End Plug Fusion	2.5%
• Fractional Non-Breeding Area for Start-Up Heating	0.5%

The fractional end plug fusion mentioned in Table 6.10-2 stands for the ratio of the DT fusion taking place in the end plug regions to the total fusion power. Reference (6.10-3) cites a fusion power of about 80 MW in the end plug regions for a 3000 MW central-cell fusion plant. This estimate leads to a net breeding loss due to the external fusion, of ~2.6% (=80/3080) which is favorably compared to ~2.5% (=89/3500) derived in Ref. (6.10-4). The blanket area lost for start-up heating is estimated to be ~0.5% (=19/3500) in Ref. (6.10-4). Thus, the overall breeding loss that must be compensated for in the central blanket regions comes to ~3%.

The neutron leakage through the end cells is explicitly accounted for in the computation by assuming a 130-m long finite cyliner with vacuum boundary conditions at both ends.

The characteristic STARFIRE parameters used for the tokamak analyses are given in Table 6.10-3. The overall blanket configuration of the tokamak designs is illustrated in Fig. 6.10-1. The reference limiter for the present study is based on the FED/INTOR Phase-2A Study(6.10-5) published in 1982. This is a bottom limiter with a front surface area of ~90 m^2, a radial width of 2.0 m, the central axis located at a major radius of 6.34 m, and the leading edge positioned at ~2.56 m below the reactor midplane. The width of the limiter plenum is assumed to be 57 cm, resulting in a total opening area of ~23 m^2 at the first wall surface. This limiter design is subject to a total power load of 224 MW, or 2.5 MW/m^2. The reference limiter is constructed of a copper-alloy (Cu-2Be) heat-sink with water coolant, and a 10-mm beryllium coating on the front side facing the plasma. An alternate limiter design that

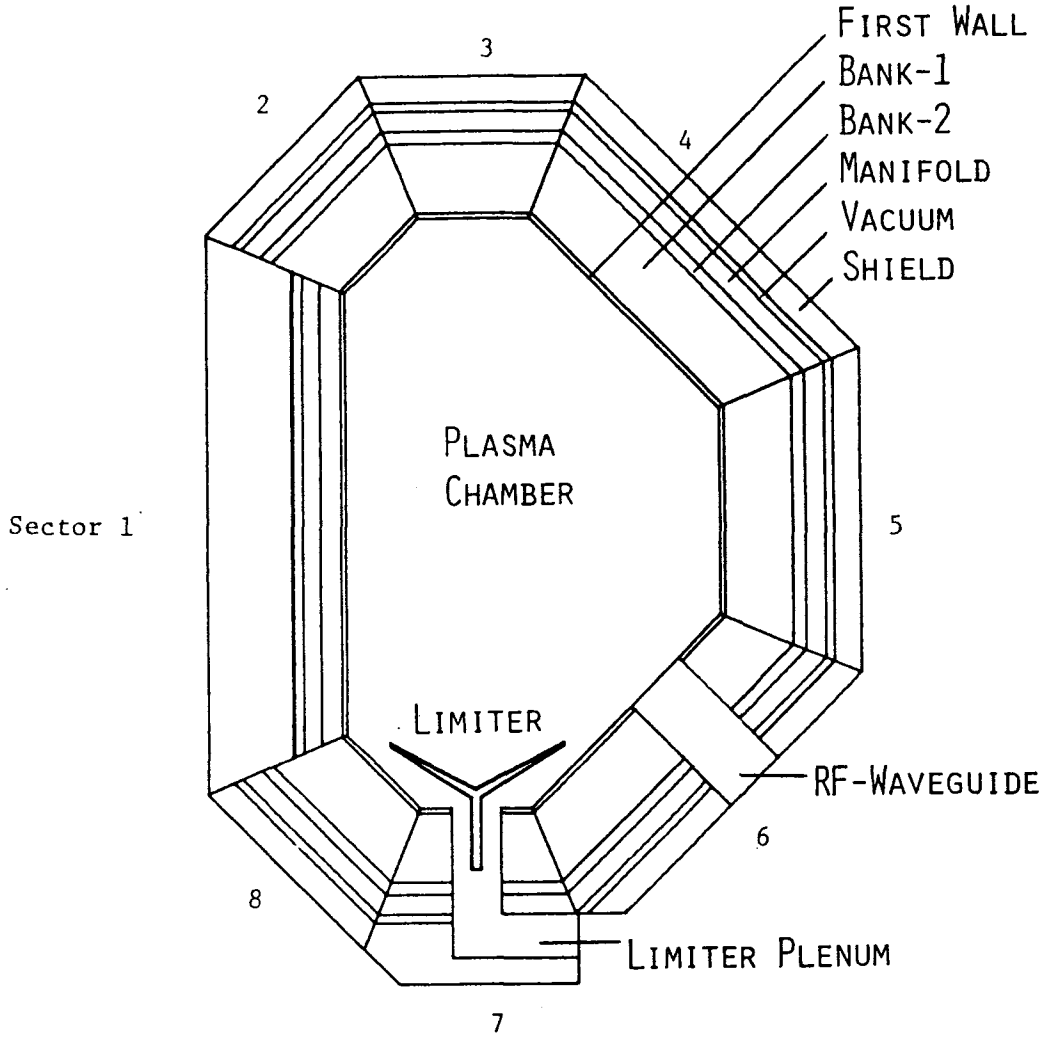


Figure 6.10-1. A vertical cross-section of tokamak design.

is used for the two liquid-lithium blanket concepts, Li/Li and Li/He, employs a lithium-cooled vanadium-alloy (V15Cr5Ti) heat-sink along with a 10-mm beryllium front coating. The back side and the vertical surface of both limiter designs are coated with 2-mm of beryllium. The thickness of the heat-sink materials is varied from 1.5 cm at the leading edge to 10 cm at the central-axis portion. A schematic view of the limiter designs is shown in Fig. 6.10-2.

TABLE 6.10-3.
THE CHARACTERISTIC TOKAMAK PARAMETERS RELEVANT TO NEUTRONICS ANALYSIS

• Plasma Major Radius	7.0 m
• Plasma Minor Radius	1.94 m
• Scrape-Off at Midplane	0.20 m
• Plasma Elongation Factor	1.6
• Plasma Triangularity Factor	0.5
• MHD Plasma Shift	0.79 m

The geometrical configuration of the RF-waveguide which penetrates perpendicularly through the lower outboard sector (Sector 6), is modeled after the STARFIRE design. This RF design is assumed to have a rectangular opening dimension of 68 cm (toroidal) × 77 cm (poloidal) and a smeared-out material composition of 53% HT9 + 8% H_2O + 39% void by volume. The duct length coincides with the total dimension of the first-wall, blanket and shield thicknesses. The center of the opening surface at the first wall is positioned at a major radius of 8.39 m and 1.9 m below the reactor midplane. There exist twelve RF-waveguides in the toroidal direction, located at thirty degree intervals. Although the water-cooled RF design might not be compatible with a certain class of the blanket designs (e.g., Li/Li), this single RF design is used for all the blanket concepts studied considering the relatively small RF area (~6.3 m^2) compared to the total first wall area of ~756 m^2.

The spatial dependence of the source neutron distribution for tokamak is assumed to be

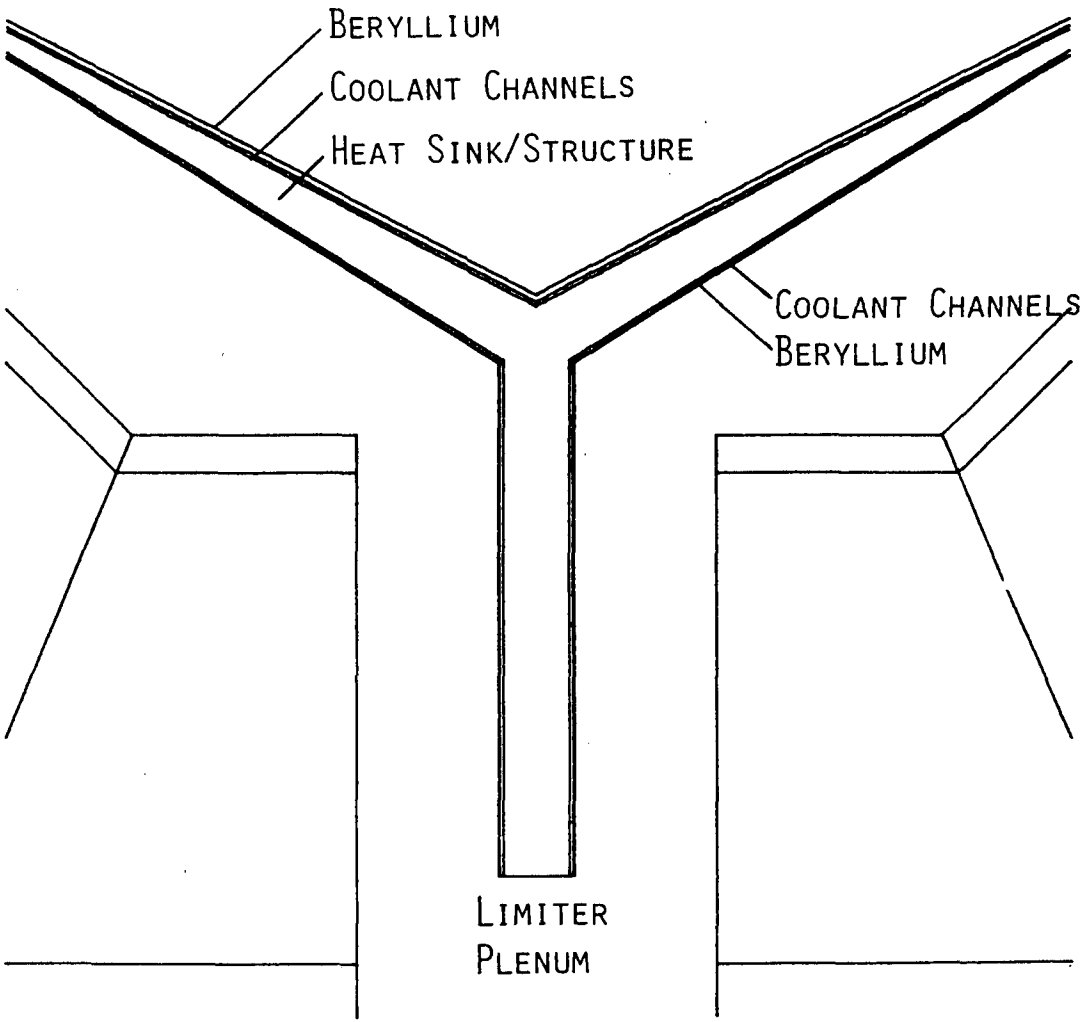


Figure 6.10-2. A vertical cross-section of limiter design.

$$f(r) \propto [1 - (r/r_m)^2]^2 \qquad [6.10\text{-}1]$$

taking into account the plasma shift due to the MHD equilibrium. The r and r_m stand, respectively, for the source point distance and the plasma boundary distance, both measured from the shifted plasma center of 7.79 m. The plasma boundary contour is determined by parametric equations with regard to parameter, t:

$$Z_b = a\kappa \sin t \qquad [6.10\text{-}2]$$

and

$$\rho_b = R_m + a \cos(t + d\sin t) \qquad [6.10\text{-}3]$$

where R_m is 7 m, Z_b is the boundary contour height in the direction perpendicular to the reactor midplane, and ρ_b is the major radius of the boundary contour. The constants, a, κ and d are the plasma minor radius (=1.94 m), the plasma elongation factor (=1.6) and the plasma triangularity (=0.5), respectively.

All multi-dimensional analyses were performed with a continuous-energy Monte-Carlo code, MCNP[6.10-6] [version 3], and its associated cross-section libraries based on the latest ENDF/B-V[6.10-7] data [RMCCS13/23 - MCPLIB2][6.10-8]. For the sake of comparison, the ENDF/B-IV[9] based MCNP libraries [XMCCS3] were also utilized. In addition, some complemental computations were performed using a one-dimensional discrete-ordinates transport code, ANISN,[6.10-10] with the $S_8 - P_3$ approximation.

Table 6.10-4 summarizes all material compositions used in the present study. Note that the lithium-6 enrichment is design dependent.

TABLE 6.10-4. MATERIAL COMPOSITIONS

@ 100% T.D.	Element	Atom/b-cm
Lithium[a]	^{6}Li	3.430-3
	^{7}Li	4.286-2
Li_2O[a]	^{6}Li	6.020-3
	^{7}Li	7.513-2
	O	4.058-2
γ-$LiAlO_2$[a]	^{6}Li	1.724-3
	^{7}Li	2.156-2
	Al	2.331-2
	O	4.661-2
17Li-83Pb[a]	^{6}Li	4.216-4
	^{7}Li	5.275-3
	Pb	2.715-2
FLIBE[a]	^{6}Li	1.135-3
	^{7}Li	1.420-2
	Be	1.729-2
	F	4.991-2
HT-9	Fe	7.058-2
	Cr	1.070-2
	Mo	4.833-4
V15Cr5Ti	V	5.754-2
	Cr	1.060-2
	Ti	2.835-3
Fe1422	Fe	7.028-2
	Mn	1.219-2
	Cr	1.849-3
	Ni	1.581-3
Cu-2Be	Cu	7.639-2
	Be	1.099-2
Nitrate Salt (60 % $NaNO_3$ - 40% KNO_3)	Na	7.823-3
	K	3.670-3
	N	1.149-2
	O	3.448-2
H_2O	H	6.686-2
	O	3.348-2
SiC	Si	4.834-2
	C	4.834-2
Beryllium	Be	1.236-1

aAssume naturally abundant lithium.

6.10.2 Tritium Breeding and Energy Multiplication

6.10.2.1 TMR Designs

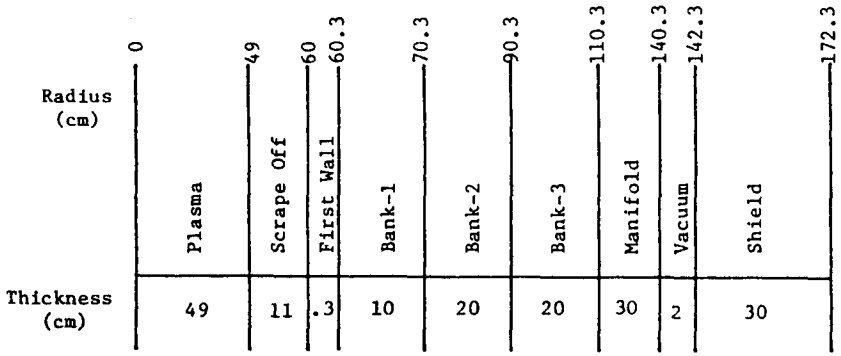
Figures 6.10-3 through 6.10-11 describe the nine TMR designs analyzed. The nuclear performance of these designs in terms of tritium production and energy deposition is summarized in Table 6.10-5. The evaluation is based on the MCNP Monte-Carlo method along with the ENDF/B-V data. Shown in Table 6.10-5 are the statistical mean values as estimated by MCNP for 10,000 neutron histories in each case. The standard deviation (although it is not indicated in the Table) has been estimated to be ~±1% or less.

All TMR blankets designed with beryllium neutron multipliers result in 3-D tritium breeding ratios (TBR's) of greater than 1.2 except for the $LiAlO_2$/He blanket. Evidently, these high TBR's have been brought about by the large neutron multiplication of the Be(n,2n) reaction. The net neutron multiplication in these systems amounts to $\gtrsim$ 1.6/DT-fusion neutron as compared to 1.1-1.2/DT-fusion neutron in the systems without beryllium or lead. For instance, the FLIBE design, which employs a 20-cm thick beryllium multiplier (10.6 cm effective thickness), yields a multiplication factor of ~2.0 (±0.5%). Namely, every neutron born by the DT fusion is doubled in the FLIBE blanket. This neutron-rich system also yields a substantially high energy multiplication factor of ~1.5 per 14.06 MeV neutron, which is 20-40% higher than any other systems studied.

The 3-D TBR of 1.16 (or 1.19 without the 3% adjustment mentioned earlier) for the $LiAlO_2$/He/HT9/Be design is somewhat discouraging compared to the other designs with beryllium multiplier. This is because of the relatively thin helium-cooled blanket design (58 cm in total and ~19 cm net $LiAlO_2$ material thickness). The relatively low blanket performance is also evident from the large heat deposition in the shield (2 MeV per DT fusion neutron). In fact, the blanket performance in this system can significantly improve, just by extending the outermost $LiAlO_2$ breeding zone by 10 cm. The TBR that results is 1.24 (or 1.27 without the adjustment) and the blanket energy deposition becomes 18 MeV/DT fusion neutron which reduces the energy loss in the shield by about 1 MeV/DT neutron.

The relatively low TBR in the 17Li-83Pb blanket in spite of its large neutron multiplication (~1.8/DT neutron) is due simply to the insufficient ^6Li

TANDEM MIRROR/ TMRANL1/Li-Li-V15Cr5Ti



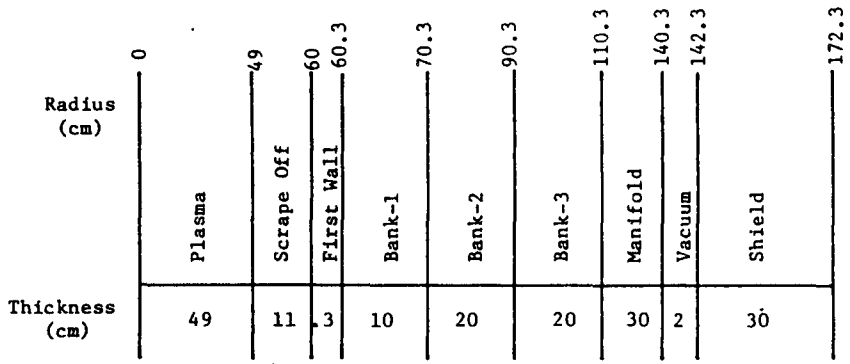
Material Compositions (vol-%)

	V15Cr5Ti		Li*	Fe1422
First Wall	100		---	---
Bank-1	7.1		73.7	---
Bank-2	7.1		73.7	---
Bank-3	7.1		73.7	---
Manifold	10		10	80
Shield	80 (Fe1422)	20 (H_2O)		

*Li density = 100% of T.D.; ^{6}Li enrichment = 7.4%.

Figure 6.10-3. System description of the TMR/Li-Li-V15Cr5Ti design.

TANDEM MIRROR/ TMRANL2/Li-Li-HT9



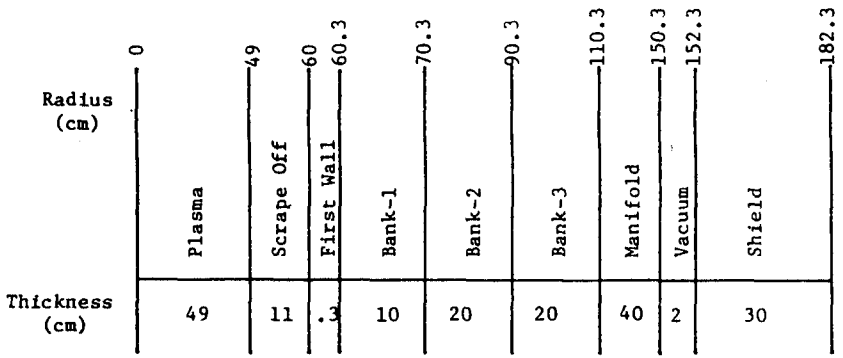
Material Compositions (vol-%)

	HT9		Li*	
First Wall	100		---	
Bank-1	7.1		73.7	
Bank-2	7.1		73.7	
Bank-3	7.1		73.7	
Manifold	90		10	
Shield	80 (Fe1422)	20 (H_2O)		

*Li density = 100% of T.D.; ^{6}Li enrichment = 7.4%.

Figure 6.10-4. System description of the TMR/Li-Li-HT9 design.

TANDEM MIRROR/TMRANL3/17Li83Pb-17Li83Pb-V15Cr5Ti



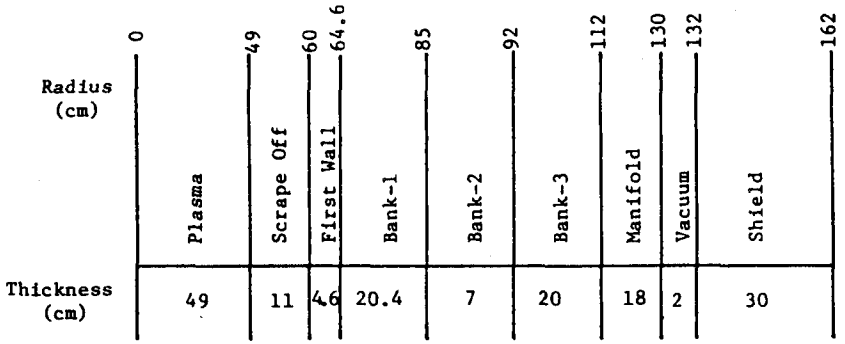
Material Compositions (vol-%)

	V15Cr5Ti		17Li83Pb*	Fe1422
First Wall	100		---	---
Bank-1	7.1		73.7	---
Bank-2	7.1		73.7	---
Bank-3	7.1		73.7	---
Manifold	10		20	70
Shield	80 (Fe1422)	20 (H_2O)		

*17Li83Pb density = 100% of T.D.; ^{6}Li enrichment = 30%.

Figure 6.10-5. System description of the TMR/17Li83Pb-17Li83Pb-V15Cr5Ti design.

TANDEM MIRROR/ TMRANL4/γ-$LiAlO_2$-H_2O-HT9-Be



Material Compositions (vol-%)

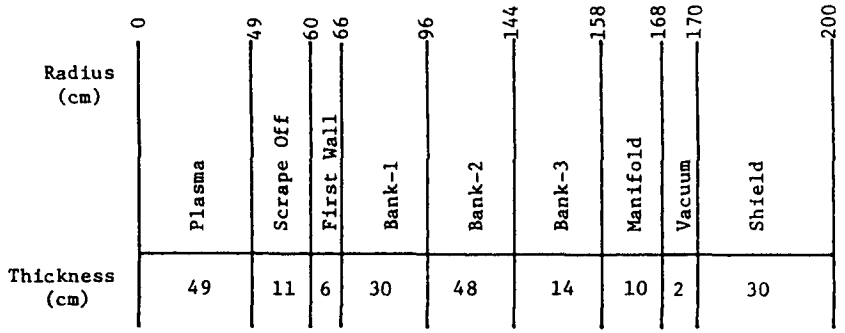
	HT9	H_2O	γ-$LiAlO_2$*	Be**
First Wall	22	8	---	---
Bank-1	19.5	21.5	5(4.35)	45(39.15)
Bank-2	12.5	11.5	70(60.9)	---
Bank-3	7	4	84(73.08)	---
Manifold	33	67	---	---
Shield	80 (Fe1422)	20		

*γ-$LiAlO_2$ density = 87% of T.D.; ^{6}Li enrichment = 90%.

**Be density = 87% of T.D.

Figure 6.10-6. System description of the TMR/γ-$LiAlO_2$-H_2O-HT9-Be design.

TANDEM MIRROR/TMRGA1/Li-He -HT9



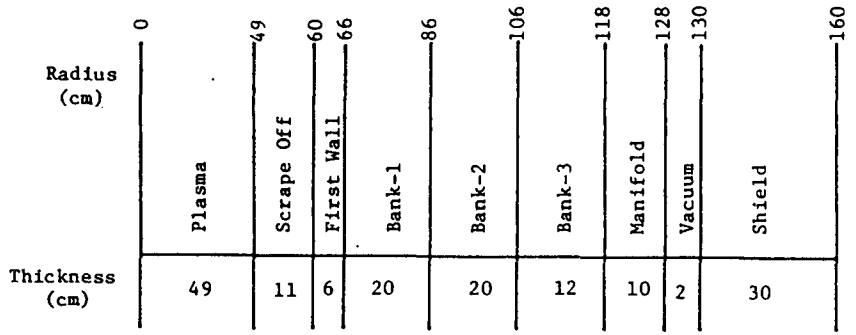
Material Compositions (vol-%)

	HT9	He	Li*	
First Wall	10.3	89.7	---	
Bank-1	8.3	23.3	68.4	
Bank-2	8.3	23.3	68.4	
Bank-3	88	12	---	
Manifold	20	80		
Shield	80 (Fe1422)	20 (H_2O)		

*Li density = 100% of T.D.; ^{6}Li enrichment = 7.4%.

Figure 6.10-7. System description of the TMR/Li-He-HT9 design.

TANDEM MIRROR/ TMRGA2/Li_2O-He-HT9



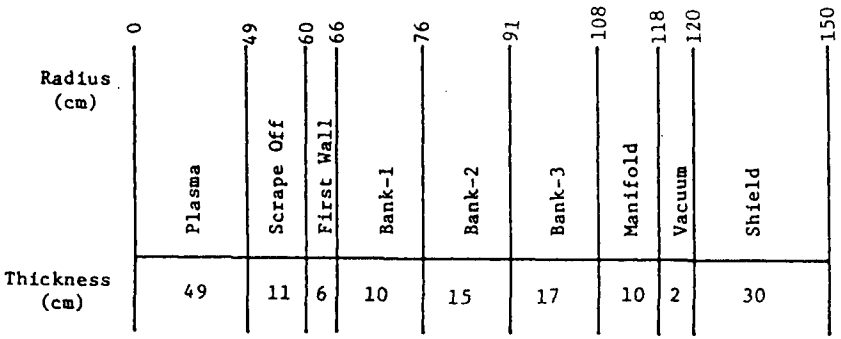
Material Compositions (vol-%)

	HT9	He	Li_2O*	
First Wall	10.3	89.7	---	
Bank-1	8	11	81(64.8)	
Bank-2	8	11	81(64.8)	
Bank-3	29	8	63(50.4)	
Manifold	20	80	---	
Shield	80 (Fe1422)	20 (H_2O)		

*Li_2O density = 80% of T.D.; ^6Li enrichment = 7.4%.

Figure 6.10-8. System description of the TMR/Li_2O-He-HT9 design.

TANDEM MIRROR/ TMRGA3/γ-$LiAlO_2$-He-HT9-Be



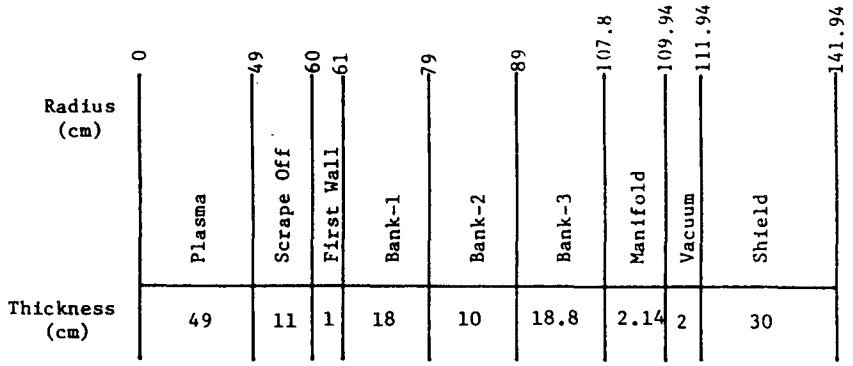
Material Compositions (vol-%)

	HT9	He	γ-$LiAlO_2$	Be**
First Wall	8.3	91.7	---	---
Bank-1	4.7	41.3	---	54(43.2)
Bank-2	16	9	75(60.0)	---
Bank-3	16	9	75(60.0)	---
Manifold	20	80	---	---
Shield	80 (Fe1422)	20 (H_2O)		

*γ-$LiAlO_2$ density = 80% of T.D.; ^6Li enrichment = 60%.
**Be density = 80% of T.D.

Figure 6.10-9. System description of the TMR/γ-$LiAlO_2$-He-HT9-Be design.

TANDEM MIRROR/ TMRTRW1/γ-$LiAlO_2$-Draw Salt-HT9-Be



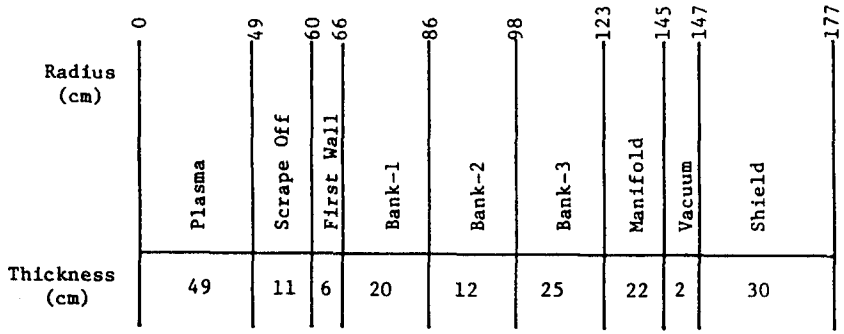
Material Compositions (vol-%)

	HT9	Draw Salt	γ-$LiAlO_2$*	Be**
First Wall	55	45	---	---
Bank-1	8	12.5	21(17.85)	58.5(40.95)
Bank-2	6	7	87(73.95)	---
Bank-3	6	7	87(73.95)	---
Manifold	15	85		
Shield	80 (Fe1422)	20 (H_2O)		

*γ-$LiAlO_2$ density = 85% of T.D.; ^6Li enrichment = 50%.
**Be density = 70% of T.D.

Figure 6.10-10. System description of the TMR/γ-$LiAlO_2$-Draw Salt-HT9-Be design.

TANDEM MIRROR/ TMRLLL1/FLIBE-He-HT9-Be



Material Compositions (vol-%)

	HT9	He	FLIBE*	Be**	SiC***
First Wall	8.7	91.3	---	---	---
Bank-1	6	32	9	53	---
Bank-2	6	10	9	---	75
Bank-3	28	10	9	---	53
Manifold	27	73	---	---	---
Shield	80 (Fe1422)	20 (H_2O)			

*FLIBE density = 100% of T.D.; ^6Li enrichment = 7.4%.

**Be density = 100% of T.D.

***SiC density = 100% of T.D.

Figure 6.10-11. System description of the TMR/FLIBE-He-HT9-Be design.

TABLE 6.10-5.
NUCLEAR PERFORMANCE OF TMR CONCEPTS

Breeder Material	(^{6}Li-content/ % of T.D.)	Coolant	Structure	Blanket[a] Thickness (cm)	Beryllium Thickness (cm)	3D-TBR[b]	Blanket Energy Deposition (MeV/DT)	Total Energy Deposition (MeV/DT)
Li	(7.4%/100%)	Li	V15Cr5Ti	80.3	--	1.19	16.7	17.8
Li	(7.4%/100%)	Li	HT9	80.3	--	1.14	15.8	17.6
17Li-83Pb	(30%/100%)	17Li-83Pb	V15Cr5Ti	90.3	--	1.18	18.6	19.2
Li	(7.4%/100%)	He	HT9	108.0	--	1.17	15.5	17.1
Li_2O	(7.4%/80%)	He	HT9	68.0	--	1.14	14.5	16.0
γ-$LiAlO_2$	(60%/80%)	He	HT9	58.0	10	1.16	17.0	19.0
γ-$LiAlO_2$	(90%/87%)	H_2O	HT9	70.0	20.4	1.22	18.3	18.4
γ-$LiAlO_2$	(50%/85%)	Draw Salt	HT9	49.9	18	1.29	17.4	18.4
FLIBE	(7.4%/100%)	He	HT9	85.0	20	1.29	21.0	21.6

[a]Includes first wall/blanket/manifolds.

[b]Adjusted for end cell fusion and neutron losses in choke coils and for start-up heating penetration.

enrichment (30%) used.[6.10-11] The TBR of this system can increase to ~1.44 merely by changing the enrichment to ~90%, although the energy performance becomes slightly worse due to the less-effective energy production of the $^6Li(n,\alpha)t$ reaction as compared to parasitic neutron absorption by the structural material.

Table 6.10-6 compares the TBR's for three helium-cooled blanket designs, Li/He, Li_2O/He and $LiAlO_2$/He, to those calculated by GA.[6.10-12] The GA evaluation was performed using ANISN (with the $S_8 - P_3$ approximation) with the Los Alamos MATXS5[6.10-13] cross-section library (which has an energy structure of 30 neutron groups). As indicated in the table, both evaluations show good agreement within the statistical errors except for the Li/He/HT-9 design that will be discussed further shortly. It should be noted that the Monte-Carlo method accounts for a neutron leakage through the end cells that can not be included in the ANISN calculation although it is small in our case (estimated to be ~1% or less) because of the large ratio of related dimensions, the reactor length over the first wall radius.

TABLE 6.10-6.
A COMPARISON OF TRITIUM BREEDING PERFORMANCE
EVALUATED BY MONTE-CARLO AND DISCRETE-ORDINATES METHODS

Concept	Monte-Carlo[a]	Discrete-Ordinates[b]
Li/He/HT9	1.20 (±1%)	1.26
Li_2O/He/HT9	1.18 (±1%)	1.17
γ-$LiAlO_2$/He/HT9/Be	1.19 (±1%)	1.22

[a]ANL - Evaluation based on MCNP/ENDF-B/V.

- 130 m-long finite cylinder calculation.
- No adjustment for end plug fusion and neutron losses in choke coils and for start-up heating.

[b]GA - Evaluation based on ANISN/MATXS5.

- Infinite-cylinder calculation.

Table 6.10-7 lists the TBR's calculated by several different methods and data libraries for three liquid-lithium blanket designs, viz., Li/Li/V15Cr5Ti, Li/Li/HT9, and Li/He/HT9. When the MCNP/ENDF/B-V results are compared to those of MCNP/ENDF/B-IV, one finds a consistently higher breeding evaluation (by ~6%) based on ENDF/B-IV due to the higher $^{7}Li(n,n'\alpha)t$ cross-section data file in this ENDF version. When the ^{7}Li contribution (T_7) is reduced to 85% of the ENDF-B/IV evaluation, however, the MCNP results indicate a good agreement between ENDF/B-IV and V for the three cases studied. On the other hand, the TBR's evaluated by ANISN are consistent with the MCNP/ENDF/B-IV calculation only for the V15Cr5Ti structure blanket. The two HT9-structure designs exhibit non-trivial difference in TBR between the MCNP and ANISN evaluations. In particular, the same TBR of 1.22 (or 1.30 without the T_7 correction) obtained both for Li/Li/V15Cr5Ti and Li/Li/HT9 in the ANISN calculation seems unreasonable because vanadium generally has larger (n,2n) and less parasitic neutron absorption cross sections than iron. The observations made above and for the GA evaluation for the Li/He/HT9 design mentioned earlier lead to a postulation that the energy group structure used in the VITAMIN-C[6.10-14]/MACKLIB-IV[15] and MATXS[6.10-13] libraries for the ANISN calculation might not be appropriate on the iron cross sections for systems that are characterized by a liquid-lithium breeder.

6.10.2.2 Tokamak Designs

Figures 6.10-12 through 6.10-18 describe the seven tokamak designs modeled for the neutronics analysis, and the result on their nuclear performance is summarized in Table 6.10-8. The computations were performed using MCNP/ENDF/B-V with 10,000 neutron histories. The typical statistical standard deviation is, as the TMR cases, ~±1% or less.

It is assumed in the present study that the two liquid-lithium blanket designs (Li/Li and Li/He) use the alternate lithium-cooled V15Cr5Ti limiter while all other blanket designs use the reference water-cooled limiter. With regard to the RF waveguides, the single H_2O-cooled HT9 design described earlier is assumed for all the designs.

The most important consideration for the breeding analysis in tokamaks is the presence of these major penetrations. In particular, the selection of limiter design is of great importance in terms of the breeding perturbation to a full breeding blanket. This is not only because a part of the breeding

TABLE 6.10-7.
A COMPARISON OF TRITIUM BREEDING PERFORMANCE
BASED ON ENDF/B-IV AND V DATA

Blanket Concept	MCNP[a] ENDF/B-V	MCNP[a,b] ENDF/B-IV	ANISN[b,c] ENDF/B-IV
Li/Li/V15Cr5Ti	1.23 (±1%)	1.22 (±1%) [1.30 (±1%)][d]	1.22 [1.30][d]
Li/Li/HT9	1.17 (±1%)	1.16 (±1%) [1.23 (±1%)][d]	1.22 [1.30][d]
Li/He/HT9	1.20 (±1%)	1.20 (±1%) [1.27 (±1%)][d]	1.26 [1.33][d]

[a]
- 130 m-long finite cylinder calculation.
- No adjustment for end cell fusion and neutron losses in choke coils and for start up heating.

[b]Evaluation based on $T_6 + 0.85T_7$.

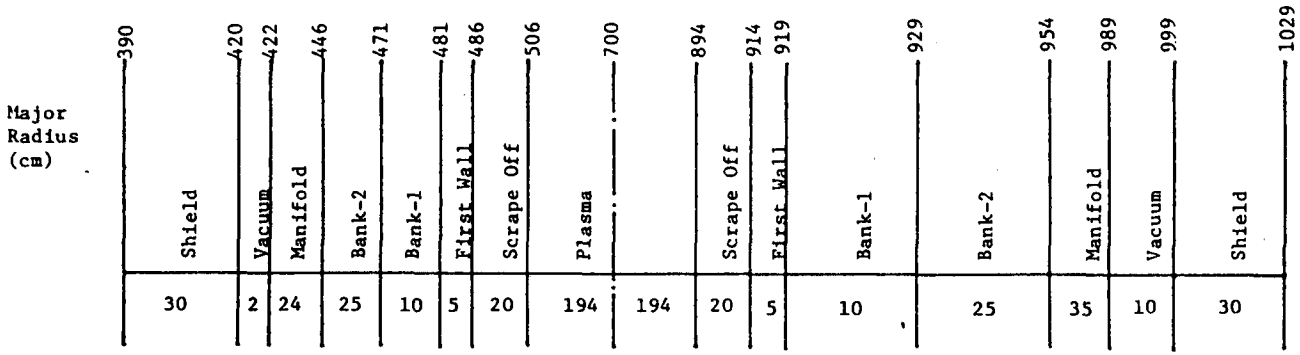
[c]Infinite cylinder calculation based on the VITAMIN-C/MACKLIB-IV data libraries.

[d]$T_6 + T_7$.

blanket area is lost for the limiter plenum, but because a large number of neutrons are possibly absorbed in the limiter itself. In general, the possible adverse effect on tritium production, due to the presence of limiter is caused by a drastic spectrum change (softening) in the limiter region, leading to an enhancement of parasitic neutron loss in the limiter materials. In this regard, for the systems where the blanket and limiter designs possess a close spectrum homogeneity, (such as the Li/Li and Li/He blankets with the lithium-cooled limiter, and the $LiAlO_2/H_2O$ blanket with the water-cooled limiter), one finds the least adverse effect of the limiter design.

As shown in Table 6.10-9 which compares the 3D-TBR's with and without the limiter/RF systems, the breeding losses in the Li/Li, Li/He, and $LiAlO_2/H_2O$ designs mentioned above amount only to 2-4%, which is more or less proportion-

TOKAMAK/TOKANL1/Li-Li-V15Cr5Ti (Li/V15Cr5Ti Limiter)



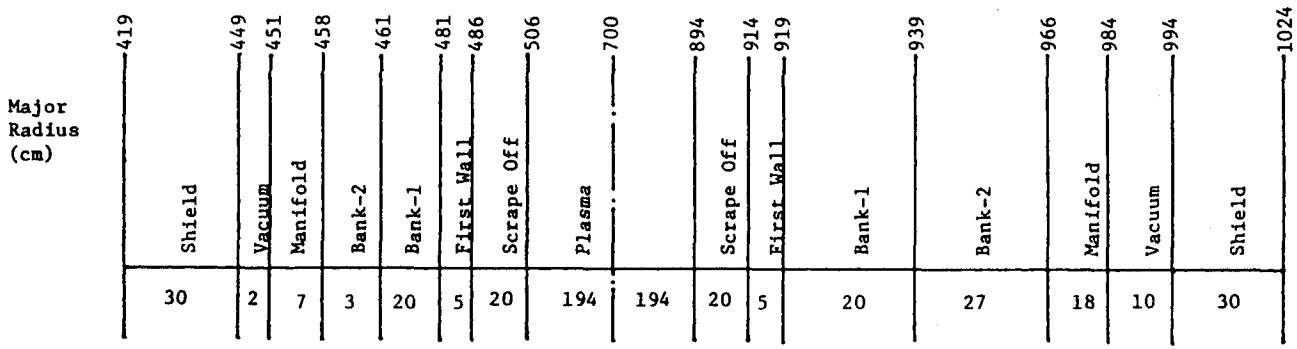
Material Compositions (vol-%)

	Inboard				Outboard			
	V15Cr5Ti		Li*	Fe1422	V15Cr5Ti		Li*	Fe1422
First Wall	20		80	---	20		80	---
Bank-1	7.5		92.5	---	7.5		92.5	---
Bank-2	7.5		92.5	---	7.5		92.5	---
Manifold	10		50	40	10		10	80
Shield	80 (Fe1422)	20 (H_2O)			80 (Fe1422)	20 (H_2O)		

*Li density = 100% of T.D.; ^{6}Li enrichment = 7.4%.

Figure 6.10-12. System description of the tokamak/Li-Li-V15Cr5Ti design.

TOKAMAK/TOKANL4/γ-$LiAlO_2$-H_2O-HT9-Be (H_2O/Cu-2Be Limiter)



Material Compositions (vol-%)

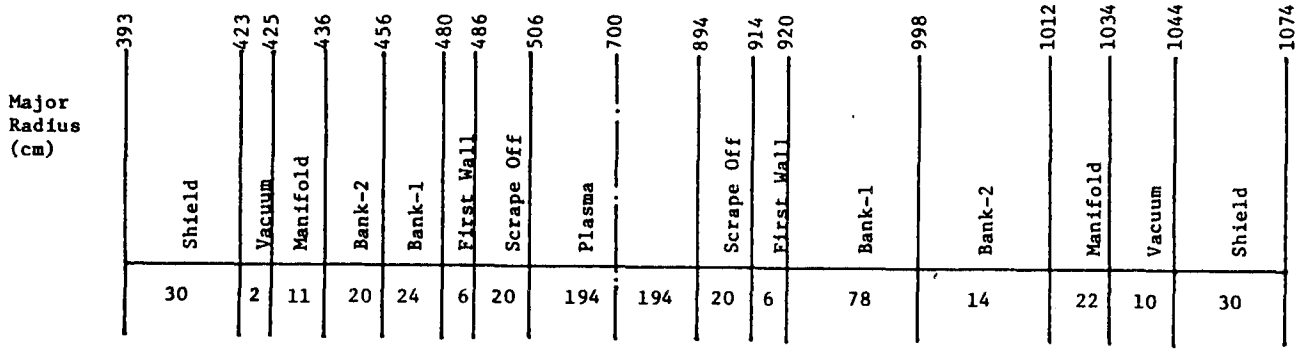
	Inboard				Outboard			
	HT9	H_2O	γ-$LiAlO_2$*	Be**	HT9	H_2O	γ-$LiAlO_2$*	Be**
First Wall	32	7	---	---	32	7	---	---
Bank-1	19.5	21.5	5(4.35)	45(39.15)	19.5	21.5	5(4.35)	45(39.15)
Bank-2	12.5	11.5	70(60.9)	---	8.5	6.0	80(70.04)	---
Manifold	33	67	---	---	33	67	---	---
Shield	80 (Fe1422)	20			80 (Fe1422)	20 (H_2O)		

*γ-$LiAlO_2$ density = 87% of T.D.; ^6Li enrichment = 90%.

**Be density = 87% of T.D.

Figure 6.10-13. System description of the tokamak/γ-$LiAlO_2$-H_2O-HT9-Be design.

TOKAMAK/TOKGA1/Li-He-HT9 (Li/V15Cr5Ti Limiter)



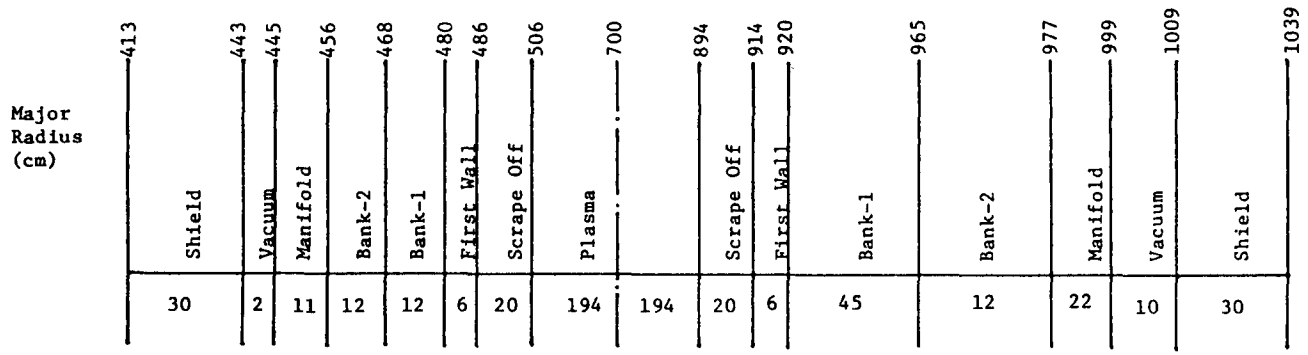
Material Compositions (vol-%)

	Inboard				Outboard			
	HT9	He	Li*		HT9	He	Li*	
First Wall	11.7	88.3	---		11.7	88.3	---	
Bank-1	8	26	66		8	26	66	
Bank-2	88	12	---		88	12	---	
Manifold	20	80	---		20	80	---	
Shield	80 (Fe1422)	20 (H_2O)			80 (Fe1422)	20 (H_2O)		

*Li density = 100% of T.D.; ^6Li enrichment = 7.4%.

Figure 6.10-14. System description of the tokamak/Li-He-HT9 design.

TOKAMAK/TOKGA2/Li_2O-He-HT9 (H_2O/Cu-2Be Limiter)



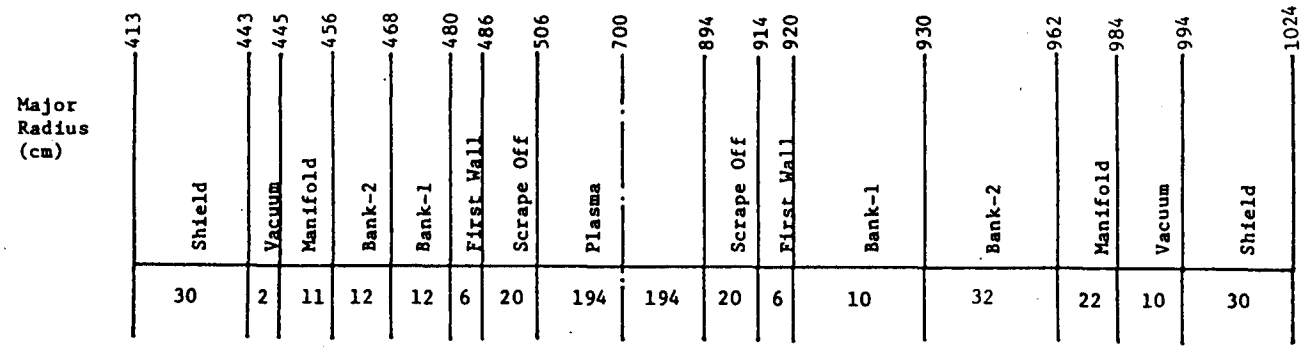
Material Compositions (vol-%)

	Inboard				Outboard			
	HT9	He	Li_2O*		HT9	He	Li_2O*	
First Wall	12	88	---		12	88	---	
Bank-1	8	11	81(64.8)		8	11	81(64.8)	
Bank-2	29	8	63(50.4)		29	8	63(50.4)	
Manifold	20	80	---		20	80	---	
Shield	80 (Fe1422)	20 (H_2O)			80 (Fe1422)	20 (H_2O)		

*Li_2O density = 80% of T.D.; ^6Li enrichment = 7.4%.

Figure 6.10-15. System description of the tokamak/Li_2O-He-HT9 design.

TOKAMAK/TOKGA3/γ-$LiAlO_2$-He-HT9-Be (H_2O/Cu-2Be Limiter)



Material Compositions (vol-%)

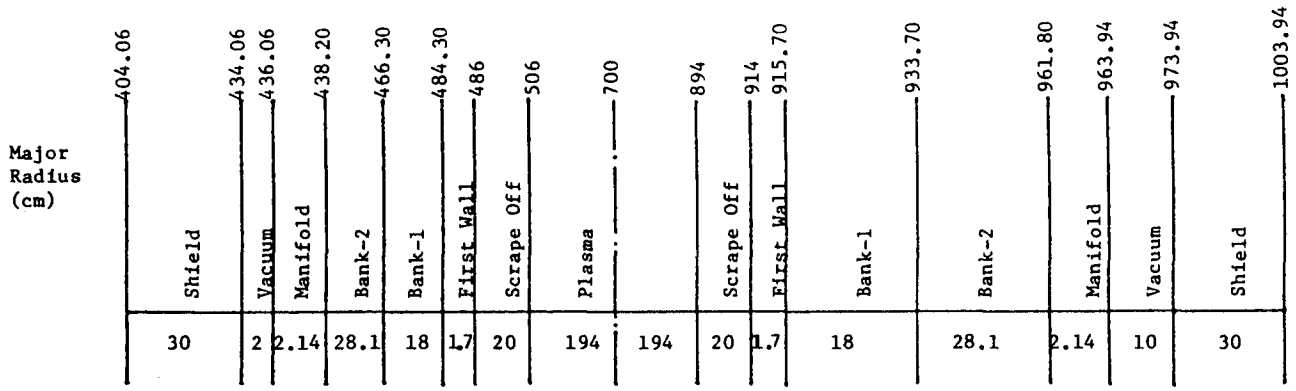
	Inboard				Outboard			
	HT9	He	γ-$LiAlO_2$*	Be**	HT9	He	γ-$LiAlO_2$*	Be**
First Wall	12	88	---	---	12	88	---	---
Bank-1	7.9	11.5	80.6(64.48)	---	4.7	41.3	---	54(43.2)
Bank-2	28.6	8.9	62.5(50.0)	---	15.7	9	75.3(60.24)	---
Manifold	20	80	---	---	20	80	---	---
Shield	80 (Fe1422)	20 (H_2O)			80 (Fe1422)	20 (H_2O)		

*γ-$LiAlO_2$ density = 80% of T.D.; ^6Li enrichment = 60%.

**Be density = 80% of T.D.

Figure 6.10-16. System description of the tokamak/γ-$LiAlO_2$-He-HT9-Be design.

TOKAMAK/TOKTRW1/γ-$LiAlO_2$-Draw Salt-HT9-Be (H_2O/Cu-2Be Limiter)



Material Compositions (vol-%)

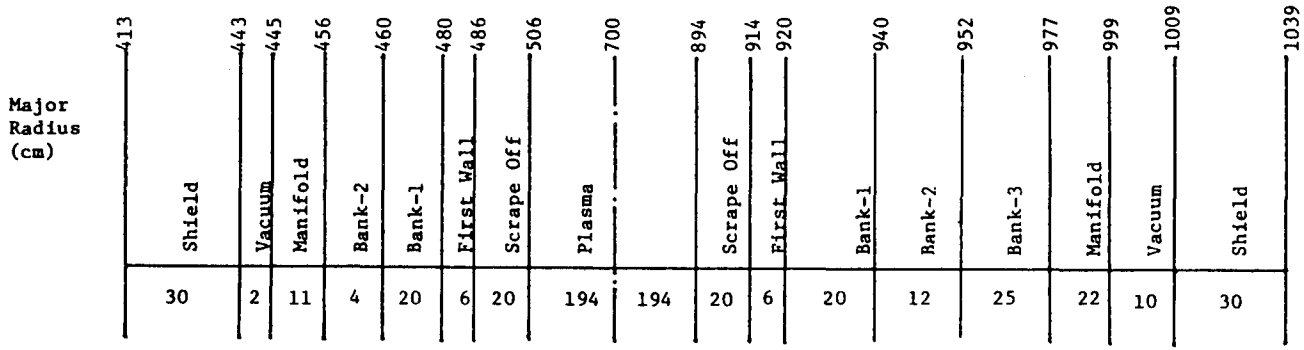
	Inboard				Outboard			
	HT9	Draw Salt	γ-$LiAlO_2$*	Be**	HT9	Draw Salt	γ-$LiAlO_2$*	Be**
First Wall	63	37	---	---	63	37	---	---
Bank-1	8	12.5	21(17.85)	58.5(40.95)	8	12.5	21(17.85)	58.5(40.95)
Bank-2	6	7	87(73.95)	---	6	7	87(73.95)	---
Manifold	15	85	---	---	15	85	---	---
Shield	80 (Fel422)	20 (H_2O)			80 (Fel422)	20 (H_2O)		

*γ-$LiAlO_2$ density = 85% of T.D.; ^6Li enrichment = 50%.

**Be density = 70% of T.D.

Figure 6.10-17. System description of the tokamak/γ-$LiAlO_2$-Draw Salt-HT9-Be design.

TOKAMAK/TOKLLL1/FLIBE-He-HT9-Be (H_2O/Cu-2Be Limiter)



Material Compositions (vol-%)

	Inboard					Outboard				
	HT9	He	FLIBE*	Be**	SiC***	HT9	He	FLIBE*	Be**	SiC***
First Wall	11.7	88.3	---	---	---	11.7	88.3	---	---	---
Bank-1	6	32	9	53	---	6	32	9	53	---
Bank-2	6	10	9	---	75	6	10	9	---	75
Bank-3						28	10	9	---	53
Manifold	27	73	---	---	---	27	73	---	---	---
Shield	80 (Fe1422)	20 (H_2O)				80 (Fe1422)	20 (H_2O)			

*FLIBE density = 100% of T.D.; ^6Li enrichment = 7.4%.

**Be density = 100% of T.D.

***SiC density = 100% of T.D.

Figure 6.10-18. System description of the tokamak/FLIBE-He-HT9-Be design.

TABLE 6.10-8.
NUCLEAR PERFORMANCE OF TOKAMAK CONCEPTS

Breeder Material	(^{6}Li-content/ % of T.D.)	Coolant	Structure	Blanket[a] Thickness (cm) Inb./Outb.	Beryllium Thickness (cm) Inb./Outb.	3D-TBR	Blanket Energy Deposition (MeV/DT)	Total Energy Deposition (MeV/DT)
Li	(7.4%/100%)	Li	V15Cr5Ti	64/75	--	1.28[b]	17.1	17.8
Li	(7.4%/100%)	He	HT9	61/120	--	1.16[b]	16.0	17.5
Li_2O	(7.4%/80%)	He	HT9	41/85	--	1.11[c]	15.5	16.5
$LiAlO_2$	(60%/80%)	He	HT9	41/70	0/10	1.04[c]	16.9	18.7
$LiAlO_2$	(90%/87%)	H_2O	HT9	35/70	20/20	1.16[c]	18.3	18.7
$LiAlO_2$	(50%/85%)	Nitrate Salt	HT9	49.9/49.9	18/18	1.24[c]	17.6	18.3
FLIBE	(7.4%/100%)	He	HT9	41/85	20/20	1.17[c]	20.8	22.1

[a]Includes first wall/blanket/manifolds.

[b]Li-cooled V15Cr5Ti limiter.

[c]H_2O-cooled Cu-2Be limiter.

al to the limiter/RF opening area of $\lesssim$4% ($[23\ m^2 + 6\ m^2]/756\ m^2$). The quite high TBR of 1.28 for the Li/Li/V15Cr5Ti blanket design, for instance, has been thus maintained in virtue of the minimal detrimental effect of the limiter. In the case of the Li/He blanket, approximately half of the breeding loss stems from parasitic neutron absorption in the water-cooled HT9 structure of the RF waveguides rather than the limiter materials. Considering the small size of RF relative to the limiter it is evident that the adverse effect on breeding performance is caused by the spectrum softening (due to the water coolant of RF in this case).

TABLE 6.10-9.
THE IMPACT OF LIMITER AND RF DESIGNS ON TRITIUM BREEDING FOR TOKAMAK BLANKET DESIGNS

System Breeder/Coolant/Structure/Multiplier	3D-TBR with Limiter/RF	3D-TBR without Limiter/RF	Relative Difference (%)
• Li/Li/V15Cr5Ti/-	1.28[a]	1.31	- 2.4
• Li/He/HT9/-	1.16[a]	1.20	- 3.1
• Li_2O/He/HT9/-	1.11[b]	1.18	- 5.8
• $LiAlO_2$/He/HT9/Be	1.04[b]	1.15	- 9.0
• $LiAlO_2$/H_2O/HT9/Be	1.16[b]	1.21	- 4.1
• $LiAlO_2$/Draw Salt/HT9/Be	1.24[b]	1.32	- 5.9
• FLIBE/He/HT9/Be	1.17[b]	1.34	-12.5

[a]Li-cooled V15Cr5Ti limiter.
[b]H_2O-cooled Cu-2Be limiter.

The largest breeding loss due to the presence of limiter/RF, is found in the helium-cooled blanket designs with the water-cooled limiter. Three such designs, Li_2O/He, γ-$LiAlO_2$/He and FLIBE/He, result in breeding losses of ~6% (or 0.07 in net TBR loss), 9% (0.11) and 12.5% (0.17), respectively. These neutron losses well coincide with the neutron capture rates in the limiter (mostly in the heat-sink material) which are respectively, ~0.06, 0.09, and 0.15. The impact of the limiter design is most serious for the $LiAlO_2$/He design. The TBR of 1.04 in this design is too marginal to guarantee a self-sufficient tritium-fuel production, and in fact, fails to meet the minimum

breeding goal of 1.05. The poor breeding performance is due in part to the insufficient breeding margin in the overall blanket design, as indicated by the full breeding ratio of 1.15 in Table 6.10-9. As discussed previously for the corresponding TMR design, the blanket performance in this system can significantly improve, simply by widening the outboard breeding zone by ~10 cm. The TBR that results is ~1.11 with the limiter/RF penetrations.

Table 6.10-10 presents a detailed breakdown of the breeding loss for the FLIBE/He design.

TABLE 6.10-10.
THE IMPACT OF LIMITER/RF DESIGN ON TRITIUM BREEDING* FOR THE TOKAMAK/FLIBE-He-HT9-Be DESIGN

Region	3D-TBR Full Breeding	3D-TBR with Limiter/RF	Relative Difference (%)	Net Breeding Loss
Bank-1	0.993 (±1.0%)	0.866 (±1.1%)	-12.8	-0.127
Bank-2	0.140 (±2.0%)	0.124 (±2.1%)	-11.1	-0.016
Bank-3	0.208 (±1.9%)	0.184 (±2.0%)	-11.7	-0.024
Sector-1	0.189 (±2.4%)	0.171 (±2.5%)	- 9.1	-0.017
Sector-2	0.064 (±4.4%)	0.063 (±4.4%)	- 0.9	-0.001
Sector-3	0.093 (±3.6%)	0.086 (±3.9%)	- 7.6	-0.007
Sector-4	0.294 (±2.1%)	0.271 (±2.1%)	- 7.8	-0.023
Sector-5	0.259 (±2.2%)	0.262 (±2.2%)	0.9	0.002
Sector-6	0.290 (±2.1%)	0.250 (±2.2%)	-13.7	-0.040
Sector-7	0.088 (±3.7%)	0.025 (±5.9%)	-71.3	-0.062
Sector-8	0.065 (±4.2%)	0.045 (±5.4%)	-30.4	-0.020
Total T_6	1.330 (±0.9%)	1.164 (±0.9%)	-12.5	-0.166
T_7	0.011 (±0.9%)	0.010 (±1.0%)	- 9.9	-0.001
$T_6 + T_7$	1.341 (±0.9%)	1.174 (±0.9%)	-12.5	-0.167

*Based on MCNP/ENDF/B-V Evaluation with 10,000 neutron histories.

It is found that the breeding loss persistently previals in all three blanket layers (Banks 1 through 3). It is evident from the breakdown by sectors that the breeding is drastically reduced in Sector-7 where the limiter resides and in the closest neighboring sectors (Sectors 6 and 8). The total breeding loss of ~0.17 is far more than what one can expect from the opening dimensions of the limiter/RF penetrations at the first wall, and is rather close to the ratio of the overall limiter surface area to the total first wall area, i.e., ~12% (=90 m^2/756 m^2).

REFERENCES FOR SECTION 6.10

6.10-1. B. G. Logan, "The Mirror Advanced Reactor Study (MARS)," Nucl. Technol/Fusion 4 (563) (1983).

6.10-2. C. C. Baker, et al., "STARFIRE-A Commercial Tokamak Fusion Power Plant Study," ANL/FPP-80-1, Argonne National Laboratory (1980).

6.10-3. J. D. Lee et al., "Feasibility Study of a Fission-Suppressed Tandem Mirror Hybrid Reactor," UCID-19327 (1982).

6.10-4. J. D. Gordon, "Tandem Mirror TBR Considerations," Presented at BCSS Meeting at UCLA. Jan. 31 - Feb. 1 (1984).

6.10-5. W. M. Stacey, Jr., et al., "U.S. FED-INTOR Activity and U.S. Contribution to the International Tokamak Reactor Phase-2A Workshop," USA FED-INTOR/82-1, Vol. I (1982).

6.10-6. Los Alamos Montel Carlo Group, "MCNP-Monte Carlo Neutron and Photon Transport Code," RSIC/CCC-200, Radiation Shielding Information Center (1983).

6.10-7. R. Kinsey, Ed., "ENDF-102 Data Formats and Procedures for the Evaluated Nuclear Data File, ENDF," BNL-NCS-50496 (ENDF-102) 2nd Ed. (ENDF/B-V), Brookhaven National Laboratory (1979).

6.10-8. R. C. Little and R. E. Seamon, Private Communication, Los Alamos National Laboratory, March 13, 1984.

6.10-9. D. Garber (compiler), "ENDF/B Summary Documentation," BNL-17541, Brookhaven National Laboratory (1975).

6.10-10. W. W. Engle, Jr., "A User's Manual for ANISN, A One-Dimensional Discrete Ordinates, Transport Code with Anisotropic Scattling," K-1693 Oak Ridge Gasious Diffusion Plant (1967).

6.10-11. J. Jung and M. Abdou, "Assessments of Tritium Breeding Requirements and Breeding Potential for the STARFIRE/DEMO Design," Nucl. Technol./Fusion (Special Issue) 4(2), Pt. 2, 361 (1983).

6.10-12. E. Cheng, Personal communication, GA Technologies, August, 1984.

6.10-13. R. E. MacFarlane, "Nuclear Data Libraries from Los Alamos for Fusion Neutronics Calculations," Trans. Am. Nucl. Society, 46 271, June 1984.

6.10-14. R. W. Roussin et al., "VITAMIN-C:. The CTR Processed Multigroup Cross Section Library for Neutronics Studies," ORNL/RSIC-37 (DLC-41), Oak Ridge National Laboratory (1980).

6.10-15. Y. Gohar and M. Abdou, "MACKLIB-IV:. A Library of Nuclear Response Functions Generated with the MACK-IV Computer Program from ENDF/B-IV," ANL/FPP/TM-106, Argonne National Laboratory (1978).

BLANKET COMPARISON AND SELECTION STUDY

SECTION 6.11

ENERGY MULTIPLICATION, FIRST WALL ATOMIC DISPLACEMENT, AND SHIELDING REQUIREMENTS FOR ALL BLANKET CONCEPTS

SECTION 6.11

TABLE OF CONTENTS

PAGE NO.

6.11 Energy Multiplication, First Wall Atomic Displacement, and Shielding Requirements for All Blanket Concepts.....6.11-1

6.11.1 Design Criteria.....6.11-1

6.11.2 Procedure and Assumptions for the Analysis.....6.11-4

6.11.3 Energy Deposition and First Wall Atomic Displacement.....6.11-5

6.11.4 Shielding Requirements.....6.11-9

REFERENCES.....6.11-20

LIST OF FIGURES FOR SECTION 6.11

FIGURE NO.	TITLE	PAGE NO.
6.11-1	Maximum thermal insulator dose as a function of the shield thickness normalized to 150 MW • y/m^2 D-T neutron fluence at the first wall	6.11-12
6.11-2	Maximum nuclear heating rate as a function of the shield thickness normalized to 5 MW/m^2 D-T neutron wall loading at the first wall	6.11-12
6.11-3	Nuclear heating in the central cell coil materials normalized to 5 MW/m^2 D-T wall loading at the first wall	6.11-13
6.11-4	Maximum neutron fluence in the winding material as a function of the shield thickness normalized to 150 MW • y/m^2 D-T neutron fluence at the first wall	6.11-13
6.11-5	Maximum copper induced resistivity in the superconductor coils as a function of the shield thickness normalized to 150 MW • y/m^2 D-T neutron fluence at the first wall	6.11-14
6.11-6	Maximum atomic displacement in the copper stabilizer of the superconductor in the central cell coils normalized to 150 MW • y/m^2 D-T neutron fluence and the first wall	6.11-14
6.11-7	Neutron flux at the outer shield surface between the central cell coils normalized to 5 MW/m^2 D-T neutron wall loading at the first wall	6.11-15

LIST OF TABLES FOR SECTION 6.11

TABLE NO.	TITLE	PAGE NO.
6.11-1	OCCUPATIONAL DOSE LIMITS	6.11-3
6.11-2A	TOKAMAK BLANKET ENERGY DEPOSITION	6.11-6
6.11-2B	MIRROR BLANKET ENERGY DEPOSITION	6.11-7
6.11-3	FIRST WALL ATOMIC DISPLACEMENT RATE	6.11-8
6.11-4A	GEOMETRICAL MODEL FOR THE INBOARD TOKAMAK SECTION USED IN THE SHIELDING ANALYSIS	6.11-10
6.11-4B	GEOMETRICAL MODEL FOR THE OUTBOARD TOKAMAK SECTION USED IN THE SHIELDING ANALYSIS	6.11-10
6.11-4C	GEOMETRICAL MODEL FOR THE CENTRAL CELL SECTION WITH SUPERCONDUCTOR COIL USED IN THE SHIELD ANALYSIS	6.11-11
6.11-4D	GEOMETRICAL MODEL FOR THE CENTRAL SECTION BETWEEN THE COILS	6.11-11
6.11-5A	SHIELD THICKNESSES FOR THE TOKAMAK INBOARD SECTION AND THE CORRESPONDING NUCLEAR RESPONSES IN THE TOROIDAL FIELD COILS NORMALIZED TO 5 MW/m^2 DT NEUTRON WALL LOADING OR 150 MW • y/m^2 DT NEUTRON FLUENCE AT THE FIRST WALL	6.11-17
6.11-5B	TOKAMAK OUTBOARD SHIELD THICKNESS FOR THE DIFFERENT BLANKET CONCEPTS	6.11-17
6.11-5C	SHIELD THICKNESSES FOR THE MIRROR CENTRAL CELL SECTION UNDER THE COILS AND THE NUCLEAR RESPONSES IN THE CENTRAL CELL COILS NORMALIZED TO 5 MW/m^2 DT NEUTRON WALL LOADING OR 150 MW • y/m^2 DT NEUTRON DT NEUTRON FLUENCE AT THE FIRST WALL	6.11-18
6.11-5D	MIRROR SHIELD THICKNESS BETWEEN THE CENTRAL CELL COILS FOR THE DIFFERENT BLANKET CONCEPTS	6.11-18

6.11 Energy Multiplication, First Wall Atomic Displacement, and Shielding Requirements for All Blanket Concepts

A nucleonic analysis was performed for each R=1 blanket concept of the BCSS to determine the energy multiplication factors, the first wall atomic displacement rate, shielding requirements, and the nuclear responses in the superconducting coils. The shielding materials selection, composition, arrangement, and thickness were considered in the analysis. The shield thickness was defined to protect the superconductoring coils from radiation damage during reactor operation and to protect the workers in the reactor hall from decay gamma rays after shutdown. The analysis employed the same ground rules for all the concepts with respect to design criteria, nuclear data libraries, radiation transport codes, and shielding materials. The blanket energy multiplication factor, the energy deposition in the shield, the atomic displacement in the first wall, and the shielding requirements obtained from this study were used in the evaluation process to compare the different concepts. The design criteria, the analysis procedure, and the results for each concept are the subject of this section.

6.11.1 Design Criteria

The effect of irradiation on superconducting coils tends to lower their performance.[6.11-1] For superconductor materials, neutron irradiation reduces the critical current density (J_c) and the critical temperature (T_c). For NbTi material it has been shown that J_c is decreased by about 10% at a fast neutron fluence of about 4×10^{18} n/cm^2 (E > 0.1 MeV) while T_c is unchanged.[6.11-1,6.11-2]. Irradiation experiments at RTNS-II[6.11-3] on NbTi superconductors show consistent results with previous work. On the other hand, J_c of Nb_3Sn generally increases, reaching a maximum and then decreases as the neutron fluence increases.[6.11-4] Irradiation experiments on Nb_2Sn at 6°K6.[11-1,6.11-2] with a fast neutron fluence of 4×10^{18} n/cm^2 show that the maximum value and the increased rate of J_c increase with the magnetic field. At a magnetic field of 5T, the 6°K experiment resulted in a 16% increase in J_c at a fast neutron fluence of 2×10^{18} n/cm^2 without reaching a peak. Irradiation experiments at higher temperatures (~ 350°K) show the same behavior for J_c. However, the J_c peak was lower than the corresponding value at lower temperature for the same magnetic field. For example, the 350°K irradiation gave

an 8% increase corresponding to the 16% mentioned before at 6°K. Other experiments at 400°K and a 10T field[6.11-5] resulted in a 90% increase for J_c at a fast neutron fluence of 4.4×10^{18} n/cm^2 and dropped to the original value of J_c as the neutron fluence increased to 10^{19} n/cm^2. Based on these experimental results[6.11-1,-4,-5], the comparison between the room temperature and the 6°K irradiation results, and a maximum field of 11T; a neutron fluence above 10^{19} n/cm^2 for Nb_3Sn is possible to achieve without a decrease in the critical current density. At this neutron fluence the T_c value is about 0.9 the original value.[6.11-5]

The stabilizer material carries the current in the event that the superconductor temporarily acts as a normal conductor. The coil is designed to remove the generated heat (I^2R) so that the normal region does not propagate. The resistance (R) of the copper stabilizer is the key parameter for this process. The total resistivity, ρ, of the copper stabilizer can be described as the sum of three components: the initial resistivity, ρ_o; the magneto-resistivity, ρ_μ; and the irradiation induced resistivity ρ_{irr}. Magneto-resistance is a function of ρ_o, ρ_{irr}, and the magnetic field which complicates the evaluation of $\rho\mu$. Few experimental studies[6.11-3,6.11-6 - 6.11-10] have been done on the change of the copper resistivity as a function of magnetic field, neutron fluence, and number of cycles of alternate neutron irradiation (4°K) and annealing (300°K). The change in the copper resistivity can be accommodated by using more copper stabilizer which will increase the thickness of the coils, can be partially annealed out by warming the coils, or can be reduced by improving the shielding performance (increase shielding thickness or better materials). The maximum irradiation induced resistivity is limited to about 5×10^{-8} $\Omega \cdot$ cm in the copper stabilizer at the end-of-life based on the analyses of the previous studies.[6.11-11 - 6.11-14]

The most sensitive component in the coils is the insulator material because the radiation damage is irreversible and limits the operating life of the coils. The properties of interest for the coil designs are the electrical resistivity, dielectric strength, mechanical strength, and thermal insulation. Experimental results[6.11-15 - 6.11-17] from neutron irradiation at 5°K suggests that polyimides can withstand a radiation dose of 10^{10} rads and retain high resistivity and mechanical strength. Glass cloth reinforced epoxy type G10-CR or G11-CR shows a serious degradation at 2×10^9 rads. A 10^{10} rads

maximum tolerable dose in the insulator material at the end-of-life was assumed for the current analysis.

The nuclear energy deposited in the coils impacts the refrigeration power required since about 500 W of electrical power is consumed to remove one watt from the superconductor coils at 4°K. This low removal efficiency calls for minimizing the nuclear energy deposited in the superconductor coils. The maximum nuclear heating was chosen to be less than 1.0 mW/cm^3 to avoid any cryogenic instability concerns and to reduce the required refrigeration capacity.

For personnel protection, the International Commission on Radiological Protection (ICRP) recommendations and the U.S. Federal Regulations[6.11-18] classify exposed individuals into two categories: (a) people exposed in the course of their work, and (b) general public. The occupational exposure limit is 5 rem/y with a maximum of 3 rem/quarter. The occupational exposure based on working 8 h per day and 40 h per week is 2.5 mrem/h. The cumulative dose shall not exceed 5(N-18) rem, where N is the age of the worker in years. Higher doses are permitted to the hands as shown in Table 6.11-1. However, the current practice in the nuclear industry, the exposure policy of the Department of Energy (DOE) and the national laboratories' guidelines are to reduce radiation exposure as low as reasonably achievable (ALARA). Specifically, DOE-5980.1 states the following: "Exposure rates in work areas should be reduced as low as reasonably achievable by proper facility design layout. Design efforts to consider are: occupancy time, source terms, spacing, processes, equipment, and shielding. On-site personnel exposure level less than one-fifth of the permissible dose equivalent limits, prescribed in this chapter should be used as a design objective." This guideline limits on-site workers to less than 1 rem/y (0.5 mrem/h).

TABLE 6.11-1. OCCUPATIONAL DOSE LIMITS

Organ	Rem/quarter	Rem/year
Whole body	1.25	5
Hands and feet	18.75	75
Skin of whole body	7.50	30

For the general public, the limits are guided by the recommendations of the Environmental Protection Agency. The proposed radiation dose guideline in the "Clean Air Act, Radiological Emission Standards," is 10 mrem/y for any member of the public assumed to reside at the site boundary.

6.11.2 Procedure and Assumptions for the Analysis

One-dimensional nucleonics calculations were performed for each blanket concept of the BCSS as a function of the shield thickness. The analysis for the inboard and the outboard section of each tokamak blanket concept were carried out separately to account for the difference in the blanket parameters and the design criteria. The total thickness of the inboard blanket and shield is an important parameter for tokamak designs. The inboard shield was designed to protect the inner leg of the toroidal field coils. In the outboard section, the shield was designed to permit personnel access to the reactor hall one day after shutdown. A similar analysis was performed for the mirror blanket concepts. For each mirror blanket concept, two shield thicknesses were also defined. Between the central cell coils, a shield thickness was determined based on the personnel access criterion. Under the central cell coils, another shield thickness was defined to protect the coils from radiation damage.

The materials for the shielding system were selected based upon tradeoff studies and the results of the previous designs.[6.11-11,-14,-19] In the selection process, cost, resource availability, and performance were considered. The shielding materials selected for this study are Fe14Mn2Ni2Cr steel alloy (Fe1422), boron carbide (B_4C), water (H_2O), and lead. Fe1422 is the main shielding material where the low concentration of nickel and chromium motivated its use. Low nickel concentration reduces the dose equivalent after shutdown and the production of long-lived isotopes; low chromium concentration minimizes the consumption of strategic materials. Water and Fe1422 are the coolant and the structural material for the shield, respectively. A small amount of B_4C is employed at the back of the shield as a neutron absorber to reduce the activation in the reactor components and the structural materials. A 0.7 density factor was assumed for the B_4C to avoid the fabrication cost required for a high density material. Lead is used as a gamma ray attenuator at the outer most surfaces of the outboard shield in the tokamak reactors and the

shield section between the central cell coils in the mirror reactors so that the dose equivalent in the reactor building is reduced after shutdown.

The one-dimensional calculations were performed using the discrete ordinate code ANISN[6.11-20] with an S_8 symmetric angular quadrature set and a P_3 legendre expansion for the scattering cross sections. A 67-multigroup cross section set (46 neutrons and 21 photons) collapsed from the CTR library[6.11-21] was used for the ANISN calculations. The MACKLIB-IV[6.11-22] was employed to calculate the nuclear responses (nuclear heating, radiation damage, etc.). A 5 MW/m^2 DT average neutron wall loading and a 150 $MW \cdot y/m^2$ DT neutron exposure at the first wall were assumed for the analysis. For tokamak concepts, 20% of the total first wall surface area was assumed to be associated to the inboard section similar to the STARFIRE design.

6.11.3 Energy Deposition and First Wall Atomic Displacement

The analysis was performed for the sixteen blanket concepts, seven tokamaks and nine mirrors, using their reference parameters as defined in the other chapters. Table 6.11-2 gives the calculated energy deposition results for each concept which includes the energy multiplication factors and the total energy deposition per fusion neutron in the blanket and the shield separately. The highest energy deposition per fusion neutron occurs with the FLIBE blanket concept because of the large Be fraction used. In fact, the blanket concepts with Be produce higher energy deposition per fusion neutron than the others considered in this study. The liquid lithium blanket (Li/Ferritic/Li) has the highest blanket energy multiplication factor among the blanket concepts without Be as well as the $LiAlO_2$/Ferritic/He/Be blanket concept. The $LiAlO_2$/Ferritic/He/Be blanket has a 1.4 energy multiplication factor but 8% of the energy is lost to the shield. In general, the percentage of the total energy deposited in the shield should be minimized to reduce the energy losses and increase the recoverable energy from the blanket. This indicates that the $LiAlO_2$/Ferritic/He/Be blanket concept can be modified to increase the blanket energy multiplication factor. The water cooled blanket has the lowest energy loss to the shield relative to the other concepts due to the good moderation properties of hydrogen.

TABLE 6.11-2A. TOKAMAK BLANKET ENERGY DEPOSITION

Blanket Concept Breeder/Structure/Coolant/Multiplier	Energy Multiplication Factor		Total Energy	Shield Energy	Percentage of Energy in the Shield
	Blanket	Total	MeV per DTn	MeV per DTn	
Li_2O/Ferritic/He	1.223	1.298	18.24	1.05	5.7
$LiAlO_2$/Ferritic/He/Be	1.280	1.399	19.67	1.68	8.5
$LiAlO_2$/Ferritic/H_2O/Be	1.372	1.399	19.67	0.38	1.9
Li/Ferritic/He	1.279	1.364	19.17	1.21	6.3
FLIBE/Ferritic/He/Be	1.511	1.608	22.61	1.37	6.1
Li/V/Li	1.272	1.311	18.43	0.55	3.0
$LiAlO_2$/Ferritic/NS/Be	1.323	1.365	19.19	0.59	3.1

TABLE 6.11-2B. MIRROR BLANKET ENERGY DEPOSITION

Blanket Concept Breeder/Structure/Coolant/Multiplier	Energy Multiplication Factor		Total Energy	Shield Energy	Percentage of Energy in the Shield
	Blanket	Total	MeV per DTn	MeV per DTn	
Li_2O/Ferritic/He	1.228	1.284	18.05	0.77	4.3
$LiAlO_2$/Ferritic/He/Be	1.291	1.408	19.80	1.65	8.3
$LiAlO_2$/Ferritic/H_2O/Be	1.386	1.394	19.60	0.11	0.6
Li/Ferritic/He	1.270	1.345	18.91	1.06	5.6
FLIBE/Ferritic/He/Be	1.549	1.582	22.24	0.46	2.1
Li/V/Li	1.254	1.297	18.24	0.61	3.3
Li/Ferritic/Li	1.313	1.368	19.23	0.77	4.0
LiPb/V/LiPb	1.294	1.319	18.55	0.35	1.9
$LiAlO_2$/Ferritic/NS/Be	1.316	1.371	19.27	0.76	3.9

The atomic displacement rate in the first wall is given in Table 6.11-3 for all the concepts. The lithium-lead breeder increases the atomic displacement rate in the first wall by about 70% relative to the other breeder. This is due to an increase in the fast neutron flux (MeV range) from the (n,xn) reactions and the back scattering from the lead material. The water coolant causes a 10% reduction in the first wall atomic displacement rate relative to the He coolant as shown in Table 6.11-3 for the $LiAlO_2$ breeder blankets. The softening of the neutron spectrum caused by the water coolant is responsible for this decrease. Also, the analysis of a specific blanket concept for tokamak and mirror type reactors shows that the tokamak geometry causes a 10% increase in atomic displacement rates in the first wall relative to the mirrors. In fact, the small plasma radius increases the neutron incident angle on the first wall, which decreases the travelling distance and the reaction rate in the first wall.

TABLE 6.11-3. FIRST WALL ATOMIC DISPLACEMENT RATE

Blanket Concept Breeder/Structure/Coolant/Multiplier	Atomic Displacement Rate dpa/5 MW•y/m^2	
	Tokamak	Mirror
Li_2O/Ferritic/He	59.1	53.2
$LiAlO_2$/Ferritic/He/Be	57.1	54.5
$LiAlO_2$/Ferritic/H_2O/Be	52.5	48.7
Li/Ferritic/He	59.7	51.4
FLIBE/Ferritic/He/Be	61.7	55.7
Li/V/Li	55.4	49.4
Li/Ferritic/Li	--	52.6
LiPb/V/LiPb	--	83.8
$LiAlO_2$/Ferritic/NS/Be	59.8	52.9

6.11.4 Shielding Requirements

A nucleonic analysis was performed to define the shielding requirements for each blanket concept for the evaluation process. A steel shield was used for all the concepts without tailoring the shield design to a specific concept. For the inboard section in tokamak reactors and sections under the central cell coils for the mirrors, the shield thickness was determined based on 10^{10} rads maximum radiation dose in the thermal insulator due to the 150 MW•y/m^2 DT neutron exposure at the first wall. At this shield thickness, the other nuclear responses were determined to check that the different components of the superconductor coils are adequately protected as expected. The outboard shield of the tokamaks and the sections between the central cell coils of the mirrors were defined based on the 0.5 mrem/hr dose equivalent in the reactor hall one day after shutdown with all shields in place.

The steel shield composition and arrangement shown in Table 6.11-4 for this study are based on previous studies.(6.11-11 - 6.11-14) Reoptimization of the shield design for each blanket concept is not expected to vary very much from the specified shield in Table 6.11-4. This is due to the fact that the radiation response parameters have a broad peak around this composition. In addition, the neutron spectra after few mean free paths in the bulk shield are similar and are dominated by the steel-water mixture.

As an example of the analysis, Figs. 6.11-1 through 6.11-7 give the nuclear responses in the superconducting coil of the central cell and the neutron flux at the back of the shield for the sections between the central cell coils performed for the Li_2O/Ferritic/He mirror concept. The maximum dose result shown in Fig. 6.11-1 indicates that a 55 cm shield thickness is required to limit the dose in the thermal insulator to 10^{10} rads at the end-of-life (150 MW•y/m^2 DT neutron fluence at the first wall). At this shield thickness, the maximum nuclear heating in the superconductor winding is 0.1 MW/cm^3, as shown in Fig. 6.11-2. This value is very close to the optimum configuration(6.11-23,-24) and it does not cause any difficulty for the superconducting coil design. The corresponding total heating in the coil winding and the case is 2.8 W/cm of the coil length as shown in Fig. 6.11-3. The maximum neutron fluence in the superconductor material is 2.5×10^{18} n/cm^2 which is expected to produce less than 10% reduction in the critical current density of the NbTi superconductor. The induced resistivity in the copper stabilizer is about

TABLE 6.11-4A. GEOMETRICAL MODEL FOR THE INBOARD TOKAMAK SECTION USED IN THE SHIELDING ANALYSIS

Zone Description	Thickness, cm	Composition, Vol. %
Plasma	194	Vacuum
Scrape-off	20	Vacuum
Blanket[a]	--	--
Gap	2	Vacuum
Steel Shield	X[b]	80% Fe1422 steel alloy, 20% H_2O
Boron Shield	5	60% B_4C (0.7 DF), 20% Fe1422 steel alloy, 20% H_2O
Gap	2	Vacuum
Dewar	3	100% type 304 steel
Thermal Insulator	5	5% insulator
Case	7	100% type 304 steel
Winding	123	2% NbTi, 32% Cu, 38% type 304 steel, 24% Liquid He, 4% insulator
Case	7	100% type 304 steel

[a]Ref. blanket parameter as defined for each concept in the other chapters.
[b] X is a variable.

TABLE 6.11-4B. GEOMETRICAL MODEL FOR THE OUTBOARD TOKAMAK SECTION USED IN THE SHIELDING ANALYSIS

Zone Description	Thickness, cm	Composition, Vol. %
Plasma	194	Vacuum
Scrape-off	20	Vacuum
Outboard Blanket[a]	--	--
Gap	50	Vacuum
Steel Shield	X[b]	80% Fe1422 steel alloy, 20% H_2O
Boron Shield	5	60% B_4C (0.7 DF), 20% Fe1422 steel alloy, 20% H_2O
Lead Shield	5	100% Pb

[a]Ref. blanket parameter as defined for each concept in the other chapters.
[b]X is a variable.

TABLE 6.11-4C. GEOMETRICAL MODEL FOR THE CENTRAL CELL SECTION WITH SUPERCONDUCTOR COIL USED IN THE SHIELD ANALYSIS

Zone Description	Thickness,cm	Composition, Vol. %
Plasma	45	Vacuum
Scrape-off	15	Vacuum
Blanket[a]	--	--
Cap	2	Vacuum
Steel Shield	X[b]	80% Fe1422 steel alloy, 20% H_2O
Boron Shield	5	60% B_4C (0.7 DF), 20% Fe1422 steel alloy, 20% H_2O
Dewar	1	100% type 304 steel
Thermal Insulator	3	5% insulator
Liquid Nitrogen	1	31.75% type 304 steel, 68.25% liquid N_2
Thermal Insulator	7	5% insulator
Case	5	100% type 304 steel
Winding	120	3.6% NbTi, 31.5% Cr, 35% type 304 steel, 15% liquid He, 15% insulator
Case	5	100% type 304 steel

[a]Ref. blanket parameter as defined for each concept in the other chapters.
[b]X is a variable.

TABLE 6.11-4D. GEOMETRICAL MODEL FOR THE CENTRAL SECTION BETWEEN THE COILS

Zone Description	Thickness,cm	Composition, Vol. %
Plasma	45	Vacuum
Scrape-off	15	Vacuum
Blanket[a]	--	--
Gap	2	Vacuum
Steel Shield	X[b]	80% Fe1422 steel alloy, 20% H_2O
Boron Shield	5	60% B_4C (0.7 DF), 20% H_2O 20% Fe1422 steel alloy
Lead Shield	5	100% Pb

[a]Ref. blanket parameter as defined for each concept in the other chapters.
[b]X is a variable.

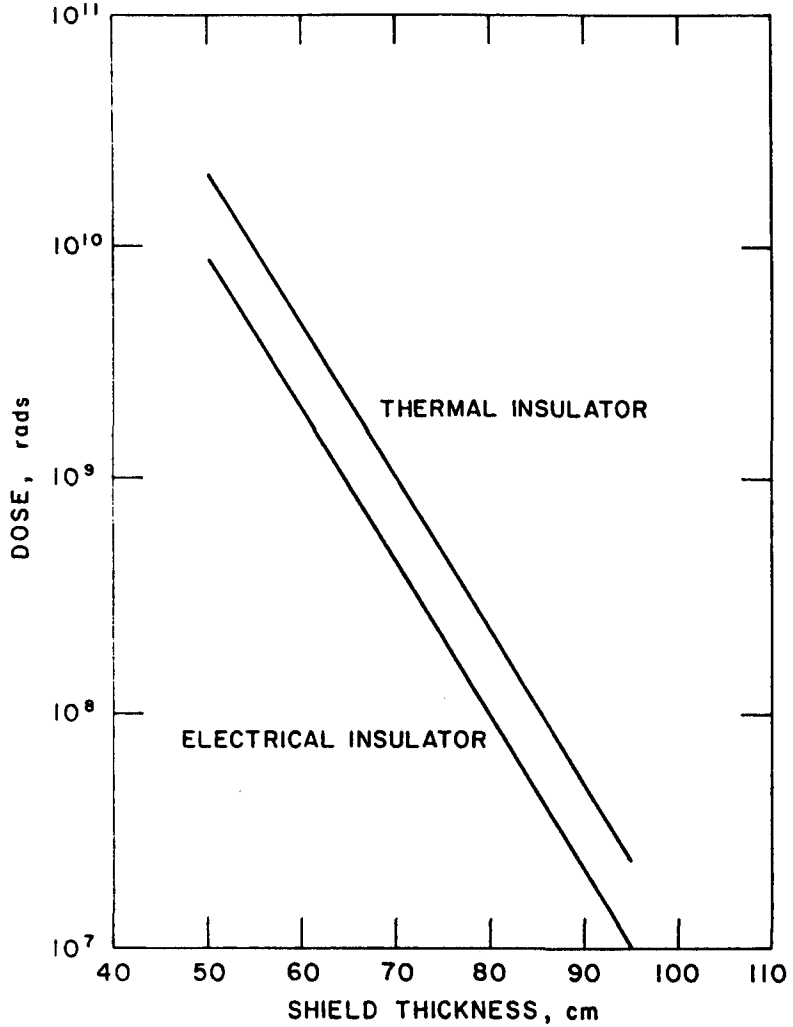


Fig. 6.11-1. Maximum thermal insulator dose as a function of the shield thickness normalized to 150 MW·y/m^2 D-T neutron fluence at the first wall.

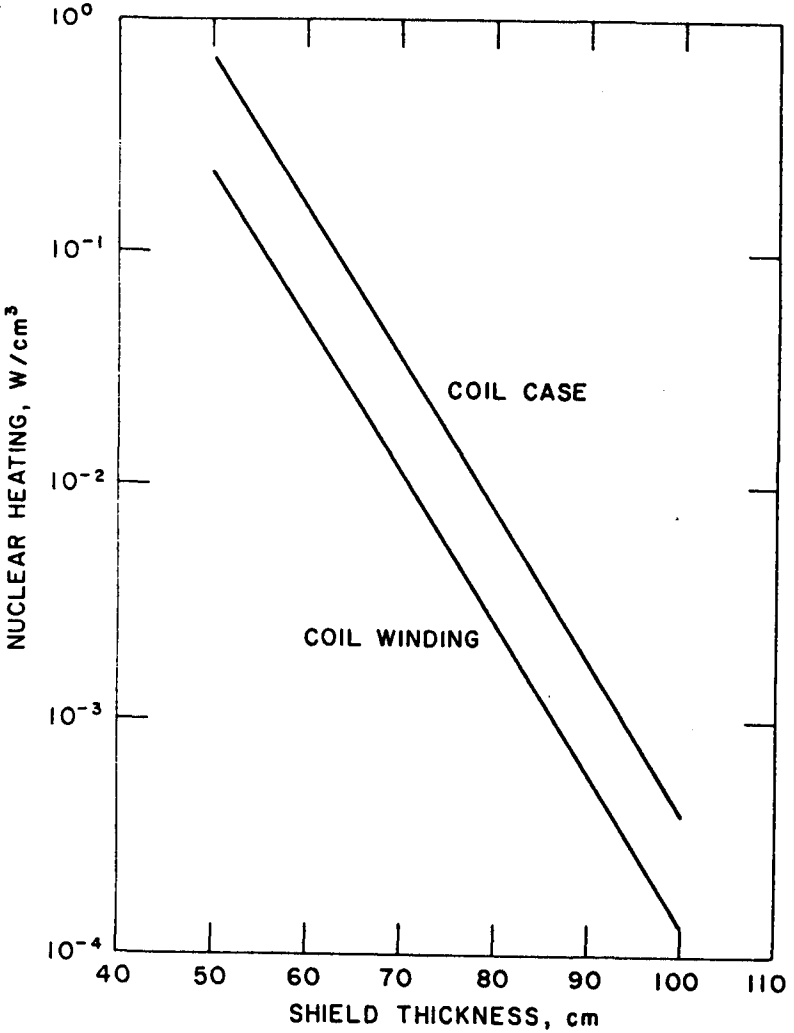


Fig. 6.11-2. Maximum nuclear heating rate as a function of the shield thickness normalized to 5 MW/m^2 D-T neutron wall loading at the first wall.

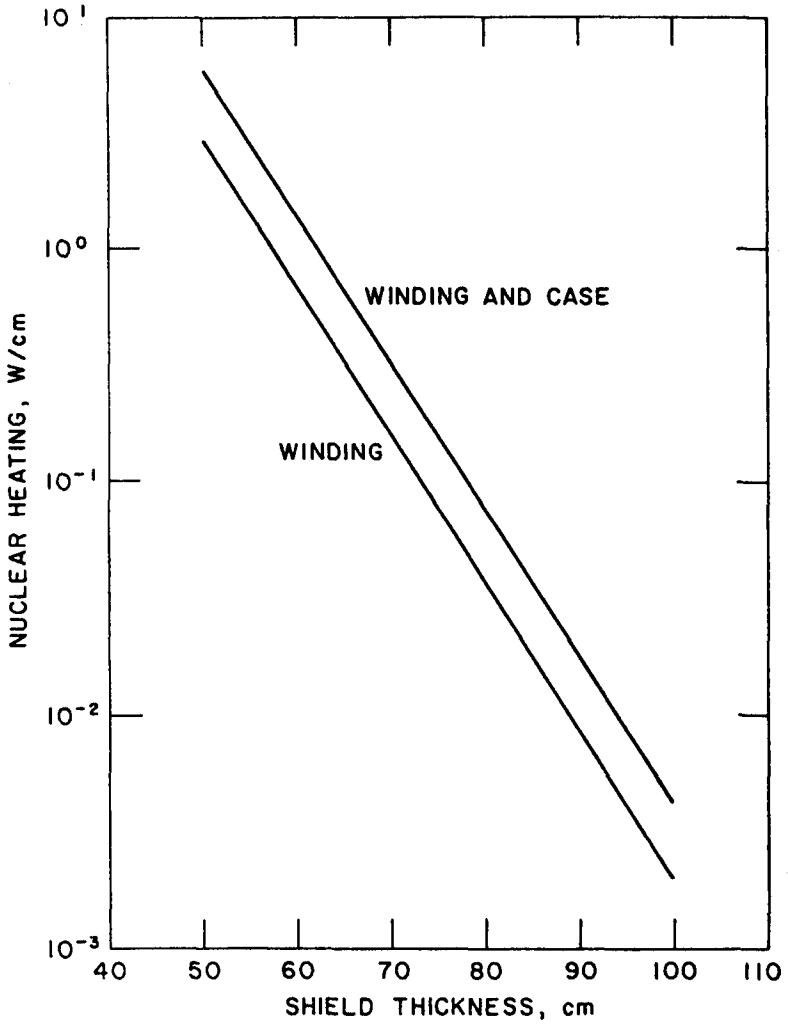


Fig. 6.11-3. Nuclear heating in the central cell coil materials normalized to 5 MW/m^2 D-T wall loading at the first wall.

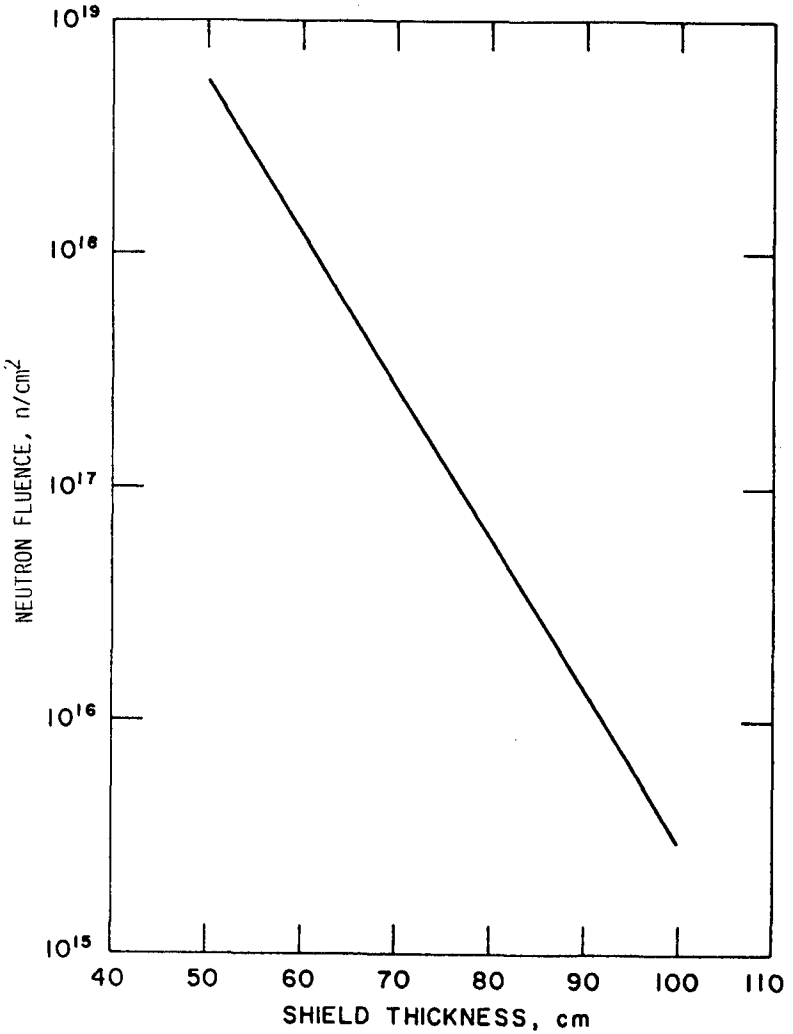


Fig. 6.11-4. Maximum neutron fluence in the winding material as a function of the shield thickness normalized to 150 $MW \cdot y/m^2$ D-T neutron fluence at the first wall.

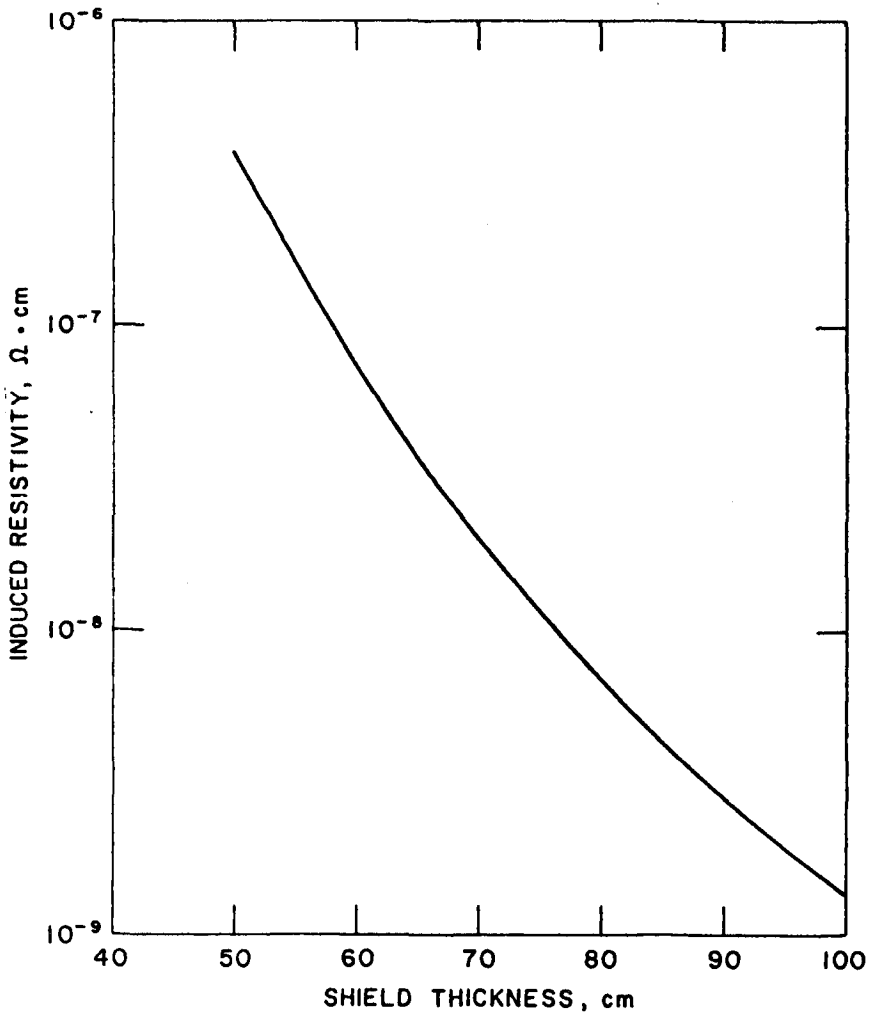


Fig. 6.11-5. Maximum copper induced resistivity in the superconductor coils as a function of the shield thickness normalized to 150 MW•y/m^2 D-T neutron fluence at the first wall.

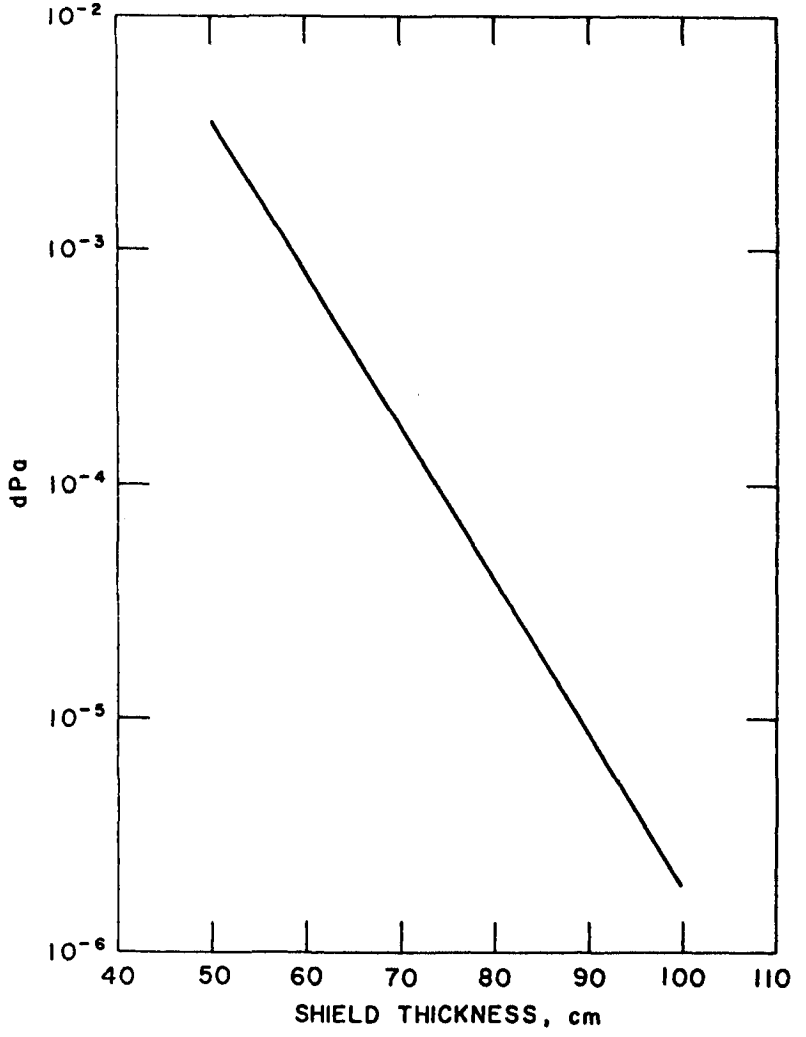


Fig. 6.11-6. Maximum atomic displacement in the copper stabilizer of the superconductor in the central cell coils normalized to 150 MW•y/m^2 D-T neutron fluence and the first wall.

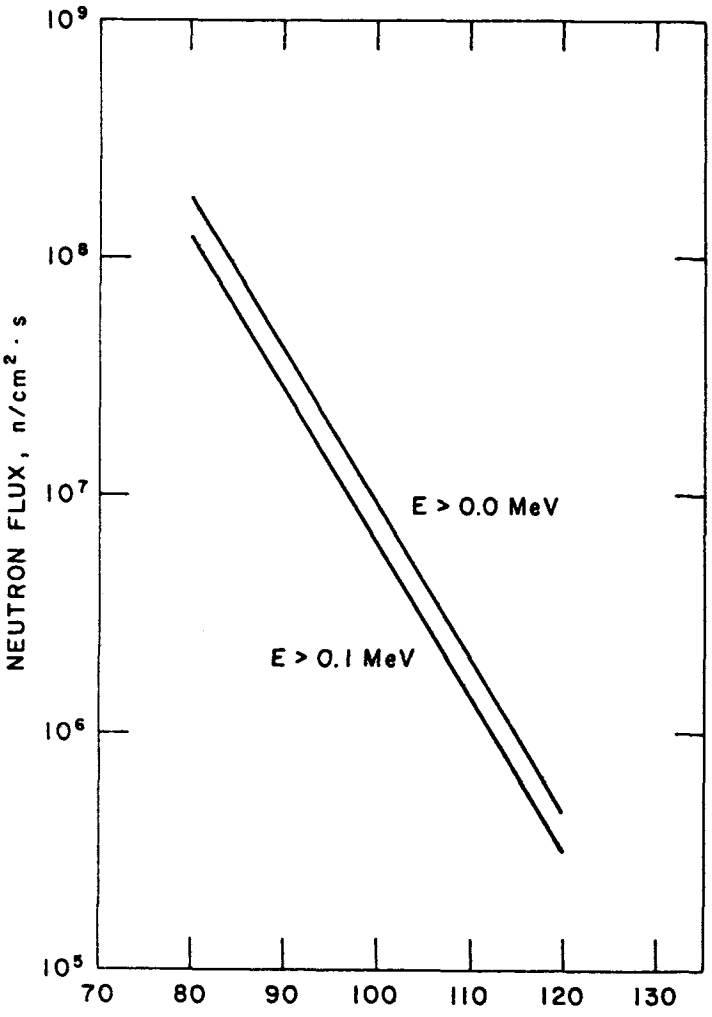


Fig. 6.11-7. Neutron flux at the outer shield surface between the central cell coils normalized to 5 MW/m^2 D-T neutron wall loading at the first wall.

1.6×10^{-7} $\Omega\cdot$cm which requires the coils to be annealed two times during the 40 years operating life of the reactor. Based on these values for the different nuclear responses, it appears that the use of the 10^{10} rads design criterion for the thermal insulator provides adequate protection to the superconducting coils with respect to all the other nuclear responses. Under this criterion, the lithium-lead concept achieves the lowest fast neutron fluence in the superconductor coil which reduces the induced resistivity in the copper stabilizer and the change in the critical current density of the superconductor material.

As mentioned before the outboard shield thickness for the tokamak concepts and the shield thickness between the central cell coils for the mirror concepts were designed with the 0.5 mrem/hr dose equivalent in the reactor hall one day after shutdown. Our previous analysis for this shield(6.11-14) and other studies for high fluence designs show that a 5×10^{6} n/cm$^2\cdot$s flux level at the outer shield surface results in the required dose equivalent. This was compared to the calculated neutron flux at the outer surface of the shield for each concept as a function of the shield thickness. From these calculations the shield thickness for each concept was defined as shown in Tables 6.11-5B and 6.11-5D. In addition, radioactivity calculations were performed for two blanket concepts (Li/V/Li and LiPb/V/LiPb mirror blanket concepts) to confirm the flux value used to determine the shield thickness. The decay gamma sources for both blankets one day after shutdown were used in transport calculations with the shield thickness as defined in Table 6.11-4D. The results confirmed the 0.5 mrem/h dose equivalent in the reactor hall one day after shutdown within ±0.07 mrem/h. This tolerance translates to ±1 cm adjustment for the shield thickness used in the calculations which is quite adequate accuracy for the evaluation process of the different blanket concepts.

Comparing the shielding thicknesses for the different concepts, the following observations can be obtained: a) the liquid lithium blanket/shield has the largest inboard thickness due to the large lithium fraction in the reflector zone dictated by MHD pressure drop considerations; b) the solid breeder blanket/shield with water coolant has the smallest inboard thickness because the water fraction is near optimum conditions from shielding point of view, c) the salt-cooled concept has the smallest blanket/shield thickness to achieve the 0.5 mrem/h dose criterion one day after shutdown, d) the helium-cooled

TABLE 6.11-5A. SHIELD THICKNESSES FOR THE TOKAMAK INBOARD SECTION AND THE CORRESPONDING NUCLEAR RESPONSES IN THE TOROIDAL FIELD COILS NORMALIZED TO 5 MW/m^2 DT NEUTRON WALL LOADING OR 150 $MW \cdot y/m^2$ DT NEUTRON FLUENCE AT THE FIRST WALL

Blanket Concept Breeder/Structure/ Coolant/Multiplier	Blanket Thickness, (cm)	Shield Thickness, (cm)	Total Thickness, (cm)	Maximum Nuclear Heating in the Winding, mW/cm^3	Nuclear Heating in the Coil (Case + winding) W/cm	Maximum Dose in the Electrical Insulator, rads	Maximum Neutron Fluence in the Winding (E>0.1 MeV) n/cm^2	Maximum Induced Resistivity in the Copper $\Omega \cdot cm$	Maximum Atomic Displacement dpa
Li_2O/Ferritic/He	41	73	114	7.1×10^{-2}	4.6	4.2×10^{9}	3.8×10^{18}	2.1×10^{-7}	1.8×10^{-3}
$LiAlO_2$/Ferritic/He/Be	41	74	115	7.2×10^{-2}	4.6	4.3×10^{9}	3.4×10^{18}	2.0×10^{-7}	1.9×10^{-3}
$LiAlO_2$/Ferritic/H_2O/Be	35	70	105	6.7×10^{-2}	4.1	4.1×10^{9}	3.3×10^{18}	1.9×10^{-7}	1.8×10^{-3}
Li/Ferritic/He	61	64	125	7.5×10^{-2}	5.0	4.0×10^{9}	3.2×10^{18}	1.8×10^{-7}	1.9×10^{-3}
FLIBE/Ferritic/He/Be	41	75	116	7.1×10^{-2}	4.5	4.1×10^{9}	3.3×10^{18}	1.9×10^{-7}	1.8×10^{-3}
Li/V/Li	64	62	126	7.3×10^{-2}	4.9	4.1×10^{9}	3.3×10^{18}	1.9×10^{-7}	1.8×10^{-3}
$LiAlO_2$/Ferritic/NS/Be	51	60	111	7.1×10^{-2}	4.5	4.1×10^{9}	3.3×10^{18}	1.9×10^{-7}	1.8×10^{-3}

TABLE 6.11-5B. TOKAMAK OUTBOARD SHIELD THICKNESS FOR THE DIFFERENT BLANKET CONCEPTS

Blanket Concept Breeder/Structure/ Coolant/Multiplier	Blanket Thickness (cm)	Shield Thickness (cm)	Total Thickness (cm)
Li_2O/Ferritic/He	85	102	187
$LiAlO_2$/Ferritic/He/Be	70	116	186
$LiAlO_2$/Ferritic/H_2O/Be	70	99	169
Li/Ferritic/He	120	104	224
FLIBE/Ferritic/He/Be	85	99	184
Li/V/Li	75	95	170
$LiAlO_2$/Ferritic/NS/Be	51	112	163

TABLE 6.11-5C. SHIELD THICKNESSES FOR THE MIRROR CENTRAL CELL SECTION UNDER THE COILS AND THE NUCLEAR RESPONSES IN THE CENTRAL CELL COILS NORMALIZED TO 5 MW/m^2 DT NEUTRON WALL LOADING OR 150 $MW\cdot y/m^2$ DT NEUTRON DT NEUTRON FLUENCE AT THE FIRST WALL

Blanket Concept Breeder/Structure/ Coolant/Multiplier	Blanket Thickness, (cm)	Shield Thickness, (cm)	Total Thickness, (cm)	Maximum Nuclear Heating in the Winding, mW/cm^3	Nuclear Heating in the Coil (Case + winding) W/cm	Maximum Dose in the Electrical Insulator, rads	Maximum Neutron Fluence in the Winding (E>0.1 MeV) n/cm^2	Maximum Induced Resistivity in the Copper $\Omega\cdot cm$	Maximum Atomic Displacement dpa
Li_2O/Ferritic/He	68.0	55.0	123.0	0.10	2.8	4.1×10^9	2.5×10^{18}	1.6×10^{-7}	1.6×10^{-3}
$LiAlO_2$/Ferritic/He/Be	58.0	64.0	122.0	0.11	3.0	4.5×10^9	2.9×10^{18}	1.7×10^{-7}	1.8×10^{-3}
$LiAlO_2$/Ferritic/H_2O/Be	70.0	45.0	115.0	0.09	3.0	4.1×10^9	2.7×10^{18}	1.7×10^{-7}	1.7×10^{-3}
Li/Ferritic/He	108.0	52.0	160.0	0.12	3.7	4.1×10^9	2.4×10^{18}	1.5×10^{-7}	1.5×10^{-3}
FLIBE/Ferritic/He/Be	85.0	47.0	132.0	0.11	3.0	3.8×10^9	2.2×10^{18}	1.4×10^{-7}	1.4×10^{-3}
Li/V/Li	80.3	48.2	128.5	0.13	3.4	4.0×10^9	2.2×10^{18}	1.4×10^{-7}	1.4×10^{-3}
Li/Ferritic/Li	80.3	48.7	129.0	0.13	3.5	3.7×10^9	2.0×10^{18}	1.3×10^{-7}	1.2×10^{-3}
LiPb/V/LiPb	90.3	40.0	130.3	0.14	3.9	2.5×10^9	6.6×10^{17}	5.0×10^{-8}	3.1×10^{-4}
$LiAlO_2$/Ferritic/NS/Be	51.0	59.0	110.0	0.11	2.7	4.3×10^9	2.7×10^{18}	1.7×10^{-7}	1.7×10^{-3}

TABLE 6.11-5D. MIRROR SHIELD THICKNESS BETWEEN THE CENTRAL CELL COILS FOR THE DIFFERENT BLANKET CONCEPTS

Blanket Concept Breeder/Structure/ Coolant/Multiplier	Blanket Thickness (cm)	Shield Thickness (cm)	Total Thickness (cm)
Li_2O/Ferritic/He	68	104	172
$LiAlO_2$/Ferritic/He/Be	58	114	172
$LiAlO_2$/Ferritic/H_2O/Be	70	95	165
Li/Ferritic/He	108	101	209
FLIBE/Ferritic/He/Be	85	95	180
Li/V/Li	80.3	96.2	176.5
Li/Ferritic/Li	80.3	95.7	176
LiPb/V/LiPb	90.3	75	165.3
$LiAlO_2$/Ferritic/NS/Be	51	108	159

concepts require the largest blanket/shield thickness for tokamak and mirror due to the large helium fraction in the blanket, and e) the mirror concepts have about the same blanket/shield thickness except for the helium cooled concepts.

REFERENCES FOR SECTION 6.11

6.11-1 B. S. Brown, "Radiation Effects in Superconducting Fusion Magnet Materials," Journal of Nuclear Materials 97 (1981) 1.

6.11-2 M. Soell, "Influence of Radiation Damage on the Maximum Attainable Magnetic Field for Toroidal Fusion Magnet Systems," Journal of Nuclear Materials 72 (1978) 168.

6.11-3 R. A. VanKonynenburg, et al., "Fusion Neutron Damage in Superconductors and Magnet Stabilizer," Journal of Nuclear Materials 103 & 104 (1981) 739.

6.11-4 B. S. Brown and T. H. Blewitt, "Critical Current Density Changes in Irradiated Nb_3Sn," Journal of Nuclear Materials 103 & 104 (1979) 18.

6.11-5 C. L. Snead, Jr., et al., "High-energy-neutron Damage in Nb_3Sn: Changes in Critical Properties, and Damage-energy Analysis," Journal of Nuclear Materials 103 & 104 (1981) 749.

6.11-6 C. E. Klaburde, et al., "The Effects of Irradiation on the Normal Metal of Composite Superconductor: A Comparison of Copper and Aluminum," Journal of Nuclear Materials 85 & 86 (1979) 185.

6.11-7 J. M. Williams, et al., "The Effects of Irradiation on the Copper Normal Metal of a Composite Superconductor," IEEE Trans. on Magnetics 15 (1979) 731.

6.11-8 S. Tokamura and T. Kato, "The Effects of Low Temperature Irradiation and Other Materials for Superconducting Magnets," Journal of Nuclear Materials 103 & 104 (1981) 729.

6.11-9 M. W. Guinan, "Radiation Effects Limits on Copper in Superconducting Magnets," Lawrence Livermore National Laboratory Report, UCID-19800 (1983).

6.11-10 R. R. Coltman, Jr., "Organic Insulators and the Copper Stabilizer for Fusion Reactor Magnets," International Conference on Neutron Irradiation Effects, November 9-12, 1981, Argonne National Laboratory, Argonne, IL.

6.11-11 C. C. Baker, et al., "STARFIRE - A Commercial Tokamak Fusion Power Plant Study," Argonne National Laboratory Report, ANL/FPP-80-1 (1980).

6.11-12 Y. Gohar and M. A. Abdou, "INTOR Radiation Shielding for Personnel Access," Proceedings of the Ninth Symposium on Engineering Problems of Fusion Research, Chicago, IL, October 26-29, 1981.

6.11-13 Y. Gohar and M. A. Abdou, "U.S. INTOR Radiation Shield Design," Proceeding of the Sixth International Conference on Radiation Shielding, Tokyo, Japan, May 16-20, 1983.

6.11-14 Y. Gohar, "Low Cost Shield for Tokamak Fusion Reactors," Nuclear Technology/Fusion, Vol. 4, No. 2 (1983) 373.

6.11-15 R. R. Coltman, Jr., et al., "Radiation Effects on Organic Insulators for Superconducting Magnets," Oak Ridge National Laboratory Report ORNL/TM-7077 (1979).

6.11-16 R. H. Kernohan, et al., "Radiation Effects on Organic Insulators for Superconducting Magnets," Oak Ridge National Laboratory Report ORNL/TM-6708 (1978).

6.11-17 F. W. Clinard, Jr., and G. F. Hurley, "Ceramic and Organic Insulators for Fusion Applications," Journal of Nuclear Materials 103 & 104 (1981) 705.

6.11-18 U.S. Nuclear Regulatory Commission, "Standard for Protection Against Radiation: U.S. NRC Rules and Regulations," Title 10, Chapter 1, Part 20 (1977).

6.11-19 M. Abdou, et al., "A Demonstration Tokamak Power Plant Study," Argonne National Laboratory Report, ANL/FPP/82-1 (September 1982).

6.11-20 W. W. Engle, Jr., "A User's Manual for ANISN, A One Dimensional Discrete Ordinates Code with Anisotropic Scattering," Oak Ridge Gaseous Diffusion Plant, ORGDP-K-1963 (1967).

6.11-21 R. W. Roussin, et al., "The CTR Processed Multigroup Cross Section Library for Neutronics Studies," Oak Ridge National Laboratory ORNL/RCSIC-37.

6.11-22 Y. Gohar and M. A. Abdou, "MACKLIB-IV: A Library of Nuclear Response Functions Generated with MACK-IV Computer Program from ENDF/B-IV," Argonne National Laboratory, ANL/FPP/TM-106 (1978).

6.11-23 J. H. Huang and M. E. Sawan, "Neutronics Analysis for the MARS Li-Pb Blanket and Shield," Journal of Nuclear Technology/Fusion, Vol. 6, No. 2, 883 (1983).

6.11-24 B. G. Logan et al., "MARS: Mirror Advanced Reactor Study - Final Report," Lawrence Livermore National Laboratory, UCRL-53480 (1984).

BLANKET COMPARISON AND SELECTION STUDY

SECTION 6.12 - ACTIVATION/WASTE MANAGEMENT

SECTION 6.12

TABLE OF CONTENTS

PAGE NO.

6.12 Activation/Waste Management.....6.12-1
6.12.1 Introduction.....6.12-1
6.12.2 Qualitative Comparisons of Remote Maintenance Ratings.....6.12-3
6.12.3 Qualitative Comparisons of Waste Disposal Ratings.....6.12-5
REFERENCES.....6.12-19

LIST OF TABLES FOR SECTION 6.12

TABLE NO.	TITLE	PAGE NO.
6.12-1A	ELEMENTAL COMPOSITIONS USED FOR BCSS ACTIVATION ANALYSIS	6.12-7
6.12-1B	ELEMENTAL COMPOSITIONS USED FOR BCSS ACTIVATION ANALYSIS	6.12-9
6.12-2	RELATIVE RANKINGS OF MATERIALS BY RMR	6.12-11
6.12-3	MAJOR NUCLIDES FOR HIGH RMR	6.12-12
6.12-4	LIMITS FOR CLASS C WASTES APPROPRIATE FOR ACTIVATION WASTES IN FUSION AND DEFINED IN 10CFR61	6.12-13
6.12-5	ESTIMATED LIMITS FOR CLASS C LONG HALF LIFE GAMMA EMITTERS IN FUSION ACTIVATION WASTES NOT LISTED IN 10CFR61	6.12-14
6.12-6	WASTE DISPOSAL RATING AT 10 YEARS AFTER SHUTDOWN	6.12-15
6.12-7	SUITABILITY OF MATERIALS FOR NEAR-SURFACE BURIAL	6.12-16
6.12-8	MAJOR NUCLIDES PREVENTING NEAR-SURFACE BURIAL	6.12-17
6.12-9	ALPHA EMITTER CONCENTRATIONS FOR LiPb	6.12-18

6.12 Activation/Waste Management

6.12.1 Introduction

The selection of materials and the design of the blankets for fusion reactors have significant effects upon the radioactivity generated by neutron activation in the materials.[6.12-1 through 6.12-4] This section considers some aspects of materials selection with respect to waste management. The activation of the materials is key to remote handling requirements for waste, to processing and disposal methods for waste, and to accident severity in waste management operations. In order to realize the desirable environmental potentials of fusion power systems, there are at least three major goals for waste management. These are: a) near-surface burial; b) disposal on-site of the fusion reactor; c) acceptable radiation doses at least cost during and after waste management operations.

Although meeting the above goals will depend finally upon specific reactor designs and upon specific materials chosen for the blankets, early design guidance can be provided by qualitative comparisons of blanket materials under a standard set of conditions. In reference 6.12-5, the conclusion states that: "...all fusion reactors, regardless of geometric shape and first wall radius, having unprotected first walls made of similar material and operated for the same amount of time, will have roughly equal total radioactivities, adjusted only in proportion to the product of their thermal power and their first wall thickness." This allows using a standard reference configuration of a fusion reactor to investigate qualitative comparisons of materials with respect to properties dependent upon radioactivity from activation in the first wall zone. Extensions of results to specific reactor designs is then only a matter of scaling based on thermal power and first wall thickness for stationary blanket/first wall materials. If the materials flow through the first wall zone (like liquid coolants and breeders), then the data in this section must be modified by a factor F to account for the reduced exposure time of the liquid to the first wall neutron flux. The factor F has the form at equilibrium:

$$F = (1-e^{-\lambda t_r})/(1-e^{-\lambda t_c}) \qquad [6.12\text{-}1]$$

where λ = decay constant of a particular radionuclide.

t_r = residence time of the liquid in the first wall zone.

t_c = circulating time of the liquid in the whole reactor system.

If the circulating time is small compared to the half life of the nuclide:

$$F = t_r/t_c \qquad [6.12\text{-}2]$$

For this study, the reference neutron environment (flux and spectrum) is the first wall zone of MARS[6.12-6] with a 5 MW/m^2 wall loading, a first wall thickness of 0.003 m and a two year exposure time. The neutron flux and spectrum were the same for all the materials. They were the ones calculated with TART specifically for the first wall of the MARS blanket. This blanket consists of HT-9 for structural material and 17Li83Pb for the coolant/breeder material. The spectra for other combinations of blanket materials would be different, but the integrated values of cross-sections would be roughly the same for all combinations. Thus, qualitative comparisons of materials, as opposed to evaluations of detailed design differences among blankets, will be roughly independent of materials combinations in the first wall where 14 Mev neutrons dominate. The reference compositions of materials for this study are shown in Table 6.12-1.

The bases for comparisons of these materials are the Remote Maintenance Rating (RMR) and the Waste Disposal Rating (WDR).[6.12-7, 6.12-8] The RMR is an index that gives a measure of the gamma ray contact dose at the surface of a thick infinite slab of activated material. The slab is considered thick when the thickness dimension is several mean free paths of the gamma rays. As described in reference 6.12-7, the RMR can be converted to contact doses for small spheres or thin sheets by multiplying the RMR by a factor containing the ratio of the radius of the sphere or thickness of the sheet to the mean free path of the gamma rays in the materials. However, such conversions will not change the relative ordering of qualitative comparison of materials. The units of the RMR are mrem/hr. If the RMR is less than 2.5 mrem/hr, workers can be in contact with the material without any special protection for gamma radiation. However, since the RMR is defined here only for gamma radiation, there is still the possibility that protection may be needed for inhalation and ingestion of alpha and beta emitters. This is in accordance

with the NRC 10CFR20 regulations on worker safety.[6.12-9] As the RMR becomes greater and greater than 2.5 mrem/hr, more and more protection against contact and exposure is needed in the form of gamma shielding and/or use of remote handling equipment.

The WDR is an index that gives a measure for classifying wastes in accordance with the NRC 10CFR61 regulation on licensing requirements for land disposal of radioactive wastes.[6.12-10] The WDR is defined as:

$$WDR = \sum_i C(i)/L(i) \qquad [6.12\text{-}3]$$

where C(i) is the concentration of the ith radionuclide in the waste material (curies/m^3) and L(i) is the corresponding allowable concentration limit for a given waste class as provided in 10CFR61. The intent of 10CFR61 is to protect inadvertent intruders at disposal sites from radiation doses greater than 500 mrem/year.[6.12-10,6.12-11] The radionuclides explicitly covered by limits in 10CFR61 are appropriate for waste classification of fission products, fission reactor activation products and transuranics. However, in fusion there are other nuclides (especially long-lived gamma emitters) that must be considered explicitly to ensure limiting doses to inadvertent intruders to 500 mrem/year or less. Several additional nuclides of this type will be discussed below.[6.12-12]

For alloys and mixtures of materials, near-surface land disposal can be used when WDR = < 1. If WDR > 1, the materials are not suitable for near-surface disposal without some kind of processing to reduce the WDR to 1 or less. As will be mentioned later, this processing may be simple dilution with inert materials in the waste package so that the WDR of the radionuclides averaged over the total volume of the package is less than 1.

The RMR and WDR are calculated from activation product concentrations obtained with the LLNL computer codes TARTNP,[6.12-13] ORLIB,[6.12-14] ACTL,[6.12-15] and FORIG.[6.12-16] The data inputs are the reference neutron environment (MARS) and the materials compositions listed in Table 6.12-1.

6.12.2 Qualitative Comparisons of Remote Maintenance Ratings

The relative rankings by RMR of blanket materials considered in this

study are shown in Table 6.12-2 for various times after removal from the neutron flux. Inspection of Table 6.12-2 reveals that there are spreads among the materials of four to six orders of magnitude in the RMR at a given time after shutdown with the greatest spreads at the later times. Also, the relative rankings of materials change from one time to another. Depending upon the material, the RMR drops four to nine orders of magnitude from the 1 hour to 100 year time for that material. Only the RMR for Li_2O, FLIBE, and lithium drop enough for the materials to be handled without worker protection at 100 years. However, even these materials require worker protection at 10 years or less for large bodies of the materials or for close contacts with components made with them. The degree of protection needed will depend upon specific dimensions of components as well as upon the material but the RMR can be helpful in assessing the consequences of materials selection early in the design phase of a reactor and in planning waste disposal.

The major radionuclides contributing to the RMR for the materials at various times are shown in Table 6.12-3. Many of these are activation products of elements that are impurities in the materials. Thus, it is important to consider carefully the purity of materials to control costs of remote handling and shielding. The task of detailed identification of the sources (essential or impurity elements) is beyond the scope of this study. However, it can be noted that, in general, Co60 is an undesirable component in all of the materials at 10 years. It originates mainly from cobalt, nickel and copper. Therefore, if these elements are impurities, they should be carefully controlled if significant materials handling is expected at 10 years (say for waste processing). For 1 hour and 1 day times, Na22 and Na24 are prominent nuclides in the breeding/multiplier materials and must be carefully considered if they come from impurities like elemental sodium or magnesium. (Note that Nitrate salt has a high sodium content as an essential element.) Both breeding/multiplier and structural materials contain Mn54 and Mn56 as major contributors to RMR at early times. In both cases these two nuclides come from natural elemental manganese and iron.

At 100 years, the prominent radionuclides are Al26, Co60, Nb94, Ag108m, Bi207 and Bi208. Except for $LiAlO_2$ which has aluminum as an essential element, the Al26 content of the materials can perhaps be controlled to reduce RMR. The Nb94 comes from molybdenum and niobium and can be

controlled only to the extent that it is possible to control these two elements. The Ag108m comes from elemental silver which appears to be an impurity and as such should be reduced as much as possible consistent with costs for shielding and handling. The bismuth nuclides come from bismuth and lead. Thus, Bi207 and Bi208 will always be generated in the LiPb breeding/multiplier; control of bismuth as an impurity can reduce but not eliminate the bismuth gamma emitters.

6.12.3 Qualitative Comparisons of Waste Disposal Ratings

As discussed above, the Waste Disposal Rating is defined in terms of the ratios of the concentrations of radioactivity in a waste package to the allowable concentrations set by regulation for specific nuclides. The underlying reason for the selection of the limits is to protect inadvertent intruders at disposal sites from radiation exposures greater than 500 mrem/year. The current regulation for near-surface disposal of radioactive waste, 10CFR61, sets limits for the nuclides significant to fusion activation wastes as shown in Table 6.12-4. However, as discussed in reference 6.12-12, some additional nuclides must be included to cover nuclides from fusion activation that present hazards from gamma radiation. These supplemental nuclides are shown in Table 6.12-5. Their limits are based upon the dose limit of 500 mrem/year as calculated by an adaptation of the INVERSI and INVERSW codes developed for the NRC as a tool in determining concentration limits for 10CFR61.[6.12-10]

The WDR at 10 years after shutdown for the materials of interest to the BCSS are displayed in Table 6.12-6. The ratings for individual nuclides are shown as well as for subtotals of nuclides grouped according to Tables 6.12-4 and 6.12-5. Note the contributions of the supplemental nuclides in Table 6.12-5 to the total WDR for $LiAlO_2$, LiPb, TENELON, and ModHT9. The supplemental nuclides increase the WDR to values greater than 1 for each of these materials. Thus, they are significant factors in determining suitability for near-surface disposal of $LiAlO_2$, LiPb, TENELON and ModHT9.

Upon consideration of the WDR in Table 6.12-6 and the 10CFR61 regulations, the suitability of materials for near-surface disposal can be summarized as shown in Table 6.12-7. Column 1 indicates that beryllium, Li_2O, lithium and FLIBE are well within the limits for near-surface

disposal. However, as pointed out in Section 6.12.2, at 10 years or less after removal from a reactor, all of these materials require worker protection during handling. At 100 years, the last three would not require protection but beryllium would still be too hazardous to handle without protection even though it can be disposed near-surface. Note that all of the materials in column 1 are breeding/multiplier materials.

The alloys in column 2 are structural materials whose WDR are greater than 1 but it is expected that, when they are packaged with other inert and less active materials from a reactor, the WDR integrated over the volume of the waste package will be less than 1 and near-surface disposal is permissible. Again, however, worker protection will be required even at 100 years because of the high RMR.

The materials in column 3 have values for WDR too high to be reduced by simple dilution. Therefore, they must be processed in some way to remove the highly active components for near-surface burial of the bulk of the materials. The high activity components would then need to be disposed of as high level waste as suggested in note (c) of Table 6.12-7.

The major nuclides preventing near-surface disposal of materials in column 3 are listed in Table 6.12-8. Note that the limiting source elements for $LiAlO_2$ and Nitrate salt are essential to the composition of the materials and cannot be reduced or eliminated. The WDR for HT9, PCA and LiPb can be reduced by reducing the amounts of the indicated source nuclides.

It should be noted that activation and subsequent decay chains in lead and lead with bismuth impurities produce several alpha emitting nuclides (see Table 6.12-9). These may cause safety problems in accident and materials handling scenarios for inhalation and ingestion. For waste management under the current 10CFR61, none of these nuclides would be limited for near surface burial since only transuranic nuclides are explicitly covered. If 10CFR61 is modified to cover any alpha emitting nuclide with an effective half life greater than five years, then Pb210, Bi 210m and Po210 may have limits. However, if the limit is 100 nCi/g (the current level for transuranic alpha emitters), there would still be no problem for waste disposal since the concentrations predicted for MARS are much less than 100 nCi/g for all the alpha emitters at 10 years after shutdown as shown in Table 6.12-9.

Table 6.12-1A.
ELEMENTAL COMPOSITIONS USED FOR BCSS ACTIVATION ANALYSIS

		Structural Materials				
		PCA	V15Cr5Ti	HT-9	Modified HT-9	TENELON Fe 1518
Z-#	Element	Wt. %	Wt. %	Wt. %	Wt. %	Wt. %
3	Li					
4	Be					
5	B	0.005		0.01	0.001	0.001
6	C	0.005	0.005	0.2	0.15	0.15
7	N	0.01	0.01	0.05	0.001	0.005
8	O		0.01	0.01	0.007	0.007
9	F					
11	Na					
12	Mg					
13	Al	0.03	0.02	0.01	0.008	0.008
14	Si	0.5	0.03	0.35	0.2	0.2
15	P	0.01	0.003	0.02	0.013	0.013
16	S	0.005	0.001	0.02	0.004	0.004
17	Cl		0.0001			
19	K	0.0003	0.00001	0.0003	0.0003	0.0003
20	Ca					
22	Ti	0.30	5.0	0.09	0.1	0.003
23	V	0.10	79.80	0.3	0.3	0.002
24	Cr	14.0	15.0	12.0	11.0	15.0
25	Mn	2.0		0.55	0.53	15.0
26	Fe	64.88	0.004	85.0	Balance	Balance

Table 6.12-1A. Continued

			Structural Materials			
		PCA	V15Cr5Ti	HT-9	Modified HT-9	TENELON Fe 1518
Z-#	Element	Wt. %	Wt. %	Wt. %	Wt. %	Wt. %
27	Co	0.03		0.02	0.005	0.005
28	Ni	16.0	0.0004	0.5	0.006	0.006
29	Cu	0.02	0.0002	0.09	0.003	0.003
30	Zn					
33	As	0.02	0.0002			
38	Sr					
40	Zr	0.005		0.001	0.001	0.001
41	Nb	0.03	0.0004	0.11	0.00011	0.00011
42	Mo	2.0	0.001	1.0	0.00027	0.00027
47	Ag	0.0001		0.0001	0.00009	0.00009
48	Cd	0.0002		0.0001	0.0001	0.0001
50	Sn	0.005		0.003	0.003	0.003
51	Sb	0.001		0.001	0.0005	0.0005
56	Ba	0.001		0.001	0.0002	0.0002
65	Tb	0.001		0.0005	0.0002	0.0002
73	Ta	0.01	0.001	0.001	0.0004	0.0004
74	W	0.05	0.0002	0.5	2.50	0.01
77	Ir	0.001		0.0005	0.0002	0.0002
82	Pb	0.001		0.001	0.0005	0.0005
83	Bi	0.001		0.001	0.0002	0.0002

Table 6.12-1B

ELEMENTAL COMPOSITIONS USED FOR BCSS ACTIVATION ANALYSIS

				Breeding/Multiplier Materials				
		Li	FLIBE	17Li-83Pb	Nitrate Salt	Li_2O	$LiAlO_2$	Be
Z-#	Element	Wt. %	Wt. %	Wt. %	Wt. %	Wt. %	Wt. %	Wt. %
1	Li	99.9	8.60	0.68			10.3	0.0003
4	Be		13.0	0.001			0.001	99.0
5	B			0.001			0.001	0.0002
6	C	0.001						0.10
7	N	0.005		0.001	15.0			0.03
8	O			0.026	51.6		48.6	0.7
9	F		78.4					
11	Na	0.03		0.01	12.3	0.005	0.005	
12	Mg			0.001				0.08
13	Al			0.005		0.002	40.9	0.09
14	Si	0.008		0.001		0.001		0.06
15	P			0.05			0.05	
16	S		0.0005	0.03				
17	Cl	0.004		0.002		0.01	0.01	
19	K	0.02		0.03	21.0	0.037	0.05	
20	Ca	0.03		0.01		0.021	0.003	0.02
22	Ti			0.003			0.003	
23	V	0.0003		0.003			0.003	
24	Cr	0.0002	0.0019	0.002	0.08		0.003	0.01
25	Mn			0.001		0.002	0.001	0.015
26	Fe	0.001	0.0166	0.01	0.005	0.010	0.003	0.06

Table 6.12-1B (Continued)

		Breeding/Multiplier Materials						
		Li	FLIBE	17Li-83Pb	Nitrate Salt	Li_2O	$LiAlO_2$	Be
Z-#	Element	Wt. %	Wt. %	Wt. %	Wt. %	Wt. %	Wt. %	Wt. %
27	Co			0.003	0.00001		0.003	0.0005
28	Ni		0.0026	0.001	0.001	0.002	0.002	0.03
29	Cu			0.001		0.0006	0.001	0.01
30	Zn			0.05			0.05	0.02
33	As			0.03			0.05	
38	Sr			0.10			0.10	
40	Zr			0.03			0.01	
41	Nb				0.0001			
42	Mo			0.003	0.001		0.003	0.002
47	Ag			0.001			0.001	
48	Cd			0.005			0.01	0.0002
50	Sn			0.001			0.03	
51	Sb			0.003			0.01	
56	Ba			0.01			0.01	
73	Ta							
74	W							
82	Pb			99.32		0.008	0.001	0.002
83	Bi			0.01			0.001	

Table 6.12-2

RELATIVE RANKINGS OF MATERIALS BY RMR

Time After Shutdown							
1 Hour		1 Day		10 Years		100 Years	
Material	RMR(mrem/hr)	Material	RMR(mrem/hr)	Material	RMR(mrem/hr)	Material	RMR(mrem/hr)
TENELON	9.14E+10	$LiAlO_2$	2.83E+10	PCA	2.30E+08	$LiAlO_2$	2.09E+04
$LiAlO_2$	8.17E+10	VCrTi	1.36E+10	Nitrate salt	4.61E+07	HT9	2.07E+04
PCA	3.69E+10	TENELON	1.33E+10	HT9	4.41E+07	PCA	9.44E+03
ModHT9	2.93E+10	PCA	1.16E+10	TENELON	1.39E+07	LiPb	9.24E+03
HT9	2.89E+10	ModHT9	4.24E+09	ModHT9	1.11E+07	ModHT9	4.26E+02
VCrTi	1.93E+10	HT9	4.17E+09	$LiAlO_2$	5.36E+06	TENELON	4.22E+02
Nitrate Salt	8.55E+09	Nitrate salt	3.25E+09	LiPb	4.16E+06	VCrTi	1.83E+02
Be	4.92E+08	Be	1.67E+08	Be	1.26E+06	Be	4.99E+01
LiPb	1.42E+08	LiPb	8.85E+07	Lithium	9.13E+04	Nitrate salt	2.33E+01
Li_2O	2.17E+07	Lithium	5.86E+06	Li_2O	4.44E+04	Li_2O	1.72E+00
Lithium	1.48E+07	Li_2O	5.53E+06	FLIBE	2.79E+04	FLIBE	2.02E-01
FLIBE	6.06E+06	FLIBE	1.73E+06	VCrTi	6.53E+03	Lithium	1.87E-02

Table 6.12-3

MAJOR NUCLIDES FOR HIGH RMR

Material	1 Hour	1 Day	10 Years	100 Years
PCA	Mn54, Mn56 Co58, Co60	Mn56 Co58, Co60	Co60	Co60, Nb94 Ag108m, B1207
HT9	Mn54, Mn56	Mn54 Co58, Co60	Co60	Nb94
ModHT9	Mn54, Mn56 W187	Mn54 W187, Ta182	Mn54 Co60	Co60, Nb94 Ag108m, Bi207
TENELON	Mn54, Mn56	Mn54, Mn56	Mn54 Co60	Co60 Ag108m, Bi207
V15Cr5Ti	Sc46, Sc48	Sc46, Sc48	Co60 K42*	Nb94 K42*, Al26
$LiAlO_2$	Na24	Na24	Co60	Al26 Ag108m
17Li83Pb	As76, Co60 Na24, Zn65 Pb203, Sb124 Zr89, Mn56 Y89m	As76, Co60 Zn65, Sb124 Na24, Zr89 Ti202, Y89m	Co60	Ag108m Bi207, Bi208
Be	Na24 Mn54, Mn56	Na24 Mn54, Co58	Co60	Al26 Co60
Li_2O	Mn54, Mn56 Na24	Mn54 Na24, Co58	Co60 Na22	Al26, Co60 Bi207
Lithium	Na22, Na24	Na22, Na24	Na22 Co60	K40 K42*
Nitrate salt	Na22, Na24 Ar41	Na22, Na24	Na22	Nb94 C136
FLIBE	Mn54, Mn56 Co58	Co58, Mn54 Co60	Co60	Co60

*Daughter from Argon 42.

Table 6.12-4
LIMITS FOR CLASS C WASTES APPROPRIATE FOR ACTIVATION WASTES IN FUSION AND DEFINED IN 10CFR61

Nuclide	Limit (Ci/m^3)
All nuclides with less than 5-year half life	No limit
H3	No limit
Co60	No limit
C14 in activated metal	80
C14	8
Ni63 in activated metal	7000
Ni63	700
Ni59 in activated metal	220
Nb94 in activated metal	0.2
Tc99	3
Sr90	7000
Cs137	4600
Alpha emitting transuranic nuclides with half lives greater than five years	100 (nanocuries/gram)

Table 6.12-5

ESTIMATED LIMITS FOR CLASS C LONG HALF LIFE
GAMMA EMITTERS IN FUSION ACTIVATION WASTES
NOT LISTED IN 10CFR61

Nuclide	Estimated Limit (Ci/m^3)
Al26	0.1
Nb92	0.3
Ag108m	3
Bi207	17000
Bi208	0.1
Bi210m	2

Table 6.12-6

WASTE DISPOSAL RATING AT 10 YEARS AFTER SHUTDOWN

	WDR (dimensionless ratio)											
Material Nuclide	HT9	PCA	$LiAlO_2$	Nitrate Salt	LiPb	VCrTi	TENELON	Mod HT9	Be	Li_2O	FLIBE	Li
C14	1.0	0.21	0.38	70.9	0.03	0.16	0.10	0.02	0.15	0.33	0.14	0.01
Ni59	0.08	2.4										
Ni63	0.40	6.6			0.01		0.01	0.01	0.01			
Nb94	477	176	0.02	0.10	0.10	1.32	0.46	0.46	0.01			
Tc99	5.38	11.0	0.01		0.02							
Sub Total	484	196	0.41	71	0.16	1.48	0.57	0.49	0.17	0.33	0.14	0.01
Al26	0.11	0.33	147		0.07	0.17	0.09	0.09	0.23	0.01		
Ag108m	0.85	0.86	2.8		10.6		0.77	0.76				
Bi207					0.02							
Bi208	0.25	0.26	0.08		13.6		0.05	0.05				
Sub Total	1.2	1.45	150		24.3	0.17	0.91	0.90	0.23	0.01		
Total	485	198	150	71	24.5	1.65	1.5	1.4	0.40	0.34	0.14	0.01

Table 6.12-7

SUITABILITY OF MATERIALS FOR NEAR-SURFACE BURIAL

WDR<1	1 < WDR < 5	WDR > 5
Class A(a)	Class C(b)	Not suitable for near-surface Burial(c)
Be	V15Cr5Ti	HT9
Li_2O	ModHT9	PCA
Lithium	TENELON	$LiAlO_2$
FLIBE		17Li83Pb
		Nitrate Salt

(a) Requires only packaging to provide physical, mechanical and chemical stability for near-surface burial.

(b) Will be diluted to Class C by normal mixing with inert and less active materials from reactor during waste packaging. Requires packaging for physical, mechanical and chemical stability for near-surface burial.

(c) WDR and total quantities of material make reduction to Class C by dilution impractical. Processing is required to remove high activity nuclides to bring the remaining material to Class C for packaging for near-surface burial. The high activity nuclides require at least a "hot" waste facility or perhaps even deep geological burial.

Table 6.12-8

MAJOR NUCLIDES PREVENTING NEAR-SURFACE BURIAL

Material	Major Nuclides	Source Elements
HT9	Nb94 Tc99	Nb, Mo Mo
PCA	Nb94 Tc99	Nb, Mo Mo
$LiAlO_2$	Al26	Al
17Li83Pb	Bi208 Ag108m	Bi, Pb Ag
Nitrate salt	C14	N

Table 6.12-9.

ALPHA EMITTER CONCENTRATIONS FOR LiPb

Nuclide	Concentration (nCi/g)	
	Shutdown	10 yr after Shutdown
Pb210	1.31E+1	9.56E00
Bi210	6.55E+5	1.82E+1
Bi210m	3.25E-1	3.25E-1
Po210	4.93E+5	1.83E00

REFERENCES FOR SECTION 6.12

6.12-1. Background Information and Technical Basis for Assessment of Environmental Implications of Magnetic Fusion Energy, U.S. Department of Energy, DOE/ER-0170, August 1983.

6.12-2. S. Vogler, et al., "Materials Recycle and Waste Management in Fusion Power Reactors - Progress Report for 1982," Argonne National Laboratory ANL/FPP/TM-163 (Jan 1983).

6.12-3. S. Vogler, et al., "Waste Management of First Wall and Blanket Structural Materials for Tokamak Fusion Reactors," Nuclear Technology/Fusion, Vol. 4, pp. 415-420 (Sept. 1983).

6.12-4. J. A. Blink and G. P. Lasche, "The Influence of Steel Type on the Activation and Decay of Fusion Reactor First Walls," Nuclear Technology/Fushion, Vol. 4, pp. 1146-1151 (Sept. 1983).

6.12-5. G. P. Lasche and J. A. Blink, "The Dependence of Neutron-Induced Radioactivity in Fusion Reactors on Geometric Design Parameters," Nuclear Technology/Fusion, Vol. 4, pp. 823-828 (Sept. 1983).

6.12-6. B. G. Logan, et al., "Mirror Advanced Reactor Study (MARS) Final Report," Lawrence Livermore National Laboratory, Livermore, CA, UCRL-53480 (1984).

6.12.7. D. W. Dorn and R. C. Maninger, "Issues in Radioactivity for Fusion Energy: Remote Maintenance Rating," Proc. of the IEEE 10th Symposium on Fusion Engineering, Philadelphia, PA, Dec. 5-9, 1983.

6.12-8. R. C. Maninger and D. W. Dorn, "Issues in Radioactive Waste Management for Fusion Power," IEEE Transactions on Nuclear Science, NS-30, (1), pp. 571-576 (Feb. 1983).

6.12-9. Code of Federal Regulations, 10CFR Part 20, "Standards for Protection Against Radiation."

6.12-10. a) Draft Environmental Impact Statement on 10CFR61, "Licensing Requirements for Land Disposal of Radioactive Waste," NUREG-0782 (4 volumes) (Sept. 1981).
b) Final Environmental Impact Statement on 10CFR Part 61, "Licensing Requirements for Land Disposal of Radioactive Waste," NUREG-0945 (3 volumes) (Nov. 1982).

6.12-11. J. A. Blink, D. W. Dorn, R. C. Maninger, "Disposal of Activated Fusion Wall Materials," Journal of Nuclear Materials, 122 and 123 (1984) 977-981, North Holland, Amsterdam.

6.12-12. R. C. Maninger and D. W. Dorn, "Radiation Safety Criteria for Maintenance and Waste Management in the Mirror Advanced Reactor Study," Lawrence Livermore National Laboratory, Livermore, CA, UCRL 90385, Revision 1 (1984).

6.12-13 E. F. Plechaty and J. R. Kimlinger, "TARTNP: A Coupled Neutron-Photon Monte Carlo Transport Code," Lawrence Livermore National Laboratory, Livermore, CA, UCRL-50400, Vol. 14 (1976).

6.12-14. J. A. Blink, R. E. Dye, and J. R. Kimlinger, "ORLIB: A Computer Code That Produces One-Energy Group, Time, and Spatially Averaged Neutron Cross Sections," Lawrence Livermore National Laboratory, Livermore, CA, UCRL-53262 (1981).

6.12-15. M. A. Gardner and R. J. Howerton, "ACTL: Evaluated Neutron Activation Cross-Section Library-Evaluation Techniques and Reaction Index," Lawrence Livermore National Laboratory, Livermore, CA, UCRL-50400, Vol. 18 (1978).

6.12-16. J. A. Blink, "FORIG: A Modification of the ORIGEN2 Isotope Generation and Depletion Code for Fusion Problems," Lawrence Livermore National Laboratory, Livermore, CA, UCRL-53263 (1982).

BLANKET COMPARISON AND SELECTION STUDY

SECTION 6.13 - ELECTROMAGNETIC EFFECTS

SECTION 6.13

TABLE OF CONTENTS

PAGE NO.

6.13 Electromagnetic Effects.....6.13-1
6.13.1 Mirror Plasma Loss.....6.13-1
6.13.2 Tokamak Plasma Disruption.....6.13-1
6.13.2.1 Pressure on First Wall.....6.13-2
6.13.2.2 Forces on Sides of Blanket Sector.....6.13-2
6.13.2.3 Loss of Plasma Diamagnetism.....6.13-3
6.13.2.4 Semi-Cylindrical First Wall Modules.....6.13-3
6.13.3 Assumptions.....6.13-3
6.13.3.1 Tokamak Fields and Time Constants.....6.13-3
6.13.3.2 Tokamak Field Solution.....6.13-4
6.13.3.3 Diamagnetism in a Tokamak Plasma.....6.13-4
6.13.3.4 Pulsed Loads on Mirror First Wall & Blanket....6.13-5
6.13.4 Conclusions.....6.13-6

6.13 Electromagnetic Effects

The blanket and other electrically conducting components of a fusion reactor are pervaded by magnetic fields. Changes in these magnetic fields, either in normal operation or in off-normal events, produce eddy currents with accompanying forces, torques, and voltages. The four most likely causes of changing fields are:

1. Operational cycling of poloidal field (tokamak only).
2. Abnormal discharge of magnets (both tokamak and mirror).
3. Loss of plasma current (tokamak only).
4. Loss of plasma diamagnetism (both tokamak and mirror).

Electromagnetic effects from operational poloidal field changes are readily handled. The likelihood of an abnormal magnet discharge is much less than that of a tokamak plasma disruption or a mirror plasma loss, and the time scale is much longer (many seconds, compared to many milliseconds). Hence, electromagnetic effects from the abnormal magnet discharge are both less likely and less severe. Attention should be focussed on the last two causes. The following describes the electromagnetic forces on the first wall and blanket of a mirror or tokamak reactor due to plasma current disruption or plasma loss.

6.13.1. Mirror Plasma Loss

Following a plasma dump for which the plasma disappears in a time of about 100 ms, the first wall will experience a pressure much smaller than 0.016 MPa (2.40 psi) in the direction toward the plasma. For a multi-layer tube-bank first wall and blanket, a higher pressure will appear in the tubes if they carry a liquid metal. The added pressure wil be 0.30 MPa (43 psi) for LiPb and 0.54 MPa (78 psi) for Li. For a water, helium, or LiPb coolant the forces will be distributed among all layers of the tube bank. The pressure arises from loss of plasma diamagnetism.

6.13.2 Tokamak Plasma Disruption

The electromagnetic forces consist of a pressure specified on the first wall and a tangential force per unit area (shear stress) acting on the sides

of each blanket sector. If the sectors are connected electrically at the first wall, the tangential forces need not be considered.

6.13.2.1 Pressure on First Wall

A plasma disruption induces currents in the first wall. The currents interact with the poloidal field and produce pressure on the first wall.

On the outboard first wall, the pressure pushes inward, toward the plasma. It rises to 0.61 MPa (88 psi) in 25 ms and then falls to zero in a further 160 ms.

On the inboard first wall, the pressure initially is toward the plasma, rising to 0.11 MPa (16.5 psi) in 18 ms. The pressure then decreases, changes sign, and peaks at -0.038 MPa (-5.5 psi), 127 ms later. Finally it goes to zero in a further 40 ms.

At the top and bottom of the first wall, the pressure sequence is similar to that on the inboard first wall, but of smaller magnitude. The pressure is initially toward the plasma, rising to 0.034 MPa (4.9 psi) in 18 ms. The pressure then changes sign and peaks at -0.0094 MPa (-1.4 psi) 130 ms later. Then it drops to zero in a further 100 ms.

The top and bottom of the first wall also experience a tangential force per unit area in the direction of decreasing radius, i.e., toward the central support cylinder. The tangential force slowly rises to 0.044 MPa (6.4 psi) in 95 ms, and then returns to zero in a further 150 ms.

These values are for a plasma current of 10 MA. The force is proportional to the square of the plasma current.

6.13.2.2 Forces on Sides of Blanket Sector

If the blanket sectors are electrically connected further back rather than at the first wall, the induced current will flow radially along the side of the blanket sector from the first wall to the electrical connector, then back to the first wall along the side of the next blanket sector. The current will interact with the toroidal field to produce forces upward or downward as the currents flow radially outward or inward.

On the outboard side the tangential force (shear stress) rises to 2.9 MPa (420 psi) in 40 ms then falls to zero in a further 100 ms.

On the inboard side the tangential force rises to 2.7 MPa (390 psi) in 40 ms then falls to zero in a further 100 ms.

These values are for a plasma current of 10 MA. For a fixed toroidal field, the shear force is proportional to the plasma current.

As currents on opposite sides of a blanket sector are in opposite directions, so are these tangential forces. Thus they produce a net torque (about a radial axis) but not net force. Also, the forces inboard and outboard are in opposite directions.

6.13.2.3 Loss of Plasma Diamagnetism

To the forces of Section 6.13.2.1 above must be added an additional inward pressure, peaking in 22 ms and then falling in another 100 ms. The peak pressure is:

inboard first wall:	0.56 MPa = 81 psi
outboard first wall:	0.16 MPa = 23 psi
top and bottom of the first wall:	0.27 MPa = 39 psi

6.13.2.4 Semi-Cylindrical First Wall Modules

The overall force acting on a curved (semi-cylindrical or semi-spherical) first wall structure is the same as that for a flat first wall, namely a force per unit area toward (or away from) the plasma as given above. That force will have components both normal and tangential to the local first wall surface.

6.13.3. Assumptions

6.13.3.1 Tokamak Fields and Time Constants

The first wall plasma is assumed to have a 20 ms current disruption time and the L/R time of 100 ms. Recent experiments with TFTR, JET, and other large devices suggest that the disruption time is more likely to be 100 ms and that the forces will be lower than calculated here. The values of poloidal

field (equilibrium field plus field from plasma) are based on a plasma current of 10 MA, and are calculated at r=5 m and r=9 m.

In Section 6.13.2.2, the toroidal field was taken as 10 T at r=3.7 m and to vary as 1/r. The inboard value is 7.7 T, calculated at r=4.8 m; the outboard value is 3.9 T, calculated at r=9.4 m.

6.13.3.2 Tokamak Field Solution

When the plasma current decays, the induced toroidal current in the first wall tends to maintain the same total poloidal field outside the first wall and a zero poloidal field on the plasma side of the first wall. On the outboard side of the first wall, the equilibrium field and the field from the plasma current are in the same directions, but on the inboard side the equilibrium field and plasma field are of opposite signs. That is why the force on the inboard wall changes sign as the induced current and its field decay.

In the midplane, both inboard and outboard, neither the equilibrium field nor the field from the plasma has a component normal to the first wall. Hence there is no tangential component of force, either initially or later. At other locations on the first wall, in particular on the top and bottom, the equilibrium field and field from the plasma have normal components which initially cancel each other. Hence initially there is no tangential component of force. Later, as the field from the plasma decays, the normal component of the equilibrium field remains; that field component produces a tangential force.

6.13.3.3 Diamagnetism in a Tokamak Plasma

A tokamak plasma exhibits both diamagnetic and paramagnetic effects; in plasmas under consideration for power reactors, the diamagnetism predominates. A plasma with a peaked current density and a STARFIRE geometry is found to have $\beta = 8\%$ and a peak toroidal magnetic field of 9.67 T at r=3.66 m, conditions similar to the case analyzed in Section 6.13.3.1. With no plasma, the toroidal flux bounded by the first wall is 127.42 Wb. With the diamagnetic plasma present, the flux is reduced to 126.15 Wb.

If a plasma disruption rapidly eliminates the diamagnetism, the flux initially remains at the lower value but is redistributed within the volume bounded by the first wall. At the inboard first wall, the toroidal field is reduced from 7.28 T to 7.21 T. Poloidal currents are induced in the first wall which interact with the toroidal field to produce an inward pressure. At the inboard first wall, with a toroidal field 7.28 T outside and 7.21 T inside, the pressure is 0.42 MPa (61 psi).

However, this net flux change can be imagined as resulting from the difference between a diamagnetism of three times the net flux change and a paramagnetism of twice this amount. The paramagnetism is taken to decay exponentially with the current disruption time of 20 ms, the diamagnetism with the thermal disruption time of 10 ms. The net flux change peaks at 22 ms at a value 33% above the final value. Hence the peak pressure is increased by 33% to 0.56 MPa (81 psi). Pressures at other positions are stated in Section 6.13.2.3. For other decay times this 33% increase could change to other values between zero and 100%.

6.13.3.4 Pulsed Loads on Mirror First Wall and Blanket

The L/R time for the first wall of 60 cm radius and 1 cm thickness is a few milliseconds. The current induced by a plasma dump penetrates into the blanket more than the thickness of the first wall on an even faster time scale. Under the assumption that the plug plasma disappears in a time that is short compared to the time that the central cell plasma can disappear by end leakage, the central cell plasma will decay at the rate the ions leak through the loss cone. The ions in the loss cone leave as fast as the end plug plasma goes away, but their density fraction [approximately equal to $(2R)^{-1}$] is negligible. The electrons then cool quickly by end conduction until the electron temperature reaches its equilibrium value which is lower than the ion temperature. Fokker-Planck calculations for that case show that

$$n\tau = 4.9 \times 10^{10} E^{3/2} \log_{10} R \qquad [6.13\text{-}1]$$

For a 5-to-1 mirror ratio, 30 keV ion temperature ($E = \frac{3}{2} T$), and 10^{14} cm^{-3} ion density, the plasma decay time is 100 ms.

After the disappearance of the plasma, the magnetic field relaxes toward the vacuum field at a different rate for thin walls than for thick walls. For a wall thin compared to the radius, then the L/R time controls the relaxation. If the wall thickness is comparable to or greater than the inner radius, then the redistribution of the flux contained within the wall dominates the problem.

A difference in magnetic field strength across the wall requires electrical current in the wall. The magnetic force on this current appears as a pressure, directed inward if $B_{out} > B_{in}$. The magnetic pressure is:

$$\Delta p = p_{out} - p_{in} = \left(B_{out}^2 - B_{in}^2(t)\right)/2\mu_0 \quad . \qquad [6.13\text{-}2]$$

The variation of the pressure with time across a one cm thick stainless steel wall was calculated numerically from the heat equation.

For a plasma decay time constant assumed to be 1 ms, a peak pressure difference of 90 psi occurs at 2 ms. For an assumed time constant of 10 ms, a peak of 36.5 psi is reached at 7 ms. For an assumed time constant of 10 ms, the peak pressure is only 6.5 psi, which is reached only after 17 ms.

These thin wall results can be reproduced very accurately from the analytic expressions. The thick wall case requires the solution of the full heat equation. For a 1 m thick LiPb blanket with an inner radius of 0.6 m, as in MARS, and a plasma decay time of 100 ms, the decay time constant of the numerically calculated pressure is asymptotically equal to 313 ms, while the simple expression for L/R gives 225 ms. The peak pressure difference across the blanket is 43 psi at 125 ms. The corresponding value for a liquid Pb blanket is 78 psi.

6.13.4. Conclusions

Electromagnetic forces on the first wall and blanket of the mirror reactor are small for cooling by water or helium, moderate for cooling by liquid PbLi, and manageable for cooling by liquid Pb. For a tokamak, the forces are manageable for all the concepts considered.

DISTRIBUTION FOR ANL/FPP-84-1

Internal:

C. Baker
M. Billone
J. Brooks
Y. Cha
R. Clemmer
D. Diercks
D. Ehst
K. Evans
Y. Gohar
D. Gruen
A. Hassanein
P. Finn
A. Fischer
C. Johnson
J. Jung
R. Leonard
Y. Liu
B. Loomis
S. Majumdar
R. Mattas
B. Misra
B. Picologlou
D. L. Smith
D. K. Sze
S. W. Tam
L. Turner
S. Vogler
S. Yang
FPP Files (53)
ANL Contract File
ANL Libraries
ANL Patent Dept.
TIS Files (6)

External:

DOE-TIC (27)
Manager, Chicago Operations Office, DOE
University of Chicago Special Committee for the Fusion Program:
S. Baron, Burns and Roe, Inc.
H. Forsen, Bechtel Group, Inc.
J. Maniscalco, TRW, Inc.
G. Miley, University of Illinois-Urbana
P. Reardon, Brookhaven National Laboratory
P. Rutherford, Princeton University
D. Steiner, Rensselaer Polytechnic Institute
K. Symon, University of Wisconsin-Madison
K. Thomassen, Lawrence Livermore National Laboratory
S. Abdel-Khalik, University of Wisconsin-Madison
M. A. Abdou, University of California-Los Angeles (6)
J. Anderson, Los Alamos National Laboratory
W. Bauer, Sandia Laboratories
S. Berk, U.S. Department of Energy/Office of Fusion Energy
D. H. Berwald, TRW, Inc.
R. Bourque, GA Technologies Inc.
W. Bjorndahl, TRW, Inc.
G. Carlson, Lawrence Livermore National Laboratory
F. Carre, , CEN-Saclay, FRANCE
G. Casini, Joint Research Centre, Ispra Establishment, ITALY
E. Cheng, GA Technologies Inc.
D. Cohn, Massachusetts Institute of Technology
R. Conn, University of California-Los Angeles
L. Creedon, GA Technologies Inc.
J. Crocker, EG&G Idaho, Inc.
J. W. Davis, McDonnell Douglas Astronautics Company
S. O. Dean, Fusion Power Associates
D. DeFreece, McDonnell Douglas Astronautics Co.
J. DeVan, Oak Ridge National Laboratory
R. Dowling, U.S. Department of Energy/Office of Fusion Energy
T. Drolet, Ontario Hydro, CANADA
C. Flanagan, Fusion Engineering Design Center/Oak Ridge National Laboratory

J. V. Foley, Princeton University
K. Furuta, University of Tokyo, JAPAN
F. Garner, Hanford Engineering Development Laboratory
J. Garner, TRW, Inc.
N. Ghoneim, University of California-Los Angeles
J. D. Gordon, TRW, Inc.
R. A. Gross, Columbia University
R. Hancox, Culham Laboratory
C. Henning, Lawrence Livermore National Laboratory
S. Herring, EG&G Idaho, Inc.
M. Hoffman, Lawrence Livermore National Laboratory
N. Hoffman, Energy Technology Engineering Center
G. Hollenberg, Hanford Engineering Development Laboratory
M. Kazimi, Massachusetts Institute of Technology
I. A. Knobloch, Max-Planck-Institute fur Plasmaphysik, WEST GERMANY
R. Krakowski, Los Alamos National Laboratory
G. Kulcinski, University of Wisconsin-Madison
T. Lechtenberg, GA Technologies Inc.
J. D. Lee, Lawrence Livermore National Laboratory
R. Little, Princeton University
G. Logan, Lawrence Livermore National Laboratory
P. S. Lykoudis, Purdue University
S. Malang, Kernforschungszentrum Karlsruhe, Federal Republic of Germany
R. C. Maninger, Lawrence Livermore National Laboratory
H. Mantz, McDonnell Douglas Astronautics Co.
L. Masson, EG&G Idaho, Inc.
I. Maya, GA Technologies Inc.
C. Maynard, University of Wisconsin-Madison
R. Micich, Grumman Aerospace Corporation
R. Moir, Lawrence Livermore National Laboratory
D. B. Montgomery, Massachusetts Institute of Technology
G. D. Morgan, McDonnell Douglas Astronautics Co.
D. Moyer, Technical Support Services Staff
L. Muhlestein, Hanford Engineering Development Laboratory
G. R. Nardella, U.S. Department of Energy/Office of Fusion Energy
W. S. Neef, Jr., Lawrence Livermore National Laboratory
A. L. Opdenaker, III, U.S. Department of Energy/Office of Fusion Energy
S. Piet, EG&G Idaho, Inc.
T. Reuther, U.S. Department of Energy/Office of Fusion Energy
F. Ribe, University of Washington
M. Rogers, Monsanto Research Corporation
D. Rowe, Rowe and Associates
D. E. Ruester, McDonnell Douglas Astronautics Co.
R. Ryder, GA Technologies Inc.
M. Sawan, University of Wisconsin-Madison
J. Schmidt, Princeton Plasma Physics Laboratory
K. Schultz, GA Technologies Inc.
F. R. Scott, Electric Power Research Institute-Palo Alto
J. Scott, Oak Ridge National Laboratory
T. Shannon, Fusion Engineering Design Center, Oak Ridge National Laboratory
A. E. Sherwood, Lawrence Livermore National Laboratory
K. Shin, University of California-Los Angeles
W. M. Stacey, Jr., Georgia Institute of Technology
W. G. Steele, TRW, Inc.

K. Sumita, Osaka University, JAPAN
I. Sviatoslavsky, University of Wisconsin-Madison
A. Tobin, Grumman Aerospace Corporation
T. Tomabechi, Japan Atomic Energy Research Institute, JAERI
P. Tortorelli, Oak Ridge National Laboratory
C. Trachsel, McDonnell Douglas Astronautics Co.
W. Verbeeck, CEC, Belgium
Prof. Vetter, Kernforschungszentrum Karlsruhe und Verwaltung, GERMANY
G. Vieider, Max-Planck-Institut fur Plasmaphysik, GERMANY
E. Vold, University of California-Los Angeles
L. Waganer, McDonnell Douglas Astronautics Co.
K. Wenzel, Massachusetts Institute of Technology
F. W. Wiffen, Oak Ridge National Laboratory
C. P. C. Wong, GA Technologies Inc.
G. L. Woodruff, University of Washington
L. Yang, GA Technologies Inc.
M. Z. Youssef, University of California-Los Angeles
Bibliothek, Max-Planck-Institute fur Plasmaphysik, WEST GERMANY
C.E.A. Library, Fontenay-aux-Roses, FRANCE
Librarian, Culham Laboratory, ENGLAND
Library Laboratorio Gas Ionizati, ITALY
Thermonuclear Library, Japan Atomic Energy Research Institute, JAPAN